Cumhuriyet Sci. J., 45(2) (2024) 182-187
DOI: https://doi.org/10.17776/csj.1334182

Cumhuriyet Science Journal

| csj.cumhuriyet.edu.tr | Founded: 2002 ISSN: 2587-2680 e-ISSN: 2587-246X Publisher: Sivas Cumhuriyet University

Antigenotoxic Properties of Different Plant Oils and the Influence of Olfactory Bias

Begumhan Yilmaz Kardas [1,a,*]

[1] *Department of Molecular Biology and Genetics, Faculty of Science and Literature, Balikesir University, Balikesir, Türkiye.*

**Corresponding author*

Research Article

History
Received: 28/07/2023
Accepted: 19/04/2024

ABSTRACT

In this study, antigenotoxic effects and developmental toxicity of frankincense and blue anemone oils were aimed to be analysed and the olfactory bias was aimed to be checked to see the possibility of an interaction between the olfactory perception and antigenotoxicity of the plant oils. The somatic mutation and recombination test was used to analyze genotoxicity, developmental process of *Drosophila melanogaster* was screened and the feeding assay was used to perform an olfactory bias test. Genotoxicity test results showed that none of the oils affected the spot frequencies compared to negative control and they caused 73.3 - 100 % inhibitions after the cotreatment with H_2O_2. None of them caused any significant difference in puparation and eclosion. The frankincense and blue anemone oils were also found antigenotoxic in this study and these effects were independent from the olfactory perception because the rates of feeding were similar to the one observed with negative control.

Keywords: Plant oils, Somatic mutation and recombination test, Drosophila melanogaster, Olfactory perception.

[a] *begumhanyilmaz@balikesir.edu.tr* *https://orcid.org/0000-0002-8446-1116*

Introduction

Plant oils which are mainly isolated from different part of the plants like fruits, seeds and pulps are used in cooking, cosmetic products and health supplements [1]. They are considered as the important part of the human nutrition because they account for 75% of daily dietary lipids worldwide [2]. The nutritional value is very critical considering the fact that the essential fatty acids found in plant oils are crucial for the healthy function of the human body and the developmental pathways [2]. Biomaterial industry also takes the advantage of plant oils because they are considered as renewable resources and their unique structures improve the biomaterial characteristics [3]. Plant oils are composed of triglycerides which are the esters of three fatty acids with a glycerol and the fatty acid chain contains unique functional groups affected by the type and growth conditions of the plant [4]. They are rich in important phytochemicals like tocopherols, carotenoids, phenolic compounds, sterols, minerals and vitamins [2]. The cold pressed plant oils are especially known to have antioxidant phenolic compounds and they were shown to prevent inflammations, hyperlipidaemia, allergic reactions and oedema [5]. According to the previous findings, plant oils like canola, peanut, sesame and olive oils were found protective against type two diabetes and inflammations in addition to their antioxidant and anticarcinogenic properties [6-10]. The plant oils can be categorized as fixed and essential oils. The plant seeds are known to contain fixed oils in addition to proteins, sugars, mucilage, organic acids, alkaloids, tannins, minerals, vitamins etc. [11]. Fixed oils are considered as the provider of energy, essential fatty acids and fat soluble vitamins for body so they are the important components of the immune system [12]. On the other hand, essential oils are the complex mixtures of low molecular weight compounds extracted from plants by solvent extraction or distillation methods. They contain terpenoids and phenylpropanoids responsible for the biological properties of the plants.

Several essential oils isolated from the plants are known to have antimicrobial/viral, anticancer/mutagenic, antidiabetic and antiinflammatory properties [13]. Therefore, the evaluation of the nutritional and health impacts of these oils is very important considering the fact that the ease of the access to the public. In this study, the toxicologic effects of two different plant essential oils (frankincense (*Boswellia sacra* Flück.) (Burseraceae) and blue anemone (*Anemone apennina* Auct. Orient. ex Boiss.) (Ranunculaceae) essential oils) and the influence of olfactory bias were aimed to be investigated. Frankincense (*Boswellia sacra* Flück.) oil was chosen because of the beneficial properties of the *Boswellia* species reported before. It is known that frankincense is a medicinal plant with anti tumorigenic, anti inflammatory properties and have been used traditionally against asthma and wounds. The *Boswellia* species are known to have terpenes and boswellic acids that are responsible for the medical properties for the traetment of age-related disorders, neurorecovery, skin disorder, cancer and depression [14, 15]. In addition, the clinical studies have shown the antiinflammatory properties of these plants

[15]. In another study, cardiac, genetic, hepatic and neuromuscular toxicity of *Frankincense* essential oil from *Boswellia sacra* using the zebrafish embryo were analysed and it didn't show any toxicity on zebrafish [16]. The frankincense plant also showed antigenotoxic properties when it was used in a gum form [17]. However, it is the first time that antigenotoxic effects and developmental toxicity of the frankincense oil were analysed in this study using *Drosophila melanogaster* model organism and the olfactory bias was checked to see the possibility of an interaction between the olfactory perception and antigenotoxicity of the plant oil. The blue anemone (*Anemone apennina* Auct. Orient. ex Boiss.) (Ranunculaceae) essential oil was also chosen in this study because of its characteristics reported before. *Anemone* genus members have been used against cancer, microbial infections and inflammations in addition to their sedative, analgesic, anti-convulsant and anti-histamine properties [18-20]. It was also shown that the triterpenoids and saponins found in those plants could be responsible for their anti-cancer activities [21]. In fact, researchers provided the evidence that triterpenoid saponins isolated from *Anemone flaccida* induced apoptosis by COX-2/PGE2 pathway in HeLa cancer cells [21]. In another study, *Anemone nemorosa* L. extracts, a close relative of *Anemone apennina* Auct. Orient. ex Boiss., showed high antioxidant activities (0.1 - 5 µg [GAE] per 1 mL sample) and cytotoxic activities against Caco-2 cancer cells [22]. However, there isn't any study about the genotoxicity of blue anemone oil in literature and it is the first time that antigenotoxic effects and developmental toxicity of the blue anemone oil were analysed in this study using *D. melanogaster* model organism and the olfactory bias was checked to see the possibility of an interaction between the olfactory perception and antigenotoxicity of the plant oil.

A compound that can cause genetic damage is regarded as a genotoxic agent and there are many bioactive substances counteracting the effects of these genotoxic compounds in nature [23]. These bioactive compounds are present in many plants abundantly and effective against genotoxicity [24]. Many plant oils have antigenotoxic properties and this was generally attributed to the antioxidant activities of their phytochemical compositions [23]. Therefore, the antigenotoxicity studies should be performed for all of the plant oils available on the market to ensure that existing medicinal potentials are not overlooked.

One of the important antigenotoxicity tests is somatic mutation and recombination test (SMART). It is based on the loss of heterozygosity caused by genotoxic damage resulting in mutated wing hair patterns on *Drosophila melanogaster* [25]. *D. melanogaster* is a frequently used model organism in biomedical sciences because approximately 75% of the genes responsible for human diseases have homologs in this organism and the short observation time is needed for screening the entire developmental process [26, 27]. Thus, antigenotoxic effects of frankincense and blue anemone oils were analyzed in this study by using SMART. In addition, developmental toxicity was analyzed to evaluate the effects of plant oils on normal developmental process of *D. melanogaster*.

The influence of the olfactory bias was also analyzed in this study to show the influence of the odor evoked preference on the antigenotoxicity of plant oils. Olfactory bias means a prejudice in favor of or against a specific olfactory perception which makes an organism aware of an odor through nose, sensory neurons and cerebral centers [28]. In traditional medicine, the sense of odor is very important for humans and the aromatic essential oils have been used for a long time as painkillers, anxiety relievers and energy boosters [29]. According to the previous findings, a strong relationship between the odor and oxidative stress was also observed [30]. The researchers found that the antioxidant activity was increased after inhalation of some plant odors [29, 30]. Not only humans but also most of the terrestrial animals use olfactory perception for the detection of dangers, nutritional sources or available mating partners and *D. melanogaster* is one of those animals which is accepted as an excellent model organism having a simple version of the olfactory system [31]. Olfactory bias can allure organisms to specific compounds and this may increase or decrease the appetite, so the protective effects of the compounds can be seen better or worse. Therefore, the independency of the antigenotoxic effects of the plant oils from the behavioural effects should be examined. In this study, feeding assay was used to perform an olfactory bias test to be able to check the existence of an interaction between the olfactory perception and antigenotoxicity of the plant oils.

Material and Methods

Materials

H_2O_2 and Brilliant Blue For Coloring Food (FCF) dye were purchased from Merck (Sigma Aldrich). The plant oils were purchased from local bazaar. The frankincense (*Boswellia sacra* Flück.) (Burseraceae) essential oil was obtained by cold pressing method and it complies with Turkish food codex (TR-34-K-000495/ 700 14 060). The blue anemone (*Anemone apennina* Auct. Orient. ex Boiss.) (Ranunculaceae) essential oil was obtained by water vapor distillation method and it complies with Turkish food codex (TR-34-K-000495/ 700 14 094).

Model Organisms and Their Growth Conditions

Wild type (*Oregon R*), *flr*^{3} (*flr*^{3}*/ In (3LR) TM3 Bd*^{s}) and *mwh* (*y; mwh j*) strains of *D. melanogaster* used in this study. The flies were kept at 22 °C. The growth media was prepared according to the classical method [32, 33]. In order to prepare the medium, 8.6 % sugar (w/v), 1.8 % agar (w/v), 18 % semolina (w/v), 5 % yeast (w/v), 0.001 % antifungal drug (v/v, MikostatinDeva Holding, 228/97) and 1 % propionic acid (v/v) were dissolved in dH_2O.

Somatic Mutation and Recombination Test (SMART)

SMART was performed using previous protocols in literature [34, 35]. For this test, *flr3* female and *mwh* male flies were crossed and 72 ± 4 hours later third instar larvae with *mwh+/+flr3* genetic background were removed from the vial and washed with dH_2O. 50 larvae were added into the experimental bottles prepared with growth medium containing plant oils (5 % v/v) or H_2O_2 (6.5 mg/L) and the negative control group was prepared without adding anything into the medium. The cotreatment group was prepared by adding plant oils (5 % v/v) with H_2O_2 (6.5 mg/L) into the same medium. When they became adults, the wings were collected and hair patterns were investigated using light microscope (400x). Genotoxicities were determined by the the frequencies of spots per wing (*Fr.)*. The spots were named as single spots (*mwh* or *flr* phenotype) or twin spots (both mutated clones adjacent). *Fr.* values were calculated by dividing the number of spots (n) by the number of wings (N). [34-36]. Inhibition % values were also calculated for the cotreatment group using equation 1 [37, 38].

$$\text{Inhibition \%} = \frac{(\text{Fr.of H2O2 Group} - \text{Fr.of Cotreatment Group})}{\text{Fr. of H2O2 Group}} \text{x}100 \quad (1)$$

Developmental Toxicity Test

Developmental toxicity test was performed to screen the developmental process from the larval to adult stages of wild type *D. melanogaster*, *in vivo* [31, 39-42]. For this test, first instar larvae were added into the growth medium composed of plant oils (5 % v/v) or H_2O_2 (6.5 mg/L). The negative control group was prepared without adding anything into the medium. The cotreatment group was prepared by adding plant oils (5 % v/v) with H_2O_2 (6.5 mg/L) into the same medium. The puparation, eclosion and survival % were calculated by the equations 2, 3 and 4 [31, 39-42].

$$\text{Puparation \%} = \frac{\text{Pupae \#}}{\text{Larvae \#}} \text{ x } 100 \quad (2)$$

$$\text{Eclosion \%} = \frac{\text{Adult \#}}{\text{Pupae \#}} \text{ x } 100 \quad (3)$$

$$\text{Survival \%} = \frac{\text{Adult \#}}{\text{Larvae \#}} \text{ x } 100 \quad (4)$$

Olfactory Bias Test

Olfactory bias test (feeding assay) was performed according to the previous studies [31]. In order to perform this test, blue-growth medium containing 0.5 % (w/v) Brilliant blue FCF dye was prepared for this study. 50 larvae were added into the blue-growth medium composed of plant oils (5 % v/v) or H_2O_2 (6.5 mg/L). The negative control group was prepared without adding anything into the blue-growth medium. The cotreatment group was prepared by adding plant oils (5 % v/v) with H_2O_2 (6.5 mg/L) into the same blue-growth medium. The larvae were fed on those media for 30 minutes and washed in sterile serum physiologic solution. Then, the larvae were dried by filter paper and frozen overnight at −80 °C. The absorbances showing a direct relationship with the amount of blue-growth media ingested were measured at 625 nm.

Results

SMART Results

In Table 1 and Table 2 SMART results are given. According to the results, it was observed that an oxidative agent, H_2O_2, caused important small single, large single and twin spot frequency increases ($p<0.05$). On the other hand, frankincense and blue anemone oils didn't affect the spot frequencies compared to negative control ($p>0.05$). Cotreatment groups also showed similar results. None of the cotreatment group significantly affect the spot frequencies. In addition, inhibition % values calculated with the cotreatment group SMART results given in Table 2 showed that frankincense and blue anemone oils caused 73.3 - 100 % inhibitions.

Table 1. SMART results

Treatments	Small single spots		Large single spots		Twin spots	
	Fr.	SE	*Fr.*	SE	*Fr.*	SE
Negative Control	1.33[b]	0.33	0[b]	0	0[b]	0
H_2O_2 (6.5 mg/L)	5[a]	0.58	4.33[a]	0.67	10[a]	0.58
Frankincense oil	0.67[b]	0.33	0.67[b]	0.33	0[b]	0
Blue anemone oil	0.67[b]	0.33	0.33[b]	0.33	0[b]	0
Frankincense oil + H_2O_2	1[b]	0	0[b]	0	0.33[b]	0.33
Blue Anemone Oil + H_2O_2	1.33[b]	0.33	0[b]	0	0[b]	0

[a] $p< 0.05$, in contrary to negative control
[b] $p< 0.05$, in contrary to H_2O_2
SE: Standard error, *Fr.*: Frequency
Plant oil concentration: 5 % v/v, H_2O_2 concentration: 6.5 mg/L

Table 2. Spot inhibition % values of the cotreatments

Treatments	Small single spots	Large single spots	Twin spots
	Inhibition %	Inhibition %	Inhibition %
Frankincense oil + H_2O_2	80	100	96.7
Blue Anemone Oil + H_2O_2	73.3	100	100

Plant oil concentration: 5 % v/v, H2O2 concentration: 6.5 mg/L

Developmental Toxicity Test Results

The developmental toxicity test results are given in Figure 1. The results showed that H_2O_2 caused important decreases in puparation, eclosion and survival %. The frankincense and blue anemone oils didn't cause any significant difference in puparation, eclosion and survival %. When the cotreatment groups are examined, it was observed that the frankincense and blue anemone oils

caused significant decreases in puparation and survival % ($p< 0.05$, Figure 1 (a)(c)). On the other hand, none of the oils cotreated with H_2O_2 caused any significant decrease in eclosion % ($p>0.05$, Figure 1 (b)).

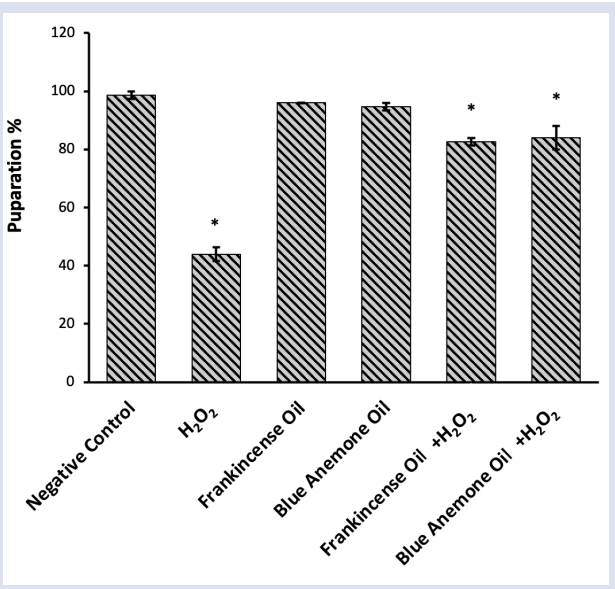

(a)

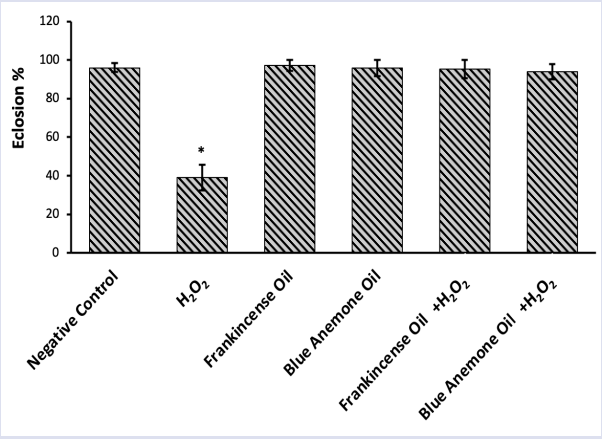

(b)

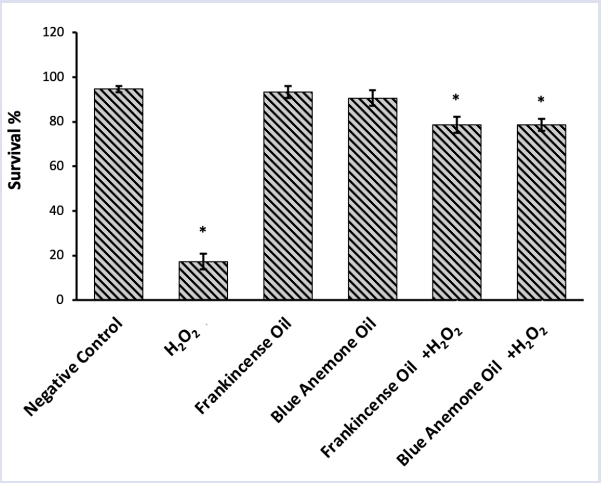

(c)

Figure 1. Developmental toxicity test results

Olfactory Bias Test Results

The olfactory bias test results are given in Figure 2. The absorbances showing the rate of feeding observed with H_2O_2, frankincense oil and blue anemone oil were similar to the one observed with the negative control ($p>0.05$).

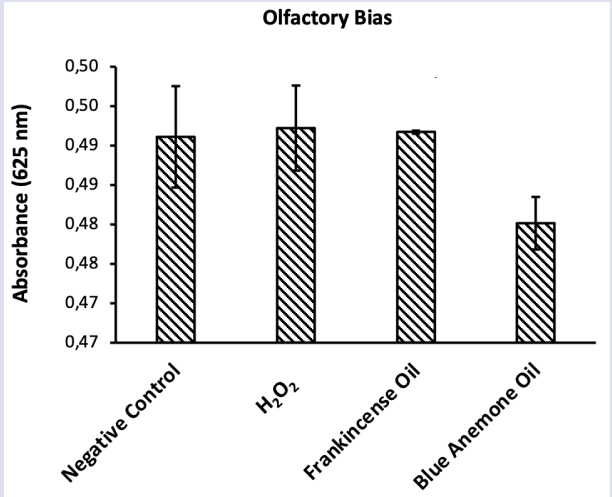

Figure 2. Olfactory bias test results

Discussion

The potential antigenotoxic effects of the frankincense oil and blue anemone oil were analysed in this study by using SMART assay. The results given in Table 1 and 2 showed that all of the plant oils used in this study was non-genotoxic. It was also clearly seen that the frankincense and blue anemone oils were able to inhibit the genotoxic effects of H_2O_2 (inhibition % of the cotreatment groups were between 73.3 - 100 %). Therefore, the frankincense and blue anemone oils can be considered as antigenotoxic oils.

As an additional toxicity assessment, the developmental toxicities were examined. The results given in Figure 1 showed that none of the plant oils studied here showed any detrimental effect on puparation and eclosion processes of *D. melanogaster*. However, according to the results of the cotreatment groups it was clearly observed that plant oils couldn't protect the organism's puparation process and survival % from the harmful effects of H_2O_2 (Figure 1(a) (c)).

An olfactory bias test was also analysed in this study to be able to check the existence of an interaction between the olfactory perception and antigenotoxicity of the plant oils. According to the results given in Figure 2 it was observed that H_2O_2, frankincense oil and blue anemone oil didn't affect the feeding rate positively or negatively ($p>0.05$). Therefore, it can be said that there isn't any olfactory bias against those plant oils.

When the assay results obtained in this study were combined, it was clearly observed that the frankincense oil and blue anemone oil were antigenotoxic and, most importantly, these effects were independent from the olfactory perception. According to the developmental toxicity test all of the plant oils were safe. In previous findings, it was also observed that frankincense oil had

anti-cancer (melanoma) activities *in vitro* and *in vivo*, while protecting the normal human epithelial melanocyte cell growth [14]. The researchers also showed that frankincense plant in a gum form was able to decrease the nuclear abnormalities and cytotoxicity observed as a result of tobacco smoking [17]. There isn't any study about the genotoxicity of blue anemone oil in literature but there are some studies about the other members of the *Anemone* genus. For example, *Anemone nemorosa* L. extracts showed antioxidant and antiproliferative activities on cancer cells (Caco-2) [22].

Conclusions

In this study, antigenotoxic effects of the frankincense and blue anemone oils were analysed by SMART, developmental toxicity was analysed to evaluate the effects of plant oils on normal developmental process of *D. melanogaster* and feeding assay was used to perform an olfactory bias test to check the existence of an interaction between the olfactory perception and antigenotoxicity of the plant oils. According to the results, all of the plant oils used in this study was non-genotoxic and none of the plant oils studied here showed any detrimental effect on puparation and eclosion processes of *D. melanogaster* while they couldn't protect the organism's puparation process and survival % from the harmful effects of H_2O_2. In addition, there wasn't any olfactory bias against frankincense oil and blue anemone oil. To conclude, the frankincense oil and blue anemone oil were found antigenotoxic in this study and, most importantly, these effects were independent from the olfactory perception.

A lot of plant oils have been introduced to the market recently while the data on the comprehensive toxicologic potential of most of them have not been reported. The evaluation of the nutritional and health impact of these oils is very important considering the fact that the ease of the access to the public. In this study, antigenotoxic effects of some plant oils (the frankincense and blue anemone oils) were analysed. In future, the medical potentials of these plant oils should be evaluated more.

Conflicts of interests

The author reports no conflicts of interest.

Acknowledgment

Author thanks Assoc. Prof. Dr. Umit Kumbicak (Nevsehir Haci Bektas Veli University) and Dr. Huzeyfe Huriyet (Uludag University) for the *Drosophila* strains used in this research.

References

[1] Zhou Y., Zhao W., Lai Y., Zhang B., Zhang D., Edible Plant Oil: Global Status, Health Issues, and Perspectives, *Front Plant Sci.*, 11(1) (2020) 1315-1315.

[2] Sumara A., Stachniuk A., Montowska M., Kotecka-Majchrzak K., Grywalska E., Mitura P., Saftić Martinović L., Kraljević Pavelić S. and Fornal E., Comprehensive Review of Seven Plant Seed Oils: Chemical Composition, Nutritional Properties, and Biomedical Functions, *Food Reviews International*, (2022) 1-21.

[3] Zhang W., Wang T., Zheng Z., Quirino R. L., Xie F., Li Y. and Zhang C., Plant oil-based non-isocyanate waterborne poly(hydroxyl urethane)s, *Chemical Engineering Journal*, 452 (2023).

[4] Yang J., Liu Y., Zhao L., Chen Y., Sun Z., Zhang Y., Versatility of plant oil as sustainable source for advanced functional materials design, *Materials Today Sustainability*, 22 (2023).

[5] Mikołajczak N., Tańska M., Ogrodowska D., Phenolic compounds in plant oils: A review of composition, analytical methods, and effect on oxidative stability, *Trends in Food Science & Technology*, 113 (2021) 110-138.

[6] Wu F., Mao L., Zhuang P., Chen X., Jiao J. and Zhang Y., Plant-sourced cooking oil consumption is associated with lower total mortality in a longitudinal nationwide cohort study, *Clin. Nutr.*, 39(12) (2020) 3703-3710.

[7] Lin L., Allemekinders H., Dansby A., Campbell L., Durance-Tod S., Berger A., Jones P. J., Evidence of health benefits of canola oil, *Nutr. Rev.*, 71 (6) (2013) 370-385.

[8] Schwingshackl L., Lampousi A. M., Portillo M. P., Romaguera D., Hoffmann G., Boeing H., Olive oil in the prevention and management of type 2 diabetes mellitus: a systematic review and meta-analysis of cohort studies and intervention trials, *Nutr. Diabetes*, 7 (4) (2017) e262.

[9] Comba A., Maestri D. M., Berra M. A., Garcia C. P., Das U. N., Eynard A. R., Pasqualini M. E., Effect of omega-3 and omega-9 fatty acid rich oils on lipoxygenases and cyclooxygenases enzymes and on the growth of a mammary adenocarcinoma model, *Lipids Health Dis.*, 9 (2010) 112.

[10] Sankar D., Rao M. R., Sambandam G., Pugalendi K. V., Effect of sesame oil on diuretics or Beta-blockers in the modulation of blood pressure, anthropometry, lipid profile, and redox status, *Yale J. Biol. Med.*, 79 (1) (2006) 19-26.

[11] Piras A., Rosa A., Marongiu B., Porcedda S., Falconieri D., Dessì M. A., Ozcelik B., Koca U., Chemical composition and in vitro bioactivity of the volatile and fixed oils of Nigella sativa L. extracted by supercritical carbon dioxide, *Industrial Crops and Products*, 46 (2013) 317-323.

[12] Kazeem M. I., Ogunwande I. A., Role of fixed oil and fats in human physiology and pathophysiology, *Recent Progress in Medicinal Plants*, 33 (2012) 85-103.

[13] Raut J. S., Karuppayil S. M., A status review on the medicinal properties of essential oils, *Industrial Crops and Products*, 62 (2014) 250-264.

[14] Hakkim F. L., Bakshi H. A., Khan S., Nasef M., Farzand R., Sam S., Rashan L., Al-Baloshi M. S., Abdo Hasson S. S. A., Jabri A. A., McCarron P. A., Tambuwala M. M., Frankincense essential oil suppresses melanoma cancer through down regulation of Bcl-2/Bax cascade signaling and ameliorates heptotoxicity via phase I and II drug metabolizing enzymes, *Oncotarget*, 10 (37) (2019) 3472-3490.

[15] Varma K., Haponiuk J. T., Gopi S., Antiinflammatory activity of Boswellia, *City*, 2021.
[16] Rashan L., Efferth T., Bishir M., Bishir M., Essa M. M., Chidambaram S. B., Qoronfleh M. W., Acute, genetic, and target organ toxicity profiling of Frankincense essential oil from Boswellia sacra in zebrafish (Danio rerio), *Archives of Clinical Toxicology*, 5(1) (2023) 12-21.
[17] Sabah J. T., Alhachami F. R., Potential Anti-Cancer Properties of Frankincese (Boswellia Sarca) Chewing Gum and its Role in Reduction of Tobacco Smoking Genotoxicity, *Biomedical and Pharmacology Journal*, 16(1) (2023) 213-219.
[18] Swanepoel B., Venables L., Olaru O. T., Nitulescu G. M., van de Venter M., In Vitro Anti-proliferative Activity and Mechanism of Action of Anemone nemorosa, *Int. J. Mol. Sci.*, 20 (5) (2019).
[19] Hao D. C., Gu X., Xiao P., Anemone medicinal plants: ethnopharmacology, phytochemistry and biology, *Acta Pharm. Sin. B.*, 7(2) (2017) 146-158.
[20] Lukianchuk A., Khropot O., Konechnyi Y., Konechna R., Novikov V., Wood anemone. Anemone Nemorosa L. Analytical review, *ScienceRise: Pharmaceutical Science*, 3(7) (2017) 34-38.
[21] Han L. T., Fang Y., Li M. M., Yang H. B., Huang F., The Antitumor Effects of Triterpenoid Saponins from the Anemone flaccida and the Underlying Mechanism, Evid Based Complement Alternat Med., 2013 (2013) 517931.
[22] Pirvu L., Stefaniu A., Neagu G., Pintilie L., Studies on Anemone nemorosa L. extracts; polyphenols profile, antioxidant activity, and effects on Caco-2 cells by in vitro and in silico studies, Open Chemistry, 20(1) (2022) 299-312.
[23] López-Romero D., Izquierdo-Vega J., Morales-González J., Madrigal-Bujaidar E., Chamorro-Cevallos G., Sánchez-Gutiérrez M., Betanzos-Cabrera G., Alvarez-Gonzalez I., Morales-González Á., Madrigal-Santillán E., Evidence of Some Natural Products with Antigenotoxic Effects. Part 2: Plants, Vegetables, and Natural Resin, *Nutrients*, 10(12) (2018) 1954.
[24] Sinha S., Biswas D., Mukherjee A., Antigenotoxic and antioxidant activities of palmarosa and citronella essential oils, *J. Ethnopharmacol*, 137(3) (2011) 1521-1527.
[25] de Andrade H. H., Reguly M. L., Lehmann M., Wing somatic mutation and recombination test, *Methods Mol. Biol*., 247 (2004) 389-412.
[26] Tolwinski N. S., Introduction: Drosophila-A Model System for Developmental Biology, *J. Dev. Biol.*, 5(3) (2017).
[27] Mirzoyan Z., Sollazzo M., Allocca M., Valenza A. M., Grifoni D., Bellosta P., Drosophila melanogaster: A Model Organism to Study Cancer, *Front Genet*, 10 (2019) 51.
[28] Slotnick B., Weiler E. Olfactory Perception. Springer Berlin Heidelberg, City, 2009.
[29] Angelucci F. L., Silva V. V., Dal Pizzol C., Spir L. G., Praes C. E. and Maibach H., Physiological effect of olfactory stimuli inhalation in humans: an overview, *Int. J. Cosmet Sci.*, 36(2) (2014) 117-123.
[30] Atsumi T., Tonosaki K., Smelling lavender and rosemary increases free radical scavenging activity and decreases cortisol level in saliva, *Psychiatry Res*., 150(1) (2007) 89-96.
[31] Depetris-Chauvin A., Galagovsky D., Chevalier C., Maniere G. and Grosjean Y., Olfactory detection of a bacterial short-chain fatty acid acts as an orexigenic signal in Drosophila melanogaster larvae, *Sci. Rep.*, 7(1) (2017) 14230.
[32] Yakovleva E. U., Naimark E. B., Markov A. V., Adaptation of *Drosophila melanogaster* to unfavorable growth medium affects lifespan and age-related fecundity, *Biochemistry (Moscow)*, 81(12) (2016) 1445-1460.
[33] Chung H., Sztal T., Pasricha S., Sridhar M., Batterham P., Daborn P. J., Characterization of *Drosophila melanogaster* cytochrome P450 genes, *Proceedings of the National Academy of Sciences*, 106(14) (2009) 5731-5736.
[34] Patenkovic A., Stamenkovic-Radak M., Banjanac T., Andjelkovic M., Antimutagenic effect of sage tea in the wing spot test of *Drosophila melanogaster*, *Food Chem Toxicol*, 47(1) (2009) 180-183.
[35] Graf U., Würgler F. E., Katz A. J., Frei H., Juon H., Hall C. B., Kale P. G., Somatic mutation and recombination test in *Drosophila melanogaster*, *Environmental Mutagenesis*, 6 (1984) 153-188.
[36] Sarikaya R., Erciyas K., Kara M. I., Sezer U., Erciyas A. F. and Ay S., Evaluation of genotoxic and antigenotoxic effects of boron by the somatic mutation and recombination test (SMART) on *Drosophila*, *Drug Chem Toxicol*, 39(4) (2016) 400-406.
[37] Abraham S. K., Antigenotoxicity of coffee in the *Drosophila* assay for somatic mutation and recombination, *Mutagenesis*, 9(4) (1994) 383-386.
[38] Mezzoug N., Abrini J., Serano A. M., Alonso-Moraga A., Idaomar M., Study on antigenotoxic effects of Moroccan medicinal plants and spices using the *white/white+* somatic assay in *Drosophila*, *African Journal of Traditional, Complementary and Alternative Medicines*, 3(3) (2006).
[39] Rand M. D., Montgomery S. L., Prince L., Vorojeikina D., Developmental toxicity assays using the *Drosophila* model, *Current Protocols in Toxicology*, 59 (1) (2014).
[40] Liu Q. F., Lee J. H., Kim Y.-M., Lee S., Hong Y. K., Hwang S., Oh Y., Lee K., Yun H. S., Lee I.-S., Jeon S., Chin Y.-W., Koo B.-S., Cho K. S., *In vivo* screening of traditional medicinal plants for neuroprotective activity against Aβ42 cytotoxicity by using *Drosophila* models of Alzheimer's disease, *Biological & Pharmaceutical Bulletin*, 38(12) (2015) 1891-1901.
[41] Macedo G. E., Gomes K. K., Rodrigues N. R., Martins I. K., Wallau G. D. L., Carvalho N. R. D., Cruz L. C. D., Costa Silva D. G. D., Boligon A. A., Franco J. L., Posser T., Senecio brasiliensis impairs eclosion rate and induces apoptotic cell death in larvae of Drosophila melanogaster, *Comparative Biochemistry and Physiology Part C: Toxicology & Pharmacology*, 198 (2017) 45-57.
[42] Riaz B., Zahoor M. K., Zahoor M. A., Majeed H. N., Javed I., Ahmad A., Jabeen F., Zulhussnain M., Sultana K., Toxicity, phytochemical vomposition, and enzyme inhibitory activities of some indigenous weed plant extracts in fruit fly, *Drosophila melanogaster*, *Evid Based Complement Alternat. Med.*, 2018 (2018) 2325659.

Cumhuriyet Sci. J., 45(2) (2024) 188-193
DOI: https://doi.org/10.17776/csj.1409301

Cumhuriyet Science Journal

| csj.cumhuriyet.edu.tr | Founded: 2002 ISSN: 2587-2680 e-ISSN: 2587-246X Publisher: Sivas Cumhuriyet University

Protective Role of Resveratrol Against Toluene-Induced Oxidative Stress in Rats

Ahmet Barat [1,a], Egemen Dere [2,b,*]

[1] *Department of Biology, Graduate School of Natural and Applied Sciences, Bursa Uludağ University, Bursa, Türkiye.*
[2] *Department of Biology, Faculty of Arts and Sciences, Bursa Uludağ University, Bursa, Türkiye.*
**Corresponding author*

Research Article

History
Received: 17/01/2024
Accepted: 13/06/2024

ABSTRACT

Toluene is a toxic substance commonly used in the industry that leads to oxidative stress in the body and causes in the formation of reactive oxygen species. In addition to the antioxidants produced by our body, we also obtain antioxidants through foods. Resveratrol is a polyphenol found in many plant species and possesses antioxidant properties. The effects of oxidative stress induced by toluene and the protective effect of resveratrol were investigated through changes in malondialdehyde (MDA) and glutathione (GSH) levels. Male rats were administered different doses of toluene and resveratrol (5 mg/kg, 10 mg/kg, 20 mg/kg), while control groups were given physiological saline and ethanol. At the end of the experiment, blood and lung tissues of the animals were examined, and MDA and GSH levels were measured. According to the obtained data, a significant increase in GSH activity was observed after the administration of toluene. However, in groups treated with combinations of toluene and various doses of resveratrol, a significant decrease in GSH levels was detected. While a significant increase in MDA levels in lung tissues was observed between the control groups and the toluene group, no significant change was observed in blood samples.

Keywords: Toluene, Resveratrol, Malondialdehyde, Glutathione.

[a] *ahmet.baratov@mail.ru* *https://orcid.org/0000-0002-7618-9626* [b] *edere@uludag.edu.tr* *https://orcid.org/0000-0001-9572-1051*

Introduction

Toluene is an important solvent widely used in various industrial applications and consumer products. Exposure to toluene can lead to oxidative stress. Among the primary reasons for this interaction is the activation of toluene through the metabolic process [1]. Toluene is metabolized in the body, resulting in the formation of various by-products. Among these metabolic products are compounds produced when toluene is metabolized by monooxygenase enzymes. The emergence of these metabolic products can trigger oxidative stress. Exposure to toluene can contribute to the formation of free radicals. Free radicals, which can damage macromolecules such as lipids, proteins, and DNA, can increase oxidative stress in cells [2]. Exposure to toluene can affect the body's natural defense against free radicals by impacting the antioxidant system. Antioxidants neutralize free radicals to protect cells [3,4]. Exposure to toluene can disrupt the balance of the antioxidant system, leading to increased oxidative stress. It can contribute to increased oxidative stress by promoting inflammation in the body, resulting in damage to cells and tissues. Additionally, it can cause damage to mitochondria. Mitochondria are vital structures in cells that produce energy, and when damaged, they can produce free radicals. In conclusion, exposure to toluene can contribute to increased oxidative stress and cellular damage [5].

Phytoalexins are effective compounds naturally produced by plants to combat infections and harmful microorganisms and are often referred to as "plant antibiotics" [6]. Among the most effective phytoalexins of the stilbenoid type is resveratrol, which is a polyphenolic compound [7]. Specifically in grapevines, an infection by a pathogen called Botrytis cinerea leads to the specialized production of resveratrol in the leaves and skin of the grapes [8]. This particular compound is found more abundantly in the skins and seeds of grapes and other fruits. Known for its antifungal, antiviral, anti-inflammatory, antioxidant, and anti-aging properties, resveratrol also stands out for its cardiovascular health-supporting, phytoestrogenic, vasorelaxant, neuroprotective, and anticancer attributes. Possessing antioxidant properties, resveratrol has the ability to effectively neutralize free radicals. Various oxidants, such as O_2^-, •OH, H_2O_2, and $ONOO^-$, can be directly deactivated by resveratrol [9]. Many people prefer to consume this beneficial compound through fruits or as a supplement. However, there are warnings that consuming large amounts of resveratrol can lead to stomach and intestinal issues in some individuals [10].

Glutathione (GSH) is a tripeptide found within cells. It plays a critical role in neutralizing free radicals and reactive oxygen species (ROS), thereby preventing oxidative stress and maintaining cellular homeostasis. It is a central component in preserving redox homeostasis (the oxidative state within cells) [11]. The balance between oxidized glutathione (GSSG) and reduced glutathione (GSH) determines a cell's capacity to cope with oxidative stress. This ensures that cells function healthily and prevent the onset of pathological conditions. Therefore, GSH and its metabolism are considered potential

therapeutic targets in many diseases associated with oxidative stress [12, 13].

Malondialdehyde (MDA), a by-product of lipid peroxidation, is also considered an indicator of oxidative damage. It is used to assess the extent and effects of oxidative damage to membrane lipids [14, 15].

In particular, in research and clinical studies, the examination of GSH and MDA aids in understanding oxidative damage and elucidating cellular mechanisms at the cellular level. In this study, the effects of toluene exposure-induced oxidative stress in rats were investigated. Additionally, it was assessed whether resveratrol plays a protective role against these adverse effects. Levels of MDA, an indicator of lipid peroxidation, and GSH, which plays a significant role in cellular antioxidant defense, were analyzed.

Materials and Methods

Animal Experiments and Procedures

Within the scope of the experiment, 36 adult Wistar Albino male rats weighing between 200–350 grams were selected. The rats were housed in an environment with a room temperature of 20-24ºC where they could freely access food and water. The animals were divided into two main groups: control and experimental. The experimental group was prepared based on exposures to toluene and toluene+resveratrol. Over a span of 6 days, the animals received intraperitoneal (i.p) injections. The first experimental group was administered toluene at a dose of 900mg/kg, the second group received the same dose of toluene combined with 5mg/kg of resveratrol, the third group was given 10mg/kg of resveratrol, and the fourth group received 20mg/kg of resveratrol, all via the i.p route. Resveratrol was dissolved in 10% ethanol before injection. For the control groups, the first group was administered with physiological saline, and the second group received an injection of 10% ethanol.

Collection of Tissue and Blood Samples

After the 6-day experiment, the rats were euthanized in accordance with ethical guidelines using the cervical dislocation method. Lung tissue and blood samples were rapidly collected from the animals. Once obtained, the tissues were rinsed and cleaned in a phosphate buffer with a pH value of 7.4, and their weights were determined using a sensitive balance. While the blood samples were centrifuged at 1000g for 15 minutes at 0-4ºC, the lung tissues were prepared in a 1/9 (w/v) ratio with cold buffer solution on ice and homogenized at a speed of 3000 revolutions per minute. The homogenates were then centrifuged at 10,000g for 15 minutes at 0-4ºC. These procedures were meticulously performed in accordance with the instructions recommended by the analytical kits used. The obtained samples were stored at -80°C."

Determination of MDH Levels

MDH levels were calculated using the formulations recommended by the MDH kit. The standard operational table of the MDA kit used in the study is shown in Table 1.

Table 1. MDA standard operational table.

	blank tube	standard tube	sample tube	Control tube
absolute ethanol (mL)	a*			
reactive 4 (mL)		a*		
samples (mL)			a*	a*
reactive 1 (mL)	a*	a*	a*	a*
reactive 2 application solution (mL)	3.0	3.0	3.0	3.0
reactive 3 application solution (mL)	1.0	1.0	1.0	1.0
50% glacial acetic acid				1.0

a* The volume represents the volumes of the sample, standard, absolute ethanol, and reagent 1, and they are equal. For instance, if the sampling volume is 0.1 mL, then the volume for the standard, absolute ethanol, and reagent 1 is also 0.1 mL each. If the sampling volume is 0.2 mL, then the volume for the standard, absolute ethanol, and reagent 1 is also 0.2 mL each.

Determination of GSH Levels

The thiol group of the cysteine amino acid, which functions in the structure of GSH, reacts with dithionitrobenzoic acid (DTNB) to produce a yellow-colored thio-nitrobenzoic (TNB) compound. The concentration of GSH was determined based on the optical density (OD) values of TNB at a wavelength of 420nm. The standard operational table of the GSH kit used in this study is shown in Table 2.

Table 2. GSH Standard operation table.

	blank tube	standard tube	sample tube
reactive 1 (mL)	1.0		
20 µmol/L GSH standard solution (mL)		1.0	
supernatant (mL)			1.0
reactive 2 application solution (mL)	1.25	1.25	1.25
reactive 3 (mL)	0.25	0.25	0.25
reactive 4 application solution (mL)	0.05	0.05	0.05
It was thoroughly mixed and left at room temperature for 15 minutes. The OD values of each tube were measured at a wavelength of 420nm using a spectrophotometer.			

Statistical Analysis

The statistical analysis of the data was conducted using GraphPad Prism 9.3.0 software. Statistical differences between the control and experimental groups were evaluated using one-way analysis of variance (ANOVA) followed by the posthoc Tukey test. The results were presented as mean values and standard error (SE). For statistical significance, the values *p<0.05, **p<0.01, ***p=0.001, and ****p<0.001 were used.

Results

GSH findings

In the lung tissue samples, GSH levels showed a significant increase of 57% when compared to the control groups in the group that received toluene injections (p<0.001). When the toluene+resveratrol treatments were compared to the control groups, statistically significant increases of 40% (p<0.05) for 5mg/kg, 57% for 10mg/kg, and 63% for 20mg/kg were observed (p<0.001).

A decrease of 28% was observed in the group treated with toluene and toluene+resveratrol at a dose of 5mg/kg. However, no significant difference was detected at a resveratrol dose of 10mg/kg. In the 20mg/kg dose of resveratrol, an 18% increase was observed, which was statistically insignificant (p>0.05).

Upon examining serum samples; a 5% increase was observed between the saline control group and the toluene group, while a 12% decrease was seen between the ethanol control group and the toluene experimental group. These findings did not show a statistically significant difference. When compared to the saline control group, a statistically significant decrease of 36% was recorded in the toluene+resveratrol (5mg/kg, 10mg/kg) treatments (p<0.01). However, despite a 5% decrease between the saline control group and the toluene+resveratrol (20mg/kg) group, this difference was considered statistically insignificant (p>0.05).

A statistically significant decrease of 46% was observed between the ethanol control group and the toluene+resveratrol (5mg/kg, 10mg/kg) group (p<0.001). Similarly, an insignificant decrease of 21% was seen between the ethanol control group and the toluene+resveratrol 20mg/kg group. A statistically significant decrease of 39% was recorded between the toluene group and the toluene+resveratrol (5mg/kg, 10mg/kg) groups (p<0.001). However, a statistically significant increase of 32% was observed between the toluene+resveratrol (5mg/kg, 10mg/kg) groups and the toluene+resveratrol 20mg/kg group (p<0.05). GSH levels in the lungs and serum are presented in Table 3 and Figure 1.

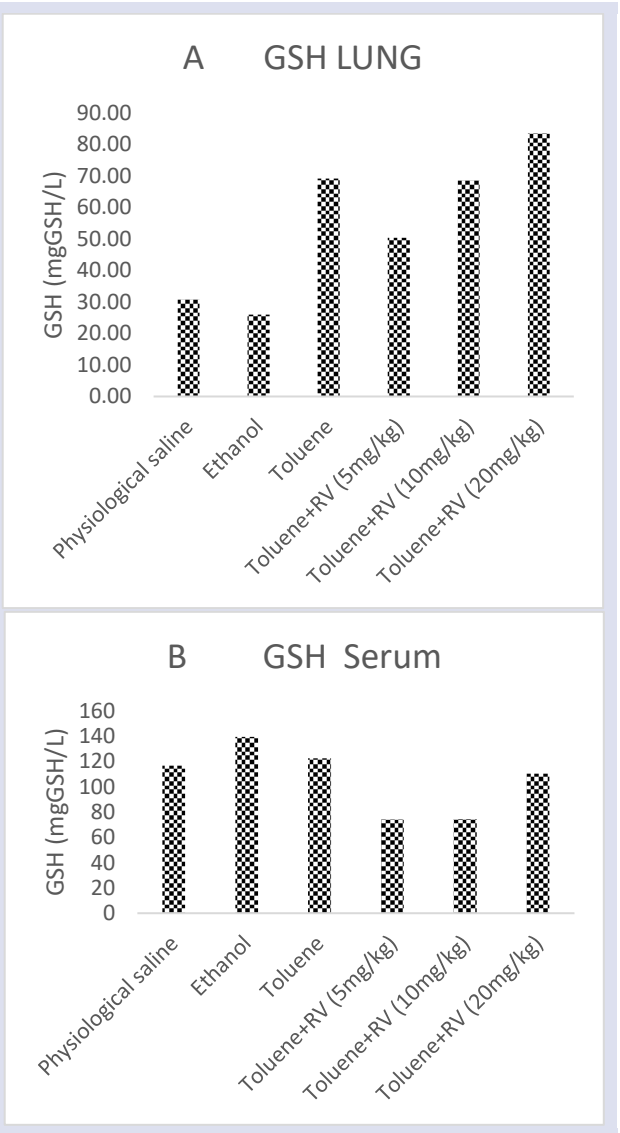

Figure 1 (A) GSH levels in rat lung. (B) GSH levels in rat serum

Table 3. GSH levels in lung and serum (mean ± standard error).

Groups	GSH Lung (µmol/L) Ort ± SE	GSH Serum (µmol/L) Ort ± SE
Control physiological saline	30.77±7.55	116.59±0.25
Control ethanol	26.00±4.45	139.35±6.57
Toluene	69.19±15.39	122.38±13.64
Toluene+Resveratrol (5 mg/kg)	50.32±4.32	74.14±8.07
Toluene +Resveratrol (10 mg/kg)	70.32±6.91	74.39±11.68
Toluene +Resveratrol (20 mg/kg)	83.43±3.77	110.21±19.36

MDA Findings

In lung tissue samples, statistically significant increases of 48% were recorded between the control saline solution group and the toluene group, and 43% between the ethanol group and the toluene group ($p<0.001$).

An increase of 35% was observed between the control saline solution group and the toluene+resveratrol 5mg/kg group, and 27% between the ethanol control group and the same group; however, these increases were not statistically significant ($p>0.05$). A statistically significant increase of 44% was detected between the control saline solution group and the toluene+resveratrol 10mg/kg group, and a 45% increase was observed between the control saline solution group and the toluene+resveratrol 20mg/kg group ($p<0.001$). Furthermore, when compared to the ethanol control group, a 39% increase was noted between the ethanol control group and the toluene+resveratrol 10mg/kg group, and a 40% increase was recorded between the ethanol control group and the toluene+resveratrol 20mg/kg group, both of which were statistically significant ($p<0.01$).

In serum samples, an increase of 21% was observed between the control saline solution group and the toluene group, but this increase was not statistically significant ($p>0.05$). Conversely, a statistically significant increase of 29% was seen between the ethanol control group and the toluene group ($p<0.01$). Significant decreases of 31%, 40%, and 32% were noted between the control saline solution group and the toluene+resveratrol groups at doses of 5mg/kg, 10mg/kg, and 20mg/kg, respectively ($p<0.01$ and $p<0.05$, respectively). When compared to the ethanol control group, decreases of 24%, 34%, and 25% were recorded in the toluene+resveratrol groups at doses of 5mg/kg, 10mg/kg, and 20mg/kg, respectively. While there was a statistically insignificant decrease in the levels of resveratrol at doses of 5mg/kg and 20mg/kg ($p>0.05$), a significant decrease was identified at a dose of 10mg/kg ($p<0.05$). Finally, statistically significant decreases of 46%, 53%, and 46% were observed between the toluene group and the toluene+resveratrol groups at doses of 5mg/kg, 10mg/kg, and 20mg/kg, respectively ($p<0.001$). The MDA levels in the lungs and serum are presented in Table 4 and Figüre 2.

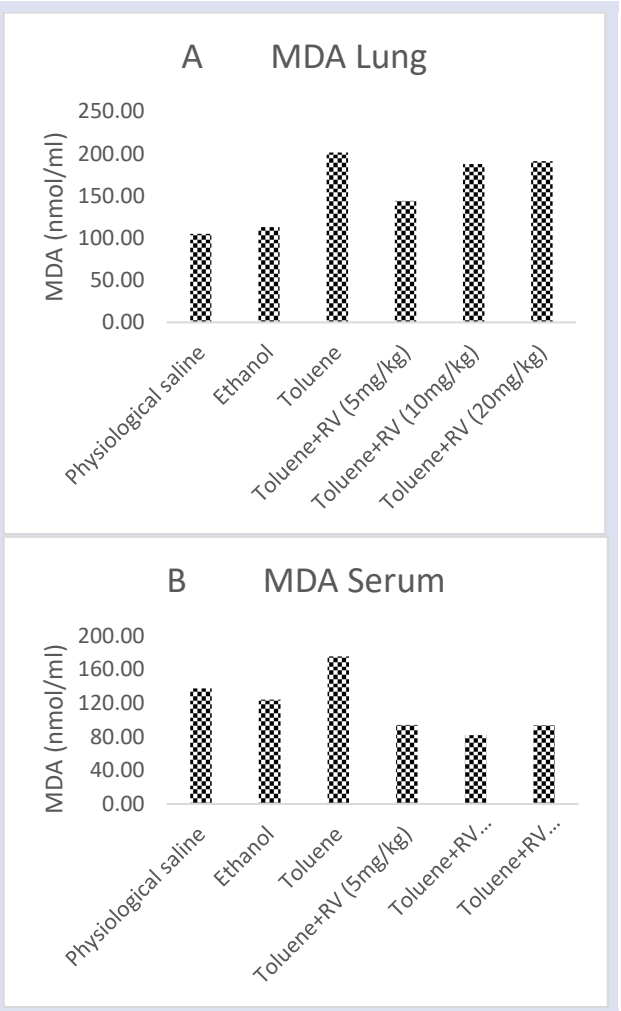

Figüre 2. (A) MDA levels in the lungs. (B) MDA levels in the serum

Table 4. MDA levels in lung and serum (mean ± standard error).

Gruplar	MDA Lung (µmol/L) Ort ± SE	MDA Serum (µmol/L) Ort ± SE
Control physiological saline	104.88±25.92	137.29±16.30
Control ethanol	113.13±7.25	124.06±13.45
Toluene	201.50±38.35	175.63±19.25
Toluene+Resveratrol (5 mg/kg)	144.17±36.22	94.06 ±13.21
Toluene+Resveratrol (10 mg/kg)	187.75±28.64	81.72 ±14.53
Toluene+Resveratrol (20 mg/kg)	191.00±14.51	93.44 ±21.58

Discussion

After injecting toluene into the rats, redness in the eyes, bleeding from the mouth and nose, and unsteady movements were observed. It is believed that these symptoms stemmed from the toxic effects of toluene. When resveratrol was administered, it was observed that the bleeding symptoms ceased and the rats regained their normal mobility. These findings support the protective properties of resveratrol. In previous studies, symptoms

induced by toluene in rabbits included vomiting within 2-3 hours, bleeding from the mouth and nose, and signs of imbalance [16].

According to the MDA analyses, it is observed that toluene injection leads to a significant increase in MDA levels. The reason for this increase may be due to toluene's lipophilic properties, allowing it to easily interfere with lipid structures in the cell membrane and interact with proteins. In a previous study, it was determined that prolonged inhalation of thinner increased lipid peroxidation in lung and liver tissues. One study suggests that inhalation of thinner can accelerate ROS formation, triggering lipid peroxidation [17].

In another study, it was noted that exposure to high doses of toluene triggers oxidative stress, increasing the formation of reactive oxygen species (ROS) and reactive nitrogen species (RNS). This condition was stated to directly cause tissue damage and have an impact on antioxidant systems [18].

In the tissue and serum samples we examined in our study, significant differences in GSH levels were identified in the group treated with toluene. It is known that in an organism exposed to organic solvents and smoking, diseases like cancer develop due to the increase of ROS and free radicals. In this context, GSH, which has antioxidant properties, plays a critical role in neutralizing accumulated free radicals. This process can lead to a decrease in the body's antioxidant capacity [19]. Additionally, GSH has various critical functions in biological processes such as DNA synthesis, repair of damaged DNA, execution of metabolic functions, neutralization of toxins, and protection against potential harms of free radicals [20].

In our study, a decrease in GSH and MDA levels was observed following the application of resveratrol. We believe that this change is due to resveratrol neutralizing ROS. Some studies indicate that resveratrol is highly effective in removing reactive oxygen species from the cell, such as O_2- anions, ROS, and H_2O_2, by preventing cellular damage and apoptosis during oxidative stress [21, 22].

Toluene has been observed to increase GSH and MDA levels in both lung tissue and serum. This increase may be attributed to toluene triggering oxidative stress and subsequently initiating lipid peroxidation. When examining lung tissue samples, although there were significant differences between the control and experimental groups, no significant change in GSH values was detected between toluene and toluene+resveratrol injections. However, in serum samples, it is evident that toluene and varying doses of toluene+resveratrol injections significantly influenced GSH activity. These findings demonstrate the enhancing effect of resveratrol, especially at high doses, on GSH activity in lung tissue. Elevated antioxidant levels can reduce the amount of ROS. This condition can lead to a decrease in lipid peroxidation by clearing free radicals, consequently resulting in a reduction in MDA levels.

When MDA levels were carefully examined, it was observed that the MDA levels in the lung tissue of groups treated with toluene increased compared to the control groups. On the other hand, a different picture emerges in serum samples; a significant difference in MDA levels was detected between groups receiving toluene and those receiving toluene+resveratrol injections.

According to the results of this study, a protective effect of resveratrol on oxidative stress and antioxidant activity has been determined. An increase in MDA levels in the lung tissue and serum due to the effect of toluene was observed, while an increase in GSH levels in the lung tissue was also noted.

These findings indicate the need for further research to more comprehensively understand the protective mechanisms of resveratrol and its regulatory effects on GSH. Evaluating the experimental results by administering resveratrol via gavage at 40 mg/kg/day and 80 mg/kg/day for 10 weeks may create new perspectives.

Conflict of interest

There is no conflict of interest among the authors.

Acknowledgement

The article is based on the master's thesis titled "Investigation of the protective properties of resveratrol on oxidative stress effects due to toluene exposure" completed by Ahmad Baratov in the Department of Molecular Biology, Biology Division, Graduate School of Natural and Applied Sciences, Bursa Uludağ University, Bursa. We would like to thank Emine Gonca PEKEL, Oğuzhan Akgün, and Raissa SOAMANJARY for their contributions to this study.

Ethical Approval Statement

This study was supported by the Scientific Research Projects Unit of Bursa Uludağ University, (QUAP(F)-2019/14). The experiments were conducted in accordance with the ethical committee decision numbered 2019/04-03 obtained from the local ethics committee for animal experiments and adhered to the Helsinki Declaration revised in 2013.

References

[1] Mohammad M.F., Mousa L.Y., Idayyir D.H., Kadim Z.M., The Toxic Effects of Toluene on Oxidative Stress Status in the Genital System of Female Mice, *TMJ*., 44 (6) (2021) 3345-3353.

[2] Özcan O., Erdal H., Çakırca G., Yönden Z., OxidativeS and Its Impacts on Intracellular Lipids, Proteins and DNA, *JCEI*., 6 (3) (2015) 331-336

[3] Cederbaum A.I., Cytochrome P450 2E1-Dependent Oxidant Stress and Upregulation of Anti-Oxidant Defense in Liver Cells, *J Gastroenterol Hepatol.*, 21 (2006) 22–S5.

[4] Finaud J., Lac G., Filaire E., Oxidative Stress, *Sports Med*., 36 (4) (2006) 327-358.

[5] Filley C.M., Halliday W., Kleinschmidt-Demasters, B.K., The Effects of Toluene on The Central Nervous System, *J Neuropathol Exp Neurol.*, 63 (1) (2004) 1-12.

[6] Jadimurthy R., Jagadish S., NayakS.C., Kumar S., Mohan C.D., Rangappa K.S., Phytochemicals as Invaluable Sources of Potent Antimicrobial Agents to Combat Antibiotic Resistance, *Life,* 13 (2023), 948.

[7] Wallerath T., Deckert G., Ternes T., Anderson H., Li H., Witte K., Förstermann U., Resveratrol, aPolyphenolic Phytoalexin Present in Red Wine, Enhances Expression and Activity of Endothelial Nitric Oxide Synthase, *Circulation,* 106 (13) (2002) 1652-1658.

[8] Montero C., Cristescu S.M., Jiménez J.B., Orea J.M., Hekkert S.L., Harren F.J.M., Ureña A.G., trans-Resveratrol and Grape Disease Resistance. A Dynamical Study by High-Resolution Laser-Based Techniques, *Plant Physiol.,* 131 (1) (2003) 129–138.

[9] Xia N., Daiber A., Förstermann U., Li H., Antioxidant Effects of Resveratrol in the Cardiovascular System, *British J Pharmacol.*, 174 (12) (2017) 1633–1646.

[10] Leifert W.R., Abeywardena M.Y., Cardioprotective Actions of Grape Polyphenols, *Nutr Res*., 28 (2008) 729–37.

[11] Lushchak V.I., Glutathione Homeostasis and Functions: Potential Targets for Medical Interventions, *J. Amino Acids.* 2012 (2012) 26

[12] Wu G., Fang Y.Z., Yang S., Lupton J.R., Turner N.D., Glutathione Metabolism and its Implications for Health, J Nutr., 134 (2004) 489–492.

[13] Cheng S.B., Liu H.T., Chen S.Y., Lin P.T., Lai C. Y., Huang Y.V., Changes of Oxidative Stress, Glutathione, and Its Dependent Antioxidant Enzyme Activities in Patients with Hepatocellular Carcinoma before and after Tumor Resection, *PLoS One*, 12(1) (2017)

[14] Tsikas D., Assessment o Lipid Peroxidation by Measuring Malondialdehyde (MDA) and Relatives in Biological Samples: Analytical and biological challenges, *Anal Biochem.,* 524 (2017) 13-30.

[15] Danuta R., Juan D.S., Gabriella W., Mohan R., Ioli M., Stefan P., Jean O., Samuel D. Lipid Profile Analysis in Spinal Trauma Patients Shows Severe Distortion of AA/DHA after Injury, *Front Immunol,* 4 (2013)

[16] Çiçek M., Şişman T., Akut Tolüen Maruziyetinin Tavşan Beyin Korteksinde Yol Açtığı Toksik Etkiler, *Etlik Vet Mikrobiyol Derg.*, 28 (1) (2017) 33-38.

[17] Ulakoğlu Z. E., Saygı A., Gümüştaş M.K., Zor E., Akkaya A., Kökoğlu E., The efEfect of Chronic Thinner İnhalation on Lipid Peroxidation in Rat Lung and Liver, *Cerrahpaşa J. Med,* 29 (2) (1998) 75-78.

[18] Choi G.S., Trinh H.K.T., Yang E.M., Ye Y.M., Shin Y.S., Kim S.H., Park H.S. Role of Clusterin/Progranulin in Toluene Diisocyanate-İnduced Occupational Asthma, *Exp Mol Med,* 50 (5) (2018).

[19] Park J.J., Chang H., Jung J.Y., Jung S.J., Song K.H., Suh W.N., Chun S.W., Lee H. Y.Yoo T.H., A Case of Tolüene-induced Renal Tubular Acidosis Presented with Hypokalemic Paralysis, *JKSEM,* 17 (6) (2006) 656-658.

[20] Chavan S., Sava L., Saxena V., Pillai S., Sontakke A., Ingole D., Reduced Glutathione: Importance of Specimen Collection, *Indian J Clin Biochem*, 20 (1) (2005) 150-152.

[21] Das D.K., Maulik N. Resveratrol in Cardioprotection: a Therapeutic Promise of Alternative Medicine, *Mol. Interv.*, 6 (1) (2006) 36-47.

[22] Bircan C.I., Merhan O., Kadmiyum Uygulanan Farelerde Oluşturulan Oksidatif Strese Karşı Resveratrolün Koruyucu Etkisinin Araştırılması, *Erciyes Üniv. Vet. Fak. Derg.,* 17 (3) (2020) 215-220.

Cumhuriyet Sci. J., 45(2) (2024) 194-200
DOI: https://doi.org/10.17776/csj.1316115

Cumhuriyet Science Journal

| csj.cumhuriyet.edu.tr | Founded: 2002 ISSN: 2587-2680 e-ISSN: 2587-246X Publisher: Sivas Cumhuriyet University

New Circular Distribution with an Application to Biology

Phani Yedlapalli [1,a,*], Venkata Sesha Girija Sagi [2,b], Peddi Raju Cherukuri [3,c], Naveen Venkata Kishore Gajula [4,d]

[1] *Department of Mathematics, Shri Vishnu Engineering College for Women (Autonomous), Vishnupur, Bhimavaram, AP-India.*
[2] *Department of Mathematics, Hindu College, Guntur, AP-India.*
[3] *Department of Mathematics, Swarnandhra College of Engineering and Technology (Autonomous), Seetharamapuram, Narsapur-AP-India.*
[4] *Department of Mathematics, SRKR Engineering College (Autonomous), Chinnaamiram, Bhimavaram, AP-India.*
**Corresponding author*

Research Article

History
Received: 17/06/2023
Accepted: 27/02/2024

ABSTRACT

In this paper, we introduce a new circular distribution known as the wrapped new weighted exponential distribution (WNWE) is introduced. We derive an explicit expression for its probability density function and establish closed-form expressions for the distribution function, characteristic function, and trigonometric moments. Furthermore, we discuss the properties of the proposed model. We employ the method of maximum likelihood estimation to estimate the parameters. To demonstrate the applicability of the proposed distribution, we analyze a real dataset consisting of 50 starhead top minnows.

Keywords: Circular data, Weighted exponential distribution, Characteristic function, Moments, Wrapped distributions.

[a] *phaniyedlapalli23@gmail.com* *https://orcid.org/0000-0002-3402-8920*
[b] *svs.girija@gmail.com* *https://orcid.org/0000-0003-4471-5203*
[c] *peddirajc@gmail.com* *https://orcid.org/0000-0001-8828-3057*
[d] *kishore.apr2@gmail.com* *https://orcid.org/0000-0001-7260-4071*

Introduction

Levy [1] put forward an innovative mechanism for introducing a wrapped variable to the symmetric and asymmetric distributions, which is acknowledged in the literature as wrapped distributions. The wrapping and inverse stereographic projection methods are established approaches to obtain circular models with the help of linear distributions [2]. Srinivasa Rao Jammalamadaka et al. [3-5] developed circular models obtained by wrapping the classical exponential and Laplace distributions on the real line around the unit circle and present explicit forms for their densities and distributions. Rao et al. [6] discuss wrapped versions of some models, such as wrapped Weibull, lognormal, extreme-value and logistic distributions and their population characteristics. Roy et al. [7] developed a new circular model called wrapped weighted exponential distribution. Roy et al. [8] derived a class of wrapped generalized Gompertz distribution and is used to analyze data on the headings of the orientation of the nests of noisy scrub birds. Girija et al. [9-10] derived some circular and semicircular models with the application of inverse stereographic projection and derived some statistical properties. Rao et al. [11] proposed a circular version of logistic distribution by inducing inverse stereographic projection. Phani et al. [12-15] constructed some semicircular distributions by using inverse stereographic projection on linear models and derived their trigonometric moments. Savitri Joshi et al. [16] explored wrapped Lindley distribution. Abdullah Yilmaz et al. [17] introduced a new wrapped exponential distribution by using the transmuted rank quadratic map method. Ahmad et al. [18-20] derived some wrapped circular distributions and studied their properties. Ayat T.R. Al-Meanazel et al. [21] constructed a wrapped Shankar distribution. Phani Yedlapalli et al. [22] derived a family of semicircular and circular Arc tan-exponential type distributions and presented some distributional properties. Ayesha Iftikhar et al. [23] developed half circular modified burr-III distribution and presented different estimation methods. In this study, we draw upon prior research contributions for contextual grounding, notably referencing Karakaya and Karakaya et al.'s [24] investigation into various estimation techniques for the one-parameter Akash distribution, Tanış et al.'s [25] examination of the Transmuted Complementary Exponential Power distribution, and Korkmaz et al.'s [26] study on parameter estimation for the Unit log-log Distribution.

In the present study, we introduce wrapped new weighted exponential distribution by wrapping the density function of the new weighted exponential distribution (Oguntunde et al. [27] along a circle of radius of unity and delve into its characteristics. In the second section of our paper, we delineate a methodology for developing a circular variant of the new weighted exponential distribution by leveraging the principle of wrapping a univariate density function. We are able to derive explicit equations for the probability density function (pdf) and cumulative distribution function (cdf) of the proposed model. In the third section, we derive the characteristic function, trigonometric moments and other

properties are discussed. The maximum likelihood estimation method is discussed to estimate the proposed model parameters in the fourth section. In the fifth section, we utilize the proposed model to analyze a real dataset comprising the orientation of fifty starhead top minnows. To evaluate its effectiveness, we compare its performance with that of the wrapped Lindley distribution (Joshi et al., [16] and the wrapped exponential distribution (S. Rao et al., [2] using model selection criteria such as Akaike Information Criteria (AIC), Bayesian Information Criteria (BIC), and log-likelihood.

Definition and Derivation

In this section, we describe a method of synthesis for the circular version of a new weighted exponential distribution following the methodology of wrapping of univariate density (Jammalamadaka et al. [11]).

Let X follows new weighted exponential distribution (Oguntunde et al. [27], then the probability density function of X is given by

$f(x) = (\alpha + \lambda\alpha)\, exp(-(\alpha + \lambda\alpha)x);$

where

$x > 0, \alpha > 0$ is the scale parameter and $\lambda > 0$ the shape parameter.

Now, the circular (wrapped) new weighted exponential random variable is defined as

$\theta = X(mod\, 2\,\pi)$, such that for $\theta \in 0,2\pi)$, the probability density function of the proposed model can be expressed as follows:

$$g_{nwe}(\theta) = \sum_{j=0}^{\infty} f_X(\theta + \pi 2j)$$

$$= (\alpha + \lambda\alpha) \sum_{j=0}^{\infty} e^{-(\alpha+\lambda\alpha)(\theta+\pi 2j)}$$

$$= (\alpha + \lambda\alpha) e^{-(\alpha+\lambda\alpha)\theta} \sum_{j=0}^{\infty} e^{-2\pi(\alpha+\lambda\alpha)j} \quad (1)$$

$$g_{nwe}(\theta) = \frac{(\alpha + \lambda\alpha)\exp\left(-(\alpha + \lambda\alpha)(\theta - \pi)\right)}{2\sinh\left(\pi(\alpha + \lambda\alpha)\right)},$$

$\theta \in [0, 2\pi)$ Where $\lambda > 0, \alpha > 0.$

The random variable θ having wrapped new weighted exponential distribution is denoted by $\theta \sim$WNWE(α, λ).

Special case:

When$\lambda \to 0$, the wrapped new weighted exponential distribution approaches to the wrapped exponential distribution.

Figures 1 and 2 depict plots of the probability density function of the wrapped new weighted exponential distribution and its circular representation for various values of the shape parameters.

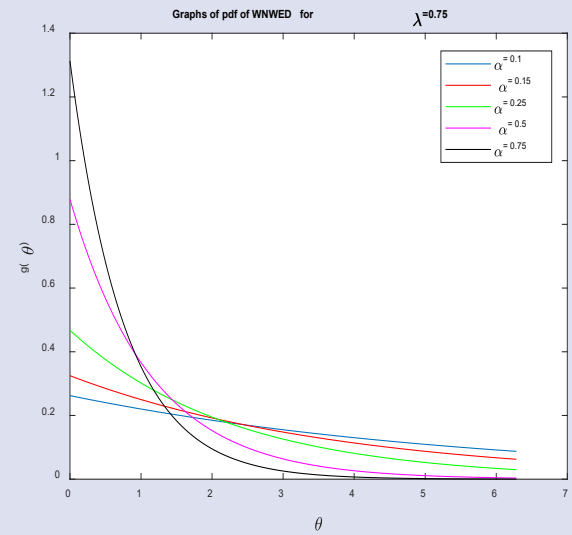

Figure 1. Pdf plots of wrapped new weighted exponential distribution.

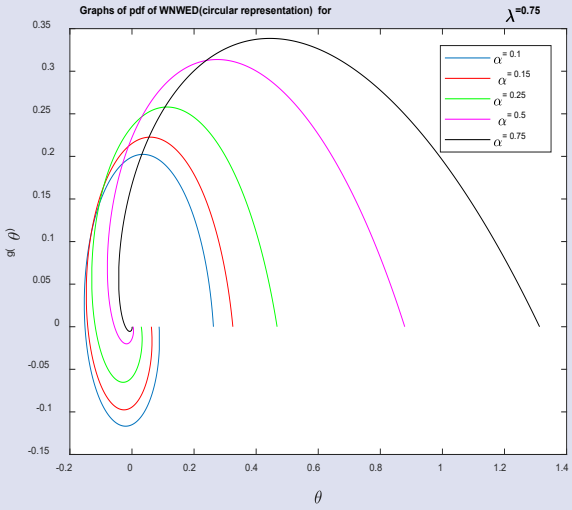

Figure 2. Pdf plots of wrapped new weighted exponential distribution (circular representation).

The cumulative distribution of WNWE(α, λ) is obtained as follows (Jammalamadaka and Sengupta (2001))

$$G_{nwe}(\theta) = \sum_{j=0}^{\infty} [F_X(\theta + \pi 2j) - F_X(2\pi j)],$$

$$G_{nwe}(\theta) = \frac{exp(\pi\alpha(1+\lambda))\,(1 - exp(-\alpha(1+\lambda)\theta))}{2\, sinh(\pi\alpha(1+\lambda))}, \quad (2)$$

$\theta \in 0,2\pi).$

Figures 3. and 4. depict plots of the cumulative distribution function for both the wrapped new weighted exponential distribution and its circular representation.

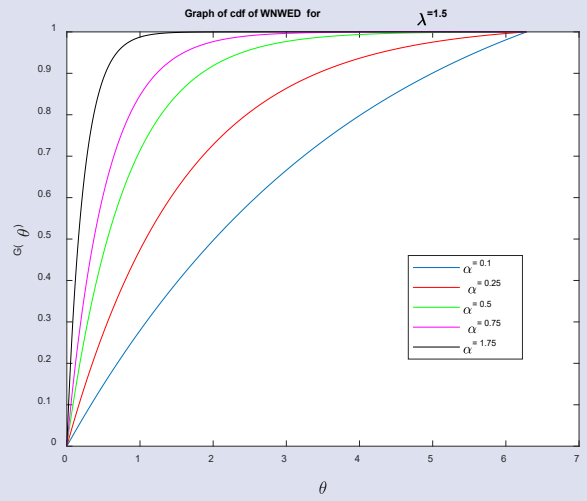

Figure 3. Plots of cdf of wrapped new weighted exponential distribution.

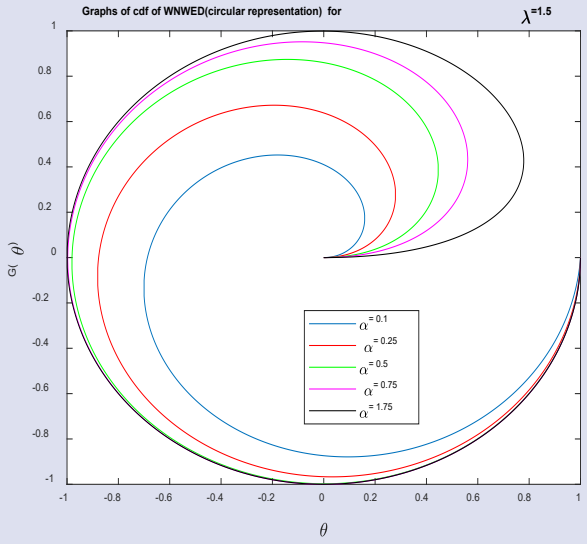

Figure 4. Plots of cdf of wrapped new weighted exponential distribution (circular representation)

Properties

In this section, we derive the closed-form expressions for various statistical properties of the proposed model. These include the characteristic function, trigonometric moments, and several other important characteristics such as the resultant length, circular mean, circular variance, standard deviation, coefficient of skewness, kurtosis, and entropy. By obtaining these analytical expressions, we gain valuable insights into the behavior and descriptive measure of the proposed model, allowing for a comprehensive understanding of its characteristics.

Characteristic Function and Trigonometric Moments

The characteristic function of a circular random variable θ is the doubly-infinite sequence of complex numbers $\{\varphi_p : p \in Z\}$ given by $\varphi_p = E(e^{ip\theta})$

$$\begin{aligned}\varphi_p &= \int_0^{2\pi} e^{ip\theta} d(G(\theta)) \\ &= \frac{\alpha(1+\lambda)}{(1-e^{-2\pi\alpha(1+\lambda)})} \int_0^{2\pi} e^{ip\theta} e^{-\alpha(1+\lambda)\theta}\, d\theta \\ &= \frac{\alpha(1+\lambda)}{(1-e^{-2\pi\alpha(1+\lambda)})} \int_0^{2\pi} e^{-(\alpha(1+\lambda)-ip)\theta}\, d\theta \\ \varphi_p &= \frac{\alpha^2(1+\lambda)^2}{\alpha^2(1+\lambda)^2+p^2} + i\frac{\alpha(1+\lambda)p}{\alpha^2(1+\lambda)^2+p^2} \\ &= \alpha_p + i\beta_p. \end{aligned} \quad (3)$$

Where $\alpha_p = \frac{\alpha^2(1+\lambda)^2}{\alpha^2(1+\lambda)^2+p^2}$, $\beta_p = \frac{\alpha(1+\lambda)p}{\alpha^2(1+\lambda)^2+p^2}$, $p \in \mathbb{Z}$.

are non-central trigonometric moments of wrapped new weighted exponential distribution.

$\varphi_p = \rho_p e^{i\mu_p^0}, p \geq 0$, so that

$$\rho_p = \sqrt{\alpha_p^2 + \beta_p^2} = \frac{(1+\lambda)\alpha}{\sqrt{(1+\lambda)^2\alpha^2 + p^2}}. \quad (4)$$

$$\mu_p^0 = tan^{-1}\left(\frac{p}{\alpha(1+\lambda)}\right). \quad (5)$$

Quantile Function

The quantile function can be obtained from the root of the equation $G(\theta) - u = 0$with respect to θ as

$$Q(u) = \frac{1}{(\alpha\lambda+\alpha)} ln\left(\frac{1}{(1-u(1-e^{-2\pi\alpha(\lambda+1)}))}\right), \quad (6)$$

where $u \in (0,1)$.

Median

$$Q(0.5) = \frac{1}{\alpha(1+\lambda)} ln\left(\frac{2}{(1+e^{-2\pi\alpha(1+\lambda)})}\right). \quad (7)$$

Resultant Length

$$\rho = \rho_1 = \frac{(1+\lambda)\alpha}{\sqrt{(1+\lambda)^2\alpha^2+1}}. \quad (8)$$

Mean Direction

$$\mu = \mu_1^0 = tan^{-1}\left(\frac{1}{\alpha(1+\lambda)}\right). \quad (9)$$

Circular Variance

$$V_0 = 1 - \rho = 1 - \frac{(1+\lambda)\alpha}{\sqrt{(1+\lambda)^2\alpha^2+1}}. \quad (10)$$

Circular Standard Deviation

$$\sigma_0 = \sqrt{-2\log_e(1-V_0)} = \sqrt{\log_e\left(1+\frac{1}{(1+\lambda)^2\alpha^2}\right)}. \quad (11)$$

Central Trigonometric Moments

$$\overline{\alpha_p} = \rho_p \cos(\mu_p - p\mu_1) = \frac{(1+\lambda)\alpha}{\sqrt{(1+\lambda)^2\alpha^2+p^2}} \cos\left(\tan^{-1}\left(\frac{p}{\alpha(1+\lambda)}\right) - p\tan^{-1}\left(\frac{1}{\alpha(1+\lambda)}\right)\right). \quad (12)$$

$$\overline{\beta_p} = \rho_p \sin(\mu_p - p\mu_1) = \frac{(1+\lambda)\alpha}{\sqrt{(1+\lambda)^2\alpha^2+p^2}} \sin\left(\tan^{-1}\left(\frac{p}{\alpha(1+\lambda)}\right) - p\tan^{-1}\left(\frac{1}{\alpha(1+\lambda)}\right)\right). \quad (13)$$

Skewness

$$\varsigma_1^0 = \frac{\overline{\beta_2}}{V_0^{\frac{3}{2}}} = \frac{\frac{(1+\lambda)\alpha}{\sqrt{(1+\lambda)^2\alpha^2+2^2}} \sin\left(\pi - \tan^{-1}\left(\frac{2}{\alpha^3(1+\lambda)(\alpha^2(1+\lambda)^2+3)}\right)\right)}{\left(\frac{(1+\lambda)\alpha}{\sqrt{(1+\lambda)^2\alpha^2+1}}\right)^{\frac{3}{2}}} \quad (14)$$

Kurtosis

$$\varsigma_2^0 = \frac{\overline{\alpha_2} - (1-V_0)^4}{V_0^2} = \frac{\frac{(1+\lambda)\alpha}{\sqrt{(1+\lambda)^2\alpha^2+2^2}} \cos\left(\pi - \tan^{-1}\left(\frac{2}{\alpha^3(1+\lambda)(\alpha^2(1+\lambda)^2+3)}\right)\right) - \left(\frac{(1+\lambda)\alpha}{\sqrt{(1+\lambda)^2\alpha^2+1}}\right)^4}{\left(\frac{(1+\lambda)\alpha}{\sqrt{(1+\lambda)^2\alpha^2+1}}\right)^2}. \quad (15)$$

Alternative representation of density function of wrapped new weighted exponential distribution as Fourier series

$$g_{nwe}(\theta) = \frac{1}{2\pi}\left[1 + 2\sum_{p=1}^{\infty}\left(\frac{\alpha^2(1+\lambda)^2}{\alpha^2(1+\lambda)^2+p^2}\cos(p\theta) + \frac{\alpha(1+\lambda)p}{\alpha^2(1+\lambda)^2+p^2}\sin(p\theta)\right)\right]. \quad (16)$$

Renyi and Shannon Entropy

Entropy serves as a metric to quantify the level of uncertainty associated with a random variable. There are two widely recognized types of entropy: Renyi entropy and Shannon entropy, with the latter being the limiting case of the former. In this section, we delve into the discussion of Renyi and Shannon entropy within the context of the wrapped new weighted distribution. The entropy of a circular random variable with a probability density function is given by $RE_\theta(\gamma) = \frac{1}{1-\gamma} ln \int_0^{2\pi} g^\gamma(\theta) d\theta$, where $\gamma \geq 0$ and $\gamma \neq 1$. Thus, Renyi entropy of WNWE (α, λ)distribution is obtained as

$$RE_\theta(\gamma) = \frac{2\pi\gamma}{1-\gamma}\left(ln\left(\frac{\alpha(1+\lambda)}{1-e^{-2\pi\alpha(1+\lambda)}}\right) - \pi\alpha(1+\lambda)\right). \quad (17)$$

Shannon entropy is obtained as

$$SE_\theta(1) = \pi\alpha(1+\lambda) - ln\left(\frac{\alpha(1+\lambda)}{1-e^{-2\pi\alpha(1+\lambda)}}\right). \quad (18)$$

Table 1: Population characteristics of wrapped new weighted exponential distribution

$\alpha = 1.5$ Trigonometric moments	$\lambda = 0.1$	$\lambda = 0.15$	$\lambda = 0.25$	$\lambda = 0.5$	$\lambda = 0.75$
α_1	07314	0.7485	0.7785	0.8351	0.8733
α_2	0.4050	0.4266	0.4678	0.5586	0.6327
β_1	0.4433	0.4339	0.4152	0.3711	0.3327
β_2	0.2454	0.2473	0.2495	0.2483	0.2410
Resultant length ρ	0.8552	0.8651	0.8824	0.9138	0.9345
Mean direction μ	0.5449	0.5254	0.4900	0.4282	0.3640
Circular variance V_0	0.3774	0.3670	0.3478	0.3077	0.2759
Circular standard deviation σ_0	0.5593	0.5383	0.5003	0.4246	0.3681
Central trigonometric moments					
$\overline{\alpha_1}$	0.7314	0.7485	0.7785	0.8351	0.8733
$\overline{\alpha_2}$	0.3962	0.4188	0.4616	0.553	0.6308
$\overline{\beta_1}$	0	0	0	0	0
$\overline{\beta_2}$	-0.0839	-0.0813	-0.0756	-0.0612	-0.0486
Coefficient of skewness ς_1^0	-1.5230	-1.6406	-1.8728	-2.4193	-2.8482
Coefficient of kurtosis ς_2^0	1.7267	1.9171	2.3205	3.4384	4.6759

Estimation of Parameters

In this section, we delve into the intricacies of the maximum likelihood estimation method for estimating the model parameters of the WNWE(α,λ) distribution. Consider a random sample denoted by $\theta_1,\theta_2,\theta_3,\ldots,\theta_m$ comprising observations drawn from the WNWE (α,λ)distribution. Then the likelihood function is given by

$L(\theta;\alpha,\lambda)=\prod_{i=1}^{m} g_{wnw}(\theta_i;\alpha,\lambda).$

The log-likelihood function is given by

$$l=log_e(L)=m\,log_e(\lambda+1)+m\,log_e(\alpha)-\alpha(\lambda+1)\sum_{i=1}^{m}(\theta_i)-m\,log_e\left(1-e^{-\pi\alpha 2(\lambda+1)}\right). \quad (19)$$

Taking first order partial differentiation of the log-likelihood function with respect to α and λ then equating them to zero, we get the following normal equations.

$$\frac{\partial l}{\partial\alpha}=\frac{m}{\alpha}-(\lambda+1)\sum_{i=1}^{m}(\theta_i)+\pi(\lambda+1)m2\left[\frac{e^{-\pi\alpha 2(\lambda+1)}}{1-e^{-\pi\alpha 2(\lambda+1)}}\right]=0. \quad (20)$$

$$\frac{\partial l}{\partial\lambda}=\frac{m}{(\lambda+1)}-(\alpha)\sum_{i=1}^{m}(\theta_i)+\pi\alpha m2\left[\frac{e^{-\pi\alpha 2(\lambda+1)}}{1-e^{-\pi\alpha 2(\lambda+1)}}\right]=0. \quad (21)$$

We are not able to get the closed form expression for maximum likelihood estimators. So we opted alternative way, therefore we employ a numerical approach to get the values for the parameters α and λ.

Application

In the following section, we aim to showcase the modeling behavior of the wrapped new weighted exponential distribution by applying it to a real-life dataset. Specifically, we consider the well-known dataset on sun compass orientations of 50-star head topminnows (Fundulus dispar), which is recognized as an endangered aquatic species. To analyze this dataset, we employ the wrapped new weighted exponential distribution and estimate its parameters using Mathematica's *NMaximize* command. Additionally, we calculate various statistics such as log-likelihood, AIC, and BIC for the derived distribution. The outcomes of these computations, along with the corresponding results for other comparable distributions (wrapped Lindley and wrapped exponential distributions), are summarized in Table 2.Directional preferences of starhead topminnows (Fisher B.4, [28], [29]

Sun compass orientations of 50 starhead topminnows, measured under heavily overcast conditions.

2	9	18	24	30	35	35	39	39	44	44	49	56
70	76	76	81	86	91	112	121	127	133	134	138	147
152	157	166	171	177	187	206	210	211	215	238	246	269
270	285	292	305	315	325	328	329	343	354	359		

Table2: Summary of statistics

Model	MLE	Log-likelihood	AIC	BIC
WE(λ)	(0.1149)	-95.8932	193.5157	195.1783
WL(λ)	(0.5138)	-94.7979	191.5958	193.5079
WNWE(α,λ)	(0.03014,0.11158)	-90.8212	185.4420	189.2660

The higher value of the log-likelihood statistic, along with the smaller values of AIC and BIC, unequivocally indicates that the wrapped new weighted exponential distribution provides a superior fit to the dataset compare to the wrapped exponential and wrapped Lindley distributions.

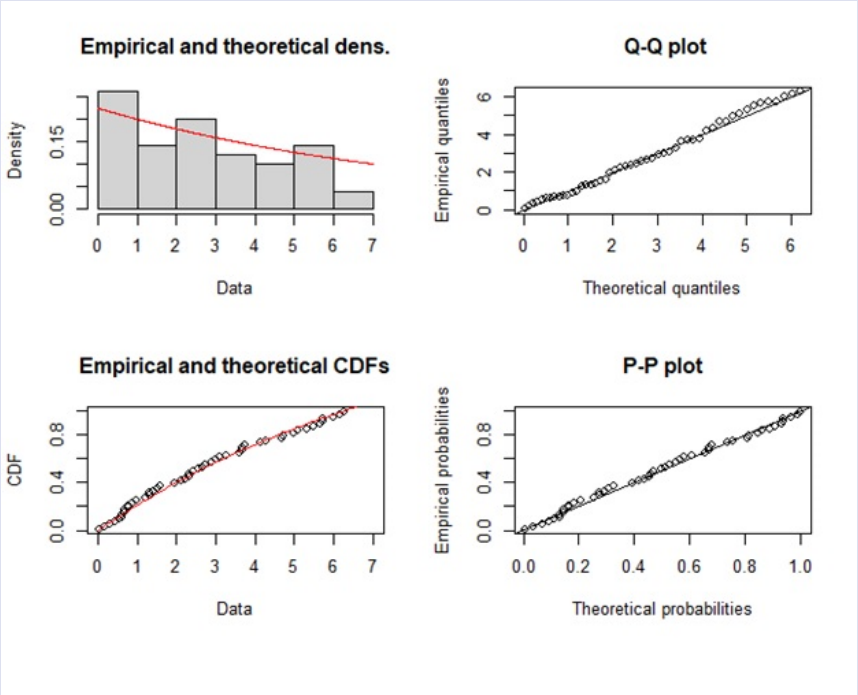

Figure 5: Depicts fitted pdf, cdf, Q-Q, and P-P plots of the wrapped new weighted exponential distribution for star head topminnows.

Closing Remarks

In the present study, we have introduced a new circular distribution referred to as the wrapped new weighted exponential (WNWE) distribution, designed specifically for modeling circular data. The probability density function (pdf), cumulative distribution function (cdf), and some characteristics have been derived in explicit form, allowing for a comprehensive understanding of the distribution's properties. To estimate the model parameters, the maximum likelihood estimation method has been employed. Furthermore, we have applied the proposed distribution to a real-life dataset for empirical validation. The performance of the proposed distribution has been rigorously examined, comparing it with that of the wrapped exponential and wrapped Lindley distributions, utilizing various statistical criteria such as log-likelihood, Akaike Information Criteria (AIC), and Bayesian Information Criteria (BIC). Based on the obtained results, it is evident that the proposed distribution exhibits a superior fit to the dataset of 50 star head top minnows compared to the wrapped exponential and wrapped Lindley distribution.

Scope for Future Work: Future research can focus on validating the WNWE distribution on diverse datasets, exploring its application in statistical and machine learning models, extending or modifying it for specific data patterns, and conducting comparative studies with other circular distributions to enhance its utility and understanding.

Conflicts of interest

The authors declare that, there are no conflicts of interest in this work.

Acknowledgments

The authors gratefully acknowledge the editor and the referees for their valuable comments and suggestions. The corresponding author, Phani Yedlapalli, would like to express sincere thanks to the management, Shri Vishnu Educational Society (SVES), of Shri Vishnu Engineering College for Women (A), Bhimavaram-534202, India, for their logistical support that helped us carry out this work.

References

[1] Levy, P.L., Addition des variables al' eateries d'efinies sur une circonf'erence. *Bull. Soc. Math*. 67(1939)1-41.

[2] Jammalamadaka S. R., Sengupta, A., Topics in Circular Statistics, New York, World Scientific, (2001).

[3] Jammalamadaka S. R., Kozubowski, T. J., A wrapped exponential circular model, *Proc. AP Acad. Sci*., 5(2001a)43–56.

[4] Jammalamadaka S. R., Kozubowski, T.J., New families of wrapped distributions for modeling skew circular data, *Communications in Statistics-Theory and Methods,*33 (9) (2004)2059-2074.

[5] S. Rao J., Tomasz J. K., A new family of circular models: The wrapped Laplace distributions, *Advances and Applications in Statistics,* (2003)1-18.

[6] Rao, A.V.D., Sarma I.R., Girija, S.V.S., On wrapped versions of some life testing models, Communications in Statistics-Theory and Methods, 36(11) (2007)2027-2035.

[7] Roy, S., Adnam, M, A, S., Wrapped weighted exponential distributions, *Statistics and Probability Letters,* 82(2012a) 77-83.

[8] Shongkour R., Arif Shams A., Wrapped Generalized Gompertz distribution: an Application to Ornithology, *Journal of Biometrics and Biostatistics,*3(6)(2012)1-4.

[9] Sagi Venkata Sesha G., A.V.Dattatreya R., and Phani Y., On Stereographic lognormal Distribution, International

Journal of Advances in Applied Sciences (IJAAS), 2(3) (2013)125-132.

[10] Sagi Venkata Sesha G., A.V. Dattatreya R., Phani Y., New Circular model induced by Inverse Stereographic projection on Double Exponential Model - Application to Birds Migration Data, *Journal of Applied Mathematics, Statistics and Informatics(JAMSI)*,10(1) (2014)5-17.

[11] Rao, A.V.D., Sagi Venkata Sesha G, and Phani Y., Stereographic Logistic Model – Application to Ornithology, *Chilean Journal of Statistics*, 7(2) (2016)69-79.

[12] Phani, Y., Girija.S.V.S., A. Dattatreya R., Circular model induced by inverse stereographic projection on extreme-value distribution, *Engineering Science and Technology,* 2 (5) (2012)881-888.

[13] Phani Y., Girija.S.V.S., A. Dattatreya R., On construction of sstereographic Semicircular Models, *Journal of Applied Probability and Statistics*, 8(1) (2013)75-90.

[14] Phani Y., A.J. Venkata R., Sagi Venkata Sesha G., A.V. Dattatreya R., On Trigonometric moments of the Stereographic Semicircular Gamma distribution, *European Journal of Pure and Applied Mathematics,* 10(5) (2017)1124-1134.

[15] Phani Yedlapalli, G.N.V.Kishore, Waddi Boulila, Anis Koubaa, and Nabil Mlaiki, Toward Enhanced Geological Analysis: a Novel Approach Based on Transmuted Semicircular Distribution. *Symmetry*, 15(2023)1-18. https://doi.org/10.3390/sym15112030.

[16] Savitri J., Jose K.K., Wrapped Lindley distribution, *Communications in Statistics-Theory and Methods*, 47(5) (2018)1013-1021.

[17] Abdullah Y., Cenker B., A new wrapped exponential distribution, *Mathematical Sciences*, 12(2018) 285-293.

[18] Ahmad M.H.Al-K., Ayat T.R.Al-M., Wrapped Akash Distribution, *Electron. J. Appl. Stat. Anal.,* 14(2) (2021)305-317.

[19] Ahmad M.H.Al-K., Ayat T.R. Al-M., Wrapped Ishita Distribution, J. *Stat. Appl. Pro.* 10(2) (2021a)293-299.

[20] Ahmad M.H.Al-K., Shawkat Al- K., On wrapping of quasi Lindley distribution, *Mathematics (MDPI),* 7(10) (2019) 1-9.

[21] Ayat T.R.Al-M., Ahmad M.H.Al-K., Wrapped Shanker Distribution*, Ital. J. Pure Appl.Math.* 46(2021) 184-194.

[22] Phani Y., Sagi Venkata Sesha G, A.V. Dattatreya R., and Sastry.K.L.N., A new family of semicircular and circular arc tan-exponential type distributions, *Thai Journal of Mathematics*,18 (2) (2020)775-781.

[23] Ayesha I., Azeem A., Muhammad H., Half circular modified burr-III distribution, application with different estimation methods, *Plos One*,7(5) (2022) 1- 21.

[24] Karakaya, K., Tanış, C., Different methods of estimation for the one parameter Akash distribution. *Cumhuriyet Science Journal*, *41*(4) (2020) 944-950.

[25] Tanış, C., Saraçoğlu, B., Kuş, C., Pekgör, A., Transmuted complementary exponential power distribution: properties and applications. *Cumhuriyet Science Journal*, (2020) *41*(2) 419-432.

[26] Korkmaz, M. Ç., Karakaya, K., Akdoğan, Y., Ünal, Y., Parameters Estimation for the Unit log-log Distribution. *Cumhuriyet Science Journal*, *44*(1) (2023) 224-228.

[27] Oguntunde, P.E., Owoloko, E.A., Balogun, O.S., On a New Weighted Exponential Distribution: Theory and Application, Asian *Journal of Applied Sciences,*9 (1) (2016) 1-12.DOI: 10.3923/ajaps.

[28] C.P. Goodyear, Terrestrial and Aquatic Orientation in the Starhead Topminnow, *Fundulus Notti, Science*,168(1970)603-605.

[29] N.I. Fisher, Statistical Analysis of Circular Data, Cambridge University Press, Cambridge, (1993).

Cumhuriyet Sci. J., 45(2) (2024) 201-209
DOI: https://doi.org/10.17776/csj.1427594

Cumhuriyet Science Journal

| csj.cumhuriyet.edu.tr | Founded: 2002 ISSN: 2587-2680 e-ISSN: 2587-246X Publisher: Sivas Cumhuriyet University

Evaluation of Bioactivity of Ethanol and Water Extracts and Determination of Nutrient Concentrations of Laurel (*Laurus nobilis*) Plants Grown in İzmir Province

Taner Dastan [1,a], Handan Sarac [1,b,*], Sevgi Durna Dastan [3,c], Ahmet Demirbas [2,d]

[1] *Department of Biochemistry, Faculty of Science, Sivas Cumhuriyet University, Sivas, Türkiye.*
[2] *Department of Plant and Animal Production, Sivas Technical Sciences Vocational School, Sivas Cumhuriyet University, Sivas, Türkiye.*
[3] *Department of Biology, Faculty of Science, Sivas Cumhuriyet University, Sivas, Türkiye.*
**Corresponding author*

Research Article

History
Received: 29/01/2024
Accepted: 19/04/2024

ABSTRACT

This study was conducted to determination of ethanol and water extracts obtained from the leaves of *Laurus nobilis* (Laurel) plant of the general content by GC-MS analysis, antimicrobial activities of these extracts on some microorganisms, total antioxidant levels (TAS), total oxidant levels (TOS), oxidative stress index (OSI) values, anti-carcinogenic effects on various cell lines and macro and micronutrient concentrations of Laurel (*Laurus nobilis*) plants cultivated for decorative purposes in parks and gardens of Izmir province of Turkey. TAS, TOS, and OSI values were determined with the aid of Rel Assay Diagnostics kits. In antimicrobial activity analysis, the minimum inhibition concentration (MIC) of the plant extracts against microorganisms was determined by microdilution broth method. *Staphylococcus aureus* (ATCC 29213), *Pseudomonas aeruginosa* (ATCC 27853), *Escherichia coli* (ATCC 25922), *Bacillus cereus* (ATCC11778), *Candida albicans* (ATCC 10231) and *Candida tropicalis* (DSM11953) microorganisms were used in this analysis. Furthermore, cytotoxic activities of plant extracts were determined by XTT method in normal rat fibroblast cell line, HUVEC, and 2 different human cancer cell lines. At the end of the study, it was found that ethanol and water extracts of the Laurel plants had no antimicrobial activity, low oxidative stress index and good antioxidant activity, and moderate cytotoxic activity on experimented cell lines. Nitrogen (N), Phosphorus (P), Potassium (P), Calcium (Ca), Magnesium (Mg), Iron (Fe), Zinc (Zn), Manganese (Mn) and Copper (Cu) concentrations of plant extracts were respectively identified as 1.68% N, 0.72% P, 1.12% K, 2.40% Ca, 0.45% Mg, 147.4 mg/kg Fe, 13.6 mg/kg Zn, 326.3 mg/kg Mn and 27.8 mg/kg Cu.

Keywords: Antimicrobial activity, Antioxidant activity, Nutrient, *Laurus nobilis* (Laurel).

[a] *tdastan@cumhuriyet.edu.tr* *https://orcid.org/0000-0003-0296-6979*
[b] *handansarac@cumhuriyet.edu.tr* *https://orcid.org/0000-0001-7481-7978*
[c] *sdurna@cumhuriyet.edu.tr* *https://orcid.org/0000-0003-4946-5602*
[d] *ademirbas@cumhuriyet.edu.tr* *https://orcid.org/0000-0003-2523-7322*

Introduction

The use of plants for treatment purposes has a long history as old as the history of humanity [1-2]. Since synthetic drugs are found to be insufficient for various diseases and have various side effects, the use of herbal natural products has become quite widespread. Therefore, many plant species have been investigated in many ways not only from microbiological and pharmacological aspects but also in terms of plant defense mechanisms [2]. Researchers especially focus on obtaining antioxidant and antimicrobial substances from the plant extracts [3].

Laurus nobilis L. (*L. nobilis,* Laurel) is a characteristic species of maquis plant cover of Mediterranean climate. Laurel is defined as ever-green shrub or tree with a height of 3-10 m [4]. Dried laurel leaves are commonly used as spice [5] and Turkey is the leading exporter of laurel leaves [6]. Researchers revealed antibacterial, diaphoretic, analgesic, antiseptic, and insecticidal effects of laurel leaves, and plant leaves were also found to be effective and alleviative for various diseases including stomach disorders, diabetes, migraine, asthenia, dyspepsia, abnormal menstruation, rheumatism, and insomnia [1, 6]. Anthocyanins in fruits of laurel plants are used in food, pharmaceutics, and cosmetic industries as pigment material [7-11].

All biological activities of the laurel plant, which is ethnobotanically widespread among people and consumed in many countries as a spice, have not been studied experimentally and the available literature information is insufficient. In addition, depending on the geography where it is grown, different activities can be observed in plants. So, this study was conducted to analyze the antimicrobial activities of ethanol and water extracts of laurel (*L. nobilis*) leaves, widespread in Turkey, against some microorganisms, determine the total antioxidant levels (TAS), total oxidant levels (TOS), oxidative stress index (OSI) values, anti-carcinogenic effects on various cell lines, and concentrations of macro and micronutrients in laurel leaves.

Material and Methods

Plant Material

Laurel (*L. nobilis*) plants were selected as the plant material. Plants were collected from the parks and gardens of İzmir province in July 2019 in Turkey. Plants were taxonomically identified by Dr. Mustafa Sevindik. Leaves were separated from the shoots and dried in the shade under room conditions.

Extraction

Dried leaves were ground into powder form in a home-type grinder. For extractions, 100 g ground leaf sample and 1000 mL ethanol and water solvents were used. For water extraction, weighed ground samples were supplemented with 80˚C distilled water and brewed for 30 min [12]. Following the brewing, it was filtered through filter paper (Whatman blue band) and lyophilized to remove water. For ethanol extraction, weighed samples were supplemented into 70% ethanol and extraction was performed for 6 hours in a Soxhlet device. Resultant extracts were filtered through filter papers (Whatman blue band) and evaporated in an alcohol rotary evaporator (Buchi) at 40˚C.

Macro and Micronutrient Analyses

Dry laurel leaves were ground in an agate mortar and subjected to wet-digestion in H_2O_2-HNO_3 acid mixture. Phosphorus (P) concentration was determined colorimetrically in a spectrophotometer at 882 nm in accordance with method of Murphy and Riley [13]; calcium (Ca), magnesium (Mg), potassium (K), iron (Fe), manganese (Mn), zinc (Zn) and copper (Cu) concentrations was determined in an Atomic Absorption Spectrophotometer (Shimadzu AA-7000). Nitrogen (N) concentration of laurel leaves was determined by Kjeldahl distillation method [14]. Each analysis was conducted 3 times.

GC-MS Analyses

In GC-MS analyses of resultant plant extracts, Shimadzu GCMS QP 2010 ULTRA device equipped with RTX-5MS capillary column (30 m; 0.25 mm; 0.25 μm) apparatus was used. Helium (0.7 mL/min) was used as the carrier gas, the column oven temperature was set at 40˚C and the injection temperature was set at 250˚C. Pressure was set at 100 kPa, injection mode was selected as split and split rate was selected as 5. Injection volume was 1.0 microliter, and oven temperature program was arranged as: 3 min at 40˚C, 53 min from 40˚C to 240˚C with 4˚C/min gradients. Interface temperature was preferred as 250˚C and ion source temperature as 200˚C. Finally, dilution was performed with 1/10 hexane.

Antimicrobial Activity

The antimicrobial activity of laurel plants was determined through finding out the minimum inhibition concentration (MIC) of the extracts against microorganisms with the aid of the "Microdilution Broth Method" [15]. The microorganism strains used in this study were *Staphylococcus aureus* (ATCC 29213), *Pseudomonas aeruginosa (*ATCC 27853), *Escherichia coli* (ATCC 25922), *Bacillus cereus* (ATCC11778), *Candida albicans* (ATCC 10231) and *Candida tropicalis* (DSM11953).

Plant extracts were dissolved in 40% dimethyl sulfoxide (DMSO) to get concentrated solutions. Mueller Hinton Broth (Accumix® AM1072) broth medium was used for bacteria strains and Saboraud Dextrose Broth (Himedia ME033) broth medium was used for *Candida albicans* and *Candida tropicalis*. The wells on the first row of microtiter plates were supplemented with 90 µL broth medium and the other wells were supplemented with 50 µL broth medium. The wells on the 11th row were used as sterile control and each of them was supplemented with 100 µL broth medium [16-17]. The wells on the 12th row were used as propagation control. The wells on the first row were then supplemented with 10 µL extract and serial dilutions were performed. Microorganisms propagated in blood agar broth medium were taken with a loop and a suspension was prepared with these microorganisms at McFarland 0.5 turbidity. Each well was supplemented with 50 µL bacterial suspension as to have 5 x10^5 CFU/mL for bacteria and 0.5-2.5 x10^3 CFU/mL for *Candida albicans* and *Candida tropicalis*. Plates containing bacteria were incubated at 37˚C, while those containing *Candida albicans* and *Candida tropicalis* were incubated at 35˚C for 16-24 hours. Herein, the first wells with the reduced image of bacteria colony were accepted as MIC values. Tests were repeated 3 times and similar results were obtained on each time.

Antioxidant Activity

Total antioxidant levels (TAS), total oxidant levels (TOS) and oxidative stress index (OSI) values were determined with the aid of commercially available Rel Assay Diagnostic kits [18-19]. Trolox standard was used for TAS analyses, hydrogen peroxide standard was used for TOS analyses. Oxidative stress index (OSI) was calculated with the aid of the following equation (Arbitrary Unit = AU) [19].

$$\text{OSI (AU)} = \frac{\text{TOS, } \mu\text{mol } H_2O_2 \text{ equiv./L}}{\text{TAS, mmol Trolox equiv./L X 10}} \quad (1)$$

Cell Cultures

Breast cancer cell line (MCF-7) (Human breast adenocarcinoma cell), healthy human endothelial cell line (HUVECs; human umbilical vein endothelial cell), human glioblastoma cell line (U87) and rat fibroblast cell line (L929) were used in this study.

Cell Growth and Propagation

All cell lines were cultured in an incubator including 37˚C 5% CO_2 in 25 cm^2 flasks (Corning-Sigma-Aldrich St. Louis, MO, USA) with Dulbecco's modified Eagle's medium (DMEM) containing high glucose, 2 mM L-glutamine and sodium pyruvate and 10% Fetal Bovine serum (FBS) medium. Cell growth and morphology were monitored and sowing was performed when 90% density was achieved (Nuve MN 120). Each well (96 of them, 100 µl/plate empty space as to have 5x10^3 cells) was supplemented with 200 µL mixture. DMEM, fetal bovine serum (FBS), and sterile phosphate buffer (PBS) were supplied from commercial Gibco (Invitrogen). Before sowing them into plates, cells were passaged, stained with Triptan Blue and cell counts were performed on the Thoma Glass slide (Iso Lab) just to sow certain number of cells to each well. For this process, counting regions over the Thoma glass slide was used. In this stage, dead cells were stained with Methylene Blue and living cells were not stained. Only the unstained cells were counted to get living cell counts. A dilution factor was also considered in calculation of number of cells per mL to get quantity of cells to be sown in each cell.

Cell proliferation test

Cytotoxic effects of plant extracts on cancerous and healthy cell lines were measured with the aid of XTT cell proliferation kit (Biotium). About 5 mL XTT solution was supplemented with 25 µL PMS and vortexed. The plant extracts prepared at 1 mg/mL stock concentration were arranged between 1 µg/mL – 1000 µg/mL doses and applied to cell cultures for 24 hours. At the end of this process, 50 µL XTT solution was supplemented into each well to get number of living cells, 96-well plates were then placed into incubator and incubated at 37˚C for 5 hours. At the end of the incubation duration, plates were placed into a microplate reader and absorbance readings were performed at 450-500 nm. At the end of XTT tests, IC_{50} values were calculated with the aid of GraphPad software. Detailed anti-cancer impact potential works were not performed on plant extracts with IC_{50} values over 100 µM. The Cancer Institute of NCBI (National Center for Biotechnology Information) assumed that the isolates with an IC_{50} value of greater than 100 µM did not have a remarkable anti-cancerogenic effect.

Statistical Analyses

SPSS 22.0 (IBM Corporation, Armonk, New York, United States) software was used in statistical analyses. Data were assessed at 95% confidence level and the ones with a p-value of less than 0.05 were considered as significant.

Results and Discussion

GC-MS Analyses Results

The GC-MS analysis results indicating the chemical composition of water and ethanol extracts of laurel leaves collected from İzmir province are provided in Table 1 and 2. GC-MS chromatograms and chromatogram peaks revealed that there were 50 different components in water extracts and 43 different components in ethanol extracts. The 2,3 Butanediol was the highest component of water and ethanol extracts (Fig. 1-2, Table 1-2).

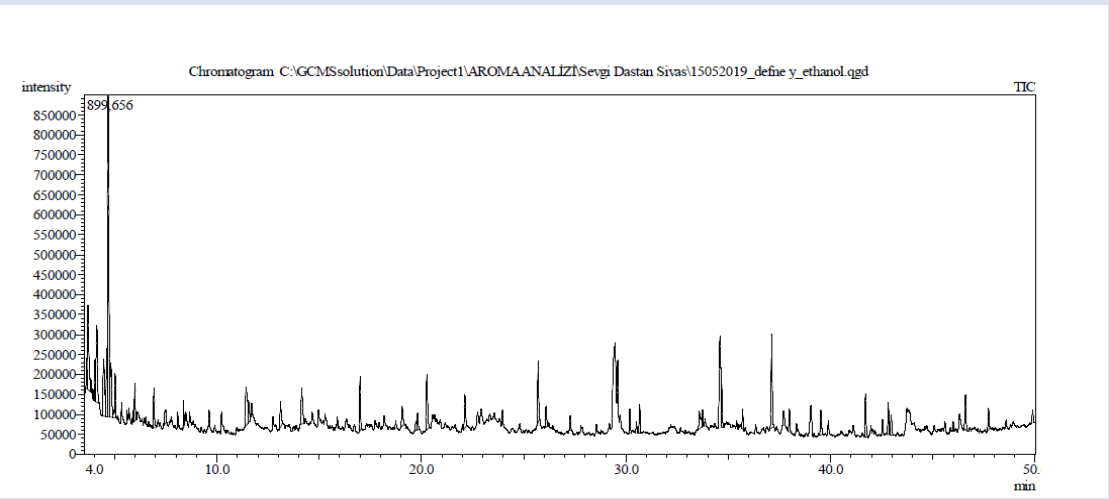

Figure 1: GC-MS chromatogram of ethanol extract of *L. nobilis*

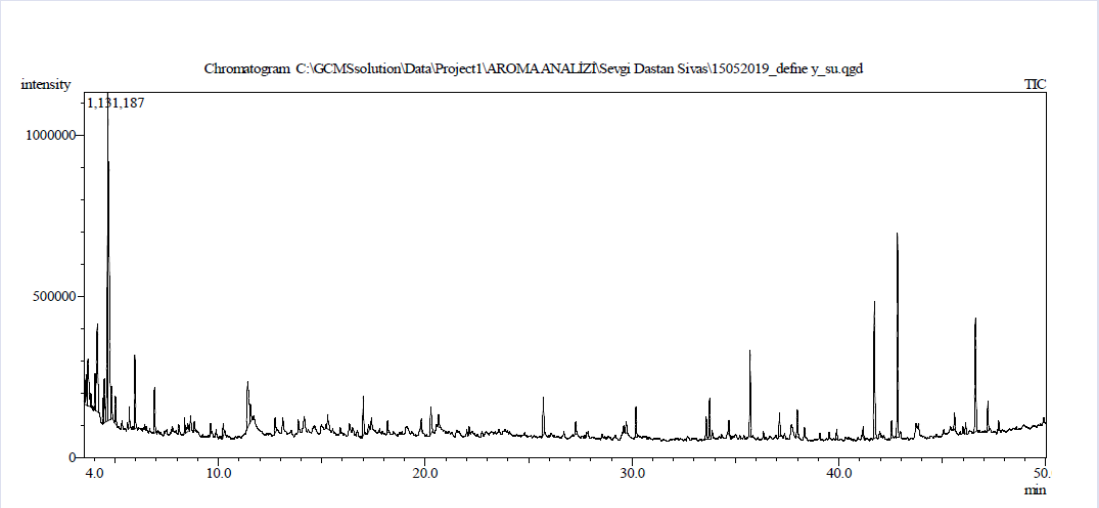

Figure 2: GC-MS chromatogram of water extract of *L. nobilis*

Table 1. Chemical composition of *L. nobilis* ethanol extract

Peak	R. Time	Area	Area%	Name
1	3.624	178222	1.00	(S)-(+)-1,2-Propanediol
2	3.698	939944	5.25	1,2-PROPANEDIOL
3	4.041	234799	1.31	Propane, 2-fluoro-2-methyl- (CAS)
4	4.141	972207	5.43	Propanoic acid, 1-methylethyl ester (CAS)
5	4.478	759617	4.24	2,3 Butanediol (CAS)
6	4.620	549220	3.07	Propanoic acid, 2-oxo-, methyl ester (CAS)
7	4.691	3632265	20.28	2,3 Butanediol (CAS)
8	4.825	622335	3.47	Hydroperoxide, 1,1-dimethylethyl (CAS)
9	5.038	407783	2.28	Propanoic acid, 2-hydroxy-, 2-methylpropyl ester
10	5.950	114915	0.64	2-Pentanone, 4-hydroxy-4-methyl- (CAS)
11	6.002	246118	1.37	2-Pentanone, 4-hydroxy-4-methyl- (CAS)
12	6.936	280395	1.57	2-Propanone, 1-(acetyloxy)- (CAS)
13	7.506	167990	0.94	Styrene
14	8.082	114813	0.64	2-Cyclopenten-1-one, 2-methyl- (CAS)
15	8.371	166509	0.93	2(3H)-Furanone, dihydro- (CAS)
16	11.420	617991	3.45	2-Hydroxy-gamma-butyrolactone
17	11.555	241142	1.35	1,2-Cyclohexanedione
18	13.117	269924	1.51	2-Cyclopenten-1-one, 2,3-dimethyl-
19	14.162	475753	2.66	Cyclohexanone, 3-methyl-, (2,4-dinitrophenyl)hydrazone (CAS)
20	17.006	366085	2.04	Silane, diethoxydimethyl-
21	19.067	227307	1.27	3,7-dimethyl-1,5-octadien-3,7-diol
22	19.710	123698	0.69	exo-2-Hydroxycineole
23	19.806	126887	0.71	Propanoic acid, di(tert-butyl)silyl ester
24	20.266	605836	3.38	2-Oxabicyclo[2.2.2]octan-6-ol, 1,3,3-trimethyl-
25	22.131	318864	1.78	2,6-DIMETHYL-1,7-OCTADIENE-3,6-DIOL #
26	25.709	522274	2.92	2b,4-dihydroxy-1,8-cineole
27	26.100	205166	1.15	Skatole
28	27.284	114754	0.64	1,3,3-Trimethyl-2-oxabicyclo[2.2.2]octane-6,7-endo,endo-diol
29	30.192	200771	1.12	Phenol, 3,5-bis(1,1-dimethylethyl)-
30	30.672	252910	1.41	2(4H)-Benzofuranone, 5,6,7,7a-tetrahydro-4,4,7a-trimethyl-, (R)-
31	33.575	295694	1.65	exo-7-(2-Propenyl)bicyclo[4.2.0]oct-1(2)-ene
32	33.746	118015	0.66	Triisobutyl(3-phenylpropoxy)silane
33	34.670	464829	2.60	
34	35.712	154377	0.86	
35	37.123	845090	4.72	Bicyclo[3.2.0]hept-2-ene, 2-methyl-
36	37.987	214742	1.20	2-Hydroxy-1,1,10-trimethyl-6,9-epidioxydecalin
37	39.535	254650	1.42	Santalol <beta->
38	41.706	391154	2.18	Hexadecanoic acid, methyl ester
39	42.544	129062	0.72	Bicyclo[3.2.0]hept-2-ene, 2-methyl-
40	42.828	256160	1.43	
41	42.966	227098	1.27	
42	46.598	317364	1.77	Methyl stearate
43	47.728	185409	1.04	1H-Pyrrole, 1-butyl-
		17910138	100.00	

Table 2. Chemical composition of *L. nobilis* water extract

Peak	R. Time	Area	Area%	Name
1	3.617	328072	1.46	Propanoic acid, 2-hydroxy-, methyl ester, (,+,)-
2	3.703	637042	2.83	1,2-PROPANEDIOL
3	3.850	106994	0.48	2-Propyn-1-ol (CAS)
4	4.047	331013	1.47	N-methyl-N-(methyl-d3)aminoheptane
5	4.160	1268209	5.64	1-Propanol, 2,2-dimethyl-, acetate
6	4.433	176771	0.79	2,3 Butanediol (CAS)
7	4.494	467707	2.08	2,3 Butanediol, [R-(R@,R@]-
8	4.663	2755610	12.25	2-Butanone, 3-hydroxy- (CAS)
9	4.713	3063565	13.61	2,3 Butanediol (CAS)
10	4.850	399272	1.77	Propane, 2-methoxy- (CAS)
11	5.035	294948	1.31	Propanoic acid, 2-hydroxy-, methyl ester
12	5.711	158896	0.71	2-Cyclopenten-1-one
13	5.984	612068	2.72	2-Pentanone, 4-hydroxy-4-methyl- (CAS)
14	6.931	340143	1.51	2-Propanone, 1-(acetyloxy)-
15	8.373	126530	0.56	2(3H)-Furanone, dihydro- (CAS)
16	8.525	140948	0.63	1-Octene, 3-ethyl- (CAS)
17	8.850	80759	0.36	2-Hydroxy-2-cyclopenten-1-one
18	9.636	74909	0.33	2,5-DIMETHYL-3(2H)FURANONE
19	10.252	95358	0.42	2-Cyclopenten-1-one, 3-methyl-
20	11.420	886872	3.94	2-Hydroxy-gamma-butyrolactone
21	11.555	195772	0.87	1,2-Cyclohexanedione
22	12.753	159276	0.71	1,2-Cyclopentanedione, 3-methyl- (CAS)
23	15.305	166064	0.74	anhydro - sugar
24	17.015	328462	1.46	Silane, diethoxydimethyl- (CAS)
25	17.255	69145	0.31	1-Tridecene
26	18.192	105795	0.47	Silanediol, dimethyl-, diacetate (CAS)
27	19.811	101333	0.45	Propanoic acid, di(tert-butyl)silyl ester
28	20.279	372956	1.66	2-Oxabicyclo[2.2.2]octan-6-ol, 1,3,3-trimethyl-
29	20.644	144869	0.64	2-Hexenal, 2-ethyl-
30	25.716	411269	1.83	2b,4-dihidroxy-1,8-cineole
31	27.289	131764	0.59	1,3,3-Trimethyl-2-oxabicyclo[2.2.2]octane-6,7-endo,endo-diol
32	29.724	131911	0.59	
33	30.195	286917	1.28	Phenol, 3,5-bis(1,1-dimethylethyl)-
34	33.587	242622	1.08	(3aS*, 5aR*, 9aS*)-3Methyldecahydro-4H-cyclopenta[c]inden-4-one
35	33.751	377720	1.68	Triisobutyl(3-phenylpropoxy)silane
36	34.688	145653	0.65	
37	35.716	772294	3.43	
38	37.127	244520	1.09	Bicyclo[3.2.0]hept-2-ene, 2-methyl-
39	37.994	306136	1.36	2-Hydroxy-1,1,10-trimethyl-6,9-epidioxydecalin
40	38.338	73733	0.33	3,7,11,15-Tetramethyl-2-hexadecen-1-ol
41	39.903	99154	0.44	Bicyclo[3.2.0]hept-2-ene, 2-methyl-
42	41.166	88777	0.39	
43	41.710	1460232	6.49	
44	42.547	161820	0.72	
45	42.837	1779015	7.91	
46	45.585	164212	0.73	1-Octadecanol (CAS)
47	46.124	116565	0.52	
48	46.602	1165995	5.18	Methyl stearate
49	47.203	258338	1.15	
50	47.728	93953	0.42	1H-Pyrrole, 1-butyl-

Antimicrobial Activity Results

Table 3. Antimicrobial activities of *L. nobilis* extracts

	E.coli	*S.aureus*	*P.aeruginosa*	*B.cereus*	*C.albicans*	*C.tropicalis*
	ATCC 25922	ATCC 29213	ATCC 27853	ATCC 11778	ATCC 10231	DSM 11953
L. nobilis water extract	2.5	5	>5	>5	>5	>5
L. nobilis ethanol extract	5	>5	>5	>5	>5	>5

The antimicrobial activity of water and ethanol extracts of laurel leaves are provided in Table 3. When the MIC values were ≤ 0.1 mg/mL, the substance is identified as important; if they have MIC values of 0.1 < MIC ≤ 0.625 mg/mL, they are classified as moderately effective and the ones with a MIC value of > 0.625 mg/mL are classified as poorly effective [20-21]. Present findings revealed that laurel leaf extracts did not have antimicrobial effects on 6 different microorganism strains.

Nutrient Concentrations Results

Macro and micronutrient concentrations of water and ethanol extracts of laurel plants collected from İzmir province are provided in Table 4.

Table 4. Some macro and micronutrient concentrations of *L. nobilis* leaf

Macro elements	N	P	K	Ca	Mg
	(%)				
L. nobilis Leaf	1.68	0.72	1.12	2.40	0.45
Micro elements	Fe	Zn	Mn	Cu	
	(mg/kg)				
L. nobilis Leaf	147.4	13.6	326.3	27.8	

For macronutrients, nitrogen concentration was identified as 1.68% N, phosphorus concentration as 0.72% P, potassium concentration as 1.12% K, calcium concentration as 2.40% Ca, and magnesium concentration as 0.45% Mg. For micronutrients, iron concentration was identified as 147.4 mg/kg Fe, zinc concentration as 13.6 mg/kg Zn, manganese concentration as 326.3 mg/kg Mn, and copper concentration as 27.8 mg/kg Cu (Table 4). Saraç with co-workers [22] reported nutrient concentrations of knotweed plants collected from Sivas region as 3.5% N, 0.259% P, 3.9% K, 0.51% Ca, 0.44% Mg, 144.7 mg/kg Fe, 40.3 mg/kg Zn, 30.1 mg/kg Mn and 7.5 mg/kg Cu. In another study, macro and micronutrient concentrations of redweed plants were reported as 3.25% N, 0.110% P, 2.13% K, 0.44% Ca, 0.10% Mg, 205.9 mg/kg Fe, 21.1 mg/kg Zn, 22.7 mg/kg Mn and 6.1 mg/kg Cu [23].

Antioxidant Activity Results

Antioxidant potentials of medicinal plants generally come from their anti-scavenging activity on reactive oxygen species. The greater the antioxidant quantity is, the greater the therapeutic impact is [23]. In the present study, water and ethanol extracts of *L. nobilis* plants had a good antioxidant capacity and extracts had oxidant substances. However, the oxidative stress index (OSI) is principally important in the assessment of antioxidant-oxidant loads of the plant extracts. *L. nobilis* extracts had low OSI values (Table 5).

Table 5. TAS, TOS, and OSI values of *L. nobilis* leaf extract

	TAS (mmol/L)	**TOS** (μmol/L)	**OSI**
L. nobilis water extract	4.839±0.102	3.712±0.076	0.075±0.063
L. nobilis ethanol extract	4.746±0.187	3.843±0.249	0.080±0.214

Values are presented as mean±SD; Experiments were made in 3 parallels.

In vitro Cytotoxic Activity Results

Different concentrations (1, 10, 100, and 1000 µg/mL) of two different extracts of laurel plants were applied to 4 different cell lines and left for incubation for 24 hours. Cytotoxic effects of extracts on different cell lines (IC_{50} values) are provided in Table 6. IC_{50} values were generally quite greater than 100 µg/mL dose. Therefore, it is possible to state that present isolates did not have remarkable cytotoxic effects on experimented cell lines. While both extracts had a moderate cytotoxic effect on MCF-7 and U87 cell lines, they had a poor cytotoxic effect on HUVEC and L929 cell lines (Table 6).

Table 6. IC_{50} levels in different cell lines of *L. nobilis* extracts

	IC-50 (µg/mL)			
	HUVEC	MCF-7	U87	L929
	Human umbilical vein endothelial cell line	Human breast adenocarcinoma cell line	Human gliablastoma cell line	Mouse fibroblast cell line
L. nobilis water extract	459.63	178.84	285.905	415.70
L. nobilis ethanol extract	548.12	237.48	621.631	472.41

As it was in the world, medicinal and aromatic plants, their extracts and drugs are widely used in treatment of various diseases in Turkey. There is still limited information available about the biological effects and impact mechanism of extracts of medicinal plants. In this study, nutrient concentrations of *L. nobilis* plants were investigated and their nutritive values, antimicrobial, antioxidant, and anticancerogenic characteristics were assessed in an integrated fashion. With IC_{50} values of 237.48 µg/mL (ethanol extract) and 178.84 µg/mL (water extract) on MCF-7 cell line, present extracts reduce the cell vigor in breast cancer cell line (MCF-7), but slightly affected cell vigor in human healthy endothelial cell line (HUVEC). With an IC_{50} value of 285.905 µg/mL, water extracts of *L. nobilis* plants had a moderate cytotoxic effect on U87 cell line. For rat fibroblast cell line, plant extracts did not have any harmful cytotoxic effects. Since a natural plant extract did not generate any damages on healthy cells, but had cytotoxic effects on cancerous cells, it was thought that these extracts could potentially be used in the development of drug preparations.

On the other hand, both water and ethanol extracts of L. nobilis plants did not have antimicrobial effect on the experimented microorganism (MIC > 0.625 mg/mL). However, there are several other microorganisms to be investigated for antimicrobial effects of these extracts. Antimicrobial effects on the other microorganisms could be investigated to better elucidate the antimicrobial activity of these extracts. Different from the present findings, antimicrobial effects of essential oils of L. nobilis plants collected from different countries, especially on S. aureus, C. albicans, E. coli-like microorganisms were reported [24-26]. In another study [27-28], antimicrobial effects of the extracts of L. nobilis plants collected from different provinces of Turkey on S. aureus and C. tropicalis-like various microorganisms were reported. In previous studies [24-26, 29], essential oils of L. nobilis plants were subjected to GC-MS analysis and 34-68 different components were identified. In the present study, 50 components were identified in water extracts and 43 components were identified in ethanol extracts of L. nobilis plants collected from Izmir province. In both extracts, 2,3 Butanediol was the major component. It is possible to identify different chemical compositions of the same plant just because of polarity of extraction solvent and geographical status of the plant collection locations [30] (Jamilah et al., 2012).

There are some earlier studies investigating antioxidant activity of different extracts of laurel plants [29, 31]. However, Rel Assay Diagnostic kits with the ability to yield outcomes at 99% confidence were used for the first time in the assessment of TAS, TOS, and OSI values of laurel extracts [32]. Antioxidant substances eliminate harmful reactions of free radicals and thus prevent degenerative diseases [23]. Present findings revealed that laurel extracts exhibit a high antioxidant capacity and low oxidative stress index thus they can be identified as a promising source of antioxidants. Therefore, they could be further investigated for their potential in obtaining and producing effective substances for the prevention of free radical-induced damages. Antioxidant activity of various other medicinal plants was investigated in previous studies. In a previous study, TAS of Mentha longifolia subsp. longifolia species, a medicinal and aromatic plant, was reported as 3.628, TOS value as 4.046 and OSI value as 0.112 [33]. In another study [34], TAS value of Salvia multicaulis plants was reported as 6.434, TOS value as 22.441, and OSI value as 0.349. When the present findings on antioxidant activity of laurel plants were compared with the above-mentioned plants, it was

seen that TAS values were between these two plants, TOS and OSI values were quite lower than Mentha sp. and Salvia sp. plants. The water extract of laurel plants had a slightly greater antioxidant capacity than the ethanol extract.

Conclusions

In this study, antioxidant, oxidant, antimicrobial, and anticancerogenic potential of *L. nobilis* plants collected from İzmir province were investigated, nutrient concentrations were determined spectrophotometrically, and the chemical composition of water and ethanol extracts were investigated through GC-MS analysis. The findings indicate that the *L. nobilis* plant has a high antioxidant potential. Although the plant extracts did not have antimicrobial effect on experimented microorganisms, they had a moderate cytotoxic effect on the tested cell lines. This study conducted to investigate the bioactive pharmacological characteristics of laurel plants, is believed to provide significant contributions to existing literature. Present findings could be used in model molecules for further studies and the design of further pharmacognosy projects.

Acknowledgement

The authors would like to thank Dr. Mehmet Atas for his aid and support, and Dr. Mustafa Sevindik for his aid in plant species identification. This study was supported by the Scientific Research Projects Department of Sivas Cumhuriyet University (Project code: YMYO-007 and V-066). This research was also presented as a summary paper at 1st International and 13th National Field Crops Congress, at the date 01-04 November 2019, Antalya, Turkey.

Conflicts of interest

The authors declare no conflict of interest.

References

[1] Baytop T. Therapy by Plants in Turkey. İstanbul University Faculty of Pharmacy Press. No: 40, İstanbul, Turkey, (1984).

[2] Kırbağ S., Kurşat M., Zengin F.K., Elazığ'da Tıbbi Amaçlar İçin Kullanılan Bazı Bitki Ekstraktlarının Antimikrobiyal Aktiviteleri*, Fırat Üni. Doğu Araş. Derg.,* 3(3) (2005) 168-171.

[3] Faydaoğlu E., Sürücüoğlu, M., Tıbbi ve Aromatik Bitkilerin *Antimikrobiyal*, *Antioksidan Aktiviteleri ve Kullanım Olanakları, Erzincan Uni. J. Sci. and Tech.,* 6(2) (2013) 233-265.

[4] Bilgin F., Şafak İ., Kiracıoğlu, Ö., Ege Bölgesinde Defne Üreticilerinin Profili, 1st International Non-Wood Forest Products Symposium, Trabzon, Turkey, *Karadeniz Technical University (KTU): Faculty of Forestry*, (2006) 60-65.

[5] Ölmez F. N., Farklı Kaynatma Sürelerinde Defneden (*Laurus nobilis* L.) Elde Edilen Renkler ve Bazı Haslık Değerleri, *YYU J. Agri. Sci.,* 14(1) (2004) 35-40.

[6] Karık Ü., Çiçek F., Oğur E., Tutar M., Ayas, F., Essential Oil Compounds of Turkey Laurel (*Laurus nobilis* L.) Populations, *Anadolu J. AARI,* 25 (2015) 1-16.

[7] Özer, S., Ülkemizdeki Bazı Önemli Orman Tali Ürünlerinin Teşhis ve Tanıtım Kılavuzu. Orman Genel Müdürlüğü Yayını, Yayın 659, Ankara, (1987).

[8] Hammer K.A., Carson C.F, Riley T.V., Antimicrobial Activity of Essential Oils and Other Plant Extracts, *J. Appl. Microbio.,* 86 (1999) 985-990.

[9] Cooper-Driver G.A., Contributions of Jeffrey Harborne and Co-workers to the Study of Anthocyanins, *Phytochem.,* 56(3) (2001) 229-236.

[10] Longo L., Vasapollo G., Anthocyanins from Bay (*Laurus nobilis* L.) Berries*, J. Agric. Food Chem.,* 53(20) (2005) 8063-8067.

[11] Ayanoğlu F., Mert A., Kaya A., Köse, E., Hatay Yöresinde Doğal Olarak Yetişen Defne (*Laurus nobilis* L.) Bitkisinin Kalite Özelliklerinin Belirlenmesi ve Seleksiyonu. Tübitak Project Report No: 108O878, 268p, Hatay, Turkey, (2010).

[12] Mata A.T., Proença C., Ferreira A.R., Serralheiro M.L.M., Nogueira J.M.F., Araújo, M.E.M., Antioxidant and Antiacetylcholinesterase Activities of Five Plants Used as Portuguese Food Spices, *Food Chem.,* 103(3) (2007) 778-786.

[13] Murphy J., Riley J.P., A Modified Single Solution for the Determination of Phosphate in Natural Waters, *Analtica Chemica Acta.,* 27 (1962) 31-36.

[14] Bremner J.M., Method of soil analysis, Part 2, Chemical and Microbiological Methods. Madison, USA: American Society of Agronomy Inc., (1965) 1149-1178.

[15] Eloff J.N., A Sensitive and Quick Microplate Method to Determine the Minimal Inhibitory Concentration of Plant Extracts for Bacteria, *Planta Med.,* 64 (1998) 711–713.

[16] CLSI, Reference Method for Broth Dilution Antifungal Susceptibility Testing of Yeasts, Approved Standard. 2nd ed., NCCLS document M27- A2. CLSI, 940 West Valley Road, Suite 1400, Wayne, Pennsylvania, USA, (2002) 19087- 1898.

[17] CLSI, Methods for Dilution Antimicrobial Susceptibility Tests for Bacteria that Grow Aerobically, Approved Standard. 9th ed., CLSI document M07-A9. Clinical and Laboratory Standards Institute, 950 West Valley Road, Suite 2500, Wayne, Pennsylvania USA, (2012) 19087.

[18] Erel O., A Novel Automated Direct Measurement Method for Total Antioxidant Capacity Using A New Generation, More Stable ABTS Radical Cation, *Clinical Biochem.,* 37(4) (2004) 277- 285.

[19] Erel O., A New Automated Colorimetric Method for Measuring Total Oxidant Status, *Clinical Biochem.,* 38(12) (2005) 1103-1111.

[20] Kuete V., Potential of Cameroonian Plants and Derived Products Against Microbial Infections: A Review, *Planta Med.,* 76 (2010) 1479–1491.

[21] Awouafack M.D., McGaw L.J., Gottfried S., Mbouangouere R., Tane P., Spiteller M., Eloff J.N., Antimicrobial Activity and Cytotoxicity of the Ethanol Extract, Fractions and Eight Compounds Isolated from *Eriosema robustum* (Fabaceae), *BMC Complementary and Alternative Med.,* 13(1) (2013) 1-9.

[22] Saraç H., Daştan T., Demirbaş A., Daştan S.D., Karaköy T., Durukan, H., Madımak (*Polygonum cognatum* Meissn.) Bitki Özütlerinin Besin Elementleri ve In vitro Antikanserojen Aktiviteleri Yönünden

Değerlendirilmesi, *SDU Ziraat Fakül. Derg.,* (2018a) 340-347.

[23] Saraç H., Daştan T., Durukan H., Daştan S.D., Demirbaş A., Karaköy T., Kırmızı Gelincik (Fam: Papaveraceae, *Glaucium grandiflorum* Boiss.&Huet var. *grandiflorum*) Bitkisinin Farklı Özütlerinin Besin Elementi İçeriğinin ve In vitro Antiproliferatif Etkilerinin Değerlendirilmesi, *SDU Ziraat Fakül. Derg.,* (2018b) 417-428.

[24] Merghni A., Marzouki H., Hentati H., Aouni M., Mastouri M., Antibacterial and Antibiofilm Activities of *Laurus nobilis* L. Essential Oil Against *Staphylococcus aureus* Strains Associated With Oral İnfections, *Current Research in Translational Med.,* 64 (2016) 29-34.

[25] Ivanović J., Mišić D., Ristić M., Pešić O., Žižović I., Supercritical CO_2 Extract and Essential Oil of Bay (*Laurus nobilis* L.) – Chemical Composition and Antibacterial Activity, *J. the Serbian Chem. Soci., 75*(3) (2010) 395-404.

[26] Marzouki H., Khaldi A., Chamli R., Bouzid S., Piras A., Falconieri D., Marongiu B., Biological Activity Evaluation of the Oils from *Laurus nobilis* of Tunisia and Algeria Extracted by Supercritical Carbon Dioxide, *Natural Product Res., 23*(3) (2009) 230-237.

[27] Digrak M., Alma M.H., Ilçim A., Antibacterial and Antifungal Activities of Turkish Medicinal Plants, *Pharmaceutical Bio.,* 39(5) (2001) 346-350.

[28] Dadalioğlu I., Evrendilek G.A., Chemical Compositions and Antibacterial Effects of Essential Oils of Turkish Oregano (*Origanum minutiflorum*), Bay laurel (*Laurus nobilis*), Spanish Lavender (*Lavandula stoechas* L.), and Fennel (*Foeniculum vulgare*) on Common Foodborne Pathogens, *J. Agric. Food Chem.,* 52(26) (2004) 8255-8260.

[29] Li R., Jiang S., Jiang Z.T., β-cyclodextrin Supramolecular Microcapsules and Antioxidant Activity of *Laurus nobilis* Essential Oil, *J. Essen. Oil Bearing Plants, 20*(6) (2017) 1511-1524.

[30] Jamilah J., Sharifa A., Sharifah N.R.S.A., GC-MS Analysis of Various Extracts from Leaf of *Plantago major* Used as Traditional Medicine, *World Appl. Sci. J., 17* (2012) 67-70.

[31] Simić M., Kundaković T., Kovačević N., Preliminary Assay on the Antioxidative Activity of *Laurus nobilis* Extracts, *Fitoterapia,* 74 (2003) 613-616.

[32] Sevindik M., Investigation of Antioxidant/Oxidant Status and Antimicrobial Activities of *Lentinus tigrinus*, *Advan. in Pharma. Sci.,* (2018) vol. 2018, Article ID 1718025.

[33] Sevindik M., Akgul H., Pehlivan M., Selamoglu Z., Determination of Therapeutic Potential of *Mentha longifolia* ssp. l*ongifolia*, *Fresen. Environ. Bull.,* 26 (2017) 4757-4763.

[34] Pehlivan M., Sevindik M., Antioxidant and Antimicrobial Activities of *Salvia multicaulis*, *Turkish J. Agri.-Food Sci. and Tech.,* 6(5) (2018) 628-631.

Cumhuriyet Sci. J., 45(2) (2024) 210-215
DOI: https://doi.org/10.17776/csj.1348667

Cumhuriyet Science Journal

| csj.cumhuriyet.edu.tr | Founded: 2002 ISSN: 2587-2680 e-ISSN: 2587-246X Publisher: Sivas Cumhuriyet University

Northernmost Locality Record of the Near Eastern Fire Salamander, *Salamandra infraimmaculata* (Martens, 1885) (Amphibia: Salamandridae) in Türkiye

Hatice Özkan [1,a], Ufuk Bülbül [1,b,*]

[1] *Department of Biology, Faculty of Science, Karadeniz Technical University, Trabzon, Türkiye.*
**Corresponding author*

Research Article

History
Received: 23/08/2023
Accepted: 30/05/2024

ABSTRACT

We provided a new locality record of *Salamandra infraimmaculata*, which is distributed in Türkiye, Syria, Lebanon, Iraq, Iran, and Israel. Five juvenile individuals belonging to the species were recorded from Yoncabayırı village located in the İmranlı district of Sivas province, Türkiye. This is the evidence for the northernmost locality of *S. infraimmaculata*. The new locality record shows that the distribution of the species may extend along the branches of the Kızılırmak River and Tozanlı and Kelkit streams. Future field observations to be performed in the northern districts of Sivas and neighboring provinces to the north may extend the distribution of the species in Türkiye. Morphometric measurements and color-pattern characteristics of the specimens of the species from the new locality were described according to the subspecies distinction. SVL ranged between 63.14 and 78.43 mm in the juveniles of *S. infraimmaculata*. The color-pattern characteristics of the specimens from the Yoncabayırı population were found similar to the color-pattern features reported in other studies for *S. i. orientalis* subspecies. The specimens caught in Yoncabayarı had the presence of small yellow spots on the dorsal, which corresponds to the general characteristic of the subspecies.

Keywords: Distribution, Morphometric measurement, İmranlı, Population, Sivas.

[a] *haticeozkan@ktu.edu.tr* *https://orcid.org/0000-0002-7810-864X*
[b] *ufukb@ktu.edu.tr* *https://orcid.org/0000-0001-6691-6968*

Introduction

The Near Eastern fire salamander, *Salamandra infraimmaculata* which is the largest species in the Salamandra genus, inhabits coastal mountainous forests from southeastern Anatolia to Israel (Türkiye, Syria, Lebanon, Iraq, Iran, and Israel) where it is threatened by habitat destruction. The species breeds during the coolest months of the year, although the subspecies *S. i. orientalis* and *S. i. semenovi*, which are restricted to high altitudes, are active during the summer months. It is entirely terrestrial, with only the females making brief visits to water to deposit their larvae [1].

A female lays 20-40 or more larvae in the water. The habitat of this nocturnal species is not far from water. The species inhabits humid forests and woodlands in mountainous and hilly regions, often found beneath leaves, between rocks, or in holes. Their habitat typically includes a nearby freshwater source [2]. *S. infraimmaculata* is classified in the Least Concern (LC) category in the IUCN Red List. The species is distributed between altitudes of 180-2000 m [3]. Although *S. infraimmaculata* is classified in the LC category, it is threatened by pesticide pollution, predation by introduced fish, residential development, transportation and service corridors, human intrusions and disturbance, climatic change (droughts), and habitat destruction, notably the damming of breeding streams [1, 3].

The species was described from Syria in 1885. There are three different subspecies of the species. *S. i. infraimmaculata* is distributed in the Hatay province of Türkiye, Syria, Lebanon, and northern Israel, while *S. i. orientalis* is found in southeastern Türkiye, and *S. i. semenovi* occurs in easternmost Türkiye, western Iran, and northern Iraq [1, 4-11].

Previously, the Turkish specimens in the Salamandra genus were accepted as the Common fire salamander, *Salamandra salamandra* (Linnaeus, 1758) [12-17]. On the other hand, the Kemaliye (Erzincan) population was assigned to *S. s. infraimmaculata* [18]. Later, this subspecies was raised to the full species level based on blood-serum protein patterns. The whole Turkish populations of the species were classified as *Salamandra infraimmaculata* [5, 19]. Molecular phylogenetic findings confirmed this classification [6, 7, 20, 21]. Subsequently, the differences in color-pattern of the three subspecies distributed in Türkiye were reported [10].

In Türkiye, the distribution of *S. infraimmaculata* is known among the Eastern (Erzincan, Tunceli, Bitlis, Bingöl, and Malatya provinces) Southern (Adana, Mersin, Hatay, Kahramanmaraş, and Osmaniye provinces), Southeastern (Gaziantep, Şanlıurfa, Adıyaman, and Diyarbakır provinces) and Central Anatolia regions (Niğde and Konya provinces) [2, 4, 22]. The distribution and taxonomic status of *S. infraimmaculata* are not clear for Turkish populations [11]. Scientific studies continue to solve this complexity. In addition to these data, the catalogue of Amphibia and Reptilia specimens in the Çanakkale Onsekiz Mart University Zoology Museum was reported and the collection of *S. infraimmaculata* from Divriği district of

Sivas province was stated without providing any locality details [23].

This study provides information on the distribution of *S. infraimmaculata* in a second district (İmranlı) of Sivas province. The new location (Yoncabayırı village of İmranlı district) is the northernmost locality record of the species in Türkiye. With the record of the present study, the known distribution area of the species has been extended about 40 km northward. This new record is an indication that the species can be found in other districts in the north of Sivas and neighboring provinces in the north of the province.

Materials and Methods

Sampling

A total of 5 juveniles of *Salamandra infraimmaculata* (Figure 1) were observed in Yoncabayırı village (N: 39° 38′ 19″ E: 38° 16′ 19″, 1606 m a.s.l.) of İmranlı district, Sivas province (Figure 2) between 4 April and 8 August 2022.

(a)

(b)

(c)

(d)

Figure 1. The juvenile individuals of *Salamandra infraimmaculata* observed in the Yoncabayırı population

In this locality, where the continental climate prevails, the habitat is composed of rocks, stabilized roads, and occasionally sparse trees. Vegetation consists of trees such as poplar (*Populus* sp.), willow (*Salix* sp.), walnut (*Juglans* sp.), oak (*Quercus* sp.), and herbaceous plants such as thyme (*Thymus* sp.) and gum tragacanth (*Astragalus* sp.).

The salamanders described in this study were observed in a water reservoir used by the villagers to store water, during a day excursion between 13.00-18.00. The geographic locations of the specimens were recorded with a GPS receiver (Garmin eTrex 20). The salamanders were caught by hand, and the morphometric measurements were performed without any anaesthesia procedure on the salamanders using a digital caliper (Mitutoyo, Kawasaki, Japan) with an accuracy of 0.01 mm. After the morphometric measurements were taken and the color and pattern characteristics of the specimens were recorded in the field, the salamanders were released back to their habitat.

According to our observations, other reptiles shared their living areas with *S. infraimmaculata* are *Pelophylax ridibundus*, *Bufotes viridis*, *Lacerta media*, *Eirenis modestus*, and *Testudo graeca* in Yoncabayırı.

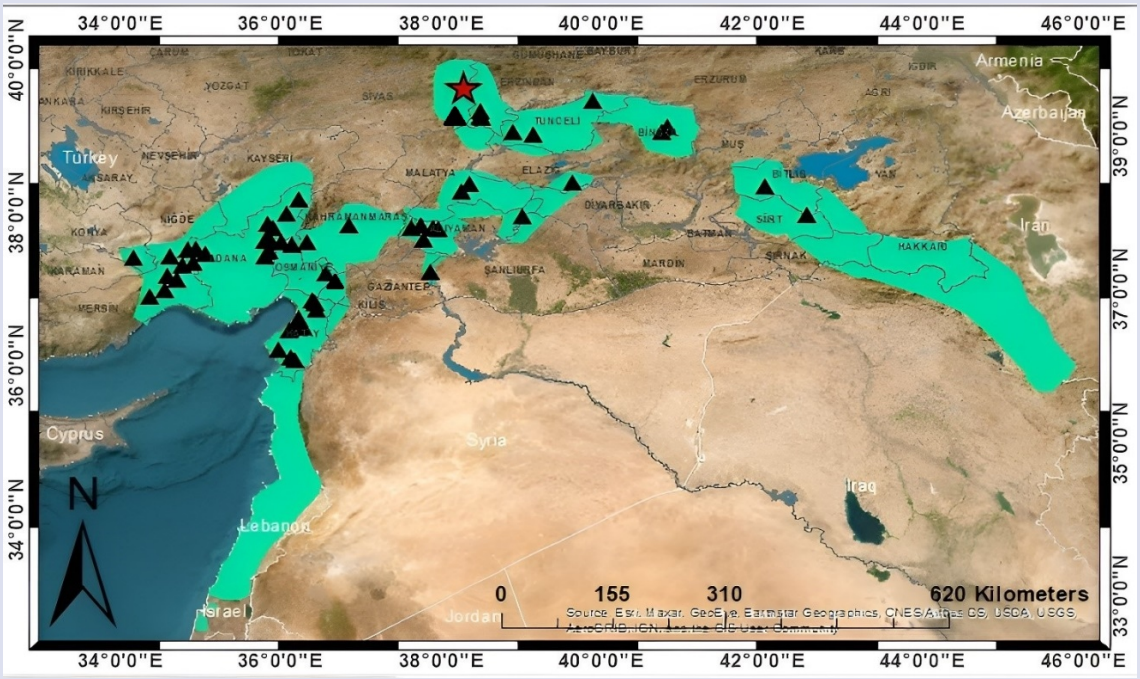

Figure 2. Map showing the localities of *Salamandra infraimmaculata*. The black triangles indicate localities previously reported in the literature and the red colored star shows the new locality (This map has been modified using the IUCN map and the locations of *S. infraimmaculata* reported in the literature [4, 10, 11, 17, 22, 23, 24-29]).

Morphological Data

All morphological measurements are given in Table 1. The following morphometric characteristics were evaluated in a manner, similar to the previous studies [4, 11, 14] related to *Salamandra infraimmaculata*: Total body length (TBL), tip of snout to tip of tail; body length (LCP), length from snout to anterior end of cloaca opening; snout-vent length (SVL), tip of snout to posterior end of cloaca opening; tail length (TL), length from posterior end of cloaca opening to tip of tail; forelimb length (FLL); hindlimb length (HLL); distance between fore and hind limbs length (DFHL); head length (HL), distance from snout to gular fold; head width (HW); parotid length (PL); parotid width (PW); distance between anterior of each parotids (DAP). The ratios of TBL/TL, TL/SVL, DFHL/SVL/, PL/HL, PW/HW, PW/PL and HW/HL were used to comparison. The morphometric measurements and ratios were compared to previously published data.

The color and pattern characteristics of the specimens were determined according to subspecies distinction. *S. i. infraimmaculata* is distinguished by its mostly large yellow dots (solid larger flecks) spread throughout the whole body, except the belly. In general, there are four yellow spots on the head (One on each paratoid and one above each eye). *S. i. orientalis* closely resembles *S. i. infraimmaculata* in appearance (having the larger broad solid flecks), except for the presence of small yellow spots covering its entire body, excluding the belly. *S. i. semenovi* is characterized by rose-like, circular spots (typical scrolled pattern of yellow rings) covering its entire body and having semicircles. The head exhibits a rather rounded shape [10, 30, 31].

Results and Discussion

SVL ranged between 63.14 and 78.43 mm in the juveniles of *S. infraimmaculata*. TBL changed from 96.18 mm to 113.52 mm. LCP varied between 60.02 and 74.27 mm. Other measurements and ratios of the specimens are given in Table 1.

In all specimens, the ground color of the upper part of the head was black and there was a yellow spot on the upper part of each eye (Figure 1). These spots above the eyes were not in contact with each other. The parotid glands were devoid of pigmentation, forming a pale dark spot. The ground color of the back was black with fire-yellow spots in a wide variety of patterns, sometimes in contact with each other, along the entire back. Different sizes of yellow spots were observed in the black background of the extremities in all specimens. Although there were large yellow spots on the dorsal parts of the specimens, there were also small yellow spots, which is a characteristic of the *S. i. orientalis*.

Salamandra infraimmaculata, whose taxonomic status and distribution are still the subject of research, is currently divided into three distinct subspecies [1, 7, 10]. *S. i. infraimmaculata* is distributed in parts close to the sea from the Hatay province in Türkiye to Israel; *S. i. orientalis* is distributed in south and southeast Türkiye, and *S. i. semenovi* is distributed in southeastern Türkiye through western Iran and northern Iraq [1, 4, 5, 7, 10] (Figure 1).

Table 1. Morphometric characteristics of the juveniles of *Salamandra infraimmaculata* from Yoncabayarı population.

Characters	1st Specimen	2nd Specimen	3rd Specimen	4th Specimen	5th Specimen
TBL	105.18	113.52	104.24	96.18	112.32
LCP	72.46	74.27	71.63	60.02	74.03
SVL	75.57	78.43	74.70	63.14	78.10
TL	29.61	35.09	29.54	33.04	34.22
FLL	21.35	22.62	20.13	18.42	22.03
HLL	24.43	26.71	23.35	21.51	26.15
DFHL	40.27	42.11	39.78	33.77	42.02
HL	20.13	21.63	19.88	16.96	21.38
HW	13.90	14.68	13.78	11.82	14.38
PL	11.73	12.12	11.38	9.79	12.01
PW	4.93	5.13	4.87	4.52	5.05
DAP	9.88	10.08	9.77	8.62	10.02
TBL/TL	3.55	3.26	3.53	2.91	3.28
TL/SVL	0.39	0.44	0.39	0.52	0.43
DFHL/SVL	0.53	0.54	0.53	0.53	0.54
PL/HL	0.58	0.56	0.57	0.58	0.56
PW/HW	0.35	0.35	0.35	0.38	0.35
PW/PL	0.42	0.42	0.43	0.46	0.42
HW/HL	0.69	0.68	0.69	0.70	0.67

The northernmost locality record (İmranlı district of Sivas province) is provided in this study. The closest locality of the Yoncabayırı-İmranlı site in the literature is the Divriği district of Sivas province [23]. The new locality record shows that the distribution of the species may extend along the branches of the Kızılırmak River. The results of this study are similar to the color-pattern features reported in other studies for *S. i. orientalis*. The color-pattern of individuals belonging to the Yoncabayırı population is the presence of small yellow spots on the dorsal of the salamanders, which corresponds to the general characteristic of the subspecies. On the other hand, the individuals of *S. i. infraimmaculata* mostly have large yellow patches on their dorsal, and the individuals of *S .i. semenovi* have rounded yellow spots on their dorsal [1, 10]. However, it is difficult to reliably distinguish between *S. i. infraimmaculata* and *S. i. orientalis* on morphological grounds [10]. Even within the same subspecies, two distinctly different color morphs can be found, as in Iraq specimens of *S. i. orientalis*. Although there was a color-pattern variation among the specimens of Iraq, Iran, and Türkiye, it was reported that the two Iraqi populations (having different color morphs), not only among each other but also with the neighboring samples from western Iran (southeast of Marivan, near Sarvabad) and eastern Türkiye (Kemaliye district of Erzincan), constituted one unit with almost no genetic distances between the specimens (range from 0.0029 to 0.0064%) after performing a barcoding test based on the fast-evolving mitochondrial COI gene. Slightly more distant from the other samples was the sample from the southeast of Türkiye (Darıpınarı, in Çamlıyayla district of Mersin province) with a genetic divergence of 0.0129-0.0151% [10]. The authors concluded that no specific difference but subspecific rank could be admitted at best.

The present study gives morphometric characters of juvenile individuals which were collected from Yoncabayırı population. However, the reports based on the morphometric measurements of *S. infraimmaculata* in the literature [4, 11, 14, 16] were generally performed the adult individuals except providing data also on juveniles [11, 14, 25, 32]. The mean SVL was 73.9 mm (63.14-78.43 mm) in the juvenile specimens of Yoncabayırı. Similar to our results, the mean SVL was 65.9 mm (53.38-78.42 mm) in two juvenile specimens of *S. i. orientalis* from Mersin province (Mezitli population) [32]. Moreover, the average body length was found to be 45.7 mm (24.2–64.8 mm) in 14 juvenile specimens of *S. i. orientalis* from Bingöl province [25]. On the other hand, it was found to be 59.7 mm (45.6–79.4 mm) in 4 subadult specimens of *S. i. orientalis* from Tunceli province [11].

The mean total body length (TBL) was 106.28 mm (96.18-113.52 mm) in the five juvenile specimens of Yoncabayırı. In addition, the average body length was found to be 81.2 mm (61.5–109.8 mm) in 14 juvenile specimens of *S. i. orientalis* from Bingöl province [25] and it was 96.4 mm (74.5–129.0 mm) in 4 subadult specimens of *S. i. orientalis* from Tunceli province [11].

Except from the mean SVL and mean total length, the ranges of LCP, TL, FLL, HLL, DFHL, HL, HW, PL, PW, DAP values and the ratios of DFHL/SVL/, PL/HL, PW/HW, PW/PL and HW/HL in the juveniles from Sivas (Yoncabayırı) were found to be almost similar to these values and ratios in the subadult specimens of *S. i. orientalis* from Tunceli [11].

The morphometric measurements of the juveniles in the Yoncabayırı population are similar to the specimens of *S. i. orientalis* used in the literature. Because of the color-pattern and morphometric similarities and the geographic distribution, we concluded that the Yoncabayırı (İmranlı, Sivas) specimens are representatives of *S. i. orientalis* subspecies.

However, the color and pattern characteristics alone do not provide adequate distinction for taxonomically assigning individuals of *Salamandra infraimmaculata* [10]. Moreover, the results obtained from morphometric measurements do not exactly coincide with the

geographical distinctions of the subspecies in some cases [33]. Phylogenetic and phylogeographic information acquired through various molecular techniques can be integrated with morphology and distribution data, resulting in a more precise taxonomic classification for the specimens of *S. infraimmaculata* [4].

In this study, we did not investigate the phylogenetic relationships of the individuals of *S. infraimmaculata* from the Yoncabayırı population with other Anatolian populations of the species. The color-pattern features alone are not sufficient to distinguish *Salamandra infraimmaculata* to taxonomically designate individuals [4, 10]. Although there are phylogenetic studies using *Salamandra infraimmaculata* samples from Türkiye, the taxonomic status of the subspecies in Türkiye has not been clearly resolved due to a limited number of samples [7, 10, 21, 22]. The taxonomic placement of the species can be made more reliable with studies containing different phylogenetic and phylogeographic information.

In conclusion, our findings show that the species can be found in different places than its known localities. Comprehensive field observations, that will be carried out along the branches of Kızılırmak River, and Tozanlı and Kelkit streams, especially in the northern districts of Sivas (Zara, Hafik, Gölova, Akıncılar, Suşehri, Koyulhisar, and Doğanşar) and other neighboring provinces (Giresun, Ordu, and Tokat), may reveal the existence of new populations of the species.

Conflicts of interest

There are no conflicts of interest in this work.

Acknowledgments

The authors thank Bayram Özdemir for his assistance in the field studies.

References

[1] Dufresnes C., Amphibians of Europe, North Africa & the Middle East: A photographic guide. London, Bloomsburgy Wildlife, (2019) 1-224.

[2] Baran İ., Avcı A., Kumlutaş Y., Olgun K., Ilgaz Ç., Türkiye Amfibi ve Sürüngenleri. Ankara, Palme Yayınevi, (2012) 1-223.

[3] IUCN SSC Amphibian Specialist Group. (2023). *Salamandra infraimmaculata*. The IUCN Red List of Threatened Species 2023: e.T59466A175607822. Available at: https://www.iucnredlist.org/species/59466/175607822. Retrieved April 25, 2024.

[4] Candan K., Distribution Range Expansion of *Salamandra infraimmaculata* Martens, 1885 (Caudata: Salamandridae) in Anatolia, Turkey, with a New Locality Record, *Amphib. Reptile Conserv.*, 16 (1) (2022) 136-147.

[5] Joger J., Steinfartz S., Protein Electrophoretic Data on Taxonomic Problems in East Mediterranean *Salamandra* (Urodela: Salamandridae). In: Llorente G.A., Montori A., Santos X., Carretero M.A. (Eds). Scientia Herpetologica (SEH). Barcelona: Asociación Herpetológica Española, (1995) 33-36.

[6] Veith M., Steinfartz S., Zardoya R., Seitz A., Meyer A., A Molecular Phylogeny of 'True' Salamanders (Family Salamandridae) and the Evolution of Terrestriality of Reproductive Modes, *JZSER*, 36 (1998) 7-16.

[7] Steinfartz S., Veith M., Tautz D., Mitochondrial Sequence Analysis of *Salamandra* Taxa Suggests Old Splits of Major Lineages and Postglacial Recolonizations of Central Europe from Distinct Source Populations of *Salamandra salamandra*, *Mol. Ecol.*, 9 (4) (2000) 397-410.

[8] Steinfartz S., Veith M., Joger U., Taxonomy Goes Evolution: the Case Study of the Genus *Salamandra* (Caudata: Salamandridae), *Zoology*, 9 (Suppl. IV) (2001) 37.

[9] Dubois A., Raffaelli J., A New Ergotaxonomy of the Family Salamandridae Goldfuss, 1820 (Amphibia, Urodela), *Alytes*, 26 (1/4) (2009) 1-85.

[10] Böhme W., Hartmann T., Fleck J., Schöttler T., Miscellaneous Notes on Oriental Fire Salamanders (*Salamandra infraimmaculata* Martens, 1885) (Lissamphibia: Urodela: Salamandridae), *Russ. J. Herpetol.*, 20 (1) (2013) 66-72.

[11] Olgun K, Avcı A, Bozkurt E, Üzüm N, Tural M, Olgun M.F., Range Extensions of Two Salamanders [*Neurergus strauchii* (Steindachner, 1887) and *Salamandra infraimmaculata* Martens, 1885] (Caudata: Salamandridae) from Anatolia, Turkey, *Russ. J. Herpetol.*, 22 (4) (2015) 289-296.

[12] Eiselt V.J., Ergebnisse Zoologischer Sammelreisen in der Türkei: Amphibia Caudate, *Ann. Naturhistor. Mus. Wien.*, 69 (1966) 427-445.

[13] Schmidtler J.J., Schmidtler J.F., Morphologie, Biologie und Verwandtschaftsbeziehungen von *Neurergus strauchii* aus der Türkei, *Senck. Biol.*, 51 (1/2) (1970) 41-53.

[14] Öz M., Anadolu'daki *Salamandra salamandra*'nın Taksonomi, Biyoloji ve Dağılışı Üzerine Araştırmalar, *Turk. J. Zool.*, 11 (3) (1987) 136-154.

[15] Arıkan H., Özeti N., Öz M., Doğu Anadolu'dan Bitlis *Salamandra salamandra* (Urodela, Salamandridae) Populasyonlarının Serum Proteinleri Üzerinde Bir Ön Çalışma, *Turk. J. Zool.*, 14 (1990) 188-194.

[16] Öz M., Arıkan H., Bitlis Çevresindeki *Salamandra salamandra* (Urodela, Salamandridae) Populasyonu Üzerinde Taksonomik Araştırmalar, *Turk. J. Zool.*, 14 (1990) 195-199.

[17] Baran İ, Öz M., *Salamandra salamandra* of Anatolia, *Mertensiella*, 4 (1994) 25–32.

[18] Fachbach G., Zur Klärung verwandtschaftlicher Beziehungen bei Vertretern der Gattung *Salamandra* mit Hilfe der Polyacrylamid-Disk Elektrophorese: II. *Z. Zool. Syst. Evolutionsforsch.*, 9 (1971) 181-187.

[19] Gasser F., Le Polytypisme de L'espèce Paléarctique *Salamandra salamandra* (L.) (Amphibien. Urodèle), *Arch. Zool. Exp. Gén.*, 19 (1978) 585-617.

[20] Weisrock D.W., Macey J.R., Uğurtaş İ.H., Larson A., Papenfuss T.J., Molecular Phylogenetics and Historical Biogeography Among Salamandrids of the "True" Salamander Clade: Rapid Branching of Numerous Highly Divergent Lineages in *Mertensiella luschani* Associated with the Rise of Anatolia, *Mol. Phylogenet. Evol.*, 18 (3) (2001), 434-448.

[21] Weisrock D.W., Papenfuss T.J., Macey J.R., Litvinchuk S.N., Polymeni R., Uğurtaş İ.H., Zhao E., Jowkar H., Larson A., A Molecular Assessment of Phylogenetic Relationships and Lineage Accumulation Rates with in the Family Salamandridae (Amphibia, Caudata), *Mol. Phylogenet. Evol.*, 41 (2006) 368-383.

[22] Burgon J.D., Vences M., Steinfartz S., Bogaerts S., Bonato L., Donaire-Barroso D., Martínez-Solano I., Velon-Antón G., Vieites D.R., Mable B.K., Elmer K.R., Phylogenomic Inference of Species and Subspecies Diversity in the Palearctic Salamander Genus *Salamandr*a, *Mol. Phylogenet. Evol.*, 157 (2021) 107063.

[23] Baycan B., Tosunoğlu M., The Catalog of Amphibia and Reptilia Specimens in the Çanakkale Onsekiz Mart University Zoology Museum (COMU-ZM), *Turkish J. Biosci. Collect.*, 1 (1) (2017) 38-55.

[24] Özeti N., Yılmaz İ., Türkiye Amfibileri, Ege üniversitesi Fen Fakültesi Kitaplar Serisi No:151, İzmir, Ege Üniversitesi Basımevi, (1994) 1-221.

[25] Çiçek K., Koyun M., Tok C. V. Food Composition of the Near Eastern Fire Salamander, *Salamandra infraimmaculata* Martens, 1885 (Amphibia: Urodela: Salamandridae) from Eastern Anatolia, *Zool. Middle East*, 63 (2) (2017) 130-135.

[26] Sarıkaya B, Yıldız M.Z, Sezen G. The Herpetofauna of Adana Province (Turkey), *Commagene J. Biol.* 1 (1) (2017) 1-12.

[27] Akman B, Yıldız M.Z., Özcan A.F., Bozkurt M.A., İğci N., Göçmen B., On the Herpetofauna of the East Anatolian Province of Bitlis (Turkey) (Amphibia; Reptilia), *Herpetozoa*, 31 (1/2) (2018) 69-82.

[28] Sami E, Yıldız M.Z., Amphibians of Adıyaman/Turkey Province, *Biodivers. Conserv.*, 11 (1) (2018) 1-12.

[29] Yıldız M.Z., Sarıkaya B., Bozkurt M.A., The Herpetofauna of the Province of Hatay (East Mediterranean Turkey), *Biodivers. Conserv.*, 12 (2) (2019) 197-205.

[30] AmphibiaWeb. University of California, Berkeley, CA, USA. Available at: https://amphibiaweb.org. Retrieved April 25, 2024.

[31] Rastegar-Pouyani N., Fizi H., On a Collection of the Near East Fire Salamander, *Salamandra infraimmaculata semenovi* (Salamandridae) from Kurdistan Province, Western Iran, *Zool. Middle East*, 37 (2006) 115-118.

[32] Altunışık A., Age, Survivorship and Life Expectancy in Near Eastern Fire Salamander, *Salamandra infraimmaculata* (Caudata: Salamandridae), *Russ. J. Ecol.*, 49 (2) (2018) 166-171.

[33] Karahisar S, Demirsoy A., Türkiye'deki Önemli *Salamandra infraimmaculata* Populasyonlarının Morfolojik, Histolojik ve Karyotipik Özellikleri Açısından Karşılaştırılması, *HJBC*, 40 (5) (2012) 343-352.

Cumhuriyet Sci. J., 45(2) (2024) 216-226
DOI: https://doi.org/10.17776/csj.1414168

Cumhuriyet Science Journal

| csj.cumhuriyet.edu.tr | Founded: 2002 ISSN: 2587-2680 e-ISSN: 2587-246X Publisher: Sivas Cumhuriyet University

Donepezil-Squaric Acid Hybrid: Synthesis, Characterization and Investigation of Anticholinesterase Inhibitory, DNA Binding and Antioxidant Properties

Derya Kılıçaslan[1,2,a,*]

[1] *Afsin Vocational School, Department of Chemistry and Chemical Processing Technologies, Kahramanmaras Sutcu Imam University, Kahramanmaras, Türkiye*
[2] *Research and Development Centre for University-Industry-Public Relations, Kahramanmaras Sutcu Imam University, Kahramanmaras, 46050, Türkiye*
**Corresponding author*

Research Article

History
Received: 03/01/2024
Accepted: 14/06/2024

ABSTRACT

A novel donepezil-squaric acid (DS) hybrid compound was designed, synthesized and biologically evaluated as multi-target-directed ligands against neurodegenerative disease by fusing a fragment of donepezil (D) and squaric acid (S). This study focuses on investigating the binding mechanism of double-stranded fish sperm DNA (Fsds-DNA) with DS and S. The interaction between DS and S with Fsds-DNA was explored using spectrophotometric and viscometric methods. Besides, DNA binding constants (K_b) were determined. The results reveal that DS binds to Fsds-DNA via the minor groove binding mode. The hybrid molecule demonstrates potent inhibitory activity against acetylcholinesterase (AChE) and butyrylcholinesterase (BuChE). Furthermore, it exhibits significant antioxidant activity, surpassing the scavenging ability of 2,2-diphenyl-1-picrylhydrazyl (DPPH) radicals compared to squaric acid alone. In conclusion, these results suggest that the hybrid molecule may serve as a potential multifunctional agent for the treatment of Alzheimer's disease.

Keywords: Donepezil, Squaric acid, DNA binding, Acetylcholinesterase, Butyrylcholinesterase.

[a] *deryatrnc@ksu.edu.tr* *https://orcid.org/0000-0001-7830 8214*

Introduction

Alzheimer's disease (AD) is an irreversible neurological disorder that leads to cognitive impairment, the loss of cholinergic neurons at basal forebrain synapses and neuronal death. The etiology of AD is intricate and definitive therapeutics are still unavailable. A variety of pathological features contributes to the pathogenesis of AD, encompassing low acetylcholine level, increased monoaminoxidase concentration, oxidative stress, Aβ accumulation, inflammation, intracellular neurofibrillary tangles, metal ion dysregulation, etc [1]. The precise pathology of AD remains unknown in spite of ongoing research [2]. For a considerable period, researchers have concentrated on boosting acetylcholine (ACh) levels in patients' brains through inhibiting the enzyme acetylcholinesterase (AChE). Acetylcholinesterase inhibitors (AChEIs) stand out as the most commonly prescribed treatment strategy for AD. AChEIs have exhibited the ability to diminish disease progression and enhance attention span. These compounds demonstrate unique patterns of structural diversity, each having distinctive features tailored for various types of ChE. Following the introduction of AChEIs, cholinergic drugs such as galantamine, donepezil and rivastigmine emerged as primary pharmacotherapy options for mild to moderate AD [3]. Nevertheless, controlling the progression of AD necessitates more than inhibiting a single underlying cause; instead, it requires simultaneous modulations of all relevant types. This comprehensive approach is achieved through studies focused on designing and synthesizing multi-targeted ligands for AD therapy [4].

Squaric acid serves as a functional structural scaffold that can be readily transformed into amide-containing compounds featuring both hydrogen bond donor and acceptor groups. This characteristic offers the potential for forming multiple interactions with complementary sites [5]. The squaric acid scaffold is a unique molecule that has garnered significant interest, particularly in the last decade, owing to its diverse applications in synthetic [6], pharmaceutical [7] and other fields [8-12]. Squaric acid, (also known as quadratic acid; 3,4-dihydroxycyclobut-3 en-1,2-dione), adopts a planar aromatic framework and derives its distinctive name from its square shape. Its analogues exhibit various biological activities, activated by the presence of crucial H-bond donors and acceptors [13]. Squaric acid analogues hold significance in medicinal chemistry for several reasons. Firstly, unlike many other compounds designed as potential drugs, they typically do not exhibit high lipophilicity and low solubility in water. The resultant compounds demonstrate enhanced solubility, rendering them suitable as therapeutic agents particularly when squaric acid or the squaramide scaffold is combined with amine and carboxylic groups [14,15]. Besides, analogues of carboxylic acid may function as non-classical isosteres for carboxylates and amino acids in the course of drug

development [16]. The utilization of chlorogenic acid analogues in chemical biology is predominantly exemplified by their bioconjugation to proteins or carbohydrates and their application as ion receptors. Conversely, in medicinal chemistry, these compounds possess diverse biological effects, involving antichagasic, antiplasmodial, anticancer and antibacterial activity, positioning them as promising agents in drug development. Squaramide can be regarded as a noteworthy motif that facilitates the formation of H-bonds bioisosteric to functionalities like carboxylic and amino acids, guanidine urea, cyanoguanidine and various phosphate groups [16]. Squaric acid occupies a unique position among oxocarbonic acids as it has an equal number of atoms that act as donors and acceptors for the formation of hydrogen bonds. This ligand can behave quite differently depending on the conditions because it has a highly symmetrical ring structure and tends to form chains with hydrogen bonds. It also has a structure suitable for forming two- or three-dimensional structures. The equal number of acceptor and donor oxygen atoms and the planar ion form with squaric acid allow the synthesis of polymeric, two- and three-dimensional supramolecular structures. There are mixed ligand complexes containing squaric acid in the literature [17-19]. A commercial AChE inhibitor, donepezil is employed in the treatment of mild to moderate AD. In addition, it has garnered widespread attention due to its potent AChE inhibitory properties, low toxicity, high selectivity and favorable bioavailability [20]. The 1-benzylpiperidine fragment within donepezil serves as the crucial pharmacophore of AChE inhibition, contributing to its good solubility in water, and numerous donepezil hybrids have been developed as multi-target-directed ligands [21-23]. Considering the relatively simple synthesis approach of the squaramide motif and its appealing properties (rigidity, aromatic character, H-bond formation), we opted to combine this scaffold with donepezil. This study endeavours to create a multi-target active small molecule by merging squaric acid with donepezil, aiming to assess whether the new molecule exhibits diverse multifunctional potential and good drug-like properties. We synthesized a novel squuaric acid-donepezil hybrid and developed it as a multi-target-oriented ligand in the current study. It also focused on the binding mechanism of Fsds-DNA with DS and S. UV-vis absorption spectroscopy, fluorescence spectroscopy and viscosimetry were deployed to explore the interaction between the molecules and Fsds-DNA. Furthermore, the interaction of Fsds-DNA and DS was compared with the S interaction. The evaluation encompassed AChE and BuChE inhibitory activity as well as antioxidant activity.

Experimantal

Apparatus

For the analysis of the IR spectra of the DS and S, we employed the Attenuated Total Reflectance technique and conducted measurements on the Perkin Elmer Spectrum 100 FT-IR Spectrophotometer. The results were assessed in wavenumbers (cm^{-1}). ^{13}C NMR and ^{1}H spectra were acquired using the Bruker AVANCE III 400 MHz NMR Spectrometer with DMSO-d6 as the solvent. Chemical shift values (ppm) were determined on the δ scale with the solvent serving as the reference peak, and interaction constants were presented in Hertz (Hz). AChE and BuChE enzyme inhibition activities, along with antioxidant activity, were determined using the Hitachi U3900H Spectrophotometer. UV-vis absorption studies were conducted using a Perkin-Elmer Lamda 25 spectrometer. Compound photoluminescence spectra were measured with a Perkin Elmer LS55 spectrometer.

Chemicals

Starting materials donepezil hydrochloride reagent-grade analytical standard ≥98% (HPLC) was procured from ARIS (Ali Raif Ilaç Sanayi, Istanbul, Turkey) and used as received. Squaric acid (3,4-Dihydroxy-3-cyclobutene-1,2-dione) and solvents were purchased from commercial sources (Sigma-Aldrich, Germany) and used as received. Electric eel AChE (Type-VI-S, EC 3.1.1.7, Sigma) and horse serum BChE (EC 3.1.1.8, Sigma) were used, while acetylthiocholine iodide and butyrylthiocholine chloride (Sigma, St. Louis, MO, USA) were employed as substrates of the reaction. 5,5′-Dithio-bis(2-nitrobenzoic)acid (DTNB, Sigma, St. Louis, MO, USA) was used for the measurement of the anticholinesterase activity. In addition, 2,2-Diphenyl-1-picrylhydrazyl (DPPH) was obtained from Sigma-Aldrich- Germany.

Procedure

The synthesis procedure consists of two steps. In the first part, Donepezil hydrochloride was dissolved in 0.24 mmol (0.1 g) ethanol. Then, 0.24 mmol (0.0096 g) NaOH was added and the mixture was stirred under reflux for 2 hours. The resulting NaCl was filtered off and the reaction mixture was stirred for another 2 hours. In the second part, 0.24 mmol (0.0273 g) of squaric acid (5/2 ml DMF/H_2O) was added. The reaction mixture was kept under reflux at 70-80 °C for 6 hours. Slow evaporation of the solvent gave a powdery cream-colored product. The product was filtered and washed with water (Scheme 1). The progress of the reaction was monitored by TLC. The purity of the product was evaluated by single spot TLC under UV lamp.

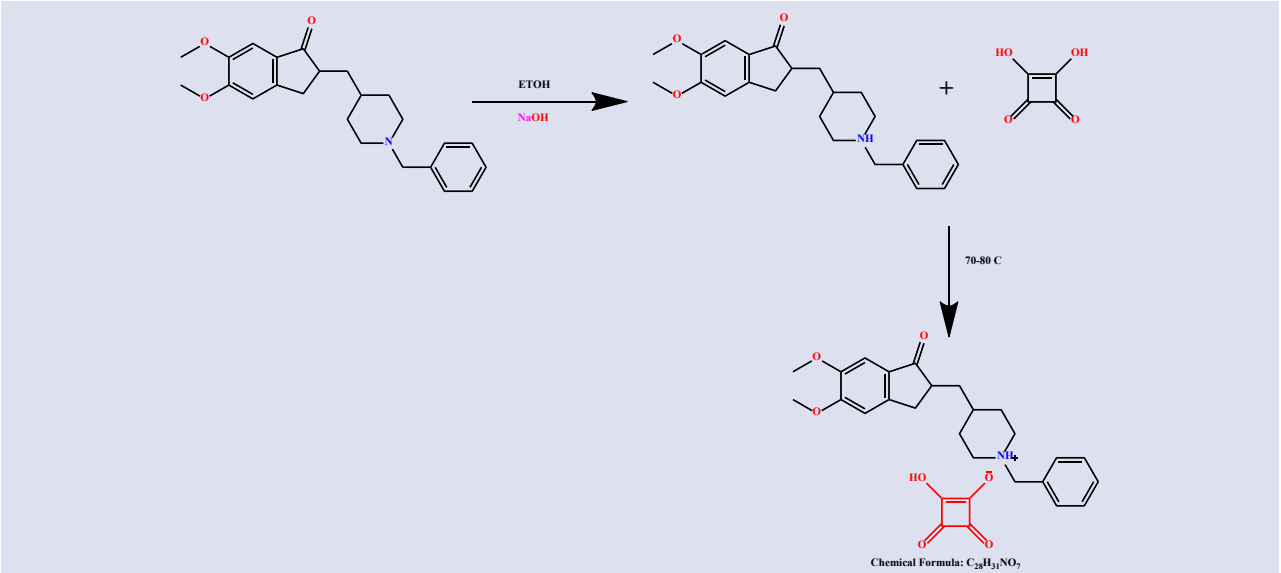

Scheme 1. Synthesis of DS

DS:$C_{28}H_{31}NO_7$, MW:493.56g/mol, Yield: %92 Color: cream, FT-IR(ATR cm^{-1}):3357 (O-H), 2929 (C-H), 2702 (N-H) 1797 (C=O), 1665 (C=C). ^{1}H NMR (DMSO-d6, ppm):4.07 ($CH_{2phenyl}$), 5.05 (NH) 7.05-7.50 ($CH_{aromatic}$), 1.26-2.67 ($CH_{aliphatic}$), 3.79 (OCH_3), 3.87 (OCH_3).^{13}C NMR (DMSO-d6, ppm) δ 206.7 ($C{=}O_{indole}$), 155.79-104.31 ($C_{aromatic}$), 56.39 and 55.89 (OCH_3), 59.65 (C_{phenyl}), 51.71-28.28 ($C_{aliphatic}$). 197.16-196.76($C_{squarat\ anion}$) HRMS (ESI) (m/z) [M+H]+: Anal. calcd. for $C_{28}H_{31}NO_7$:493.21, Found:495.24.

Interaction Studies of Compounds with DNA

DNA Binding Studies

The DNA sample employed for assessing the compounds' binding affinity was directly sourced as double-stranded fish sperm DNA (Fsds-DNA) procured from Aldrich without any specific purification. Tris-HCl buffer was formulated using 20 mM Tris-HCl and 20 mM NaCl in pH 7 medium. A fresh stock solution of Fsds-DNA (5 mg ml^{-1}) was prepared, and the concentration of the resulting Fsds-DNA solution was determined by measuring the absorbance at 260 nm. A known value of the molar extinction coefficient of 6600 M^{-1} cm^{-1} was used to calculate the concentration..

Stock solutions of compounds (1×10^{-3} M) were prepared in DMSO as co-solvent and buffer as solvent. The assay was carried out in the presence of a constant concentration of DS and S ($2{\times}10^{-4}$ M) and by titrating the increasing concentration of FSds-DNA. The Fsds-DNA concentration per nucleotide was determined through absorption spectroscopy, utilizing the molar absorption coefficient (6600 M^{-1} cm^{-1}) at 260 nm [24]. The binding constants (K_b) of the DS and S were calculated by plotting [DNA]/(ε_a/ε_f) versus [DNA]/(ε_a/ε_f), taking into account the degradation of the absorption bands of the DS and S. The following equation was used for the calculation;

$$[DNA]/(\varepsilon_a{-}\varepsilon_f) = [DNA]/(\varepsilon_b{-}\varepsilon_f) + 1/K_b(\varepsilon_b{-}\varepsilon_f)$$

[DNA] is the concentration of FSds-DNA in base pairs, εa is the extinction coefficient (A_{obs}/[compound]), and ε_b and ε_f are the extinction coefficients of the free and fully bound forms, respectively. In [DNA]/(ε_a/ε_f) vs [DNA] plots, K_b is depicted by the intersection ratio of the slope [24].

Fluorescence Competitive Binding Studies

Competitive ethidium bromide (EB) binding studies were conducted to assess the relative binding affinities of S and DS to FSds-DNA, employing the fluorescence spectroscopy technique. Fluorescence intensities of ethidium bromide bound to Fsds-DNA were measured at 610 nm upon excitation at 526 nm. The measurements were performed in the presence and absence of compounds (0-100 µM) in Tris-HCl buffer (2 mM Tris-HCl, pH 7.1). The Quenching constant (K_{sv}) value was calculated using the Stern-Volmer equation, derived from the graph generated using the collected data [24].

$$F_0/F = K_{sv}\,[Q] + 1,$$

Where F_0 represents the fluorescence intensity in the absence of the quencher; F represents the fluorescence intensity in the presence of the quencher; K_{sv} denotes the quenching constant, and [Q] signifies the quencher concentration. The K_{sv} value was determined by plotting the F value against [Q] and obtaining the slope.

Viscosity Measurement

A viscosity experiment was conducted on Ostwald's viscometer immersed in a thermostated water bath maintained at 25 ± 1 °C. The flow times of the FSds-DNA solution, in the presence of increasing concentrations of DS and S, were recorded with an accuracy of ±0.01 s using a digital stopwatch. Each sample was measured three times at room temperature. The Fsds-DNA concentration was kept constant (200 µM) and the concentration of S and DS compounds varied from 0 to 60 µM. The relative

viscosity for FSds-DNA in the absence (η_0) and presence (η) of the S and DS was calculated using the formula; $\eta=(t-t_0)/t_0$ (where 't' is the flow time for the buffer solution containing FSds-DNA and the compounds at a speacific concentration and 't_0' is the observed flow time for the buffer solution alone) and $\eta_0 = (t - t_0)/ t_0$ (where 't' is the observed flow time for buffer solution containing FSds-DNA and 't_0' is the observed flow time for buffer solution alone). The relative viscosity $(\eta/ \eta_0)^{1/3}$ versus 1/R was then plotted, where *R* = concentration of DNA/concentration of DS or S [25].

Evaluation of Cholinesterase Inhibitory Activity

The AChE and BuChE inhibitory activities of the S and DS were identified through the modified Ellman method using AChE and BuChE. The inhibitory activities of the target compound were compared with those of S. All assays were conducted in a pH 8.0, 0.1 M KH_2PO_4/K_2HPO_4 buffer. The enzyme solutions were prepared at a concentration of 0.22 units/mL. A modified Ellman's method was employed using a 96-well plate reader for the in vitro measurement of AChE activity [26]. Each well consisted of 100 µL of potassium phosphate buffer (KH_2PO_4/K_2HP0_4, 0.1 M, pH 8), 20 µL of the sample dissolved in 50% methanol and 50% DMSO and 20 µL of the enzyme. The mixture was pre-incubated for 15 minutes at room temperature. The chromatographic reagent 5,5-dithio-bis(2-nitrobenzoic acid) (DTNB) (3 mM, 50 µL/well) and substrates acetylthiocholine iodine (ATCI) (3 mM, 50 µL/well) or butrylthiocholine iodine (BTCI) (3 mM, 50 µL/well) was added to the enzyme-inhibitor mixture. The yellow anion (2-Nitro-5-thiobenzoic acid) formation was monitored at 412 nm for a duration of 10 minutes. An identical solution was prepared by including the enzyme without the tested compounds (as a control). Control and inhibitor readings were corrected with a blank read. Each concentration was assayed in triplicate. The concentrations of samples that inhibited the degradation of substrates (acetylcholine or butyrylcholine) by 50% (IC_{50}) were determined through linear regression analysis between percent inhibition and sample concentration using an Excel program.

Antioxidant Activity Assay

The method involves measuring the scavenging effects of antioxidants on DPPH (1,1-diphenyl-2-picrylhydrazyl) radical, a stable organic nitrogen radical. 9.86 mg DPPH was weighed and dissolved in methanol to achieve a total volume of 25 mL, resulting in the preparation of a DPPH solution. Varying concentrations of S and DS (1750 to 54 µM) were then added to 100 mM concentration of the DPPH solution. The quenching of the absorbance at 517 nm of the DPPH radical was monitored at regular time intervals (0-45 min). All experiments were conducted in triplicate, and the mean absorbance was measured to calculate the percentage of inhibition using the following equation.

$$\% \text{ Inhibition of the DPPH free radical}=[(A_{blank}-A_{sample})/(A_{blank})]\times 100\%$$

In which A_{blank} represents the absorbance of the DPPH radical in the absence of a sample, and A_{sample} is the absorbance of the DPPH radical in the presence of varying concentrations of sample [27,28]. The radical inhibition concentration (IC_{50}) of S and DS was determined from the plot of the percentage inhibition versus the sample concentration.

Results and Discussion

Two donor O-H groups and two carbonyl acceptors are present in squaric acid, while there is one donor and three proton acceptors in the monoanion structure. The IR spectrum of the synthesised DS complex was analyzed and the characteristic vibrations were identified. The relationship between the structures D and S forming DS and their spectra was investigated. The IR spectrum of squaric acid was initially examined to explore the similarities and differences between the IR spectrum of DS and the IR spectrum of squaric acid. Four characteristic and strong peaks were observed in the 4000-200 cm^{-1} range in both the IR spectrum of squaric acid and DS. A strong broad peak around 1505 cm^{-1} was evident, representing a mixture of C-C and C-O stretching vibrations. The peak at 1652 cm^{-1} is associated with υ(C=C) stretching vibrations. The υ(C=O) stretching vibration peak is observed at 1807 cm^{-1}. In squaric acid, weak peaks at 512 cm^{-1} and 623 cm^{-1} are attributed to localised C=O stretching vibrations [29-32]. The broad band around 2300 cm^{-1} is due to the O-H stretching vibration of squaric acid. The peak frequency values of the C-C and C-O stretching vibrations of squaric acid were observed in the range of 1490-1550 cm^{-1}, centered around 1500 cm^{-1}, with small shifts attributed to hydrogen bonds effects. The peak of the O-H stretching in the DS complex is observed at 3367 cm^{-1} respectively. Besides, the strong and broad peak of υ(C-C) and υ(C-O) vibrations, characteristic for squaric acid, is observed at 1497 cm^{-1} in the complex. These strong and broad bands indicate that the presence of the squarate anion in the complex. The absence of the diffuse band around 2300 cm^{-1} in the IR spectrum of squaric acid in the complex suggests that the hydrogen in the squaric acid ligand is separated from the structure, referring to the formation of the complex where it is coordinated to the piperidine group of donepezil. In the IR spectrum of squaric acid, the peaks of υ(C=C) at 1652 cm^{-1} and υ(C=O) stretching vibrations at 1807 cm^{-1} were observed at the expected frequencies in the DS complex. The appearance of peaks at 1665 cm^{-1} in the higher energy region in the DS complex, compared to squaric acid, is attributed to C=C stretching vibrations.

The occurence of these values in the higher energy region, as compared to the IR spectrum of squaric acid, reveals that DS coordinates through the nitrogen atoms in piperidine. In the IR spectrum of the complex, a robust peak in the range of 1313-1217 cm^{-1} contributes to the υ(C-N) and υ(C=C) stretching vibrations of the donepezil

ligand, while the aromatic υ(C-H) stretching vibrations of this ligand manifest around the 2929 cm^{-1} region. The absence of aromatic or aliphatic C-H groups in the squarate anion makes the peaks in this region indicative of the presence of the donepezil ligand in the structure. The band at 2702 cm^{-1} corresponds to υ(N-H), participating in the hydrogen bonds. As the sole proton donor, squaric acid transfers its proton from OH groups to the N atom, leading to the formation of a DS complex (Figure 1).

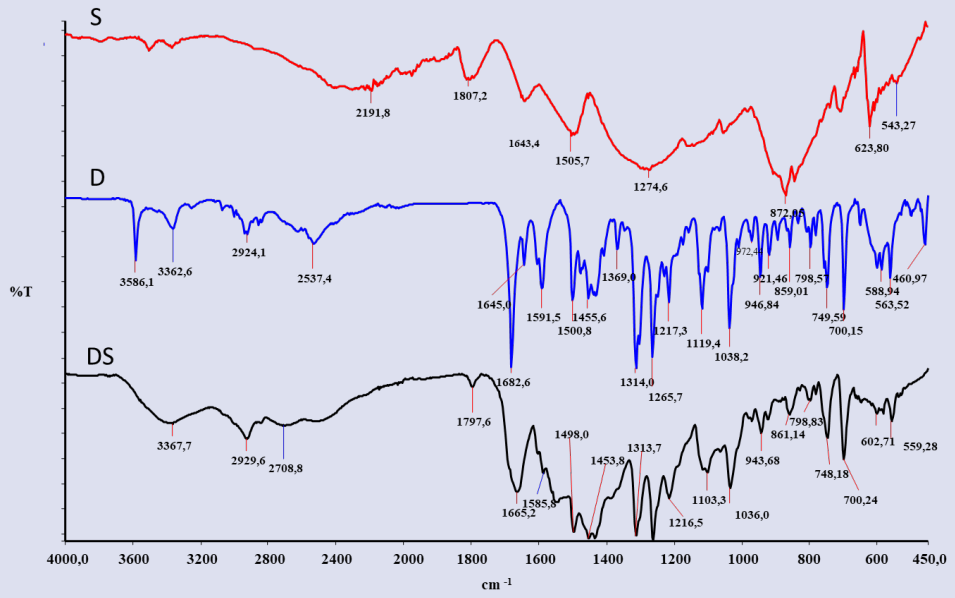

Figure 1. FT-IR spectra of S, D and DS

The aliphatic and aromatic protons in the structure of the DS hybrid compound exhibited peaks in the ^1H NMR spectra, as generally expected. Upon analyzing the hydrogen NMR results of the synthesised compound, where methoxy is at the 5th position of the indanone ring, several noteworthy details emerged. The methoxy protons observed at 3.90 ppm in the starting material did not vary significantly across the electronic environment due to the distance to altering substituents and peak at 3.87 or 3.79 ppm. The aromatic protons at the 4th, 6th and 7th position of the ring were predominantly observed as doublets, doublets of doublets and doublets, respectively, and in some cases as multiplet intertwined with other protons. Their chemical shift values were 7.05, 7.09, 7.41, 7.50 ppm, respectively (Figure 2).

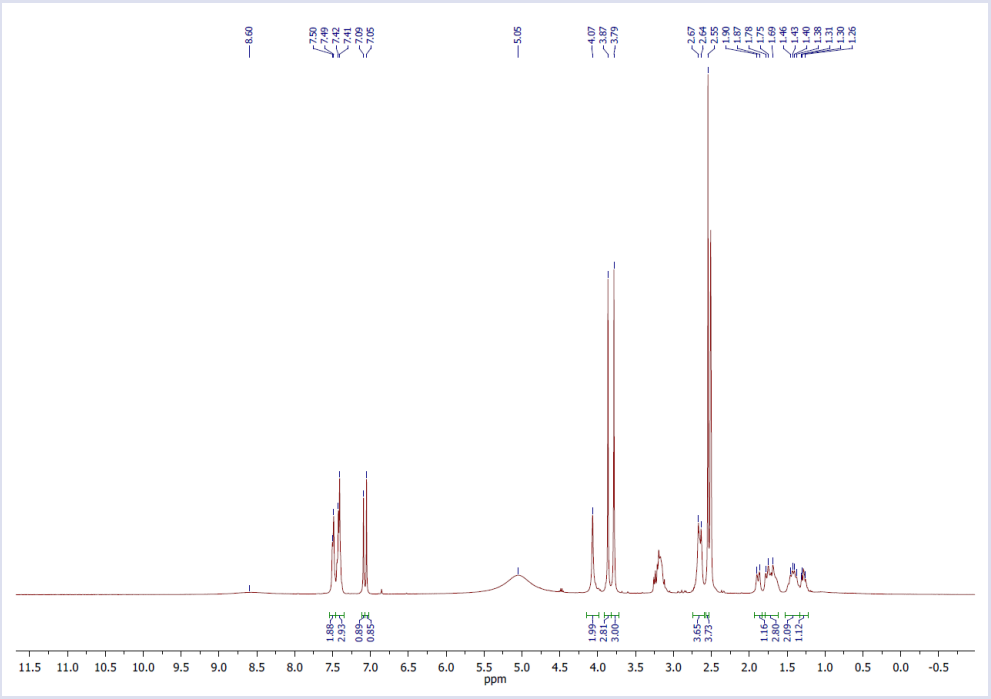

Figure 2. ^1H NMR spectra of DS

The common structural components in the synthesised compound gave peaks in the ^{13}C NMR spectra, aligning with general expectations. The total number of carbons in the spectra of the synthesised compound was determined by considering the identical carbon atoms based on their electronic environment and the expected number of peaks was observed. Specific functional groups (C=O) were observed at 206 ppm in the spectra of the compounds. The remaining aliphatic carbons peaked in the range of 51.71-28.28 ppm and aromatic carbons in the range of 104.31-155.79 ppm, consistent with findings in the literature. In the chemical structure of the synthesised compound, a disubstituted methoxy group is present at the 5th and 6th positions of the indan-1-one ring system. Carbon atoms belonging to this functional group were identified in the range of 56.39- 55.89 ppm in the spectra (Figure 3).

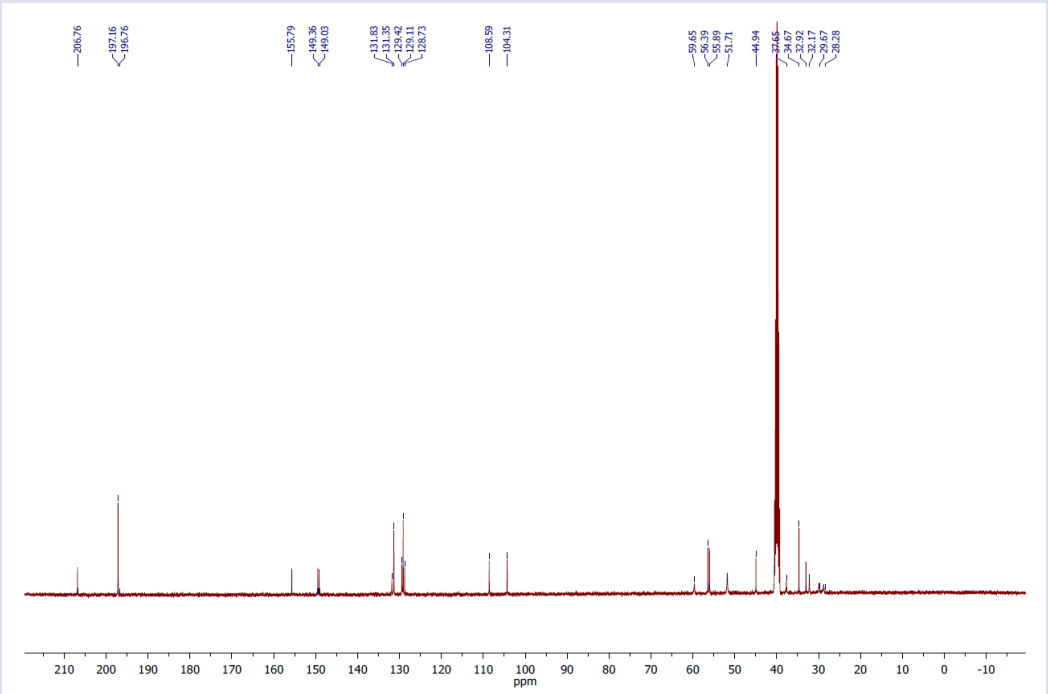

Figure 3. ^{13}C NMR spectra of DS

DNA Binding Studies

UV–Visible Titration Experiments

Many natural or synthetic drugs function as analogs in protein-nucleic acid recognition studies, offering site-specific reagents for molecular biology. Therefore, investigating drug-DNA interaction is crucial for understanding the molecular mechanisms of drug action and designing specific DNA-targeted drugs [33]. Spectroscopic methods play a pivotal role in understanding the drug-DNA binding mechanism and identifying structural deformations in the double helix during complex formation with molecules [34, 35]. Among various spectroscopic techniques, UV–vis spectroscopy stands out as one of the most simple and popular techniques employed to study small molecules-DNA interaction [34]. There are three main modes of non-covalent interactions through which drug molecules bind to DNA.

Possible bonding modes include electrostatic bonding, groove bonding, and intercalative bonding. Intercalators typically demonstrate a hypochromic effect with a significant redshift, while minor-groove binders may show an occasional hyperchromic effect with little or no wavelength shift [35]. The Figure 4-5 displays the absorption spectra of DS and S in the absence and presence of FSds-DNA. DS independently depicts an absorption maximum at 266 nm in the absence of FSds-DNA, as indicated in the dotted spectra. Significant changes in DS UV–vis bands confirmed the DS-FSds-DNA interaction. DS-FSdsDNA mixed solutions were prepared by adding different concentrations of FSdsDNA to the DS solution. Upon the addition of various concentrations of FSds-DNA solutions to the DS solution, there was a noticeable increase in the intensities of the absorption peaks. While this indicated the expected hyperchromic effect, a blue shift of up to 7 nm was observed at the wavelength of maximum absorption. Generally, the groove binding interaction between small molecules and FSds-DNA results in hyperchromism and hypsochromism in the absorption bands. The addition of FSds-DNA solution to fixed concentrations of DS and S resulted in an increase in absorbance values and a blue shift of the wavelength. Thus, the interaction mode of DS and S binding with FSds-DNA appears to be groove binding. The K_b value of DS was found to be 5.35×10^4 (λ max=266 nm) and the K_b value of S was determined to be 4.92×10^4 M^{-1} (λ max=271 nm). When compared to the known intercalator value such as EB ($1.4x\ 10^6 M^{-1}$)[24] and reported groove-binding drugs such as gefitinib (1.29×10^4 L. mol^{-1})[35], it becomes evident that the K_b values of DS and S align with the groove-binding values. Considering the K_b binding constants, the DNA binding capacity of DS was found to be higher than that of S.

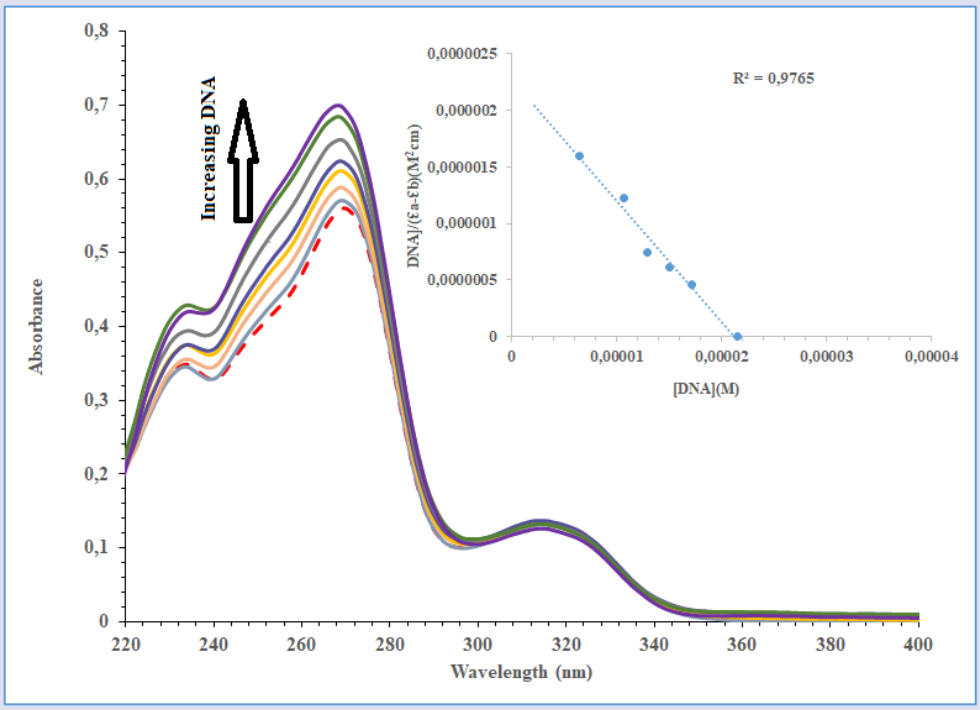

Figure 4. UV-vis absorption spectra of the DS solution resulting from cumulative amounts of FSds-DNA (changes indicated by the arrow). Inset: Graph showing [DNA/$\varepsilon_a - \varepsilon_f$] vs. [DNA]

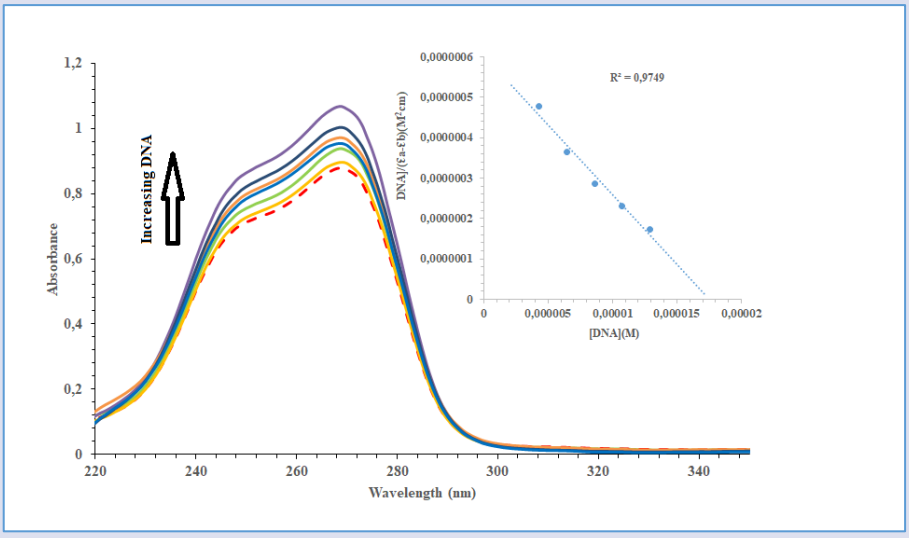

Figure 5. UV-vis absorption spectra of the S solution resulting from cumulative amounts of FSds-DNA (changes indicated by the arrow). Inset: Graph showing [DNA/εa − εf] vs. [DNA]

Fluoroscence Titration Experiments

Fluorescence-based titration experiments were conducted to validate the findings obtained from the UV–vis titration experiment. As is known, the interaction mode of EB on DNA is intercalation [36]. EB is commonly used as a fluorescent probe to verify the binding mode of DNA with small molecules. When inserted between DNA base pairs, EB enhances the fluorescence intensity upon binding to DNA. Compounds with a DNA-like binding mode, such as EB, reduce the EB binding site, thereby quenching the EB-DNA emission intensity. In other words, it reduces the frequency of EB binding to DNA. Upon the addition of the tested compounds to the medium, the intensity of the EB-DNA system in the emission band at 590 nm were noted to decrease with the increasing concentration of the compound under examination. This effective quenching mode is believed to occur by displacing EB molecules from the EB-DNA system and facilitating the binding of the compound to different regions of the DNA. This study recorded the fluorescence emission spectra of a fixed amount of FSds-DNA and EB in Tris-HCl buffer solution (pH = 7.4), with gradually increasing amounts of DS and S, and the results are summarized in Figure 6-7. The fluorescence intensities of FSds-DNA-EB solutions decreased with the gradual increase in DS and S concentration. The experimental results conclude that there is competitive binding between EB and DS and S on FSds-DNA. Hence, DS and S can bind to regions of FSds-DNA via minor groove binding interaction. K_{sv} values were calculated from the slope of

the Stern-Volmer plot for the quenching of the fluorescence intensity of EB bound to FSds-DNA by DS and S, as shown in Figure 6-7. The K_{sv} quenching constants for DS and S compounds were calculated as 3.5 x10^4 M^{-1} and 1.7 x10^4 M^{-1}, respectively. On comparing the calculated values, it becomes apparent that the DS compound exhibits a stronger capability to modify EB-DNA emission. Moreover, the binding mode of the compounds to the DNA structure involves groove binding rather than intercalation [24]. The decrease in emission intensity is presumed to result from the interaction of DS and S with EB-DNA, changes in the three-dimensional DNA structure or excited-level energy transfer.

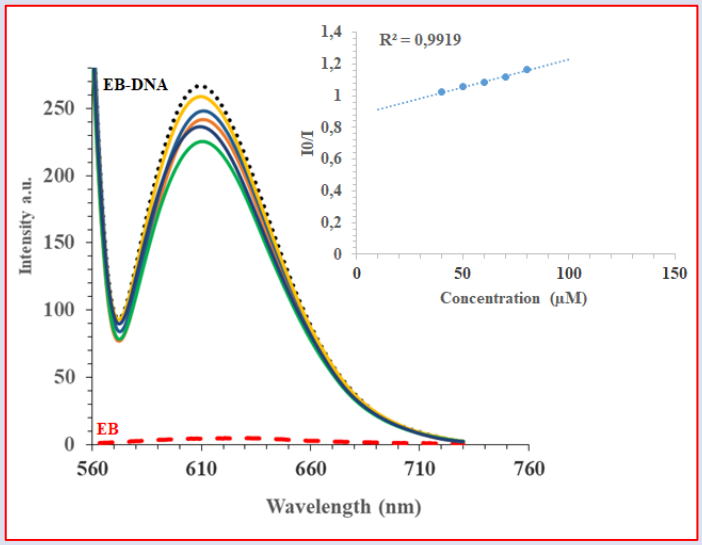

Figure 6. Effect of DS additions at concentrations of 10–100 µM on the emission intensity of the FSds-DNA-bound ethidium bromide in Tris–HCl buffer (pH 7.1); Stern-Volmer graph showing fluorescence titrations of the DS with FSds-DNA.

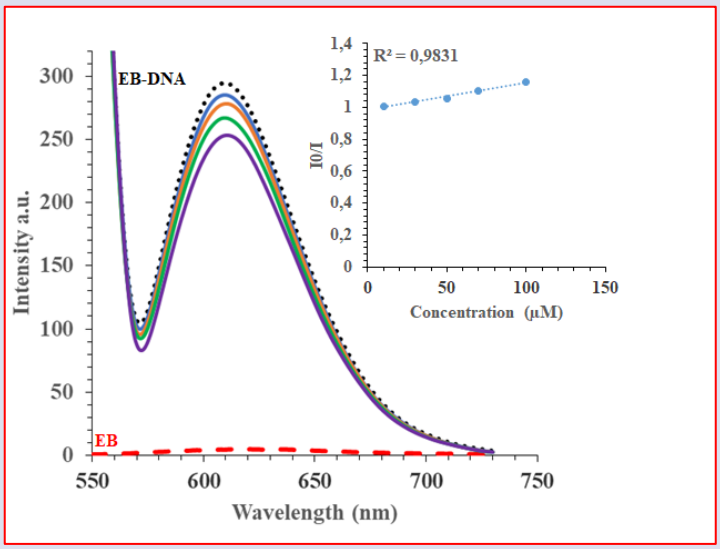

Figure 7. Effect of S additions at concentrations of 10–100 µM on the emission intensity of the FSds-DNA-bound ethidium bromide in 2 mM Tris–HCl buffer (pH 7.1); Stern-Volmer graph showing fluorescence titrations of the S with FSds-DNA

Viscosity Studies

Viscosity measurement is widely acknowledged as an effective and precise method to identify the binding mode between small molecules and DNA [37]. A classical intercalation model proposes that the DNA helix lengthens as base pairs separate to incorporate the compound between the bases, leading to increased DNA viscosity [38]. In contrast, drugs that specifically bind to DNA grooves through partial and/or non-classical intercalation can interact with the DNA strand, reducing its length and generally causing less pronounced or no change in DNA solution viscosity [38]. The viscosities of Fsds-DNA solution ((200 µM); pH = 7.4) in the absence and presence of DS and S (0 to 60 µM) were measured, and the results are depicted in Figure 8. The results suggested that a very slight change in Fsds-DNA viscosity was observed with increasing concentrations of DS and S, and this was not as pronounced as reported for EB, a classical indicator. Therefore, viscosity studies confirm that DS and S bind in the minor groove of Fsds-DNA, ruling out the possibility of intercalation [28].

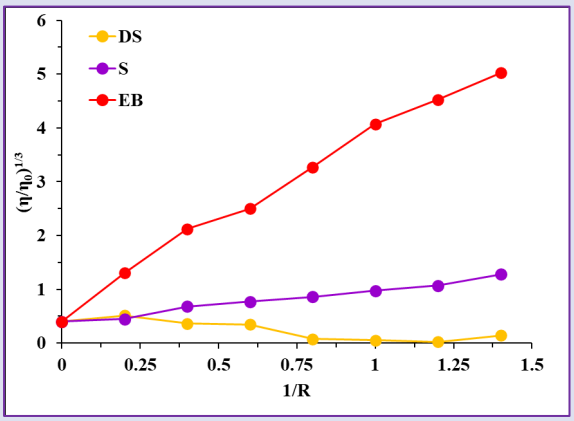

Figure 8. The relative viscosity of FSds-DNA in the presence of different amount of DS and S

Inhibitory Activity Against AChE And BuChE

Cholinesterase enzymes (ChEs) play a role in accelerating the hydrolysis of acetylcholine, a neurotransmitter, thereby reducing acetylcholine levels in the brain. Thus, blocking cholinesterase enhances cholinergic neurotransmission [39]. It utilizes ChE inhibition to alleviate AD symptoms or temporarily slow its progression by restoring cholinergic activity in the brain. The inhibitory activities of DS against AChE and BuChE were assessed using a spectrophotometric method [26], with S serving as the reference compound. For AChE, the IC_{50} value of DS was calculated as 813.7, for S was 1177.8 µM, while for BuChE, DS was 184 and S was 850µM. The results indicated that DS presented notable inhibitory activity against both AChE and BuChE, with a better selectivity for BuChE compared to S.

Antioxidant Activity

DPPH is characterized as a stable free radical due to the delocalization of the spare electron over the entire molecule, preventing dimerization, a characteristic observed in most other free radicals. The delocalization of electrons imparts a deep violet colour with absorption measured at 517nm. The DPPH radical scavinging activity assay was utilized to determine the total antioxidant activity of the S and DS based on the method described in the literature [27]. This assay was performed for various concentrations (1750µM, 875µM, 437µM, 218 µM and 109µM) of the S and DS. The Figure 9 signifies the DPPH radical scavenging activity of DS and reference compound (S), expressed as percentage of scavenged DPPH radicals. DS and S showed a decrease in the concentration of DPPH radicals, confirming their scavenging ability. DS exhibited a higher activity in scavenging DPPH radicals compared to S (Table 1).

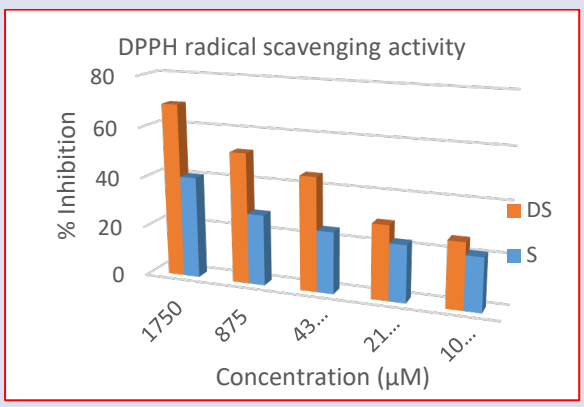

Figure 9. The antioxidant activity of S and DS with DPPH spectrophotometric assay.

Table 1. DPPH antioxidant activities of S and DS.

Sample	DPPH radical scavenging activity assay (IC_{50} value in µM)
S	1055
DS	918

Conclusion

This study synthesized a hybrid molecule by combining donepezil/squaric acid (DS), aiming for its potential application in the treatment of AD. The structure of the DS hybrid molecule was elucidated by FTIR and $^{1}H/^{13}C$ NMR spectroscopy. The binding interactipns of DS and S to Fsds-DNA were thoroughly investigated through various experimental methods, including absorption spectrum measurements, fluorescence studies and viscosity measurements. The DNA binding constants for DS and S; K_b were determined using Uv-Visible absorption and fluorescence spectroscopy methods.

The binding of DS with Fsds-DNA resulted in minor hypochromism with no change in the absorbance maximum and fluorescence quenching with minimal shift in the emission maximum, indicative of a groove binding mode of the interaction. Calculated binding constants revealed that DS had a higher interaction with DNA than S. Besides, DS demonstrated higher DPPH scavenging activity in comparison to S. In vitro inhibitory effects of DS and S against AChE and BuChE put forward that DS exhibited stronger inhibitory activity than S.

The preliminary biological activity results reported in our study are promising for obtaining more comprehensive structure-action relationships with derivatizations on the skeletal structure, determination of the type of ChE inhibition by kinetic studies, molecular modeling and toxicity studies and testing of compounds in animal models according to these possible results. In conclusion, the synthesized DS molecule is thought to be a promising scaffold structure in the treatment of neurological diseases. In future studies, we plan to carry out further bioactivity studies on this structure and to obtain broader structure-effect relationships by synthesizing possible molecules with similar skeleton.

Acknowledgments

The author is grateful to the Kahramanmaras Sutcu Imam University, Scientific Research Projects Unit (KSU-BAP 2019/3-21 M) for the financial support.

Conflict of Interest

There are no conflicts of interest in this work.

References

[1] Carmo C.M., Mendes E., Jesus P.M., Paula F.A., Marco C.J., The Multifactorial Nature of Alzheimer's Disease for Developing Potential Therapeutics, *Curr. Top. Med. Chem.*, 13 (15) (2013) 1745–1770.

[2] Mayeux R., Sano M., Treatment of Alzheimer's Disease, *N. Engl. J. Med.*, 341 (22) (1999) 1670–1679.

[3] George G., Koyiparambath V.P., Sukumaran S., Nair A.S., Pappachan L.K., Al-Sehemi A.G., ... & Mathew B., Structural Modifications on Chalcone Framework for Developing New Class of Cholinesterase Inhibitors, *International Journal of Molecular Sciences*, 23 (6) (2022) 3121.

[4] Agis-Torres A., Sollhuber M., Fernandez M., Sanchez-Montero J., Multi-Targetdirected Ligands and Other Therapeutic Strategies in The Search of A Real Solution for Alzheimer's Disease, *Curr. Neuropharmacol.*, 12 (1) (2014) 2–36.

[5] Svobodova B., Mezeiova E., Hepnarova V., Hrabinova M., Muckova L., Kobrlova T., ... & Korabecny J, Exploring Structure-Activity Relationship in Tacrine-Squaramide Derivatives as Potent Cholinesterase Inhibitors, *Biomolecules,* 9 (8) (2019) 379.

[6] Chen P.H., Dong G., Cyclobutenones and Benzocyclobutenones: Versatile Synthons in Organic Synthesis, *Chemistry–A European Journal*, 22 (51) (2016) 18290-18315.

[7] Elliott T.S., Slowey A., Ye Y., Conway S.J., The Use of Phosphate Bioisosteres in Medicinal Chemistry and Chemical Biology, *Med. Chem. Comm.*, 3 (7) (2012) 735-751.

[8] Henary M., Cyanine and Squaric Acid Metal Sensors, *Sensors and Actuators B: Chemical*, 243 (2017) 1191-1204.

[9] Tong C., Liu T., Saez T.V., Noteborn W.E.M., Sharp T.H., Hendrix M.M.R.M., Voets I.K., Mummery C.L., Orlova V.V., Kieltyka R.E., Squaramide-Based Supramolecular Materials for Three-Dimensional Cell Culture of Human Induced Pluripotent Stem Cells and Their Derivatives, *Biomacromolecules*, 19 (4) (2018) 1091-1099.

[10] Qian X., Jin C., Zhang X., Jiang Y., Lin C., Wang L., Squaramide Derivatives and Their Applications in Ion Recognition, *Prog. Chem.*, 26 (10) (2014) 1701.

[11] Castro I., Calatayud M.L., Sletten J., Julve M., Lloret F., Squarate and Croconate in Designing One-and Two-Dimensional Oxamidato-Bridged Copper (II) Complexes: Synthesis, Crystal Structures and Magnetic Properties of $[Cu_2(Apox)(C_4O_4)(H_2O)_2]N\cdot NaH_2O$ and $[Cu_4(Apox)_2(C_5O_5)_2]\cdot 6H_2O$. *Comptes, Rendus l'Académie Des Sci. IIC-Chemistry*, 4 (3) (2001) 235-243.

[12] Cheuquepán W., Martínez-Olivares J., Rodes A., Orts J.M., Squaric Acid Adsorption and Oxidation at Gold and Platinum Electrodes, *J. Electroanal. Chem.*, 819 (2018) 178-186.

[13] Chasák J., Šlachtová V., Urban M., Brulíková L. Squaric Acid Analogues in Medicinal Chemistry, *European Journal of Medicinal Chemistry*, 209 (2021) 112872.

[14] Olmo F., Rotger C., Ramírez-Macías I., Martínez L., Marín C., Carreras L., Urbanova K., Vega M., Chaves-Lemaur G., Sampedro A., Synthesis and Biological Evaluation of N, N'-Squaramides with High in Vivo Efficacy and Low Toxicity: Toward A Low-Cost Drug Against Chagas Disease, *J. Med. Chem.*, 57 (2014) 987-999.

[15] Cui D., Prashar D., Sejwal P., Luk Y.Y., Water-Driven Ligations Using Cyclic Amino Squarates: A Class of Useful SN1-Like Reactions, *Chem. Commun.*, 47 (4) (2011) 1348-1350.

[16] Storer R.I., Aciro C., Jones L.H., Squaramides: Physical Properties, Synthesis and Applications, *Chem. Soc. Rev.*, 40 (5) (2011) 2330-2346.

[17] Korkmaz U., Uçar I., Bulut A., Büyükgüngör O., Three Forms of Squaric Acid with Pyrazine and Pyridine Derivatives: An Experimental and Theoretical Study, *Structural Chemistry*, 22 (2011) 1249-1259.

[18] Bulut A., Yesilel O.Z., Dege N., Icbudak H., Olmez H., Büyükgüngör O., Dinicotinamidium Squarate, *Acta Crystallographica Section C: Crystal Structure Communications*, 59 (12) (2003) o727-o729.

[19] Bartoszak-Adamska E., Dega-Szafran Z., Komasa A., Szafran M., Structural and Spectroscopic Properties of Piperidinium-4-Carboxylic Acid Hydrogen Squarate. *Vibrational Spectroscopy*, 81 (2015) 13-21.

[20] Sang Z., Song Q., Cao Z., Deng, Y., Zhang L. Design, Synthesis, and Evaluation of Chalcone-Vitamin E-Donepezil Hybrids as Multi-Target-Directed Ligands for the Treatment of Alzheimer's Disease, *Journal of Enzyme Inhibition and Medicinal Chemistry*, 37 (1) (2022) 69-85.

[21] Li Q., He S., Chen Y., Feng F., Qu W., Sun, H., Donepezil-Based Multi-Functional Cholinesterase Inhibitors for Treatment of Alzheimer's Disease, *Eur. J. Med. Chem.*, 158 (2018) 463–77.

[22] Unzeta M., Esteban G., Bolea I., Fogel W.A., Ramsay R.R., Youdim M.B., ... & Marco C.J., Multi-Target Directed Donepezil-Like Ligands for Alzheimer's Disease, *Front Neurosci.*, 10 (2016) 205.

[23] Qiang X., Sang Z., Yuan W., Li Y., Liu Q., Bai P., ... & Deng Y., Design, Synthesis and Evaluation of Genistein-O-Alkylbenzylamines as Potential Multi-Functional Agents for the Treatment of Alzheimer's Disease, *Eur. J. Med. Chem.*, 76 (2014) 314–31.

[24] Turgut E., Gungor O., Kirpik H., Kose A., Gungor S.A., Kose M., Benzimidazole Ligands with Allyl, Propargyl or Allene Groups, DNA Binding Properties, and Molecular Docking Studies, *Appl. Organometallic Chem.*, 35 (9) (2021) e6323.

[25] Kose A., Gungor O., Ballı J.N., Erkan S., Synthesis, Characterization, Non-Linear Optical and DNA Binding Properties of A Schiff Base Ligand and Its Cu(II) and Zn(II) Complexes, *Journal of Molecular Structure*, 1268 (2022) 133750.

[26] Ellman G.L., Courtney K.D., Andres V., Feather-Stone R.M. A New and Rapid Colorimetric Determination of Acetylcholinesterase Activity, *Biochem. Pharmacol.*, 7 (2) (1961) 88-95.

[27] Liu D., Guo Y., Wu P., Wang Y., Kwaku G.M., Ma H., The Necessity of Walnut Proteolysis Based on Evaluation After in Vitro Simulated Digestion: ACE Inhibition and DPPH Radical-Scavenging Activities, *Food Chemistry*, 311 (2020) 125960.

[28] Gungor O., Kose M., The Biguanide–Sulfonamide Derivatives: Synthesis, Characterization and Investigation of Anticholinesterase Inhibitory, Antioxidant and DNA/BSA Binding Properties, *Journal of Biomolecular Structure and Dynamics*, 41 (24) (2023) 14952-14567.

[29] Catro I., Calatayud M.L., Sletten J., Lloret F., Julve M., Syntheses, Crystal Structure and Magnetic Properties of $[Ni_2(C_4O_4)(tren)_2][ClO_4]_2$ and $[Ni_2(C_4O_4)(tren)_2(H_2O)_2][ClO4]_2$ (tren=tris(2-amino-ethyl)amine), *Journal Chemical Society Dalton Translation*, 5 (1997) 811-817.

[30] Mondal A., Das D., Chaudhuri N.R., Thermal Studies of

Nickel(II) Squarate Complexes of Triamines in The Solid State, *Journal of Therma Analysis and Calorimetry*, 55 (1999) 165-172.

[31] Maji T.K., Das D., Chaudhuri, N.R., Preparation, Characterization, and Solid State Thermal Studies of Cadmium(II) Squarate Complexes of Ethane-1,2-Diamine and Its Derivatives, *Journal of Thermal Analysis and Calorimetry*, 63 (2001) 617-625.

[32] Das D., Ghosh A., Chaudhuri, N.R., Preparation, Characterization, and Solid State Thermal Studies of Nickel(II) Squarate Complexes of 1,2-Ethanediamine and Its Derivatives, *Bulletion Chemical Society, Japan*, 70 (4) (1997) 789-797.

[33] Li N., Ma Y., Yang C., Guo L., Yang X., Interaction of Anticancer Drug Mitoxantrone with DNA Analyzed by Electrochemical and Spectroscopic Methods, *Biophysical Chemistry*, 116 (3) (2005) 199-205.

[34] Chakraborty A., Panda A.K., Ghosh R., Biswas A. DNA Minor Groove Binding of A Well Known Anti-Mycobacterial Drug Dapsone: A Spectroscopic, Viscometric and Molecular Docking Study. *Archives of Biochemistry and Biophysics*, 665 (2019) 107-113.

[35] Madku S.R., Sahoo B.K., Lavanya K., Reddy R.S., Bodapati A.T.S. DNA Binding Studies of Antifungal Drug Posaconazole Using Spectroscopic and Molecular Docking Methods. *International Journal of Biological Macromolecules*, 225 (2023) 745-756.

[36] Shi J.H., Liu T.T., Jiang M., Chen J., Wang Q., Characterization of Interaction of Calf Thymus DNA with Gefitinib: Spectroscopic Methods and Molecular Docking, *Journal of Photochemistry and Photobiology B: Biology*, 147 (2015) 47-55.

[37] Shi J.H., Chen J., Wang J., Zhu Y.Y., Binding Interaction Between Sorafenib and Calf Thymus DNA: Spectroscopic Methodology, Viscosity Measurement and Molecular Docking, *Spectrochimica Acta Part A: Molecular and Biomolecular Spectroscopy*, 136 (2015) 443-450.

[38] Shahabadi N., Hashempour S. DNA Binding Studies of Antibiotic Drug Cephalexin Using Spectroscopic and Molecular Docking Techniques, *Nucleosides, Nucleotides and Nucleic Acids*, 38 (6) (2019) 428-447.

[39] Al-ghulikah H.A., Mughal E.U., Elkaeed E.B., Naeem N., Nazir Y., Alzahrani, A.Y.A., ... Shah S.W.A., Discovery of Chalcone Derivatives as Potential A-Glucosidase and Cholinesterase Inhibitors: Effect of hyperglycemia in paving a path to dementia, *Journal of Molecular Structure*, 1275 (2023) 134658.

Cumhuriyet Sci. J., 45(2) (2024) 227-234
DOI: https://doi.org/10.17776/csj.1398295

Cumhuriyet Science Journal

| csj.cumhuriyet.edu.tr | Founded: 2002 ISSN: 2587-2680 e-ISSN: 2587-246X Publisher: Sivas Cumhuriyet University

Examining the Effect of Metformin on Cell Death Mechanisms in Relation to Hippo Signaling in MDA-MB-231 Breast Cancer Cells

Özge Rencüzoğulları [1,a,*] , Zeynep Gülşah Sonalp [1,b]

[1] *Department of Science and Letter, Istanbul Kultur University, 34158, Istanbul,Türkiye.*
**Corresponding author*

Research Article

History
Received: 30/11/2023
Accepted: 30/05/2024

ABSTRACT

Breast cancer is one of the most common cancer types in women in the world and our country. Antitumorigenic activity is achieved with various therapeutic drugs by directly suppressing the constantly active PI3K/Akt/mTOR signaling pathway or enabling AMPK activation. AMPK, a positive regulator of autophagy, ensures the induction of autophagy by suppressing the Akt/mTOR pathway. Metformin, an anti-diabetic drug, achieves its anti-tumorigenic effect by activating AMPK. Deregulation of the Hippo signaling pathway is a new therapeutic target because it causes cancer cells to become aggressive and evade cell death mechanisms. The study aims to reveal the effects of metformin treatment on Hippo signaling pathway activity on apoptosis and autophagy, depending on drug treatment in MDA-MB-231 breast cancer cells. Metformin decreased the cell viability through induction of mitochondria membrane potential loss in dose and time dependent manner in MDA-MB-231 cells. The colony forming potential of the MDA-MB-231 cells were suppressed by 10 mM metformin treatment which was induced apoptotic cell death and autophagy by increasing Bim, Bad, Bak and cleavage of caspase 3, 9, PARP and Beclin1, Atg5 and Atg7. Moreover, Hippo signaling related protein levels showed remarkable increase due to metformin treatment. It was shown that metformin treatment increased the activity of the hippo signaling pathway, resulting in the induction of apoptosis and autophagy.

Keywords: Breast cancer, Metformin, Hippo signaling, Apoptosis, Autophagy.

[a] *o.berrak@iku.edu.tr* *https://orcid.org/0000-0002-2157-1289* [b] *gulsahsonalp@gmail.com* *https://orcid.org/0000-0001-9638-371X*

Introduction

Breast cancer is one of the most common cancer types in women in the world. Risk factors such as menopausal age, obesity, type 2 diabetes, personal cancer history, familial cancer history, BRCA1-2 mutations, and environmental factors such as smoking and alcohol use are involved in the development of breast cancer. According to 2018 World Health Organization (WHO) data, one in every six deaths is caused by cancer, and breast cancer ranks first in women [1]. According to research by the International Agency for Research on Cancer (IARC), breast cancer, which was seen in 2.26 million women in 2020, is predicted to be seen in 3.19 million women 20 years later. According to 2020 IARC data, 24,175 women were diagnosed with breast cancer in Turkey and 7,161 women died due to breast cancer [2]. New therapeutic agents need to be developed for the treatment of breast cancer, which is a common type of cancer among women and its incidence is increasing.

Metformin is a biguanide-class antidiabetic drug used as first-line treatment in patients with type 2 diabetes. The primary effect of metformin is to inhibit glucose production in the liver, but it also increases the insulin sensitivity of peripheral tissues [3]. In addition to regulating insulin metabolism, metformin provides weight control and is also used in the treatment of insulin resistance. The required daily dose has been determined as 500-2500 mg/day [4]. The main molecular targets of metformin are the mitochondrial electron transport chain (ETC), Adenosine monophosphate-activated protein kinase (AMPK) and mTOR [5]. ETC causes downregulation of AMPK by producing Adenosine triphosphate (ATP). Metformin, on the other hand, inhibits ETC, reducing ATP synthesis, and the high AMP/ATP ratio activates AMPK, which suppresses mTOR. Metformin-mediated inhibition of ATP synthesis provides mTOR inhibition. Many studies in colon cancer cells, breast cancer cells and the model organism *C. elegans* have shown that metformin slows down the growth of cancer cells in various types of cancer [6,7]. Studies have shown that metformin has tumorigenesis-suppressing and antiproliferative effects in various types of cancer. It shows its anticancer effect through AMPK-dependent or AMPK-independent pathways [8]. Signal transmission in cancer cells occurs through the activation of cytoplasmic kinases such as serine/tyrosine kinase and receptor tyrosine kinases (RTK). Uncontrollable and continuous RTK activity is observed during the tumor formation phase. The PI3K/Akt/mTOR signaling pathway is involved in important cellular events such as cell growth, autophagy, apoptosis and lipid metabolism. Antitumorigenic activity is achieved by directly suppressing or AMPK-dependent inhibition of the PI3K/Akt/mTOR signaling pathway using various drugs. AMPK, a positive regulator of autophagy, induces autophagy by suppressing the Akt/mTOR pathway

[9]. AMPK/mTOR signaling induces apoptosis by causing an increase in the expression of caspase-3, which provides DNA fragmentation in apoptosis as well as autophagy [10]. Metformin induced apoptosis through induction of ROS production and the effect of metformin were highly associated with the glucose concentration on MDA-MB-231 aggressive breast cancer cells. But, the relation of these mechanism with Hippo signaling still largely unknown in MDA-MB-231 cells.

The Hippo signaling pathway regulates organ size and maintains tissue stability by managing cell proliferation and apoptosis. The Hippo signaling pathway consists of mammalian STE20-like kinase 1/2 (MST 1/2), large tumor suppressor kinase 1/2 (LATS 1/2) and Yes-associated protein 1 (YAP) and its paralogue WW-domain-containing transcription regulator 1 (TAZ) elements [10]. The basis of the Hippo pathway is based on serine/threonine phosphorylation. Activation of the Hippo pathway results in phosphorylation of YAP at Ser127 *via* LATS 1/2 and consequently YAP inactivation. Phosphorylated YAP is degraded in the cytoplasm as a result of its interaction with 14-3-3, resulting in inhibition of target gene transcription [11,12]. When the Hippo pathway is inactivated, the inactive MST1/2 and LATS1/2 dephosphorylate YAP/TAZ, leading to YAP/TAZ accumulation in the nucleus. YAP/TAZ accumulates in the nucleus and binds with TEAD family transcriptional factors (TEAD1-4) to stimulate gene transcription that regulates various cellular activities such as cell proliferation [13]. Defects in the Hippo signaling pathway encourage breast cancer cells to metastasize. YAP deficiency has been observed to reduce the incidence of lung metastases in a genetically engineered mouse model of breast cancer [14]. A study showed that metformin inhibited the stem structure and epithelial-mesenchymal transition of glioma cells by regulating YAP activity [15]. The Hippo signaling related genes showed variation between various breast cancer cells. So, the oncogenic and tumor suppressor role of Hippo signaling against chemotherapeutics are still needed to be investigated

In line with the information in the literature, this study aims to demonstrate the effects of metformin treatment in breast cancer cells on the Hippo signaling pathway activity in a relation with apoptosis and autophagy, depending on the drug treatment concentrations. In addition, the results obtained are intended to be used as preliminary data in phase studies for breast cancer treatment.

Material and Methods

MTT Cell Viability Test

MDA-MB-231 (ATCC HTB-26) breast cancer cells were seeded in a 96-well/plate with $1x10^4$ cells in each well, and the cells were incubated at 37°C for 24 hours. Then, the cells are incubated with 1-10 mM metformin for 24h and 48h at 37°C. At the end of the incubation, 10 µl of 3-(4,5-dimethyltriazol-2-yl)-2-5-diphenyltetrazolium bromide (MTT) agent was added to the medium on the cells and incubated for 4 hours at 37°C. After incubation with the MTT agent, 100 µl Dimethyl sulfoxide (DMSO) was added and kept in the dark for 5 minutes to dissolve the formazan crystals formed by living cells metabolizing the MTT agent. After dissolving Formazan crystals with DMSO, the cell viability rate was measured by absorbance at 570 nm in a microplate ELISA reader (Bio-Rad, California, USA). The results were shown as the average of three experiments with at least four repetitions.

Colony Formation Test

MDA-MB-231 cells were seeded into a 6-well petri dish as $2x10^3$ cells. 10 mM metformin was treated for 24h and 48h. Then, the medium on the cells was replaced with fresh medium. Compared to the control group cells reaching 90% density, the media was removed after approximately 14 days. Cells were washed with 1X PBS and incubated for 15 minutes at RT with a 3:1 ratio of 100% methanol: acetic acid. 500 µl 0.5% crystal violet was added to the cells and incubated at RT for 20 minutes. After 20 minutes, the dye was removed by washing with distilled water. Colonies were drawn and counted.

Trypan Blue Cell Proliferation Assay

A cell survival experiment was performed to determine the effect of metformin on cell proliferation in MDA-MB 231 breast cancer cells. $5x10^4$ cells were seeded in a 6-well/plate. 10 mM metformin was treated for different time points. At the end of every 24, 48 and 72 hours, cells were collected with trypsin and centrifuged at 2000 rpm for 5 minutes. Cells were dissolved with 10 µl media and mixed with 10 µl of trypan blue and counted in a hemocytometer. Cell survival assay was examined as the average of three different experiments with at least duplicates.

Fluorescence Microscopy

$1x10^4$ cells were seeded into 6 wells/plates and then treated with various concentrations (1, 2, 5 and 10 mM) of metformin for 24h and 48h. The effect of metformin on mitochondrial membrane potential loss was examined by 3,3'-dihexyloxacarbocyanine iodide (DiOC6) (4 nM; Calbiochem, La Jolla, CA, USA) fluorescent staining and visualized by fluorescence microscopy (Ex./Em.: 488/525 nm) [16]. Propidium iodide (PI) staining was performed to observe the cell death ratio after metformin treatment (Ex./Em.: 536/617 nm) [17].

Immunoblotting

MDA-MB-231 cells were treated with the 10 mM metformin for 24h and 48 h. As was proceeded in our previous study; first, cells were washed with ice-cold 1x PBS and lysed mPER extraction buffer in the presence of a protease inhibitor cocktail (Complete, Roche)[18]. Following lysis of the cells, total protein lysate was obtained after centrifugation for 15 min at 13,200 rpm. Bradford protein assay was used to determine the protein concentrations (Bio-Rad, California, USA). Samples were kept in the -80° freezer until use. Separation of total protein lysates proceeded with a 10-12% SDS-PAGE and

proteins were transferred onto PVDF membranes (Roche, Basel, Switzerland). The membranes were then blocked with a 5% milk-blocking solution (prepared with Tris buffer saline-Tween 20) and incubated with appropriate primary and HRP-conjugated secondary antibodies (CST) in antibody. Then membranes were washed

with 1X TBS-Tween 20, the proteins were analyzed using an enhanced chemiluminescence detection system (Chemidoc Bio-Rad, California, USA).

Statistical Analysis

The results obtained are the average of three different experiments with at least two repetitions. All numerical results obtained from the experiments were converted into graphs using GraphPad Prism 6 and statistical analysis was carried out using the Two-way ANOVA method. The p value for significant changes is *p<0.05; **p<0.01, ***p<0.001, ****p<0.0001.

Results and Discussion

Metformin Reduced Cell Viability in a Time and Dose-dependent Manner in MDA-MB-231 Breast Cancer Cell

Metformin is a first-line anti-diabetic drug used to treat type 2 *diabetes mellitus* and regulate blood sugar in overweight people. The risk of breast cancer in women with diabetes increases compared to healthy people, especially the risk of breast, pancreas, colon, liver and uterine cancer increases in people with diabetes. A meta-analysis has shown that long-term metformin treatment will reduce the risk of T2D-related breast cancer [19]. In the study conducted by Phoenix et al. in 2010, long-term treatment with metformin was shown to be effective in primary tumor growth [20]. In light of this information, the mechanisms of action and signaling pathways of metformin on the MDA-MB-231 triple-negative breast cancer cell line were investigated and the research was supported by *in-vitro* experiments. MTT survival test was performed to determine the effect of metformin on cell viability. Metformin was treated to MDA-MB-231 breast cancer cells depending on dose (1-10 mM) and time (24-48 hours) (Figure 1A). Metformin caused a dose-dependent decrease in cell viability. While a 40% loss of cell viability was observed in a 24h application of 10 mM metformin, a 50% cell viability was observed in a 48h application of 10 mM metformin. The effect of 10 mM metformin on cell proliferation depending on time was examined by trypan blue assay (Figure 1B). Compared to the control group, 10 mM metformin showed a cytotoxic effect and suppressed the cell proliferation rate in a time-dependent manner in cell viability. The study on the xenograft model of breast cancer showed the anti-proliferative role of metformin at the concentration of 150 mg/kg/day led to significant reduction of tumor growth [21].

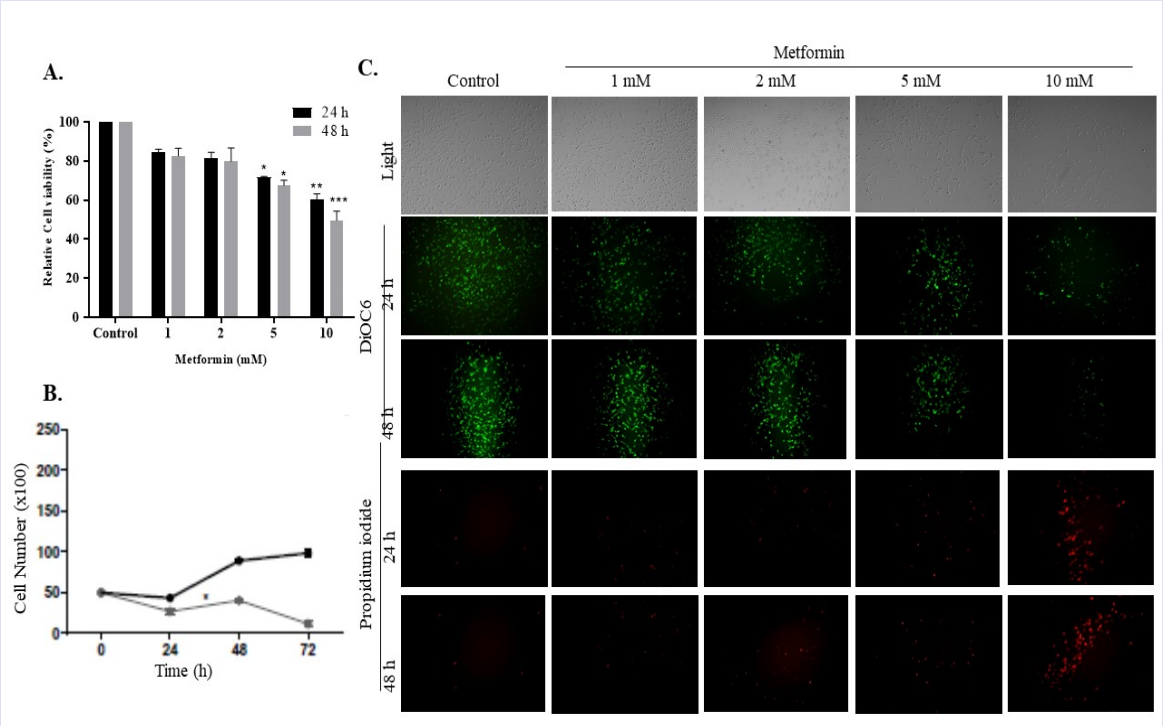

Figure 1. Metformin increased cell viability loss in MD-MB-231 breast cancer cells. A. MTT cell survival assay was performed after metformin treatment in MDA-MB-231 breast cancer cells in a dose- and time-dependent manner (* p<0.05; ** p<0.01, *** p<0.001). B. Cell survival assay (Trypan blue assay) was proceeded after metformin treatment to MDA-MB-231 cells (*p<0,05). C. The effect of metformin on cell viability was examined by DiOC6 and PI staining by fluorescence microscopy. Scale bar: 50 µm

It was examined by DiOC6 staining to observe the effect of metformin on cell viability depending on mitochondrial membrane potential (MMP) (Figure 1C). Live cells stained with DiOC6 were observed in green fluorescent color. Treatment of 1 mM and 2 mM metformin for both 24h and 48h did not cause a significant decrease in cell viability. However, although 5 mM metformin was more effective in 48h metformin treatment, it also reduced cell viability by 50% in the 24h treatment period. By increasing MMP loss, 10 mM metformin significantly reduced MDA-MB-231 breast cancer cell viability. Propidium iodide is a fluorescent intercalating agent that can bind to DNA insertion with little or no sequence preference between bases. When 10 mM metformin was treated, cells with impaired membrane integrity were observed in red color (Figure 1C). In the study with ovarian cancer, metformin enhanced the cytotoxic effect of cisplatin [22]. It was known that metformin as an anti-diabetic drug reduces the glucose levels. The cell death mechanisms under the low glucose level especially in MDA-MB-231 breast cancer cells still under investigation. The high glucose concentration (25 mM) prevent the anti-proliferative mechanism of metformin in MDA-MB-231 cells [23]. Therefore, the mechanism under induction of cell death is further investigated.

Time-dependent Metformin Treatment Increased Apoptotic Cell Death of MDA-MB-231 Triple-negative Breast Cancer Cells

Recent studies have shown that metformin may suppress tumor growth in many types of cancer, reduce cancer risk, and be associated with improved prognosis in patients with cancer [24]. When the long-term effect of metformin was examined, the effects of 24h and 48h treatment on colony formation potential were determined as 265 and 72 colonies, respectively, compared to the control group (410 colonies) (Figure 2A). Considering the number of colonies and colony diameters, it was shown that the treatment of 10 mM metformin for 48h significantly suppressed cell proliferation. A study in MCF-7 and MDA-MB-231 cells showed that the anticarcinogenic effect of metformin was induced by increasing glucose uptake [25]. Moreover, metformin treatment in these cells caused an increase in oxidative stress generation and DNA damage [26]. Therefore, in our study, we investigated the effect of metformin on the apoptotic cell death mechanism. Cells were treated with the selected concentration of 10 mM metformin for 24 and 48 h, followed by total protein isolation. Changes in the expression of apoptosis-related proteins (BIM, BAD, BAK, cleaved caspase 3, cleaved caspase 9, and PARP) were examined by immunoblotting (Figure 2A-B). Both pro-apoptotic and anti-apoptotic proteins regulate apoptotic cell death. BIM, a pro-apoptotic protein, works with pro-apoptotic proteins such as BAD to regulate cell death and survival necessary for normal tissue homeostasis. Decreased BIM expression in cancer cells induces tumor formation. As a result, a 4-fold increase in Bad and Bak protein expressions was observed and a 2-fold increase in Bim protein expression was observed compared to the control group. As consistent with our study, metformin exerted pro-apoptotic effect on HT-29 colon cancer cells by inhibiting nuclear factor-kappa B (NF-κB) signaling which activated caspases [27]. The high concentration of metformin (25 mM) induced apoptotic cell death *via* upregulation of p53 but decreasing in cyclin D1 expression. Additionally, the AMPK expression level of the breast cancer cells also effect the anti-proliferative role metformin [28]. Other proteins that are effective in apoptotic cell death are caspases. Caspases, which remain inactive until the appropriate signal arrives, take part in the apoptotic pathway after being activated. Activated caspase 9 is cleaved and acts as the initiator caspase, enabling the activation of caspase 3, which is the effector caspase, and thus causing cell death through the intrinsic apoptotic pathway [29].

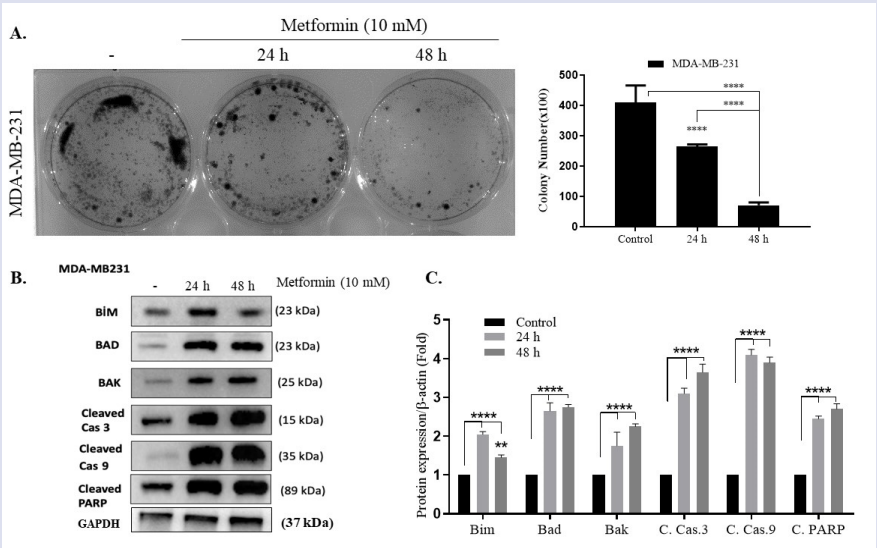

Figure 2. A. Examination of the effect of metformin on the colony formation potential of MDA-MB-231 breast cancer cells. B. Display the number of colonies formed as a result of time-dependent metformin treatment using the Image J program (****p<0.0001). C. Apoptotic marker protein expressions (Bim, Bad, Bak, Cle. Caspase 3, Cle. Caspase 9 and Cle. PARP) were analyzed by immunoblotting flowing 24h and 48h metformin treatment in MDA-MB-231 cells. D. Graphical representation of the changes in the expression of apoptotic marker proteins by using the Image J program (****p<0,0001).

A 4-fold increase was observed in cleaved caspase 9 and therefore cleaved caspase 3 protein expressions compared to the control group, depending on time, after metformin treatment. Caspase-mediated apoptotic cell death occurs through the cleavage of PARP. Due to the increase in caspase 3 expression, an increase in the expression of cleaved PARP is also observed (Figure 2A-B). A study in A498 renal cell carcinoma cells also showed the apoptotic effect of metformin which induced cleavage of caspase 3 and PARP in a dose-dependent manner. In the same study it was concluded that the metformin-induced apoptosis was modulated by degradation of caspase 8 (FLICE)-like inhibitory protein (c-FLIP$_L$) which has an inhibitory role on caspase-8 activation [30]. As a result, it has been shown that metformin treatment causes a 4-fold decrease in colony formation in MDA-MB-231 cells depending on the treatment time, proliferation is suppressed. Similar to the study conducted by Jang et al. on T4 bladder cancer cells, a positive effect on caspase-dependent apoptosis was observed in our study after metformin treatment [31]. Treatment with metformin caused an increase in the expression of intrinsic apoptosis pathway markers in breast cancer cells, causing the cell to undergo programmed cell death.

Effect of Time-dependent Metformin Treatment on the Autophagy Mechanism in MDA-MB-231 Breast Cancer Cells

Although autophagy, a process that regulates cell homeostasis that occurs under various stressful conditions such as organelle damage, the presence of abnormal proteins and nutrient deprivation, is associated with non-apoptotic cell death, it is considered a survival mechanism because it maintains intracellular balance. In the study conducted by Gözüaçık and Kimchi in 2006, p53 activation stimulates autophagy by inhibiting mTOR activity, which is effective in an antiapoptotic signaling pathway [32]. To demonstrate the effect of time-dependent metformin treatment on autophagy-induced cell death, immunoblotting with autophagy-related proteins (Atg5, Atg7, Beclin-1) was examined after 24 and 48 hours of metformin treatment (Figure 3A-B). Beclin-1 protein is the central regulator of autophagy. It is also a tumor suppressor whose expression is decreased in many types of cancer such as breast and ovarian [33,34]. Therefore, decreased Beclin-1 expression has been associated with tumorigenesis. As a result of the treatment of 10 mM metformin, which is the effective dose, for 24 and 48 h, a 2-fold and 2.3-fold increase in Beclin-1 expression was observed in MDA-MB-231 cells, respectively. Atg5, another autophagy regulator, is a central regulator required for autophagy in terms of its participation in autophagosome elongation. In studies, inhibiting Atg5 caused partial resistance to chemotherapy [35,36]. Deficiency of Atg7, which is involved in the regulation of autophagy, causes a phenotype lacking autophagy and disruption of cell homeostasis [37]. As a result of immunoblotting, no significant difference was observed in the expression of Atg5 with 24-hour metformin treatment, while 48-hour metformin caused a 2-fold increase in Atg5 expression. A 2-fold increase in Atg7 expression was observed compared to the control group, depending on both 24 h and 48 h metformin treatment duration (Figure 3A-B).

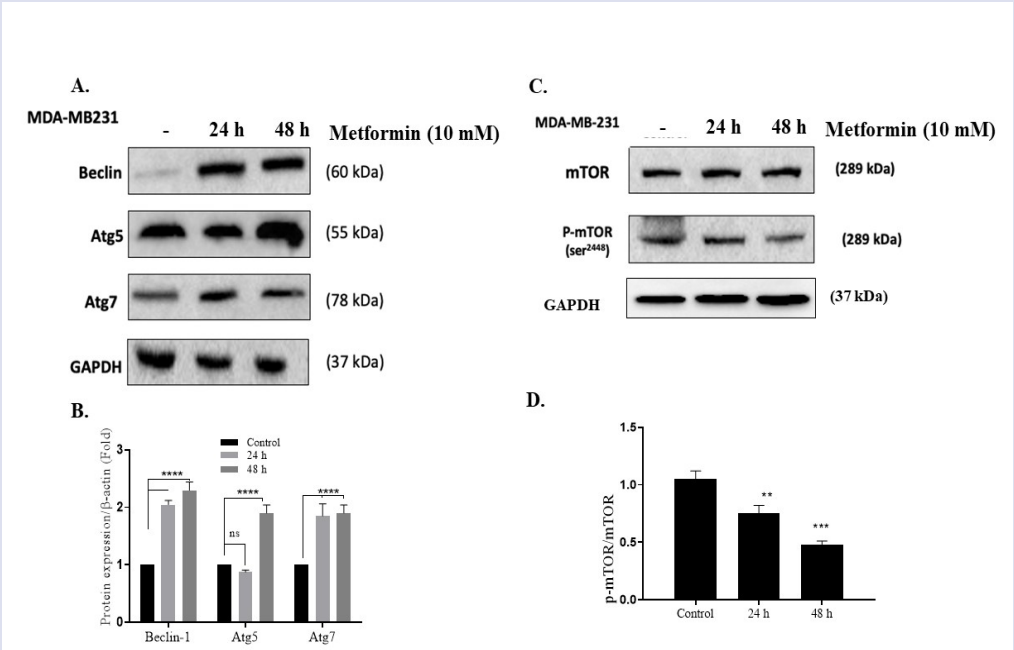

Figure 3. Demonstration of autophagy marker protein expressions (A. Beclin-1, Atg-5, Atg7) in MDA-MB-231 cells following metformin administration using the ChemiDoc MP Imaging System. B. Graphical representation of the changes in the expression of autophagy marker proteins as a result of time-dependent treatment with 10 mM Metformin in the MDA-MB-231 breast cancer cell line, using the Image J program. (****p<0.0001) C. Demonstration of mTOR and p-mTOR protein expressions in MDA-MB-231 cells following metformin treatment and analyse with the ChemiDoc MP Imaging System device. D. Graphical expression of mTOR and p-mTOR protein expression rates by using the Image J program. (** p<0.01, *** p<0.001)

After 48 hours of metformin treatment, a 2-fold decrease in phosphorylated mTOR (Ser2448) expression level was observed compared to the control group, but there was no significant change in total mTOR expression due to metformin treatment (Figure 3C-D). mTOR activity supports cell survival and energy metabolism, a mechanism that works opposite to the autophagy mechanism. In a study conducted to demonstrate the effect of metformin on Beclin-dependent autophagy in gastric cancer cells, it was shown that autophagy was induced in gastric cancer cells by decreasing the p-mTOR protein level and resulting in an increase in Beclin protein level [38]. As a result, it has been observed that Metformin induces autophagy through inhibition of mTOR activity in addition to apoptotic death in MDA-MB-231 breast cancer cells and has an inhibitory effect on tumor growth caused by autophagy-dependent cell death.

Metformin Suppressed the Proliferation and Invasion of MDA-MB-231 Breast Cancer Cells through Activation of the Hippo Signaling Pathway.

The Hippo signaling pathway, which modulates cell death, cell proliferation, and cell differentiation, plays a role in cell homeostasis by regulating cell number. YAP and TAZ, two interrelated transcriptional factors, have an important place in tissue repair and organ size control in cancer treatment [39]. In this study, to observe the effect of metformin on the Hippo signaling pathway in MDA-MB-231 triple-negative breast cancer cells, changes in Hippo signaling pathway markers YAP, TAZ and p-YAP protein expressions following 24h and 48h of metformin treatment were examined by immunoblot analysis (Figure 4A-C). It was observed that YAP protein expression, which has an anti-apoptotic, cell migration and invasion-promoting effect, decreased to 0.3-fold and 0.4-fold levels, respectively, after 24h and 48h of metformin treatment, compared to the control group. Metformin treatment for 24h and 48h caused a 2.6- and 2.7-fold increase in the level of p-YAP, which increases apoptotic activity by ensuring YAP phosphorylation, respectively, compared to the control group. When p-YAP expression is compared to total Yap expression, 24h metformin increased 3-fold and 48-h metformin increased 3.5-fold (Figure 4C). Studies have suggested that the Hippo signaling pathway can control apoptosis through the YAP protein, based on the response of the effector YAP protein regulated by the Hippo signaling pathway after DNA damage. Recent studies have suggested that YAP activation is associated with drug resistance in cancer treatment, and as a result of the experiments, it has been observed that there is more YAP expression in drug-sensitive breast cancer cells compared to non-resistant ones. Accordingly, *in vivo* experiments showed that the YAP level in the nucleus was downregulated after treatment with metformin [40].

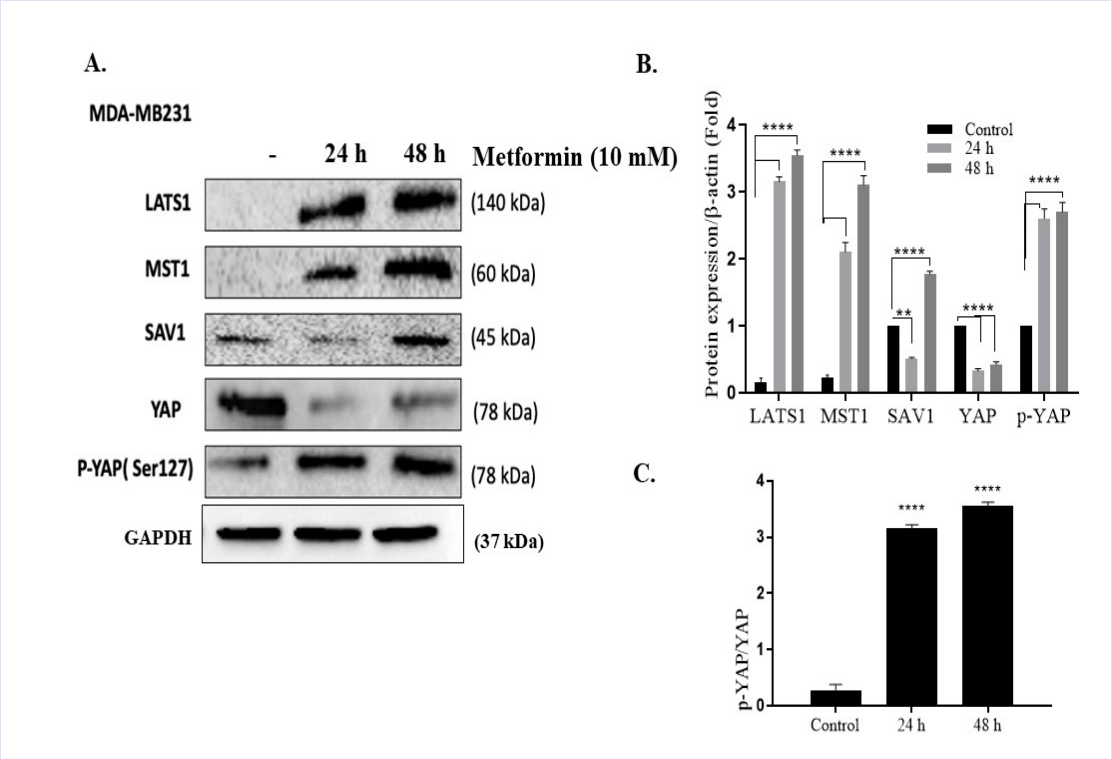

Figure 4. A. Demonstration of Hippo signaling pathway marker protein expressions (LATS1, MTS1, SAV1, YAP and p-YAP (S127) in MDA-MB-231 cells following metformin treatment. GAPDH was used as a loading control. B. Graphical expression of the changes in protein expression using the Image J program. C. Graphical representation of YAP and p-YAP protein expression rates in MDA-MB-231 breast cancer cell line as a result of 10 mM Metformin treatment (24-48 h) using the Image J program. (**p<0.01, ****p<0.0001)

Increased expression of TAZ, a Hippo signaling pathway regulator with anti-apoptotic effect that is highly expressed in many types of cancer, is associated with cancer metabolism [41]. Previous studies have observed that treatment with metformin has a dependent or independent effect on YAP inhibition, depending on the increase in MST1 and LATS1 interaction and expression [42]. In this study, metformin treatment for 24h and 48 h increased MST1 expression by 3.2 and 3.6-fold, respectively, and LATS1 expression level by 2.1 and 3.1-fold, respectively. Accordingly, it caused suppression of YAP expression. The expression of SAV1 protein, which has a tumor suppressor effect in many types of cancer, decreased by 0.5-fold in MDA-MB-231 breast cancer cells after metformin treatment within 24h while it increased by 1.8-fold with 48h metformin (Figure 4A-B). In the study conducted to demonstrate the role and mechanism of SAV1 on the development of pancreatic cancer; overexpression of SAV1 was shown to suppress cell migration and invasion and promote apoptosis [43]. Recent studies have reported that drug-sensitive and resistant cells are affected by different mechanisms of metformin treatment. *In vivo* and *in vitro* experiments indicated that metformin suppressed breast cancer by an AMPK-independent pathway to decrease YAP nuclear localization. In drug-sensitive cells, metformin activated the Hippo pathway by increasing KIBRA and FRMD6 expression, but this did not occur in drug-resistant cells [44].

As a result, following the 48h treatment of metformin, an increase in apoptotic cell death was observed due to activation of the Hippo signaling pathway.

Conclusion

As a result, in the light of the experiments performed, it has been shown that metformin treatment induced Hippo signaling pathway-dependent apoptosis in MDA-MB-231 triple negative breast cancer cells. Moreover, beside the downregulation of Hippo signaling, metformin inhibited cell proliferation and survival through upregulation of autophagy mechanism due to mTOR inhibition in breast cancer cells. The current study has some limitations, albeit the promising results. Firstly, glucose concentration is a limiting factor of metformin therefore the molecular mechanism of metformin as an anti-cancer drug in nondiabetic subjects should be investigated. Secondly, in the healthy cells, the adequate drug concentration of metformin should be determined, and thirdly, metformin-induced hippo signaling pathway in MDA-MD-231 cells should be investigated in various glucose concentration.

Acknowledgements

The authors wish to thank Scientific Research Projects Unit of Istanbul Kultur University for funding the study.

Conflict of Interest

There is not any conflict of interest or common interest with an institution/organization or a person that may affect the review process of the paper.

References

[1] Ferlay J., Colombet M., Soerjomataram I., Mathers C., Parkin DM, Piñeros M. Estimating the global cancer incidence and mortality in 2018: GLOBOCAN sources and methods, *Int J Cancer*, 144 (8) (2019) 1941–53.

[2] IARC. GLOBOCAN : Estimated Number of New Cases from 2020. *Int Agency Res Cancer.* 247 (22) (2020) 3087–3088.

[3] Erices R., Cubillos S., Aravena R., Santoro F., Marquez M., Orellana R. Diabetic concentrations of metformin inhibit platelet-mediated ovarian cancer cell progression, *Oncotarget,* 8 (13) (2017) 20865–20880.

[4] Wang YW., He SJ., Feng X., Cheng J., Luo YT., Tian L. Metformin: a review of its potential indications, *Drug Des Devel Ther.,* 11 (2017) 2421–2429.

[5] Vancura A, Bu P, Bhagwat M, Zeng J, Vancurova I. Metformin as an Anticancer Agent, *Trends Pharmacol Sci*., 39 (10) (2018) 867–878.

[6] Sabit H., Abdel-Ghany SE., M Said OA., Mostafa MA., El-Zawahry M. Metformin Reshapes the Methylation Profile in Breast and Colorectal Cancer Cells, *Asian Pac J Cancer Prev.* 19 (10) (2018) 2991–2999.

[7] Wu L., Zhou B., Oshiro-Rapley N., Li M., Paulo JA., Webster CM., An Ancient, Unified Mechanism for Metformin Growth Inhibition in C. elegans and Cancer, *Cell,* 167 (7) (2016) 1705-1718.e13.

[8] Davies G., Lobanova L., Dawicki W., Groot G., Gordon JR., Bowen M. Metformin inhibits the development, and promotes the resensitization, of treatment-resistant breast cancer, *PLoS One* 12 (12) (2017) e0187191.

[9] Liang P., Jiang B., Li Y., Liu Z., Zhang P., Zhang M. Autophagy promotes angiogenesis via AMPK/Akt/mTOR signaling during the recovery of heat-denatured endothelial cells, *Cell Death Dis.* [Internet]. 9 (12) (2018) 1152-1160.

[10] Bu H., Liu D., Zhang G., Chen L., Song Z. AMPK/mTOR/ULK1 Axis-Mediated Pathway Participates in Apoptosis and Autophagy Induction by Oridonin in Colon Cancer DLD-1 Cells, *Onco Targets Ther.* 13 (2020) 8533–8545.

[11] Mo JS., Park HW., Guan KL. The Hippo signaling pathway in stem cell biology and cancer, *EMBO Rep.,* 15 (6) (2020) 642–656.

[12] Yu FX., Guan KL. The Hippo pathway: regulators and regulations, *Genes Dev.,* 27 (4) (2013) 355–371.

[13] Moroishi T., Hansen CG., Guan KL. The emerging roles of YAP and TAZ in cancer, *Nat. Rev. Cancer,* 15 (2) (2015) 73–79.

[14] Wei C., Wang Y., Li X. The role of Hippo signal pathway in breast cancer metastasis, *Onco Targets Ther.,* 11 (1) (2018) 2185–2193.

[15] Yuan X., Wei W., Bao Q., Chen H., Jin P., Jiang W. Metformin inhibits glioma cells stemness and epithelial-mesenchymal transition via regulating YAP activity, *Biomed Pharmacother,* 102 (1) (2018) 263–270.

[16] Rencüzoğullari Ö., Arısan ED., Obakan Yerlikaya P., Çoker Gürkan A., Keskin B., Palavan Ünsal N. Inhibition of extracellular signal-regulated kinase potentiates the apoptotic and antimetastatic effects of cyclin-dependent kinase inhibitors on metastatic DU145 and PC3 prostate cancer cells, *J Cell Biochem.,* 120 (4) (2019) 5558–5569.

[17] Akkoç Y., Berrak Ö., Arısan ED., Obakan P., Çoker-Gürkan A., Palavan-Ünsal N. Inhibition of PI3K signaling triggered apoptotic potential of curcumin which is hindered by Bcl-2 through activation of autophagy in MCF-7 cells, *Biomed Pharmacother*, 71 (1) (2015) 161–171.

[18] Obakan Yerlikaya P., Mehdizadehtapeh L., Rencüzoğullari

Ö., Kuryayeva F., Çevikli SS., Özağar Ş. Gemcitabine in combination with epibrassinolide enhanced the apoptotic response in an ER stress-dependent manner and reduced the epithelial-mesenchymal transition in pancreatic cancer cells, *Turkish. J. Biol.,* 46 (6) (2022) 439–457.

[19] Park YMM., Sandler DP. Making sense of associations between type 2 diabetes, metformin, and breast cancer risk, *Br J Cancer,* 125 (7) (2021) 909–910.

[20] Phoenix KN., Vumbaca F., Fox MM., Evans R., Claffey KP. Dietary energy availability affects primary and metastatic breast cancer and metformin efficacy, *Breast Cancer Res Treat.,* 123 (2) (2010) 333–344.

[21] Rizvi F., Shaukat L., Azhar A., Jafri A., Aslam U., Imran-Ul-Haq H. Preclinical meritorious anticancer effects of Metformin against breast cancer: An In vivo trial, *J. Taibah Univ Med Sci.,* 16 (4) (2021) 504–512.

[22] Zheng Y., Zhu J., Zhang H., Liu Y., Sun H. Metformin inhibits ovarian cancer growth and migration in vitro and in vivo by enhancing cisplatin cytotoxicity, *Am J Transl Res*., 10 (10) (2018) 3086–3098.

[23] Zordoky BNM., Bark D., Soltys CL., Sung MM., Dyck JRB. The anti-proliferative effect of metformin in triple-negative MDA-MB-231 breast cancer cells is highly dependent on glucose concentration: implications for cancer therapy and prevention, *Biochim Biophys Acta,* 1840 (6) (2014) 1943–1957.

[24] Kasznicki J., Sliwinska A., Drzewoski J. Metformin in cancer prevention and therapy, *Ann Transl Med*., 2 (6) (2014) 57-67.

[25] Amaral I., Silva C., Correia-Branco A., Martel F. Metformin interferes with glucose cellular uptake by both estrogen and progesterone receptor-positive (MCF-7) and triple-negative (MDA-MB-231) breast cancer cell lines: PS156, *Porto Biomed.,* 2 (5) (2014) 218-225.

[26] Marinello PC., da Silva TNX., Panis C., Neves AF., Machado KL., Borges FH. Mechanism of metformin action in MCF-7 and MDA-MB-231 human breast cancer cells involves oxidative stress generation, DNA damage, and transforming growth factor β1 induction, *Tumor Biol*., 37 (4) (2016) 53375–53346.

[27] Sena P., Mancini S., Benincasa M., Mariani F., Palumbo C., Roncucci L. Metformin induces apoptosis and alters cellular responses to oxidative stress in Ht29 colon cancer cells: Preliminary findings, *Int J Mol Sci.,* 19 (5) (2018) 45-56.

[28] Yenmiş G., Beşli N., Yaprak Saraç E., Hocaoğlu Emre FS., Şenol K., Kanıgür G. Metformin promotes apoptosis in primary breast cancer cells by downregulation of cyclin D1 and upregulation of P53 through an AMPK-alpha independent mechanism, *Turkish J Med Sci.,* 51 (2) (2021) 826–834.

[29] Fujita E., Egashira J., Urase K., Kuida K., Momoi T. Caspase-9 processing by caspase-3 via a feedback amplification loop in vivo, *Cell Death Differ.,* 8 (4) (2001) 335–344.

[30] Jang JH., Song IH., Sung EG., Lee TJ., Kim JY. Metformin-induced apoptosis facilitates degradation of the cellular caspase 8 (FLICE)-like inhibitory protein through a caspase-dependent pathway in human renal cell carcinoma A498 cells, *Oncol Lett.,* 16 (2) (2018) 2030-2040.

[31] Jang JH., Sung EG., Song IH., Lee TJ., Kim JY. Metformin induces caspase-dependent and caspase-independent apoptosis in human bladder cancer T24 cells, *Anticancer Drugs*, 31 (7) 2020 655–662.

[32] Gozuacik D., Kimchi A. DAPk protein family and cancer, *Autophagy*, 2 (2) (2006) 74–79.

[33] Wijshake T., Zou Z., Chen B. Tumor-suppressor function of Beclin 1 in breast cancer cells requires E-cadherin, *Proc Natl Acad Sci USA*, 118 (5) (2021) e2020478118.

[34] Cai M., Hu Z., Liu J., Gao J., Liu C., Liu D. Beclin 1 Expression in Ovarian Tissues and Its Effects on Ovarian Cancer Prognosis, *Int J Mol Sci.,* 215 (4) (2014) 5292.

[35] Ge J., Chen Z., Huang J., Chen J., Yuan W., Deng Z. Upregulation of Autophagy-Related Gene-5 (ATG-5) Is Associated with Chemoresistance in Human Gastric Cancer, *PLoS One,* 9 (10) (2014).

[36] Maskey D., Yousefi S., Schmid I., Zlobec I., Perren A., Friis R. ATG5 is induced by DNA-damaging agents and promotes mitotic catastrophe independent of autophagy, *Nat Commun.,* 4(1) (2013) 2130.

[37] Zhou H, Qian X, Xu N, Zhang S, Zhu G, Zhang Y. Disruption of Atg7-dependent autophagy causes electromotility disturbances, outer hair cell loss, and deafness in mice, *Cell Death Dis.,* 11 (10) (2020).

[38] Liu S, Yue C, Chen H, Chen Y, Li G. Corrigendum: Metformin promotes beclin1-dependent autophagy to inhibit the progression of gastric cancer, *Onco Targets Ther.,* 13 (1) (2020) 4445—4455.

[39] Fu M, Hu Y, Lan T, Guan KL, Luo T, Luo M. The Hippo signalling pathway and its implications in human health and diseases, *Signal Transduct Target Ther*., 7 (1) (2020) 1–20.

[40] Liu J, Li J, Chen H, Metformin suppresses proliferation and invasion of drug-resistant breast cancer cells by activation of the Hippo pathway, *J Cell Mol Med*., 24 (10) (2020).

[41] Han Y, Liu D, Li L. Increased expression of TAZ and associated upregulation of PD-L1 in cervical cancer, *Cancer Cell Int.,* 21 (1) (2021) 592.

[42] Liu J, Li J, Chen H, Wang R, Li P, Miao Y. Metformin suppresses proliferation and invasion of drug-resistant breast cancer cells by activation of the Hippo pathway, *J Cell Mol Med.,* 24 (10) (2020) 5786–5796.

[43] Wang L, Wang M, Hu C, Li P, Qiao Y, Xia Y. Protein salvador homolog 1 acts as a tumor suppressor and is modulated by hypermethylation in pancreatic ductal adenocarcinoma, *Oncotarget,* 8 (38) (2017) 62953–62961.

[44] Liu J, Li J, Chen H, Wang R, Li P, Miao Y. Metformin suppresses proliferation and invasion of drug-resistant breast cancer cells by activation of the Hippo pathway, *J Cell Mol Med.,* 24 (10) (2020) 5786–5796.

Cumhuriyet Sci. J., 45(2) (2024) 235-239
DOI: https://doi.org/10.17776/csj.1398415

Cumhuriyet Science Journal

| csj.cumhuriyet.edu.tr | Founded: 2002 ISSN: 2587-2680 e-ISSN: 2587-246X Publisher: Sivas Cumhuriyet University

Investigating the Impact of Birt–Hogg–Dubé Syndrome Associated Folliculin (FLCN) and Retinitis Pigmentosa 2 (RP2) Loss on Cilia Function and Morphology

Oktay İsmail Kaplan [1,a]

[1] *Rare Disease Laboratory, School of Life and Natural Sciences, Abdullah Gul University, Kayseri, Türkiye.*
**Corresponding author*

Research Article

History
Received: 30/11/2023
Accepted: 13/06/2024

ABSTRACT

Folliculin (FLCN), a GTPase-activating protein (GAP), has been linked to Birt–Hogg–Dubé syndrome, the mTORC1 signaling pathway and cilia. Disruptions in cilia structure and function lead to a group of diseases known as ciliopathies. Birt-Hogg-Dubé syndrome is one of 35 different ciliopathy diseases and there are more than 250 genes that cause ciliopathy diseases. FLCN interacts with kinesin-2 along cilia. The specific role of FLCN in regulating Kinesin-IFT trafficking has, however, remained unclear. In the current study, we investigated the effects of *flcn-1* loss (the human ortholog of FLCN) on kinesin and IFT trafficking in *C. elegans*. The loss of *flcn-1* alone did not result in any apparent alterations to kinesin or IFT trafficking within the cilia. However, when we combined the deletion of *flcn-1* with the deletion of Retinitis Pigmentosa 2 (RP2), another GAP protein, the ciliary entry of a non-ciliary membrane protein TRAM-1 (Translocation Associated Membrane Protein 1) occured. Additionally, although cilia length was unaltered, our analysis of double mutants revealed the extra branch in wing AWB cilia morphology but not the single rod-like PHA/PHB cilia. In summary, our study reveals the previously unknown functions of FLCN in ciliary gating and cilia morphology in *C. elegans*.

Keywords: Folliculin, Cilia, Retinitis pigmentosa 2, Ciliary gate.

[a] *oktay.kaplan@agu.edu.tr* *https://orcid.org/0000-0002-8733-0920*

Introduction

Cilia were the first cellular organelles discovered by scientists and are characterized by the presence of microtubules as a fundamental structure [1]. The terms "motile" and "non-motile" (primary cilium) refer to two functionally and structurally distinct forms of cilia [2]. In unicellular organisms, cilia serve a crucial function in enabling the mobility of the whole organism. In higher multicellular organisms, it has been demonstrated that cilia are important not only for cellular motility and sensation but also for crucial embryonic developmental processes [2,3]. Both the motile and primary cilia are involved in a variety of rare diseases, collectively known as ciliopathies. More than 50 cilia-related disorders exist, with more than 4000 distinct symptoms [4].

A bi-directional movement process spanning the entire length of cilia was initially discovered in 1993 in the single-celled green alga *Chlamydomonas reinhardtii*, and this phenomenon was termed intraflagellar transport (IFT) [5, 6]. Further analysis, including the biochemical isolation of IFT components and genomic comparisons across various species, revealed that IFT components and motor proteins, such as cytoplasmic dynein and kinesin, are conserved in ciliated organisms [7, 8]. Subsequent work revealed that the cilia host different types of proteins, including signaling molecules, small GTPase, GTPase-activating proteins (GAP) proteins, and membrane. Folliculin (FLCN) is a protein that functions as a tumor suppressor and acts as a GTPase-activating protein (GAP). Specifically, FLCN activates the GTPase enzymes RagC and RagD. FLCN plays essential roles in a range of cellular activities, including cilia function, apoptosis, cell proliferation, and autophagy, and was implicated in Birt–Hogg–Dubé syndrome, a cancer-related syndrome [9-13]. Notably, it has been reported to reside within cilia, where it forms interactions with kinesin-2 (the anterograde kinesin motor responsible for IFT) [9, 13, 14]. The ciliary localization of FLCN is dependent on its binding with kinesin-2. Furthermore, FLCN has been associated with the regulation of mTORC1 signaling, and the loss of FLCN leads to aberrant mTORC1 signaling [9, 15]. However, the role of FLCN in the IFT trafficking remains unknown.

In our study, we obtained a null allele of *C. elegans* FLCN (flcn-1) and observed that the loss of *flcn-1* resulted in a normal length of cilia, which is consistent with findings in mammals. There are no notable IFT trafficking defects in *flcn-1* mutants. However, we observed defects in cilia morphology when FLCN deletion was coupled with the GTPase activating protein RP2 (Retinitis pigmentosa 2), but cilia length was not affected. Notably, in *flcn-1;rpi-2* double mutants, a non-cilia localizing transmembrane protein was observed to enter cilia, suggesting a potential role for FLCN in regulating ciliary gate control. In summary, our analysis of null mutants has unveiled previously undisclosed functions of FLCN in cilia.

Materials and Methods

Materials

In the preparation of Nematode Growth Medium (NGM), we used the following reagents and materials: NaCl, Agar, Peptone, cholesterol (5 mg/ml in ethanol), KH_2PO_4, K_2HPO_4, $MgSO_4$, H_2O, and 6 cm Petri plates. The medium was sterilized in an autoclave, cooled, and then

placed on Petri plates under carefully controlled conditions. These petri plates were maintained at room temperature for 48 hours, after which they were evenly coated with OP50, an *Escherichia coli* (*E. coli*) derivative.

Genetics Cross and Worm Maintenance

We employed forward and reverse primers to track mutations in both *flcn-1(ok975)* and *rpi-2(ok1863)* to carry out genetic crosses with the wild type. Specifically, strains GOU2362, ift-74(cas499[ift-74::gfp]), N2;Ex[OSM-3::GFP + pRF4], N2;Ex[MKS-2::GFP + TRAM-1::tdTOMATO + pRF4], or str-1pro::mCherry were crossed with flcn-1(ok975), rpi-2(ok1863) single mutants, as well as flcn-1(ok975); rpi-2(ok1863) double mutants [10, 16].

Primers

flcn-1(ok975)F 5'GGACCTTGCCTTCTGTCAAATG 3' (OK698)
flcn-1(ok975)R 5'GGTAGAATCCTCGCGCTTTC 3' (OK699)
rpi-2(ok1863)F 5'GAGACGCAGACATCTCATCTG 3' (OK589)
rpi-2(ok1863)R 5' CAGGTCGTTCTCGGACATCAC3' (OK590)

Microscopy Analysis

Transgenic strains expressing ift-74(cas499[ift-74::gfp], N2;Ex[MKS-2::GFP + TRAM-1::tdTOMATO + pRF4], or *str-1pro::mCherry* were imaged with the Zeiss LSM 900 confocal microscope as previously described [16].

Statistical Significance

When comparing the statistical significance of cilia lengths, we used the Kruskal-Wallis test in the R programming ("R version 4.2.2 (2022-10-31)").

Results and Discussion

A Transmembrane Protein from outside of Cilia Enters Cilia in the loss of both Folliculin (FLCN) and Retinitis Pigmentosa 2 (RP2)

Our previous work implicated GTPase-activating proteins (GAP) proteins, including RP2 (Retinitis pigmentosa 2) and ELMOD3 (ELMO Domain Containing 3) in restricting the ciliary entry of TRAM-1 (Translocation Associated Membrane Protein 1) [16]. TRAM-1 (Translocation Associated Membrane Protein 1) is a transmembrane protein that localizes to the periciliary membrane compartment but does not normally enter into cilia. We investigated the role of a GAP protein FLCN in limiting access of TRAM-1 to cilia. We obtained a previously characterized mutant of *flcn-1*(ok975) from the Caenorhabditis Genetics Center (CGC), Minnesota, USA, and established a PCR (Polymerase Chain Reaction) based genotyping strategy. We next crossed N2;Ex[MKS-2::GFP + TRAM-1::tdTOMATO + pRF4] into *flcn-1*(ok975) to visualize both TRAM-1 and the transition zone marked with MKS-2::GFP (Fig. 1a and b.). Interestingly, TRAM-1::tdTOMATO was present in the cilium of the double mutants *flcn-1* (the human ortholog of FLCN);*rpi-2* (the human ortholog of RP2) but lacking in the single mutants and wild type, suggesting FLCN and RP2 may play a role in restricting entry of non-ciliary transmembrane protein into cilia.

Cilia Morphology is Impacted by the loss of both Folliculin (FLCN) and Retinitis Pigmentosa 2 (RP2)

We next investigated the role of folliculin and RP2 in the transport of intraflagellar transport (IFT), a bidirectional motility process along the cilia. We especially wanted to find out the effects of the absence of both RPI-2 and FLNC-2 on IFT transport. We chose the human ortholog of kinesin motor KIF17 (OSM-3), and an IFT-A complex subunit, namely intraflagellar transporter protein 140 (IFT140) (the human ortholog of IFT140). Subsequently, we generated single and double mutants with them. Normally, fluorescence tagged OSM-3 and IFT-140 localize to the cilia and translocate along the cilia. Our confocal microscopy revealed that the localizations of the kinesin motor and IFT-140 are unaffected in both single and double mutants (Fig. 2a.).

Furthermore, we measured the cilia length in wild type, single and double mutants, and found that the length of cilia is comparable with that of wild type (Fig. 2b.). However, the cilia morphology of AWB cilia, Y-like cilia structure, has more extra branches in the *flcn-1;rpi-2* double mutants (Fig. 3a and b.).

Conclusions

Our current study provides the first evidence for the potential role of Birt–Hogg–Dubé syndrome associated folliculin (FLCN) in controlling the ciliary gate. Our previous work had already implicated the two GAP proteins (Retinitis Pigmentosa 2 and ELMO Domain Containing protein) in this process [16]. Surprisingly, in both the FLCN and RP2 single and double mutants, the length of the cilia is unchanged, but the existence of extra branches in the AWB cilia morphology of the flcn-1;rpi-2 double mutants raises the possibility that FLCN and RP2 are involved in the regulation of structural integrity of the cilia.

The role of folliculin in regulating the ciliary gate control is undeniably intriguing. There are, in fact, two distinct possibilities that could potentially explain the observed ciliary gate defects in the *flcn-1;rpi-2* double mutants. Firstly, it is widely recognized that the transition zone (TZ) plays a key role in governing ciliary gating, with proteins residing in the TZ known to influence this process [17]. FLCN and RP2 could potentially impact the function or localization of proteins within the transition zone, potentially facilitating the entry of non-membrane proteins into the cilia due to their loss. Alternatively, the disruption in the intraflagellar transport (IFT) process could be responsible for the ciliary entry of membrane proteins in the *flcn-1;rpi-2* double mutants. However, the lack of FLCN and RP2 did not affect the ciliary localization of the kinesin motor KIF17 (OSM-3) and the IFT-A complex member IFT140. Thus, a defect in IFT trafficking may not explain the potential mechanism behind the ciliary leakiness of non-ciliary membrane proteins. Further in-depth analysis is warranted to unravel this intriguing phenomenon. Taken together, our work expands our understanding of FLCN and RP2 in cilia biology, offering valuable insights into their contributions to ciliary gate control and morphology. Further studies may uncover the precise mechanisms underlying these intriguing observations and their implications for cellular processes.

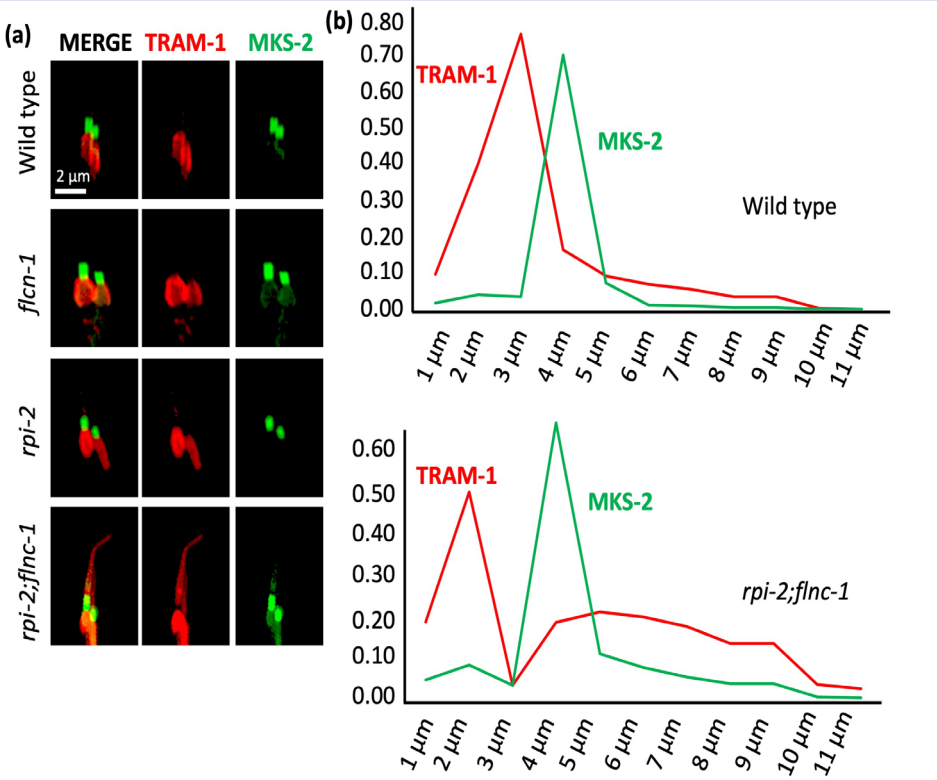

Figure 1. (a) Shown are localizations of MKS-2::GFP (green) and TRAM-1::tdTOMATO (red) in the corresponding mutants and wild type. (b) The line plot displays normalized measurements of MKS-2::GFP and TRAM-1::tdTOMATO along the distal dendrite to the cilia.

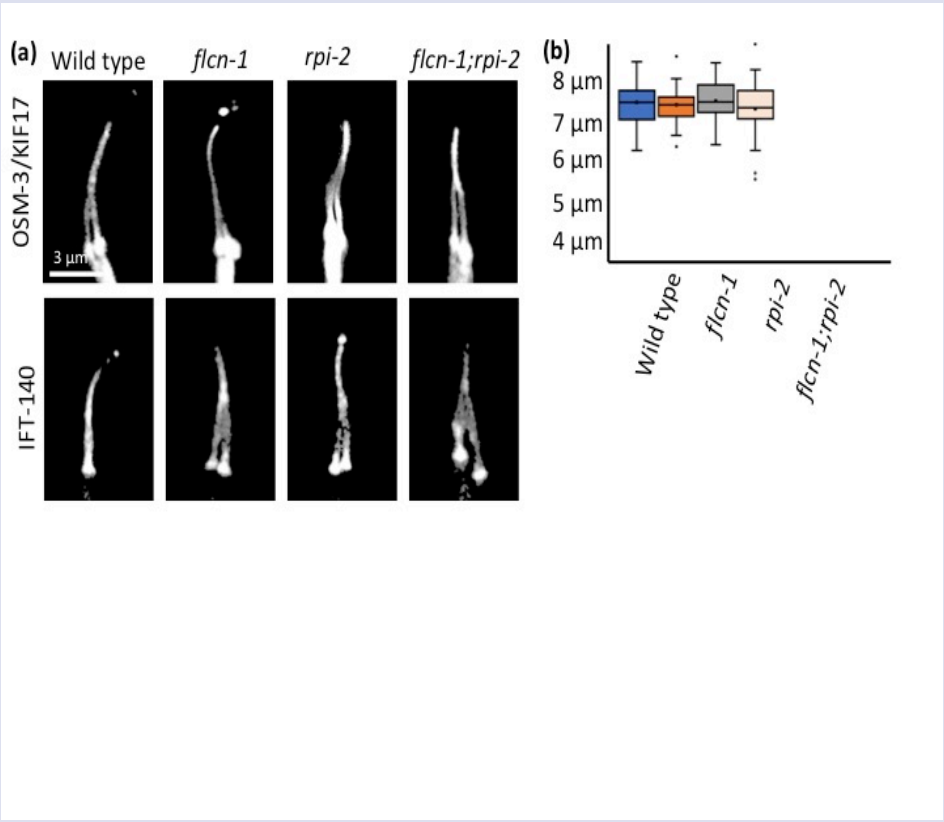

Figure 2. (a) The localization of IFT-140::GFP and OSM-3::GFP (human KIF17) were shown in the wild type and respective mutants. (b) The cilia length measurements were presented for the wild type and indicated mutants. There is no noticeable statistical significance in the cilia length between any of the mutants and the wild type.

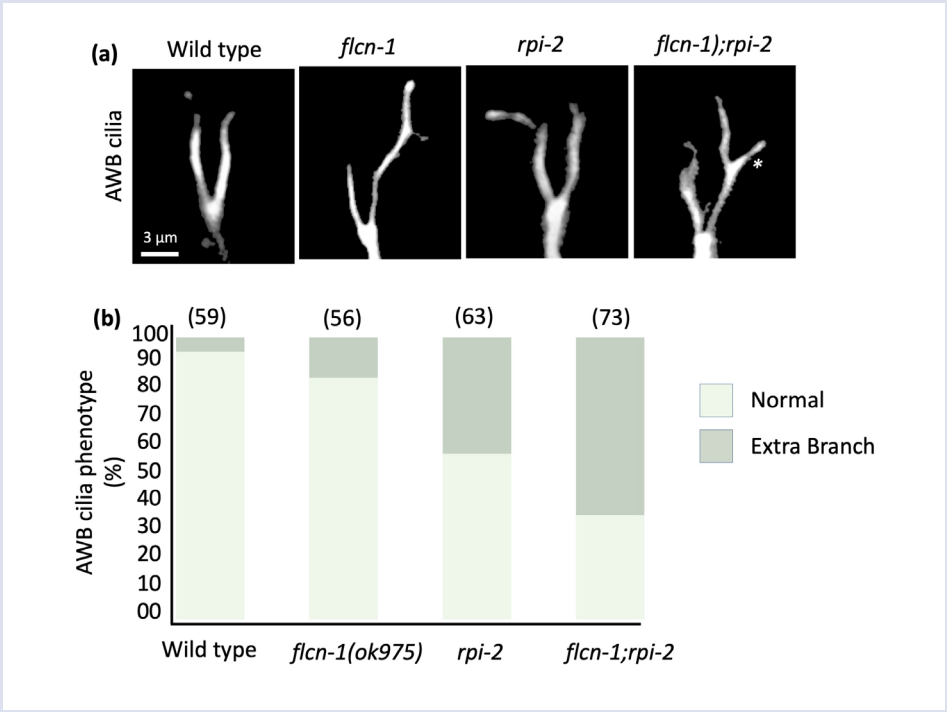

Figure 3. (a) Images for AWB cilia were displayed for wild type and indicated mutants. (b) The percentage of AWB cilia with branches and mutants displaying normal morphology was visualized in a stacked bar plot for both the wild type and the indicated mutant strains. The number of AWB cilia counted is displayed at the top of the plot within parentheses.

Acknowledgements

We thank Ali Sina Arslan and Sebiha Cevik for their technical assistance.

Conflicts of Interest

The authors declare that, there are no conflicts of interest in this work.

References

[1] Satir P, Christensen ST., Overview of Structure and Function of Mammalian Cilia, *Annu Rev Physiol*., 69(1) (2007) 377-400.

[2] Mitchison HM, Valente EM. Motile and non-motile cilia in human pathology: from function to phenotypes: Motile and non-motile ciliopathies, *J. Pathol*., 241(2) (2017) 294-309.

[3] Shah AS, Ben-Shahar Y, Moninger TO, Kline JN, Welsh MJ., Motile Cilia of Human Airway Epithelia Are Chemosensory, *Science*, 325(5944) (2009) 1131-1134.

[4] Turan MG, Orhan ME, Cevik S, Kaplan OI., CiliaMiner: an integrated database for ciliopathy genes and ciliopathies, *Database.*, (2023) baad047.

[5] Kozminski KG, Johnson KA, Forscher P, Rosenbaum JL., A motility in the eukaryotic flagellum unrelated to flagellar beating, *Proc Natl Acad Sci.,* 90(12) (1993) 5519-5523.

[6] Kozminski KG, Beech PL, Rosenbaum JL., The Chlamydomonas kinesin-like protein FLA10 is involved in motility associated with the flagellar membrane, *J Cell Biol.,* 131(6) (1995) 1517-1527.

[7] Rosenbaum JL, Witman GB., Intraflagellar transport, *Nat Rev Mol Cell Biol.,* 3(11) (2002) 813-825.

[8] Blacque OE, Cevik S, Kaplan OI., Intraflagellar transport: from molecular characterisation to mechanism, *Front Biosci.*, 13(13) (2008) 2633.

[9] Zhong M, Zhao X, Li J, Yuan W, Yan G, Tong M, Guo S, Zhu Y, Jiang Y, Liu Y, Jiang Y, Tumor Suppressor Folliculin Regulates mTORC1 through Primary Cilia, *J Biol Chem*., 291(22) (2016) 11689-11697.

[10] Possik E, Jalali Z, Nouët Y, Yan M, Gingras MC, Schmeisser K, Panaite L, Dupuy F, Kharitidi D, Chotard L, Jones RG, Hall DH, Pause A., Folliculin Regulates Ampk-Dependent Autophagy and Metabolic Stress Survival, *PLoS Genet*., 10(4) (2014) e1004273.

[11] Baba M, Toyama H, Sun L, Takubo K, Suh HC, Hasumi H, Nakamura-Ishizu A, Hasumi Y, Klarmann KD, Nakagata N, Schmidt LS, Linehan WM, Suda T, Keller JR. Loss of *Folliculin* Disrupts Hematopoietic Stem Cell Quiescence and Homeostasis Resulting in Bone Marrow Failure, *Stem Cells*., 34(4) (2016) 1068-1082.

[12] Dunlop EA, Seifan S, Claessens T, Behrends C, Kamps MA, Rozycka E, Kemp AJ, Nookala RK, Blenis J, Coull BJ, Murray JT, van Steensel MA, Wilkinson S, Tee AR., FLCN, a novel autophagy component, interacts with GABARAP and is regulated by ULK1 phosphorylation, *Autophagy*., 10(10) (2014) 1749-1760.

[13] Luijten MN, Basten SG, Claessens T, Vernooij M, Scott CL, Janssen R, Easton JA, Kamps MA, Vreeburg M, Broers JL, van Geel M, Menko FH, Harbottle RP, Nookala RK, Tee AR, Land SC, Giles RH, Coull BJ, van Steensel MA., Birt–Hogg–Dubé syndrome is a novel ciliopathy, *Hum Mol Genet.,* 22(21) (2013) 4383-4397.

[14] Zhang Y, Liu Y, Dai Y, Ren Y, Bao G, Ai B, Jiang Y., Ciliary localization of folliculin mediated via a kinesin-2-binding

motif is required for its functions in mTOR regulation and tumor suppression, *FEBS Lett.,* 595(1) (2021) 123-132.

[15] Hasumi Y, Baba M, Hasumi H, Huang Y, Lang M, Reindorf R, Oh HB, Sciarretta S, Nagashima K, Haines DC, Schneider MD, Adelstein RS, Schmidt LS, Sadoshima J, Marston Linehan W., Folliculin (Flcn) inactivation leads to murine cardiac hypertrophy through mTORC1 deregulation, *Hum Mol Genet*., 23(21) (2014) 5706-5719.

[16] Cevik S, Peng X, Beyer T, Pir MS, Yenisert F, Woerz F, Hoffmann F, Altunkaynak B, Pir B, Boldt K, Karaman A, Cakiroglu M, Oner SS, Cao Y, Ueffing M, Kaplan OI., WDR31 displays functional redundancy with GTPase-activating proteins (GAPs) ELMOD and RP2 in regulating IFT complex and recruiting the BBSome to cilium, *Life Sci Alliance*., 6(8) (2023) e202201844.

[17] Williams CL, Li C, Kida K, Inglis PN, Mohan S, Semenec L, Bialas NJ, Stupay RM, Chen N, Blacque OE, Yoder BK, Leroux MR., MKS and NPHP modules cooperate to establish basal body/transition zone membrane associations and ciliary gate function during ciliogenesis, *J Cell Biol*., 192(6) (2011) 1023-1041.

Cumhuriyet Sci. J., 45(2) (2024) 240-248
DOI: https://doi.org/10.17776/csj.1457268

Cumhuriyet Science Journal

| csj.cumhuriyet.edu.tr | Founded: 2002 ISSN: 2587-2680 e-ISSN: 2587-246X Publisher: Sivas Cumhuriyet University

Effective Biosorption of Auramin O Dye with Sustainable Chickpea Pods Waste; Isotherms, Kinetics and Thermodynamic Analysis

Zehra Saba Keskin [1,a,*]

[1] *Department of Pharmacy, Cumhuriyet University, Health Services Vocational School, Sivas 58140, Türkiye.*
**Corresponding author*

Research Article

History
Received: 22/03/2024
Accepted: 14/06/2024

ABSTRACT

This study investigated biosorbent properties in removing Auramin O (AO) dye from the aqueous solution of agricultural wastes released from chickpea (Cicer arietinum L.), which is widely produced in Turkey and the world. Biosorption studies were carried out using different values of parameters such as initial AO concentration, dye pH, contact time, temperature, and biosorbent amount. Characterization analyses of the biosorbent used before and after biosorption were carried out by scanning electron microscopy (SEM), energy dispersive X-ray (EDX), Brunauer–Emmett–Teller (BET), Fourier transform infrared spectroscopy (FTIR), and point of zero charge (PZC). Biosorption isotherms were evaluated using Langmuir, Freundlich, and Dubinin-Radushkevich (D-R) isotherm models. As a result of experimental data, it has been shown that the Langmuir isotherm model (R^2 = 0.930) is the most compatible model for biosorption, while the biosorption kinetic mechanism proceeds through the pseudo-second-order (PSO) kinetic model (R^2 = 0.965) and the intra-particle diffusion model. As a result of thermodynamic studies, it has been reported that biosorption is endothermic (ΔH0>0), spontaneous (ΔS0>0), and entropy-increasing (ΔG0 <0).

Keywords: Cicer arietinum L. pods, Auramin O, Biosorption.

[a] *zkeskin@cumhuriyet.edu.tr* *https://orcid.org/0000-0003-1334-5158*

Introduction

All living organisms require high-quality water to sustain their lives in a healthy way. However, due to demographic growth, wastewaters resulting from increasing anthropogenic activities are discharged directly into water bodies [1]. Synthetic dyes are among the pollutants that cause high water pollution levels.

Due to being low-cost, brightly coloured, and highly stable against environmental conditions, dyes are widely used in various industries such as textiles, paper, pharmaceuticals, food, plastic coating, and cosmetics [2]. However, discharging wastewater contaminated with dyes without any treatment poses a great danger in terms of aesthetics and the harm it causes to the ecosystem.

According to the United Nations World Water Assessment Programme report for 2023, water sources receive a daily discharge of 2 tonnes of wastewater [3].

The presence of dyes in water ecosystems leads to a decrease in light penetration, an increase in chemical oxygen demand, and toxicity for living organisms in the water. Furthermore, it causes respiratory disorders, skin irritation, burns, allergic reactions, cancer, and mutations in human health [4].

Auramine O (AO) dye, also referred to as Basic Yellow 2, is an easily soluble yellow cationic dye used as a colorant in various industries such as textile, ink, leather, and paper. The International Agency for Research on Cancer (IARC) has classified AO as a carcinogenic chemical. Therefore, it is crucial to purify wastewater using various methods and dispose of it in natural ecosystems. Several studies have been conducted in recent years using methods such as coagulation, photodegradation, membrane filtration, ion exchange, ozonation, solvent extraction, hyperfiltration adsorption (biosorption) [3]. The adsorption method has gained attention due to its simplicity, cost-effectiveness, environmental friendliness, high efficiency, and absence of harmful by-products.

However, the high performance and efficiency of the adsorption method also depend on the morphological characteristics of the preferred adsorbent, and whether it is edible, cheap, and abundant. Recently, agricultural wastes have been seen as an alternative to traditional adsorbents. Most agricultural wastes are lignocellulosic in structure and contain functional compounds such as hydroxyl, amine, aldehyde, ketone, and phenol. The presence of these functional compounds, which can bind dyes, and their porous and loose structures increase the effectiveness of agricultural wastes in purifying dyes from wastewater [5,6]. In addition, utilizing waste from agriculture as a biosorbent will help climate neutrality with a sustainable product strategy [7] .

Therefore, in recent years, researchers have conducted studies on removing dyes using agricultural waste as an alternative to traditional adsorbents. Examples of such waste include potato peel [8], wheat straw (*T. aestivum*) [9], jackfruit leaves [3], corn husk waste [10], rosemary waste [11], and Alfa (*Stipa tenacissima* L.) leaf powder [12].

Chickpeas (*Cicer arietinum* L.) belong to the Viceae genus of the *Leguminosae* family and are originally from West Asia and Near East Asia [13] . They are one of the most widely produced legumes globally and in Turkey, making them a crucial component of the Turkish economy. However, a significant amount of agricultural waste generated from this production is either burned or left untreated in the environment. Therefore, using these

wastes as biosorbents could yield ecological, economic, and social benefits.

This study examines the potential use of chickpea peels (CPP) as biosorbents for the removal of AO from aqueous solutions. This report presents the first study on the use of chickpea outer husks as a biosorbent for removing AO dye. We conducted characterization analyses on the unmodified biosorbent before and after biosorption and examined the effects of parameters such as pH, initial dye concentration, time, temperature, and biosorbent amount on the biosorption process.

Materials and Methods

Chemicals

Chemicals with analytical purity were used in the experiment. The AO dye (powder form) (Table 1), KNO_3, HCl, and NaOH used in the experiment were purchased from Merck. All analyses were conducted using double-distilled water.

Table 1. Properties of Auamine O

Physicochemical	Values
Chemicals formula	$C_{17}H_{21}N_3 \cdot HCl$
Molecule weight (g/mol)	303.83
Class	Cationic dye
λ_{max}(nm)	434
Molecular structure	 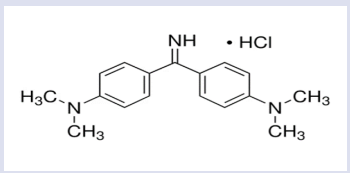

Characterization and Preparation of CPP

CPP was obtained from chickpeas harvested in the Kangal region of Sivas. The CPP was subjected to a distilled water washing process to remove any physical impurities. It was then dried in the oven at 50°C for 24 hours. To increase the surface area of the biosorbent, it was crushed with an IKA A 11 grinder. The prepared CPP biosorbent was stored in airtight propylene containers until further processing.

The equilibrium solution concentrations of AO were determined by analyzing absorbance values at 434 nm using a UV-Vis spectrophotometer (Peak, E 1000). Functional compound analysis of CPP before and after AO biosorption was conducted using FTIR spectroscopy (ATR, Bruker, Tensor II). Additionally, changes in surface morphology and elemental composition before and after biosorption were assessed using Energy Dispersive X-ray spectroscopy (EDX) coupled with a Scanning Electron Microscope (Tescan Mira3 XMU). Samples were coated with gold in an automatic coater before analysis to increase process surface conductivity and obtain better quality images. Additionally, the pH of the zero charge point (pHpzc) of CPP was determined using the solid addition method [14].

Biosorption Procedure

The batch method was used to examine the adsorptive efficiency of CPP in removing AO dye. A stock AO dye solution at a concentration of 1000 ppm was prepared by dissolving 1 g of dye in 1000 ml of distilled water. Different initial dye concentrations (10-1000 ppm) were created by diluting this stock solution at varying rates. To evaluate the biosorption process, experiments were conducted in a 10 ml volume of 500 ppm AO dye solution using 50 mg CPP at pH 6.2 at 298 K in a constantly shaking water bath for 24 hours. The equilibrium solutions were then filtered through the Whatman filter paper, and the non-adsorbed concentrations were calculated using linear regression equations based on the absorbance values read on the UV-Vis spectrophotometer.

Additionally, experiments were conducted with different values of parameters such as initial AO concentration (10-1000 ppm), dye pH (2-12), contact time (2-1440 min.), and temperature (5, 25, 40 °C) to determine the optimum conditions for biosorption.

Percentage of AO removal (%R), amount of AO adsorbed at equilibrium (Q, mg/g), and Recovery% were calculated using the following Equations [1-3], respectively [15].

$$\% R = \left(\frac{C_O - C_e}{C_O}\right) X100 \quad (1)$$

$$Q = (C_o - C_e).\frac{V}{m} \quad (2)$$

$$Recovery\% = \frac{Q_{des}}{Q_{ads}} x100 \quad (3)$$

Here, Co (ppm) and Ce (ppm) are the initial and equilibrium concentrations of the AO dye, m (g) is the amount of adsorbent, and V (L) is the volume of the AO dye solution.

Results and Discussion

FTIR

FTIR analysis was conducted before and after biosorption to identify functional groups aiding in the biosorption process of AO dye molecules onto CPP. The FTIR spectra were obtained in the range of 4000-400 cm^{-1} and are depicted in Figure 1.

The peak at 3307 cm^{-1} observed in the range of 3680-3000 cm^{-1} is attributed to the stretching vibration of the amine group (-NH_2) and the hydroxyl group (-OH) present in lignin, cellulose, and hemicellulose [16].

The small sharp peaks at 2920 and 2850 cm^{-1} correspond to the symmetric and asymmetric C-H stretching of methoxy groups in lignocellulosic structures, while the peak at 1738 cm^{-1} corresponds to the C=O stretching vibration of carboxylic acid [17].

The peak observed at 1623 cm^{-1} corresponds to the C=O stretching of carboxylic acid groups, while the peak at 1425 cm^{-1} is attributed to the C=C stretching in aromatic rings [18].

The sharp peak at 1021 cm^{-1} indicates the presence of C-O and C-N bonds, which are characteristic of proteins, alcohols, and ethers. Additionally, it suggests the presence of lignin in CPP [16,17,19]. As seen in Figure 1, changes in

the intensity and positions of peaks in the FTIR spectrum have been observed due to the interactions between the functional groups and the AO dye molecules adhering to the biosorbent surface. The peaks at 1623 and 1021 cm^{-1} shifted to 1600 and 1006 cm^{-1}, respectively, and the intensity of all peaks decreased after biosorption. The changes observed before and after biosorption may be attributed to electrostatic interactions between functional groups and AO, as well as surface complexation reactions.

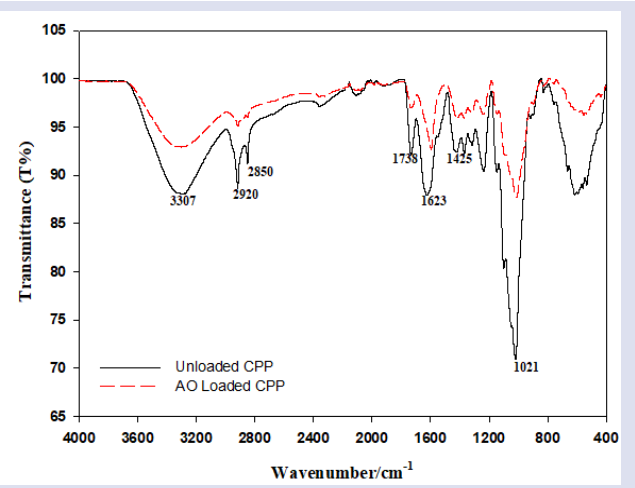

Figure 1. FTIR analysis of CPP pre- and post-AO biosorption in the panels. Error bars show ±SD values.

SEM-EDX and BET Analyzes

SEM was used to examine the morphological characteristics and surface features of CPP biomass before (Figure 2a) and after (Figure 2b) the biosorption process.

The SEM images in Figure 2a show that the surface of the CPP biosorbent was smooth before the biosorption process. However, after the biosorption process, large dye particles were observed on the biosorbent, as shown in Figure 2b, indicating successful biosorption.

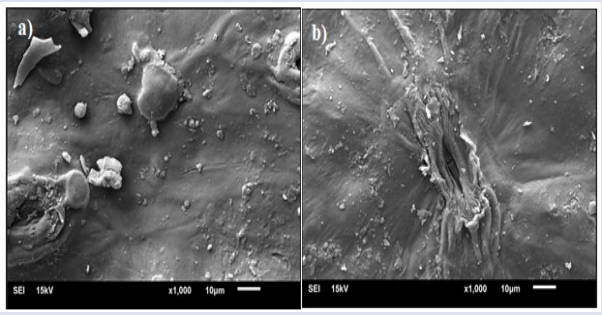

Figure 2. SEM micrographs of CPP before (a) and after (b) AO biosorption

The EDX spectrum in Figures 3a and 3b shows the elemental composition on the CPP surface before and after biosorption, respectively. In the spectrum obtained before biosorption, C (51.7% by weight), O (47.3% by weight), Ca (0.6% by weight), Mg (0.2% by weight) and Al (0.2 % by weight) its existence has been determined.

The appearance of new elements, especially nitrogen (9 wt%) and chlorine (0.2 wt%), and changes in composition in the EDX spectrum after biosorption indicate that the biosorption process has occurred. The detection of these elements, including carbon, hydrogen, nitrogen and chlorine atoms in the chemical composition of AO, in the spectrum can be shown as evidence that biosorption has occurred.

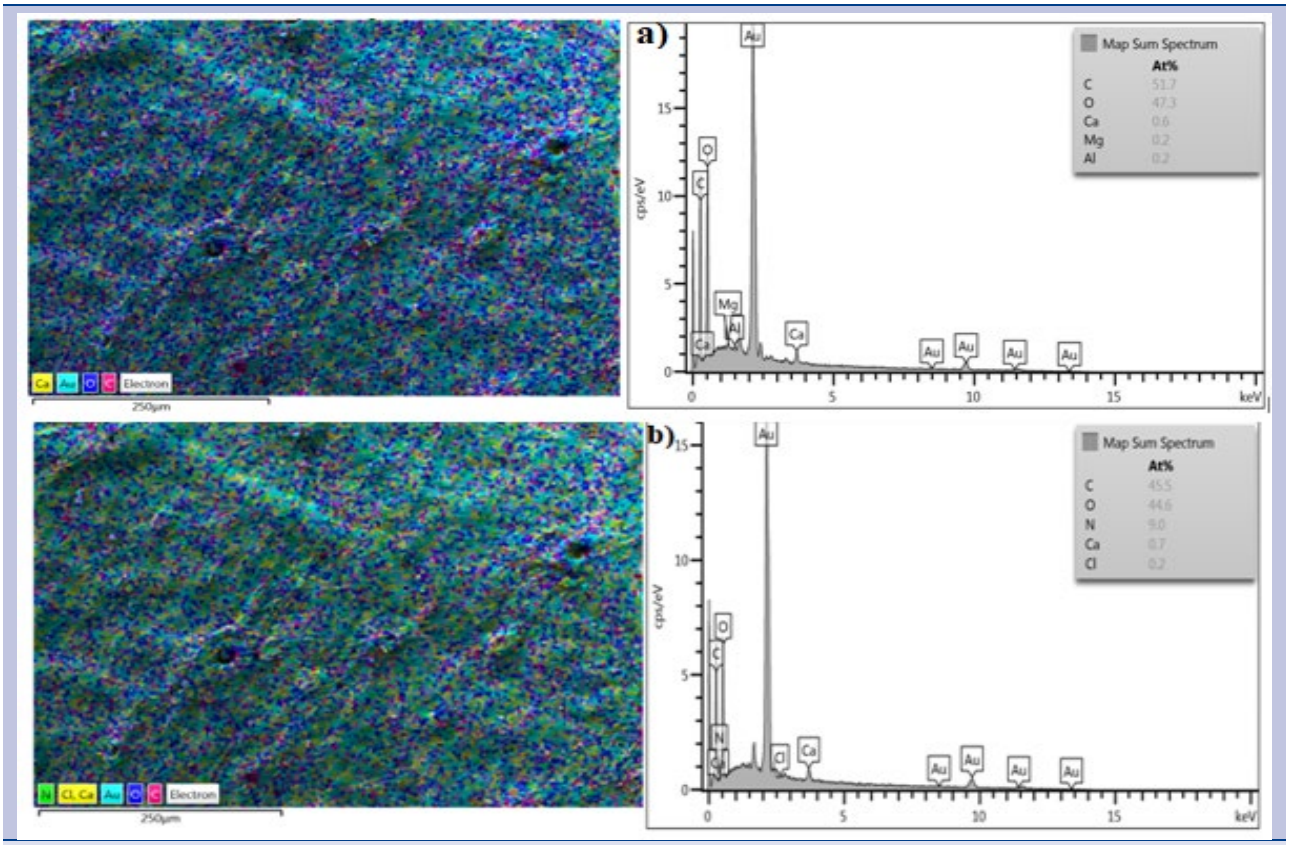

Figure 3. EDX spectra before (a) and after (b) AO biosorption

BET surface area (m^2 g^{-1}) analysis was performed for CPP biosorbent before and after biosorption. It was determined that the surface area of CPP before biosorption was 50,872 m^2 g^{-1} and after biosorption, the surface area decreased to 31,460 m^2 g^{-1}. This apparent decrease in surface area can be attributed to the adhesion of AO dye molecules to the CPP pores.

Effect of PZC and pH on Biosorption

The pH of the dye is crucial in controlling the biosorption process as it impacts the surface structure of the biosorbent and alters the electrostatic interactions between the dye and the biosorbent [20].

To determine the effect of pH on the biosorption of AO dye onto CPP, experiments were carried out at different pH values ranging from 2-12, with a contact time of 1440 minutes and an amount of 50 mg biosorbent. The findings on the relationship between solution pH and biosorption capacity are presented in Figure 4.

The neutral pH value on the surface of the biosorbent plays a critical role in understanding the surface kinetics and biosorption mechanism. This value is also important in explaining the interaction of dye molecules with the biosorbent and the chemical structures of the active sites for the biosorption process. At pH> pHpzc values, the biosorbent surface carries a negative charge, while at pH< pHpzc values, the biosorbent surface carries a positive charge [21].

As depicted in Figure 5, the pHpzc value of the CPP biosorbent was determined to be 4.91. Consequently, when the solution pH is below 4.91, the CPP surface is positively charged, whereas a solution pH above 4.91 indicates a negatively charged biosorbent surface. Hence, pH values exceeding the pHpzc are conducive to the removal of AO, which is a cationic dye.

Based on the data obtained, as seen in Figure 4, a decrease in AO removal is observed between pH 2 and pH 4.

The decrease in RhB dye biosorption by CPP at low pH can be attributed to the competition between the cationic groups in the dye and the H^+ ions in the solution for the biosorption sites in the CPP. Additionally, electrostatic repulsion between the protonated surface of CPP and the cationic dye can be shown as another reason [22].

The interaction between AO and chickpea shell is found to increase between pH 4-6 and pH 8-12 compared to lower pH values due to the heightened electrostatic attraction forces between the increasingly negatively charged regions and the positively charged cationic dye. This strong binding facilitates the biosorption of AO onto the CPP biosorbent [23].

Although the removal amount was expected to increase between pH 6 and pH 8, a slight decrease was observed. This decrease can be attributed to the NaOH used in pH adjustment of AO dye solutions and the Cl in the structure of the AO dye entering into a substitution reaction that causes the formation of NaCl [24].

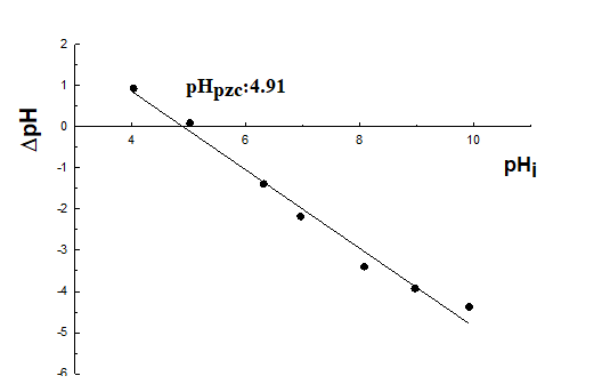

Figure 5. PZC plots of CPP biosorbent

Effect of CPP Amount on Biosorption

It is crucial to determine the optimal amount of biosorbent dose in order to achieve high biosorption efficiency and lower the cost of biosorbent. The experiment investigated the effect of different biosorbent doses (ranging from 5-20 g L^{-1}) on AO removal and its interpretation can be found in Figure 6.

The results show that as the biosorbent dose increased, the percentage of AO removal rate also increased. This is due to the increase in active biosorption sites and total surface area caused by the increase in biosorbent amount [25].

However, an increase in the biosorbent dose led to a decrease in the amount of biosorbed AO dye per unit. This is because the number of active sites was not sufficiently saturated by AO dye molecules. The highest biosorption capacity (53.03 mg g^{-1}) was obtained with an adsorbent dose of 5 g L^{-1}

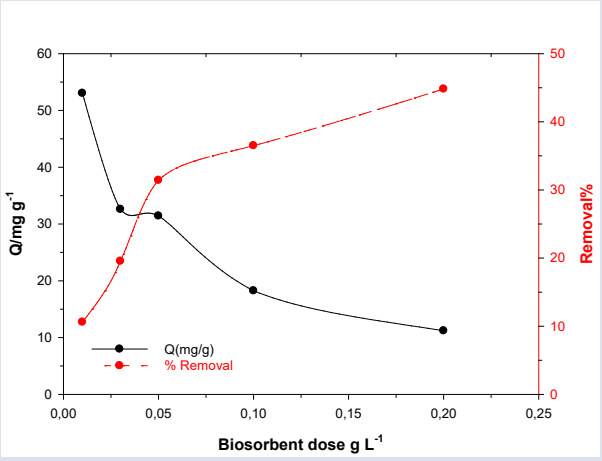

Figure 6. Effect of CPP amount on AO biosorption.

Biosorption Equilibrium Isotherm Modelling

Biosorption isotherms play a crucial role in interpreting the interaction between biosorbent and dye, explaining the biosorption mechanism, and determining the biosorption capacity of the biosorbent [26].

The investigation of AO dye molecule biosorption onto CPP involved the application of three isotherm models to the experimental data: Langmuir [27], Freundlich [28], and Dubinin-Radushkevich (D-R) [29]. Analyzes in which isotherm models were determined were carried out at

different initial concentrations of AO dye (10-1000 mg L^{-1}), 50 mg CPP, pH 6.2 and 1440 minutes contact time.

Table 2 presents the nonlinear equations for the Langmuir, Freundlich, and D-R isotherm models used in the removal of AO dye on CPP, along with the corresponding isotherm parameters.

The Langmuir isotherm model assumes biosorption occurs on monolayer homogeneous surfaces with equal energy of the biosorbent.

Although the Freundlich isotherm model assumes that biosorption occurs on reversible and multilayered heterogeneous surfaces, it also provides information about the adsorbent concentration adhering to the biosorbent.

The D-R isotherm model states that the adsorption potential on heterogeneous surfaces depends on the pore structure of the adsorbent. It also states that biosorption proceeds physically or chemically, evaluated in terms of energy.

The equilibrium of biosorption of AO dye molecules is observed at a concentration of 500 mg L^{-1}, as shown in Figure 7. The suitability of isotherm models for the biosorption process was assessed by comparing the correlation coefficients (R^2).

When comparing the R^2 values of isotherm models, it was determined that the equilibrium data was more compatible with the Langmuir model, which describes single-layer biosorption with an R^2 value close to 1. According to the Langmuir isotherm, the maximum biosorption capacity (qm) of CPP biosorbent is 177.96 mg/g. The Langmuir equilibrium constant (K_L), which is related to the appropriate surface area and porosity of the biosorbent, was calculated as 6.596 x10^{-4}. This parameter describes the binding of AO molecules in a single layer on homogeneous CPP surfaces.

The Freundlich constant (Kf) that determines the biosorption capacity and the β value that indicates surface heterogeneity intensity were determined as 0.2486 L mg^{-1} and 0.831, respectively. The β value within the range of $0 < \beta < 1$ indicates the suitability of biosorption of AO dye molecules onto CPP [30].

D-R isotherm model aims to explain the biosorption process and pore filling mechanism by distributing Gauss energy across a non-uniform surface. The D-R isotherm model can be used to calculate the average biosorption free energy per biosorbent molecule (E) and determine whether the process is physical or chemical in nature [31]. The calculated E value of 7.128 kJ mol^{-1} suggests that the interaction between AO dye and CPP surface occurred through physisorption, as it is less than 8 kJ mol^{-1}.

Table 3 presents a comparison of the maximum adsorption capacities of various adsorbents used for AO removal. The raw agricultural waste used in this study, without any modification, exhibited a higher maximum adsorption capacity than many other adsorbents. This suggests that CPP could be a cost-effective and readily available biosorbent with a high biosorption capacity for AO removal.

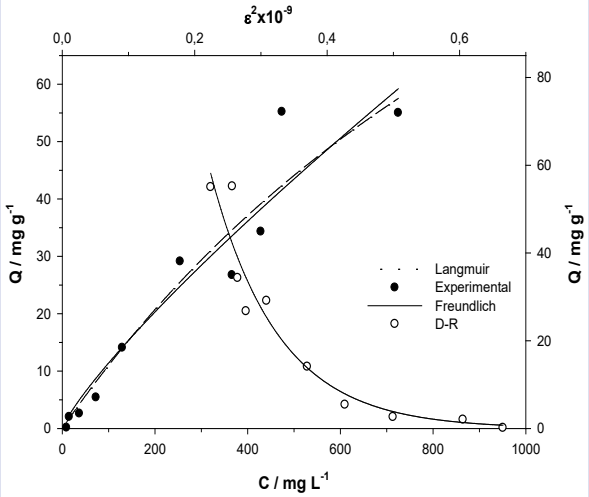

Figure 7. Biosorption isotherms

Table 2. Equations and parameters for nonlinear isotherm models

Isotherms	Equations	Parameters	Values	R^2
Langmuir	$Q = \frac{K_L . q_m . C_e}{1 + K_L . C_e}$	q_m (mg/g) K_L (L/ mg)	177,96 6,596 x10^{-4}	0,930
Freundlich	$Q = K_F . C_e^{\beta}$	K_F β	2,486 x10^{-1} 8,313 x10^{-1}	0,924
D-R	$Q = X_{DR} . e^{-KDR.\varepsilon 2}$. $\varepsilon = R.Tln(1 + \frac{1}{C_e})$ $E = \frac{1}{\sqrt{2K_{DR}}}$	X_{DR} (mg/ g) K_{DR} (mol² K/ J ²) E (kJ /mol)	5,278 x10^{-2} 9,84 x10^{-9} 7,128	0,929

Table 3. Comparison of maximum adsorption capacities (qm) for the removal of AO by various adsorbents

Sorbents	T (°C)	pH	q_m (mg/g)	References
Chickpea pods (CPP)	25	6.2	177,96	This study
Chitosan–kaolin composite	25	7.5	35,5	[32]
Activated jackfruit leaf powder	-	-	79,36	[3]
Pyracantha Coccinea	25	-	123,1	[33]
Kernel powder/kappa-carrageenan hydrogel	-	11	9,225	[34]
Fe3O4-based melamine-rich covalent organic polymer	-	-	107,11	[35]
Amazon raw clay	28	5,6	18.04	[36]

Biosorption Kinetic Modelling

In order to examine the kinetic mechanism of AO dye biosorption onto CPP, pseudo-first-order kinetic model (PFO) [37], pseudo-second-order kinetic model (PSO) [38], and intra-particle diffusion model (IPD) [27] were utilized.

The kinetic studies were conducted at varying time intervals ranging from 2 to 1440 minutes, with a CPP amount of 0.05 g, pH 6.2, and a fixed AO concentration of 500 mg L^{-1}.

Figure 8 presents the application of experimental data obtained from kinetic studies to these models. Table 4 provides the nonlinear equations and kinetic parameters corresponding to these models.

Figure 8 shows that the equilibrium time is around 300 minutes. The removal of AO was rapid until the 120th minute, after which it remained constant due to the saturation of active sites.

When comparing the R^2 values of the kinetic models, it was found that the R^2 value for PSO is closer to 1, indicating better compatibility of biosorption with PSO. This compatibility with PSO suggests that the removal of AO dye occurs chemically. This chemical process involves electron sharing or exchange between the functional groups of CPP and AO dye molecules [39].

Additionally, the closer results found between the theoretically calculated Qt value using the PSO kinetic model and the experimentally determined Qe value in this biosorption process indicate that PSO is more applicable.

It can be said that the graph of the IPD model in Figure 8, containing two linear components, encompasses the surface and intra-particle diffusion stages of the biosorption process. According to the IPD model, the first linear component indicates that dye molecules quickly adhere to the biosorbent surface, while the second linear component suggests that AO dye molecules diffuse into the pores of the biosorbent. In this case, it can be said that the biosorption kinetic mechanism is compatible with the PSO and IPD kinetic models.

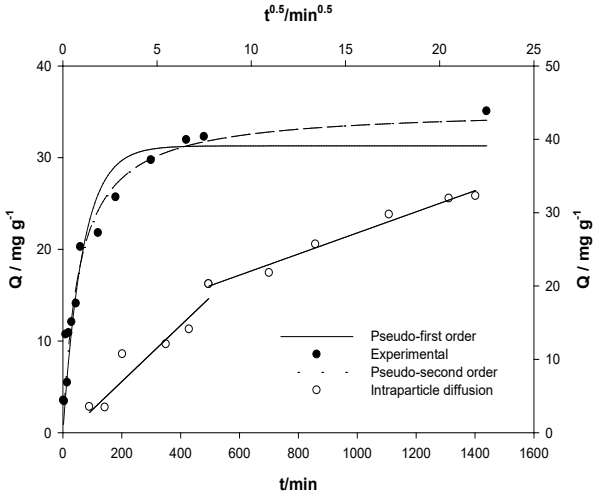

Figure 8. Biosorption kinetics of AO dye with PFO, PSO, IPD

Table 4. Equations and parameters for biosorption kinetic models

Kinetic Models	Equations	Parameters	Values	R^2
PFO	$Q_t = Q_e(1 - e^{-k_1 t})$ $H_1 = k_1 . Q_e$	Q_t (mg/ g) Qe (mg/ g) k_1 (g/ mg min) H_1 (mg/ g min)	31,29 35,06 1,485x 10^{-2} 46,46 x 10^{-2}	0,933
PSO	$Q_t = t/[k_2 . Q_e^2] + \left[\frac{1}{Q_e}\right] . t$ $H_2 = k_2 . Q_e$	Q_t (mg/ g) Qe (mg/ g) k_2 (g/ mg min) H_2 (mg/ g min)	35,38 35,06 2,55 x 10^{-5} 3,19 x 10^{-2}	0,965
IPD	$Q_{t=} k_i . t^{0,5}$	k_I (mg/ g $min^{0,5}$)	11,16 x 10^{-3}	0,976

Biosorption Thermodynamics

Temperature is a crucial factor that influences the diffusion rate through active binding sites on the biosorbent and the solubility of adsorbates in aqueous media [40] .Therefore, thermodynamic studies were conducted at various temperatures, including 278 K, 298 K, and 313 K, to elucidate the impact of temperature on the biosorption of AO dye to CPP. Thermodynamic parameters, such as enthalpy (ΔH^o, kJ mol^{-1}), entropy (ΔS^o, J mol^{-1} K^{-1}), and Gibbs free energy (ΔH^o, kJ mol^{-1}), were determined using Equation [4-7] [6] and are presented in Table 5.

$$K_d = \frac{Q}{C_e} \quad (4)$$

$$lnK_D = \frac{\Delta S^\circ}{R} - \frac{\Delta H^\circ}{RT} \quad (5)$$

$$\Delta G^\circ = -RTln(K_d) \quad (6)$$

$$\Delta G^\circ = \Delta H^\circ - T\Delta S^\circ \quad (7)$$

The ΔH^o and ΔS^o values were calculated by determining the slope and intercept of the line obtained from plotting the 1/T graph against ln K_D. A positive ΔH^o value indicates that the biosorption of AO dye onto CPP increases with temperature, suggesting an endothermic nature. ΔH^o value of less than 20 kJ mol^{-1} suggests that the biosorption is occurring physically. The positive value of ΔS^o indicates an increase in randomness and irregularity at the interface of CPP and AO dye solution during the biosorption process. The negative value of ΔG^o at increasing temperatures indicates that the biosorption process occurs spontaneously.

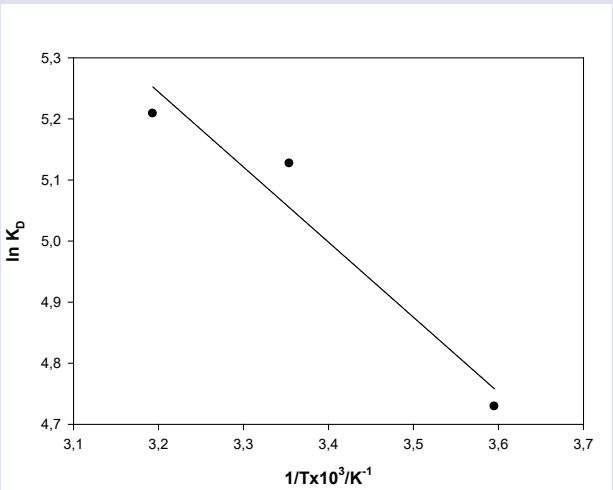

Figure 9. Temperature effect on the biosorption of RhB onto TPS

Table 5. Thermodynamic parameters

Temperature	ΔH	ΔG	ΔS	R^2
278		-14,174		
298	10,226	-15,924	76,31	0,939
313		-17,24		

Recovery

Recovery of AO molecules bound to the CPP surface is one of the most important steps determining the cost of the biosorption process. Therefore, recovery studies of AO molecules from CPP were carried out using 0.1 M HCl, ethanol and methanol solutions. As shown in Figure 10, the recovery percentages were determined as 61%, 72% and 64% for HCl, ethanol and methanol, respectively. According to these results, CPP can be considered as a promising biosorbent for the recovery of AO dye molecules.

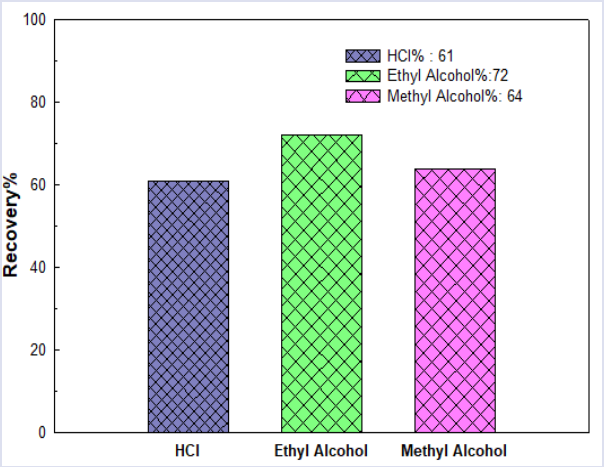

Figure 10. The effect of recovery for CPP

Conclusion

Batch adsorption experiments were conducted to investigate the potential of CPP, a sustainable and renewable agricultural waste, as a biosorbent for the removal of AO dye from aqueous solutions. The objective of this study is to investigate the influence of various operational factors on biosorption. These factors include solution pH, initial AO concentration, zero charge point, CPP quantity, temperature, and contact duration. The morphological structure and functional compounds of the CPP biosorbent were analyzed using FTIR, SEM, EDX and BET characterization techniques. In biosorption isotherm studies, the experimental data were assessed using Langmuir, Freundlich, and D-R isotherm models. The evaluation revealed that the biosorption process aligned with the Langmuir isotherm model, as indicated by its higher correlation coefficient. According to the Langmuir model, the maximum biosorption capacity of the monolayer was calculated to be 177.96 mg/g at 25 °C and pH 6.2. The E_{DR} value calculated from the D-R isotherm model is 7.128 kJ/mol, indicating that the biosorption process is progressing physically. The kinetic study of AO biosorption on CPP showed that PSO is better suited to the biosorption kinetic mechanism. The thermodynamic analysis indicates that the biosorption process is endothermic ($\Delta H^0>0$) and spontaneous ($\Delta S^0>0$). Furthermore, it has been found that the irregularity at the interface between the biosorbent and dye solution (where $\Delta G^0 < 0$) increases as the biosorption process progresses. The study results show that the CPP

biosorbent, an agricultural waste with minimal cost, can effectively remove AO dye from aqueous media.

Conflicts of interest

The authors declare that, there are no conflicts of interest in this work.

References

[1] Boukarma L, Aboussabek A, El Aroussi F, Zerbet M, Sinan F, Chiban M., Insight into mechanism, Box-Behnken design, and artificial neural network of cationic dye biosorption by marine macroalgae Fucus spiralis, *Algal. Res*., 76 (2023) 103324.

[2] Akindolie M.S, Choi H.J., Acid modification of lignocellulosic derived material for dye and heavy metals removal: A review, *Environ Eng Res.*, 28 (2023) 0–3. Gajipara Y.N, Balpande D.N., Patil P.S., Yadav A.A., Yadav M.D., Patwardhan A.V., Jackfruit Leaf–Based Natural Adsorbent for the Efficient Removal of Auramine O Dye, *Water Conserv. Sci. Eng*., 8 (2023) 1–13.

[3] Mahajan P, Jaspal D, Malviya A., Adsorption of dyes using custard apple and wood apple waste: A review, *J. Indian Chem. Soc.,* 100 (2023) 100948.

[4] Sánchez-Ponce L., Díaz-de-Alba M., Casanueva-Marenco M.J., Gestoso-Rojas J., Ortega-Iguña M., Galindo-Riaño M.D., et al, Potential Use of Low-Cost Agri-Food Waste as Biosorbents for the Removal of Cd(II), Co(II), Ni(II) and Pb(II) from Aqueous Solutions, *Separations,* 9(10) (2022) 309.

[5] Hambisa A.A., Regasa M.B., Ejigu H.G., Senbeto C.B., Adsorption studies of methyl orange dye removal from aqueous solution using Anchote peel-based agricultural waste adsorbent, *Appl. Water Sci., 13(24) (* 2023) 1–11.

[6] Kainth S., Sharma P., Panney O.P., Green sorbents from agricultural wastes: A review of sustainable adsorption materials, *Applied Surface Science Advances,* 19 (2024) 100562.

[7] Hadadi A., Imessaoudene A., Bollinger J.C., Cheikh S., Manseri A., Mouni L., Dual Valorization of Potato Peel (Solanum tuberosum) as a Versatile and Sustainable Agricultural Waste in Both Bioflocculation of Eriochrome Black T and Biosorption of Methylene Blue., *J. Polym Environ*., 31 (2023) 2983–98.

[8] Kumari S., Verma A., Sharma P., Agarwal S., Rajput V.D., Minkina T., et al., Introducing machine learning model to response surface methodology for biosorption of methylene blue dye using Triticum aestivum biomass, *Sci. Rep., 13 (* 2023) 8574.

[9] Handayani T., Emriadi, Deswati, Ramadhani P., Zein R., Modelling studies of methylene blue dye removal using activated corn husk waste: Isotherm, kinetic and thermodynamic evaluation, *South African J. Chem. Eng., 47 (* 2024) 15–27.

[10] Naboulsi A., Naboulsi I., Regti A., El Himri M., El Haddad M., The valorization of rosemary waste as a new biosorbent to eliminate the rhodamine B dye, *Microchem. J*., 191 (2023) 108790.

[11] Ouettar L., Guechi E.K., Hamdaoui O., Fertikh N., Saoudi F., Alghyamah A., Biosorption of Triphenyl Methane Dyes (Malachite Green and Crystal Violet) from Aqueous Media by Alfa (Stipa tenacissima L.) Leaf Powder, *Molecules, 28*(8) (2023) 3313.

[12] Zhang Y., Huang X., Zeng X., Li L., Jiang Y., Preparation, functional properties, and nutritional evaluation of chickpea protein concentrate, *Cereal Chem*., 100 (2023) 310–20.

[13] Keskin Z.S., Efficient adsorption of Pb(II) ions using novel adsorbent polyacrylamide/coffee ground composite: isotherm, kinetic and thermodynamic studies, *Polym. Bull.,* (2023). https://doi.org/10.1007/s00289-023-05111-x

[14] Isik B., Avci S., Cakar F., Cankurtaran O., Adsorptive removal of hazardous dye (crystal violet) using bay leaves (Laurus nobilis L.): surface characterization, batch adsorption studies, and statistical analysis, *Environ Sci. Pollut. Res.,* 30 (2023) 1333–56.

[15] Choong Lek B.L., Peter A.P., Qi Chong K.H., Ragu P., Sethu V., Selvarajoo A., et al., Treatment of palm oil mill effluent (POME) using chickpea (Cicer arietinum) as a natural coagulant and flocculant: Evaluation, process optimization and characterization of chickpea powder, *J. Environ. Chem. Eng.,* 6 (2018) 6243–55.

[16] Petrović M., Šoštarić T., Stojanović M., Milojković J., Mihajlović M., Stanojević M., et al., Removal of Pb2+ ions by raw corn silk (Zea mays L.) as a novel biosorbent, *J. Taiwan Inst. Chem. Eng.,* 58 (2016) 407–16.

[17] Fatombi J.K., Lartiges B., Aminou T., Barres O., Caillet C., A natural coagulant protein from copra (Cocos nucifera): Isolation, characterization, and potential for water purification, *Sep Purif Technol*., 116 (2013) 35–40.

[18] Garg U., Kaur M.P., Jawa G.K., Sud D., Garg V.K., Removal of cadmium (II) from aqueous solutions by adsorption on agricultural waste biomass, *J. Hazard Mater.*, 154 (2008) 1149–57.

[19] Mansour R.A., El Shahawy A., Attia A., Beheary M.S., Brilliant Green Dye Biosorption Using Activated Carbon Derived from Guava Tree Wood, *Int. J. Chem. Eng.,* 2020 (2020) 8053828.

[20] Şenol Z.M., Keskin Z.S., Şimşek S., Synthesis and characterization of a new hybrid polymer composite (pollene@polyacrylamide) and its applicability in uranyl ions adsorption, *J. Radioanal Nucl. Chem., 332 (2023) 2239–2248.*

[21] Hevira L, Zilfa, Rahmayeni, Ighalo J.O., Zein R., Biosorption of indigo carmine from aqueous solution by Terminalia Catappa shell, *J. Environ. Chem. Eng.,* 8 (2020)104290.

[22] Akkari I., Graba Z., Bezzi N., Merzeg F.A., Bait N., Ferhati A., Raw pomegranate peel as promise efficient biosorbent for the removal of Basic Red 46 dye: equilibrium, kinetic, and thermodynamic studies, *Biomass Convers Biorefinery,* 13 (2023) 8047–60.

[23] Amar I.A., Biosorption Removal of Methylene Blue Dye from Aqueous Solutions using Phosphoric Acid-Treated Balanites Aegyptiaca Seed Husks Powder, Biointerface Research in Applied Chemistry, 12(6) (2022) 7845–62.

[24] Al-Asadi S.T., Al-Qaim F.F., Al-Saedi H.F.S., Deyab I.F., Kamyab H., Chelliapan S., Adsorption of methylene blue dye from aqueous solution using low-cost adsorbent: kinetic, isotherm adsorption, and thermodynamic studies, *Environ Monit Assess,* 195 (2023) 676.

[25] Ayawei N., Ebelegi A.N., Wankasi D., Modelling and Interpretation of Adsorption Isotherms, J *Chem*., 2017 (2017) 3039817.

[26] Şenol Z.M., Gül Ü.D., Şimşek S., Bioremoval of Safranin O dye by the identified lichen species called Evernia prunastri biomass; biosorption optimization, isotherms, kinetics, and thermodynamics, *Biomass Convers Biorefinery*., 12 (2022) 4127–37.

[27] Mohammed R.A., Walli H.A., A Study of Removal of Lead (II) Ions from Aqueous Solution on Chitosan-g-poly (acrylic acid-co-crotonic acid) Hydrogel, *Int J Drug Deliv Technol.,* 12 (2022) 1844–8.

[28] Keskin Z.S., Şenol Z.M., Kaya S., Şimşek S., Prunus mahaleb shell as a sustainable bioresource for carminic acid removal from aqueous solution: Experimental and theoretical studies, J. Mol. Struct., 1275 (2023) 134618.

[29] Al-Ghouti M.A., Da'ana D.A., Guidelines for the use and interpretation of adsorption isotherm models: A review, *J. Hazard Mater.,* 393 (2020) 122383.

[30] Dada A.O., Adekola F.A., Odebunmi E.O., Dada F.E., Bello O.M., Akinyemi B.A., et al., Sustainable and low-cost Ocimum gratissimum for biosorption of indigo carmine dye: kinetics, isotherm, and thermodynamic studies, *Int. J.*

Phytoremediation,. 22 (2020) 1524–37.
[31] Şenol Z.M., Çetinkaya S., Yenidünya A.F., Başoğlu-Ünal F., Ece A., Epichlorohydrin and tripolyphosphate-crosslinked chitosan–kaolin composite for Auramine O dye removal from aqueous solutions: Experimental study and DFT calculations, *Int. J. Biol. Macromol.,* 199 (2022) 318–30.
[32] Sözüdoğru O., Investigation of Effective Removal of Auramine O Dye by Pyracantha Coccinea Biosorbent: Isotherm and Kinetics, *Brill Eng*.,4 (2023) 1–6.
[33] Vaid V., Jindal R., Biodegradable tamarind kernel powder/kappa-carrageenan hydrogel for efficient removal of cationic dyes from effluents, *Water Environ. Res.,* 95 (2023) 1–21.
[34] Shakeri S., Rafiee Z., Dashtian K., Fe3O4-Based Melamine-Rich Covalent Organic Polymer for Simultaneous Removal of Auramine O and Rhodamine B., *J. Chem. Eng. Data*, 65 (2020) 696–705.
[35] Duarte E.D.V., Vieira W.T., Góes R.O., de Azevedo L.E.C., Vieira M.G.A., da Silva M.G.C., et al., Amazon raw clay as a precursor of a clay-based adsorbent: experimental study and DFT analysis for the adsorption of Basic Yellow 2 dye, *Environ. Sci. Pollut. Res.,* 30 (2023) 62602–24. A
[36] Şenol Z.M., Şimşek S, Equilibrium, kinetics and thermodynamics of Pb(II) ions from aqueous solution by adsorption onto chitosan-dolomite composite beads, *Int. J. Environ. Anal. Chem.,* 102(17) (2022) 4926–40.
[37] Thompson C.O., Ndukwe A.O., Asadu C.O., Application of activated biomass waste as an adsorbent for the removal of lead (II) ion from wastewater, *Emerg Contam*., 6 (2020) 259–67.
[38] Şenol Z.M, El Messaoudi N., Fernine Y., Keskin Z.S., Bioremoval of rhodamine B dye from aqueous solution by using agricultural solid waste (almond shell): experimental and DFT modeling studies, *Biomass Convers Biorefinery*, (2023) https://doi.org/10.1007/s13399-023-03781-1.
[39] Zafar L., Khan A., Kamran U., Park S., Nawaz H., Eucalyptus (camaldulensis) bark-based composites for efficient Basic Blue 41 dye biosorption from aqueous stream : Kinetics , isothermal , and thermodynamic studies, *Surfaces and Interfaces* , 31 (2022) 101897.

Cumhuriyet Sci. J., 45(2) (2024) 249-255
DOI: https://doi.org/10.17776/csj.1423273

Cumhuriyet Science Journal

| csj.cumhuriyet.edu.tr | Founded: 2002 ISSN: 2587-2680 e-ISSN: 2587-246X Publisher: Sivas Cumhuriyet University

Electrochemical Oxidation of Ranitidine using a Boron-Doped Diamond Electrode in the Presence of Anionic Surfactant: A Comprehensive Investigation

Hasret Subak [1,a], Pınar Talay Pınar [1,b,*]

[1]*Department of Analytical Chemistry, Faculty of Pharmacy, Van Yuzuncü Yil University, Zeve Campus 65080 Van, Türkiye.*
**Corresponding author*

Research Article

History
Received: 21/01/2024
Accepted: 06/04/2024

ABSTRACT

Ranitidine (RAN) is a drug from the histamine H2 receptor antagonist class and is used to prevent excessive production of stomach acid. An electrochemical investigation of the RAN in pharmaceutical preparation and spiked human urine was performed for the using a boron-doped diamond electrode (BDDE). Voltammetric measurements were performed in a pH 11 BR solution supplemented with the anionic surfactant, sodium dodecyl sulfate (SDS). In the proposed method using optimized experimental conditions, linearity was obtained for RAN in the concentration range of 0.8-50.0 µM. The LOD value obtained is 0.22 µM. Good selectivity, accuracy, precision, and acceptable repeatability were also achieved in this proposed electrochemical sensor. Finally, this electrochemical sensor was successfully used for RAN detection in pharmaceutical samples.

Keywords: Ranitidine, Electrochemical detection, Boron-doped diamond electrode, Surfactant, Pharmaceutical samples.

[a] *hasret@yyu.edu.tr* *https://orcid.org/0000-0003-0100-2529* [b] *ptalay@yyu.edu.tr* *https://orcid.org/0000-0003-1027-1456*

Introduction

RAN, (N-(2-((5-((dimethylamino) methyl) furan-2-yl) methylthio) ethyl)-N'-methyl-2-nitroethene-1,1-diamine) is an H2 receptor antagonist and is often used to treat peptic ulcers by reducing stomach acid production. It is used in the treatment of RAN, duodenal and gastric ulceration, gastro-esophageal reflux disease, Zollinger-Ellison syndrome diseases [1,2]. The majority of the oral or intravenous RAN dose excreted in urine is in the unchanged drug form, but only a small fraction of the administered dose is excreted as metabolites (RAN-N-oxide, RAN-S-oxide, and desmethyl-RAN) [3,4]

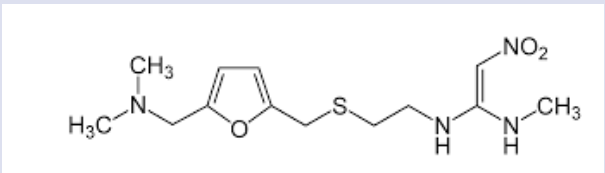

Figure 1. Chemical structure of RAN.

In the literature survey, there are various analytical methods developed for the quantitative analysis of RAN, such as high-performance liquid chromatography (HPLC), liquid chromatography (LC)-mass spectroscopy (MS), fluorescence technique, colorimetric detection, and electrophoresis [5-15]. Although these methods are effective and sensitive, they are known to be quite expensive and not environmentally friendly due to the excessive use of organic solvents. In addition, it creates disadvantages such as long analysis times and the need for experts to use analytical devices. Electrochemical methods, on the other hand, have a more environmentally friendly feature than other methods and are preferred in the analysis of electro-active compounds used in many areas (such as agriculture, food, plants, health, and drugs) [16-20]. Voltammetry, one of the most used electroanalytical techniques, is widely used especially in drug analysis. These methods have many advantages such as short analysis time, low cost, low use of organic solvents, high sensitivity, precise analytical capabilities, and analysis in low volumes.

Boron-doped diamond electrode (BDD) is a special electrode used in chemical analysis and electrochemical applications. Boron-doped diamond electrodes are widely used in electrochemical analysis, sensor applications, bioanalytical measurements, and various electrochemical research. The properties of boron-doped diamond electrodes combine high mechanical strength, chemical inertness, low surface roughness, and conductivity [21-22]. These electrodes have the potential to provide high sensitivity and durability, especially in harsh environmental conditions and when working with biological samples.

The combination of carbon-based electrodes with surfactants is a widely used strategy in electrochemical studies to improve surface properties and increase measurement sensitivity. As is known, carbon-based electrodes generally have a high surface area, and their surface properties can be further improved with the use of surfactants. This allows reactants on the electrode surface to be adsorbed more effectively and electrochemical reactions to be monitored more precisely. Surfactants have the ability to control molecular adsorption on the electrode surface. This can particularly

increase the selectivity of certain analytes and reduce undesirable interactions on the electrode [23-25].

In this study, it was aimed to obtain a more stable sensor in the anionic surfactant environment with a boron-doped diamond electrode for sensitive voltammetric detection of RAN and to examine the possible electrochemical oxidation mechanism.

Materials and Methods

RAN ($C_{13}H_{22}N_4O_3S \cdot HCl$) standard pharmaceutical active ingredient was purchased from Sigma-Aldrich (Türkiye, CAS: 66357-59-3). 1.0×10^{-3} M stock solution was prepared by dissolving the appropriate amount of RAN in salt form in water. A stock solution of the surfactant tested in this study, sodium dodecyl sulfate, SDS (anionic) (1×10^{-2} M), was prepared by dissolving it in water.0.1 M Acetate buffer (pH 4.8), 0.1 M phosphate buffer (pH 2.5, 7.4), 0.1 M Britton-Robinson buffer (pH 2.0 – 12.0), and H_2SO_4 (96%) (0.1 and 0.2 M) were used as supporting electrolytes. Additionally, dopamine, ascorbic acid, uric acid, lactose, glucose, potassium chloride, magnesium chloride, sodium sulfate, and potassium nitrate were obtained from Sigma-Aldrich to perform interference studies. The chemicals H_3PO_4 (85%), $NaH_2PO_4 \cdot H_2O$, CH_3COOH (100%), HCl (37%), H_3BO_3 (99.5%), and Na_2HPO_4 used in the preparation of supporting electrolyte solutions were obtained from Sigma-Aldrich.

Electrochemical studies were carried out with cyclic voltammetry (CV), and square wave voltammetry (SWV) techniques using Autolab PGSTAT 101 (Metrohm Autolab B.V., Netherlands) electrochemical analyzer with NOVA 2.1.6 electrochemical software.

Electrochemical studies were carried out using a triple electrochemical cell system containing a working electrode, counter electrode, and reference electrode. The BDD electrode as the working electrode (Windsor Scientific Ltd., UK, declared boron doping level of 1000 ppm, disk diameter of 3 mm); the platinum wire (MW-1032, USA) obtained from BASi was used as the counter electrode and Ag/AgCl electrode (3 M NaCl; BASi, MF 2056, USA) was used as the reference electrode. In addition, solid chemical substances were weighed with a Vibra brand electronic scale with a sensitivity of 0.01 mg. ISOLAB model ultrasonic bath was used to clean the working electrode and dissolve some substances. WTW inoLab pH7110 digital pH meter was used to adjust the pH of the solutions.

Before starting the voltammetric experiments, BDD was pretreated cathodic and anodic in 0.5 M H_2SO_4 by applying - 1.8 V, then + 1.8 V for 120 s, respectively, to activate the electrode. Between individual measurements, the BDD electrode was gently cleaned with a damp velvet cloth and then rinsed with water.

Zantac® (contains 50mg 10mL−1 RAN HCl) brand syrup was used for RAN syrup formulations. The contents of the bottle were mixed thoroughly to ensure homogeneity. The required volume for voltammetric analysis was taken and diluted with buffer containing anionic surfactant (SDS). The prepared solutions were analyzed directly voltammetrically without being subjected to any further processing.

Results and Discussion

Electrochemical Behavior of RAN

First, the CV technique was used to investigate the electrochemical response of 1×10^{-4} M RAN on BDDE in pH 11 BR buffer solution (the best medium for RAN analysis has been selected and will be mentioned later) is presented in **Fig. 2.** As seen in the voltammogram, oxidation peaks of RAN were obtained at 0.75 µA at 1.28 V in pH 11 BR buffer solution, and no reduction peak was observed in the cathodic scan. This result shows that the oxidation of the RAN molecule under all applied conditions is completely irreversible.

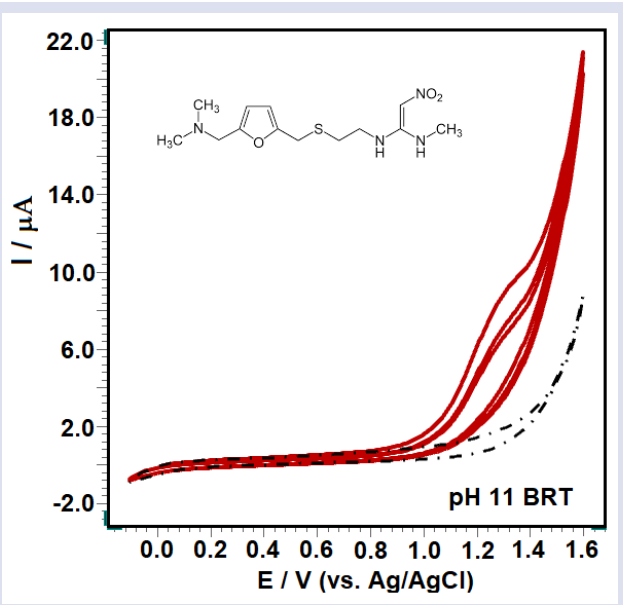

Figure 2. CVs of 1×10^{-4} M RAN at BDD electrode with three repetitions in pH 11 BR buffer solution. The scan rate is 100 mV/s.

Valuable information regarding the electrode reaction mechanism (rate determination step) can be obtained from the relationship between oxidation peak current and scan rate. The effect of scan rate on the electrochemical oxidation of 1×10^{-4} M RAN was studied using different scan rates (75-500 mV/s; n:6) with BDD electrode in pH 11 BR buffer solution and the corresponding voltammograms are shown in Fig. 3. v – Ip (Eq.1), log v –log Ip (Eq.2) graphs were drawn using the findings obtained from these voltammograms, and the linearity equations of these graphs are presented below.

$$\log I_p = 0.7809 \pm 0.16 \log v - 1.6105 \pm 0.562;\ r = 0.999 \quad (1)$$

$$\log I_p = 0.7809 \pm 0.16 \log v - 1.6105 \pm 0.562;\ r = 0.999 \quad (2)$$

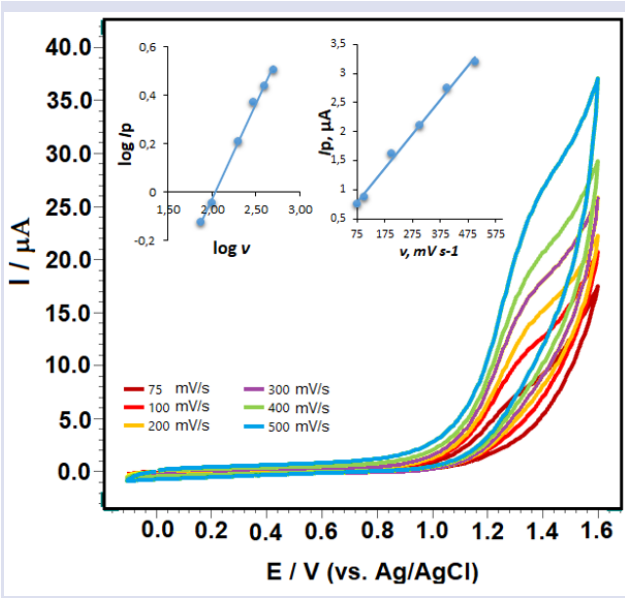

Figure 3. Cyclic voltammograms of 1×10^{-4} M RAN recorded using a BDD electrode in the scan rate range of 75-500 mV s^{-1} in pH 11 BR buffer solution. Inset: Linearity graphs of $\sqrt{v}$ – Ip and log v – log Ip.

The linearity obtained from the Ip/v relationship shows that the electrochemical oxidation of the RAN molecule is adsorption-controlled under the experimental conditions studied. When the logarithmic equations of current and scan rate are examined, the slope obtained (0.78) is between the theoretical values of 0.5 and 1.0, indicating that this reaction is adsorption-controlled in the irreversible electro-oxidation process of RAN on the BDD electrode. On the other hand, anodic peak potentials (Ep) were observed to slowly shift linearly to more positive values from 75 to 500 mV s^{-1}. This phenomenon, as is known, is characteristic of the irreversible electrochemical reaction. The plot of the Ep/log v (Eq.3) between 75-500 mV s^{-1} can be expressed as follows:

$$E\text{p} = 0.054\pm0.085\log v + 1.1978\pm1.238;\ r = 0.9949 \quad (3)$$

The number of electrons (n) transferred in the oxidation of the RAN molecule on the BDD electrode was calculated by taking measurements on CVs and using the 'Laviron's equation (Eq. 4) given below, which is valid in the adsorpsion-controlled irreversible electrode process [26].

$$E_p = E^\circ + (2.303RT / \alpha nF) \log (RTk^\circ / \alpha nF) + (2.303RT / \alpha nF) \log v \quad (4)$$

The constants T, R, F, E^0, v, n, k^0 and α in the formula are expressed as absolute temperature, universal gas constant, Faraday constant, formal redox potential, scanning speed, number of electrons transferred, heterogeneous transfer constant, respectively. Considering the slope of the graph of Ep (V) versus log v (mV s^{-1}), the resulting αn is 1.0. In irreversible systems, the α value is accepted as 0.5. Thus, the value of n is calculated as 2. This result shows that 2 electrons are transferred per molecule in the redox reaction of RAN [27].

As it is known, the pH of the analytical solution is an important step that determines whether protons will take part in electrode reaction mechanisms. In studies carried out to develop a sensitive and selective voltammetric method for the determination of RAN, sharper and well-defined peaks were obtained with the SWV technique. The effect of pH value on the anodic potential and current responses at the BDD electrode was investigated in 1×10^{-4} M RAN. In order to examine the effect of supporting electrolyte and pH on the voltammetric behavior of RAN, SW voltammograms were recorded in the (0.0) - (+1.6) V potential scan range of RAN solutions prepared in the appropriate support electrolyte. For this purpose, supporting electrolyte solutions of 0.1 M Britton-Robinson buffer (pH 2.0-12.0) were used. Figure 4 shows the effect of pH on square-wave voltammograms recorded in 1×10^{-4} M RAN solutions.

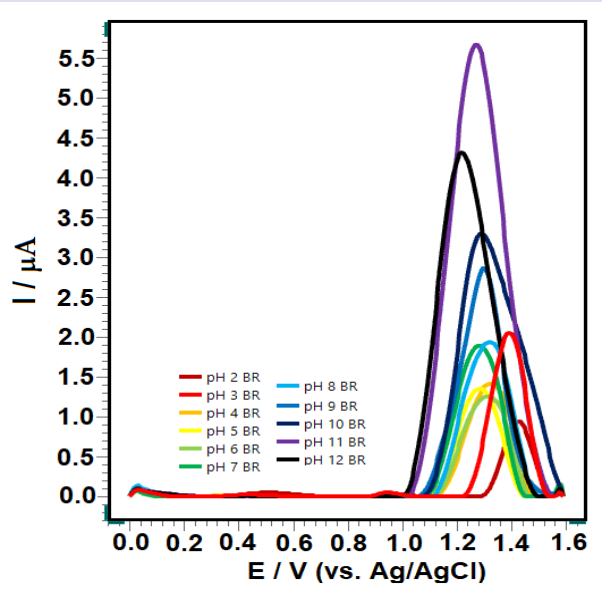

Figure 4. SWVs of 1×10^{-4} M RAN in BR buffer (pH 2.0–12.0) at a range of pH values. Electrode, BDDE; SWV parameters: 50 Hz frequency, 8 mV scan increment, and 30 mV pulse amplitude.

As seen in Fig. 4 the oxidation peak current of RAN can change with different pH values. The highest oxidation peak current was obtained at the pH 11 BR buffer. The oxidation peak potential of RAN appears to shift towards a more negative potential between pH 2 and 5. In the more basic region, pH again shifts to negative potential between 8 and 11. Therefore, there are two inclined regions of RAN on the BDD electrode surface, one being an acidic region and the other being a basic region. This result shows that protons on the BDD electrode surface are effective on the electrochemical mechanism. As can be seen from the SW voltammograms in Fig. 4, pH 11 BR buffer solution was preferred in terms of both peak morphology and oxidation peak current, and all studies

were continued in this medium. When the relationship between pH and peak potential (*E*p) of RAN is examined; It can be seen that there are two slope region. The linear regression equations of RAN are expressed as follows.

$$E_{pa}\ (V)\ (pH\ 2 - 5) = -0.047\ pH + 1.5178\ r: 0.996$$

$$E_{pa}\ (V)\ (pH\ 8 - 11) = -0.016\ pH + 1.4477\ r: 0.995$$

When the obtained slopes are examined, it is seen that the proton transfer in acidic and basic environments changes on the BDD electrode surface of RAN. Therefore, since the slope value obtained in a strongly basic solution is closer to the theoretical value of 30 mV/pH, two electrons and one proton transfer are involved in the oxidation of RAN in BR buffer, pH 11 solution. Accordingly, the possible electrochemical oxidation mechanism of RAN has been reported previously [27].

Since the signals occurring in voltammetric techniques may vary with the variables of the device used, it is necessary to optimize these variables. For this purpose, square wave pulse variables were optimized in the range of 15 - 200 Hz frequency (*f*), 4 - 20 mV step potential (ΔE_s), and 10 - 100 mV pulse amplitude (ΔE_{sw}) of 1×10^{-5} M RAN in pH 11 BR buffer. The optimization process was carried out by changing one parameter at a time and keeping the others constant. By increasing the frequency, the oxidation peak current increased up to 200 Hz, but after 125 Hz, the oxidation peak current increased but the peak morphology deteriorated. For this reason, the most appropriate frequency value was determined as 125 Hz. The best result in terms of peak shape and oxidation peak current value in the potential range of 4–20 mV was obtained at ΔEs = 14 mV, and the best result was obtained at 40 mV in oxidation peak current in the pulse amplitude range of 10–100 mV.

Finally, the effect of surfactant (SDS; anionic surfactant, CTAB; cationic surfactant, Tween 20; non-ionic surfactant) on the electrochemical oxidation of RAN was examined. As is known, the sensitivity of voltammetric methods can be increased thanks to this electrostatic interaction between the electrode surface - surfactant and analyte. Figure 5 shows the interaction of RAN with cationic, anionic and nonionic surfactants in the same medium (pH 11 BR). As can be seen from the figure 5, the oxidation peak current of RAN increases in the presence of SDS, and decreases significantly in the presence of CTAB and Tween 20.

By keeping the RAN concentration constant at 5×10^{-5} M in the pH 11 BR buffer solution, the surfactant effect was investigated by adding SDS in different concentration ranges (1×10^{-5} to 1×10^{-3} M). The maximum value was observed when 8×10^{-4} M SDS (Figure 6) was added, and the 8×10^{-4} M SDS concentration was chosen for the remainder of the present analytical study.

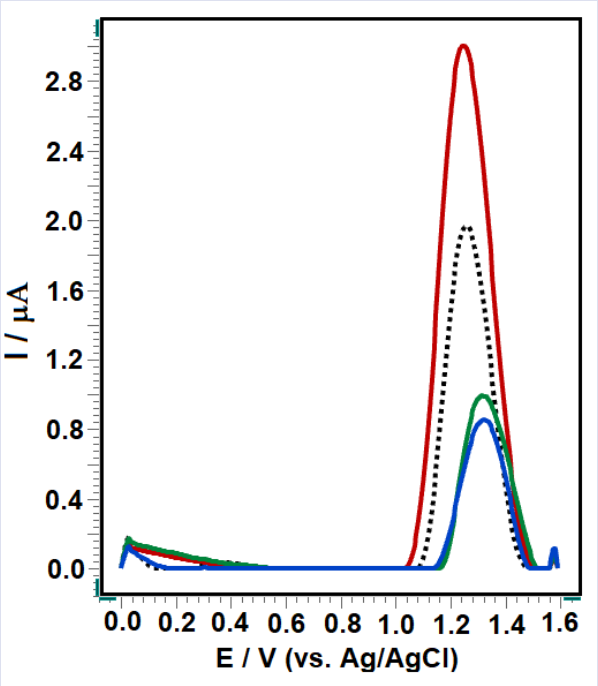

Figure 5. SWVs of 5×10^{-5} M RAN (----) in BR buffer (pH 11.0) with 8×10^{-5} M SDS (Red), CTAB (green), and Tween 20 (blue) surfactant. Electrode, BDDE; SWV parameters: 125 Hz frequency, 14 mV scan increment, and 40 mV pulse amplitude.

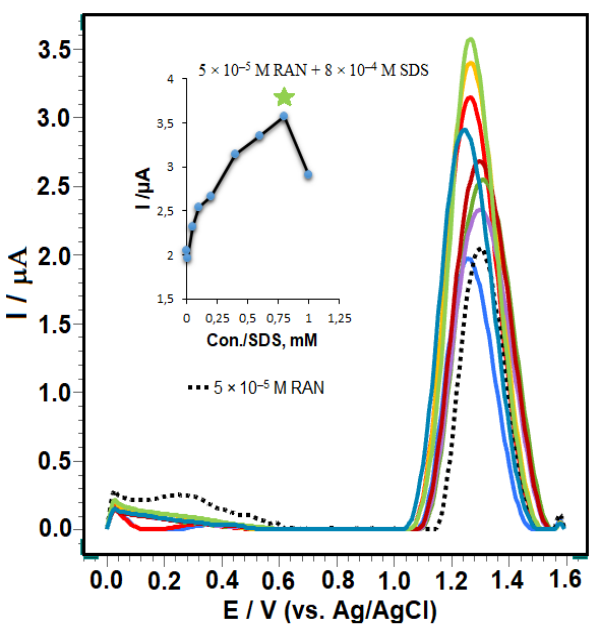

Figure 6. SW voltammograms of 5×10^{-5} M RAN in pH 11 BR buffer solution in the concentration range of 1.0×10^{-5} to 1×10^{-3} M SDS. Dashed lines represent voltammograms without SDS. Inset: *i*p plot and SDS concentration. Electrode, BDDE; SWV parameters: 125 Hz frequency, 14 mV scan increment, and 40 mV pulse amplitude.

Analytical Application of RAN

The sensitivity, selectivity, repeatability and linearity range of the studied voltammetric method were investigated in detail. To examine the effect of RAN concentration on oxidation peak current under the best experimental conditions, voltammograms of RAN solutions at different concentrations were evaluated with the BDD electrode in pH 11 BR buffer. The SW voltammograms for calibration were obtained by increasing the concentrations of RAN as shown in Fig. 7. As seen in the figure, the oxidation peak currents of RAN at increase in proportion to their concentrations, and the relevant analytical parameters are summarized in Table 1. Fig. 7 shows that RAN has a linear range between 0.8 and 50 µM, [*ip* (µA) = 0.1181 C (µM) + 0.0113], r=0.999].

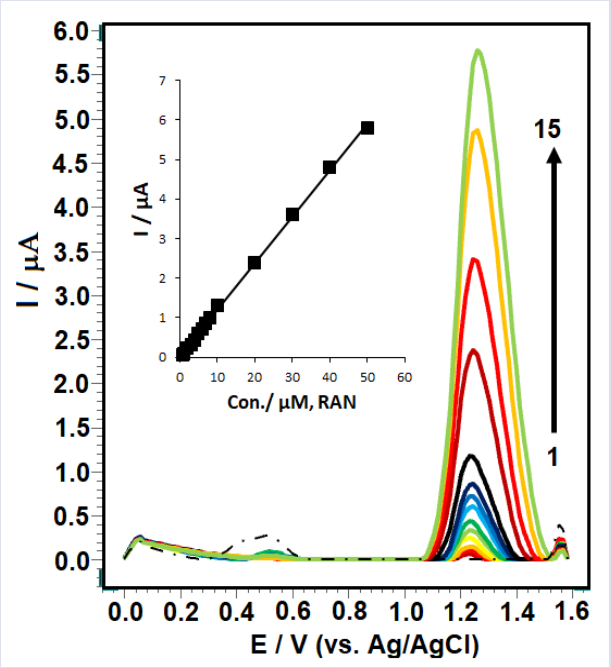

Figure 7. SWVs for RAN levels of (1–15) 0.8, 1.0, 2.0, 3.0, 4.0, 5.0, 6.0, 7.0, 8.0, 9.0, 10.0, 20.0, 30.0, 40.0, 50.0 µM in pH 11 BR solution with presence 8×10^{-4} M SDS. Inset shows the corresponding calibration plot for the quantitation of RAN. Electrode, BDDE; SWV parameters: 125 Hz frequency, 14 mV scan increment, and 40 mV pulse amplitude.

Table 1. Analytical validation parameters of the proposed SW voltammetric method

Parameters	Oxidation of RAN
Linearity range (µM)	0.8 – 50
Slope (µA/µM)	0.1181
Intercept (µA)	0.0113
Correlation coefficient	0.999
LOD (µM)	0.22
LOQ (µM)	0.74

The RSD value of the slope of calibration curve for oxidation of RAN was found to be 4.53%. This result show that the BDD electrode has very high reproducibility for the electrochemical oxidation of RAN. Comparison between previously reported methods for electrochemical oxidation of RAN and the method presented here is given in Table 2.

Table 2. Comparison of the proposed method for determination of RAN with previously reported electrochemical oxidation using different electrodes.

Electrode	LOD (µM)	Sample	Ref.
GCE	0.6	Drug	[28]
Gr-GCE	0.1	Drug, Serum	[29]
PDA-CPE	0.019	Drug, Urine	[27]
Printex 6L-GCE	0.24	Urine, Serum	[30]
BDDE	0.22	Drug	This work

GCE: Glassy carbon electrode, Gr-GCE: Graphene modified glassy carbon electrode, PDA-CPE: poly(dopamine) modified carbon paste electrode.

The precision values of the method were evaluated with the relative standard deviations (RSD) of both intraday and interday repeatability of RAN oxidation peak current values. It was taken again eight times on the same day and in three different solutions on different days, using the square wave voltammetry method. Intraday and interday % RSD values of oxidation peak currents of RSD were determined as 3.55% and 5.23%, respectively. The results show us that the repeatability of oxidation in peak current and peak potential values is quite good.

To examine the selectivity of the proposed voltammetric method, it was tested on substances that could interfere with the 3.0 µM RAN solution. In the selectivity study, no change in the peak potential of RAN was observed in the presence of Ca^{2+}, Cu^{2+}, Zn^{2+}, Ag^{+}, Na^{+}, NO^{3-}, Cl^{-}, uric acid and dopamine compounds. The results obtained from these data show that; It can be said that the method designed with BDD electrode is selective. In the next step, the amount of RAN was determined using the BDD electrode at presence 8×10^{-4} M SDS. Finally, to check the practical applicability of the determined method, the analysis of syrup containing RAN was tested using the calibration method. The assay results with recoveries for the pharmaceutical formulation examined are summarized in Table 3.

Table 3. The results for quantification and recovery of RAN from the syrup sample (Zantac®, mg/10 mL)

Declared amount	Determined amount	Recovery (%)	Bias (%)
150	148	98.66	1.34

Conclusions

Electrochemical studies of RAN in the literature are mainly related to electrochemical reduction. There are a limited number of studies on electrochemical oxidation. Here, a new electroanalytical method is proposed for the determination of RAN with BDD electrode for the first

time in the presence of SDS, an anionic surfactant. The results obtained show the sensitivity of the proposed electrochemical method and its low cost since it does not require expensive apparatus. The main advantage of the proposed method is that it is directly applicable to the analysis of biological samples without the need for separation or complex sample preparation since there are no problems caused by endogenous substances compared to other techniques. The recovery results show that the proposed procedures are sufficiently accurate and precise. Therefore, this proposed technique is quite fast, simple to implement, and most importantly, inexpensive. It can be considered as a suitable alternative to other existing analytical methods.

Conflicts of interest

There are no conflicts of interest in this work.

References

[1] Helman C. A., Tim L. O., Pharmacology and Clinical Efficacy of Ranitidine, a New H2-Receptor Antagonist, *Pharmacother. J. Hum. Pharmacol. Drug Ther.*, 3(4) (1983) 185-191.

[2] Dawson J., Richards D. A., Stables R., Dixon G. T., Cockel R., Ranitidine—Pharmacology and Clinical use, *J. Clin. Pharm. Ther.*, 8(1) (1983) 1-13.

[3] Ashiru D. A., Patel R., Basit A. W., Simple and Universal HPLC-UV Method to Determine Cimetidine, Ranitidine, Famotidine, and Nizatidine ın Urine: Application to the Analysis of Ranitidine and its Metabolites in Human volunteers, *J. Chromatogr. B*, 860(2) (2007) 235-240.

[4] Psoma A. K., Rousis N. I., Georgantzi E. N., Thomaidis N. S., An Integrated Approach to MS-based Identification and Risk Assessment of Pharmaceutical Biotransformation in Wastewater, *Sci. Total Environ.*, 770 (2021) 144677.

[5] Zendelovska D., Stafilov T., Development of an HPLC method for the Determination of Ranitidine and Cimetidine in Human Plasma Following SPE, *J. Pharm. Biomed. Anal.*, 33(2) (2003) 165-173.

[6] Castro A., Arancibia A., Romero P., Gai M. N., Validated HPLC method for the Determination of Ranitidine in Plasma, *Die Pharm. Int. J. Pharm. Sci.,* 58(10) (2003) 696-698.

[7] Haque T., Takulder M. M. U., Laila S., Fatema K., Development and Validation of RP-HPLC method for Simultaneous Estimation of Naproxen and Ranitidine Hydrochloride, *Pak. J. Pharm. Sci.,* 23(4) (2010) 379-383.

[8] Babu B., Hemnath E., Jeyaprakash M., Krishnaveni N., Meyyanathan S., Raja R., Venkatesh D., A RP-HPLC method for Simultaneous Estimation of Ondansetron and Ranitidine in Pharmaceutical Formulation, *Int. J. Heal. Allied Sci.*, 1(2) (2012) 129-129.

[9] Kiszkiel-Taudul I., Starczewska B., Jabłońska A., Ionic Liquid-based Ultrasound-assisted Emulsification Microextraction for the Determination of Ranitidine in Water Samples and Pharmaceutical Preparations, *New J. of Chem.*, 44(27) (2020) 11490-11497.

[10] El-Naem O. A., El-Maraghy C. M., A Validated Liquid Chromatography-Tandem Mass Spectrometric method for the Determination of Co-administered Ranitidine and Metronidazole in Plasma of Human Volunteers, *Anal. Met.,* 13(23) (2021) 2586-2595.

[11] Paul S., Barai L., Husen F., Sarker S., Pal T. K., Bal P., Biswas S., Analytical method Development and Validation for Estimation of Ranitidine in Solid Dosage form by UV-Spectrophotometric method, *Orient. J. Chem.*, 36(6) (2020) 1161.

[12] Berisha L., Jashari G., Veseli V., Shabani E., Lushaj F., Maxharraj F., Maloku A., Flow İnjection Analysis of Ranitidine based on Derivatization Reaction Producing 2-Methylfuran Cation as a Sensitive and Selective Amperometric Detector, *Electroanalysis*, (2023) e202200318.

[13] Alshehri Y. M., Alghamdi T. S., Aldawsari F. S., HS-SPME-GC-MS as an Alternative method for NDMA Analysis in Ranitidine Products, *J. Pharm. Biomed. Anal.,* 191 (2020) 113582.

[14] Júnior J. G. F., de Lima A. R. B., de Freitas A. J. D., de Freitas J. D., Limad P. R., de Abreu F. C., Meneses D., Paper based Device (PAD) for Colorimetric Determination of Ranitidine in Pharmaceutical Samples, *Microchem. J.*, 178 (2022) 107336.

[15] Zounr R. A., Khuhawar M. Y., Khuhawar T. M., Lanjwani M. F., Khuhawar M. Y., GC Analysis of Metformin, Ranitidine and Famotidine from Pharmaceuticals and Human Serum, *J. Chromathogr. Sci.*, 61(9) (2023) 807-813.

[16] Karahan F., Başı Z., Keskin E., Pınar P. T., Yardım Y., Şentürk Z., Electrochemical Determination of Fluoroquinolone Antibiotic Norfloxacin in the Presence of Anionic Surfactant using the Anodically Pretreated Boron-Doped Diamond Electrode, *ChemistrySelect*, 5(42) (2020) 12862-12868.

[17] Allahverdiyeva S., Pınar P. T., Yardım Y., Şentürk Z., First Report for the Electrochemical Investigation of a New HIV İntegrase İnhibitor Dolutegravir: Its Voltammetric Determination in Tablet Dosage Forms and Human Urine using a Boron-Doped Diamond Electrode, *Diam. Relat. Mater.*, 114 (2021) 108332.

[18] Pınar P. T., Yardım Y., Gülcan M., Şentürk Z., The First Approach for the Simultaneous Quantification of İsoproturon, Carbendazim, and Carbofuran at the Surface of a MIL-101 (Cr) Metal-organic Framework-based Electrode, *Inorg. Chem. Commun*., (2023) 111327.

[19] Ali H. S., Barzani H. A., Yardım Y., Utilizing Epicatechin Voltammetric Oxidation Signal for the Estimation of Total Phenolic Content in the Tea Samples via the Unmodified Boron-Doped Diamond Electrode Surface, *Microchem. J.*, 189 (2023) 108572.

[20] Pınar P. T., Yardım Y., Şentürk Z., Square-wave Voltammetric Sensing of Lawsone (2-hydroxy-1, 4-naphthoquinone) based on the Enhancement Effect of Cationic Surfactant on Anodically Pretreated Boron-Doped Diamond Electrode, *Acta Chim. Slov*, 68(4) (2021) 1027-1032.

[21] Švorc Ľ., Rievaj M., Bustin D., Green Electrochemical Sensor for Environmental Monitoring of Pesticides: Determination of Atrazine in River Waters using a Boron-Doped Diamond Electrode, *Sensors and Actuators B: Chem.,* 181 (2013) 294-300.

[22] Budak F., Cetinkay, A., Kaya S. I., Atici E. B., Ozkan S. A., Sensitive Determination and Electrochemical Evaluation of Anticancer Drug Tofacitinib in Pharmaceutical and Biological Samples using Glassy Carbon and Boron-Doped Diamond Electrodes, *Diam. Relat. Mater.*, 133 (2023) 109751.

[23] Kaya S., Cetinkaya A., Ozkan S. A., Surfactant Sensors for Pharmaceutical/Medical Applications, 23(3) (2023) 163-192.

[24] Barzani H. A., Yardım Y., First Approach for the Voltammetric Sensing of Rifabutin by the use of Cationic Surfactant Media on the Boron-Doped Diamond Electrode, *Diam. Relat. Mater.,* 132 (2023) 109658.

[25] Mete C., Pınar P. T., Using a Boron-Doped Diamond Electrode in Anionic Surfactant Media as an Improved Electrochemical Sensor for the Anticancer Drug Ibrutinib, *Chemistry Select*, 8(6) (2023) e202204492.

[26] Pilz F. H., Kielb P., Cyclic voltammetry, Square Wave Voltammetry or Electrochemical İmpedance Spectroscopy? Interrogating Electrochemical Approaches for the Determination of Electron Transfer Rates of İmmobilized Redox Proteins, *BBA Advances*, 4 (2023) 100095.

[27] Pınar P. T., Yardım Y., Şentürk Z., Electrochemical Oxidation of Ranitidine at Poly (Dopamine) Modified Carbon Paste Electrode: Its Voltammetric Determination in Pharmaceutical and Biological Samples based on the Enhancement Effect of Anionic Surfactant, *Sensors and Actuators B: Chem.*, 273 (2018) 1463-1473.

[28] Pfaffen V., Ortiz P. I., Alternative method with Amperometric Detection for Ranitidine Determination, *Ind. Eng. Chem. Res., 49*(9) (2010) 4026-4030.

[29] Xi X., Ming L., Electrochemical Determination of Ranitidine Hydrochloride in Pharmaceutical Formulations and Biological Fluids at Graphene Modified Electrode, *Asian J. Chem.,* 25(10) (2013) 5315.

[30] Silva L. P., Vicentini F. C., Lourencao B. C., Oliveira G. G., Lanza M. R., Fatibello-Filho O., A New Sensor Architecture based on Carbon Printex 6L to the Electrochemical Determination of Ranitidine, *J. Solid State Electrochem.*, 20 (2016) 2395-2402.

Cumhuriyet Sci. J., 45(2) (2024) 256-262
DOI: https://doi.org/10.17776/csj.1425012

Cumhuriyet Science Journal

| csj.cumhuriyet.edu.tr | Founded: 2002 ISSN: 2587-2680 e-ISSN: 2587-246X Publisher: Sivas Cumhuriyet University

Influence of Selected Natural Antioxidants on Iron-Induced Enzymatic Alterations Related to Oxidative Stress

Melike Karaman [1,a,*], Emine Toraman [1,b]

[1] *Department of Molecular Biology and Genetics, Faculty of Science, Atatürk University, Erzurum, Türkiye.*
**Corresponding author*

Research Article

History
Received: 24/01/2024
Accepted: 13/06/2024

ABSTRACT

Iron is required in various biological processes of the cell, but excess iron causes oxidative stress. Oxidative stress can be prevented by antioxidants with free radical scavenging properties. Tannic acid and gallic acid are phenolic compounds with antioxidant properties found naturally in plants. In this study, the effects of gallic acid and tannic acid on iron-induced oxidative stress parameters were investigated in a fruit fly model. Effect of the compounds against iron-induced oxidative stress were evaluated by determining spectrophotometrically superoxide dismutase (SOD), catalase (CAT), glutathione peroxidase (GPx) and acetylcholinesterase (AChE) enzyme activities, and levels of reduced glutathione (GSH) and malondialdehyde (MDA) in larvae (n: 10) and adults (n: 20) of wild type Oregon R strain of Drosophila melanogaster. Iron treatment decreased enzyme activities and GSH levels, but increased MDA levels. Co-treatment of these compounds with iron ameliorated iron-induced changes, especially in larvae. On the other hand, iron-induced decrease in AChE activity was increased in adults by treatment of these compounds with iron. The results showed that natural phenolic compounds have the potential to ameliorate iron-induced changes in oxidative stress parameters.

Keywords: Antioxidant, Drosophila, Phenolic compound.

[a] *melike.yildiz@atauni.edu.tr* *https://orcid.org/0000-0002-0973-2561* [b] *emine.toraman@atauni.edu.tr* *https://orcid.org/0000-0001-7732-6189*

Introduction

Iron, which plays a role in normal cellular physiology such as oxygen transport and energy production, is an essential mineral for the growth, development and survival of most organisms [1]. However, excess iron intake has been associated with many diseases such as diabetes, hormonal abnormalities, immune system disorders, neurological disorders, certain types of cancer, liver and heart diseases. Due to its chemical structure and capacity to carry out single-electron reactions, iron plays an important role in the production and metabolism of free radicals in biological systems. Therefore, it has been reported that iron toxicity is caused by free radicals that cause tissue damage [2]. In this respect, antioxidants with metal chelating and/or free radical scavenging properties are being investigated to prevent free radical formation [3,4].

Polyphenols are bioactive compounds found in plants [5]. These compounds play a role in the prevention of various diseases such as degenerative diseases, cancer, hypercholesterolemia and hyperglycemia. They also have high antioxidant properties [5]. Polyphenols have the capacity to remove lipid peroxidation, scavenge hydroxyl radicals, and prevent oxidative damage. Tannic acid (TA), a polyphenol found in the fruit and peel of many plants, has been reported to have antimutagenic, anticancer, antioxidant, and antimicrobial activities [6–9]. Gallic acid (GA), found in various plants such as tea, hazelnut, grape and pomegranate peel, is a natural phenolic compound. Phenolic hydroxyl groups in GA can scavenge reactive oxygen species and prevent the formation of new radicals. This phenolic compound has anticancer, anti-inflammatory, antimicrobial, antioxidant and neuroprotective effects [10–12]. TA and GA are preferred to investigate their protective effects in toxicity studies due to their antioxidant properties [13–17].

Drosophila melanogaster is used as a model organism to identify novel therapeutics, evaluate anti-aging compounds, study drug addiction, and conduct toxicological and cancer studies, because it has a short life cycle and is cheap and easy to maintain and homologs approximately 75% of the genes associated with human diseases. model organism Drosophila is used as a model organism to identify novel therapeutics, evaluate anti-aging compounds, study drug addiction, and conduct toxicological and cancer studies, because it is cheap and easy to maintain, has a short life cycle and homologs approximately 75% of the genes associated with human diseases [18–23].

Since excess iron intake can lead to the formation of free radicals, the use of scavenging antioxidants can ameliorate iron-induced changes. This study was carried out to investigate the ability of TA and GA, which have antioxidant properties, to alleviate the harmful effects of iron (II) sulfate on lipid peroxidation and antioxidant enzymes in fruit flies.

Materials and Methods

Chemicals

In the study, iron (II) sulfate heptahydrate (AFG Scientific) were used as the iron sources. All chemicals including tannic and gallic acids were obtained from Sigma–Aldrich.

Animals and Treatment

The flies used in the study were wild-type Oregon R strain of *Drosophila melanogaster* and were obtained from Carolina Biological Supply Company. This strain is the standard winged fruit fly with red eyes and brown body. The flies The flies were cultured in vials including standard medium (corn flour, active dry yeast, sugar, agar, water and propionic acid) at 25 °C in an incubator. The third instar larvae obtained from these flies were used for all treatments. The larvae were divided into six groups: control group (treated with distilled water), iron group (treated with 1 mM Fe^{+2} solution), TA group (treated with 2 mg/mL TA solution), GA group (treated with 2 mg/mL GA solution), TA+iron group (treated with 1 mM Fe^{+2} solution and 2 mg/mL TA solution) and GA+iron group (treated with 1 mM Fe^{+2} solution and 2 mg/mL GA solution). For each treatment, 1.5 grams of and Formula 4-24® Instant *Drosophila* Medium (Carolina) was soaked with 5 mL of test solution. Larvae were harvested for analysis 24 hours after administration. In addition, the heads of adult flies developed from treated larvae with the test solutions were dissected and used for analysis.

Preparation of Homogenate

Ten larvae and twenty heads of adult fly belonging to each group were taken into tubes containing homogenate buffer (50 mM phosphate buffer with 1mM EDTA and 1 mM DTT, pH: 7.4). The larvae and heads were homogenized in the TissueLyser LT device (Qiagen) using stainless steel beads (5 mm diameter). The homogenates were centrifuged at 10000 rpm for 30 min at 4 °C. The obtained supernatants were used for biochemical analysis.

Determination of Enzyme Activities

Total protein contents of the supernatants were measured according to the method of [24] using a standard curve prepared with bovine serum albumin. The activity of Superoxide dismutase (SOD) was determined spectrophotometrically at 560 nm as described by [25]. The activity of Catalase (CAT) was measured in a spectrophotometer at 240 nm according to the method described by [26]. The of Glutathione peroxidase (GPx) was determined spectrophotometrically at 340 nm according to the method described by [27]. The activity of Acetylcholinesterase (AChE) was measured colorimetrically at 412 nm using the method described by [28].

Determination of the Reduced Glutathione Level

The reduced glutathione (GSH) concentrations in the supernatants of samples were determined in a spectrophotometer at 412 nm using GSH standard curve according to the method described by [29].

Determination of Lipid Peroxidation

Lipid peroxidation was assessed by the measurement of malondialdehyde (MDA) level. The MDA levels in the samples were measured spectrophotometrically at 532 nm using a standard curve of 1,1,3,3-tetramethoxypropane according to the method described by [30].

Statistical Analysis

All experimental results were expressed as mean ± standard deviation. The results were analyzed with one-way ANOVA and Tukey's post-hoc test using GraphPad Prism Software version 9.0. Differences were considered statistically significant at $p < 0.05$.

Results

The Enzyme Activities in the Larvae and Heads of Adults after the Treatments

The activities of enzymes (SOD, CAT, GPx and AChE) in larvae and heads of adults after treatment with gallic acid and tannic acid were shown in Figure 1 and Figure 2. The treatment of 1 mM Fe^{+2} caused a statistically significant decrease in enzyme activities compared to the control group. Gallic acid treatment did not alter CAT and GPx activities in larvae (Figure 1B and 1C), but increased SOD activity and decreased AChE activity (Figure 1A and 1D). After gallic acid treatment, no statistical change was observed in SOD, CAT and AChE activities in adults (Figure 1E, 1F and 1H), but a decrease in GPx activity was detected (Figure 1G). Gallic acid treatment with Fe^{+2} tolerated the Fe^{+2}-induced decrease in SOD and CAT activity in larvae (Figure 1A and 1B), and AChE activity in the adult (Figure 1G). It brought other enzyme activities closer to the control group. Tannic acid treatment increased SOD activity in both larvae and adults compared to the control group, but did not change the activity of other enzymes except GPx enzyme in larvae (Figure 2A-H). Tannic acid treatment in combination with Fe^{+2} ameliorated Fe^{+2}-induced changes in SOD, CAT and GPx activities (Figure 2A-C), except AChE activity (Figure 2D) in larvae. In adults, this treatment restored GPx and AChE activities (Figure 2G and 2H) to control group values, but increased SOD activity (Figure 2E).

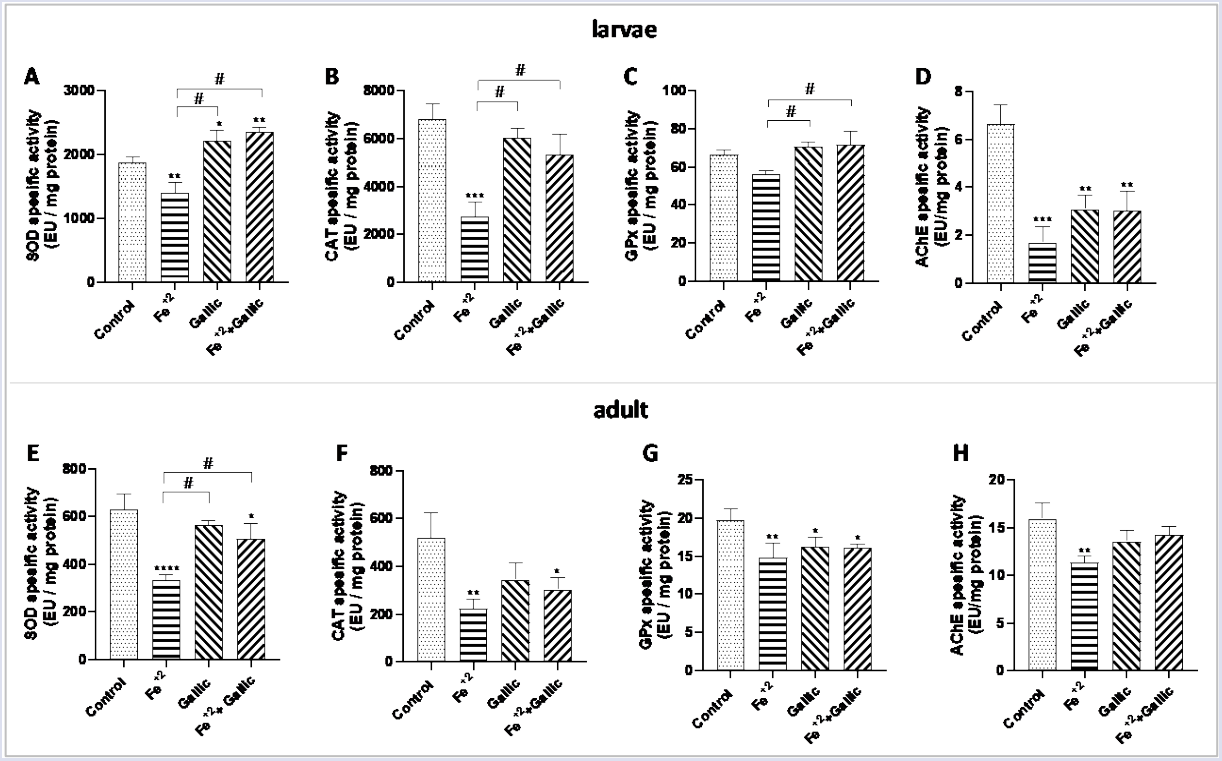

Figure 1. Superoxide dismutase (SOD), catalase (CAT), glutathione peroxidase (GPx) activity and acetylcholinesterase (AChE) activities in larvae (A-D) and heads of adults (E-H) after treatment with gallic acid. The bars represent the mean ± SD. Symbols indicate significance of differences between the groups: *p <0.05, **p < 0.01, ***p < 0.001 vs. control group; #p < 0.05 vs. other groups.

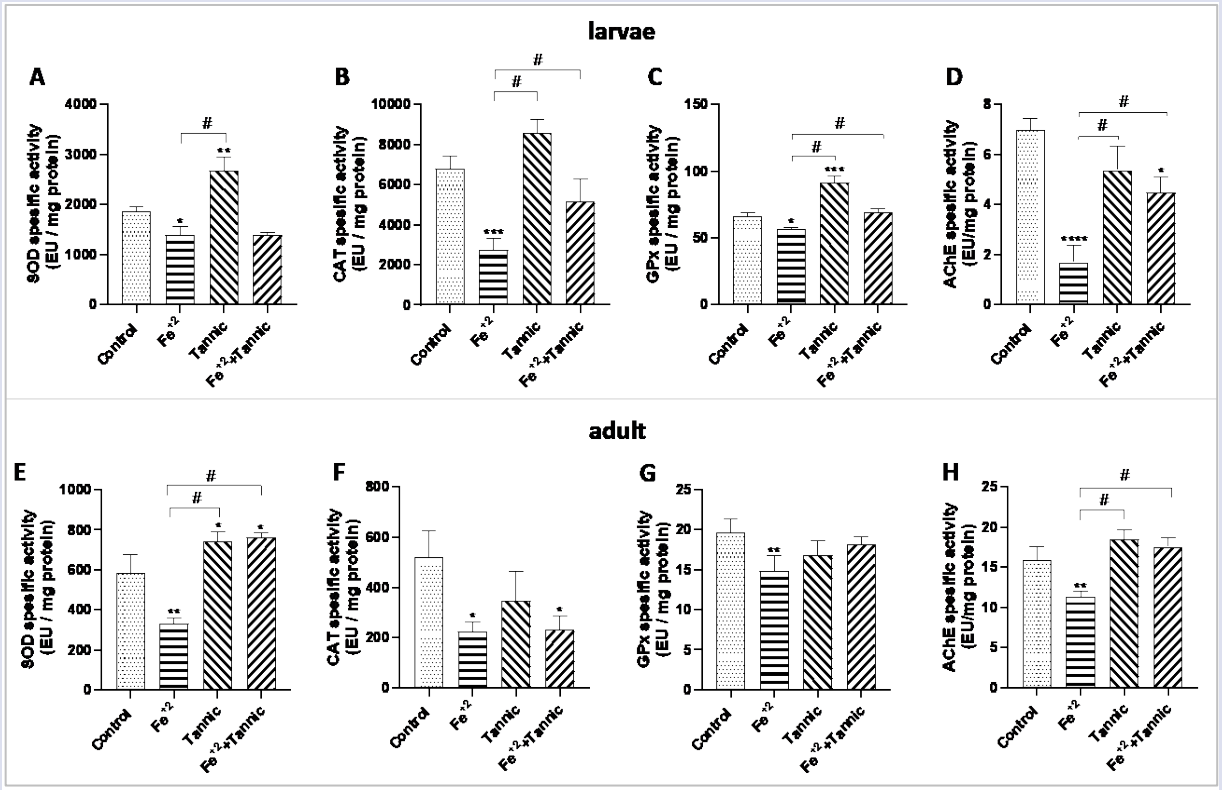

Figure 2. Superoxide dismutase (SOD), catalase (CAT), glutathione peroxidase (GPx) activity and acetylcholinesterase (AChE) activities in larvae (A-D) and heads of adults (E-H) after treatment with tannic acid. The bars represent the mean ± SD. Symbols indicate significance of differences between the groups: *p <0.05, **p < 0.01, ***p < 0.001 vs. control group; #p < 0.05 vs. other groups.

The Reduced Glutathione Levels in the Larvae and Heads of Adults after the Treatments

The reduced glutathione (GSH) levels in larvae and heads of adults after treatment with gallic acid and tannic acid were illustrated in Figure 3 and Figure 4. The Fe^{+2} treatment caused a significant decrease in GSH levels in both larvae and adults compared to the control group. However, gallic acid treatment did not change GSH levels in both larvae and adults (Figure 3A and 3B). Gallic acid treatment together with Fe^{+2} resulted in an increase in GSH level of larvae (Figure 3A). On the other hand, both alone and combined treatment of tannic acid with Fe^{+2} increased the GSH level of larvae compared to the control group (Figure 4A).

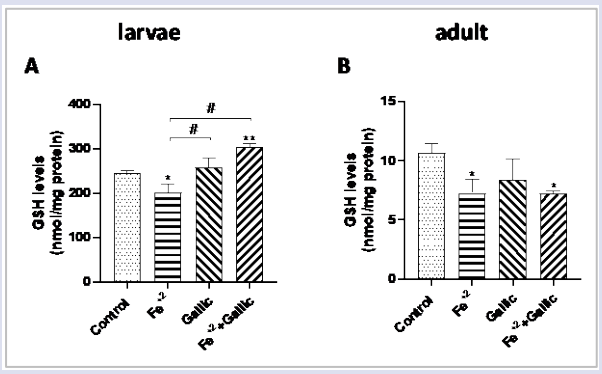

Figure 3. The levels of glutathione (GSH) in larvae (A) and heads of adults (B) after treatment with gallic acid. The bars represent the mean ± SD. Symbols indicate significance of differences between the groups: *p <0.05, **p < 0.01, ***p < 0.001 vs. control group; #p < 0.05 vs. other groups.

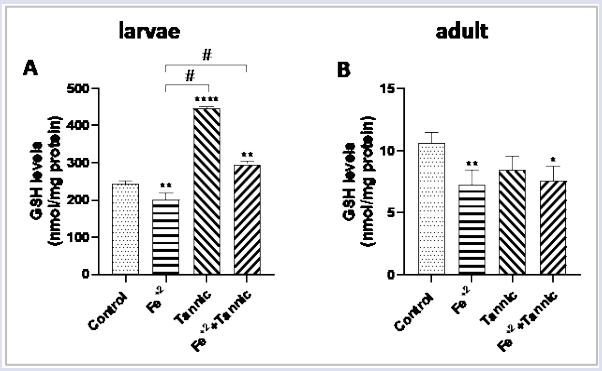

Figure 4. The levels of glutathione (GSH) in larvae (A) and heads of adults (B) after treatment with tannic acid. The bars represent the mean ± SD. Symbols indicate significance of differences between the groups: *p <0.05, **p < 0.01, ***p < 0.001 vs. control group; #p < 0.05 vs. other groups.

The Malondialdehyde Levels in the Larvae and Heads of Adults after the Treatments

The MDA levels in larvae and heads of adults after treatment with gallic acid and tannic acid were shown in Figure 5 and Figure 6. Fe^{+2} treatment increased MDA levels in larvae and adults compared to the control group. Gallic acid treatment caused a decrease in MDA levels in adults. In addition, co-treatment of gallic acid with Fe^{+2} attenuated the Fe^{+2}-induced increase in MDA levels in adults (Figure 5B). Tannic acid treatment did not change

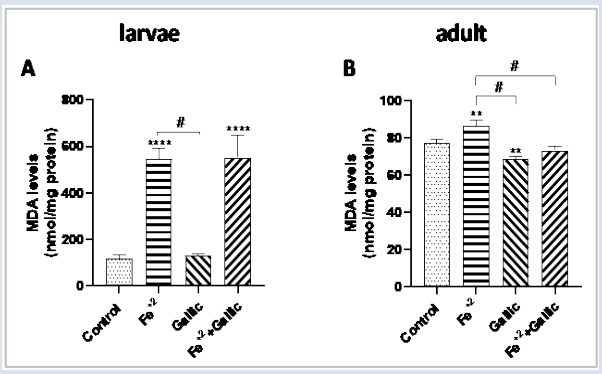

Figure 5. The level of malondialdehyde (MDA) in larvae (A) and heads of adults (B) after treatment with gallic acid. The bars represent the mean ± SD. Symbols indicate significance of differences between the groups: *p <0.05, **p < 0.01, ***p < 0.001 vs. control group; #p < 0.05 vs. other groups.

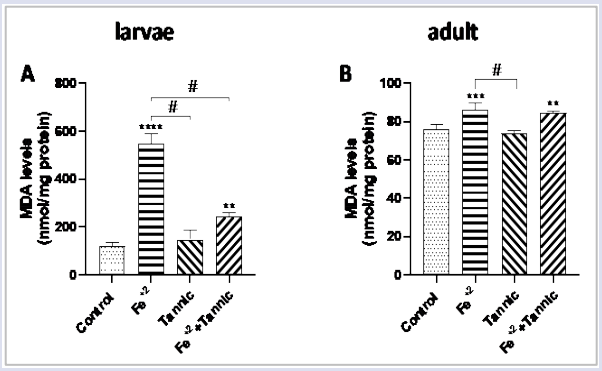

Figure 6. The level of malondialdehyde (MDA) in larvae (A) and heads of adults (B) after treatment with tannic acid. The bars represent the mean ± SD. Symbols indicate significance of differences between the groups: *p <0.05, **p < 0.01, ***p < 0.001 vs. control group; #p < 0.05 vs. other groups.

MDA levels in larvae and adults, whereas co-treatment with Fe^{+2} brought the Fe^{+2}-induced increase slightly closer to the values of the control group (Figure 6A and 6B).

Discussion

Heavy metals have entered the ecosystem as a result of natural and industrial activities. When exposed to metals through water, food and air, metals can bioaccumulate and cause toxicity in living organisms [31].

Metal-induced toxicity is associated with increased lipid peroxidation and alteration of cell homeostasis, with emphasis on the formation of reactive oxygen species and free radicals. Antioxidants play a protective role against free radical-induced attacks [32]. There are studies showing that antioxidants may provide protection against iron-related toxicity. It has been reported that vitamin E, an important antioxidant, can prevent most iron-induced damage in both in vitro and in vivo systems [33–37]. On the other hand, plant extracts and their components have been shown to have protective potential on iron-induced toxicity. For example, it has been found that baru nut and the phytic acid obtained from it have a protective effect against iron-induced oxidative stress [38]. Extracts of *Terminalia chebula* (Retz.) and *Drosera burmannii* Vahl have been reported to have iron chelation activity, which can reduce toxicity caused by iron overload [39,40]. Rutin, a natural flavonoid, was able to improve antioxidant defense systems against iron-induced hepatic oxidative stress [41]. Gallic acid (GA) and tannic acid (TA) suppressed cisplatin-induced ROS formation, lipid peroxidation and oxidative stress in rat kidney tissue [14]. TA reduced iron overload-induced liver damage in mice through ROS regulation [42]. *Molinga oleifera* leaf extract and its bioactive compound GA reduced metal-induced intracellular reactive oxygen species (ROS) accumulation in *Saccharomyces cerevisiae* [43]. It is emphasized that carboxyl and hydroxyl groups of GA and TA are important in the chelation of metals [42,43]. Therefore, since natural flavonoids and phenolic compounds are well-known antioxidants, they can be effective protective agents against oxidative stress. In this study, the preventive effect of natural phenolic compounds GA and TA against iron-induced oxidative stress in larvae and adult flies was investigated. Iron treatment reduced SOD, CAT, and GPx activities and GSH levels in larvae and adults. Since SOD, CAT and GPx are antioxidant enzymes that fight against oxidative stress, a decrease in their activities is an indicator of oxidative stress. Co-treatment of GA and TA with iron had a better effect on larvae to tolerate the decrease in enzyme activities. The compounds may have been more effective in the larvae because the organism is in the developmental stage and is in a more feeding state. The iron-induced decrease in GSH levels indicates that the primary intracellular antioxidant function is impaired. On the other hand, MDA level, which is an indicator of lipid peroxidation caused by oxidative stress, increased with iron treatment. The increase in MDA level may have been observed because the increase in iron-induced ROS formation causes membrane biochemical and functional changes [44].

AChE is an important enzyme involved in the termination of neurotransmission in cholinergic nerves. The cholinergic system and activity of AChE can be affected by metals such as copper, iron and aluminum [45]. Excessive iron intake is associated with dysfunction in cholinergic neurotransmission as a result of a decrease in acetylcholinesterase pathways involved in neurodegenerative diseases [46]. In this study, we found that iron treatment decreased AChE activity in both larvae and adults. GA and TA treatment with iron brought the iron-induced decrease closer to the control group only in adults. In a study examining the effect of copper on AChE activity at different stages of *D. melanogaster* development, it was determined that there were different changes in enzymatic parameters in larvae and adults [47]. Differences in enzyme activities in larvae and adults may be related to responses to endogenous or exogenous stressors due to complex neurochemical, metabolic and hormonal differences during development.

The fruit fly is used as a model because of its cheap and easy maintenance, short life span, homology with human genes, observable variations and large number of offspring [48]. But it is important to keep in mind that no model organism is exactly the same as a human being. The fly's body size and organization are different from that of a human, which limits its use. However biomedical and toxicological studies, epigenetics, human genetics and disease research are conducted with *D. melanogaster*, and useful results have been obtained [49,50]. Fruit flies and humans have similar metabolic pathways, such as superoxide metabolism and DNA repair, which play a role in pharmaceutical modulation [51]. In the present study, the ameliorative properties of GA and TA against iron-induced changes on antioxidant system elements were studied in a fly model. TA and GA helped to reverse iron-induced changes. The results may pave the way for further studies in this field.

Conclusion

In conclusion, this study showed that gallic acid and tannic acid can affect changes in iron-induced oxidative stress parameters. These natural compounds may be useful for applications to eliminate the negative effects of metal-induced toxicity. Therefore, the concentrations, interactions and effects of natural polyphenols on different biological parameters against the toxicity should be evaluated in further studies.

Conflicts of interest

There are no conflicts of interest in this work.

Acknowledgement

The authors acknowledge with thanks Ataturk University technical support.

References

[1] Gammella E., Recalcati S., Rybinska I., Buratti P., Cairo G., Iron-Induced Damage in Cardiomyopathy: Oxidative-Dependent and Independent Mechanisms, Oxid Med Cell Longev, 2015 (2015) 1–10.

[2] Emerit J., Beaumont C., Trivin, F. Iron metabolism, free radicals, and oxidative injury, *Biomedicine & Pharmacotherapy*, 55 (2001) 333–339.

[3] Fraga C., Iron toxicity and antioxidant nutrients, *Toxicology*, 180 (2002) 23–32.
[4] Jomova K., Valko M., Importance of Iron Chelation in Free Radical-Induced Oxidative Stress and Human Disease, *Curr. Pharm. Des.*, 17 (2011) 3460–3473.
[5] Abbas M., Saeed F., Anjum F.M., Afzaal M., Tufail T., Bashir M.S., *et al.*, Natural polyphenols: An overview, *Int. J. Food Prop.*, 20 (2017) 1689–1699.
[6] Andrade R.G., Dalvi L.T., Silva J.M.C., Lopes G.K.B., Alonso A., Hermes-Lima M., The antioxidant effect of tannic acid on the in vitro copper-mediated formation of free radicals, *Arch. Biochem. Biophys*, 437 (2005) 1–9.
[7] Dong G., Liu H., Yu X., Zhang X., Lu H., Zhou T., *et al.*, Antimicrobial and anti-biofilm activity of tannic acid against *Staphylococcus aureus*, *Nat. Prod. Res.*, 32 (2018) 2225–2228.
[8] Baldwin A., Booth B.W., Biomedical applications of tannic acid, *J Biomater Appl*, 36 (2022) 1503–1523.
[9] Kaczmarek B., Tannic Acid with Antiviral and Antibacterial Activity as A Promising Component of Biomaterials—A Minireview, *Materials*, 13 (2020) 3224.
[10] Badhani B., Sharma N., Kakkar R., Gallic acid: a versatile antioxidant with promising therapeutic and industrial applications, *RSC Adv.*, 5 (2015) 27540–27557.
[11] Al Zahrani N.A., El-Shishtawy R.M., Asiri A.M., Recent developments of gallic acid derivatives and their hybrids in medicinal chemistry: A review, *Eur. J. Med. Chem.*, 204 (2020) 112609.
[12] Bai J., Zhang Y., Tang C., Hou Y., Ai X., Chen X., *et al.*, Gallic acid: Pharmacological activities and molecular mechanisms involved in inflammation-related diseases, *Biomedicine & Pharmacotherapy*, 133 (2021) 110985.
[13] Vijaya Padma V., Sowmya P., Arun Felix T., Baskaran R., Poornima P., Protective effect of gallic acid against lindane induced toxicity in experimental rats, *Food and Chemical Toxicology*, 49 (2011) 991–998.
[14] Akomolafe S.F., Akinyemi A.J., Anadozie S.O., Phenolic Acids (Gallic and Tannic Acids) Modulate Antioxidant Status and Cisplatin Induced Nephrotoxicity in Rats, *Int. Sch. Res. Notices*, 2014 (2014) 1–8.
[15] Yesilkent E.N., Ceylan H., Investigation of the multi-targeted protection potential of tannic acid against doxorubicin-induced kidney damage in rats, *Chem. Biol. Interact*, 365 (2022) 110111.
[16] Kizir D., Karaman M., Ceylan H., Tannic acid may ameliorate doxorubicin-induced changes in oxidative stress parameters in rat spleen, *Naunyn Schmiedebergs Arch. Pharmacol.*, 396 (2023) 3605–3613.
[17] Silva R.L. dos S., Lins T.L.B.G., Monte A.P.O. do, de Andrade K.O., de Sousa Barberino R., da Silva G.A.L., *et al.*, Protective effect of gallic acid on doxorubicin-induced ovarian toxicity in mouse, *Reproductive Toxicology*, 115 (2023) 147–156.
[18] Ong C., Yung L.Y.L., Cai Y., Bay B.H., Baeg G.H. *Drosophila melanogaster* as a model organism to study nanotoxicity. *Nanotoxicology*, 9 (2015) 396–403.
[19] Read R.D. *Drosophila melanogaster* as a model system for human brain cancers, *Glia*, 59 (2011) 1364–1376.
[20] Jafari M. *Drosophila melanogaster* as a model system for the evaluation of anti-aging compounds, *Fly*, 4 (2010) 253–257.
[21] Gonzalez C. Drosophila melanogaster: a model and a tool to investigate malignancy and identify new therapeutics, *Nature Reviews Cancer*, 13 (2013) 172–183.
[22] Kaun K.R., Devineni A. V., Heberlein U. Drosophila melanogaster as a model to study drug addiction, *Human Genetics*, 131 (2012) 959–975.
[23] Mirzoyan Z., Sollazzo M., Allocca M., Valenza A.M., Grifoni D. Bellosta, P. Drosophila melanogaster: A Model Organism to Study Cancer, *Frontiers in Genetics*, 10 (2019).
[24] Bradford M.M., A rapid and sensitive method for the quantitation of microgram quantities of protein utilizing the principle of protein-dye binding, *Anal Biochem.*, 72 (1976) 248–254.
[25] Sun Y., Oberley L.W., Li Y., A simple method for clinical assay of superoxide dismutase., *Clin. Chem.*, 34 (1988) 497–500.
[26] Aebi H., [13] Catalase in vitro, In: Methods in Enzymology, (1984) 121–126.
[27] Wendel A., [44] Glutathione peroxidase, *In: Methods Enzymol*, (1981) 325–333.
[28] Ellman G.L., Courtney K.D., Andres V., Featherstone R.M., A new and rapid colorimetric determination of acetylcholinesterase activity, *Biochem Pharmacol*, 7 (1961) 88–95.
[29] Sedlak J., Lindsay R.H., Estimation of total, protein-bound, and nonprotein sulfhydryl groups in tissue with Ellman's reagent, *Anal Biochem*, 25 (1968) 192–205.
[30] Ohkawa H., Ohishi N., Yagi K., Assay for lipid peroxides in animal tissues by thiobarbituric acid reaction, *Anal Biochem*, 95 (1979) 351–358.
[31] Onuoha T., Akpafun A.S. Akpofure I.H. Effects of Heavy Metals on Soil and Water in Amai Delta State, Nigeria, *Journal of Soil Science and Plant Physiology*, 5 (2023) 1–5.
[32] Valko M., Morris H., Cronin M., Metals, Toxicity and Oxidative Stress, *Curr Med Chem*, 12 (2005) 1161–1208.
[33] Packer L., Weber S.U., Rimbach G., Molecular Aspects of α-Tocotrienol Antioxidant Action and Cell Signalling, *J. Nutr.*, 131 (2001) 369S-373S.
[34] Galleano M., Puntarulo S., Dietary α-tocopherol supplementation on antioxidant defenses after in vivo iron overload in rats, *Toxicology*, 124 (1997) 73–81.
[35] Lucesoli F., Fraga C.G., Oxidative stress in testes of rats subjected to chronic iron intoxication and α-tocopherol supplementation, *Toxicology*, 132 (1999) 179–186.
[36] Milchak L.M., Douglas Bricker J., The effects of glutathione and vitamin E on iron toxicity in isolated rat hepatocytes, *Toxicol Lett.*, 126 (2002) 169–177.
[37] Koyu A., Ozguner F., Caliskan S., Karaca H., Preventive effect of vitamin E on iron-induced oxidative damage in rabbit, *Toxicol Ind. Health*, 21 (2005) 239–242.
[38] Siqueira E.M. de A., Marin A.M.F., da Cunha M. de S.B., Fustinoni A.M., de Sant'Ana L.P., Arruda S.F., Consumption of baru seeds [Dipteryx alata Vog.], a Brazilian savanna nut, prevents iron-induced oxidative stress in rats, *Food Research International*, 45 (2012) 427–433.
[39] Sarkar R., Hazra B., Mandal N., Reducing power and iron chelating property of Terminalia chebula (Retz.) alleviates iron induced liver toxicity in mice, *BMC Complement Altern Med.*, 12 (2012) 144.
[40] Ghate N.B., Chaudhuri D., Das A., Panja S., Mandal N., An Antioxidant Extract of the Insectivorous Plant Drosera burmannii Vahl. Alleviates Iron-Induced Oxidative Stress and Hepatic Injury in Mice, *PLoS One*, 10 (2015) e0128221.
[41] Aziza S.A.H., Azab M.E., El-Shall S.K., Ameliorating Role of Rutin on Oxidative Stress Induced by Iron Overload in Hepatic Tissue of Rats, *Pakistan Journal of Biological Sciences*, 17 (2014) 964–977.
[42] Basu T., Panja S., Shendge A.K., Das A., Mandal N. A natural antioxidant, tannic acid mitigates iron-overload induced

hepatotoxicity in Swiss albino mice through ROS regulation, *Environmental Toxicology*, 33 (2018) 603–618.

[43] Kerdsomboon K., Chumsawat W., Auesukaree C. Effects of Moringa oleifera leaf extracts and its bioactive compound gallic acid on reducing toxicities of heavy metals and metalloid in Saccharomyces cerevisiae, *Chemosphere*, 270 (2021) 128659.

[44] Bermejo-Bescós P., Piñero-Estrada E., Villar del Fresno Á.M., Neuroprotection by Spirulina platensis protean extract and phycocyanin against iron-induced toxicity in SH-SY5Y neuroblastoma cells, *Toxicology in Vitro*, 22 (2008) 1496–1502.

[45] Pohanka M., Copper, aluminum, iron and calcium inhibit human acetylcholinesterase in vitro, *Environ Toxicol Pharmacol*, 37 (2014) 455–459.

[46] Perez V., Martins de Lima M., da Silva R., Dornelles A., Vedana G., Bogo M., *et al.*, Iron Leads to Memory Impairment that is Associated with a Decrease in Acetylcholinesterase Pathways, *Curr Neurovasc Res*, 7 (2010) 15–22.

[47] Halmenschelager P.T., da Rocha J.B.T., Biochemical CuSO4 Toxicity in Drosophila melanogaster Depends on Sex and Developmental Stage of Exposure, *Biol Trace Elem. Res.*, 189 (2019) 574–585.

[48] Ogienko A.A., Omelina E.S., Bylino O.V., Batin M.A., Georgiev P.G., Pindyurin A.V. Drosophila as a Model Organism to Study Basic Mechanisms of Longevity, *International Journal of Molecular Sciences*, 23 (2022) 11244.

[49] Wangler M.F., Yamamoto S., Bellen H.J. Fruit Flies in Biomedical Research, *Genetics*, 199 (2015) 639–653.

[50] Nainu F., Nakanishi Y., Shiratsuchi A. Fruit fly as a model organism in the study of human diseases and drug discovery, *Journal of Center for Medical Education Sapporo Medical University*, 10 (2019) 21–32.

[51] Jafari M., Rose M.R. Rules for the use of model organisms in antiaging pharmacology, *Aging Cell*, 5 (2006) 17–22.

Cumhuriyet Sci. J., 45(2) (2024) 263-267
DOI: https://doi.org/10.17776/csj.1453805

Cumhuriyet Science Journal

| csj.cumhuriyet.edu.tr | Founded: 2002 ISSN: 2587-2680 e-ISSN: 2587-246X Publisher: Sivas Cumhuriyet University

Determination of Serum Cathepsin G Level in Patients with Multiple Myeloma

Hatice Terzi [1,a,*]

[1] *Department of Hematology, Faculty of Medicine, Sivas Cumhuriyet University, Sivas, Türkiye.*
**Corresponding author*

Research Article

History
Received: 16/03/2024
Accepted: 13/06/2024

ABSTRACT

Multiple myeloma is a hematological malignancy identified by bone marrow infiltration of clonal plasma cells. It is still not a curable disease under current conditions. Cathepsin G is a serine protease playing a role in inflammation that is present in the azurophilic granules of neutrophils. It is known that there is a relationship between Cathepsin G and chronic inflammatory diseases and tumors. The goal of the study is to define its role in multiple myeloma. In the study, 33 patients newly diagnosed with MM who were never received treatment and 33 control subjects were included. Basic laboratory parameters and Cathepsin G levels were examined both in the myeloma patient group and control group. While the serum CathG level in the control group is 22.84 ng/mL, the serum CathG level of the MM patient group is 10.77 ng/mL. Serum CathG level in the control group is statistically significantly higher than the MM patient group. The aim of the present study is to contribute to the literature in hematological malignancies, to figure out the role of Cathepsin G in multiple myeloma, and to open a door to new treatment options for multiple myeloma, which is an incurable disease, yet.

Keywords: Cathepsin G, Inflammation, Multiple myeloma.

[a] *dr.terzi@hotmail.com* *https://orcid.org/0000-0003-3471-1305*

Introduction

Multiple myeloma (MM) is a hematological malignancy caused by excessive neoplastic reproduction of plasma cells. MM forms 1% of all malignancies and 10% of hematological malignancies. Mean age of diagnosis is 65. Despite mean survival in MM is 5-7 years, it may vary depending on the host factors, tumor load, cytogenetic anomalies, and the response to treatment [1].

In the patient group suitable for autologous stem cell transplantation, 4-year survival rate is over 80%. Among these patients, overall survival is more than 8 years. Overall survival is lower in elder patients (age >75) and it is approximately 5 years. Although there is an increase in general survival rates and response to treatment via new treatment options, MM is still an incurable disease [1]. Therefore, new treatment options are being searched for MM.

Cathepsin G (CathG) is a neutral serine protease found in azurophilic granules of neutrophils which is accepted as one of the inflammation effectors. In addition, it is also found in some non-myeloid cells such as endothelium, smooth muscle cells, brain astrocytes, and fibroblasts. CathG activates metalloproteases and plays a role in chemotaxis by degrading the extracellular proteins. CathG both helps specific immune response by antigen presentation and neutralizes toxins with its antimicrobial properties. It also has antimicrobial properties and neutralizes toxins [2].

CathG involves in the pathogenesis of some diseases related to chronic inflammatory process (such as atherosclerosis, chronic obstructive pulmonary diseases, neuropathies, and tumor). CathG has pro-inflammatory or anti-inflammatory properties depending on the physiological conditions paradoxically, location of CathG secretion, and the nature of the substrate. CathG-mediated proteolysis may cause an increase in inflammatory response or suppression of inflammation. As an example, elastolytic activity of CathG causes atherogenesis in early period. However, CathG inhibits the progress of atherosclerosis by eliminating low-density lipoproteins (LDL). It is thought that CathG, which is multifunctional protease, is of critical importance in maintaining the sensitive balance between tissue preservation and destruction during inflammatory response [2,3].

It is known that neutrophils invade several tumor tissues and affect tumor development [4]. However, the role of neutrophil proteases including CathG in the tumor metastasis is not well understood.

The goal of the study is to determine the role of CathG in MM and to elucidate new agents in myeloma for which new treatment options are being searched.

Materials and Methods

In this study, blood samples taken with approval from Sivas Cumhuriyet University Interventional Clinical Research Ethics Committee in February 2022 (Decision no: 2022-02/01) were used with the second ethics committee approval (Decision no:2023-09/02).

Thirty-three patients with newly diagnosed MM, who were applied to the Department of Internal Medicine, Division of Hematology of Sivas Cumhuriyet University

and who had never received any treatment, were included in the study. The control group consisted of 33 volunteers, who were over 18 years, had no comorbidities, no regular medication, were not pregnant, did not smoke, had no active infection, and had no diagnosed active malignancy or history of malignancy.

In the study, examinations made at the beginning of application were used as routine blood examinations. ISS (International Staging System) was used for determining the stages of the disease. The presence of fractures at the time of diagnosis were decided by examining the positron emission computerized tomography (PET/CT), computerized tomography, and if any, magnetic resonance image reports.

Serum CathG level and laboratory values were analyzed by using the blood samples taken. Bloods taken were centrifuged at 4000 Rpm for 10 minutes and kept in an Eppendorf tube at -80 degrees. Serum cathepsin G level was measured by commercial ELISA kit (Sun Red, China®).

Statistics

Data analysis was done by SPSS 26.0 program and studied with 95% confidence level. Mean, standard deviation (Mean±sd), median (M), and 1st and 3rd quartiles were given for the measurements. In the study, Mann Whitney U test was used for two groups in comparing measurements according to groups, Kruskal Wallis H test for more than two groups, Chi-square test for the relationship of group variables, and Spearman rho correlation test for the relationships between numerical measurements.

Results

In the present study, 33 MM patients applied to the Division of Hematology, Department of Internal Medicine of Sivas Cumhuriyet University Faculty of Medicine, and 33 control subjects were included. Of MM patient group, 39.4% (n=13) were under 65 years and 60.6% (n=20) were over 65 years. In the control group, 66.7% (n=22) were under 65 years and 33.3% (n=11) were over 65 years. In the MM patient group, 39.3% (n=13) were female and 60.6% (n=20) were male and in the control group, 60.6% (n=20) were female and 39.4% (n=13) were male.

A statistically significant difference was found between the MM patient group and control group in terms of age (p=0.006<0.05), BUN (p<0.001), creatinine (p=0.001<0.05), uric acid (p<0.001), total protein (p=0.001<0.05), albumin (p<0.001), phosphorus (p=0.002<0.05), magnesium (p=0.004<0.05), hemoglobin (p<0.001), platelet count (p<0.001), and erythrocyte sedimentation rate (p<0.001) measurements. In MM patient group, age (69), BUN (22.3 mg/dL), creatinine (0.95 mg/dl), uric acid (6.2 mg/dL), total protein (85 g/L), phosphorus (3.99 mg/dL), erythrocyte sedimentation rate (102 mm/h) measurements were higher and in the control group, albumin (46.4 g/L), hemoglobin (14.05 g/dL), platelet count (291 10^9/L) measurements were higher. Other measurements did not indicate any significant difference among the groups (p>0.05) (Table 1).

There was a statistically significant difference between MM patient group and control group in terms of serum CathG (p=0.040 <0.05) measurements. In the control group, CathG measurements were higher than MM patient group (Table 1).

Table 1. Comparison of Clinical Measurements According to the Groups

	MM	Control	Test/p
Age	69 (59.5-77.0)	34 (31-38)	U=8.000/ 0.000*
BUN(mg/dL)	22.3 (17.35-32.5)	12.4 (10.95-13.95)	U=154.5/ 0.000*
Creatine (mg/dl)	0.95 (0.74-1.51)	0.76 (0.64-0.88)	U=293.5/ 0.001*
Uric acid (mg/dL)	6.2 (4.7-7.7)	4.4 (3.6-5.1)	U=180.5/ 0.000*
Total protein(g/L)	85 (67.3-102.15)	74.5 (71.2-75.9)	U=356.0/ 0.016*
Albumin(g/L)	35.6 (30.55-38.5)	46.4 (44.7-48.15)	U=22.0/ 0.000*
LDH (U/L)	169 (145.5-213.0)	167 (153-181)	U=535.5/ 0.908
Ca (mg/dL)	9.1 (8.78-10.32)	9.52 (9.28-9.75)	U= 428.5/ 0.137
P (mg/dL)	3.99 (3.69-4.67)	3.4 (3.17-3.82)	U=273.0/ 0.000*
Mg (mg/dL)	1.93 (1.74-2.05)	2.08 (1.95-2.18)	U=296.5/ 0.001*
WBC (10^6/L)	6672.12±2648.42	6545.45±1520.87	t=0.238/ 0.812
Neu (10^6/L)	3420 (2390-5395)	3460 (2690-4605)	U=537.5/ 0.928
Lymp (10^6/L)	1931.52±696.55	2152.73±493.05	t=-1.489/ 0.142
Hgb (g/dL)	10.48±2.19	14.05±1.65	t=-7.466/ 0.000*
Platelet (10^9/L)	223 (157.5-268.5)	291 (244,5-342)	U=263.5/ 0.000*
ESR (mm/h)	102.0 (42.5-116.5)	6.0 (2.0-17.0)	U=31.0/ 0.000*
Cathepsin G (ng/mL)	10.77 (5.12-23.26)	22.84 (8.17-32.92)	U=384.0/ 0.040*

*p<0.05 significant difference, t/Mann Whitney U test BUN: Blood Urea Nitrogen, LDH: Lactate dehydrogenase, Ca: Calcium, P: Phosphor, Mg: Magnesium, WBC: White Blood Cell, Neu: Neutrophil, Lymp: Lymphocyte, Hgb: Hemoglobin, ESR: Erythrocyte Sedimentation Rate

In MM patient group, the rate of IgG kappa was 30.3% (n=10), the rate of IgG lambda was 24.2% (n=8), the rate of IgA kappa was 6.1% (n=2), the rate of IgA lambda was 18.2% (n=6), the rate of kappa light chain was 12.1% (n=4), the rate of lambda light chain was 6.1% (n=2), and the rate of non-secretory type myeloma was 3% (n=1) (Table 2).

Table 2. Relationship of Clinical Properties with Gender in MM Patient Group

N (%)		Female	Male	Total	p
MM type	IgG kappa	7 (53.8)	3 (15)	10 (30.3)	0,009*
	IgG lambda	3 (23.1)	5 (25)	8 (24.2)	
	IgA kappa	0 (0)	2 (10)	2 (6.1)	
	IgA lambda	0 (0)	6 (30)	6 (18.2)	
	Kappa light chain myeloma	1 (7.7)	3 (15)	4 (12.1)	
	Lambda light chain myeloma	2 (15.4)	0 (0)	2 (6.1)	
	Non-secretory type myeloma	0 (0)	1 (5)	1 (3)	
Stage at diagnosis according to ISS	Stage 1	3 (23.1)	3 (15)	6 (18.2)	0.811
	Stage 2	3 (23.1)	6 (30)	9 (27.3)	
	Stage 3	7 (53.8)	11 (55)	18 (54.5)	
	Yes	10 (83.3)	19 (95)	29 (90.6)	
	Yes	4 (100)	8 (61.5)	12 (70.6)	
Bone involvement on PET at diagnosis	No	1 (7.7)	5 (26.3)	6 (18.8)	0.164
	Yes	12 (92.3)	14 (73.7)	26 (81.3)	
Fracture at diagnosis	No	10 (76.9)	16 (84.2)	26 (81.3)	0.606
	Yes	3 (23.1)	3 (15.8)	6 (18.8)	

At the moment of diagnosis, 54.5% (n=18) of the patients were in stage 3, 27.3% (n=9) in stage 2, and 18.2% (n=6) patients in stage 1. Bone involvement on PET/CT at diagnosis was detected in 81.3% (n=26) of the patients. Fracture at the time of diagnosis was seen in 18.8% (n=6) patients (Table 2). A statistically significant relationship was found between gender and MM sub-types in MM patient group ($p=0.023<0.05$). While the incidence rate of IgG kappa in women was higher (53.8%), the incidence rate of IgA lambda in men was higher (30.0%). The relationship of other clinical properties with gender was not significant ($p>0.05$) (Table 2).

In the study, 75% of the patients in the myeloma group received ortezomib+cyclophosphamide+dexamethasone protocol as the first-line therapy, and 2% of the patients were followed up as drug-free. Of the patients, 52% responded positively to first-line therapy and 33.3% of them were subject to autologous stem cell transplantation. Second-line therapy was given to a total of 22 patients; 40.9% of these patients received lenalidomid+dexamethasone protocol and remission was obtained in 44.4%. After second-line therapy, autologous stem cell transplantation was applied to 26.7% of the patients. A total of 12 patients received third-line therapy and the most preferred protocols in the treatment were lenalidomid+dexamethasone and lenalidomid+dexamethazone+ixazomib protocols.

Remission was obtained in 4 patients and 2 of them underwent autologous stem cell transplantation. In MM patient group, the difference between the patients who responded first-, second-, and third-line therapies and the patients who did not respond in terms of CathG measurements was not statistically significant ($p>0.05$).

In MM patient group, a negative statistically significant relationship was found in terms of lactate dehydrogenase ($r=-0.428$, $p<0.05$), WBC (White blood cell) ($r=-0.349$, $p<0.05$), absolute neutrophil count ($r=-0.370$, $p<0.05$), and hemoglobin ($r=-0.353$, $p<0.05$) measurements via CathG measurement (Table 3). The relationship between other measurements was not significant ($p>0.05$).

Table 3. Relationship of Clinical Measurements and Cathepsin G Measurement in MM Patient Group

	Cathepsin G
Blood Urea Nitrogen	-.179
Creatine	-.160
Uric acid	-.135
Total protein	-.045
Albumin	.022
Lactate dehydrogenase	-.428*
Calcium	-.099
Phosphor	-.227
Magnesium	.138
White Blood Cell	-.349*
Neutrophil	-.370*
lymphocyte	-.113
Hemoglobin	-.353*
Platelet	-.195
Erythrocyte Sedimentation Rate	.194
Beta2 Microglobulin	-.305

**p<0.05 significant relationship, p>0.05 no significant relationship, 0≤r≤0.25 very weak, 0.26≤r≤0.49 weak, 0.50≤r≤0.69 moderate, 0.70≤r≤0.89 strong, 0.90≤r≤1 very strong; Spearman's rho correlation test*

Although serum CathG levels were higher in alive patients than in dead patients in the MM patient group, the difference was not statistically significant ($p>0.05$) (Table 4).

Table 4. Comparison of Cathepsin G measurements in MM Patient Group according to the Final Situation

	Final situation		
	Exitus	Alive	Test/p
Cathepsin G (ng/mL)	10.24 (4.79-23.05)	11.71(5.22-24.64)	U=129.0/ 0.828

**p<0.05 significant difference, t/Mann Whitney U test*

Discussion

Inflammation is defined as one of the necessary factors of cancer; inflammatory cells and secreted factors play a role in almost every step of tumor development and progression. Neutrophils is one of the important factors of tumor-related inflammatory cell infiltration. Their roles in tumor biology have been progressively recognized. Indeed, it is shown that neutrophils have both pro- and anti-tumorigenic properties [5]. Although neutrophils morphologically appear in the same way under a light microscope, it is thought that they have more than one sub-type with different genetic expression profiles. In recent years, neutrophil extracellular traps (NETs) are accepted as a main antimicrobial effector mechanism released by neutrophils as a response to several stimulus. Previous researchs have shown that NETs are involved in many parts of tumor biology, from tumor progression to tumor-related thrombosis [6]. Among them, neutrophil elastase, calprotectin, proteinase 3, matrix metalloproteinase 9, myeloperoxidase, cathepsin G, and bactericidal/permeability-increasing protein take place. Even though the role of NETs in inflammation is well known, its role in tumor progression is not clear [7]. However, there are researchs showing the relationship between NETs and breast, lung, colorectal, pancreas, skin, neurological cancers, and hematological cancers [8-14].

CathG is characteristically stored in the azurophilic granules of neutrophils and released via various stimuli such as the presence of bacteria. CathG is not only related to the resistance to bacterial or fungal infections, but also has diverse physiological functions such as the induction of thrombocyte activation, reshaping of extracellular matrix, induction of leucocyte chemotaxis, activation of inflammatory cytokine release, induction of endothelium-dependent vascular relaxation, anonychia of cardiomyocytes, and endothelial cell damage [15].

Previous researchs have notified that CathG has a role in the forming of metastasis by facilitating angiogenesis and tumor cell dissemination. It is thought that tumor cells form tumor aggregates through homotypic cell-cell interaction as they move away from the main tumor site and tumor emboli and metastases occur. CathG facilitates the formation of tumor aggregates in in vitro breast cancer models. In their study, Yui et al., showed that cell aggregation induced with CathG depended on E-cadherin [16]. Then, in their other study conducted on MCF-7 and MDA MB-231 human breast cancer cell lines, they concluded that CathG induced multicellular aggregate formation in low metastatic and E-cadherin-positive MCF-7 cells; whereas, it decreased the adhesion capacity of high metastatic and E-cadherin-negative MDA MB-231 cells to culture substrates [15]. They argued that CathG secreted by neutrophils infiltrating intra-tumor environments may be an important factor affecting the metastatic capacity of tumor cells and may facilitate dissemination of tumor cell aggregates by acting on E-cadherin-positive tumor cells and inducing detachment from the extracellular matrix, whereas it may inhibit metastasis by suppressing the adhesion capacity between highly metastatic E-cadherin-negative tumor cells and the extracellular matrix. However, they also stated that further studies are needed [15].

There are in vivo evidence showing that CathG plays a role on cancer metastasis. Previous researchs have indicated that high CathG levels in human lung cancers are related to the tumor degree and stage [17].

Wilson et al., indicated that CathG facilitated the formation of osteolytic bone lesions in breast cancer metastasis models. It is thought that high CathG level induced by tumor cells have increased osteoclast activation and thus, the bone lesions have occurred [18].

In the study conducted by Tomoya et al., on MCF-7 human breast cancer cell line, it was shown that cathepsin G inhibited cancer cell contact not over type IV collagen but over fibronectin and had induced cell-cell adhesion [19].

Depending on various researchs in the literature, it has been concluded that CathG facilitates the reshaping of extracellular matrix and potentialize the tumor progress and metastasis [18].

Previous researchs in the literature notified that there was a high level of CathG transcription in the promyelocytic stage of granulocyte development [20]. In their study, Zhang et al., suggested that CathG is highly expressed in myeloid leukemia blasts, and it may be an ideal immunotherapeutic target candidate in patients with acute myeloid leukemia [21].

Conclusion

Upon the literature review, any study on the role of CathG in MM could not be found. In the present study, a statistically significant difference was found between the MM patient group and the control group in terms of serum CathG measurements (p=0.040 <0.05). CathG measurements were higher in the control group than in the MM patient group. This result gives a clue that CathG may have a role in the etiopathogenesis. However, when the literature is examined, most studies conducted on CathG revealed that the presence of CathG was examined in tumor tissue and serum CathG level was not examined.

It is thought that the difference in CathG level in the study may be caused by this reason. Thus, further studies regarding CathG level in multiple myeloma tumor tissue are needed. Any relationship was not found between CathG and general survival; however, a negative and a statistically significant relationship was observed in MM patient group between CathG level and lactate dehydrogenase ($r=-0.428$, $p<0.05$), WBC (White blood cell) ($r=-0.349$, $p<0.05$), absolute neutrophil count ($r=-0.370$, $p<0.05$), and hemoglobin ($r=-0.353$, $p<0.05$) values. These provide clues that CathG may be relatively related to the prognosis.

Consequently, it is considered that CathG plays a role in the etiopathogenesis of MM. However, in vivo, in vitro, and clinical studies are required via further techniques. It is thought that determining the role of CathG in MM will provide new treatment alternatives in the future.

Acknowledgement

I would like to thank Biochemistry faculty member Halef Okan DOĞAN for supporting my laboratory studies and ECEM DEMİR YURTSEVEN for her help with statistics.

Conflict of Interest

Authors declared no conflict of interest.

References

[1] Rajkumar SV., Multiple myeloma: Every year a new standard?, *Hematological oncology*, 37 (2019) 62-65.

[2] Zamolodchikova T.S., Tolpygo S.M., Svirshchevskaya E.V., Cathepsin G—not only inflammation: the immune protease can regulate normal physiological processes, *Frontiers in immunology*, 11 (2020) 411.

[3] Wang J., Sjöberg S., Tang T.T., Oörni K., Wu W., Liu C., Secco B., Tia V., Sukhova G.K., Fernandes C., Lesner A., Kovanen P.T., Libby P., Cheng X., Shi G.P., Cathepsin G activity lowers plasma LDL and reduces atherosclerosis, *Biochimica et Biophysica Acta (BBA)-Molecular Basis of Disease*, 1842(11) (2014) 2174-2183.

[4] Tazawa H., Okada F., Kobayashi T., Tada M., Mori Y., Une Y., Sendo F., Kobayashi M., Hosokawa M., Infiltration of neutrophils is required for acquisition of metastatic phenotype of benign murine fibrosarcoma cells: implication of inflammation-associated carcinogenesis and tumor progression, *American Journal of Pathology*, 163(6) (2003) 2221– 2232.

[5] Smith H.A., Kang Y., The metastasis-promoting roles of tumor-associated immune cells, *J Mol Med*., 91(4) (2013) 411–429.

[6] Fridlender Z.G., Albelda S.M., Tumor associated neutrophils: friend or foe?, *Carcinogenesis*, 33(5) (2012) 949–955.

[7] Pham C.T., Neutrophil serine proteases: specific regulators of inflammation, *Nat Rev Immunol*., 6(7) (2006) 541–550.

[8] Martins-Cardoso K., Almeida V.H., Bagri K.M., Rossi M.I.D., Mermelstein C.S., König S., Monteiro R.Q., Neutrophil extracellular traps (Nets) promote pro-metastatic phenotype in human breast cancer cells through epithelial–mesenchymal transition, *Cancers*, 12(6) (2020) 1542.

[9] Li Y., Yang Y., Gan T., Zhou J., Hu F., Hao N., Yuan B., Chen Y., Zhang M., Extracellular RNAs from lung cancer cells activate epithelial cells and induce neutrophil extracellular traps, *International journal of oncology*, 55(1) (2019) 69-80.

[10] Shang A., Gu C., Zhou C., Yang Y., Chen C., Zeng B., Wu J., Lu W., Wang W., Sun Z., Li D., Exosomal KRAS mutation promotes the formation of tumor-associated neutrophil extracellular traps and causes deterioration of colorectal cancer by inducing IL-8 expression, *Cell Communication and Signaling*, 18(1) (2020) 1-14.

[11] Yu M., Li T., Li B., Liu Y., Wang L., Zhang J., Jin J., Guan Y., Zuo N., Liu W., Jing H., Li Y., Du J., Dong Z., Jiang T., Xie R., Zhou J., Shi J., Phosphatidylserine-exposing blood cells, microparticles and neutrophil extracellular traps increase procoagulant activity in patients with pancreatic cancer, *Thrombosis Research*, 188 (2020) 5-16.

[12] Schedel F., Mayer-Hain S., Pappelbaum K.I., Metze D., Stock M., Goerge T., Loser K., Sunderkötter C., Luger T.A., Weishaupt C., Evidence and Impact of Neutrophil ExtracellularTraps in Malignant Melanoma, *Pigment Cell Melanoma Res.*, 33(1) (2020) 63–73.

[13] Zha C., Meng X., Li L., Mi S., Qian D., Li Z., Wu P., Hu S., Zhao S., Cai J., Liu Y., Neutrophil Extracellular Traps Mediate the Crosstalk Between Glioma Progression and the Tumor Microenvironment via the HMGB1/RAGE/IL-8 Axis, *Cancer Biol Med*., 17(1) (2020) 154–168.

[14] Li M., Lin C., Deng H., Strnad J., Bernabei L., Vogl D.T., Burke J.J., Nefedova Y., A Novel Peptidylarginine Deiminase 4 (PAD4) Inhibitor BMS-P5 Blocks Formation of Neutrophil Extracellular Traps and Delays Progression of Multiple *Myeloma, Mol Cancer Ther*., 19(7) (2020) 1530-1538.

[15] Yui S., Osawa Y., Ichisugi T., Morimoto-Kamata R., Neutrophil Cathepsin G, but Not Elastase, Induces Aggregation of MCF-7 Mammary Carcinoma Cells by a Protease Activity-Dependent Cell-Oriented Mechanism, *Mediators Inflamm*., 2014(1) (2014) 971409.

[16] Yui S., Tomita K., Kudo T., Ando S., Yamazaki M., Induction of multicellular 3-D spheroids of MCF-7 breast carcinoma cells by neutrophil-derived cathepsin G and elastase, *Cancer Science*, 96(9) (2005) 560–570.

[17] Cools-Lartigue J., Spicer J., Najmeh S., Ferri L., Neutrophil extracellular traps in cancer progression, *Cell Mol Life Sci.*, 71(21) (2014) 4179–4194.

[18] Wilson T.J., Nannuru K.C., Futakuchi M., Sadanandam A., Singh R.K., Cathepsin G enhances mammary tumor-induced osteolysis by generating soluble receptor activator of nuclear factor-kappaB ligand, *Cancer Res*., 68(14) (2008) 5803–5811.

[19] Kudo T., Kigoshi H., Hagiwara T., Takino T., Yamazaki M., Yui S., Cathepsin G, a neutrophil protease, induces compact cell-cell adhesion in MCF-7 human breast cancer cells, *Mediators Inflamm*., 2009(1) (2009) 850940.

[20] Garwicz D., Lennartsson A., Jacobsen S.E., Gullberg U., Lindmark A., Biosynthetic profiles of neutrophil serine proteases in a human bone marrow-derived cellular myeloid differentiation model, *Haematologica*, 90(1) (2005) 38–44.

[21] Zhang M., Sukhumalchandra P., Enyenihi A.A., St John L.S., Hunsucker S.A., Mittendorf E.A., Sergeeva A., Ruisaard K., Al-Atrache Z., Ropp P.A., Jakher H., Rodriguez-Cruz T., Lizee G., Clise-Dwyer K., Lu S., Molldrem J.J., Glish G.L., Armistead P.M., Alatrash G., A novel HLA-A*0201 restricted peptide derived from cathepsin G is an effective immunotherapeutic target in acute myeloid leukemia, *Clin Cancer Res*., 19(1) (2013) 247-257.

Cumhuriyet Sci. J., 45(2) (2024) 268-273
DOI: https://doi.org/10.17776/csj.1401967

Cumhuriyet Science Journal

| csj.cumhuriyet.edu.tr | Founded: 2002 ISSN: 2587-2680 e-ISSN: 2587-246X Publisher: Sivas Cumhuriyet University

Design, Synthesis, Biological Evaluation and Docking, ADME Studies of Novel Phenylsulfonyl Piperazine Analogues as α-Amylase Inhibitors

Kerem Buran [1,a,*]

[1] *Department of Pharmaceutical Chemistry, Hamidiye Faculty of Pharmacy, University of Health Sciences, 34668, İstanbul, Türkiye.*
**Corresponding author*

Research Article

History
Received: 08/12/2023
Accepted: 13/06/2024

ABSTRACT

Diabetes mellitus (DM) stands as one of the most widespread diseases encountered today. It is primarily characterized by diminished insulin levels and heightened blood glucose concentrations. Inhibition of the α-amylase enzyme plays a pivotal role in the management of diabetes mellitus. Piperazine and sulfonamide groups are recognized for their extensive range of biological effects. The current study involved synthesizing five phenylsulfonyl piperazine derivatives. An evaluation of their α-amylase inhibitory capacities was conducted. Phenylsulfonyl piperazine derivatives (compounds 1-5) exhibited notable α-amylase enzymatic inhibition, with compound 4 showing the most substantial potential for inhibition. The inhibitory percentage of compound 4 (80.61±0.62) surpassed that of the standard drug acarbose (78.81±0.02). The molecular docking studies identified compound 4 as possessing the most substantial inhibitory effect on the α-amylase enzyme, with notable binding energy -8.2 kcal/mol. This compound exhibited specific interactions, including π-π stacking and π-anion interactions with key enzyme residues, solidifying its role as a potent inhibitor.

Keywords: Diabetes mellitus, α-Amylase, Piperazine, Sulfonamide.

[a] *kerem.buran@sbu.edu.tr* *https://orcid.org/0000-0002-7783-7533*

Introduction

Heterocyclics rings are of paramount importance in medicinal chemistry due to their versatility and wide-ranging biological activities that translate into diverse therapeutic applications. Their prevalence in an extensive array of pharmaceuticals underlines this significance. Heterocyclic rings are categorized into several types, each exhibiting a wide range of biological activities — for instance, thiazoles [1–3], thiophenes [4], quinolines [5]. Notably, heterocyclic molecules containing nitrogen, such as the piperazine heterocycle illustrated in Figure 1, have garnered significant attention for their biological efficacy. Piperazine is a non-aromatic heterocycle ring characterized by its two nitrogen atoms. This functional group is present in various FDA-approved medications, including members of the fluoroquinolone family of antibiotics (norfloxacin, ciprofloxacin, lomefloxacin), antihistamines (cyclizine, levocetirizine, cetirizine, hydroxyzine, cinnarizine), and antihypertensive agents (prazosin, terazosin, doxazosin) [6]. Moreover, piperazine derivatives exhibit a multitude of biological activities, functioning as anticonvulsants [7], antianginal [8], anti-inflammatory [9], carbonic anhydrase enzyme inhibitor [10] and antidiabetic [11].

Furthermore, the sulfonyl group stands as another moiety of significant interest due to its contribution to a wide array of biological activities (Fig 1).

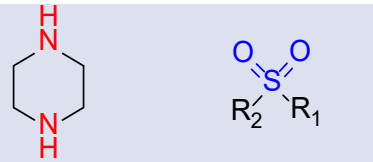

Piperazine **Sulfonyl group**

Figure 1. Molecular structures of piperazine and sulfonyl group.

Commonly, the integration of the sulfonyl group into other molecules either augments their biological activity or results in sulfonylated derivatives with unique biological functions. Prominent among the biological efficacies attributed to the sulfonyl group are antidiabetic [11], anticancer [12] and anti-inflammatory [13]. The combination of piperazine and the sulfonyl group, both of which independently display substantial biological activity, often leads to compounds with enhanced biological effects through a synergistic relationship. A prime example of such a compound is sildenafil, which has achieved notable success as a leading pharmaceutical agent, primarily employed in the treatment of erectile dysfunction (Fig 2) [14].

Diabetes mellitus (DM) poses a formidable challenge to global health. This condition is marked by dysregulated blood glucose regulation and impaired insulin secretion, often attributable to malfunction of pancreatic beta-cells, culminating in a state of hyperglycemia.

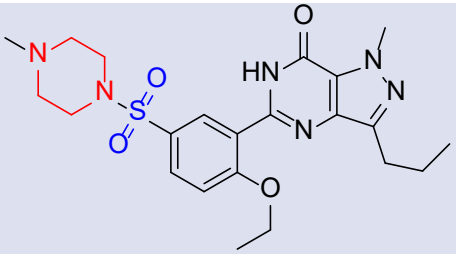

Figure 2. Molecular structure of Sildenafil

Elevated blood glucose levels are critically implicated in the development of major complications affecting vital organs, notably the heart, retina, and vascular system [15]. DM primarily presents as Type 1 and Type 2, with both conditions commonly linked to inadequate insulin production [16]. Beyond compromised insulin function, other physiological processes, including the action of the α-amylase enzyme (E.C. 3.2.1) — responsible for breaking down carbohydrates into monosaccharides — significantly contribute to elevated blood glucose levels [17]. Consequently, inhibition of α-amylase activity is a strategic approach in the management of hyperglycemia, especially in Type 2 DM therapy. Clinically, α-amylase inhibitors such as Acarbose, Voglibose, and Miglitol (Fig 3) are employed to control the postprandial surge in blood glucose typical of Type 2 DM. Nonetheless, these agents are associated with side effects, including gastrointestinal disturbances like flatulence and diarrhea [18,19].

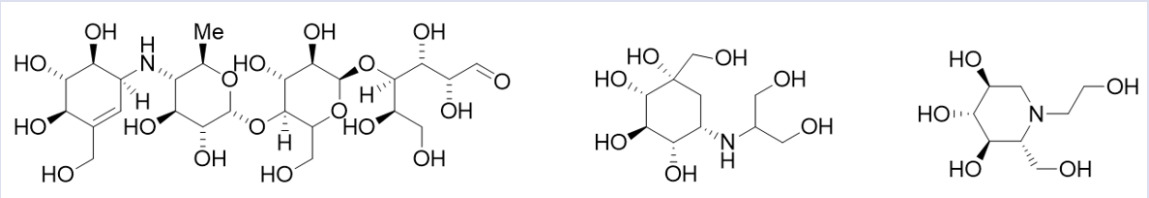

Figure 3. Molecular structure of Acarbose, Viglibose and Miglitol respectively

In a prior investigation [6], a series of piperazine sulfonamide derivatives was crafted and their antidiabetic efficacies were meticulously probed via enzyme inhibition assays. Nonetheless, analyses regarding the influence of substituent groups linked to the piperazine core on enzyme inhibitory action remained unaddressed. In another study, although compounds 1 and 2 were synthesized, their antidiabetic or α-amylase enzyme inhibition potential were not investigated [20]. The current study seeks to bridge this knowledge gap by evaluating the inhibition potency of novel sulfonyl-piperazine hybrids, with a focus on the impact of varying substituents attached to the piperazine scaffold on α-amylase enzyme activity. This was achieved using a combination of in vitro assays and in silico docking simulations. The integration of the sulfonyl group into the molecular architecture was purposeful, leveraging its documented biological activities, while the piperazine segment was chosen for hybridization due to its prevalence in a range of pharmacologically active compounds [6,11].

Table 1. Compounds 1-5, sulfonyl-piperazine hybrid molecules

Compounds	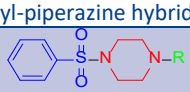
1	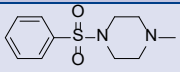
2	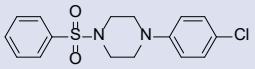
3	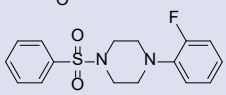
4	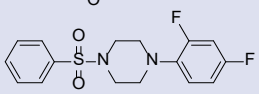
5	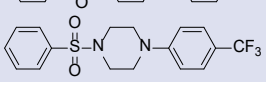

Within the framework of this research, five distinct derivatives [1-5] cataloged in Table 1 were synthesized for the goal of biological evaluation. To dissect the influence of the substituents on the piperazine ring in terms of enzyme inhibition, a systematic exploration involving both methyl-substituted and phenyl-substituted derivatives was undertaken. It is anticipated that this comparative study will shed light on the structure-activity relationships, thereby facilitating the innovative advancement of antidiabetic therapies.

Material and Methods

Chemicals

Materials and Reagents

All the chemicals were purchased from Fluka Chemie AG Buchs and Sigma Aldrich and used without further purification. Reactions were monitored by thin-layer chromatography (TLC) on silica gel 60 F254 aluminium sheets. The mobile phase was ethyl acetate: *n*-Hexane, and detection was made using UV light. ^{1}H NMR and ^{13}C NMR spectra were registered in $CDCl_3$ on Agilent 400/54 (400 MHz) NMR. The mass spectra were obtained on Agilent 6530 Accurate Mass Q-TOF LC/MS.

General procedure for the synthesis of compounds 1-5

Triethylamine (3.0 eq) was added to a solution of piperazine derivatives (1.0 eq) CH_2Cl_2 at 0 °C, then benzene sulfonyl chloride (1.0 eq) was added and stirred for 2 hours. The completion of reaction was checked with TLC (*n*-hexane and ethyl acetate (1:3)). After the reaction was finished, the solution was quenched with water and extracted with CH_2Cl_2. The combined organic layer was

dried over anhydrous Na_2SO_4 and evaporated to give compounds 1-5 [11].

1-Methyl-4-(phenylsulfonyl)piperazine (1)

Yield: 95%, white solid. ^{1}H NMR (400 MHz, $CDCl_3$) δ 7.71 (d, *J* = 7.7 Hz, 2H), 7.53 (dt, *J* = 26.3, 7.2 Hz, 3H), 3.00 (s, 4H), 2.43 (t, *J* = 4.4 Hz, 4H), 2.22 (s, 3H); ^{13}C NMR (400 MHz, CDCl3) δ 135.2, 132.8, 128.9, 127.7, 53.9, 45.9, 45.6; HRMS (ESI) calcd for $C_{11}H_{16}N_2O_2S$ [M + H]+ m/z: 241.0932, found 241.1004.

1-(4-Cholorophenyl)-4-(phenylsulfonyl)piperazine (2)

Yield: 80%, grey solid.^{1}H NMR (400 MHz, $CDCl_3$) δ 7.77 (d, *J* = 7.9 Hz, 2H), 7.68 – 7.51 (m, 4H), 7.43 – 7.28 (m, 1H), 7.12 (s, 2H), 3.36 (s, 8H). ^{13}C NMR (400 MHz, $CDCl_3$) δ 135.2, 133.3, 130.2, 129.7, 129.3, 128.3, 127.6, 125.7, 44.9; HRMS (ESI) calcd for $C_{16}H_{17}N_2O_2SCl$ [M+H]+ m/z: 336.8502, found 336.8508.

1-(2-Fluorophenyl)-4-(phenylsulfonyl)piperazine (3)

Yield: 42%, white solid ^{1}H NMR (400 MHz, $CDCl_3$) δ 7.79 (d, *J* = 7.7 Hz, 2H), 7.66 – 7.50 (m, 3H), 6.98 (ddd, *J* = 29.3, 15.8, 7.9 Hz, 4H), 3.16 (d, *J* = 17.1 Hz, 8H); ^{13}C NMR (400 MHz, $CDCl_3$) δ 156.8, 154.40 139.16 135.3, 133.0, 129.1, 127.8, 124.5, 123.3, 119.2, 116.2, 49.9, 46.2. HRMS (ESI) calcd for $C_{16}H_{17}N_2O_2FN_2S$ [M+H]+ m/z: 321.1062 found 321.0329.

1-(2,4-Difluorophenyl)-4 (phenylsulfonyl) piperazine (4)

Yield: 73%, white solid. ^{1}H NMR (400 MHz, $CDCl_3$) δ 7.78 (d, *J* = 7.5 Hz, 2H), 7.59 (dt, *J* = 27.0, 7.4 Hz, 3H), 6.94 – 6.69 (m, 3H), 3.13 (dd, *J* = 37.4, 4.3 Hz, 8H); ^{13}C NMR (400 MHz, $CDCl_3$) δ 159.5, 157.0, 154.3, 135.3, 133.0, 129.1, 127.7, 119.9, 110.7, 105.0, 50.3, 46.1; HRMS (ESI) calcd for $C_{16}H_{16}F_2N_2O_2S$ [M+H]+ m/z: 339.0965 found 339.0972.

1-(Phenylsulfonyl)-4-(4-(trifluoromethyl)phenyl) piperazine (5)

Yield: 65%, brown solid. ^{1}H NMR (400 MHz, $CDCl_3$) δ 7.81 (dd, *J* = 15.2, 7.5 Hz, 2H), 7.57 (ddd, *J* = 33.6, 20.6, 7.9 Hz, 5H), 7.00 (d, *J* = 8.4 Hz, 2H), 3.37 (d, *J* = 4.6 Hz, 4H), 3.24 (s, 4H); ^{13}C NMR (400 MHz, $CDCl_3$) δ 135.2, 133.2, 129.2, 127.7, 126.5, 125.8, 116.1, 48.6, 45.4; HRMS (ESI) calcd for $C_{17}H_{17}F_3N_2O_2S$ [M+H]+ m/z: 371.1026 found 371.1035.

Biological Activity Assay

α-Amylase Enzyme Inhibition Assay

α-Amylase inhibition activity of samples was calculated by following the method described earlier reference [21]. 3,5-dinitrosalicylic acid (DNS) reagent was used to determine α-amylase inhibition potential of the samples spectrophotometrically. According to the method, maltose is formed from the conversion of the starch and the yellow colour of alkaline DNS is turned into the orange-red colour due to produced maltose from starch. Thus, 96 mM DNS solution was prepared from the mixture of sodium potassium tartrate solution (dissolved in 2 M NaOH) and a certain amount of DNS (dissolved in distilled water). Then, 20 mM sodium phosphate buffer with 6.7 mM NaCl (co-factor of α-amylase enzyme) was prepared at 20°C (pH: 6.9). α-amylase enzyme (1U/mL) and starch (10 mg/mL) were dissolved in this buffer. After that, 50 µL of sodium phosphate buffer and 10 µL of α-amylase enzyme solution were added to 20 µl of the sample solutions. This mixture was incubated at 37°C for 45 minutes. After the incubation period, 20 µL of the starch solution was added to the mixture. Another incubation period was started at 37°C for 45 minutes. The same procedure was applied to the samples without inserting α-amylase enzyme solution called "sample background". The control group was studied with the same procedure in the absence of sample solutions. Absorbance was measured at 540 nm. Acarbose was used as a reference solution at 31.25, 62.5, 125, 250, 500 and 1000 µg/mL concentrations. Results were presented as a percentage of inhibitory activity in 1 mg/mL of samples.

Molecular Docking Study

Ligand Preparation: Data Warrier was utilized to generate SDF files of ligands. In a nutshell, conformers are generated using SMILES codes and the following settings: Random, Low Energy Bias, Energy Minimization Based on MMFF94s+ Forcefield, Torsions Based on Crystallographic Database. 3D atom coordinates from the SD file version 3 have been utilized. Protein Preparation and Docking Parameters: PDB number: 4W93 The structure of the human α-amylase protein in combination with montbretin A has been utilized in docking experiments. In a nutshell, proteins' crystal structures were acquired from https://www.rcsb.org in pdb format. In the PDB ID: 4W93, receptor structures were examined for improper charges and missing atoms. Water molecules, montbretin A, and calcium and chloride ions were eliminated to optimize the structures. 30°A x 24°A x 24°A in a grid box and AutoDockTools 1.5.6 was used to construct the coordinates of x=-11.254, y=0.864, z=-28.914 and spacing of 1°A around the montbretin A binding pocket (for PDB ID: 4W93). With PaDelADV, ligand docking was done automatically. The amino acid interactions between molecules and enzymes were examined using the BIOVIA Discovery studio.

ADME Study

ADME (absorption, distribution, metabolism and excretion) parameters were examined with the help of the publicly available silico SwissADME web tool (http://www.swissadme.ch). This tool offers boiled-egg charts and bioavailability radar. The physicochemical features and drug-likeness properties of compounds are explored using the physicochemical parameters found in bioavailability radar charts.

Results and Discussion

Chemistry

With a few modifications, compounds 1–5 were synthesized in accordance with reference [6]. In short, 1.0 eq of piperazine was dissolved in CH_2Cl_2 (DCM) derivatives, and 3.0 eq of triethylamine was slowly added to the solution at 0 °C. After that, this mixture was added to 1.0 eq of benzene sulfonyl chloride and allowed to stir at room temperature for two hours. TLC was used to ensure that the reaction had finished. Following the completion of the reaction, DCM extraction was carried out and water was added. Compounds 1 through 5 were obtained by evaporating the mixed organic layer over anhydrous Na_2SO_4 (Scheme 1).

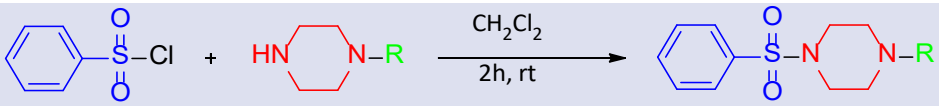

Scheme 1. Synthesis pathway of compound 1-5

^{1}H-NMR, ^{13}C-NMR and HRMS were used to characterize the compounds. Basic peaks of compounds' aromatic hydrogens have been observed in the ^{1}H-NMR spectra at 7.70 and 7.50 ppm. 3.50 - 2.0 ppm of the piperazine ring's aliphatic hydrogens have been identified. These hydrogens' peaks were identified in two separate ways. Depending on the substituent on the piperazine ring, some of them had only one peak, while others had two peaks.

Biological Activity

α-Amylase Enzyme Inhibition

α-Amylase enzyme inhibition study of synthesized piperazine sulfonamide molecules were performed using acarbose as a reference molecule. As a result of the study, all compounds had variable degree of α-amylase enzyme inhibition percentages between 65.95± 0.41 – 80.61 ± 0.62 (Table 2). Compared to acarbose, the compound 4 showed the best (80.61 ± 0.62) and higher inhibition value than acarbose (78.81 ± 0.02). Compound 4 is composed of two fluorine (F) atoms which are electron withdrawing groups (EWG).

Table 2. α-Amylase enzyme inhibition results of compounds 1-5

Compounds	R	α-Amylase enzyme inhibition (%)
1	-CH_3	65.95±0.41
2	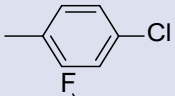	69.17±0.37
3	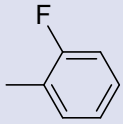	71.90±0.22
4	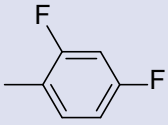	80.61±0.62
5	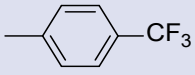	68.84±0.65
Acarbose		78.81±0.02

[a] Results were presented as α- amylase enzyme inhibition experiments were performed independently three different times. [b] standard deviation was symbolized with ±.

Compound 3 has one F atom and showed high enzyme inhibition but not as good as compound 4. The other F contained compound is compound 5 which has three F atoms but showed the lowest inhibition percentage among the substances containing F atoms (3, 4). These results may indicate that, for these molecular structures, optimum F atoms that was located on the piperazine ring was two. Apart from this, we can also conclude that the binding of all three fluorine atoms to the same carbon may have caused a decrease in enzyme inhibition percentage. Investigation of other halogen substituted phenyl ring derivative 2 has good inhibition value but it is lower than acarbose. Compound 2 has chlorine atom at *para* position of phenyl ring. When inhibition value of 2 is compared the other halogenated compounds (3, 5), although it has almost the same inhibition value as other F- containing molecules, it has been found to have a lower value than compound 4. Compound 1 has aliphatic group (methyl) electron donating groups (EDG).

Molecular Docking

Molecular docking is an important tool for elucidating the structural properties of ligands that have biological activity for target enzymes. In this part, the most active compounds were investigated based on their molecular interactions and binding energies for α-amylase enzyme. It was calculated and confirmed with their binding energy which was in the range of -5.9 to -8.2 kcal/mol for α-amylase enzyme. According to binding mode prediction results, the most potent compound for α-amylase enzyme is compound 4 (Fig.4). Compound 4 has π-π stacking between phenyl ring bound to piperazine and TRP59. Moreover, sulfonamide group has π-anion interaction with TRP58 and HIS299. In addition, a phenyl ring bound to sulfonamide interacts with GLU233. There are van der Waals interactions between LEU162, TYR62, LEU165, THR163, GLN63, HIS101, ASP300 and ASP197. According to the results obtained, compound 4 with the highest enzyme inhibition activity is also the molecule with the highest binding energy (-8.2 kcal/mol). When docking results are examined, it is seen that the molecule has strong interactions with the active site of the enzyme.

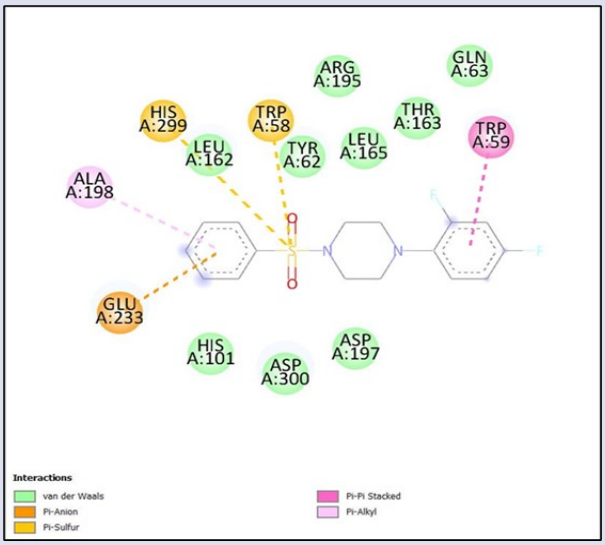

Figure 4. Docking result of compound 4 for α-amylase enzyme

ADME profiling

To investigate the physicochemical properties of the compounds 1-5 SwissADME web tool was used. Using the free SwissADME online program, the physicochemical characteristics of compounds 1–5 were predicted [22]. The bioavailability radar shows a quick predetermination of a drug-likeness properties. Six primary physicochemical properties—lipophilicity, polarity, size, solubility, saturation, and flexibility—are examined in this chart (Fig. 5). The boundary delineating the physicochemical features of the molecules that make them drug-likeness is the portion enclosed by the pink region. Once the red frame of the molecules is in the pink area, it shows that the physicochemical values of the molecule remain within the desired limits. Calculated physicochemical properties of compounds (1 – 5) are in desired limits and in pink area. These charts indicate that lipophilicity, oral bioavailability, and solubility of compounds are suitable for drug-likeness properties.

A technique for predicting ADME parameters like brain penetration (BBB) and passive gastrointestinal absorption (HIA) is the BOILED-Egg method [23]. WLOG and TPSA, two parameters, serve as the basis for these predictions. They serve as indicators of apparent polarity and lipophilicity. The results demonstrate that compounds 1 through 5 were able to enter the yolk and penetrate the BBB (Fig. 6). The substrate of permeability glycoprotein (P-gp) is indicated by red dots. Not every compound is included in the P-gp mechanism for active efflux. The compound's physicochemical properties can help it progress toward becoming a drug-like molecule, even though BBB penetration and not efflux from brain properties may have some negative effects on central nervous systems.

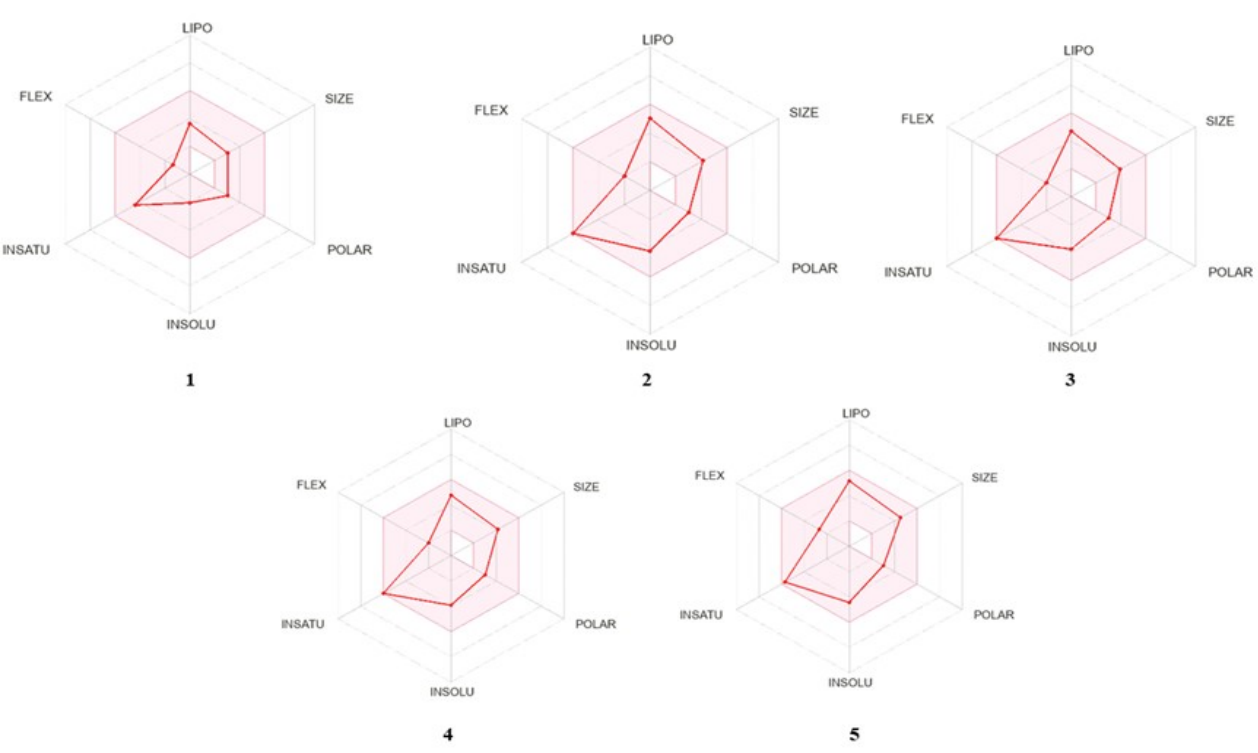

Figure 5. Bioavailability radar chart of compounds 1-5

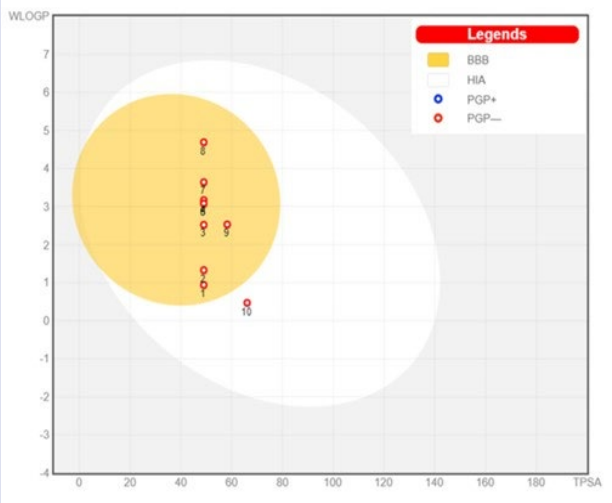

Figure 6. Boiled-egg chart for the compounds 1 -5

Conclusion

In the present study, we synthesized five phenylsulfonyl piperazine derivatives and evaluated their inhibitory effects on the α-amylase enzyme. Notably, compound 4 exhibited an inhibition value that surpassed that of the reference molecule, acarbose, as well as the other derivatives in the series. To assess the physicochemical properties bioavailability radar charts and the boiled-egg model were employed. These analyses predicted favorable drug-like characteristics and pharmacokinetic profiles for the synthesized compounds. Furthermore, molecular docking studies were conducted to elucidate pivotal interactions between the compounds and the enzyme. The promising nature of these findings is supported by binding energies ranging from -5.9 to -8.6 kcal/mol for the α-amylase enzyme, demonstrating strong affinity. Compound 4 possessing the most substantial inhibitory effect on the α-amylase enzyme, with notable

binding energy -8.2 kcal/mol. This compound exhibited specific interactions, including π-π stacking and π-anion interactions with key enzyme residues, solidifying its role as a potent inhibitor.

Conflict of Interest

The authors declare no conflicts of interest.

Acknowledgements

This project was supported by University of Health Sciences, unit of scientific research project (BAP) (Project No:2020/040

References

[1] Mittal K.R., Mishra R., Sharma V., Mishra I., 1,3,4-Thiadiazole: A Versatile Scaffold for Drug Discovery [Internet]. Vol. 21, *Letters in Organic Chemistry*, 21 (2024) 400–413.

[2] Mishra R., Sharma P.K., Verma P.K., Tomer I., Mathur G., Dhakad P.K., Biological Potential of Thiazole Derivatives of Synthetic Origin, J. Heterocycl Chem., 54(4) (2017) 2103-2116.

[3] Mishra I., Chandra P., Sachan N., Thiazole Derivatives as RORγt Inhibitors: Synthesis, Biological Evaluation, and Docking Analysis, *Letters in Drug Design & Discovery*, 21 (2024) 905–17.

[4] Mishra R., Kumar N., Mishra I., Sachan N., A Review on Anticancer Activities of Thiophene and Its Analogs, *Mini-Reviews in Medicinal Chemistry*. 20 (2020) 1944–1965.

[5] Mittal K.R., Purohit P., Quinoline-3-carboxylate Derivatives: A New Hope as an Antiproliferative Agent, *Anti-Cancer Agents in Medicinal Chemistry*. 20 (2020) 1981–1991.

[6] Vitaku E, Smith DT, Njardarson JT. Analysis of the Structural Diversity, Substitution Patterns, and Frequency of Nitrogen Heterocycles among U.S. FDA Approved Pharmaceuticals. J Med Chem [Internet]. 2014 Dec 26;57(24):10257–74.

[7] Mukherjee D., Mukhopadhyay A., Bhat K.S., Shridhara A.M., Rao K.S., Synthesis, characterization and anticonvulsant activity of substituted 4- chloro-2-(4-piperazin-1-YL) quinazolines, Int. J. Pharm. Sci., 6(5) (2014) 567–571.

[8] Kálai T., Khan M., Balog M., Kutala V.K., Kuppusamy P., Hideg K., Structure-activity studies on the protection of Trimetazidine derivatives modified with nitroxides and their precursors from myocardial ischemia-reperfusion injury, *Bioorg Med Chem.*, 14(16) (2006) 5510–5516.

[9] Buran K., Reis R., Sipahi H., Önen Bayram F.E., Piperazine and piperidine-substituted 7-hydroxy coumarins for the development of anti-inflammatory agents, Arch. Pharm. (Weinheim) 354(7) (2021) 2000354.

[10] Buran K., Bua S., Poli G., Bayram F.E.Ö., Tuccinardi T., Supuran C.T., Novel 8-substituted coumarins that selectively inhibit human carbonic anhydrase IX and XII, *Int. J. Mol. Sci.,* 20(5) (2019).

[11] Taha M., Irshad M., Imran S., Chigurupati S., Selvaraj M., Rahim F., Synthesis of piperazine sulfonamide analogs as diabetic-II inhibitors and their molecular docking study, Eur. J. Med. Chem., 141 (2017) 530–537.

[12] Finch R.A., Shyam K., Penketh P.G., Sartorelli A.C., 1,2-Bis(methylsulfonyl)-1-(2-chloroethyl)-2-(methylamino)carbonylhydrazine (101M): A novel sulfonylhydrazine prodrug with bbroad-spectrum antineoplastic activity, *Cancer Res.*, 61(7) (2001) 3033–3038.

[13] Ignat A., Zaharia V., Mogoşan C., Palibroda N., Cristea C., Silaghi-Dumitrescu L., Heterocycles 25. Microwave assisted synthesis of some p-toluensulfonyl-hydrazinothiazoles with analgesic and anti-inflammatory activity, *Farmacia*, 58(3) (2010) 290–302.

[14] Goldstein I., Lue T.F., Padma-Nathan H., Rosen R.C., Steers W.D., Wicker P.A., Oral Sildenafil in the Treatment of Erectile Dysfunction, *New England Journal of Medicine,* 338(20) 1998 1397–404.

[15] Fowler M.J., Microvascular and Macrovascular Complications of Diabetes, *Clinical Diabetes*, 26(2) 2008 77–82.

[16] Dehghan M., Ghorbani F., Najafi S., Ravaei N., Karimian M., Kalhor K., Progress toward molecular therapy for diabetes mellitus: A focus on targeting inflammatory factors, *Diabetes Res. Clin. Pract.,* 189 (2022) 109945.

[17] Alqahtani A.S., Hidayathulla S., Rehman M.T., Elgamal A.A., Al-Massarani S., Razmovski-Naumovski V., Alpha-amylase and alpha-glucosidase enzyme inhibition and antioxidant potential of 3-oxolupenal and katononic acid isolated from Nuxia oppositifolia, *Biomolecules*, 10(1) (2020) 61.

[18] Gunawan-Puteri M.D.P.T., Kato E., Kawabata J., α-Amylase inhibitors from an Indonesian medicinal herb, Phyllanthus urinaria, *J. Sci. Food Agric.,* 92(3) (2012) 606–609.

[19] Williams L.K., Zhang X., Caner S., Tysoe C., Nguyen N.T., Wicki J., The amylase inhibitor montbretin A reveals a new glycosidase inhibition motif., *Nat. Chem. Biol.,* 11(9) (2015) 691–696.

[20] Kumar Parai M., Panda G., Srivastava K., Kumar Puri S., Design, synthesis and antimalarial activity of benzene and isoquinoline sulfonamide derivatives, Bioorg Med. Chem. Lett., 18(2) (2008) 776–781.

[21] Balan K., Ratha P., Prakash G, Viswanathamurthi P., Adisakwattana S., Palvannan T., Evaluation of invitro α-amylase and α-glucosidase inhibitory potential of N2O2 schiff base Zn complex, *Arabian Journal of Chemistry*, 10(5) (2017) 732–738.

[22] Daina A., Michielin O., Zoete V., SwissADME: A free web tool to evaluate pharmacokinetics, drug-likeness and medicinal chemistry friendliness of small molecules, *Sci. Rep.,* 7 (2017) 1–13.

[23] Daina A., Zoete V., A Boiled-Egg To Predict Gastrointestinal Absorption and Brain Penetration of Small Molecules, Chem. Med. Chem., 11(11) (2016) 1117–1121.

Cumhuriyet Sci. J., 45(2) (2024) 274-281
DOI: https://doi.org/10.17776/csj.1410033

Cumhuriyet Science Journal

| csj.cumhuriyet.edu.tr | Founded: 2002 ISSN: 2587-2680 e-ISSN: 2587-246X Publisher: Sivas Cumhuriyet University

In Silico Studies of a Novel Scaffold of Acetylsalicylic Acid Derivatives Against EGFR by Molecular Docking and Molecular Dynamics Simulations

Alpaslan Bayrakdar [1,a,*]

[1] *Department of Medical Services and Techniques, Vocational School of Health Services, Igdır University, Igdır, Türkiye.*
**Corresponding author*

Research Article

History
Received: 26/12/2023
Accepted: 06/06/2024

ABSTRACT

In this study, a molecular docking study was performed to propose the acetylsalicylic acid derivative 2-[(4-Acetylphenyl)carbamoyl]phenyl acetate (AMPBS) as a potential cancer candidate targeting the Epidermal Growth Factor Receptor (EGFR). The native ligand erlotinib was used as a control compound. The calculated docking score of -7.4 kcal/mol compared to the native ligand erlotinib of -7.0 kcal/mol of AMPBS compound revealed a promising anticancer activity. The stability of the complex was interpreted by careful analysis of the root mean square deviation (RMSD), root mean square fluctuations (RMSF) and mean hydrogen bond number (Hb) plots obtained from the MD trajectories. The ADMET properties of AMPBS were evaluated using relevant online tools. Drug-likeness studies showed that AMPBS is suitable for use in living organisms. It was predicted that AMPBS in the active pocket could be a promising inhibitor due to its high binding energy, interaction mechanism and retention in the active pocket.

Keywords: DFT, Molecular docking, Molecular dynamic, Acetylsalicylic acid, ADMET.

[a] *alpaslan.bayrakdar@igdir.edu.tr* *https://orcid.org/0000-0001-7967-2245*

Introduction

Cancer is a dangerous disease that threatens people's lives after cardiovascular disease and is very common worldwide [1]. There are many types of cancer, including melanoma, leukemia, colorectal, lung, ovarian, brain, prostate, kidney and breast cancer. Advances in technology, molecular biology and immunotherapy are enabling the development of treatment strategies for this relentless disease. Advances in clinical trials are playing a key role in the discovery of more effective treatments with fewer side effects, leading to an important transformation in cancer treatment.

EGFR is a receptor-type tyrosine kinase involved in cellular growth, division and survival [2, 3]. Activation of EGFR regulates cell growth and proliferation by affecting cellular signal transduction networks. 1M17 refers to the tyrosine kinase domain of EGFR [4]. This tyrosine kinase domain of EGFR is important for initiating intracellular signal transduction and regulating cell growth signals. This region plays a critical role for the activation of EGFR and affects various cellular processes within the cell. Because over-activation of EGFR has the potential to cause an uncontrolled increase in cell growth, drugs that target the tyrosine kinase activity of EGFR are used specifically in cancer therapy [5]. Therefore, EGFR tyrosine kinase inhibitors are targeted therapeutic agents specifically used in the treatment of certain types of cancer [6].

Medical research into cancer treatment has revealed that some known drugs may have unexpected benefits beyond their primary application. One of these drugs is acetylsalicylic acid (ASA), known as aspirin. ASA has long been recognized for its pain-relieving and anti-inflammatory properties [7]. However, recent studies have shown that the positive impact of ASA can extend to the field of cancer prevention and treatment. One of the main potential positive effects of ASA on cancer is its anti-inflammatory power [8, 9]. Inflammation has been recognized as the driving force behind the development and progression of cancer cells. ASA's powerful anti-inflammatory properties offer a unique opportunity to disrupt this process, potentially inhibiting the formation and spread of cancer cells [9, 10].

Moreover, studies show that ASA may go beyond simply inhibiting inflammation; it may also play an important role in breaking tumor cells' resistance to the body's immune system. This dual mechanism of action of ASA has led to an increased interest in the synthesis of ASA-based scaffolds with cancer-protective propertiesIn this context, Mohamed-Ezzat et al. synthesized AMPBS compound that can be used in the prevention of colorectal cancer and investigated *its in vitro* anti-proliferative activities. [11].

Computer-aided analysis methods have been widely used in recent years in the design of new drugs and elucidation of the interaction mechanisms and physicochemical properties of existing drugs with target receptors [12]. Computer-aided simulation studies and quantum mechanical calculation-based methods used for

this purpose contribute greatly to *in vivo* and *in vitro* studies in terms of cost and time savings.

In this study, we first evaluated the drug-likeness properties of the newly synthesized AMPBS compound. The next step was to elucidate the mechanisms of EGFR interaction with the kinase domain through molecular docking and molecular dynamics simulation (MDS) studies. Gefitinib, an EGFR tyrosine kinase inhibitor, was used as a control compound to interpret the results of molecular docking and molecular dynamics studies [13]. In summary, the study investigated the potential of the synthesized title compound as an anti-cancer compound against the target EGFR.

Materials and Methods

Density Functional Theory (DFT) Calculations

The basic level design of the molecular structure of AMPBS was carried out using Gaussview 5.0, a very useful tool for molecular modelling [14]. On the other hand, the molecular structure of the native ligand erlotinib (CID: 176870) was obtained from Pubchem database (https://pubchem.ncbi.nlm.nih.gov). The most stable structures corresponding to the ground states of both compounds and their properties such as HOMO-LUMO orbitals were theoretically calculated with Gaussian 09 software using quantum chemical calculation techniques [15] and given in Figures 1a and 1b. Quantum mechanical calculations were performed using DFT/B3LYP method and 6-31G basis set. HOMO-LUMO molecular orbital analysis was performed on the optimized structures to determine the reactivity of the compounds.

Molecular Docking Study

The three-dimensional crystal structure of the target protein for molecular docking, Tyrosine Kinase Domain from the EGFR (PDB: 1M17), was obtained from the Protein Data Bank database [16]. The drug-likeness properties of the compound were investigated with the help of SwissADME web tool (http://www.swissadme.ch). UCSF Chimera and AutoDock Vina tool, which are very useful in molecular docking studies to create complex structures of proteins and ligands and to visualise and analyse the interactions of molecular structures, were used together [17]. The drug-likeness and ADMET (Absorption, Distribution, Metabolism, Excretion and Toxicity) properties of the native ligand erlotinib and AMPBS were analyzed for prediction using SwissADME and pkCSM web tool (https://biosig.lab.uq.edu.au/pkcsm / prediction), respectively. For the docking study, components such as water molecules and hetatm were removed from the receptor by UCSF and polar hydrogen atoms and charges were assigned to the receptor. In this study, Discovery Studio 2019 Client molecular imaging software was used, which provides comprehensive tools to visualise molecular interactions, analyse binding affinities and assess the stability and quality of predicted ligand-receptor complexes.

Molecular Dynamic Simulation Study

Unlike molecular docking studies, MDS studies allow protein-ligand interactions to be expanded biomolecularly, not at a single moment but over a certain time period [18]. In this study, MD Simulations were performed using Gromacs 2023.3 to analyse the interactions between protein and ligand. The input files and topology elements required for MD simulations were prepared using the CHARMM-GUI server [19] and the open access Swissparam web tool [20], respectively. MD simulations were performed in time steps of 2 fs for 50 ns. The RMSD, RMSF and Hb of protein-ligand interactions were analyzed by MDS.

Results and Discussion

Density Functional Theory (DFT) Calculations

The first step in investigating the physicochemical, biological, and pharmacokinetic properties of compounds using quantum chemical calculations is the optimization of the compounds. The optimized structures of AMPBS and erlotinib compounds obtained using DFT/B3LYP method and 6-31G basis set are given in Fig. 1a and 1b, respectively.

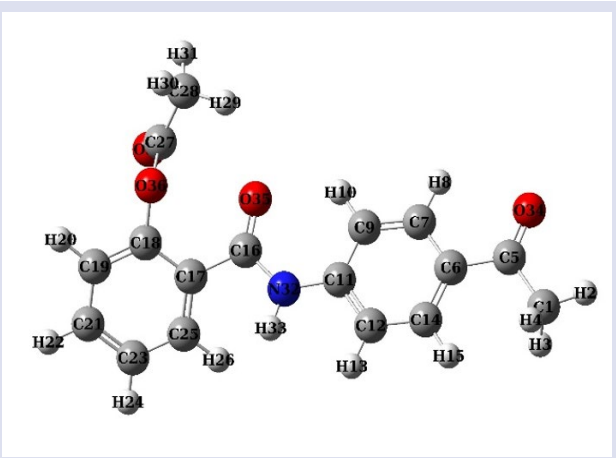

(a)

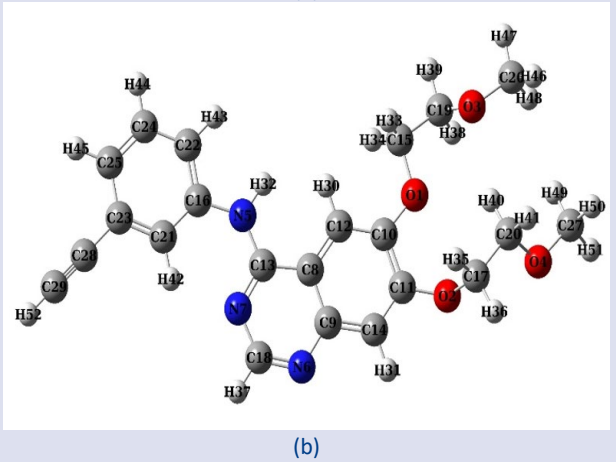

(b)

Figure 1. Optimized molecular structures of AMPBS and erlotinib compounds by DFT/B3LYP method and 6-31G basis set, a) AMPBS, b) erlotinib

HOMO-LUMO molecular orbital analysis is a measure of intramolecular charge transfer through conjugated pathways between electrophilic and nucleophilic functional groups [21]. In molecules, the highest filled molecular orbit (HOMO) corresponds to nucleophilic centers, while the lowest empty molecular orbit (LUMO) corresponds to electrophilic centers. HOMO-LUMO molecular orbital energies are very important in the calculation of the reactivity of chemical systems as well as other global descriptors (Ionization potantial, electron affinity, chemical hardness/ softness, electronegativity, chemical potential, electrophilicity index). The HOMO-LUMO orbitals and related parameters for the compounds were calculated by DFT/B3LYP method and 6-31 G(d) basis set and are given in Table 1. In addition, the predicted 3D structure of the HOMO-LUMO orbitals is given in Fig 2. The energy gaps between the HOMO-LUMO orbitals characterize the biological reactivity of compounds. The HOMO energy levels of AMPBS and erlotinib compounds were -6.35 eV and -5.58 eV, respectively, while the LUMO orbital values were -1.72 and -1.31 eV. The energy gap between HOMO and LUMO was found to be 4.60 eV for AMPBS and 4.27 eV for erlotinib. Large energy gap indicates high stability and low chemical reactivity for molecules. The results showed that AMPBS had a higher kinetic stability than erlotinib.

Tablo 1. HOMO-LUMO orbital energies of the compounds and other calculated global descriptors.

Parameters (eV)	ligand	erlotinib	Parameters (eV)	ligand	erlotinib
LUMO energy	-1.72	-1.31	Chemical hardness (η)	2.30	2.14
HOMO energy	-6.32	-5.58	Chemical softness (S)	0.22	0.23
Energy Gap (ΔG)	4.60	4.27	Electronegativity (χ)	4.02	3.45
Ionization potantial (I)	6.32	5.58	Chemical potential (μ)	-4.02	-3.45
Electron Affinity (A)	1.72	1.31	Electrophilicity index (ω)	3.51	2.78

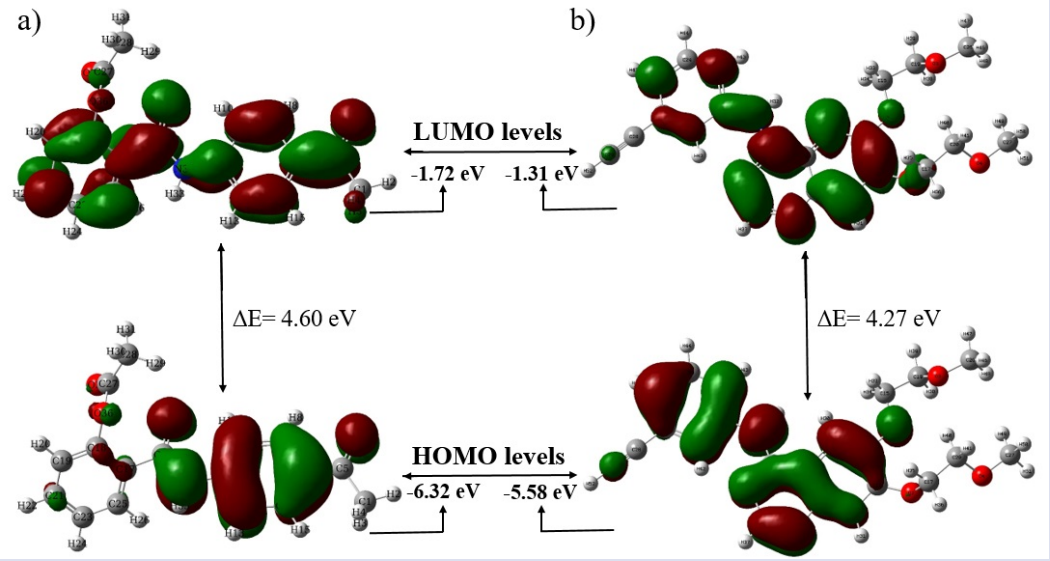

Figure 2. 3D drawing of HOMO, LUMO orbitals obtained from the optimized structure of compounds, a) AMPBS, b) erlotinib

Molecular Docking Study

The EGFR receptor coded 1M17 with a resolution of 2.60Å, which was retrieved from the protein databank for use in the molecular docking study, consists of several binding sites to which ligands can bind. TA pharmacophore model has been proposed for the binding pocket of EGFR, including hydrophobic region I, adenine site, hydrophobic region II, sugar pocket and phosphate binding site, respectively [22]. For AMPBS and Erlotinib compounds, the binding pocket of the EGFR receptor was identified using BIOVIA Discovery Studio software as the region containing the active residues Leu694, Ala719, Leu764, Thr766, Gln767, Leu768, Met769, Pro770, Phe771, Gly772, Leu820, Thr830 and Asp831. The region containing these active residues plays a key role in EGFR inhibition. Therefore, this region of the 1M17 receptor was used in the molecular docking study. As a result of the molecular docking study, the conformations with the best binding energy for protein-ligand interactions were selected and their h-bond, hydrophobic, electrostatic and Van der Waals interaction mechanisms were analyzed using BIOVIA Discovery Studio molecular visualization software. The interactions of the native ligand erlotinib and AMPBS compounds with the EGFR receptor are given in Fig. 3 and Fig. 4, respectively. Summary results of the interactions are presented in Table 2. As clearly seen in Table 2, the binding energies of AMPBS compound and erlotinib were found to be 7.4 kcal/mol and 7.0 kcal/mol,

respectively. The magnitude of the binding energy provides important information about the binding strength, efficacy and specificity of the drug to the target receptor. Lower (more negative) binding energy is one of the leading parameters of a more effective and specific drug development process [23]. Fig. 3 and Fig. 4 showed that both ligands travelled to the active site of the receptor and placed there. Erlotinib showed conventional hydrogen bond with amino acids Lys721 and Met769 from the active site residues of 1M17 and C-H bond interactions with residues Arg817 and Gln767 according to the interaction mechanism given in Fig. 3. Pi-Pi-stacked with Phe699, Pi-Alkyl hydrophobic interactions with residues Phe699, Val702, Lys721 and Leu820 and It showed 2 Pi-Anion electrostatic interactions with Asp831 residue. On the other hand, Van der Waals interactions were observed between Thr830, Ala719, Leu768, Leu694 and Cys773.

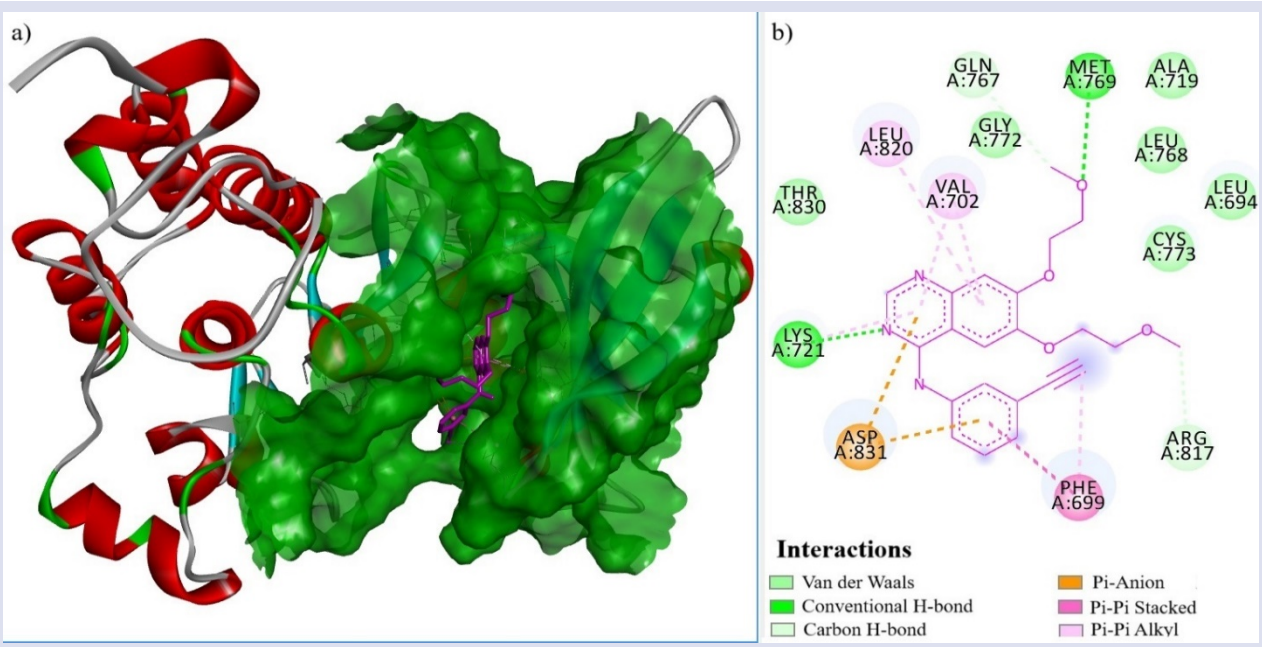

Figure 3. Post docking interactions between active site residues of EGFR with erlotinib, a) 3D solid surface drawings of the interaction, (b) 2D interaction diagram of ligand with EGFR protein.

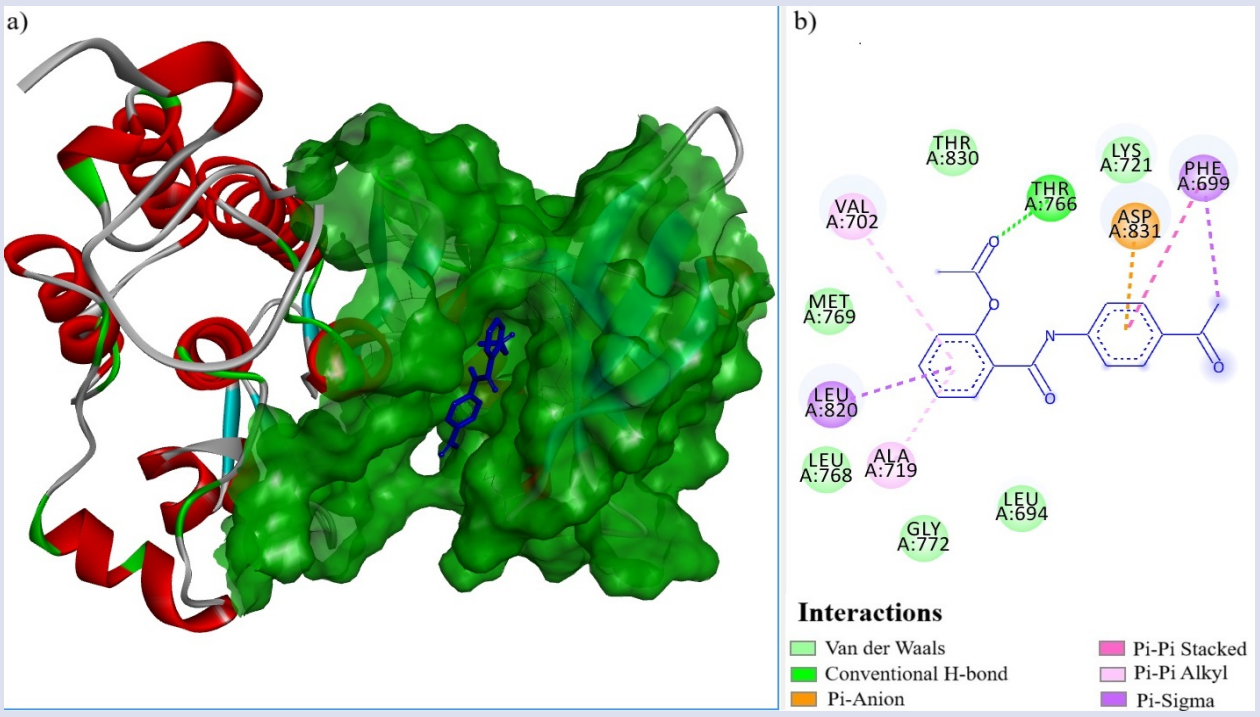

Figure 4. Post docking interactions between active site residues of EGFR with AMPBS, a) 3D solid surface drawings of the interaction, (b) 2D interaction diagram of ligand with EGFR protein.

AMPBS in Fig. 4 showed conventional hydrogen bond with residue Thr766 in the active site of 1M17, Pi-Pi-stacked with residue Phe699, Pi-Sigma with residues Leu820, Pi-Sigma with residues Phe699, Pi-Alkyl hydrophobic interaction with residues Val702 and Ala719 and 2 Pi-Anion electrostatic interactions with residue Asp831. On the other hand, Van der Waals interactions were observed between Thr830, Leu694, Lys721, Gly772, Leu768 and Met769.

Table 2. Summarative results of Post docking interactions between EGFR with ligands

Protein	Ligands	ΔG (kcal/mol)	Hydrogen Bond interactions (Å)	Hydrophobic interaction (Å)	Electrostatic interaction (Å)	Van der Waals
1M17	Erlotinib	-7.0	Conventional H-Bond Lys721(3.04), *Met769(2.92) Carbon H-Bond Arg817(3.70), *Gln767(3.72)	Pi-Pi stacked Phe699(3.80) Pi-Alkyl Phe699(5.18), Val702(4.80-4.13), Lys721(5.05), *Leu820(5.37)	Pi-Anion *Asp831(3.64-3.63-3.96)	Ala719, Leu768, Leu694, Cys773, Thr830
	AMPBS	-7.4	Conventional H-Bond *Thr766(2.75)	Pi-Pi stacked Phe699(4.83) Pi-Sigma *Leu820(3.75), Phe699(3.90), Pi-Alkyl Val702(5.40), *Ala719(4.75)	Pi-Anion *Asp831(3.58-4.50)	Thr830, Lys721, Leu694, Gly772, Leu768, Met769

*Active residues of 1M17

Drug-Likeness and ADMET Properties

Drug synthesis studies to be used for the treatment of many diseases that threaten living health are both time consuming and very costly. In this respect, the combination of computer technologies and multi-disciplinary approaches has made significant contributions to new drug designs. Although drug-likeness studies do not provide conclusive results, they provide useful predictions for the early stages of new drug design. There are some criteria used in drug-likeness studies and developed based on previous drug designs. One of the most common of these is the Lipinsky rule of five [24]. The drug-likeness of erlotinib and AMPBS compounds were evaluated within the framework of Lipinski's five criteria and presented in Table 3. It is clear from Table 3 that there are no violations of the Lipinski criterion for either compound that would preclude their use in living organisms.

Table 3. Drug-likeness analysis of AMPBS and Erlotinib.

Lipinski's five criteria	Accepted range	Erlotinib		AMPBS	
		Value	result	Value	result
Molecular Weight (Da) (MW)	≤500	393.44	✓	293.3	✓
Num. H-bond donors	≤5	1	✓	1	✓
Num. H-bond acceptors	≤10	6	✓	4	✓
LogP	≤5	3.67	✓	2.43	✓

According to these results, AMPBS is expected to be permeable through the cell membrane, easy absorption, transport and distribution [25]. ADMET study was performed to evaluate these properties. ADMET predictions performed through the web-based online pkCSM tool for erlotinib and AMPBS compounds are summarized in Table 4. Absorption part of the ADMET study both compounds exhibited excellent intestinal (human) absorbance values around 95%. In the distribution part of the ADMET study, the blood brain barrier (BBS) penetrability values of erlotinib and AMPBS compounds were found to be -0.465 and -0.16, respectively, and the central nervous system (CNS) penetrability values were found to be -3.418 and -2.212,

respectively. Accepted penetrability values for BBS and CNS are expected to be between -1 and 0.3 and -3 and -2, respectively [26]. Toxicity analysis is an important and guiding method for safer new drug designs. When the Ames toxicity values of the compounds in the table are analyzed, it is estimated that erlotinib is not toxic but AMPBS may be toxic. On the other hand, the opposite is the case in hepatotoxicity values. Cytochrome P450 (CYP) enzymes form the major metabolizing enzyme system in humans and are responsible for the chemical changes that many molecules synthesized as drugs undergo in the body. Cytochrome P450 (CYP) enzymes (CYP2D6, CYP2C9, CYP2C19, CYP3A4, CYP1A2) constitute the major metabolising enzyme system in humans and are responsible for the chemical changes that many molecules synthesized as drugs undergo in the body. Of these enzymes, CYP3A4 is the most common and important in terms of interactions [27]. Metabolism results showed that both compounds were substrates of CYP3A4, while only erlotinib was an inhibitor of CYP3A4. The term clearance refers to the rate of excretion of the drug from the body (Clearance n High: >15 mL/min/kg; moderate: 5-15 mL/min/kg; low: <5 mL/min/kg [28] A high clearance indicates that the drug is cleared from the body rapidly, while a low clearance means that the drug is cleared more slowly. This is important in determining how long a drug can be effective and in adjusting its dosage. The clearance values of the compounds in Table 4 showed that the compounds have a high persistence in the body.

Table 4. ADMET analysis results obtained by using pkCSM tools.

Properties	Compounds		Properties	Compounds	
Absorption	Erlotinib	AMPBS	**Distribution**	Erlotinib	AMPBS
Water solubility (log mol/L)	-5.081	-3.693	VDss (human) (log L/kg)	-0.02	-0.036
Caco2 permeability (log Papp in 10^{-6} cm/s)	1.185	1.183	Fraction unbound (human) (Fu)	0.05	0.102
Human intestinal absorption (HIA+, %)	95.43	94.432	BBB permeability (log BB)	-0.465	-0.16
Skin Permeability (log Kp)	-2.758	-2.877	CNS permeability (log PS)	-3.418	-2.212
P-glycoprotein substrate	No	No	**Metabolism**		
P-glycoprotein I inhibitor	Yes	No	CYP2D6 substrate	No	No
P-glycoprotein II inhibitor	Yes	No	CYP3A4 substrate	Yes	Yes
Toxicity			CYP1A2 inhibitior	No	Yes
AMES toxicity	No	Yes	CYP2C19 inhibitior	Yes	Yes
Max. tolerated dose (human) (log mg/kg/day)	0.714	0.411	CYP2C9 inhibitior	Yes	No
hERG I inhibitor	No	No	CYP2D6 inhibitior	No	No
hERG II inhibitor	Yes	No	CYP3A4 inhibitior	Yes	No
Oral Rat Acute Toxicity (LD50) (mol/kg)	2.499	1.988	**Excretion**		
Oral Rat Chronic Toxicity (LOAEL) (log mg/kg_bw/day)	1.183	1.555	Total Clearance (log ml/min/kg)	0.63	0.314
Hepatotoxicity	Yes	No	Renal OCT2 substrate	No	No
Skin Sensitization	No	No			
T. Pyriformis toxicity (log ug/L)	0.34	1.331			
Minnow toxicity (log mM)	-1.76	1.088			

Molecular Dynamic Simulation

Important information on the conformation of ligand molecules in the active cavity of the target receptor and the interactions that occur were obtained from molecular docking studies. MDS studies were performed using the Gromacs 2023.3 package at time steps of 2 fs for 50 ns to understand the behavior of erlotinib and AMPBS compounds in the active site and the stability of receptor-ligand interactions. In this study, RMSD, RMSF and Hb plots were generated and the results analyzed to investigate the actual mechanisms of the interactions.

RMSD analysis is used to obtain information about the conformational stability of pharmacological molecules [29]. The RMSD plot in Fig. 5a clearly shows that erlotinib exhibited a stable behavior around the equilibrium point around 0.67 nm after 20 ns until the end of the simulation, initially showing high fluctuations that gradually decreased. On the other hand, the RMSD plot in Figure 3b shows that AMPBS behaved unstably around 0.8 nm after 20 ns until 40 ns and exhibited a stable behavior after 40 ns until the end of the simulation. The RMSD plots obtained from MDS clearly showed that erlotinib

oscillated stably around the equilibrium point, reaching a plateau in the first 10 ns, unlike AMPBS. On the other hand, RMSD graphs revealed that both compounds exhibited similarly stable movements around the equilibrium point at the end of the MDS. For the analysis of the positional fluctuations of protein residues, the RMSF plot obtained from MDS is very useful. In this study, the RMSF plot was plotted against each atom based on the MDS trajectory for each of the atom mobility complexes and is given in Fig. 5b. Figure 5b clearly shows that the fluctuation profiles of the complexes are quite overlapping. This implies that AMPBS can form a stable complex with EGFR and inhibit it like the native ligand erlotinib. It is well known that hydrogen bonding interactions play an important role in the structural stability of proteins. It provides information about the number of hydrogen bonds formed in the complex. As seen in Fig. 5c, the maximum number of hydrogen bonds formed in the erlotinib and AMPBS complexes are 3 and 2, respectively .

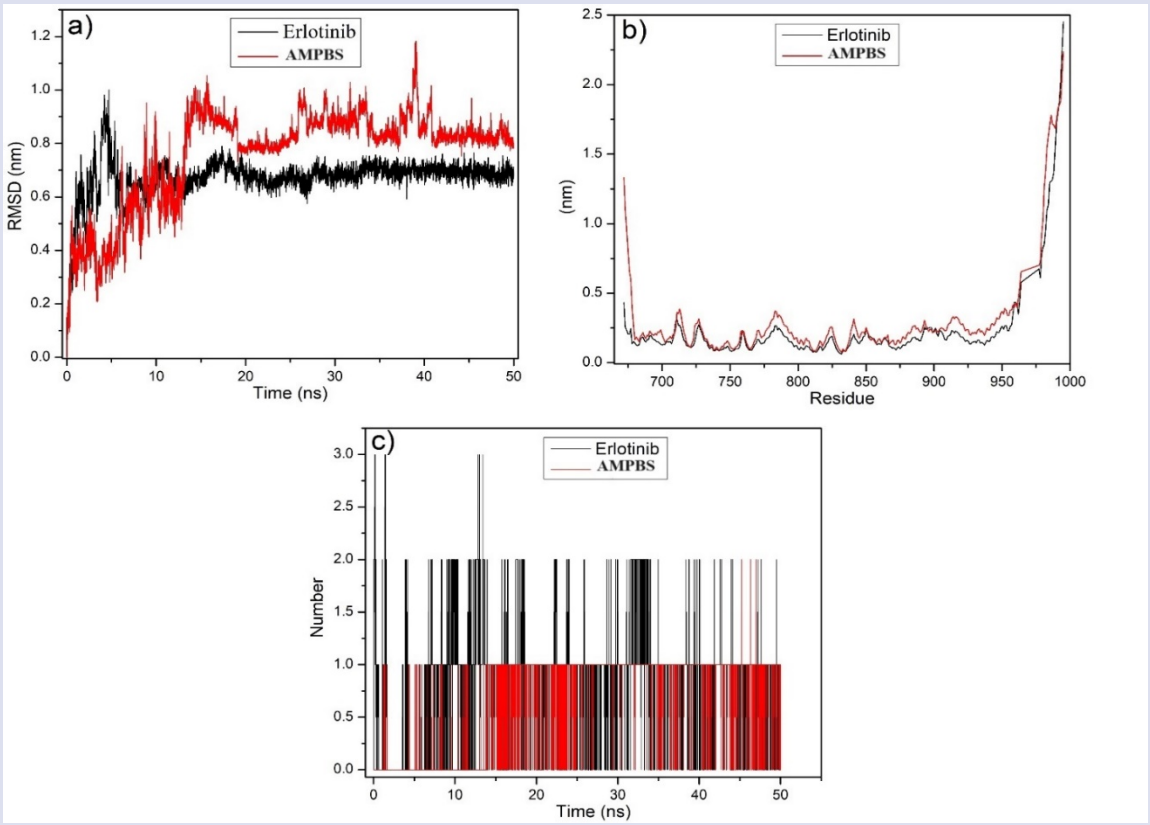

Figure 5. a) RMSD of protein and ligands; b) RMSF of the amino acid residues; c) H-bond count of the protein-ligands complex.

Conclusion

In this study, molecular docking, ADMET and MDS studies were used to identify possible therapeutic inhibitors of pharmacological importance that are predicted to show antiproliferative activity against EGFR. The native ligand erlotinib was used as a control compound. Chemical stability of the compounds was calculated by DFT calculations. The results obtained from ADMET analysis strongly indicated that the studied compounds can behave like a drug and exhibit remarkable biological activities. In addition to ADMET studies, when drug-likeness was evaluated according to Lipinski criteria, the compounds were found to obey Lipinski's rule without any violation. In the docking study, both molecules travelled to the active site and docked there. In addition, when the binding scores obtained were compared, it was observed that AMPBS had higher binding energy than erlotinib. The results of the docking studies were evaluated by MDS, especially the RMSF analysis almost overlapped with the control compound. In conclusion, the positive results obtained from *in silico* studies for AMPBS often encourage *in vitro* (laboratory) and *in vivo* (animal) testing for a new drug compound. These studies are necessary to confirm the biological activity, safety and pharmacokinetic properties of the compound. Successful results can lead to the initiation of clinical trials and ultimately the development of the compound as a medicine.

Conflicts of interest

There are no conflicts of interest in this work.

Acknowledgment

I would like to thanks for the software support provided by Pamukkale University grant project number 2013FBE013.

References

[1] Jemal A., Bray F., Center M.M., Ferlay J., Ward E., Forman D., Global cancer statistics, *CA Cancer J. Clin.*, 61 (2) (2011) 69-90.

[2] Shang D., Sun D., Shi C., Xu J., Shen M., Hu X., Liu H., Tu Z., Activation of epidermal growth factor receptor signaling mediates cellular senescence induced by certain pro-inflammatory cytokines, *Aging Cell*, 19 (5) (2020) e13145.

[3] Ukirde R., Sawant R., Nerkar A., Role of Epidermal Growth Factor Receptor Inhibitors in Treating Cancer, *Curr Trends Pharm Pharm Chem*, 2 (1) (2020) 57-63.

[4] Stamos J., Sliwkowski M.X., Eigenbrot C., Structure of the epidermal growth factor receptor kinase domain alone and in complex with a 4-anilinoquinazoline inhibitor, *J. Biol. Chem.*, 277 (48) (2002) 46265-46272.

[5] Cordover E., Minden A., Lehman S., Zhao O., Signaling pathways downstream to receptor tyrosine kinases: Targets for cancer treatment, *J. Cancer Metastatis Treat.*, 2020 (2020) 1-19.

[6] Raymond E., Faivre S., Armand J.P., Epidermal growth factor receptor tyrosine kinase as a target for anticancer therapy, *Drugs*, 60 (2000) 15-23.

[7] Ahmad, A. A., Hussain, K., Shah, M. R., Ashhad Halimi, S. M., Rabbi, F., Ahmad, Z., Khan, I., Rauf, A., Alshammari, A., Rasul Suleria, H. A. (2023). Molecular Insights into the In Vivo Analgesic and Anti-Inflammatory Activity of Indomethacin Analogues, *ACS Omega*, 8(33), 30048-30056.

[8] Das A.J., Das M.K., Singh S.P., Saikia P.P., Singh N., Islam J., Ansari A., Chattopadhyay P., Rajamani P., Miyaji T., Synthesis of salicylic acid phenylethyl ester (SAPE) and its implication in immunomodulatory and anticancer roles, *Sci. Rep.,* 12(1) (2022) 8735.

[9] Thiruchenthooran V., Sánchez-López E., Gliszczyńska A., Perspectives of the application of non-steroidal anti-inflammatory drugs in cancer therapy: Attempts to overcome their unfavorable side effects, *Cancers*, 15 (2) (2023) 475.

[10] Ramos-Inza S., Ruberte A.C., Sanmartin C., Sharma A.K., Plano D., NSAIDs: Old Acquaintance in the Pipeline for Cancer Treatment and Prevention– Structural Modulation, Mechanisms of Action, and Bright Future, *J. Med. Chem.*, 64(22) (2021) 16380-16421.

[11] Mohamed-Ezzat R.A., Kariuki B.M., Srour A.M., Synthesis, crystal structure and in vitro anti-proliferative activity of 2-[(4-acetylphenyl) carbamoyl] phenyl acetate, *Acta Cryst. E*, 79 (11) (2023).

[12] Ibrahim M.T., Uzairu A., Shallangwa G.A., Uba S., Structure-based design and activity modeling of novel epidermal growth factor receptor kinase inhibitors; an in silico approach, *Sci. Afr.,* 9 (2020) e00503.

[13] Lin S.-Y., Chang Hsu Y., Peng Y.-H., Ke Y.-Y., Lin W.-H., Sun H.-Y., Shiao H.-Y., Kuo F.-M., Chen P.-Y., Lien T.-W., Discovery of a furanopyrimidine-based epidermal growth factor receptor inhibitor (DBPR112) as a clinical candidate for the treatment of non-small cell lung cancer, *J. Med. Chem.*, 62 (22) (2019) 10108-10123.

[14] GaussView V., 6.1, R. Dennington, T.A. Keith, J.M. Millam, Semichem Inc, (2016).

[15] Frisch M., Trucks G., Schlegel H., Scuseria G., Robb M., Cheeseman J., Scalmani G., Barone V., Petersson G., Nakatsuji H., Gaussian 16 Rev. C. 01, Gaussian 16 Rev C01, (2016).

[16] Bourne P.E., Beran B., Bi C., Bluhm W.F., Dimitropoulos D., Feng Z., Goodsell D.S., Prlić A., B. Quinn G., W. Rose P., The evolution of the RCSB Protein Data Bank website, *Wiley Interdiscip. Rev. Comput. Mol. Sci.*, 1 (5) (2011) 782-789.

[17] Pettersen E.F., Goddard T.D., Huang C.C., Couch G.S., Greenblatt D.M., Meng E.C., Ferrin T.E., UCSF Chimera—a visualization system for exploratory research and analysis, *J. Comput. Chem.*, 25 (13) (2004) 1605-1612.

[18] Vidal-Limon A., Aguilar-Toala J.E., Liceaga A.M., Integration of molecular docking analysis and molecular dynamics simulations for studying food proteins and bioactive peptides, *J. Agric. Food Chem.*, 70 (4) (2022) 934-943.

[19] Jo S., Vargyas M., Vasko-Szedlar J., Roux B., Im W., PBEQ-Solver for online visualization of electrostatic potential of biomolecules, *Nucleic Acids Res.*, 36 (suppl_2) (2008) W270-W275.

[20] Bugnon M., Goullieux M., Röhrig U.F., Perez M.A., Daina A., Michielin O., Zoete., SwissParam 2023: A Modern Web-Based Tool for Efficient Small Molecule Parametrization, *J Chem Inf Model .*, 63 (21) (2023) 6469-6475.

[21] Bulat F.A., Murray J.S., Politzer P., Identifying the most energetic electrons in a molecule: The highest occupied molecular orbital and the average local ionization energy, *Comput Theor Chem.*, 1199 (2021) 113192.

[22] Traxler P., Furet P.,. Strategies toward the design of novel and selective protein tyrosine kinase inhibitors, *Pharmacology & Therapeutics*, 82(2-3) (1999) 195-206.

[23] Iwaloye O., Elekofehinti O. O., Olawale F., Chukwuemeka P. O., Kikiowo B., Folorunso I. M., Fragment-based drug design, 2D-QSAR and DFT calculation: Scaffolds of 1, 2, 4, triazolo [1, 5-a] pyrimidin-7-amines as potential inhibitors of Plasmodium falciparum dihydroorotate dehydrogenase, *Lett Drug Des Discov.*, 20(3) (2023) 317-334.

[24] Lipinski C.A., Lombardo F., Dominy B.W., Feeney P.J., Experimental and computational approaches to estimate solubility and permeability in drug discovery and development settings, *Adv. Drug Deliv. Rev.*, 64 (2012) 4-17.

[25] Ibrahim M.T., Uzairu A., Shallangwa G.A., Uba S., Structure-based design of some quinazoline derivatives as epidermal growth factor receptor inhibitors, *Egypt. J. Med. Hum. Genet.*, 21 (2020) 1-12.

[26] Clark D.E., In silico prediction of blood–brain barrier permeation, *Drug Discov. Today*, 8 (20) (2003) 927-933.

[27] Zhou S.-F., Xue C.C., Yu X.-Q., Li C., Wang G., Clinically important drug interactions potentially involving mechanism-based inhibition of cytochrome P450 3A4 and the role of therapeutic drug monitoring, *Ther. Drug Monit.*, 29 (6) (2007) 687-710.

[28] Loganathan T., Barathinivas A., Soorya C., Balamurugan S., Nagajothi T., Ramya S., Jayakumararaj R., Therapeutics, Physicochemical, Druggable, ADMET Pharmacoinformatics and Therapeutic Potentials of Azadirachtin-a Prenol Lipid (Triterpenoid) from Seed Oil Extracts of Azadirachta indica A. Juss, *J. Drug Deliv.,* 11 (5) (2021) 33-46.

[29] Zaki M.E., Al-Hussain S.A., Masand V.H., Akasapu S., Bajaj S.O., El-Sayed N.N., Ghosh A., Lewaa I., Identification of anti-SARS-CoV-2 compounds from food using QSAR-based virtual screening, molecular docking, and molecular dynamics simulation analysis, *Pharm.*, 14(4) (2021) 357.

Cumhuriyet Sci. J., 45(2) (2024) 282-290
DOI: https://doi.org/10.17776/csj.1403956

Cumhuriyet Science Journal

| csj.cumhuriyet.edu.tr | Founded: 2002 ISSN: 2587-2680 e-ISSN: 2587-246X Publisher: Sivas Cumhuriyet University

Theoretical Investigations on Phytochemicals: Physical Chemistry, FMO, MEP, Lipophilicity, Water Solubility, Drug-likeness, and Bioavailability

Nihat Karakuş [1,a,*]

[1] *Department of Chemistry, Faculty of Science, Sivas Cumhuriyet University, 58140, Sivas.*
**Corresponding author*

Research Article

History
Received: 12/12/2023
Accepted: 30/03/2024

ABSTRACT

Naturally-existing chemicals especially phytochemicals have been commonly used for medicinal purposes in terms of both traditional and contemporary respects. Allyl isothiocyanate structure exhibits antimicrobial and anticancer activity, whereas the allitridin, as one of the main components of the garlic, showed antifungal, antitumor, and antioxidant activity. Arabinose and galactose as monosaccharides also play a main role in drug-design research to facilitate drug delivery to target cells and regulate insulin resistance, respectively. Herein, the 3-isothiocyanatoprop-1-ene (Allyl isothiocyanate, AITC), 2,3,4,5-tetrahydroxypentanal (Ar, Arabinose), 1,3-diallyltrisulfane (Allitridin, DATS), 6-(hydroxymethyl)tetrahydro-2H-pyran-2,3,4,5-tetraol (Galactose, Gal), 6-methyltetrahydro-2H-pyran-2,3,4,5-tetraol (Rhamnose, Rh), and tetrahydro-2H-pyran-2,3,4,5-tetraol (cyclic-Arabinose, C-Ar) agents were investigated by using DFT. The B3LYP/6-311G** level computations were used to optimize the compounds' geometries and then to predict the reactivity indexes of the compounds. Also, lipophilicity and water-solubility features were determined to enlighten the physicochemical characteristics of the compounds. Then, the studied agents' pharmacokinetics were evaluated using the BOILED-Egg and radar graphs. Last, the bioavailability and drug-likeness behaviors were predicted. This trial work will be hoped to provide fundamental electronic and physicochemical insight into the relationship between drug-likeness and electronic structure.

Keywords: Phytochemicals, Arabinose, DFT study, Lipophilicity& water solubility, Drug-likeness.

[a] *nkarakus@cumhuriyet.edu.tr* *https://orcid.org/0000-0001-6223-7669*

Introduction

Naturally occurring compounds have been important in the necessities of daily life, such as the clothing industry, nutritional needs, and medicinal purposes since ancient times. Nowadays, computational research is crucial in the basic science, engineering, and medical fields in terms of the controlled use of natural resources for greener chemistry. Although many compounds can be obtained from synthetic routes due to limited natural resources, computational tools provide very important information for preliminary predictions of the processes of interest due to their adverse effects on the economy, time, and, more importantly, humans and the environment.

Among the studied compounds, galactose and arabinose [1,2] as member of the monosaccharides known very well due to their biological importance and are commonly studied now. Also, the DATS derived from garlic has been reported to have a potential anticancer effect via binding the cysteine residues in β-tubulin to produce the sallylmercaptocystein [3]. Furthermore, the DATS obtained from allium vegetables as bioactive dietary agents can regulate the cancer hallmark pathways [4]. In this regard, organosulphur compounds obtained from allium vegetables were investigated to explore the prevention and therapy of human cancer using preclinical and limited clinical data [5]. In addition, the DATS has been reported regarding the possible antimetastatic agent by exploring the migration and invasion of human colon cancer cells [6]. In research on antimicrobial and cytotoxic activities of lepidium latifolium L. hydrodistillate, the pure allyl isothiocyanate exhibited the cytotoxic effect on bladder cancer UM-UC-3 and glioblastoma LN229 cell lines with the similar trend to hydrodistillate [7]. Rhamnose, as a naturally occurring deoxy sugar, has a crucial role in synthetic biology and biotechnology research [8,9]. In the past, the E. coli rhamnose-inducible rhaBAD promoter has been reported to explore the possible effects on freshwater cyanobacterium; the obtained results revealed that it is superior to cyanobacterial inducible promoter model with a non-toxicity, photostability, non-metabolizable inducer, etc [8]. Furthermore, the L-rhamnose and L-fucose have been observed in terms of the potential anticancer capabilities; the optimal L-rhamnose dose has been determined as 3.64 g/kg/day, and the tumour-inhibitory effect of L-rhamnose has been more promising than the L-Fucose [10]. However, the selected compounds are naturally occurring and applicable for medicinal purposes; the possible toxicity works on the living body and/or environment of these molecules have also been investigated [11,12].

Also, the quantum chemical computations at M062X−D3/6-311++G** level have been performed to explore the ciprofloxacin interactions with glucuronic acid, arabinose, glucosamine, and rhamnose; the results indicate that ciprofloxacin in the zwitterion form is preferable to complex carbohydrates and probably induce the proton exchange between these structures [13]. In a paper reported the molecular mechanism of diallyl trisulfide (DATS) on trans-crotonaldehyde (TCA), the Raman spectroscopic properties of DATS were estimated by using the DFT/B3LYP/6-31+g (d, p) level [14]. Recently, the phytochemicals extracted from mustard, including AITC, DATS, Gal, Ar, and Rh, have been explored for possible use in corrosion inhibition [15].

In this study, well-known compounds extracted from natural sources were selected to explore the relationships between electronic structure and possible chemical direction. The compounds were optimized and confirmed by the B3LYP/6-311G** level computations. The FMO "Frontier Molecular Orbitals" investigations were performed to determine the reactivity tendencies and directions of the compounds. Also, *in silico* works were performed to estimate the compounds' physicochemical characteristics and structure relationships. For this purpose, the lipophilicity and water solubility properties were assessed and evaluated. The pharmacokinetics and bioavailability properties of the compounds were determined by using *in silico* analyses as well. From the results obtained, this work will hopefully provide the main information on the structural requirements for evaluating chemical and biological reactivity tendencies and directions.

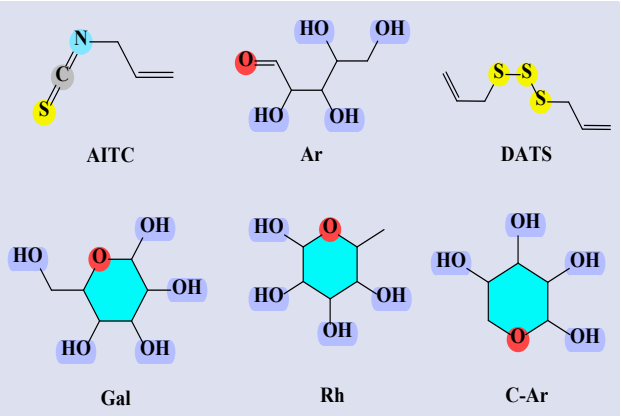

Scheme 1. Chemical Structures of the studied compounds

Computational Methods

DFT Computational Study

All quantum mechanical computations of AITC, Ar, DATS, Gal, Rh, and C-Ar agents were conducted by the G09W [16] package, at B3LYP [17,18] / 6-311G(d,p) level [19]. GaussView 6.0.16 [20] package was used for visualizations of the optimized geometries, and FMO plots as well as to perform the FMO and MEP analyses.

The thermochemical functions of the compounds were evaluated on the basis of statistical mechanics [21,22]. Accordingly, the total partition and vibrational partition functions are given below

$$Q = Q_{trans.}\, x\, Q_{rot.}\, x\, Q_{vib.}\, Q_{elec.}$$

$$Q_{vib.} = \prod_{j=1}^{3N-6} \frac{e^{-\Theta_{v,j}/2T}}{\left(1-e^{-\frac{\Theta v,j}{T}}\right)}$$

Here, the terms are defined as follows: Q→ "total partition function", $Q_{trans.}$→ "translational partition function", $Q_{rot.}$→ "rotational partition function", $Q_{vib.}$→ vibrational partition function", and $Q_{elec.}$→ "electronic partition function". Hence, the thermodynamic quantities, $E_{vib.}$ "vibrational thermal energy", $S_{vib.}$ "vibrational entropy", and $Cv_{vib.}$ "vibrational heat capacity". Here, the notations are expressed as $\Theta_{vj} = \frac{h\nu_j}{k}$ "the vibrational temperature", h→ "Planck constant", k→ "Boltzmann constant", and ν_j→" j^{th} fundamental frequency".

$$E_{vib.} = Nk \sum_{j=1}^{3N-6} \left(\frac{\Theta_{v,j}}{2} + \frac{\Theta_{vj}\, e^{-\Theta_{v,j}/T}}{\left(1 - e^{-\frac{\Theta v,j}{T}}\right)} \right)$$

$$S_{vib} = Nk \sum_{j=1}^{3N-6} \left[\frac{\Theta_{v,j}/T}{\left(e^{\Theta_{v,j}/T} - 1\right)} - ln\left(1 - e^{-\Theta_{v,j}/T}\right) \right]$$

$$Cv_{vib.} = Nk \sum_{j=1}^{3N-6} \left[\left(\frac{\Theta_{vj}}{T}\right)^2 \frac{e^{\Theta_{vj/T}}}{\left(e^{\Theta_{v,j}/T} - 1\right)^2} \right]$$

The *I* "ionization energy" and *A* "electron affinity" [23] were calculated according to the Koopmans Theorem through the energies HOMO and LUMO. Then, the possible reactivity indexes of the compounds were calculated by using the following equations

$$I = -E_{HOMO}$$

$$A = -E_{LUMO}$$

$$\chi = -\left(\frac{I+A}{2}\right)$$

$$\eta = \frac{I-A}{2}$$

$$\omega = \frac{\mu^2}{2\eta}$$

$$\Delta N_{max} = \frac{I+A}{2(I-A)}$$

$$\omega^{+} \approx (I+3A)^2/(16(I-A))$$

$$\omega^{-} \approx (3I+A)^2/(16(I-A))$$

$$\Delta\varepsilon_{back-donation} = -\frac{\eta}{4}$$

Here, the terms are described as χ → "electronic chemical potential" η → "global hardness", ω → "electrophilicity", ΔN_{max} → "the maximum charge transfer capability index" [24,25], ω- "the electrodonating power" and ω+ "the electroaccepting power" [26], and $\Delta E_{back\text{-}donat.}$ "back-donation energy" [27].

Lipophilicity and water solubility features

The lipophilicity indexes of the studied agents were estimated using five approaches: the ILOGP [28], XLOGP3 [29], WLOGP [30], MLOGP [31], and SILICOS-IT [32], by performed SwissADME [33]. The lipophilicity index (Log P) is described depending on the concentrations of a specific system in octanol (C_o) and water (C_w) as follows

$$Log\ P_{o/w} = Log\ \frac{C_o}{C_w}$$

In addition, the water-soluble features were estimated by using ALI described by Ali et al [34] and ESOL [35] provided by Delaney. The relevant equations for both of them are defined as follows

$$\log S = -1.0239\ \log P - 0.0148\ TPSA - 0.0058\ (m.p.(C) - 25) + 0.3295\ aroOHdel + 0.5337\ (ALI)$$

$$\log Sw = 0.16 - 0.63\ clogP - 0.0062\ MWT + 0.066\ RB - 0.74\ AP\ (ESOL)$$

In the ALI method, the terms are described as the aroOHdel → "the number of the aromatic –OH group(s)", the TPSA → "topological surface area", and m.p → "melting point". On the other hand, the Delaney method depends on the "Molecular weight, MWT", "Rotatable bonds, RB", and "Aromatic proportion, AP".

Pharmacokinetics, Druglikeness, and Bioavailability Study

Herein, the GI "Gastrointestinal" absorption (white) and BBB "blood–brain barrier" permeation (yolk) have been illustrated and evaluated depending on the BOILED-Egg model. The selected Cytochrome P450 characteristics, which are CYP1A2, CYP2C19, CYP2C9, CYP2D6, and CYP3A4, and gp (glycoprotein) substrate potency have also been estimated by SwissADME [33] via the SVM "support vector machine" model.

Also, the Lipinski [31], Ghose [36], Veber [37], Egan [38], and Muegge [39] approaches have been used to predict the drug-likeness characteristics of the compounds and the Abbott score [40] for bioavailabilities has been computed by using the SwissADME [33] tools.

Result and Discussion

Molecular Geometry and Thermochemistry

In computational research, the elucidation of the thermochemistry and physical characteristics of the relevant molecular systems is the main first step for further investigation and analysis.d In this work, the computed thermodynamic parameters and physical characteristics of the studied ligands are presented in Table 1.

Depending on the structural isomerism, the ΔE (au) of the C-Ar molecule would have been lower than the corresponding open-chain form (Ar): the ΔE (au) values of Ar and C-Ar were determined as -572.640688 au and -572.645566 au, respectively. Like being in ΔE (au), the other thermochemical and physical values of these molecules were also close to each other. Namely, the ΔH quantity of Ar and C-Ar were determined in -572.628692 and -572.634697 au, respectively, whereas the ΔG of them was predicted as -572.677490 and -572.679951 au. On the other hand, the lowest thermodynamic quantities among the studied molecules were estimated for the DATS molecule due to the existence of three sulfur atoms, as expected from the quantum statistics or statistical mechanics [21]. Namely, the ΔE, ΔH, and ΔG values of DATS were calculated as -1429.185987, -1429.172523, and -1429.228069 au, respectively. In addition, the ΔG value of the AITC, Gal, and Rh molecules was computed as -608.374666, -687.209130, and -611.978951 au, respectively. Also, the $E_{therm.}$ values of the compounds were determined as 55.451 (AITC), 108.178 (Ar), 99.238 (DATS), 131.531 (Gal), 127.579 (Rh), and 109.162 au (C-Ar). The Cv and S values of the Gal were determined as 47.346 and 106.823 cal/molK, respectively, whereas these quantities of DATS were estimated as 41.393 and 116.906 cal/molK. On the other hand, the Cv and S values of the Ar molecule were determined as 40.183 and 102.704 cal/mol, respectively, while these values for the closed-ring Ar were determined as 38.464 and 95.245 cal/molK. The dipole moment order of the compounds was determined as DATS (1.542)< C-Ar (1.571)< Ar (2.943)< Gal (3.636)< AITC (3.735)< Rh (3.802), whereas the α (au) order of the molecules was computed as AITC (69.143)< C-Ar (71.352)< Ar (73.194)< Rh (82.541)< Gal (85.993)< DATS (139.315).

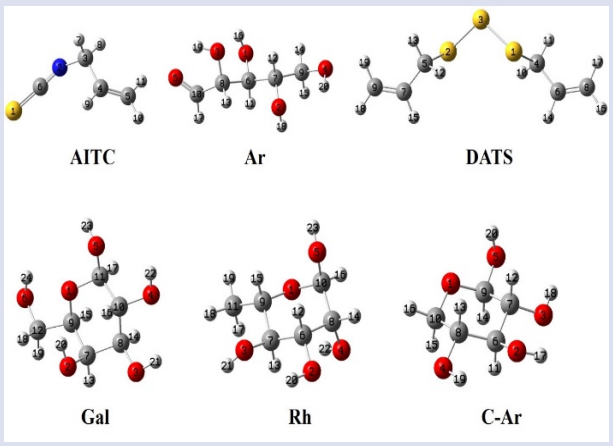

Figure 1. The optimized geometries

Table 1. The thermochemical and physical parameters of the studied compounds

	AITC	Ar	DATS	Gal	Rh	C-Ar
ΔE (au)	-608.341498	-572.640688	-1429.185987	-687.171634	-611.943046	-572.645566
ΔH (au)	-608.333658	-572.628692	-1429.172523	-687.158375	-611.930723	-572.634697
ΔG (au)	-608.374666	-572.677490	-1429.228069	-687.209130	-611.978951	-572.679951
$E_{therm.}$(kcal/mol)	55.451	108.178	99.238	131.531	127.579	109.162
Cv (cal/molK)	22.083	40.183	41.393	47.346	44.203	38.464
S (cal/molK)	86.308	102.704	116.906	106.823	101.503	95.245
μ (D)	3.735	2.943	1.542	3.636	3.802	1.571
α (au)	69.143	73.194	139.315	85.993	82.541	71.352

Lipophilicity and Water Solubility Features

The lipophilicity and water-soluble characteristics of the molecular systems have an essential role in investigating the physicochemical properties that help predict, evaluate, and provide a deep understanding of the chemical processes. In addition to the basic information of the molecular systems, especially, they are critical properties in drug-design research. In this respect, the determined lipophilic and water-soluble scores of the studied compounds were summarized in Table 2.

The lipophilicity indexes of the compounds were estimated by using five different approaches, and the average lipophilicity was given in Table 2 as well. Depending on the approach used, the lipophilicity indexes changed in the following orders:

iLOGP: DATS (2.65)> AITC (1.93)> Rh (0.85)> Gal (-0.12)> C-Ar (-0.39)> Ar (-0.65)

XLOGP3: DATS (2.64)> AITC (2.41)> Rh (-2.09)> Ar (-2.32)> C-Ar (-3.02)> Gal (-3.24)

WLOGP: DATS (3.39)> AITC (1.28)> Rh (-2.19)> C-Ar (-2.58)> Ar (-2.74)> Gal (-3.22)

MLOGP: DATS (2.35)> AITC (1.98)> Rh (-1.94)> C-Ar (-2.32)> Ar (-2.48)> Gal (-2.75)

SILICOS-IT: DATS (2.38)> AITC (2.37)> Ar (-1.29)> C-Ar (-1.70)> Rh (-1.72)> Gal (-2.30)

Avg.: DATS (2.68)> AITC (1.99)> Rh (-1.42)> Ar (-1.90)> C-Ar (-2.00)>Gal (-2.33)

Table 2. Lipophilicity and water solubility of the studied compounds

	AITC	Ar	DATS	Gal	Rh	C-Ar
Formula	C4H5NS	C5H10O5	C6H10S3	C6H12O6	C6H12O5	C5H10O5
Molecular weight(g/mol)	99.15	150.13	178.34	180.16	164.16	150.13
Num. heavy atoms	6	10	9	12	11	10
Num. arom. heavy atoms	0	0	0	0	0	0
Fraction Csp3	0.25	0.80	0.33	1.00	1.00	1.00
Num. rotatable bonds	2	4	6	1	0	0
Num. H-bond acceptors	1	5	0	6	5	5
Num. H-bond donors	0	4	0	5	4	4
Molar Refractivity	30.03	31.00	52.78	35.74	34.57	29.77
TPSA (Å²)	44.45	97.99	75.90	110.38	90.15	90.15
Lipophilicity						
iLOGP	1.93	-0.65	2.65	-0.12	0.85	-0.39
XLOGP3	2.41	-2.32	2.64	-3.24	-2.09	-3.02
WLOGP	1.28	-2.74	3.39	-3.22	-2.19	-2.58
MLOGP	1.98	-2.48	2.35	-2.75	-1.94	-2.32
SILICOS-IT	2.37	-1.29	2.38	-2.30	-1.72	-1.70
Avg. LogPo/w	1.99	-1.90	2.68	-2.33	-1.42	-2.00
Water Solubility						
Log S (ESOL)	-1.84	0.95	-2.21	1.15	0.46	1.13
Solubility (mg/mL)	1.43	1350	109	2550	4.72	2030
Class	VS	HS	S	HS	HS	HS
Log S (Ali)	-2.99	0.80	-3.88	1.49	0.72	1.69
Solubility (mg/mL)	0.103	944	0.0233	5610	870	7340
Class	S	HS	S	HS	HS	HS
Log S (SILICOS-IT)	-0.85	1.94	-1.91	2.62	2.06	2.23
Solubility (mg/mL)	14.1	13000	2.18	74200	19100	25600
Class	S	S	S	S	S	S

*The abbreviations are defined as S, Soluable; VS, very soluable. HS; Highly soluble

As known well, the water-solubility classification of the relevant molecule is as Insoluble< -10 < poorly< -6 < moderately < -4< soluble < -2< very < 0 < highly. Accordingly, all compounds were determined water soluble depending on all approaches used, but the most soluble one would be Gal while the less soluble was found to be DATS, as implied by the lipophilicity indexes. Considering the importance of both the lipophilicity and water solubility properties of the compounds due to their role in the ADMET characteristics of the molecular systems, the computed results will be hoped to help further early-stage drug-design research.

Accordingly, the DATS, including the -S-S-S bridge between the two allyl terminals was determined the most lipophilic compound, as expected by the structural nature of the aliphatic chain and the presence of the sulfurs. Due to the presence of the hydrophilic -OH groups, Gal, C-Ar, Ar, and Rh compounds were determined to be less lipophilic among the compounds, as expected. Although the Ar was determined to be less lipophilic according to the iLOGP scores, the Gal molecule was found to be less lipophilic based on the other approaches and the average scores.

Furthermore, the water solubility scores of the compounds were calculated in the following orders:

Log S (ESOL): Gal (1.15)> C-Ar (1.13)> Ar (0.95)> Rh (0.46)> AITC (-1.84)> DATS (-2.21)

Log S (Ali): C-Ar (1.69)> Gal (1.49)> Ar (0.80)> Rh (0.72)> AITC (-2.99)> DATS (-3.88)

Log S (SILICOS-IT): Gal (2.62)> C-Ar (2.23)> Rh (2.06)> Ar (1.94)> AITC (-0.85)> DATS (-1.91)

Druglikeness and Bioavailability Study

Also, computational tools have been efficiently applied to explore potential agents by predicting the structural necessities of drug-design research in terms of pharmacokinetics. Herein, the BOILED-Egg model and pharmacokinetic radar graphs of the compounds were visualized in Fig. 2; the calculated bioavailability and drug-likeness characteristics were presented in Table 3.

The five approaches like Lipinski, Ghose, Veber, Egan, and Muegge were used to determine the drug-likeness properties of the compounds. According to the Lipinski, Veber, and Egan formulae, all compounds could be bioavailable since there were not determined a violations in terms of structural and physical views. Moreover, the DATS molecule could not be a bioavailable agent because of the atom number<20 depending on the Ghose rules and MW<200 depending on the Muegge rules. On the other hand, AITC, Ar, and C-Ar molecules would have 3 violations depending on the Ghose scales, and thus their bioavailability could be in danger. According to Ghose, the limitations for the bioavailability of AITC were related to the structural properties that were MW<160, MR<40, and Natoms<20, while the possible contravening for Ar and C-Ar molecules were also related to the physicochemical properties (WLOGP<-0.4). According to Muegge, the C atom number of the AITC could be a problem in possibly being used for biological purposes due to it being calculated lower than 5. In summary, the bioavailability values of all compounds were determined to be 0.55, which implied that the studied compounds could be promising bioavailable agents, depending on the Abbott scores.

According to the BOILED-Egg model, the AITC and DATS molecules would have the capability of BBB permeation (yolk region of the BOILED-Egg), while the other molecules would have no ability in terms of the BBB permeation due to their location out of the yolk of the egg. Among the studied compounds, the Rh molecule could have a potency of P-gp substrate because it was positioned in the range of the white of the BOILED-Egg, while the other compounds could have no potential for P-gp substrate. Here, it could be said that the -CH3 substitution makes the Rh gain P-gp substrate potency because the C-Ar molecule included the -H substitution in the same position as -CH3 of Rh. On the other hand, the hydroxymethyl substitution on the pyran ring of Gal could be responsible for being far away from the possible power in terms of pharmacokinetics. Also, the red frame on the radar plots of the compounds showed the optimal physicochemical space for oral bioavailability.

Table 3. Druglikeness and bioavailability scores

	AITC	*Ar*	*DATS*	*Gal*	*Rh*	*C-Ar*
Lipinski	Yes	Yes	Yes	Yes	Yes	Yes
Ghose	No 3 violations: MW<160, MR<40, #atoms<20	No 3 violations: MW<160, WLOGP<-0.4, MR<40	No 1 violation: #atoms<20	No 2 violations: WLOGP<-0.4, MR<40	No 2 violations: WLOGP<-0.4, MR<40	No 3 violations: MW<160, WLOGP<-0.4, MR<40
Veber	Yes	Yes	Yes	Yes	Yes	Yes
Egan	Yes	Yes	Yes	Yes	Yes	Yes
Muegge	No 2 violations: MW<200, #C<5	No 2 violations: MW<200, XLOGP3<-2	No 1 violation: MW<200	No 2 violations: MW<200, XLOGP3<-2	No 2 violations: MW<200, XLOGP3<-2	No 2 violations: MW<200, XLOGP3<-2
Bioavailability Score	0.55	0.55	0.55	0.55	0.55	0.55

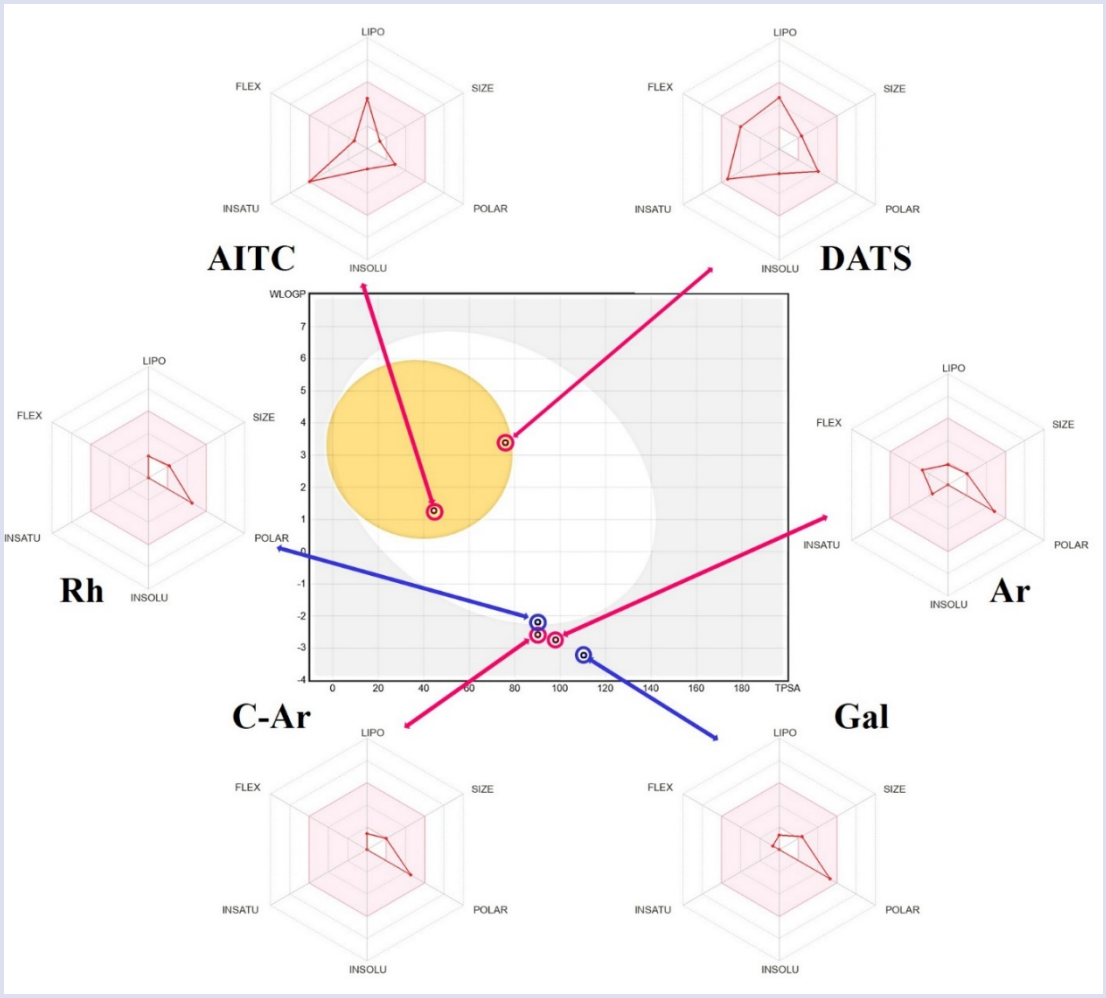

Fig. 2. BOILED-Egg model and pharmacokinetic radar graphs

FMO (Frontier Molecular Orbital) Analysis and MEP (Molecular Electrostatic Potential)

The energies and shapes of the FMOs of the molecular systems have provided helpful information by pointing out the possible reactivity directions and region(s) and applying them to different types of molecular systems, from simple organics to complex structures. Herein, the calculated reactivity values of the compounds were presented in Table 4; the surfaces of the HOMO, LUMO, and MEP of them were displayed in Fig. 3.

The global reactivity parameters of the compounds changed as the following orders:

H (-I): DATS (-6.681)> AITC (-6.788)> Rh (-7.180)> Gal (-7.233)> C-Ar -7.284)> Ar (-7.371)

L (-A): C-Ar (0.645)> Rh (0.488)> Gal (0.359)> AITC (-0.823)> C-Ar (-1.547)> DATS (-1.635)

ΔE (L-H): C-Ar (7.930)> Rh (7.668)> Gal (7.592)> AITC (5.965)> Ar (5.824)> DATS (5.046)

χ: C-Ar (-3.319)> Rh (-3.346)> Gal (-3.437)> AITC (-3.805)> DATS (-4.158)> Ar (-4.459)

η: C-Ar (3.965)> Rh (3.834)> Gal (3.796)> AITC (2.983)> Ar (2.912)> DATS (2.523)

ω: DATS (0.126)> Ar (0.125)> AITC (0.089)> Gal (0.057)> Rh (0.054)> C-Ar (0.051)

ω^+: DATS (0.061)> Ar (0.057)> AITC (0.033)> Gal (0.011)> Rh (0.010)> C-Ar (0.008)

ω^-: Ar (0.221)> DATS (0.214)> AITC (0.173)> Gal (0.138)> Rh (0.133)> C-Ar (0.130)

ΔN_{max}: DATS (1.648)> Ar (1.531)> AITC (1.276)> Gal (0.905)> Rh (0.873)> C-Ar (0.837)

ΔE_{back}: DATS (-0.631)> Ar (-0.728)> AITC (-0.746)> Gal (-0.949)> Rh (-0.958)> C-Ar (-0.991)

According to the HOMO energy order, the DATS could be the best nucleophile, while the Ar could be the less nucleophilic character. Also, the C-Ar would prefer to interact with the external system, whereas the intramolecular charge transfer for the DATS would be possible. In terms of the electronic chemical stability, the χ orders implied that the Ar would be more stable than the others. Also, C-Ar could be the hardest agent, whereas the DATS was determined to be the softer agent among the compounds. The DATS compound would have the most electrophilic character and electron-accepting power, whereas the C-Ar could have the lowest electrophilic character and less electroaccepting potency. Also, the electron-donating capability of all compounds could be domineering in comparison to the electron acceptance

potency. Last, the C-Ar agent could gain more stability via back-donation than the other compounds.

Furthermore, the FMO graphs are used as a popular tool for studying the electronic properties of molecular structure in drug discovery, design, and pharmacokinetic profiling, as they help to understand the reactivity of a molecule, i.e., how it can behave in chemical reactions. In this regard, the HOMO density of the compounds Ar, Gal, Rh, and C-Ar expanded on the whole surface, while the HOMO of both AITC and DATS molecules separated on the surface except for the allyl group(s). Except for the Ar compound, the LUMO of the other agents was also distributed on the whole surface. The LUMO for the Ar agent was half expanded on the surface. Moreover, Molecular Electrostatic Potential (MEP) diagrams are visual representations of the electron density on the surface of molecules of interest, where the positive and negative charge densities in various regions of the molecule are expressed in colors. Generally, red represents electron-rich regions, and blue represents electron-poor regions. Other colors, such as yellow and green, indicate neutral or intermediate potential values. From Fig. 3, the red color (V<0) as a marker of the electron-abundance site appeared on the allyl group(s) for both the AITC and DATS molecules, whereas the blue color (V>0) as a sign of the electron-poor field appeared on the sulfur (s) of these compounds. Also, the tri-sulfur bridge of the DATS and sulfur atom of the AITC molecules would seem blue. For the compounds, the H atom of the -OH group could wear blue, while the oxygens of these compounds appeared by orange color as a marker of the electron-rich region at a moderate-level.

Table 4. The chemical reactivity indices

	AITC	Ar	DATS	Gal	Rh	C-Ar
H (-I)	-6.788	-7.371	-6.681	-7.233	-7.180	-7.284
L (-A)	-0.823	-1.547	-1.635	0.359	0.488	0.645
ΔE (L-H)	5.965	5.824	5.046	7.592	7.668	7.930
χ	-3.805	-4.459	-4.158	-3.437	-3.346	-3.319
η	2.983	2.912	2.523	3.796	3.834	3.965
ω	0.089	0.125	0.126	0.057	0.054	0.051
ω^+	0.033	0.057	0.061	0.011	0.010	0.008
ω^-	0.173	0.221	0.214	0.138	0.133	0.130
$\Delta N_{max.}$	1.276	1.531	1.648	0.905	0.873	0.837
$\Delta E_{back.}$	-0.746	-0.728	-0.631	-0.949	-0.958	-0.991

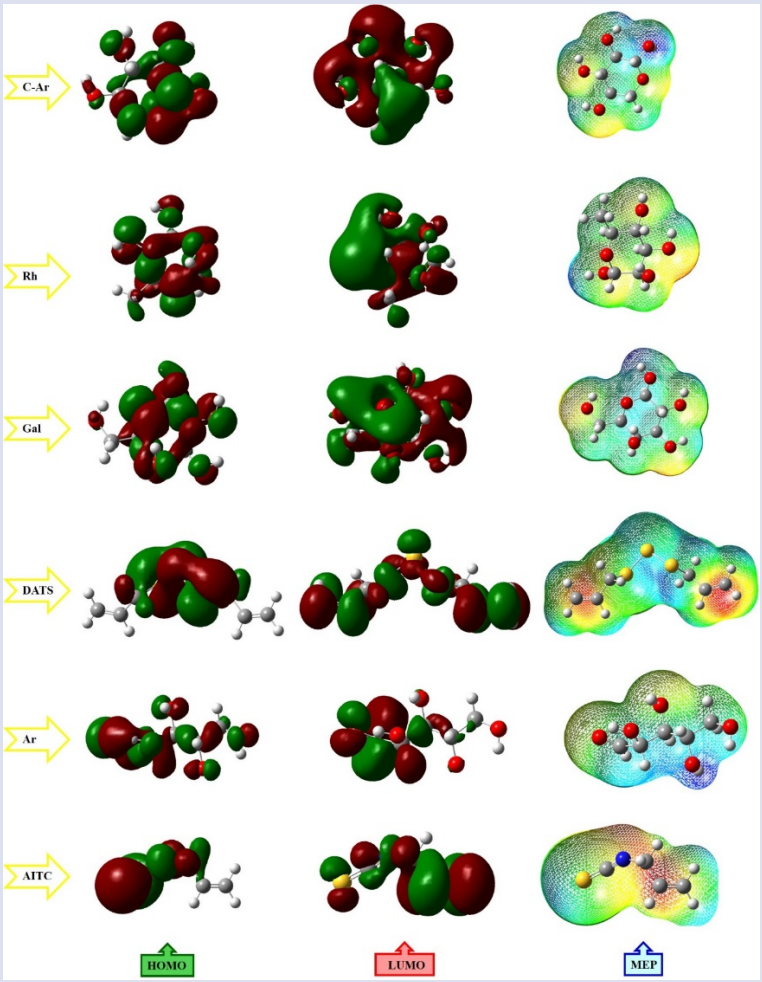

Fig. 3. HOMO& LUMO (isoval:0.02), and MEP (isoval:0.0004) plots

Conclusions

Herein, the phytochemical agents AITC, Ar, DATS, Gal, Rh, and C-Ar have been explored in relation to the electronic structure and drug-likeness relationship. In this regard, the optimized and confirmed structures were used for future analyses of the compounds. According to the average lipophilicity indices, the DATS agent was predicted as the most lipophilic compound, with the order of Avg.: DATS (2.68)> AITC (1.99)> Rh (-1.42)> Ar (-1.90)> C-Ar (-2.00)>Gal (-2.33). Depending on the Log S (SILICOS-IT) approach, Gal (2.62)> C-Ar (2.23)> Rh (2.06)> Ar (1.94)> AITC (-0.85)> DATS (-1.91), the DATS was predicted the less water-soluble agent whereas the Gal was estimated to have the most water solubility. The FMO analyses revealed the possible reactivity features of the compounds. Namely, the hardness order of the compounds displayed that the C-Ar C-Ar (3.965 eV) would be the hardest, whereas the DATS (2.523 eV) would be the softest one among the compounds. Furthermore, the C-Ar (-0.991) could gain the most stability via back-donation, whereas the DATS (-0.631 eV) could gain less stability via back-donation. From the results obtained, this work is hoped to help the deep understanding of the relationship between the electronic structure and bioavailability & drug-likeness.

Conflicts of interest

The authors declare that, there are no conflicts of interest in this work.

Acknowledgments

All calculations have been carried out at TUBITAK ULAKBIM, High Performance and Grid Computing Center (TR-Grid e-Infrastructure).

References

[1] Whittaker M. M., Whittaker J. W., The active site of galactose oxidase, *Journal of Biological Chemistry*, 263 (13) (1988) 6074-6080.

[2] Jansen L. M., van Rijbroe, K. W. M., den Bakker P. C., Klaassen-Heshof D. J., Kolkman W. J. B., Venbrux N., Migchielsen V., Hutzezon J., Lenferink W. B., Lücker S., Ranoux A., Raaijmakers H. W. C., Boltje T. J., Synthesis and Performance of Biobased Surfactants Prepared by the One-Pot Reductive Amination of l-Arabinose and d-Galacturonic Acid, *ACS Sustainable Chemistry & Engineering*, 11 (45) (2023) 16117-16123.

[3] Seki T., Hosono T., Hosono-Fukao T., Inada K., Tanaka R., Ogihara J., Ariga T., Anticancer effects of diallyl trisulfide derived from garlic, *Asia Pac. J. Clin. Nutr.*, 17 (1) (2008) 249-252.

[4] Puccinelli M. T., Stan S. D., Dietary Bioactive Diallyl Trisulfide in Cancer Prevention and Treatment, *International Journal of Molecular Sciences*, 18(8) (2017) 1645.

[5] Powolny A. A., Singh S. V., Multitargeted prevention and therapy of cancer by diallyl trisulfide and related Allium vegetable-derived organosulfur compounds, *Cancer Letters*, 269(2) (2008) 305-314.

[6] Lai K. C., Hs S. C., Kuo, C. L., Yang J. S., Ma C. Y., Lu H. F., Tang N., Hsia T., Ho H., Chung J. G., Diallyl sulfide, diallyl disulfide, and diallyl trisulfide inhibit migration and invasion in human colon cancer colo 205 cells through the inhibition of matrix metalloproteinase-2,-7, and-9 expressions, *Environmental Toxicology*, 28(9) (2013) 479-488.

[7] Blažević I., Đulović A., Maravić A., Čikeš Čulić V., Montaut S., Rollin P., Antimicrobial and cytotoxic activities of Lepidium latifolium L. Hydrodistillate, extract and its major sulfur volatile allyl isothiocyanate, *Chemistry & Biodiversity*, 16(4) (2019) e1800661.

[8] Kelly C. L., Taylor G. M., Hitchcock A., Torres-Méndez, A., Heap, J. T., A Rhamnose-Inducible System for Precise and Temporal Control of Gene Expression in Cyanobacteria, *ACS Synthetic Biology,* 7(4) (2018) 1056-1066.

[9] Kelly C. L., Liu Z., Yoshihara A., Jenkinson S. F., Wormald M. R., Otero J., Estévez A., Kato A., Marqvorsen M. H. S., Fleet G. W. J., Estévez R. J., Izumori K., Heap J. T., Synthetic Chemical Inducers and Genetic Decoupling Enable Orthogonal Control of the rhaBAD Promoter, *ACS Synthetic Biology*, 5(10) (2016) 1136-1145.

[10] Tomsik P., Soukup T., Cermakova E., Micuda S., Niang M., Sucha L., Rezacova M., L-rhamnose and L-fucose suppress cancer growth in mice, *Central European Journal of Biology*, 6 (2011) 1-9.

[11] Lin H., Ramesh S., Chang Y., Tsai C., Tsai C., Shibu M. A., Tamilselvi S., Mahalakshmi B., Kuo W., Huang C., D-galactose-induced toxicity associated senescence mitigated by alpinate oxyphyllae fructus fortified adipose-derived mesenchymal stem cells, *Environmental Toxicology*, 36(1) (2021) 86-94.

[12] Liu G., Hale G. E., Hughes C. L., Galactose metabolism and ovarian toxicity, *Reproductive Toxicology*, 14(5) (2000) 377-384.

[13] Coba-Jiménez L., Maza J., Guerra M., Deluque-Gómez J., Cubillán N., Interaction of Ciprofloxacin with Arabinose, Glucosamine, Glucuronic Acid and Rhamnose: Insights from Genetic Algorithm and Quantum Chemistry, *Chemistry Select*, 7(2) (2022) e202103836.

[14] Su Y., Chen L., Cheng Y., Zhang F., Su Y., Li Z., Raman spectroscopic characteristics of diallyl trisulfide acting on trans-crotonaldehyde, *Journal of Raman Spectroscopy*, 46(11) (2015) 1067-1072.

[15] Dehghani A., Mostafatabar A. H., Ramezanzadeh B., Synergistic anticorrosion effect of Brassica Hirta phytoconstituents and cerium ions on mild steel in saline media: Surface and electrochemical evaluations, *Colloids and Surfaces A: Physicochemical and Engineering Aspects*, 656 (2023) 130503.

[16] Frisch M. J., Gaussian 09W, Revision D.01, Gaussian, Inc, Wallingford CT, (2013).

[17] Becke A. D., A new mixing of Hartree–Fock and local density-functional theories, *J. Chem. Phys.,* 98 (1993) 1372-1377.

[18] Lee C., Yang W., Parr R. G., Development of the Colle-Salvetti correlation-energy formula into a functional of the electron density, *Phys. Rev.,* B37 (1988) 785-789.

[19] Raghavachari K., Binkley J. S., Seeger R., Pople J. A., Self-Consistent Molecular Orbital Methods. 20. Basis set for correlated wave-functions, *J. Chem. Phys*., 72 (1980) 650-654.

[20] GaussView 6.0.16, Gaussian, Inc, Wallingford CT, 2016.
[21] Herzberg G., Molecular Spectra and Molecular Structure III, 1st Edition, D. Van Nostrand Company, Inc., New York, (1964).
[22] Serdaroglu G., Durmaz S., DFT and statistical mechanics entropy calculations of diatomic and polyatomic molecules, *Indian J. Chem*., 49 (2010) 861-866.
[23] Koopmans T., Über die Zuordnung von Wellenfunktionen und Eigenwerten zu den Einzelnen Elektronen Eines Atoms, *Physica*, 1 (1934) 104-113.
[24] Perdew J. P., Parr R. G., Levy M., Balduz J. L., Density-Functional Theory for Fractional Particle Number: Derivative Discontinuities of the Energy, *Phys. Rev. Lett*., 49(23) (1982) 1691-1694.
[25] Parr R. G., Pearson R. G., Absolute hardness: companion parameter to absolute electronegativity, *J. Am. Chem. Soc.*, 105 (1983) 7512-7516.
[26] Gazquez J. L., Cedillo A., Vela A., Electrodonating and Electroaccepting Powers, *J. Phys. Chem. A*, 111 (10) (2007) 1966-1970.
[27] Gomez B., Likhanova N. V., Domínguez-Aguilar M. A., Martínez-Palou R., Vela A., Gazquez J. L., Quantum Chemical Study of the Inhibitive Properties of 2-Pyridyl-Azoles, *J. Phys. Chem. B*, 110(18) (2006) 8928-8934.
[28] Daina A., Michielin O., Zoete V., iLOGP: a simple, robust, and efficient description of n-octanol/water partition coefficient for drug design using the GB/SA approach, *J. Chem. Inf. Model.*, 54(12) (2014) 3284-3301.
[29] Cheng T., Zhao Y., Li X., Lin F., X Y., Zhang, X., Lai L., Computation of octanol–water partition coefficients by guiding an additive model with knowledge, *J. Chem. Inf. Model.*, 47(6) (2007) 2140-2148.
[30] Wildman S. A., Crippen G. M., Prediction of physicochemical parameters by atomic contributions, *J. Chem. Inf. Comp. Sci.,* 39(5) (1999) 868-873.
[31] Lipinski C. A., Lombardo F., Dominy B. W., Feeney P. J., Experimental and computational approaches to estimate solubility and permeability in drug discovery and development settings, *Adv. Drug Deliv. Rev.,* 64 (2012) 4-17.
[32] Computational approaches streamlining drug discovery. Available at: https://www.silicos-it.be. Retrieved April 28, (2023).
[33] Daina A., Michielin O., Zoete V., SwissADME: a free web tool to evaluate pharmacokinetics, drug-likeness, and medicinal chemistry friendliness of small molecules, *Sci. Rep.-UK*, 7(1) (2017) 1-13.
[34] Ali J., Camilleri P., Brown M. B., Hutt A. J., Kirton S. B., In silico prediction of aqueous solubility using simple QSPR models: the importance of phenol and phenol-like moieties, *J. Chem. Inf. Model*., 52(11) (2012) 2950-2957.
[35] Delaney J. S., ESOL: estimating aqueous solubility directly from molecular structure, *J. Chem. Inf. Comp. Sci*., 44(3) (2004) 1000-1005.
[36] Ghose A. K., Viswanadhan V. N., Wendoloski J. J., A knowledge-based approach in designing combinatorial or medicinal chemistry libraries for drug discovery. 1. A qualitative and quantitative characterization of known drug databases, *J. Comb. Chem*., 1(1) (1999) 55-68.
[37] Veber D. F., Johnson S. R., Cheng H. Y., Smith B. R., Ward K. W., Kopple K. D., Molecular properties that influence the oral bioavailability of drug candidates, *J. Med. Chem*., 45(12) (2002) 2615-2623.
[38] Egan W. J., Merz K. M., Baldwin J. J., Prediction of drug absorption using multivariate statistics, *J. Med. Chem*., 43(21) (2000) 3867-3877.
[39] Muegge I., Heald S. L., Brittelli D., Simple selection criteria for drug-like chemical matter, *J. Med. Chem*., 44(12) (2001) 1841-1846.
[40] Martin Y. C., A bioavailability score, *J. Med. Chem*., 48(9) (2005) 3164-3170.

Cumhuriyet Sci. J., 45(2) (2024) 291-298
DOI: https://doi.org/10.17776/csj.1465192

Cumhuriyet Science Journal

| csj.cumhuriyet.edu.tr | Founded: 2002 ISSN: 2587-2680 e-ISSN: 2587-246X Publisher: Sivas Cumhuriyet University

The Causes of Thyrotoxicosis, Clinical Features, and Treatment Strategies in a Former Iodine Deficient Area

Osman Akidan [1,a,*], Mustafa Kocak [2,b], Hülya Coskun [2,c], Halil Onder Ersöz [2,d]

[1] *Department of Internal Medicine, Faculty of Medicine, Karadeniz Technical University, Trabzon, Türkiye.*
[2] *Department of Endocrinology, Faculty of Medicine, Karadeniz Technical University, Trabzon, Türkiye.*
**Corresponding author*

Research Article

History
Received: 04/04/2024
Accepted: 13/06/2024

ABSTRACT

Thyrotoxicosis is a hypermetabolic condition caused by excess thyroid hormones in the circulation with/without increased production from the thyroid gland. In this prospective study, we aimed to investigate the causes of thyrotoxicosis, clinical features, and treatment strategies in a former iodine-deficient area. Thyroid function tests, antithyroid and antithyroid receptor antibodies, and routine thyroid ultrasonography was obtained, and a thyroid scintigraphy/radioactive iodine uptake test was performed on need. A statistically significant difference was found between toxic multinodular goiter (TMNG) and Graves' disease (GD) groups when mean corpuscular volume (MCV), mean corpuscular hemoglobin (MCH), alanine aminotransferase (ALT), and aspartate aminotransferase (AST) values were analyzed. TSH levels were significantly lower in GD patients compared to those in TMNG and TNG patients, but free triiodothyronine (FT3) and free thyroxine (FT4) values were higher. A high level of TSH receptor antibody (TRAb) was observed in patients with normal antithyroid peroxidase (Anti-TPO). TRAb levels were found to be high. Anti-TPO and anti-thyroglobulin (Anti-Tg) levels were observed to be positively correlated with sT3 and sT4 levels. TMNG is the leading cause of thyrotoxicosis; despite sufficient iodide intake in our former iodine-deficient region, TMNG is characteristically seen in older patients with much lower thyroid hormone levels than GD. According to the study results, the diagnosis of patients with thyrotoxicosis, their clinical presentation, the treatment they will receive, early detection of postoperative complications were predicted.

Keywords: Thyrotoxicosis, Toxic multinodular goiter, Graves' disease, TSH.

[a] *osmanakidandr@hotmail.com* *https://orcid.org/0000-0002-4211-7309*
[b] *mkocak19@ktu.edu.tr* *https://orcid.org/0000-0002-8269-2869*
[c] *hulyacoskun82@hotmail.com* *https://orcid.org/0000-0002-7837-4251*
[d] *hersoz@yahoo.com* *https://orcid.org/0000-0001-7157-1116*

Introduction

"Thyrotoxicosis" describes the classical clinical symptoms caused by excessive circulating thyroid hormones [1]. Although the term "hyperthyroidism" is frequently used instead of "thyrotoxicosis," this term refers to instances when the thyroid gland's excessive synthesis of thyroid hormones results in "thyrotoxicosis"[2]. Thyrotoxicosis is a significant health issue that affects women more commonly than males. Thyrotoxicosis is observed more frequently in the elderly, Caucasians, and regions with iodine deficiency [3]. The most common reason for non-iatrogenic thyrotoxicosis in regions without iodine deficiency is Graves' disease (GD), which constitutes 80% of the cases, as nodular thyroid disease and thyroiditis [4]. However, the prevalence of these etiologies varies depending on the degree of iodine consumption (in iodine-deficit areas, nodular thyroid disorders make up around 50% of cases), the population's age (toxic-nodular goiter affects the elderly more commonly), and the region [4,5]. The prevalence of thyrotoxicosis is about 2%, and GD causes 70 to 90% of the cases [6]. Graves' disease is an autoimmune disorder that causes hyperthyroidism, diffuse goiter, ophthalmopathy, and dermopathy. In regions with adequate iodine intake, this is the most frequent cause of thyrotoxicosis. In women, it occurs 7 to 10 times more frequently than men [2]. The overgrowth and overfunctioning of thyroid cells are caused by stimulating antibodies against the TSH receptor on the thyroid cell membrane in GD [7].

The second most frequent cause of thyrotoxicosis is toxic multinodular goiter (TMNG). Functional nodules, which had gained autonomy among the multiple nodules of thyroid glands, cause the typical TMNG symptoms. It is inversely correlated with iodine intake, and TMNG is more prevalent in iodine-deficient areas. It is stated that the pathogenesis may be associated with the receptor activation caused by somatic mutation that has occurred in the thyroid-stimulating hormone receptor (TSHR) gene and with cyclic adenosine monophosphate (cAMP) upregulation [8].

Toxic nodular goiter (toxic adenoma, TNG) develops as a result of a single hyperfunctioning adenoma in the thyroid gland, which produces too many thyroid hormones. Similar to TMNG, it is more prevalent in areas with an iodine deficiency. TNG generally develops slowly and occurs when the nodule, which has been present for years, gains autonomy. It displays the increased Thyroxine (T4) and Triiodothyronine (T3) levels along with the suppressed Thyroid stimulating hormone (TSH) [9].

A surplus of thyroid hormone has an impact on numerous organ systems. Fatigue, anxiety, palpitations,

sweating, heat intolerance, anxiety, sleep disorders, and weight loss are examples of clinical symptoms [9]. These clinical signs and symptoms are generally not very specific and might change based on the patient's age, sex, comorbidities, and the duration and cause of the disease [10]. The variety of non-specific symptoms and signs makes diagnosing or evaluating the disease state difficult based on traditionally obtained information on the symptoms and findings. Clinical examination is the first step in the diagnostic evaluation of thyrotoxicosis, and then the proper biochemical tests, nuclear medicine data, and ultrasound are used to make the diagnosis [1].

This prospective study aims to determine the causes of thyrotoxicosis, clinical features, and treatment strategies in a former iodine-deficient area, which will be very important for clinical practice.

Material and Methods

Study Design and Patient Selection

In this study, a total number of 195 patients with thyrotoxicosis who had been admitted to Karadeniz University Endocrinology outpatient clinics were evaluated. The patient's demographic characteristics, symptoms, and signs were questioned. Thyroid function tests, antithyroid and antithyroid receptor antibodies, and routine thyroid ultrasonography were obtained, and thyroid scintigraphy or radioactive iodine uptake test was performed on need. Treatment choice, medical care, and post-treatment problems were also assessed.

Patients over 18 years old who received a de novo thyrotoxicosis diagnosis were included in the study. In comparison, patients under 18 years old, pregnant patients, and patients who had received treatment for thyrotoxicosis previously were excluded. The characteristics of the patients with thyrotoxicosis who were followed up in this study were recorded, including age, sex, clinical symptoms, physical examination findings, diagnosis techniques (laboratory values, imaging methods), treatment options, treatment side effects, and treatment outcomes.

The study was performed according to the principles of the Declaration of Helsinki as revised in 1983 and approval was obtained by the Ethics Committee of Karadeniz University Medical Faculty. The permission has been granted by Karadeniz University Medical Faculty of Ethics Committee via the resolution dated 18.11.2014 and no. 2014/81. All participants in the study obtained informed consent before entering the study.

Biochemical Analysis

TSH, free triiodothyronine (FT3), free thyroxine (FT4), anti-thyroglobulin (Anti-Tg), and anti-thyroid peroxidase (Anti-TPO) analyses were performed by using Beckman Coulter DX1-800 (Minnesota, USA) device. Biochemistry analyses Alanine aminotransferase (ALT), Aspartate aminotransferase (AST), albumin, glucose, sodium, potassium, calcium, phosphorus, cholesterol, Low-density lipoprotein-cholesterol (LDL-C), triglyceride) were measured by the Beckman Coulter AU-5800 (Shizuoka, Japan) autoanalyzer. The whole blood count was performed by using Beckman Coulter LH-780. TSH receptor antibody (TRAb) analysis has been determined via an immunoassay kit at Anka laboratory. TRAb levels were performed following kit protocol.

Ultrasound Evaluation of Thyroid Gland

Thyroid gland ultrasound assessment was performed using ToshibaAplio 500 Series No: 00134z04 Version of the software: AB V5.00*R204.

Scintigraphic Evaluation

Scintigraphic evaluation of the patients was performed via Scintigraphy Siemens E. Cam Signature Serie Series No:9231.

Statistical Analysis

All data were analyzed using IBM SPSS Statistics for Windows (version 20.0; Chicago, IL). The distribution of variables was assessed using Kolmogorov-Smirnov test. Data were expressed as the normal distribution's mean ± standard deviation (SD). One-way ANOVA test was carried out for normal distribution followed by the Bonferroni post-hoc test and the Kruskal-Wallis test for non-normal distribution followed by the Mann Whitney U post-hoc test among groups. Correlation coefficients and statistical significance were evaluated using Spearman's correlation test. $p < 0.05$ were considered as statistically significant.

Results

The demographic properties and clinical diagnoses of all patients with thyrotoxicosis are given in Table 1. The patients with thyrotoxicosis were identified to have TMNG:100 (51%), GD:73 (37%), TNG:14 (7%), subacute granulomatous thyroiditis:4 (2%), Hashimoto's disease with Hashitoxicosis:2 (1%), subacute lymphocytic thyroiditis:2 (1%). GD was primarily observed in younger cases, whereas TNG and TMNG were observed mainly in the elderly. The mean age of the GD group was 36.9±13.5, while this was 64.08±14.5 in the patients with TMNG (p=0.0001).

Table 1. Demographic characteristics and clinical diagnosis of thyrotoxicosis patients

		N	%
Age	Male	74	37.9
	Female	121	62.1
Symtoms/Signs	Palpitation	78	%40
	Weight Loss	67	%34.4
	Sweating	49	%25.1
	Shaking Hands	40	%20.5
	Irritability	38	%19.5
	Insomnia	14	%7.2
	Hair loss	14	%7.2
	Diarrhea Complaint	6	% 3.1
	Palpable Goiter	32	%16.4
	Exophthalmos	23	%11.8
	HT	18	%9.2
	Tachycardia	22	%11.3
Accompanying Diesases	Hypertension	23	%11.7
	Diabetes Mellitus	14	%7
	Osteoporosis	10	%5

N: Number

The most common accompanying medical conditions of patients were hypertension (11.7%), diabetes mellitus (7%), and osteoporosis (5%). When the patient symptoms were questioned, the most common complaints were palpitation (40%), weight loss (34.4%), sweating (25.1%), hand tremors (20.5%), irritability (19.5%), insomnia (7.2%), alopecia (7.2%) and diarrhea (3.1%). The patients' physical examination results revealed palpable goiter (16.4%), hypertension (9.2%), tachycardia (11.3%), and exophthalmos (11.8).

A comparison of biochemical values between patient groups with TMNG, TNG, and GD is shown in Table 2.

Table 2: Comparison of biochemical values of patients with TMNG, TNG and GD

	Thyrotoxicosis (N=195)	TMNG (N=100)	TNG (N=14)	GD (N=73)	p
TSH (µIU/mL)	0.062±0.09	0.077±0.081	0.090±0.080	0.032±0.033[a,b]	0.0001*
FT4 (ng/dL)	2.21±1.41	1.55±0.726	1.72±1.27	3.18±1.60 [a, b]	0.0001*
FT3 (pg/mL)	7.11±6.05	4.16±1.54	4.94±2.03	11.4±7.61 [a, b]	0.0001*
Anti Tg (IU/ml)	91.1±278	11.9±5.95	79.4±50.5	199±48.7 [a, b]	0.0001*
Anti TPO (IU/ml)	101±214	10.9±4.61	36.7±29.9	257±38.2 [a, b]	0.0001*
TRAb (U/l)	49.32±70.5	8.55±8.26	6.54±4.94	61.1±75.9 [a, b]	0.0001*
Haemoglobin(Hb) (mg/dL)	13.3±1.70	13.3±1.50	13.9±1.63	13.3±1.87	0.406
MCV (fL)	84.68±7.60	86.9±5.79	83.9±15.7	82.5±6.57 [a]	0.0001
MCH (pg)	28.2±2.53	28.8±2.17	28.9±2.30	27.5±2.69 [a]	0.002
MPV (fL)	8.85±1.3	8.92±1.35	8.74±1.66	8.81±1.29	0.794
Glucose (mg/dL)	104.3±33	109±37.2	106±46.0	98.4±23.2	0.132
Sodium (mEq/L)	138±2.4	139±2.55	139±2.17	138±2.17	0.466
Potassium (mEq/L)	4.41±0.44	4.41±0.435	4.51±0.428	4.31±0.327	0.095
Calcium (mg/dL)	9.5±0.51	9.49±0.501	9.50±0.406	9.57±0.414	0.519
Phosphorus (mg/dL)	3.6±0.83	3.52±0.838	3.26±0.366	3.79±0.813 [b]	0.022
Albumin (mg/dL)	4.1±0.4	4.02±0.468	4.13±0.360	4.19±0.352 [a]	0.028
ALT (U/L)	21.7±13.4	18.0±10.6	19.0±11.3	27.4±15.5 [a]	0.0001
AST (U/L)	22.9±7.5	21.8±6.08	21±6.08	24.8±8.90 [a]	0.018
LDL-C(mg/dL)	149±82.5	131±43.1	135±51.2	113±38.5 [a]	0.013
TG(mg/dL)	47.0±10.3	148±81.8	185±143	141±67.1	0.200

P values according to One way ANOVA test, post hoc Bonferroni test.
*P values according to Kruskal-Wallis test, post hoc Mann Whitney U test.
a; Significantly different from TMNG.
b; Significantly different from TNG.
Data were expressed as mean ± SD.

ALT and AST values of the patients with thyrotoxicosis were 21.7±13.4 and 22.9±7.5 U/L, respectively. It was determined that hemoglobin (Hb) levels anemia (Hb<12 mg/dL) was found in 36 patients (18.5%), and the mean Hb value was found to be 13.3±1.70 mg/dL. The values for mean corpuscular volume (MCV), mean corpuscular hemoglobin (MCH) and mean platelet volume (MPV) were 84.68±7.60 fL, 28.2±2.53 pg, and 8.85±1.3 fL, respectively. Lipid levels were high in 87 patients (44.6%). The sodium, potassium, calcium, and phosphorus values were found to be 138±2.4 mEq/L, 4.41±0.44 mEq/L, 9.5±0.51 mg/dL, and 3.6±0.83 mg/dL, respectively. When the glucose values were examined, the glucose values of 140 patients were within the normal range, while 40 patients had impaired fasting glucose and 15 had diabetes. The mean glucose level was found to be 104.3±33 mg/dL. While 180 patients' albumin levels were normal, 15 were low; the mean albumin value was 4.1±0.4 mg/dL. The mean TSH level was 0.062±0.09 IU/mL, the FT3 level was 7.11±6.05 pg/mL, and the FT4 level was 2.21±1.41 ng/dL. The mean TRAb was found to be 49.32±70.5 U/L. TRAb values were measured to be above average (>14 U/L) in 55 patients and above 100 U/L in 35 patients.

Comparing the MCV and MCH values in patients with TMNG, TNG, and GD, a statistically significant difference was observed between the TMNG and GD groups, both lower in the GD group (p=0.0001, p=0.002, respectively). ALT and AST levels were higher in patients with GD compared with the TMNG patients group, although in the normal range (p=0.0001, p=0.018, respectively). LDL levels were lower in GD patients, statistically significant between GD and TMNG groups (p=0.013). The group of patients with TMNG had lower albumin values than the GD group (p=0.028). When the average TSH, FT3, and FT4 values of patients with TMNG, TNG, and GD were compared, a statistically significant difference was observed for all, with FT3 and FT4 being significantly higher and TSH being significantly lower in the GD group compared with TMNG and TNG groups. There was no significant difference regarding other biochemical parameters.

The relationship of TSH, FT3, and FT4 with Anti-TPO and Anti-Tg levels are shown in Table 3.

Anti-TPO levels were compared with TSH, TRab, sT3, and sT4 levels, and there happened to be a statistically significant correlation of Anti-TPO with FT3 and FT4 levels (p=0.0001). While 40% of patients with normal Anti-TPO values had high levels of TRAb, 74.5% of patients with high Anti-TPO values had high levels of TRAb. There is also a statistically significant correlation of Anti-Tg with FT3 and FT4 levels (p=0.0001). Anti-Tg levels were positively correlated with TRab. A negative, weak correlation was found between TRAb and TSH (rho:-0.283 p=0.007). A positive correlation was observed between FT3-TRAb (rho:0.418, p=0.0001) and between FT4-TRAb (rho:0.332, p=0.001).

Table 3. TSH, sT3, sT4 relationship between Anti-TPO and Anti-Tg levels in patients with thyrotoxicosis

		Anti TPO (-) N=125 rho	P- value	Anti TPO (+) N=70 rho	P- value
	TSH	-0.187	0.013	-0.128	0.075
N=95	FT3	0.472	0.0001	0.466	0.0001
	FT4	0.415	0.0001	0.391	0.0001
		Anti TPO (-)		Anti TPO (+)	
		N=35		N=55	
N=90	TRAb	0.400	0.0001	0.331	0.001
		Anti Tg (-)		Anti Tg (+)	p value
		N=145		N=50	
	TSH	0.012	0.869	0.008	0.907
N=95	FT3	0.325	0.0001	0.331	0.0001
	FT4	0.245	0.001	0.256	0.0001
		Anti Tg (-)		Anti Tg (+)	
		N=54		N=36	
N=90	TRAb	0.257	0.014	0.188	0.078

p and rho values according to Spearman tests. N:number

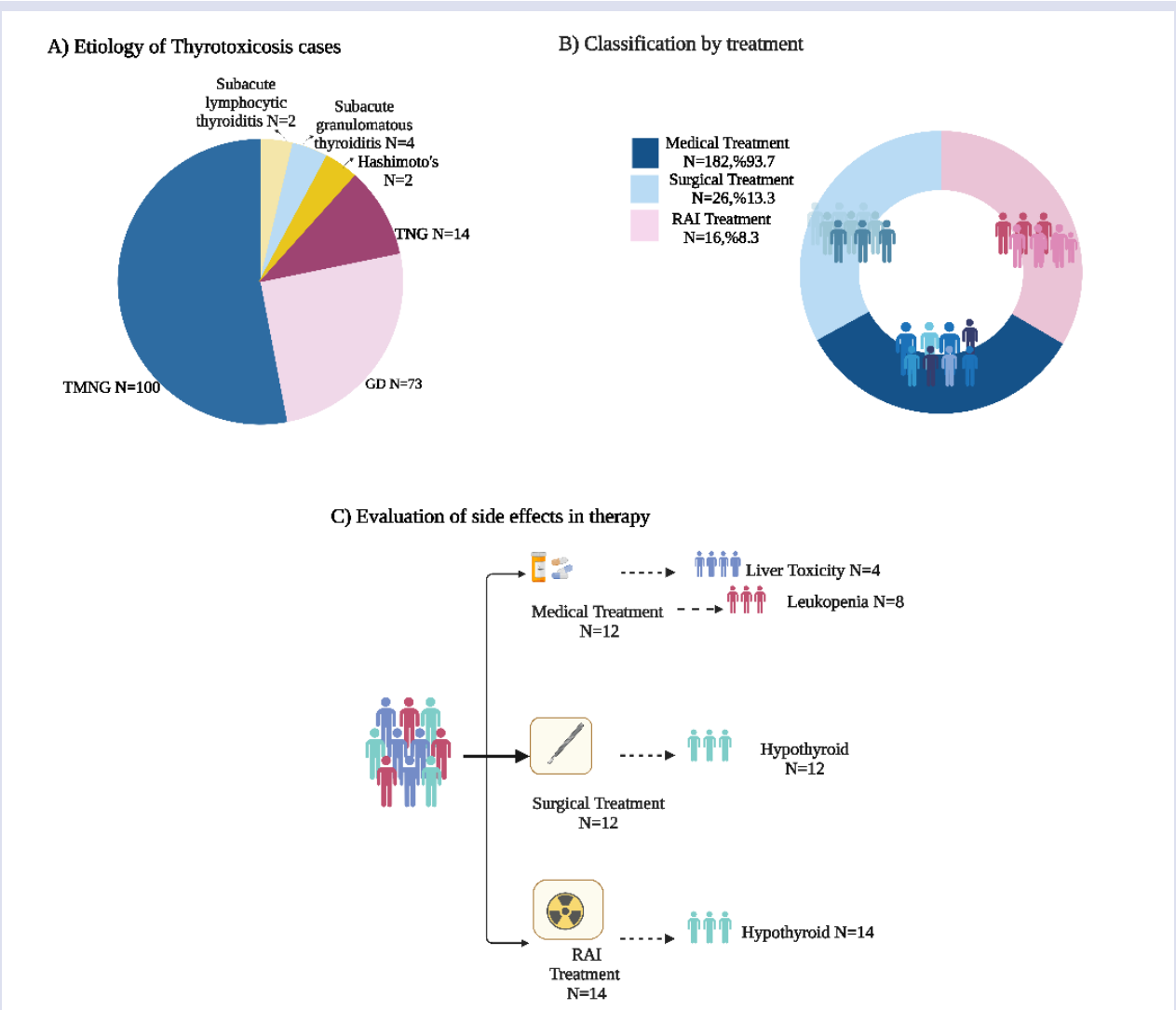

Figure 1. A) Etiology of Thyrotoxicosis cases, B) Classification by treatment, C) Evaluation of side effects in treatment

The etiology of thyrotoxicosis cases, the classification according to treatment and the side effects that occurred in the patients receiving treatment are shown in Figure 1. A total number of 182 patients received medical therapy (93.7%), 16 (8.3%) received surgical treatment, and 26 patients received radioactive iodine (RAI) therapy (13.3). Propylthiouracil (PTU) in 54 patients and methimazole (MMI) in 128 patients were used as a medical treatment agent. Leukopenia (6 patients) and elevation of liver function tests (3 patients) were observed in 9 cases

(16.7%) who received PTU. In contrast, one case experienced elevated liver enzymes, and two patients developed leukopenia in the MMI group (2%). In total, 12 (75%) of the 16 patients who had undergone surgical treatment developed hypothyroidism during the post-op period, while only 14 (53.8%) of the 26 patients who had undergone RAI treatment experienced hypothyroidism

Discussion

Thyrotoxicosis is a significant health issue that is more prevalent in women than men [11]. It is frequently observed in the elderly, Caucasians, and regions with iodine deficiency [3]. GD most frequently causes thyrotoxicosis; in areas with adequate iodine intake, GD causes 80% of thyrotoxicosis, while TNG-dependent hyperthyroidism occurs at a rate of 50% in areas with an iodine deficit [4]. The diagnosis of thyrotoxicosis is obtained through a careful clinical examination and the appropriate laboratory and imaging techniques [6]. The treatment options for hyperthyroidism include surgery, antithyroid medication, and radioactive iodine; however, the clinical profile of the patient and readily available therapy options determine a treatment strategy [12].

In this prospective study, we analyzed the causes of thyrotoxicosis, clinical features, and treatment strategies in a former iodine-deficient area. A total number of 195 patients with thyrotoxicosis were examined. Surprisingly, TMNG was still the leading cause, affecting 51% of patients, while GD was only apparent in 37%; TNG was the third common cause, affecting 7% of the patients. As expected, female patients took the lead with 62% while male patients were only 38% with an overall mean age of 52.3 ±.19.1. Considering the age distribution, GD claimed the top spot in the younger patients group, while TMNG was the leading cause in the older.

The finding of a higher prevalence of TMNG compared to GD amongst thyrotoxicosis cases should have resulted from endemic iodine deficiency in the Eastern Black Sea Region. It was much earlier established by a study by Kologlu et al. in 1966 in the Black Sea region when iodine levels in food and water were low [13]. The overall prevalence of goiter had been calculated as 30.5% by palpation in a national survey conducted by Urgancıoglu and Hatemi in 1987, being most prominent in the Black Sea region [14]. In a comparative study by Erdogan et al., they measured sonographic thyroid volumes (STV) and urinary iodine concentrations (UIC) in 1226 school-age children (SAC) (9–11 years old) from Ankara, located in central Anatolia and three highly endemic goiter areas of the Black Sea region on of them being Trabzon. A considerable number of school-age children (SAC) were found to have STV exceeding the recommended upper normal limits for their age and gender obtained from iodine-replete European children (26.7, 40.3, 44.8 and 51.7% of children from Ankara, Kastamonu, Bayburt, and Trabzon respectively). UIC indicated moderate to severe ID in these areas with median concentrations of 25.5, 30.5, 16.0, and 14 µg/L, respectively. This study showed severe to moderate ID as the primary etiological factor for the goiter endemic observed in Ankara and the Black Sea region of Turkey, with goiter prevalence and iodine deficiency being most prominent in the Trabzon region [15].

According to research released by the WHO in 2007, the average person should excrete between 100-199 g/L of iodine through their urine. Furthermore, in endemic goiter etiology, selenium deficiency, other goitrogenic factors affecting iodine bioavailability, dietary habits, and soil structure should be considered in endemic goiter etiology [16].

Legislation for mandatory iodization of household salt in Turkey was passed in July 1999. The overall scenery before the legislation was again established by another study by Erdogan et al., which ascertained the prevalence of goiter and iodine nutrition in school-age children (SAC) living in known endemic areas of Turkey. Sonographic thyroid volumes (STV) and urinary iodine concentrations (UIC) of 5.948 SAC from 20 cities were measured between 1997 and 1999. STV of 31.8% of the SAC examined stayed above the upper-normal limits for the same age and gender recommended by the World Health Organization (WHO). Goiter prevalence ranged between 5 and 56%, and median UIC ranged between 14 and 78 microg/l, indicating severe to moderate ID in 14 and mild ID in 6 surveyed cities. Both of the cities were found to have insufficient median UIC levels. That study showed that endemic goiter was an essential public health problem and iodine nutrition was inadequate nationwide [17].

Subsequent studies by Erdogan et al. revealed a significant reduction in iodine deficiency in Turkey. In 2007, moderate to severe ID was still prevalent in 27.8% of the population, a marked improvement from the 1997 and 2002 surveys of the same group (58% and 38.9%, respectively). The follow-up monitoring study showed that ID had been eliminated in 20 of 30 cities surveyed, with a median UIC of 130 µg/l. This progress, while significant, also highlighted the ongoing challenge of addressing iodine deficiency in rural areas and specific geographical regions [18].

In a subsequent study by Koçak et al. in the Trabzon region, it was found that the mean urine iodine excretion was 122.79 µg/L, males had a urine iodine level of 124.52 g/L, while females had 121.20 g/L, being quite similar by the study of Erdogan et al. The range of urinary iodine excretion was still below 100 µg/L in 37% of participants. The median UIE value in subjects with goiter was 122.78 lg/L and 122.80 lg/L in those without being not statistically significant. Iodized salt was used by 98.5 % of participants, while only 0.24 % of all subjects in the study used iodine-free salt, and 1.24 % used other salts. Koçak et al. stated that the province of Trabzon's urine iodine excretion largely complies with WHO standards [19].

However, a novel study performed in Turkey demonstrated a different dilemma for older subjects. In a senior group with a mean age of 70.9 years, the mean urinary iodine concentration was 98 µg/L. Goiter was found in 18.2% of women, 6.7% of men, and 43.8% of men

had nodules. Overt hyperthyroidism was present in 0.8%, T3 thyrotoxicosis in 0.3%, and subclinical hyperthyroidism in 2.2%. Toxic multinodular goiter and toxic adenoma caused 80% of hyperthyroidism cases. After the iodization of table salt, iodine levels have not yet reached favorable levels in older people. Iodization of salt seems insufficient to achieve these levels in older people for whom alternative iodine supplementation should be considered [20].

As previously stated, the pathogenesis of thyrotoxicosis is proposed to be associated with the receptor activation caused by a somatic mutation that has occurred in the thyroid-stimulating hormone receptor (TSHR) gene and with cyclic adenosine monophosphate (cAMP) upregulation [8]. In the study by Gozu et al. performed in Turkey in TNG and TMNG patients, TSHR mutations were identified in 70.2% of 74 toxic thyroid nodules (TTN). A Gs alpha mutation was identified in one TTN, and three new TSHR mutations were detected (A627V, I640K, I486N). However, there was no significant difference between frequencies of TSHR mutations in iodine deficient/sufficient regions. The frequency of non-random X-chromosome inactivation was similar in iodine-sufficient or -deficient regions and TSHR mutation-positive or negative hot nodules [21]. These findings suggest that TTNs in iodine deficient/sufficient areas predominantly arise from aberrant growth of a single cell, and they suggested that neither the prevalence of TSHR mutations nor that of monoclonal TTNs is related to iodine supply.

The most common symptoms in patients with thyrotoxicosis are palpitation, weight loss, sweating, irritability, heat intolerance, hand tremors, menstrual irregularity, and diarrhea. The patients mainly complained about palpitation at a rate of 40% and weight loss at 34.4%. A similar study by Esen et al. performed in Turkish children found that the most common presenting features were tachycardia and palpitations, weight loss, and excessive sweating, which were quite similar to our adult population [22]. In our study, goiter, thyroid nodules, hypertension, tachycardia, and exophthalmos are the most typical signs we observed in patients with thyrotoxicosis. Exophthalmos occurs at a rate of 11.8%; GD findings are observed to be less common because TMNG is the more common cause in the Black Sea region. According to the literature, an average of 20-50% of ophthalmopathy in GD was reported as 40% in the study by Burch et al. [23], and Bartley GB et al. found it 62% [24].

Graves' disease is diagnosed using TSH, sT3, sT4, Anti-Tg, anti-TPO, and TRAb. According to the literature, the TRAb test, in particular, is recommended in differential diagnosis. A study stated that the TRAb test has a 98% specificity and 99% sensitivity for diagnosing GD [25]. Another study found that the TRAb test had a 99.6% specificity and a 98.8% sensitivity [26]. According to two studies, the TRAb positivity rate in GD is 88.2% [27] and 80% [28]. In a study performed in the UK, the specificity of the TRAb test was once more emphasized, and in patients with GD, a correlation between the degree of thyrotoxicosis and the TRAb value was found [29]. Regarding thyroid antibodies' role in diagnosing GD, it is remarkable that anti-TPO has been found positive at 74% [30] and anti-Tg positivity at 53% in another study [27]. According to our research, the TRAb, anti-TPO, and anti-Tg positive percentages in GD were 75.3%, 71.2%, and 49.3%, respectively.

In this study, we also assessed the liver function tests in the patients diagnosed with thyrotoxicosis. Of the 195 patients whose ALT-AST values were tested, we found that the ALT value was above average in 11 (5.6%) of them, while the AST value was higher than usual in 13 (6.7%). The rate of abnormal liver function tests reported in the literature is 15 to 76% for different series [31, 32].

Anemia was identified in 36 (18.5%) of 195 patients. The literature states that erythrocyte mass has increased in hyperthyroid individuals; however, due to various metabolic factors, the erythrocyte lifecycle has been reduced, resulting in a fall in Hb and hematocrit values [33]. Omar S et al. reported that 40.9% of the patients had anemia, a strong association between erythrocyte count and hemoglobin level, and anemia was treated to improve the condition [34]. On the other hand, Hambsch K et al. showed that 38% of the patients had normochromic normocytic anemia [35].

When 195 patients diagnosed with thyrotoxicosis were examined, it was determined that 182 (93.7%) of them had received anti-thyroid medical treatment, 16 (8.3%) had undergone surgery, and 26 (13.3%) received RAI treatment. In the studies performed, it was stated that the medical treatment should be the first-line treatment, with methimazole being the first option [36,37]. The incidence of hypothyroidism after surgical therapy is higher than the rate of hypothyroidism after RAI. We assessed the incidence of hypothyroidism after surgery and after RAI. Following surgical therapy, hypothyroidism incidence was found to be 75%, while post-RAI hypothyroidism incidence was reported to be 53.8%. Therefore, it was determined that hypothyroidism developed in most of the patients who received surgical treatment and in some of the patients who received RAI treatment. According to the literature, research performed in Turkey found that 16.9% of patients developed hypothyroidism after a year of receiving RAI [38], and another study found that around 50% of patients developed hypothyroidism within ten years [39]. This rate is 67.9% after a year in another study [40]. This discrepancy is assumed to be caused by the treatment dose given, the length of the post-treatment follow-up period for RAI, and the operation technique.

Conclusion

Based on the study's findings, a fundamental prediction was ensured regarding the diagnosis of thyrotoxicosis patients, the clinical picture they would present, the therapy they will receive, the early

identification of post-operative problems, and the changing biochemical parameters.

Conflicts of interest

There are no conflicts of interest in this work.

References

[1] Sharma A., Stan M.N., Thyrotoxicosis: Diagnosis and Management, *Mayo Clin. Proc.*, 94(6) (2019) 1048-1064.

[2] Brent G.A., Clinical practice. Graves' disease, *N Engl J Med*, 358 (2008) 2594-2605.

[3] Golden S.H., Robinson K.A., Saldanha I., Anton B., Ladenson P.W., Prevalence and incidence of endocrine and metabolic disorders in the United States: a comprehensive review, *J. Clin. Endocrinol. Metab.*, 94(6) (2009) 1853-1878.

[4] Laurberg P., Pedersen I. B., Knudse, N., Ovesen, L., Andersen S., Environmental iodine intake affects the type of nonmalignant thyroid disease, *Thyroid*, 11(5) (2001) 457-469.

[5] Schwartz F., Bergmann N., Zerahn B., Faber J., Incidence rate of symptomatic painless thyroiditis presenting with thyrotoxicosis in Denmark as evaluated by consecutive thyroid scintigraphies, *Scand J. Clin. Lab. Invest..*, 73(3) (2013) 240-244.

[6] Weetman A.P., Graves' disease, *N Engl J Med*, 343 (2000) 1236-1248.

[7] Morshed S.A., Davies T.F., Graves' Disease Mechanisms: The Role of Stimulating, Blocking, and Cleavage Region TSH Receptor Antibodies,. *Horm. Metab. Res.*, 47(10) (2015) 727-734.

[8] Tonacchera M., Agretti P., Chiovato L., Rosellini V., Ceccarini G., Perri A., et al., Activating thyrotropin receptor mutations are present in nonadenomatous hyperfunctioning nodules of toxic or autonomous multinodular goiter*, J. Clin. Endocrinol. Metab.*, 85(6) (2000) 2270-2274.

[9] Davies T. F. and Larsen, P.R., Thyrotoxicosis. Williams Textbook of Endocrinology, 10th edition, Saunders, Philadelphia, (2003) 374-422.

[10] Boelaert K., Torlinska B., Holder R. L., Franklyn J. A. Older subjects with hyperthyroidism present with a paucity of symptoms and signs: a large cross-sectional study, *J. Clin. Endocrinol. Metab.*, 95(6) (2010) 2715-2726.

[11] Vaidya B., Pearce S.H., Diagnosis and management of thyrotoxicosis, *BMJ*, 349 (2014).

[12] Schneider D. F., Sonderman P. E., Jones M. F., Ojomo K. A., Chen H., Jaume J. C., et al., Failure of radioactive iodine in the treatment of hyperthyroidism, *Ann. Surg. Oncol.*, 21 (2014). 4174-4180.

[13] Kologlu S., Kologlu B., Su ve gıda maddeleri ile vücuda giren günlük iyod miktarı (Daily iodide intake by water and nutrients). *AU Tip Fak. Mec.*, 19(3) (1966) 372.

[14] Urgancıoglu I., Hatemi H., Türkiye'de Endemik Guatr (Endemic goiter in Turkey), *İstanbul: Cerrahpaşa Tıp Fak. Nükleer Tıp ABD Yayın*, (1989) 14.

[15] Erdogan G., Erdoğan M. F., Delange F., Sav H., Güllü S., Kamel N., Moderate to severe iodine deficiency in three endemic goitre areas from the Black Sea region and the capital of Turkey, *Eur. J. Epidemiol*,16 (2000). 1131-1134.

[16] World Health Organization. Assessment of iodine deficiency disorders and monitoring their elimination A Guide For Program Managers. 2007. Available at: https://www.who.int/publications/i/item/9789241595827.

[17] Erdogan G., Erdoğan M. F., Emral R., Baştemir M., Sav H., Haznedaroğlu D.,et al., Iodine status and goiter prevalence in Turkey before mandatory iodization, *J. Endocrinol Invest.*, 25 (2002) 224-228.

[18] Erdoğan M. F., Ağbaht K., Altunsu T., Özbaş S., Yücesan F., Tezel B., et al., Current iodine status in Turkey, *J. Endocrinol. Invest.*, 32 (2009) 617-622.

[19] Kocak M., Erem C., Deger O., Topbas M., Ersoz H. O., Can E., Current prevalence of goiter determined by ultrasonography and associated risk factors in a formerly iodine-deficient area of Turkey, *Endocrine*, 47 (2014) 290-298.

[20] Atmiş V., Bulbul B., Bahsi R., Gumussoy M., Yalçin A., Dogan Z., et al., Iodine concentration and prevalence of thyroid disease in older people after salt iodization in Turkey, *East Mediterr. Health J.*, 27(2) (2021) 151-158.

[21] 5Gozu H. I., Bircan R., Krohn K., Müller S., Vural S., Gezen C.,et al.,Similar prevalence of somatic TSH receptor and Gsα mutations in toxic thyroid nodules in geographical regions with different iodine supply in Turkey, *Eur. J. Endocrinol.*,155(4) (2006) 535-545.

[22] Esen I., Bayramoğlu E., Yıldız M., Aydın M., Özturhan E. K., Aycan Z., et al., Management of thyrotoxicosis in children and adolescents: a Turkish multi-center experience, *J. Clin. Res. Pediatr. Endocrinol.*, 11(2) (2019) 164-172.

[23] Burch H.B., Wartofsky L., Graves' ophthalmopathy: current concepts regarding pathogenesis and management, *Endocr. Rev.*, 14(6) (1993) 747-793.

[24] Bartley G. B., Fatourechi V., Kadrmas E. F., Jacobsen S. J., Ilstrup D. M., Garrity J. A., Gorman C. A., Clinical features of Graves' ophthalmopathy in an incidence cohort, *Am. J. Ophthalmol.*, 121(3) (1996) 284-290.

[25] Paunkovic N., Paunkovic J., The diagnostic criteria of graves diseas and especially the thyrotropin reseptör antibody, our own experience, *Hell J. Nucl. Med.*, 10(2) (2007) 89-94.

[26] Costagliola S., Morgenthaler N. G., Hoermann R., Badenhoop K., Struck J., Freitag D., et al., Second generation assay for thyrotropin receptor antibodies has superior diagnostic sensitivity for Graves' disease, *J. Clin. Endocrinol. Metab.*, 84(1) (1999) 90-97.

[27] Zingrillo M., D'Aloiso L., Ghiggi M. R., Di Cerbo A., Chiodini I., Torlontano M., Liuzzi A. Thyroid hypoechogenicity after methimazole withdrawal in Graves' disease: a useful index for predicting recurrence?, *Clin. Endocrinol.*, 45(2) (1996) 201-206.

[28] Gauna A., Segura G., Sartorio G., Soto, R., Segal-Eiras A., Immunological aspects of Graves' disease patients in different clinical stages, *J. Endocrinol. Invest.*, 12 (1989) 671-677.

[29] Myint K. S., Andappa G. S., MacFarlane I., Gurnell M., Wood D., Chatterjee K., et al., Use of anti thyroid hormone receptor antibody (TRAB) in Graves' Disease, *Endocrine*, 13 (2007) 81.

[30] Mariotti S., Caturegli P., Piccolo P., Barbesino G., Pinchera A., Antithyroid peroxidase autoantibodies in thyroid diseases, *J. Clin. Endocrinol. Metab*., 71(3) (1990) 661-669.

[31] Fong T.L., McHutchison J.G., Reynolds T.B., Hyperthyroidism and hepatic dysfunction. A case series analysis, *J. Clin. Gastroenterol.*, 14(3) (1992) 240-244.

[32] Huang M.J., Li K.L., Wei J.S., Wu S.S., Fan K.D., Liaw Y.F., Sequential liver and bone biochemical changes in hyperthyroidism: prospective controlled follow- up study, *Am J. Gastroenterol.,* 89(7) (1994) 1071-1076.

[33] Ford H.C, Carter J.M., The haematology of hyperthyroidism: abnormalities of erythrocytes, leucocytes, thrombocytes and haemostasis, *Postgrad Med. J.*, 64(756) (1988) 735-742.

[34] Omar S., Kanoun F., Hammami M. B., Kamoun S., Romdhane B., Feki M., et al., Erythrocyte abnormalities in thyroid dysfunction. *La Tunis Med.*, 88(11) (2010) 783-788.

[35] Hambsch K, Fischer H, Langpeter D, Müller P, Hyperthyroidism and anemia. *Zeitschrift fur die Gesamte Innere Medizin und Ihre Grenzgebiete* 36(6) (1981) 203-208.

[36] Franklyn J.A., Boelaert K., Thyrotoxicosis, *Lancet*, 379 (2012) 1155-1166.

[37] Gilbert J., Thyrotoxicosis – investigation and management, *Clin. Med. (Lond),* 17(3) (2017) 274–277.

[38] Dokmetas H.S., Erselcan T., Yüksel I., Ataseven H., Dogan, D., Koyuncu A., Yönem Ö., Hipertiroidizmi Olan Hastalarımızda Radyoaktif İyot Tedavisinin Sonuçları (Results of radio active iodine treatment in patients with hyperthyroidism), *Cerrahpaşa Üniv. Tıp Fak. Derg*., 23(3) (2001) 121-125.

[39] Farrar J.J., Toft A.D., Iodine-131 treatment of hyperthyroidism: current issues, *Clin. Endocrinol.*, 35(3) (1991) 207-212.

[40] Ghadban W. K., Zirie M. A., Al-Khateeb D. A., Jayyousi A. A., Mobayedh H. M., Ahmed S., Radioiodine treatment of hyperthyroidism, *Saudi Med. J.*, 24(4) (2003) 347-351.

Cumhuriyet Sci. J., 45(2) (2024) 299-308
DOI: https://doi.org/10.17776/csj.1440382

Cumhuriyet Science Journal

| csj.cumhuriyet.edu.tr | Founded: 2002 ISSN: 2587-2680 e-ISSN: 2587-246X Publisher: Sivas Cumhuriyet University

Chlorogenic Acid: HPLC Quantification and In Vitro Assessment of Proliferative and Migration Effects on Human Dermal Fibroblast Cells

Abdulbaki Akpınar [1,a,*], Fatma Demirkaya Miloğlu[2,b], Gülşah Gündoğdu[3,c], Leyla Güven [4,d], Burak Bayrak [2,e], Yücel Kadıoğlu [2,f]

[1] *Department of Pharmacy Services, Inebolu Vocational School, Kastamonu University, Türkiye.*
[2] *Department of Analytical Chemistry, Faculty of Pharmacy, Ataturk University, Türkiye.*
[3] *Department of Physiology, Faculty of Medicine, Pamukkale University, Türkiye.*
[4] *Department of Pharmaceutical Botany, Faculty of Pharmacy, Atatürk University, Türkiye.*
**Corresponding author*

Research Article

History
Received: 20/02/2023
Accepted: 21/06/2024

ABSTRACT

Chlorogenic acid (CA) exhibits diverse biological activities, including antioxidant and antiinflammatory effects. This research aims to develop, optimize, and validate an HPLC method to quantify CA in methanol and investigate its *in vitro* proliferative and cell migration effects on human-dermal-fibroblast (HDF) cell lines in a dose-dependent manner. The HPLC experimental conditions were optimized using the central composite design (CCD) method for determining CA. Chromatographic separation occurred at a wavelength of 330 nm. Under the optimized conditions, the method exhibited linearity across a concentration range of 0.1-100 µg/mL, demonstrating sensitivity (LOQ:0.1µg/mL), precision (RSD%≤3.32), and accuracy (RE%≤4.05). To evaluate the in vitro proliferative and cell migration effects on HDFs, we employed the XTT cell proliferation assay and TAS-TOS commercial kits. The XTT assay revealed that CA displayed a proliferative effect within the concentration range of 75-250 µM (P <0.01), and at a concentration of 125 µM, TAS levels increased significantly (P<0.05). The scratch assay demonstrated that HDF cell migration increased at 12 h, with substantial closure of the wound area at 24 h when treated with CA concentrations between 75-125 µM. The results demonstrate that pure chlorogenic acid extracted from plants exhibits dose-dependent effects on cell proliferation, antioxidant, and cell migration.

Keywords: Chlorogenic acid, HPLC, Experimental design, Central composite design, Proliferative and migration effects.

[a] *abakiakpinar@kastamonu.edu.tr* *https://orcid.org/0000-0001-7318-6529*
[b] *fdkaya@atauni.edu.tr* *https://orcid.org/0000-0001-5729-7181*
[c] *ggundogdu@pau.edu.tr* *https://orcid.org/0000-0002-9924-5176*
[d] *leyla.guven@atauni.edu.tr* *https://orcid.org/0000-0002-3189-6415*
[e] *burak.bayrak@atauni.edu.tr* *https://orcid.org/0000-0001-6550-6916*
[f] *yucel@atauni.edu.tr* *https://orcid.org/0000-0001-6590-7306*

Introduction

Phenolic acids have recently played an important role in human health due to their various pharmacological and biological effects. Additionally, chlorogenic acid (CA), one of the polyphenols found in large amounts in the human diet, is found in large amounts in foods, certain plant species, fruits, and coffee types, especially in green coffee [1]. CA [1,3,4,5-Tetrahydroxycyclohexanecarboxylic acid 3-(3,4-Dihydroxycinnamate], named 5-O-caffeoylquinic acid (5-CQA) by the International Union of Pure and Applied Chemistry (IUPAC), is an ester from the hydroxycinnamic acid family (Figure 1).

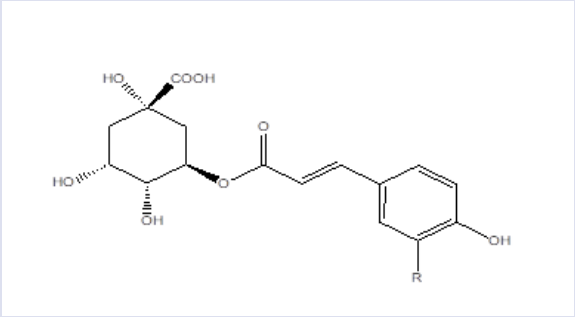

Figure 1. Structure of Chlorogenic Acid

It has been reported that CA has an antimicrobial effect against various bacteria and antifungal effect against *Candida albicans*, and it has been found that it is suitable as an ideal preservative and food additive with these properties. It has been reported that, similar to other phenolic acids, OH groups and numbers on CA positively affect antioxidant activity. In addition, it has been reported that CA, interleukin-8 (IL-8), and mRNA expression significantly inhibit their secretion due to oxidative stress. Thus, it is a compound with antioxidant and antiinflammatory potential [2]. In addition, it has antibacterial, antiviral, antifungal, antidiabetic, and anticarcinogenic properties [3-5]. Furthermore, it was observed that chronic use of CA in high doses for a long time increased the lipid peroxidation level of liver and kidney samples without affecting the heart and muscle tissue [6,7]. Therefore, it is crucial to determine the amount of CA in plants and foods containing CA. Obviously, a simple and rapid analytical method is needed for the routine measurement of this substance. A review of the literature reveals numerous analytical methods, such as high-performance liquid chromatography (HPLC) with UV detection, employed to determine chlorogenic acid (CA), the primary phenolic acid, in different *Helichrysum* species [8-10], other plants [11], and various foods, particularly coffee [12, 13], following diverse

extraction processes [14-17]. In many HPLC methods for CA determination, separation is achieved by adding acid to the mobile phase [8-13]. Researchers commonly reported that the peak area, retention times, and peak resolution of CA are significantly influenced by the mobile phase solvent ratio and acid percentage in HPLC analysis. Typically, single-factor optimization, lacking interactions between factors, was employed, which was time-consuming and necessitated numerous experiments to determine the optimal level for each factor. Currently, green analytical chemistry is a prominent topic in analytical chemistry, focusing on environmentally friendly approaches to enhance the quality of analytical results [18]. Chemometric techniques, incorporating experimental design and principles of green analytical chemistry (such as reducing interferences of the analyzed substance and using fewer chemicals and time while maintaining acceptable accuracy and precision), have been recently applied to determine experimental conditions in chemistry. The application of the CCD method allowed for the simultaneous determination of various parameters with their interrelation [19].

Wound healing is a complex process that includes hemostasis, inflammation, cell proliferation, extracellular matrix synthesis, and remodeling. Different factors are involved in regulating and controlling these phases [20]. Therefore, when investigating the sufficient attributes for wound healing, it is evident that cell proliferation and cell migration are particularly effective on the wound. This is because wounds cannot be successfully repaired without an adequate level of cell division [21]. Therefore, the substance used as a wound healer should affect the factors that play an essential role in wound healing (inflammatory cells, platelets, cytokines, extracellular matrix, etc.). In addition, it should shorten the duration of these periods and provide ideal neovascularization and scar tissue formation [22]. Antioxidants and antiseptics are used to increase the number of fibroblast cells in wound healing. The wound is cleansed in the fibrin matrix by the release of oxygen radicals, which kill the invading foreign organisms. This accelerates the healing process. Fibroblasts play an essential role in wound healing. They initiate the proliferative repair phase. Today, to accelerate and regulate wound healing, studies on the use of many medical and traditional drugs are still being carried out, and new products are being researched. In this context, the studies conducted on CA showed that it has different pharmacological effects containing antimicrobial, anti-inflammatory, and antioxidant properties ([11], [23-25])

In an *in vivo* study evaluating the effectiveness of CA on wound healing, it was reported that CA has a high wound healing capacity due to its potent antioxidant capacity and accelerates the wound healing process by increasing collagen synthesis in different phases of wound healing [6]. Another study stated that CA increased glutathione, catalase, and superoxide dismutase and decreased lipid peroxidation, thus having strong antioxidant activity. It has been shown that CA increases the wound healing process by increasing collagen synthesis and antioxidant activity through TNF-α and TGF-β upregulation during wound healing [7]. However, there is no study of an *in vitro* dose-dependent proliferative and cell migration effects on the HDF cell line of CA.

Therefore, this study aims to develop an optimized HPLC method using CCD, an experimental design method, and investigate the effects of CA on proliferation, oxidative stress, and *in vitro* cell migration using HDF cell line.

Materials and Methods

Reagents

CA was procured from Sigma (USA). Methanol (HPLC grade) and acetonitrile (HPLC grade) were supplied by Merck (Germany), while analytical grade orthophosphoric acid (OPA) was acquired from Sigma–Aldrich (USA). A Milli-Q system (Thermo Scientific, USA) was used to obtain ultrapure water. ATCC® PCS-201-012™ was used as Adult HDFa. The commercial TAS-TOS kits were obtained from REELASSAY (Turkey). XTT kits, Dulbecco's modified Eagle's medium (DMEM), fetal bovine serum (FBS), dimethyl sulfoxide (DMSO), phosphate buffer (PBS), L-glutamine, Pen-strep solution, and trypsin-EDTA were provided by Sigma (USA).

HPLC Method

Preparation of Stock, Working, and Quality Control Solutions of Chlorogenic Acid

Stock solutions of CA were prepared with methanol at a 10 mg/mL concentration. Working solutions (WC; 0.1, 0.5, 1, 2.5, 5, 10, 20, 40, 60, 80, and 100 µg/mL) and quality control (QC; 0.5, 10, and 80 µg/mL) solutions for CA were prepared in acetonitrile. All solutions were stored at +4°C pending analysis.

Optimization of Mobile Phases in HPLC Analysis by Central Composite Design (CCD)

In the central composite design (chemometric experimental design method, CCD), the percentage concentration of acetonitrile (A), which is effective in obtaining the highest peak area and the most regular peak shape in HPLC analysis, and the percentage concentration of OPA in water (B) were selected as significant factors of CCD in the mobile phase for the determination of CA. The A and B factor ranges were 30%-95% and 0.01%-0.5%, respectively. CA solutions (10 µg/mL) were prepared to monitor the response variables.

HPLC Apparatus and Analytical Conditions

An Agilent 1200 Series HPLC instrument was equipped with a G1311A/Quat Pump, and a G1314B/VWD detector was used. Chromatographic separation was achieved on a BRISA LC2 C18 column (250 × 4.6 mm, 5-µm particle size). Isocratic elution with a mobile phase consisting of acetonitrile and water containing 0.2% OPA (95:5 v/v) was used for HPLC analysis. The detection wavelength was set at 330 nm. Chromatographic separation was performed at

a 7 min run time using a 1 mL/min flow rate, 10 µL injection volume and ambient column temperature.

Cell Culture Experiments

The medium used in the cell culture study to be carried out in *in vitro* environments should contain the necessary substances suitable for cell growth, survival, and proliferation. Therefore, this study used DMEM containing 10% FBS, 2 mM L-glutamine, 20 IU/mL penicillin, and 20 mg/mL streptomycin to grow HDFs. Routine cell culture steps such as thawing, propagation, passaging, and freezing of the cells were performed on HDFs.

XTT Assay for Chlorogenic Acid

Cell viability was determined by inducing the effect of CA on cell proliferation using the XTT kit. HDF cells (10000/well) were seeded into 96-well plates, and then these cells were incubated under 5% CO_2 for 24 h at 37°C and grown to 80% confluence. Cell counts were made in all experimental steps to ensure experimental standardization. The cells were treated with control (C; untreated cells), 0.5% DMSO, and CA (final concentration 10-1000 µM in each well) dissolved in 0.5% DMSO culture media and incubated under 5% CO_2 for 24 h and 48 h at 37°C to determine a dose-dependent manner. After cultivation for 24 h and 48 h, XTT reagent solution was added to the medium as recommended by the manufacturer, followed by the measurement of absorbance at 450 nm with a correction wavelength of 630 nm in a microplate reader.

Determination of Total Oxidant Status (TOS) and Total Antioxidant Status (TAS)

TOS and TAS of CA were determined with commercial kits according to methods developed by Erel [26]. First, HDFs (10000/well) were seeded in 96-well plates and incubated under 5% CO2 for 24 h at 37°C. After that, 10, 25, 50, 75, 100, 125, 250, 500, and 1000 µM concentrations of CA in HDF cells were added and incubated for 24 and 48 h. After incubation, supernatants of HDF cells were separated (number of repetitions: 3) and stored at -20°C until analysis.

TOS analysis: The method measures the color intensity in the presence of oxidants in samples with spectrophotometry. For this purpose, supernatants removed at 24 h and 48 h were analyzed as recommended by the manufacturer using the TOS commercial kit to determine the TOS levels of CA. The method was calibrated with H_2O. The method's precision was expressed as RSD% and found to be ≤ 2%. The obtained results are given in µmol H_2O_2 Equiv./L sample.

TAS analysis: The method is based on the OH* radicals produced by the Fenton reaction and its reaction with the colorless substrate O-dianisidine to produce dianisyl radicals by antioxidants in samples against potent free radical reactions. For this purpose, supernatants removed at 24 h and 48 h were analyzed as recommended by the manufacturer using a TAS commercial kit to determine the TAS of CA. The obtained results were given as µmol Trolox Equiv./L sample.

Scratch Assay

HDF cells were used for the *in vitro* wound healing model for cell migration by performing a scratch assay. HDF cells were seeded in 6-well plates (3×10^5 cells/well) and incubated until 100% confluence was achieved in DMEM solution (containing 10% FBS, 1% penicillin–streptomycin, and 1% L-glutamine) under 5% CO_2 at 37°C. Later, the scratch was formed in one direction of approximately the same size using a micropipette tip (0.1-10 µL). Then, the floating cells and the medium were exchanged with fresh medium. Different concentrations of CA (containing 10, 25, 50, 75, 100, 125, 250, and 500 µM concentrations) were added to each well, and the microscopic image was monitored with an inverted fluorescence microscope (Leica, ebq 100-04, Germany) at 0, 12, 18, and 24 h. The experiment was terminated when cell migration was completed entirely in one group [26].

Statistical Analyses

Experimental design and statistical analyses (one-way ANOVA with Tukey's post hoc test) were performed using Design-Expert8.0 (Stat-Ease Inc., Minneapolis, MN, USA) and SPSS 20 (SPSS, Chicago, IL, USA) software, respectively. *P* values<0.05 were taken into consideration to indicate statistical significance.

Results

Chlorogenic Acid Analysis with HPLC

Optimization of HPLC Analysis with the CCD Method:

CA was prepared at a 10 µg/mL concentration by dilution with acetonitrile. Chromatographic separation was achieved on a C18 (250x4.6 mm, 5 µm) column at 330 nm. To determine the mobile phase composition consisting of acetonitrile, water, and OPA%, the CCD method was applied to determine the percentages of acetonitrile (A %) and OPA in water (OPA %), which were selected as mobile phase components in the HPLC method. The ranges of the A and B factors are specified in Section 2.3. The peak area of CA (10 µg/mL) was monitored as a response variable, and 13 different experiments were carried out. The peak area of CA experimentally determined from CCD is shown by the response surface curve (three-dimensional graph) (Figure 2A). Experimental data were placed on the response surface to obtain optimum conditions. The resulting quadratic regression model is shown below with coded terms:

$$RF = 301.96 – 22.80A -43.34B + 8.58\ AB-11.81\ B -31.81B$$

where RF is the response factor corresponding to the peak area of CA. A and B factors. According to the parameters obtained from the ANOVA statistical method

for the model, the *P* value was 0.0057. Since this *P* value was significant at < 0.05, the A and B factors significantly affected the peak area of CA. The coordinates producing the maximum desirability were A: 95% and B: 0.2%. The predicted response peak areas from the numerical optimization are 319.52. Experiments (n=10) were performed to compare the point predicted values with the experimental results, and the response peak area values were recorded. Based on the predicted outcome, the mean recovery of the obtained results was calculated as 100.26 ± 0.8023%. In all HPLC conditions mentioned above, CA showed a retention time of 2.7 min with a maximum peak at 330 nm (Figure 2B).

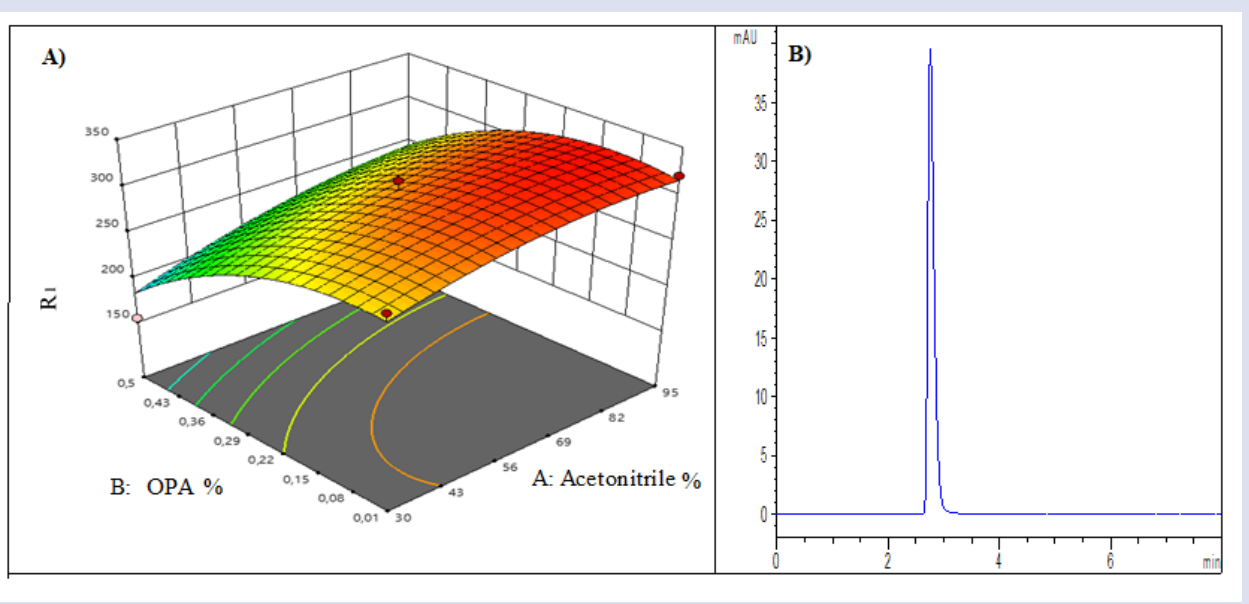

Figure 2. A) Three-dimensional plot of the response surface for peak area (R1) shown as a function of A and B. B) HPLC chromatogram of CA (10 µg/mL)

HPLC Method Validation: The calibration curve was obtained by plotting the peak areas and CA concentrations. The equations for calibration curves in the 0.1-100 µg/mL concentration range for determination of CA were obtained by:

PA = 32.421x – 8.530 (Sa: 0.325, Sb: 0.068 and R^2 = 0.9999; n: 6)

where PA is the peak area of CA, Sa is the standard deviation of the shift in the calibration curve, Sb is the standard deviation of the slope in the calibration curve, and R is the correlation coefficient.

The method precision and accuracy were determined by analyzing the QC samples (0.5, 10, and 80 ng/mL) with intraday (6 times per day) and interday (6 times once daily for 6 days) measurements. The method's precision was given as the relative standard deviation (RSD %: (standard deviation/mean) × 100), and it was < 3.320%. The accuracy of the method was given as relative error (RE %: [(found concentration-known concentration)/known concentration × 100] and found to be less than ± 4.052 (Table 1). With acceptable values, the method is accurate and precise for the determination of CA.

Table 1. Precision and accuracy of CA using the proposed method.

Added (µg/mL)	Intraday			Interday		
	Found ± SD (µg/mL)	Accuracy (RE)	Precision (RSD %)	Found±SD (µg/mL)	Accuracy (RE)	Precision (RSD %)
0.5	0.479± 0.016	-4.052	3.320	0.501± 0.009	0.191	1.806
10	9.970± 0.283	1.129	2.835	10.018±0.023	1.605	0.232
80	79.887± 1.191	-0.165	1.491	80.047±0.741	0.068	0.925

SD: standard deviation (n=6). RE: relative error, RSD: relative standard deviation.

The limits of detection (LOD) and the limit of quantification (LOQ) were calculated as 3xσ (standard deviation of y-intercepts)/S (slope of the calibration curve) and 10xσ/S and found to be 0.031 µg/mL and 0.1 µg/mL, respectively.

The extraction recoveries of CA in the extracts of plants were determined using the standard addition method of QC samples (0.5, 10, and 80 µg/mL) to plant solution. All of the experiments were repeated six times. The quantification of CA was calculated by comparing the found and added concentrations in each case. The

obtained recovery results for 0.5, 10, and 80 µg/mL CA were 99.85%, 101.04%, and 100.56%, respectively, and showed the good accuracy of the HPLC method.

To determine the stability of the stock and calibration solutions of CA during the study, the QC solutions of CA were kept at +24°C, at 6, 24, and 48 h at +4°C, analyzed at the end of these periods, and the recovery (%) was obtained by comparison with the immediately measured values. ±10 values were determined as the acceptance criteria. According to these criteria, CA was stable for at least 6 h at +24°C and at least 48 h at +4°C.

To showcase the suitability of the established method for plant samples, the developed and validated HPLC method was utilized to quantify chlorogenic acid (CA) isolated from the capitulum of *H. plicatum subsp. pseudoplicatum* plant using methanol. For this investigation, the extracted sample weighing 1 mg was diluted to 500 µg extract/mL (n:10) and subsequently analyzed with the developed and validated method. The relative quantity of CA was determined to be 9.770 ± 1.818 µg/mg extract.

Cell Culture Experiments for for Chlorogenic Acid

XTT Analysis Results for Proliferative Effect: The effects of CA on HDF cell proliferation were studied using the XTT assay. Figure 3 shows the XTT results obtained at between 10-1000 µM concentrations of CA in HDF cells at 24 and 48 h. We found that CA concentrations in a dose range of 75-250 µM have a significantly positive proliferative effect on HDF cells compared to control (untreated cells) at 24 and 48 h (P<0.01).

TOS-TAS Level Results for Oxidative Stress Activities: The effects of CA on oxidative stress were determined in HDFs using the TAS-TOS commercial assay. Figures 4 and 5 show the effects of CA at concentrations between 10-1000 µM on oxidative stress in HDF cells obtained after 24 and 48 h of incubation. It was determined that the TOS of CA decreased in HDF cells treated with 75-125 µM concentrations compared to the C group (untreated cells) at both 24 and 48 h (Figure 4). However, this decrease was not statistically significant (P > 0.05). The obtained TOS results were in line with our XTT results. It was determined that the TOS of CA at high concentrations increased while causing the highest increase in cell viability.

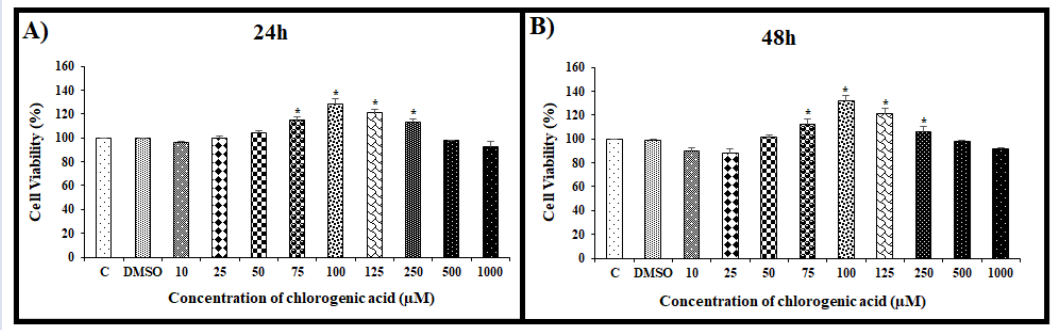

Figure 3: Proliferation effect obtained at different CA concentrations treated with HDF cells using XTT assay A) 24 h and B) 48 h (Results are given as the mean ± SD, n=8,*statistically significant compared with the control (untreated cells); C: control, DC: 0.5% DMSO (DMSO control)).

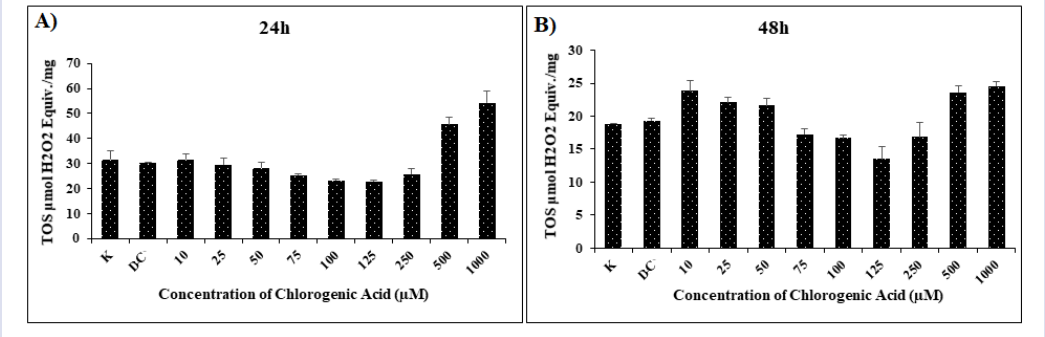

Figure 4: TOS levels of CA on HDF cells. A) 24 h and B) 48 h ((Results are given as the mean ± SD, n=8; C: control, DC: 0.5% DMSO))

The TAS of CA increased in HDF cells treated with 100-250 µM CA compared to the C group (untreated cells) at both 24 and 48 h (Figure 5). Only at 125 µM was the increase in CA statistically significant (P <0.05). Similar to the TOS results, the TAS results of CA were consistent with the XTT results. It was determined that 100-250 µM CA had the highest effect on cell viability and antioxidant capacity.

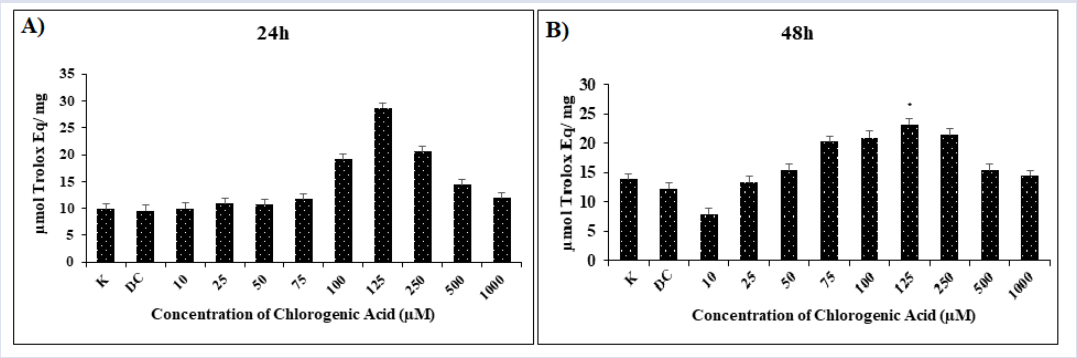

Figure 5: TAS levels of CA in HDF cells. A) 24 h and B) 48 h ((Results are given as the mean ± SD; n=8; *statistically significant compared with the control (untreated cells); C: control, DC: 0.5% DMSO).

Scratch Assay Results for Cell Migration Effects

In the current study, the effect of CA on cell migration was investigated in the range of 10-500 µM by using a starch assay test because it is toxic at concentrations above 500 µM according to XTT analysis. We found that CA had a dose-dependent effect on the HDF cell line.

We have demonstrated that CA at 50-250 µM concentrations had a stimulatory effect on cell migration, especially at 75-125 µM concentrations. CA increased cell migration at 12 h and significantly closed the wound area at 24 h (Figure 6). At the same time, it was determined that the cell migration results were parallel to the XTT results, and 75-125 µM CA had the strongest effect on cell viability and cell migration .

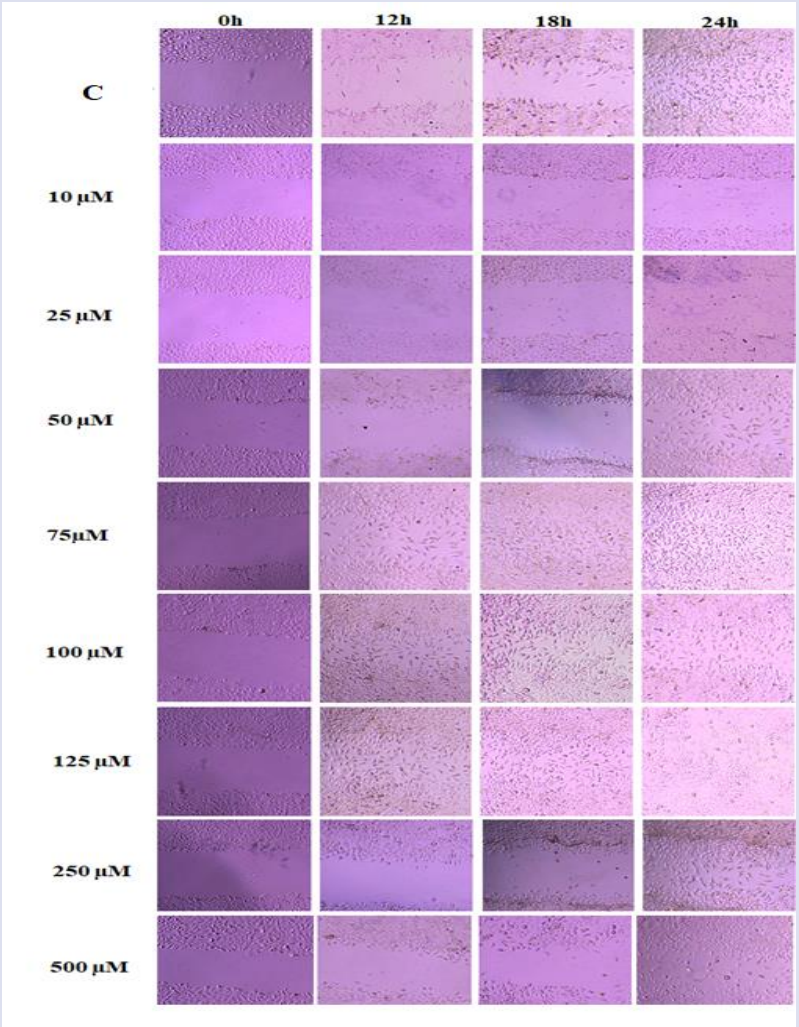

Figure 6. Photographs were taken at 0, 12, 18, and 24 hours by microscopy at 4× magnification to determine the effect of CA on HDF cell migration.

Discussion

In recent years, there has been an increasing focus on the study of phenolic compounds, which are vital bioactive compounds possessing various beneficial properties. Among these compounds, CA has garnered significant attention because it serves as the primary phenolic compound/metabolite present in plants and foods [27]. However, before recommending the traditional use of these bioactive compounds for wound healing, it is crucial to quantitatively determine their levels. While bioactive compounds undergo rigorous quality control, improper dosages may result in insufficient effects or even harmful consequences. Growing concerns about the potential carcinogenic effects of chemical preservatives in the food industry have spurred interest in natural and herbal alternatives. Natural antioxidants derived from various plants, which are well received by consumers, are preferred over synthetic chemical preservatives for food products. CA, in particular, stands out as an ideal natural and safe food additive due to its antioxidant properties [28, 29]. To harness the potential of plants as a source of CA, it is essential to optimize the isolation of CA from plant extracts, a task made possible through the selection of an appropriate analytical method. The HPLC method is widely used for the analysis of drug compounds, active components in plants, and residues in food [30]. Its broad applicability and effectiveness make it a valuable tool for these types of analyses. For quantitative determination of CA with the HPLC method, stock and dilution solutions of CA were prepared in water, acetonitrile, methanol or their different mixtures used in previous studies [8-13, 27, 31, 32]. To determine the solvent medium in which the CA chromatogram has the most regular and the highest peak in the HPLC. CA was prepared by dilution with the solvents mentioned above, and HPLC chromatograms were taken. Acetonitrile was selected as a solvent because CA was dissolved and achieved the highest peak. A C18 reversed-phase column was used for chromatographic separation of CA in HPLC studies in the literature for the determination of CA in food and plants and for good separation, 0.1% formic acid [13, 27, 31], 0.2% formic acid [8], 0.5% acetic acid [9], 0.1% acetic acid [10, 11], acetic acid [12], 0.05% trifluoroacetic acid [32], and 0.1% formic acid were added to the mobile phase, which usually contains acetonitrile or methanol and water. Experimental design methods determine the optimum experimental conditions by mathematical modeling. The CCD method is one of the experimental design methods. This method can determine the factors affecting the experiment and the interaction between experimental errors and optimum experimental conditions [33].

In our study, chromatographic separation was achieved on a C18 (250×4.6 mm, 5 µm) column at 330 nm, and different solvent mixtures of methanol-water and acetonitrile solvents as mobile phases were tried. The mobile phase mixture was selected as acetonitrile-water. It was stated that the mobile phase composition should be acidic to determine CA by the HPLC method. Preliminary experiments and prior knowledge of the literature were decisive for selecting these two parameters as significant. Therefore, OPA was added to water, one of the mobile phase components, to make the mobile phase acidic. At the end of 13 experiments with the CCD method, the selected parameters A% and OPA% were determined to be 9% and 0.2%, respectively, with the CCD method. Then, the optimization of the HPLC method was validated with different validation parameters following ICH Q2B guidance [33]. The validation study supported the HPLC method conditions by confirming that the assay was linear, specific, sensitive, accurate, and precise. The developed, optimized and validated HPLC method was demonstrated to be applicable by determining the amount of CA in the selected *H. plicatum subsp. pseudoplicatum* plant with capitulums. It can be easily applied to both plant and food samples if a suitable extraction process is found depending on the matrix.

Plants and food have had an important place in human life in terms of improving health since ancient times. Wound healing is characterized by epithelial, endothelial, inflammatory cells, platelets, and fibroblasts coming together and performing their normal functions in a particular order [35]. Plants and food contain antifungal, antibacterial, and bioactive antioxidant compounds, which provide coagulation, inflammation, collagen production, epithelial formation, and wound healing properties [34]. Bağdaş et al. [6] investigated the potential role of CA treatment on wound healing and oxidative stress markers and whether the treatment has side effects on vital organs and bone marrow using an experimental wound model *in vivo*. CA as IP at various doses was applied and showed that CA treatment accelerated wound healing. CA decreased malondialdehyde (MDA) and nitric oxide (NO) levels in the wound area, increased glutathione (GSH), superoxide dismutase (SOD) and catalase (CAT) levels, and increased hydroxyproline content in the scar tissue. It was concluded that CA treatment accelerated wound healing by increasing antioxidant defense. In addition, it has been shown that long-term high-dose chronic use of CA may cause side effects due to its pro-oxidant effect on the liver, kidney, and bone marrow. In another study, the effects of topical CA treatment on wound healing were investigated by Chen et al. [7], and it was found that CA caused a significant increase in wound contraction. The study showed that CA has potent antioxidant activity by increasing superoxide dismutase, catalase, and glutathione and decreasing lipid peroxidation. It causes upregulation of TNF-α and TGF-β levels in the inflammatory phase of wound healing (12-72 hours). It was concluded that it increases the wound healing process by increasing collagen synthesis and antioxidant activity through TNF-α and TGF-β upregulation. Antioxidant and antiseptic agents used in wound healing treatment cause an increase in the number of fibroblast cells. Because the release of oxygen radicals kills invading foreign organisms and the wound in the fibrin matrix is cleaned. In other words, it accelerates the

healing process. In this context, fibroblasts, which initiate the proliferative repair phase, have an important role in wound healing [11,25].

Various *in vitro* wound healing models utilizing cell lines and methods derived from human or murine (rodent) keratinocyte and fibroblast cells have been employed to explore potential therapeutic agents [36]. For instance, Moghadam et al. [37] demonstrated the wound-healing effect of *Parrotia persica* extract, which contains chlorogenic acid and myricetin-3-O-β-rhamnoside, using normal human keratinocyte and HDF cell lines *in vitro*. Similarly, Alexandru et al. [38] investigated the wound-healing activity of plant extracts containing polyphenols, such as chlorogenic acid, caffeic acid, luteolin, and apigenin, on L929 fibroblast cells. They observed an increase in collagen synthesis and antioxidant activity. Several studies have shown the *in vitro* wound healing and antioxidant activity of various plant extracts containing chlorogenic acid. However, the efficacy of CA isolated directly from the plant or pure CA remains unexplored. Additionally, a few studies have demonstrated the antioxidant and wound healing efficacy of CA *in vivo*. The scratch assay using an HDF cell line is one of the most commonly used wound models for cell migration in cell culture studies [39,40].

Nevertheless, the specific proliferative and migration properties of CA using human dermal fibroblast cells and its antioxidant activity using TAS-TOS have not been adequately explored in the literature.

In this line, our study evaluated the proliferative effect on cell viability with the XTT test after 24 and 48 incubations using various concentrations of CA (final concentration of 10-1000 µM in each well). The XTT results showed that CA had a significant dose-dependent proliferative effect in the dose range of 75-250 µM (Figure 3).

Since measuring oxidant species with different properties is expensive, time-consuming, and requires intensive labor, it is preferred to measure TAS-TOS, a reliable and sensitive method that researchers can easily apply in recent years with a short duration and high linearity. Therefore, in our study, the efficacy of CA on oxidative stress was evaluated using the TAS-TOS kit. It was observed that they have a dose-dependent antioxidant effect, similar to the literature [6, 7]. Additionally, CA significantly increased TAS compared with the control group, especially at 100-250 µM (Figure 5). These results were found to be compatible with the XTT results.

The effects of CA on *in vitro* cell migration were evaluated using the *scratch* assay. Our study found that CA increased cell migration at 50-250 µM, especially at 75-125 µM. CA increases cell migration at 12 h and significantly closes the wound area at 24 h. CA has the most substantial effect on cell viability, antioxidant effect, and *in vitro* cell migration effects, especially at concentrations of 75-125 µM. It has been shown that the cell migration effect of CA may depend on its antioxidant effect in a dose-dependent manner. In this study, we observed that the proliferative, antioxidant, and cell migration activities of CA exhibit dose dependency, and all these activities are evident within the same dose range. Consequently, it was hypothesized that the cell migration effect of CA is directly influenced by its antioxidant properties, as the observed effects seem to correlate with the varying doses applied.

Conclusion

This study aimed to develop and optimise an HPLC method using a central composite design (CCD) approach for the quantitative analysis of chlorogenic acid (CA). The method was carefully validated for accuracy, precision and sensitivity, establishing it as a robust tool for the determination of pure CA concentrations in isolated from *H. plicatum subsp. pseudoplicatum*. In addition, we investigated the dose-dependent effects of CA on cell proliferation and migration in HDF cell lines, highlighting its potential therapeutic applications in wound healing and tissue regeneration. The results of this research span analytical chemistry and pharmacology, providing a reliable means of quantifying CA and uncovering significant biological activities, laying the groundwork for future studies to explore the full therapeutic potential of CA.

Moving forward, it is recommended that future research focus on elucidating the specific mechanisms of action of CA, conducting clinical trials to validate its efficacy, and optimising its application in clinical settings.

Conflict of Interest

There is no conflict of interest among the authors.

Acknowledgement

We gratefully thank Prof. Dr. A.M.Abd El- Aty for editing this manuscript.

References

[1] Kremr D., Bajer T., Bajerová P., Surmová S., Ventura K., Unremitting problems with chlorogenic acid nomenclature: A

[2] Review, *Química Nova.*, 39 (2016) 530-533.

[3] Naveed M., Hejazi V., Abbas M., Kamboh A.A., Khan G.J., Shumzaid M., XiaoHui Z., Chlorogenic acid (CGA): A pharmacological review and call for further research, *Biomedicine & pharmacotherapy.*, 97 (2018) 67-74.

[4] Budama-Kılınç Y., Klorojenik Asit Yüklü PLGA Nanopartiküllerinin Üretimi ve Antimikrobiyal Etkinliğinin Belirlenmesi, *Türk Mikrobiyoloji Cemiyeti Dergisi.,* 49(1) (2019) 47-54.

[5] Feng R., Lu Y., Bowman L.L., Qian,Y., Castranova V., Ding M., Inhibition of activator protein-1, NF-κB, and MAPKs and induction of phase 2 detoxifying enzyme activity by chlorogenic acid, *Journal of Biological* Chemistry., 280 (2005) 27888-27895.

[6] Zhong C., Wall N.R., Zu Y., Sui G., Therapeutic application of natural medicine monomers in cancer treatment, *Current Medicinal Chemistry.*, 24(34) (2017) 3681-3697.

[7] Bagdas D., Gul N.Y., Topal A., Tas S., Ozyigit M.O., Cinkilic N., Gurun M.S., Pharmacologic overview of systemic chlorogenic acid therapy on experimental wound healing, *Naunyn-Schmiedeberg's archives of pharmacology.*, 387 (2014) 1101-1116.

[8] Chen W.C., Liou S.S., Tzeng T.F., Lee S.L., Liu I.M., Effect of topical application of chlorogenic acid on excision wound healing in rats, *Planta medica.*, (2013) 616-621.

[9] Chaowuttikul C., Palanuvej C., Ruangrungsi N., Quantification of chlorogenic acid, rosmarinic acid, and caffeic acid contents in selected Thai medicinal plants using RP-HPLC-DAD, *Brazilian Journal of Pharmaceutical Sciences.*, 56 (2020) e17547.

[10] Kolaylı S., Şahin H., Ulusoy E., Tarhan Ö., Phenolic composition and antioxidant capacities of *Helichrysum* plicatum, *Hacettepe Journal of Biology and Chemistry.*, 38(4) (2010) 269-276.

[11] Albayrak S., Aksoy A., Sagdic O., Hamzaoglu E.,Compositions, antioxidant and antimicrobial activities of *Helichrysum* (Asteraceae) species collected from Turkey, *Food chemistry.*, 119(1) (2010) 114-122.

[12] Albayrak S., Aksoy A., Sağdıç O., Budak Ü., Phenolic compounds and antioxidant and antimicrobial properties of *Helichrysum* species collected from eastern Anatolia, Turkey,*Turkish Journal of Biology.*, 34(4) (2010) 463-473.

[13] Ayelign A., Sabally K., Determination of chlorogenic acids (CGA) in coffee beans using HPLC, *American Journal of Research Communication.*, 1(2) (2013) 78-91.

[14] De Luca S., Ciotoli E., Biancolillo A., Bucci R., Magrì A.D.,Marini F., Simultaneous quantification of caffeine and chlorogenic acid in coffee green beans and varietal classification of the samples by HPLC-DAD coupled with chemometrics, *Environmental Science and Pollution Research.*, 25 (2018) 28748-28759.

[15] Li H., Chen B., Yao S., Application of ultrasonic technique for extracting chlorogenic acid from Eucommia ulmodies Oliv.(E. ulmodies), *Ultrasonics sonochemistry.*, 12(4) (2005) 295-300.

[16] Zhang B., Yang R., Liu C.Z., Microwave-assisted extraction of chlorogenic acid from flower buds of Lonicera japonica Thunb, *Separation and Purification Technology.*, 62(2) (2008) 480-483.

[17] Mullen W., Nemzer B., Ou B., Stalmach A., Hunter J., Clifford M.N., Combet E., The antioxidant and chlorogenic acid profiles of whole coffee fruits are influenced by the extraction procedures, *Journal of agricultural and food chemistry.*, 59(8) (2011) 3754-3762.

[18] Tan Z., Wang C., Yi Y., Wang H., Li M., Zhou W., Li F., Extraction and purification of chlorogenic acid from ramie (Boehmeria nivea L. Gaud) leaf using an ethanol/salt aqueous two-phase system, *Separation and Purification Technology.*, 132 (2014) 396-400.

[19] Płotka J., Tobiszewski M., Sulej A.M., Kupska M., Górecki T., Namieśnik J., Green chromatography, *Journal of Chromatography A.*, 1307 (2013) 1-20.

[20] Demirkaya-Miloglu F., Yaman M. E., Kadioglu Y., Optimization of a spectrofluorimetric method based on a central composite design for the determination of potassium losartan in pharmaceutical products, *Brazilian Journal of Pharmaceutical Sciences.*, 50 (2014) 611-619.

[21] Theoret C.L., Update on wound repair, *Clinical Techniques in Equine Practice.*, 3(2) (2004) 110-122.

[22] Zanca A., Flegg J.A., Osborne J. M., Push or Pull? Cell Proliferation and Migration During Wound Healing, *Frontiers in Systems Biology.*, 2 (2022) 876075.

[23] Ayla Ş., Günal M.Y., Sayın Şakul A.A., Biçeroğlu Ö., Özdemir E.M., Okur M.E., Bilgiç B. E., Effects of Prunus spinosa L. fruits on experimental wound healing, *Medeniyet medical journal.*, 32(3) (2017).

[24] Bigović D., Šavikin K., Janković T., Menković N., Zdunić G., Stanojković T., Djurić Z., Antiradical and cytotoxic activity of different *Helichrysum* plicatum flower extracts, *Natural product communications.*, 6(6) (2011) 1934578X1100600617.

[25] Bigović D.J., Stević T.R., Janković T.R., Noveski N.B., Radanović D.S., Pljevljakušić D.S.,Djurić Z.R., Antimicrobial activity of *Helichrysum* plicatum DC, *HEMIJSKA INDUSTRIJA (Chemical Industry).,* 71(4) (2017) 337-342.

[26] Steenkamp V., Mathivha E., Gouws M.C., Van Rensburg C.E.J., Studies on antibacterial, antioxidant and fibroblast growth stimulation of wound healing remedies from South Africa, *Journal of ethnopharmacology.*, 95(2-3) (2004) 353-357.

[27] Erel O., A new automated colorimetric method for measuring total oxidant status, *Clinical biochemistry*, 38(12) (2005) 1103-1111.

[28] Pereira J.C., Paulino C.L.D.A., Granja B.D.S., Santana A.E.G., Endres L.,Souza R.C.D., Allelopathic potential and identification of secondary metabolites in extracts of Canavalia ensiformis L, *Revista Ceres.*, 65 (2018)243-252.

[29] Santana-Gálvez J., Cisneros-Zevallos L., Jacobo-Velázquez D.A.,Chlorogenic acid: Recent advances on its dual role as a food additive and a nutraceutical against metabolic syndrome, *Molecules.*, 22(3) (2017) 358.

[30] Rofouei M.K., Kojoori S.M.H.,Moazeni-Pourasil R.S., Optimization of chlorogenic acid extraction from Elm tree, Ulmus minor Mill., fruits, using response surface methodology,*Separation and Purification Technology.*, 256 (2021) 117773.

[31] Skoog D.A., Holler F.J., Crouch S.R., Principles of instrumental analysis, Cengage learning (2017).

[32] Gouveia S.C., Castilho P.C., Validation of a HPLC-DAD–ESI/MSn method for caffeoylquinic acids separation, quantification and identification in medicinal *Helichrysum* species from Macaronesia, *Food research international.*, 45(1) (2012) 362-368.

[33] Silva L., Rodrigues A.M., Ciriani M., Falé P.L.V., Teixeira V., Madeira P.,Serralheiro M.L.M., Antiacetylcholinesterase activity and docking studies with chlorogenic acid, cynarin and arzanol from *Helichrysum* stoechas (Lamiaceae), *Medicinal Chemistry Research.*, 26 (2017) 2942-2950.

[34] Dinç, E., Kemometri Çok Değişkenli Kalibrasyon Yöntemleri,*Hacettepe Üniversitesi, Eczacılık Fakültesi Dergisi.,* (2007) 61-92.

[35] Özkorkmaz E.G., Özay Y., Yara iyileşmesi ve yara iyileşmesinde kullanılan bazı bitkiler, *Türk Bilimsel Derlemeler Dergisi.*, (2) (2009) 63-67.

[36] Gundogdu G., Nalci K.A., Ugur Kaplan A.B., Gundogdu K., Demirci T., Demirkaya-Miloglu F., Cetin M.,The evaluation of the effects of nanoemulsion formulations containing boron and/or zinc on the wound healing in diabetic rats, *The International Journal of Lower Extremity Wounds.*, 21(4) (2022) 492-501.

[37] Villegas J., McPhaul M., Establishment and culture of human skin fibroblasts, *Current protocols in molecular biology.*, 71(1), (2005) 28-3.

[38] Moghadam S.E., Ebrahimi S. N., Salehi P., Moridi Farimani M., Hamburger M., Jabbarzadeh E., Wound healing

potential of chlorogenic acid and Myricetin-3-O-β-Rhamnoside isolated from Parrotia persica, *Molecules.*, 22(9) (2017) 1501.

[39] Alexandru V., Gaspar A., Savin S., Toma A., Tatia R., Gille E.,Phenolic content, antioxidant activity and effect on collagen synthesis of a traditional wound healing polyherbal formula, *Studia Universitatis" Vasile Goldis" Arad. Seria Stiintele Vietii (Life Sciences Series).*, 25(1) (2015) 41.

[40] Muniandy K., Gothai S., Tan W.S., Kumar S.S., Mohd Esa N., Chandramohan G., Arulselvan P., In vitro wound healing potential of stem extract of Alternanthera sessilis, *Evidence-based complementary and alternative medicine.*, (2018) 2018.

[41] Gundogdu G., Gundogdu K., Nalci K. A., Demirkaya A. K., Yılmaz Tascı S., Demirkaya Miloglu F., Hacimuftuoglu, A., The effect of parietin isolated from rheum ribes l on in vitro wound model using human dermal fibroblast cells, *The International Journal of Lower Extremity Wounds.*, 18(1) (2019) 56-64.

Cumhuriyet Sci. J., 45(2) (2024) 309-321
DOI: https://doi.org/10.17776/csj.1418035

Cumhuriyet Science Journal

| csj.cumhuriyet.edu.tr | Founded: 2002 ISSN: 2587-2680 e-ISSN: 2587-246X Publisher: Sivas Cumhuriyet University

Impact of Solar Cell Infrastructures on Energy Efficiency in Power Grid Integration

Derya Betul Unsal [1,2,3] *

[1] *Department of Electrical and Electronics Engineering, Sivas Cumhuriyet University, Sivas, Türkiye.*
[2] *Renewable Energy Research Center, Sivas Cumhuriyet University, Sivas, Türkiye.*
[3] *Sustainability Coordinating Office, Rectorate of Sivas Cumhuriyet University, Sivas, Türkiye.*
**Corresponding author*

Research Article

History
Received: 11/01/2024
Accepted: 24/06/2024

ABSTRACT

Photovoltaic technology harvest electrical energy by stimulating liberated electrons within the semiconductor layers using solar radiation. Photovoltaic technology produces electrical energy by collecting electrons that are liberated in a semiconductor pn-junction by solar radiation. Photovoltaic solar cells have layered semiconductor structures and this study utilised for this objective. Current researches on energy storage with solar cells, focused to optimise the utilisation of the generated energy with cell efficiency. This study offers a thorough analysis of the energy efficiency of solar cells based on their infrastructures. The study involved obtaining computational visuals and doing efficiency verification. This was done by comparing the impact of different chemical structures on energy production. The MATLAB software was used with fixed parameters and varying efficiency. The results show that the Monocrystalline N-Type IBC model exhibits the maximum efficiency in terms of PV cell structure. The MIBC structure is more efficient than polycrystalline cells and also standard monotypes with high temperatures. This allows the cell to reflect itself and passivise the cell base, resulting in a 5% or more increase in energy production. Standard monotype cell has %16.2 efficiency and Monotype IBC has %20.1 efficiency results achieved with PVsyst and Matlab softwares. The results of the calculations were applied in real time and confirmed by testing the impact of structural differences on efficiency with real climate data..

Keywords: Solar cell, Energy efficiency, Renewables integration, Power grid.

[a] *dbunsal@cumhuriyet.edu.tr* *https://orcid.org/0000-0002-7657-7581*

Introduction

Solar cells and photovoltaic (PV) systems have made significant progress in recent decades. Crystalline silicon accounted for 90% of the PV systems built worldwide in 2019 [1]. Nevertheless, inorganic structure as silicon solar cells have an inherent efficiency threshold of 29.4% [2], which contemporary cell technologies are rapidly nearing. An alternative solution to surpass this limitation is presented through the use of silicon-based tandem solar cells [3]. In order to enhance the conversion efficiency to above 30%, several novel cell designs that include silicon as the bottom cell are being examined.

Photovoltaic or solar cells are devices that directly convert solar energy into direct current (DC) electricity by using semiconductors like silicon, gallium, arsenide, cadmium telluride, or copper indium diselenide when exposed to sunlight. Solar cells typically have a square, rectangular, or circular shape with an area ranging from approximately 100 to 243 cm2 with a thickness between 0.2 and 0.4 mm [1-5]. The efficiency of single-junction solar cells varies between 5% and 25%, contingent upon their construction. Nevertheless, 0.5 Volt cells thus photovoltaic systems that include panels are constructed by connecting cells in series to provide higher voltage. int current (Immp) of a 6-inch (silicon?) crystalline cell is 7.83 Amperes, while the maximum power point voltage (Vmmp) averages at 0.49 Volts under an irradiance of 1000 Watts per square meter. A 6-inch cell measures 15.6 cm x 15.6 cm, whereas a 5-inch cell measures 12.5 cm x 12.5 cm [1, 6, 7].

Solar cell efficiency is the measure of the ability of a solar cell to convert solar light energy into electricity using photovoltaic technologies. The annual energy output of a photovoltaic system is determined by the efficiency of its solar cells, as well as factors such as density of energy and climate. For instance, when a solar panel with a 20% efficiency and a surface area of 1 m2 is subjected to 2.74 hours of sunlight per day at the 1000 W/m2 standard test condition, it will produce 200 kWh/year of energy under the same test conditions. Usually, solar panels receive sunshine for an extended duration throughout the day while the intensity of the sun's radiation remains below 1000W/m2 for the majority of the day. A solar panel's energy production is maximised when the sun is at a high position in the sky, as the light reaches the panel at a more perpendicular angle. Conversely, during overcast weather or when the sun is near the horizon, the panel's energy output decreases. In winter, the sun's position in the sky is more inclined towards the horizon. Within a remarkably productive solar area, like central Colorado, where there is an annual sunlight intensity of 2000 kWh/m2 [1], a solar panel of this kind is projected to produce approximately 400 kWh of energy annually. Nevertheless, in Michigan, where the energy availability is limited to 1400kWh/m2/year, the annual energy output for the

same panel will decrease to 280kWh. In contrast, the energy efficiency in the northern European suburbs is much reduced. For instance, in the South of England, it is possible to attain an annual energy efficiency of 175kWh under identical circumstances [2].

Figure 1 illustrates the temporal evolution of solar cell efficiency [3]. According to research conducted at the NREL laboratory, multijunction-type solar cells have recently achieved the greatest efficiency of 47%.

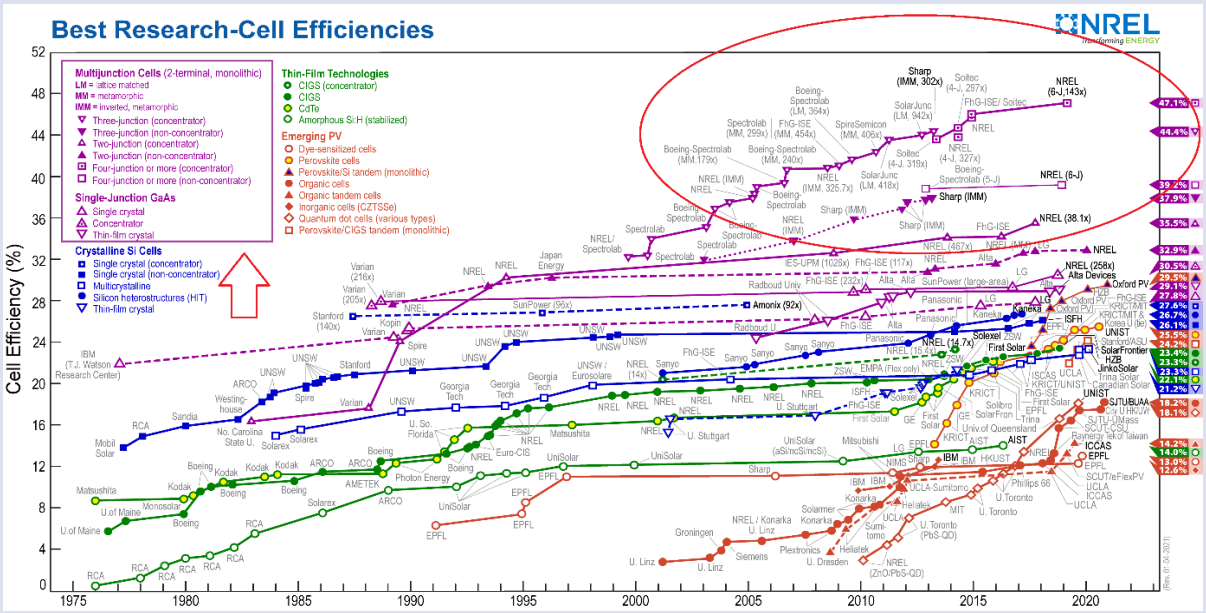

Figure 1. Temporal evolution of solar cell efficiency [3]

Currently, grid-connected systems have approved the use of 72-cell 24 Volt systems. The front side of these panels is coated with tempered glass, while the back surface is coated with a protective and water-resistant substance. Additionally, the corners and connection points are encapsulated. A panel array is formed by interconnecting panels either in parallel or in series, depending on the desired voltage or current specifications.

Edmund Becquerel discovered photo-electric effect in 1839, and Albert Einstein further developed it in 1905, earning him the Nobel Prize in physics that same year. He found that the voltage across electrodes submerged in electrolyte solution fluctuates in response to the intensity of light incident on the electrolyte. Adams and Day discovered a comparable occurrence on solid surfaces during their work on selenium crystallines in 1876. In subsequent years, light metres in the field of photography extensively utilised photodiodes constructed from copper oxide and selenium. In 1954, Chapin et.al. introduced Si crystalline cells and also panels with an efficiency of 6%. In subsequent years, photovoltaic technology was employed in spacecraft and is in a state of ongoing advancement at present [1–3, 8].

Enhancing the compatibility between the inverter and PV groups can augment the efficiency of the PV system. It is crucial to select an inverter that is appropriate for the nominal voltage operating range. When analysed based on the sorts of cells used, first, crystalline silicon cells were investigated. Monocrystalline solar cells and polycrystalline solar cells Polycrystalline band cells EFG, String Ribbon, Dentritic web, and Polycrystalline thin film cells are all types of solar cells manufactured by Apex. B-Thin cells made of amorphous silicon, copper-indium-diselenide (CIS), and cadmium telluride (CdTe) Microcrystalline and micromorphological cells [2, 4, 9–14].

Infrastructures of Solar Cells for panels are commonly used Crystalline and there exist two distinct categories of structures: Monocrystalline and Polycrystalline. Their mean life expectancy exceeds 20 years.

Monocrystalline Cells

The product excels in both quality and efficiency, however, its production entails significant time and technological challenges, resulting in relatively higher prices. It is a favorable choice for tasks that require a significant amount of time to complete. A monocrystalline cell is composed entirely of crystalline and possesses a uniform atomic structure, indicating homogeneity. In order to manufacture monocrystalline cells, silicon must possess a high level of purity. Consequently, their prices are exorbitant. To accomplish this, individual ingots made of single-crystalline silicon are extracted from the molten silicon. An optimal characteristic for this sort of panel is to have a module tolerance of +5% or more. Monocrystalline possess a uniform structure and commonly exhibit color shades ranging from deep blue to black. The shape of an object might vary depending on the degree of diffusion, ranging from circular to rectangular. Panels with

monocrystalline cells are employed for measuring high power outputs in the megawatt range [2, 4, 9–14].

Polycrystalline Cells

The process involves pouring (casting) molten silicon into the rectangular molds to create these cells. The polycrystalline blocks, measuring 40 cm x 40 cm and 30 cm in length, are subsequently sliced into “bricks” and then into wafers. The crystalline exhibits a grain size of around 1 cm and is distinctly visible against a dark blue background. Due to the highly crystalline nature of the cell structure, the crystallines are readily visible in the light reflections. The colours of wafers are blue with an anti-reflective coating, and silver grey without any coating. Due to its poorer quality and efficiency compared to a monocrystalline cell, the cost of this type of cell is significantly lower. Polycrystalline lack a singular crystalline structure, thereby rendering them non-homogeneous. The presence of cracks within the crystalline has a detrimental impact on the level of effectiveness, however, the manufacturing of these cell types is more cost-effective. Polycrystalline panels consist of vessels with crystalline structures that share identical electrical, optical, and structural properties, with the exception of their opposite orientations. The magnitude of the veins is directly proportional of the crystalline [2, 4, 9–14].

The lack of consistency between the vessels poses a substantial obstacle, particularly in the transit of electrical load carriers. Due to the proportional reduction in electrical characteristics with the size of the container, the efficiency of polycrystalline material is lower compared to monocrystalline cells. Nevertheless, the production methods for Polycrystalline Si are characterized by lower energy consumption and reduced weight, resulting in a lower cost for manufacturing polycrystalline cells. Consequently, they are favored in regions that necessitate minimal power production, in regions with abundant sunshine, and in regions that do not prioritise efficiency [15–19].

Silicon cells with enhanced power output

These cells are derived from polycrystalline structures formed during injection. In addition, they also undergo mechanical forming procedures. Microscopic perforations are created on both the front and back surfaces of silicon plates using a high-speed rotating milling blade. The processed pieces are arranged in a rectangular shape, with minor gaps intentionally left at the cutting sites. These holes facilitate the cell's permeability. The permeability ranges from 0% to 30% and is contingent upon the magnitude of the gaps. The efficiency of the cell that passes by 10% is once again around 10%. The forms have dimensions of 10cm x 10cm and are square in shape. The colour matches that of the Polycrystalline cell [2, 4, 9–14].

Ribbon created

About 50% of the brick material is wasted during the wafer slicing process in conventional manufacturing techniques. Various strip extraction methods are implemented to mitigate this loss and enhance utilisation. These techniques generate fluids by directly melting silicon. The fibres possess the necessary plate thickness and are exclusively divided into strip pieces by laser cutting. This strategy uses less quantities of resources and energy. Moreover, it is a more economical alternative to injection casting or crystalline pulling methods. Three technologies have been developed specifically for mass production [2, 4, 9–14].

The Cells are Made of aa-Polycrystalline EFG silicon

These cells, which have an efficiency of 14% and an average thickness of 0.28 mm, are manufactured using a technique called Edge-Defined Film-Fed Growth (EPG). They are typically made in a rectangular or square shape. The colour of the object is blue [2, 4, 9–14].

Polycrystalline string ribbon silicon

The cells possess a rectangular shape, exhibiting an efficiency of 12% and an average thickness of 0.3 mm. Their structure closely resembles that of EFGs, appearing in shades of blue or silver grey [2, 4, 9–14].

Monocrystalline dendritic web silicon (cc-monocrystalline dendritic web silicon)

The cells possess a homogenous structure, similar to monocrystalline silicon cells, with an efficiency of 13% and a rectangular thickness of 0.13 mm. The structure, in fact, calls double-crystalline or Apex cells represent the initial utilisation of thin film technology in the manufacturing of crystalline silicon that is ready for use. The conductive ceramic substrate, which contains silicon, is substituted with a thick layer of silicon. This silicon layer is then coated with a thin film of Polycrystalline silicon, measuring 0.03-0.1 mm in thickness, using a sequential process. This technique yields solar cells of greater dimensions that possess polycrystalline characteristics. By employing this technique, lower temperatures prove enough for the fabrication of superior semiconductors, resulting in a decreased cost for accelerated manufacturing.

Thin manufactured solar panels

The method of coating the semiconductor material in a thin film across large surfaces has effectively addressed the reduction in materials and labour, as well as the simplification of technology and cost reduction, in the manufacturing of solar panels. These panels are multi-layered and have the ability to absorb photons across a larger range of wavelengths. This approach involves the application of photoactive semiconductors in thin layers onto a mostly glass substrate. The employed techniques encompass chemical processes such as electrolytic baths and cathode toning.

Thin film panels have the advantage of not being restricted by the size of the plate. In theory, the substrate can be precisely sliced to the desired dimensions and then

covered with semiconductor material. Nevertheless, it represents the maximum achievable rectangular area with an electrically conductive region for an asymmetrical shape, as only cells of identical dimensions may be connected in a series. Regions beyond this domain lack electrical activity and cannot be discerned from an optically active domain.

Crystalline cells rely on external means for intercellular communication, whereas thin film cells are interconnected in a monolithic structure. During the forming steps of the production process, the cells are electrically isolated from one other. Consequently, sticky folds are formed between these cells. In order to enhance energy efficiency, these waves are minimised to the greatest extent feasible and are imperceptible to the unaided human eye [15].

Although thin film cells have a rather low efficiency, it is certainly worth considering energy recovery under some circumstances. They exhibit superior performance compared to other cells in both low-light and high-temperature situations. They persist in manufacturing during overcast and indoor conditions. Their cell morphologies, which are thin and elongated strips, make them more resistant to shade.

Their electrical connections are established through the application of an opaque metal coating on the back surface. The technique is carried out on the front surface, which is exposed to light, using a highly polished and conductive coating called the TCO (Syddam or Transparent conductive oxide layer). Zinc oxide (ZnO), tin oxide (SnO2), and indium tin oxide (ITO) are the most often utilised metal oxides [7, 16, 17, 20, 21].

Solar cells serve as the primary components for manufacturing solar modules/panels, which produce electrical energy by harvesting sunlight. A solar panel harvests solar radiation to generate renewable energy. Research findings indicate that a wide range of semiconductor materials can be applied as a coating on various substrates, including glass, metal, or plastic foil. Thin-film photovoltaic (PV) products typically possess a polycrystalline structure and contain vascular defects that vary in density from one in a thousand to one in a million per millimeter. The semiconductor material exhibits favourable electrical, optical, and structural characteristics for photovoltaic (PV) applications in various devices. However, the presence of structural imperfections at the microscopic scale, such as intervascular borders, poses significant challenges in polycrystalline materials [21–25].

Based on its optical qualities, a certain semiconductor has the ability to effectively dissipate nearly all of the sun's radiation within a thickness of 0.001 millimeters. Transitioning from this point, there are limited applications for cells composed of thick silicon in thin film photovoltaic material. Simultaneously, thin film semiconductor material can be applied on expansive surfaces on virtually any type of material, whereas silicon batteries are constrained by increased crystalline sizes [15, 24, 25].

An impressive characteristic of the NREL's 18.8% efficient cell was orientation of the CIGS films. Typically, chalcopyrite CIGS films have a random orientation. Currently, absorbers with orientation are widely used in high-efficiency devices [15]. Figure 2 describes the imagination of standard structure of solar cells [2].

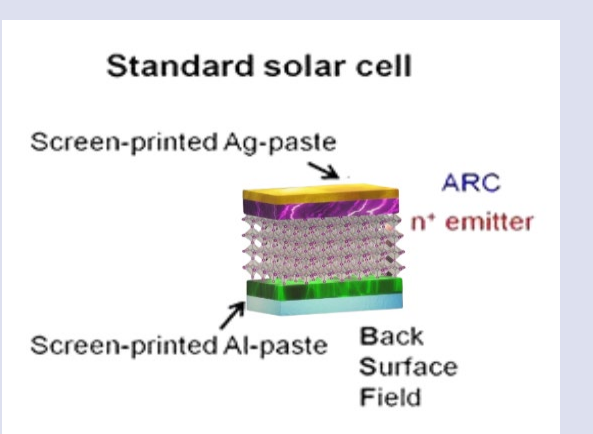

Figure 2. Standard solar cell structure in PV.

The cellular modules are equipped with windows, glass enclosures, and various surfaces, including side fronts. These shade devices, known as "Shadow-Voltaic", offer protection from the sun's disruptive effects while also generating electricity for users, resulting in a rapid return on investment. Control systems can be optionally integrated with shading systems, allowing for both horizontal and vertical use in sunbeds, and storefronts. The integrated modules and designs, in the form of glass that is incorporated, can also be used without frames. These structures are referred to as synergy fronts and roofs. There are two available applications: one that is integrated into the roof structure and another that is separate and installed on the rooftop. The laboratory efficiency of these panels is approximately 18%, but, their long-term durability does not meet the acceptable standard [14, 16].

Amorphous silicon, cadmium, cadmium telluride (CdTe), and copper-indium-diselenide (CulnSe2) are notable compound semiconductors used in thin film panels [15–18].

Amorphic Silicon Thin Film Cells possess a notable cooling coefficient and may be uniformly applied to expansive surfaces at a temperature of 250 degrees. The key characteristic that sets the material apart from crystalline silicon is the random arrangement of silicon atoms, which are positioned beyond the surrounding atoms in close proximity. Amorphous silicon, instead of adopting a normal crystalline structure, produces an irregular network. Consequently, unoccupied bonds have the capacity to retain hydrogen. The hydrogen silicon is synthesised in a plasma reactor using the chemical vapour deposition of gaseous silicon (SiH4). The addition is performed by combining the gases that contain the pertinent components [14, 18, 26]. Despite the negative impact of a haphazard arrangement of structural stones

on the efficiency of amorphous-silicon electricity, the inclusion of hydrogen in the semiconductor can enhance its electrical characteristics by 5-10%, making it suitable for the PV circuit. Despite the challenges they pose, Amorphous Silicon cells are widely utilised as power sources in applications that demand small-scale power. Due to advancements in addressing issues of inconsistent performance, these solar cells have also been implemented in extensive projects.

The primary drawback of amorphous cells is their suboptimal efficiency. Stacked cells have been developed as a means of preventing this. Every segment of these cells is specifically designed to maximise efficiency for a particular colour wavelength, hence enhancing the total effectiveness. Additionally, it mitigates the impact of light-induced fatigue by decreasing light sensitivity. The cell shapes can be customised according to preference. The efficiency of the modules varies between 5% and 8% depending on their static state. The standard dimensions of a module are 0.77 m × 2.44 m, while individual modules measuring 2m x 3m can also be produced. The substrate has a thickness ranging from 1 to 3 mm, and it is coated with a layer of amorphous silicon that is roughly 0.001 mm thick. Their composition is uniform, however their colour ranges from crimson to ebony [2, 8, 27]. Amorphous-silicon PV panels have the benefit of being highly responsive to wavelengths in the transmission spectrum, resulting in a greater energy generation capability. It generates a reduced amount of raw materials and consumes a lower amount of energy. An exemplary illustration of hybrid panels is provided by Kaneka, comprising a total of 53 interconnected cells. Every individual cell produces an electrical voltage of 1.02 V. The current generated by the panel under 1000W/m^2 radiation is 2.04 Amperes, while the voltage is calculated as 1.02 multiplied by 53, resulting in 54.0 Volts. The power output (Wp) is determined by multiplying the voltage (54 Volts) by the current (2.4 Amperes), resulting in 100 Wp [8].

Cadmium telluride thin film solar cells

Cadmium telluride (CdTe) cells are manufactured using a glass substrate coated with a solid conductive layer, often indium mould oxide (ITO). The front connector is coated with a very thin coating of n-type CDS. Subsequently, the p-type CdTe coolant layer is introduced. Common production techniques such as serigraphy, galvanization, or spray pyrolysis are employed.

The issue with this technology lies in Cadmium contamination, which has the potential to impact the level of adoption in the market. Cadmium telluride (CdTe) is a chemically stable molecule that does not emit pollutants. Health-risk circumstances only develop in the gas phase, namely under closed production conditions. The module's efficiency varies between 6% and 9%. The cells can be moulded according to one's preference. The cells possess a covering with a thickness of 0.008 mm, in addition to a substrate that is 3 mm thick. The maximum dimensions are 1.20 millimeters in length and 0.60 square meters in area. Their structures exhibit uniformity, but their colours range from lustrous dark green to black [1, 3, 28]. The forbidden energy range of CdTe at ambient temperature is Eg = 1.5 eV, which is in close proximity to the threshold needed for optimal conversion of solar energy into electricity from the solar spectrum [14, 19, 29]. Furthermore, the CdTe compound semiconductor has gained prominence in the manufacturing of large-scale solar cells due to its high cooling coefficient and the ease of production offered by various thin film enlargement technologies.

Solar cells made of copper indium diselenide

This compound semiconductor exhibits high cooling ratios and allows for precise adjustment of the energy gaps to optimally align with the sun spectrum. The group known as CIS is commonly referred to as solar cells, and CdTe is the most formidable competitor to solar cells. Today, the incorporation of the Ga element in these cells has led to a higher yield. Nevertheless, the production method becomes increasingly intricate as the number of components comprising the semiconductor increases. During the production of cells, a glass substrate is initially covered with a thin coating of molybdenum to provide a back surface connection. The P-type CIS cooling layer is formed through the reverse evaporation of copper, indium, and selenium at a temperature of 500 degrees within a vacuum chamber. CIS cells do not experience light-induced reduction in efficiency, unlike Amorphous cells.

In addition, stability issues develop in environments characterised by high temperatures and humidity. Hence, it is crucial to prioritise insulation in humid settings. The current most efficient thin film technology available today is CIS cells [14, 17, 19, 29]. Mass production yields significantly lower production costs in comparison to crystalline silicon cells. An inherent drawback is the necessity for further investigation to eliminate the use of cadmium in the CdS buffer layer. Selenium is considered safe due to its low overall toxicity [14, 18]. The shapes can be customised according to one's preferences. The dimensions of the cells do not exceed 1.20 mm x 0.60 mm^2 and they are coated with a layer that is 0.003 mm thick. The cells are mounted on a 3 mm substrate made of warmed glass [7, 15–17]. They exhibit a uniform structure and possess a dark coloration. Silicon (Si) cells exhibit greater productivity in hot climes and offer a more affordable pricing compared to Si. batteries.

However, the coverage area of the cells is significantly greater than that of the Si. cells. Photovoltaic cells generate a greater amount of energy from light compared to other types of cells. Additional cell types are positioned at an average incline of 30 degrees, whilst thin film panels are affixed to external facades with a 90-degree inclination relative to the floor [17, 18].

Bifacial solar panels

Bifacial cells, which are panels composed of various cell combinations such as monocrystalline and amorphous

silicon, have the ability to generate electricity on both their front and rear surfaces. This is achieved by harnessing solar radiation from direct sunlight as well as utilising solar rays. This product is not derived from a homogeneous cell population. N-PERT technology refers to the production of panels using p-PERC+ and Heterojunction cell types [2, 5, 30, 31]. The panel's transparent rear covering and entrance window allow for angular positioning, which enhances the reflection of light from the ground

PERC standards for passive emitter rear cell

PERC solar cells, or solar panels including these cells, have a higher efficiency in converting sunlight into electricity. Perc solar panels, equipped with solar cells, have demonstrated superior performance compared to conventional panels under conditions of low light and high temperature [8]. The incorporation of a thin film layer created using SiO2 or Al2O3 chemicals in the PERC structure enhances the efficiency of the conventional solar cell, resulting in numerous advantages for the cell's efficiency. This design enables the reflection of some photons within the cell, enhancing energy production. Additionally, the cell base is passivised to reduce energy production losses at high temperatures. The Multi Bus Bar is a system that allows for the simultaneous stripping and connecting of many wires using a single bar. This is a cellular technology designed to increase the number of tin alloy wire strips used in standard (typical) cell types while reducing the amount of silver paste required in the metallization process, hence lowering costs. It is feasible to apply to a wide range of cell types. 12-busbar technology has gained significant popularity in recent times.Furthermore, transitioning to PERC production necessitates minimal alteration to current cell production procedures. Manufacturers can easily transition to producing more efficient PERC cells at a reduced cost. These structures are referred to as PERC or Aluminium cells.

Half-Cut — Refers to cells that have been physically divided into two halves

A panel refers to a specific form of panel that is achieved through the process of laser cutting Mono and Poly structured cells. The purpose of this cutting is to maximise power output within a limited area by combining the cells on the surface, effectively doubling the number of cells. This advancement has enabled the production of solar panels with a power output of 400 Watts peak (Wp) or more [9, 10].

Also it used for Dual Glass refers to a type of glass that consists of two layers, commonly known as Double Glass. Double-glass panels without frames. The level of efficiency is contingent upon the specific type of cell employed.

Biosol Panels

These foldable thin film solar panels are particularly effective when utilised for roof applications. If mounting the PV system proves challenging, it is possible to install it on the roof without causing any harm to the roof insulation. Furthermore, this installation might serve as an extra layer of protection for the rooftop [27, 31]. The Biosol panels are offered in different options, including crystalline and thin film cells. The Biosol panels are composed of thin film cells, which are also referred to as the Thin Film Tandem. It possesses great adaptability and can be utilised in uppercase format. It does not require an additional structure. Thin-film panels have a weight that is 70% lighter than crystalline panels. The multi-layer (tandem) solar cells have a theoretical yield of 40%.

Nanocrystalline cells

These cells serve as a substitute for silicon technology. The fundamental constituent of this cell is titanium dioxide (TiO2), which functions as a semiconductor [9, 32]. This semiconductor utilises the absorption of solar light by chlorophyll during plant photosynthesis to convert sunlight into a cooler organic form, rather than relying on the p-n connection concept. Upon exposure to light, the cell undergoes activation, causing the transmission of an electron through Titanium Dioxide in the paint. The electron travels to the higher electrode from inside the particles. An electron is conveyed via a platinum catalyst to an electrolyte solution.

The electrolyte facilitates the transfer of electrons back to the paint, thereby closing the circuit. This technique is entirely devoid of any harmful properties. Their production is cost-effective and straightforward. However, addressing the issue of long-term commitment is vital. The cell yield in laboratory conditions is approximately 12%. It exhibits high tolerance for shadows and suboptimal angles of incidence. Conversely, crystalline cells exhibit enhanced productivity in elevated temperatures, making them particularly well-suited for compact devices and building-integrated systems designed for indoor applications [21, 29].

Tandem or multijunction cells

These cells utilise layers of different materials with differing bandgaps to catch a wider range of sunlight wavelengths, hence enhancing the overall effectiveness of the cells.

Micro-crystalline and micromorphic solar cells

Silicon is an abundant chemical that is absolutely non-toxic. It is spontaneously created by cells in the form of a thin film derived from crystalline silicon. This technology capitalises on the benefits of silicon as a material, as well as the ease of thin film technology. The production method utilised in the aforementioned Apex cells is pioneering. In this process, a superior silicon coating is applied over a low-cost substrate using high temperatures, resulting in the formation of huge granular formations similar to those found in polycrystalline cells.

The second category involves procedures conducted at reduced temperatures. Due of the low temperatures, inexpensive substrates made of glass, metal, or plastic can

be utilised. The silicon films generated through this procedure exhibit micro-crystalline characteristics and are manufactured using methodologies akin to Amorphous Silicon Technology. The maximum efficiency reached in these cells is 8.5%, and superior outcomes are obtained by utilising Tandem cells composed of micro-crystallines and employing amorphous silicon in combination. The term "micromorphic" refers to these tandem cells, which are a fusion of the words "microcrystalline" and "amorphous". The cells exhibit a remarkable steady efficiency of 12% and were initially manufactured by the Japanese business company named Kaneka [8].

Hybrid (HIT) cells

HIT solar cells consist of a hybrid structure that combines traditional crystalline and thin film solar cell technologies. The name HIT (Hetero-Junction with Intrinsic Thin layer) refers to the specific construction of these solar cells. The HITs structure comprises crystalline and amorphous silicon, along with an extra non-contributing thin film layer. Similar to thin film cells, the effectiveness of the cells does not diminish based on the intensity of light. HIT cells exhibit higher efficiency than crystalline cells in high temperature conditions. Production procedures are more cost-effective. Due to the specified processing temperature of 200 degrees, the plates are not subjected to excessive heat conditions, allowing for a reduction in their thickness to 0.2 mm. The cell dimensions are 104 mm × 104 mm, forming square forms. The cellular composition is uniform, with cells exhibiting a mostly dark blue to black coloration [5, 26].

Thin-Film Solar Cells consist of Cadmium Telluride (CdTe)

This type of material with a high absorption coefficient and lower production expenses. This combination allows for good efficiency and cost-effectiveness. Copper Indium Gallium Selenide (CIGS) is capable of attaining high levels of efficiency and can be applied onto flexible substrates.

Materials and Methods

A thorough comprehension of certain principles is necessary for optimising solar panel efficiency. The effectiveness of a solar cell is intricately linked to its inner structure, specifically the elements employed and their organisation. Different simulation programs were used to compare the efficiency of PV panels with different structures. In order to change the internal structure of the panels, the results obtained in the Matlab program were tested on another simulation program, PVsyst, and the results were compared. In practice, real climate data was used when testing the production of panels, ensuring real panel production results were achieved. Details of study explain below of how the compositions impacts the efficiency of solar cells.

Choosing the Optimal Semiconductor Material

Energy efficiency is related with the bandgap of a semiconductor material dictates the specific wavelengths of light that it is capable of absorbing. An optimal efficiency can be achieved by utilising a material having a bandgap that closely aligns with the photons in the sun spectrum. The efficiency of a substance is influenced by its absorption coefficient, which measures its capacity to absorb light. Materials possessing high absorption coefficients have the capacity to collect a greater number of photons, resulting in enhanced efficiency Carrier mobility refers to the ease with which charge carriers, such as electrons or holes, can travel within a material. Enhanced mobility leads to a decrease in carrier recombination and enhances efficiency. The previous section also discussed the many types of solar cells. Monocrystalline solar panels have superior efficiency as a result of their consistent crystalline structure, however they are more expensive to manufacture. On the other hand, Polycrystalline solar panels have lower efficiency but are more cost-effective due to their less complex production method.

Furthermore, Perovskite materials have garnered significant interest because to their remarkable capacity for high efficiency and their cost-effective manufacturing methods. Manipulating the chemical composition enables the enhancement of bandgap and carrier transport capabilities, which are vital for increasing efficiency. The term "chemical enhancements" refers to the process of doping, which involves injecting impurities into a semiconductor to modify its electrical characteristics, hence improving conductivity and increasing carrier mobility. Surface passivation refers to the application of surface treatments or coatings to decrease the presence of defects or states that capture charge carriers on the surface of a semiconductor. This process aims to reduce recombination and enhance carrier efficiency.

The effectiveness of a system is significantly influenced by nanostructures and morphology. Nanowires or nanotubes can augment light absorption and charge carrier collection by offering a larger surface area and diminishing carrier travel distances. Furthermore, meticulous management of material morphology, such as nanostructuring and surface texturing, can enhance light trapping and minimise losses caused by reflection. Comprehending and controlling the chemical composition of materials used in solar cells is essential for advancing efficiency limits, cutting down expenses, and broadening the range of potential applications for solar technology.

The general structure of grid connected real time working principles of PV could be seen in Figure 3. The material differences used in the PV cell inner structure provide the opportunity to control nominal power and gain changes within the VSC together with the cell parameters.

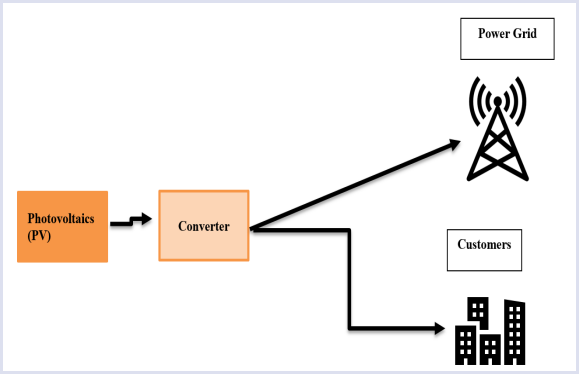

Figure 3. Grid Connected Solar Panel Infrastructure.

The efficiency of a solar panel is determined by comparing the power consumed by the panel to the power it generates when exposed to a light source that closely resembles sunshine in laboratory settings. Typically, solar cells that are used on land are evaluated at AM0 and AM1.5 circumstances, while maintaining a consistent temperature of 25°C and insident light power is same for each panel. Figure 4 shows Matlab software application for the efficiency formula for the actual designs of the photovoltaic (PV) panels, and using ideal parameters for calculation with SunPower SPR-315E, as follows within the Matlab software. This calculation is conducted under appropriate conditions and the efficiency of solar panels and solar cells can be quantified using different equations that correspond to their performance.

Equations for Solar Cell Efficiency

The Shockley-Queisser Limit refers to the maximum theoretical efficiency of a single-junction solar cell. The Shockley-Queisser limit represents the highest possible efficiency that a solar cell can achieve, based on the bandgap of the material it is made of. Equation 1 used voltage, current and power values in Matlab calculations.

$$\eta_{SQ} = \frac{V_{OC} \times I_{SC}}{P_{in}} \quad (1)$$

V_{oc}= Open Circuit Voltage

I_{sc}= Short Circuit Current

P_{in} = Incident Light Power

The efficiency of a solar panel can be calculated using the following equation :

$$Solar\ Panel\ Efficiency = \frac{Power\ Output}{Solar\ Energy\ Input} \times 100\% \quad (2)$$

Power Output: The tangible electrical power generated by the solar panel, commonly quantified in watts (W).

Solar Energy Input: The quantity of solar energy that reaches the panel, typically measured in watts per square metre (W/m²) or kilowatt-hours per square metre per day (kWh/m²/day).

Equation 2 measures the efficacy of the solar panel in converting incoming sunlight into practical electrical energy. When assessing the efficiency of solar panels in real-world scenarios, it is crucial to consider variables such as temperature, angle of incidence, shading, and climatic conditions. Meteonorm and Weatherspark database used for climate parameters.

A comprehensive understanding of certain principles is necessary for optimising solar panel efficiency. The principles can be summarised as follows: the output forces are measured by comparing them with the monocrystalline values obtained from the NREL, as stated in the Efficiencies section. Figure 1. Distinct panel values were inputted for the polycrystalline configuration, and distinct computations were performed for the monocrystalline. The temperature and irradiance values were consistent, however the efficiency values varied among the 400kW solar panels. The National Renewable Energy Laboratory provides the average efficiency numbers for solar panel structures as follows [3].

The polycrystalline has a composition ranging from 15% to 18%. The Standard Monocrystalline has a purity level ranging from 16.5% to 19%. The Monocrystalline PERC (Mono PERC) solar panel has an efficiency range of 17.5% to 20%. The Monocrystalline solar cells have an N-type doping concentration (Mono N-Type) ranging from 19.5% to 20.5%. The Monocrystalline N-type HJC (Mono HJC) has an efficiency of 19 to 21%. The Monocrystalline N-Type IBC (Mono IBC) has a power output efficiency of 20 to 22%. The values are manually inputted into the parameters in the equations, and the output voltage and output forces are generated by utilising derived graphs.

Results and Discussion

The objectives of the solar panel efficiency notification, depicted in Figure 4, is to ascertain the impact of varying efficiency values on output power. The result charts clearly indicate that comparing polycrystalline and monocrystalline cells in places inside the borders of Sivas, Turkey with average Irradiation values of 25 degrees. Polycrystalline cells are suitable for regions experiencing extreme regional temperatures and limited power generation. The Matlab Application was used to conduct a comprehensive analysis of monocrystalline solar panels. The measurement results were acquired by inputting specific parameters into the 400kW networked photovoltaic cell construction. The resulting data is displayed in the graphs in Figure 5 and Figure 6. The Energy Generation results were evaluated using the 400kW PV panel model displayed in the MATLAB application. The model data includes four photovoltaic arrays, each with a maximum power production of 100 kW when exposed to sun irradiation of 1000 W/m2.

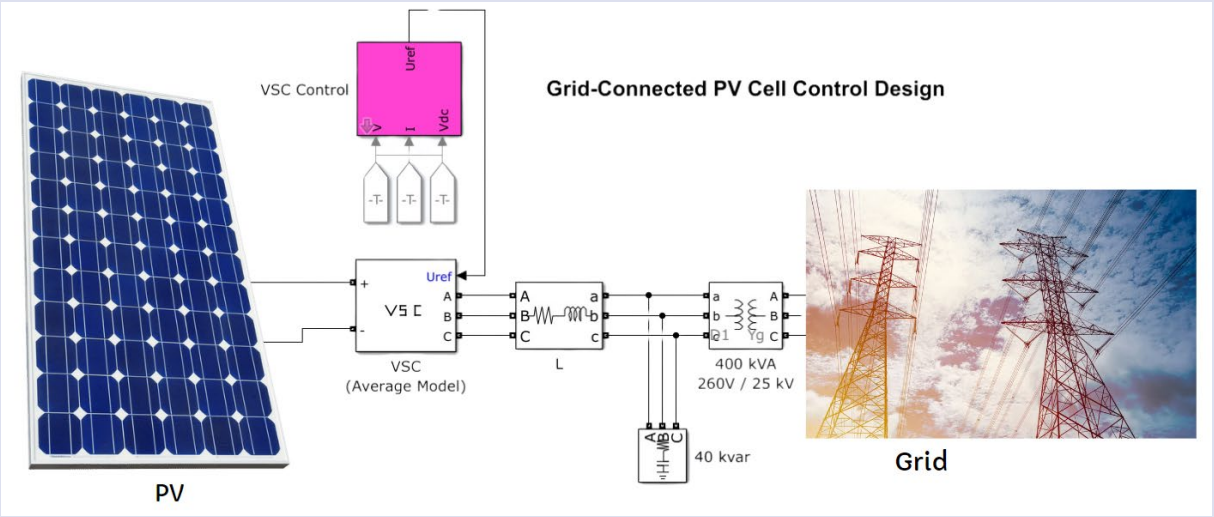

Figure 4. Grid Connected Solar Panel Efficiency Application in Matlab.

The PV array block is composed of 64 parallel threads, it is designed with based on Figure 4 Matlab PV array block diagram, then it is developed and improved with different parameters, where each thread is made up of a series connection of 5 different location same power in simulation as SunPower SPR-315E modules. Every solar array is linked to a direct current to direct current converter, specifically employing an simulation model. The outputs of the boost converters are linked to a shared DC bus operating at a voltage of 500 V. Every boost is regulated by separate Maximum Power Point Trackers (MPPT). MPPTs employ the "Perturb and Observe" method to control the voltage across the terminals of the PV array in order to attain the highest attainable power. The three-phase Voltage Source Converter (VSC) transforms the 500 V DC input into a 260 V AC output, maintaining a power factor of unity. A 400kVA three-phase coupling transformer is utilised to link the converter to the grid. The transformer possesses a primary voltage rating of 260 volts and a secondary voltage rating of 25 kilovolts. The grid model has standard 25 kV distribution feeders and a 120 kV transmission system that faithfully reproduces actual transmission networks.

The model parameters depict in Figure 4 and the boost and VSC converters as voltage sources that produce the mean AC voltage across a single cycle of the switching frequency. While this model may not accurately depict harmonics, it does effectively maintain the dynamics that arise from the interplay between the control system and the power system. This model enables the usage of significantly longer time periods (50 microseconds), leading to a significantly faster simulation. When the efficiencies of the panels remain constant, the power output chart of identical solar panels, with irradiance as a linear output, follows the same pattern, while maintaining a consistent efficiency.

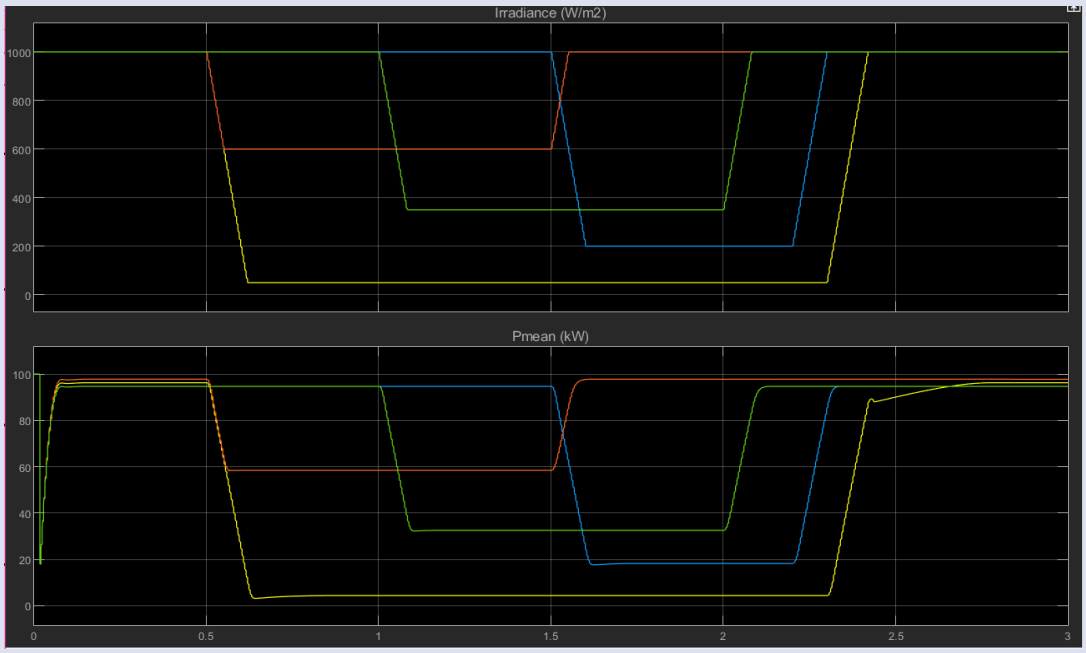

Figure 5. Irradiance and Power Output Correction Graphs.

The colour codes employed in obtaining the findings are based on values associated with the chemical structure of efficiency, which are altered by adjusting the parameters inside the panels' internal structure. The output forces for each panel are also displayed in Figure 5 to verify if the outputs corresponding to these colour codes exhibit a linear relationship with constant irradiance levels.

The outcome graphs were analysed in depth, using data from the Panel efficiency account. The data was focused on the ideal values of the matching cells in the solar cell parameters, which solely consider efficiency. The temperature was set at 25 degrees. Figure 6 displays the computed results for current in Matlab, voltage, and power outputs utilising efficiency equations.

It is apparent that the maximum efficiency value belongs to the Mono N Type IBC cells, while the polycrystalline cells do not demonstrate sufficient performance even in modest power production. Different mono types also simulated with 1MW power capacity and results are compared with Matlab and PVsyst simulation. In the Matlab model data includes four photovoltaic arrays, each with a maximum power production of 100 kW when exposed to sun irradiation of 1000 W/m2.

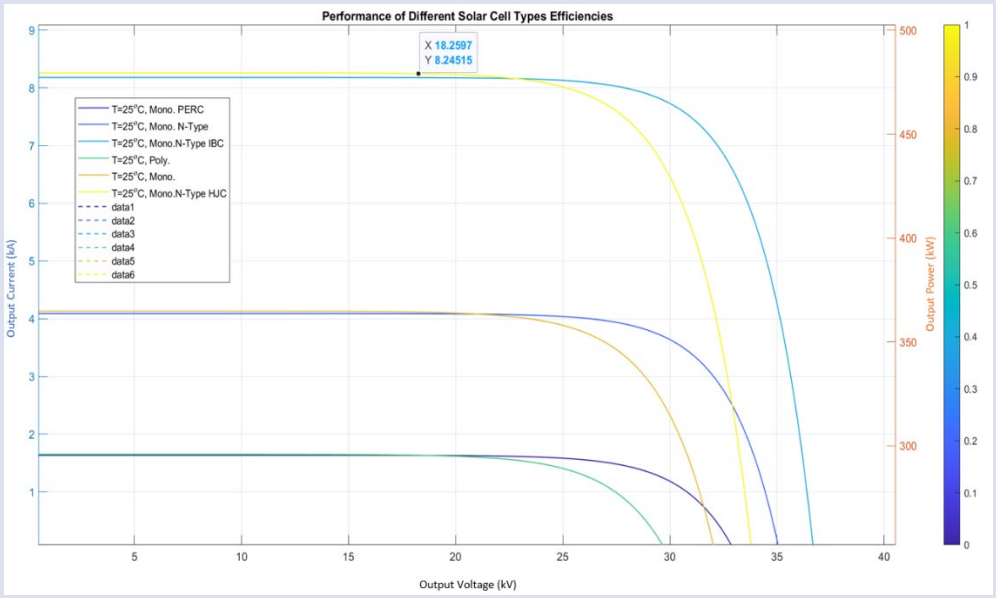

Figure 6. Solar Cell Efficiency Performance results.

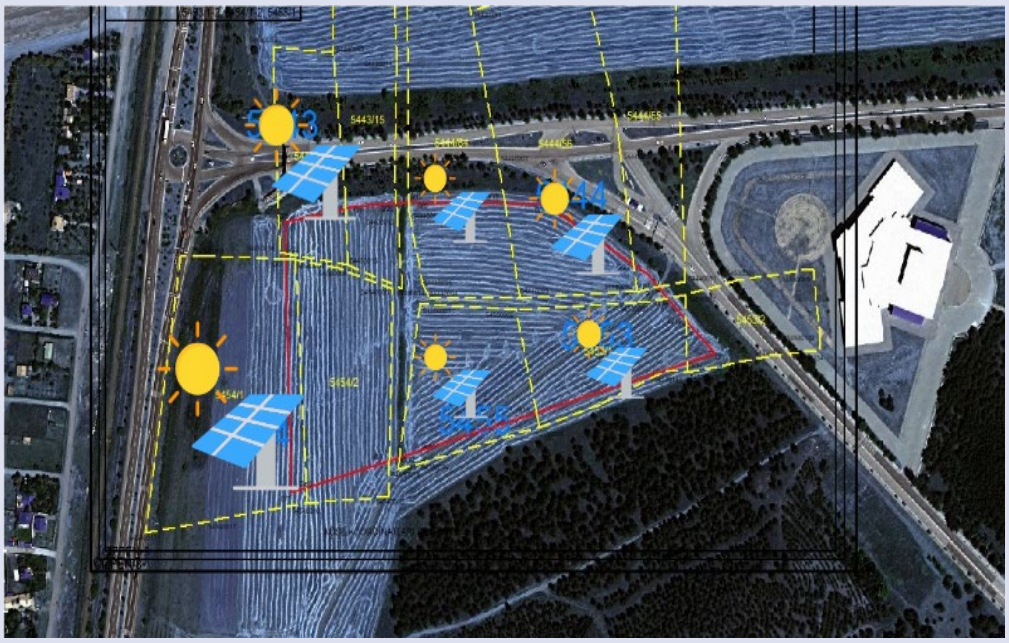

Figure 7. Suitable Areas for PV Application in Sivas Cumhuriyet University.

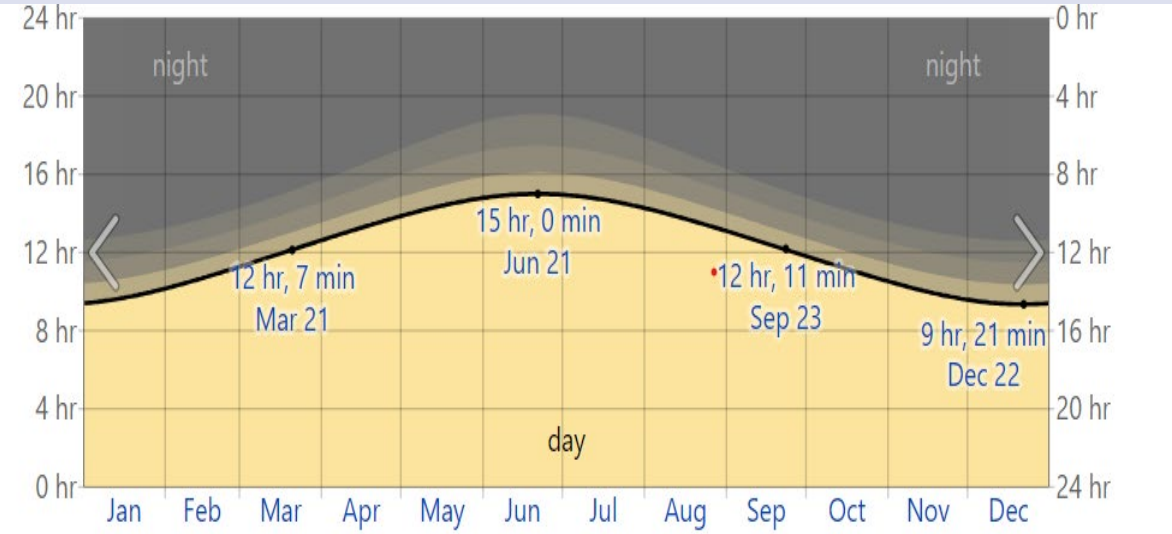

Figure 8. Sivas city daylight and Twilight values from Weatherspark database, the number of hours during which the Sun is visible (black line). From bottom (most yellow) to top (most gray), the color bands indicate: full daylight, twilight (civil, nautical, and astronomical), and full night.

In order to verify the results on a real system, areas where solar panels could be applied were identified within Sivas Cumhuriyet University and real-time application was made. According to the analysis, areas must have some characteristics in order to apply the pv system [3].

In this context, the PV application areas marked in yellow and shown in Figure 7. PV application details could be find in our previous study [33] for determined and selected areas characterisation where panels can be applied.

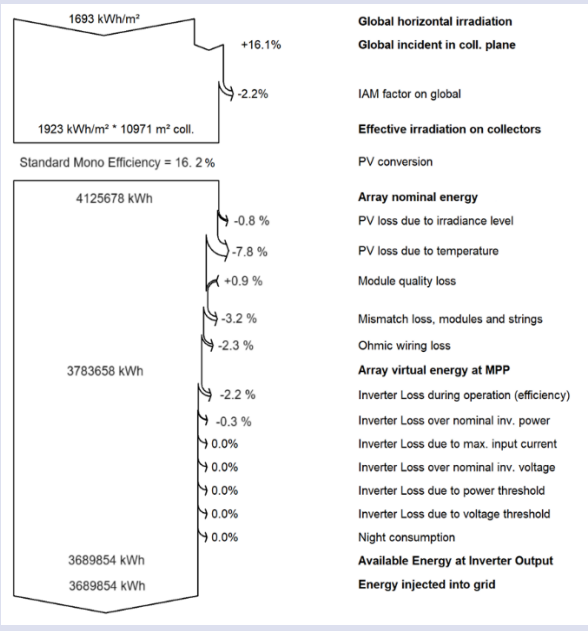

Figure 9. Standard Mono Cell losses and efficiency results.

According to the simulation results along with the climate data of the region shown in Figure 8 taken in real time, the cells giving the highest and lowest efficiency results were tested with the PVsyst simulation for different PV characteristics and efficiency results were obtained. The efficiency results of MONO IBC and standard Mono cells are shown in Figure 9 ,10 and 11.

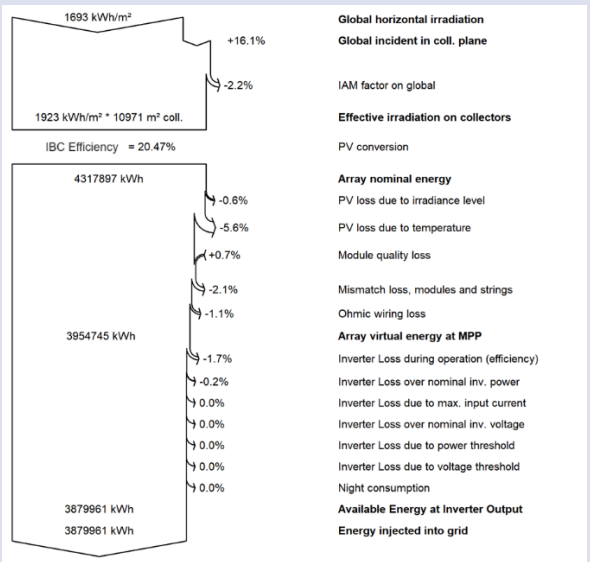

Figure 10. Mono IBC Cell losses and efficiency results.

The reason for choosing a capacity of 1 MW is to compare the efficiency of energy production in the region. Since 100 kW PV cells were selected both Matlab and PVsyst application. In addition, simulation results which made with the PVsyst, used Meteonorm 8.2 climate database and show real-time production values of PV cells.

New simulation variant
Balances and main results

	GlobHor	DiffHor	T_Amb	GlobInc	GlobEff	EArray	E_Grid	PR
	kWh/m²	kWh/m²	°C	kWh/m²	kWh/m²	kWh	kWh	ratio
January	62.7	29.78	-3.81	99.6	97.7	218117	215084	0.963
February	85.3	34.80	-2.13	122.0	119.9	261789	257980	0.943
March	124.8	49.64	3.42	156.3	153.2	323811	318809	0.910
April	159.8	61.45	8.42	173.3	169.4	348922	343215	0.883
May	196.2	71.65	13.04	193.6	188.5	383160	376599	0.867
June	219.3	65.31	16.77	206.5	200.9	400965	393696	0.850
July	219.9	61.55	20.52	210.8	205.2	401156	393560	0.833
August	207.9	56.69	21.10	219.3	214.3	417924	409984	0.834
September	165.5	43.23	16.34	198.9	195.0	384516	377458	0.846
October	115.2	42.57	10.84	158.6	155.7	320985	315755	0.887
November	75.5	29.02	4.40	120.9	118.9	254221	250453	0.923
December	60.8	25.80	-1.30	106.2	104.1	230550	227367	0.955
Year	1693.0	571.50	9.03	1965.9	1922.6	3946115	3879961	0.880

Figure 11. PVsyst simulation Pv Cell loss calculation and efficiency results.

Conclusion

The analyses conducted on the Solar Panel cell and the matlab model indicate that the Monocrystalline N-Type IBC model exhibits the maximum efficiency in terms of pv cell structure. Both polycrystalline cells and cells in the Mono structure have demonstrated inadequate power efficiency in power generation, even when considering solar panels with a capacity as low as 400kW. The Mono IBC structure is more efficient than polycrystalline cells and all monocrystalline at high temperatures. This allows the cell to reflect itself and passivise the cell base, resulting in a 5% or more increase in energy production. However, the Mono Perc cell type is less efficient in generating energy at high temperatures, leading to a lower yield compared to other mono and polycrystalline cells. Although the data obtained under constant temperatures did not provide a reason for the decrease in yields at higher temperatures, future investigations could potentially draw conclusions by comparing the efficiency at various temperature levels. The graphs exhibit findings that align with the calculated results and the different infrastructures of the solar cell.

The design of the system with an installed power of 1 MW was carried out separately in Matlab and PVsyst simulation programs, using poly panels with the lowest efficiency. 14% of the global radiation, which is 1,693 kWh/m2 annually, falls on the collector, and 2.5% turns into losses as the angle conversion factor. The efficiency obtained when standard mono panel cells were used was 16.1%. The efficiency rate in MIBC has increased up to 20%. PV loss depending on radiation level, PV loss depending on temperature, module quality loss, cabling losses, etc. When included, the annual energy given to the grid is 1,693 MWh. Figure 9 shows the annual generated energy and losses diagram obtained from the PVsyst software for the power plant built using standard monocrystalline panels. According to the results obtained with the climate data added in Figure 8, it is shown in Figure 10 that the most efficient among mono cells is the MIBC model, since the inefficiency of poly cells is clearly known in literature.

Conflict of Interest

The Author has no conflict of interests.

References

[1] V. A. Milichko et al., Solar photovoltaics: current state and trends, *Physics-Uspekhi*, 59(8) (2016) 727–772.

[2] L. Scalon, Y. Vaynzof, A. F. Nogueira, C. C. Oliveira, How organic chemistry can affect perovskite photovoltaics, *Cell Rep Phys Sci*, 4(5) (2023) 101358.

[3] National Renewable Energy Laboratory, NREL-Solar Photovoltaic Technology Basics | NREL. Available: https://www.nrel.gov/research/re-photovoltaics.html, Retrieved: Jan. 10, 2024.

[4] E. Klugmann-Radziemska, P. Ostrowski, Chemical treatment of crystalline silicon solar cells as a method of recovering pure silicon from photovoltaic modules, Renew Energy, 35(8) (2010) 1751–1759.

[5] E. Kobryn, S. Gusarov, K. Shankar, Multiscale modeling of active layer of hybrid organic-inorganic solar cells for photovoltaic applications by means of density functional theory and integral equation theory of molecular liquids, *J. Mol. Liq.*, 289 (2019) 110997.

[6] R. Schmager, M. Langenhorst, J. Lehr, U. Lemmer, B. S. Richards, U. W. Paetzold, Methodology of energy yield modelling of perovskite-based multi-junction photovoltaics, *Opt. Express*, 27(8) (2019) 507.

[7] R. Uhl et al., Liquid-selenium-enhanced grain growth of nanoparticle precursor layers for CuInSe2 solar cell absorbers, *Progress in Photovoltaics: Research and Applications*, 23(9) (2015) 1110–1119.

[8] Kaneka Corporation Official Reports Database. Available: https://www.kaneka.co.jp/en/, Retrieved: Jan. 10, (2024).

[9] V. M. Andreev et al., Effect of postgrowth techniques on the characteristics of triple-junction InGaP/Ga(In)As/Ge solar cells, *Semiconductors*, 48(9) (2014) 1217–1221.

[10] N. Mohr, A. Meijer, M. A. J. Huijbregts, L. Reijnders, Environmental impact of thin-film GaInP/GaAs and multicrystalline silicon solar modules produced with solar electricity, *International Journal of Life Cycle Assessment*, 14(3) (2009) 225–235.

[11] D. V. Boguslavsky, K. S. Sharov, N. P. Sharova, Using Alternative Sources of Energy for Decarbonization: A Piece of Cake, but How to Cook This Cake?, *Int. J. Environ. Res. Public Health*, 19(23) (2022).

[12] N. J. Mohr, J. J. Schermer, M. A. J. Huijbregts, A. Meijer, L. Reijnders, Life cycle assessment of thin-film GaAs and GaInP/GaAs solar modules, *Progress in Photovoltaics: Research and Applications*, 15(2) (2007) 163–179.

[13] B. Sagyndykov, Z. K. Kalkozova, G. S. Yar-Mukhamedova, K. A. Abdullin, Fabrication of nanostructured silicon surface using selective chemical etching, *Technical Physics*, 62(11) (2017) 1675–1678.

[14] Eeles et al., High-efficiency nanoparticle solution-processed Cu(In,Ga)(S,Se)2 solar cells, IEEE J Photovolt, 8(1) (2018) 288–292.

[15] M. Kemell, M. Ritala, M. Leskelä, Thin film deposition methods for CuInSe2 solar cells, *Critical Reviews in Solid State and Materials Sciences*, 30(1) (2005) 1–31.

[16] P. Jackson *et al.*, Properties of Cu(In,Ga)Se2 solar cells with new record efficiencies up to 21.7%, *Physica Status Solidi - Rapid Research Letters*, 9(1) (2015) 28–31.

[17] P. Jackson, R. Wuerz, D. Hariskos, E. Lotter, W. Witte, M. Powalla, Effects of heavy alkali elements in Cu(In,Ga)Se2 solar cells with efficiencies up to 22.6%, *Physica Status Solidi - Rapid Research Letters*, 10(8) (2016) 583–586.

[18] H. Azimi, Y. Hou, and C. J. Brabec, Towards low-cost, environmentally friendly printed chalcopyrite and kesterite solar cells, *Energy Environ. Sci.*, 7(6) (2014) 1829–1849.

[19] Q. Guo, G. M. Ford, H. W. Hillhouse, R. Agrawal, Sulfide nanocrystalline inks for dense Cu(In 1-xGa x)(S 1-ySe y) 2 absorber films and their photovoltaic performance, *Nano Lett.*, 9(8) (2009) 3060–3065.

[20] R. Gottschalg, D. G. Infield, M. J. Kearney, Experimental study of variations of the solar spectrum of relevance to thin film solar cells, *Solar Energy Materials and Solar Cells*, 79(4) (2003) 527–537.

[21] M. Morales-Masis, S. De Wolf, R. Woods-Robinson, J. W. Ager, C. Ballif, Transparent Electrodes for Efficient Optoelectronics, *Adv Electron Mater*, 3(5) (2017).

[22] O. Hohn et al., Impact of irradiance data on the energy yield modeling of dual-junction solar module stacks for one-sun applications, *IEEE J Photovolt*, 11(3) (2021) 692–698.

[23] P. Faine, S. R. Kurtz, C. Riordan, J. M. Olson, The influence of spectral solar irradiance variations on the performance of selected single-junction and multijunction solar cells, *Solar Cells*, 31(3) (1991) 259–278.

[24] G. Nofuentes, B. García-Domingo, J. V. Muñoz, F. Chenlo, Analysis of the dependence of the spectral factor of some PV technologies on the solar spectrum distribution, *Appl Energy*, 113 (2014) 302–309.

[25] H. W. Hillhouse, M. C. Beard, Solar cells from colloidal nanocrystallines: Fundamentals, materials, devices, and economics, *Curr Opin Colloid Interface Sci*, 14(4) (2009) 245–259.

[26] K. Sarker, A. K. Azad, M. G. Rasul, A. T. Doppalapudi, Prospect of Green Hydrogen Generation from Hybrid Renewable Energy Sources: A Review, *Energies (Basel)*, 16(3) (2023) 16031556.

[27] J. C. Bijleveld, M. Fonrodona, M. M. Wienk, R. A. J. Janssen, Controlling morphology and photovoltaic properties by chemical structure in copolymers of cyclopentadithiophene and thiophene segments, *Solar Energy Materials and Solar Cells*, 94(12) (2010) 2218–2222.

[28] L. V. Kontrosh, V. S. Kalinovsky, A. V. Khramov, E. V. Kontrosh, Estimation of the chemical materials volumes required for the post-growth technology manufacturing InGaP/GaAs/Ge with a concentrator and planar α–Si:H/Si solar cells for 1 MW solar power plants, *Clean Eng Technol*, 4 (2021) 100186.

[29] Helbig, T. Kirchartz, R. Schaeffler, J. H. Werner, U. Rau, Quantitative electroluminescence analysis of resistive losses in Cu(In, Ga)Se2 thin-film modules, *Solar Energy Materials and Solar Cells*, 94(6) (2010) 979–984.

[30] Z. Bi and W. Ma, Calculating Structure-Performance Relationship in Organic Solar Cells, *Matter*, 2(1) (2020) 14–16.

[31] C. Ciobotaru, S. Polosan, C. C. Ciobotaru, Organometallic compounds for photovoltaic applications, *Inorganica Chim Acta*, 483 (2018) 448–453.

[32] Y. P. Varshni, Temperature dependence of the energy gap in semiconductors, *Physica*, 34(1) (1967) 149–154.

[33] Unsal D.B., Aksoz A., Oyucu S., Guerrero J.M., Guler M. A, Comparative Study of AI Methods on Renewable Energy Prediction for Smart Grids: Case of Turkey, *Sustainability,* 16 (2024) 2894.

Cumhuriyet Sci. J., 45(2) (2024) 322-330
DOI: https://doi.org/10.17776/csj.1452166

Cumhuriyet Science Journal

| csj.cumhuriyet.edu.tr | Founded: 2002 ISSN: 2587-2680 e-ISSN: 2587-246X Publisher: Sivas Cumhuriyet University

Polyacrylamide@Tangerine Peel Composite: A Novel Adsorbent for Efficient Removal of Pb^{2+} Ions from Water

Zeynep Mine Şenol [1,a,*]

[1] *Department of Nutrition and Diet, Faculty of Health Sciences, Sivas Cumhuriyet University, 58140 Sivas, Türkiye.*
**Corresponding author*

Research Article

History
Received: 22/03/2024
Accepted: 14/06/2024

ABSTRACT

In this study, hydrogel@fruit peel composite was synthesized by using polyacrylamide (PAA), a hydrogel, and tangerine peel (TP) as biowaste. The removal performance of PAA@TP was investigated for the Pb^{2+} ions. The FT-IR and SEM-EDX structural characterizations of PAA@TP showed that PAA@TP has various functional groups. The adsorption data fit to the isotherm models was investigated and the best fit was found with the Langmuir model. This showed that the binding sites on the surface of the PAA@TP composite showed a homogeneous distribution and that Pb^{2+} ions formed a monolayer on this homogeneous. The results show that PAA@TP can alternatively be efficiently used to treat wastewater containing Pb^{2+} ions.

Keywords: Polyacrylamide, Tangerine peel, Composite, Pb2+, Adsorption.

[a] *msenol@cumhuriyet.edu.tr* *https://orcid.org/0000-0002-5250-1267*

Introduction

With the rapid advancement of industrial activities in recent years, facilities are discharging wastewater containing heavy metals into the environment. Heavy metal pollution discharged into the environment mixes with groundwater and harms the environment [1]. This pollution mixed into water is very worrying in terms of environmental safety and public health. Because heavy metal ions cannot be biodegraded. Increasing concerns about water pollution underscore the urgent demand for effective approaches to eliminating heavy metal pollutants from water supplies [2]. The removal and recovery of heavy metals, which cause environmental pollution and harm human health, are very important. One of the dangerous heavy metals that attracts a lot of attention and causes environmental pollution is lead ions [3]. Lead is a highly toxic heavy metal and poses significant risks to both human health and aquatic ecosystems. Lead can disrupt the delicate balance of aquatic ecosystems, affecting aquatic life and overall biodiversity [4]. Long-term exposure to lead ions can cause a variety of health problems, including kidney damage, developmental disorders, and cancer. For these reasons, it is vital to remove lead from wastewater, which poses a threat to the environment and public health. Various methods such as adsorption, reverse osmosis, ion exchange, membrane filtration, and chemical precipitation are used in the treatment of heavy metals from wastewater [5]. Among these methods, the adsorption method is very interesting in terms of efficiency, low cost, and ease of application. In the adsorption method, the selection of the appropriate adsorbent is of critical importance [6]. The preferred adsorbent should be low-cost, reusable, easily accessible, and should not cause secondary pollution. In addition, the adsorbent must have advantages such as being selective to the adsorbent and having a high removal rate and capacity. Adsorbents commonly used in the removal of heavy metal ions from wastewater include various fruit peels [7], minerals [8], natural and artificial polymers [9], and composite materials [10]. The use of natural material-based composite adsorbents in the removal of heavy metal pollution has become quite widespread.

Tangerine (Citrus reticulata) is a fruit belonging to the citrus family that grows in temperate climates [11]. Vitamin A, B, C, potassium, phosphorus, calcium, etc. It has an important nutritional content for health as it contains minerals, pectin, and folic acid, is used as dietary fiber, and contains many phytochemical substances [12]. During the processing of tangerine fruits, approximately half of the fruit weight is converted into juice, while the remaining 50% is converted into peel, pulp, seeds, etc. remains as waste. While most of the acid, sugar, and mineral substances found in the fruit pass into the fruit juice, most of the water-soluble and insoluble polysaccharides, carotenoids, and lipids remain in the pulp [12]. These fruit peels, which are agricultural waste, are preferred because they are an alternative to high-cost materials in the removal of heavy metals from aqueous solutions. Overall, the interest in tangerine peels as adsorbents for different metal types and dyes underscores the potential of natural and renewable materials in addressing environmental pollution and wastewater treatment challenges.

Marques [13] used tangerine peels in the removal of Ni (II) from aqueous solutions. Unugul and Nigiz [14]

prepared activated carbon adsorbent from waste tangerine peel and used it in the removal of synthetic dyes. Husein [15] used raw and chemically modified tangerine peel for the adsorption of mercury ions. Yılmaz et al. [16] investigated the removal of Acid Brown 14 dye onto tangerine-CO TETA obtained from the tangerine peel. Inagaki et al., [17] used Mexerica tangerine (Citrus nobilis) peel to remove Cu(II), Cd(II), and Pb(II) from industrial wastewater. Özdemir et al., [18] examined the adsorption of phosphate ions and Remazol Brilliant Blue-R dye from an aqueous solution using thermally activated tangerine peel waste. Although there are many studies on using tangerine peels as adsorbents, there is no existing study on their use by creating a composite with a hydrogel. This study aims to fill this gap in the literature.

In this study, the PAA@TP composite was synthesized using tangerine peels, a biowaste, and polyacrylamide, a hydrogel, and its adsorptive properties were investigated for the removal of Pb^{2+} ion from aqueous media. PAA@TP composite was characterized by the point of zero charge (pHpzc), FT-IR, and SEM-EDX analyses. The adsorbent properties of the PAA@TP for Pb^{2+} ions were evaluated in terms of pH, concentration, kinetics, and thermodynamics of adsorption.

Materials and Methods

Chemicals and Devices

Acrylamide (AA), N, N'-methylenebisacrylamide (MBS), N, N, N', N'-tetramethylenediamine (TEMED), and ammonium persulphate (APS) were obtained from Sigma (St. Loius, MO, USA). $Pb(NO)_3$, and PAR were obtained from Merk (Germany). KNO_3, HCl, HNO_3, NaOH, ethyl alcohol, and all other chemicals were of analytical purity (Sigma Aldrich).

The functional groups on the TP, PAA@TP, and Pb^{2+} adsorbed PAA@TP were determined using the FT-IR (ATR, Bruker Model: Tensor II) technique. The surface morphology of the TP, PAA@TP, and Pb^{2+} adsorbed PAA@TP, along with the identification of different elements, was analyzed by SEM-EDX (TESCAN MIRA3 XMU).

Preparation of PAA@TP Composite

Tangerine peel was first washed with pure water and separated from its impurities. It was then left to dry at room temperature. Dried tangerine peel was ground to increase the contact surface and used in composite synthesis. To synthesize the PAA@TP composite; 1 g of tangerine peel and 1 g AA monomer were weighed and mixed in 20 mL of water in a magnetic stirrer until a homogeneous appearance was achieved. Then, MBS was added to this mixture, and mixing continued. Then, 300 µL TEMED and APS were added in a fast cycle to allow the polymerization reaction to occur. The obtained PAA@TP composite was washed with pure water until it reached approximately the conductivity of pure water. The composite was dried at 40 °C, then ground and stored in a polypropylene container.

Adsorption Procedure

Pb^{2+} adsorption studies on PAA@TP were carried out in a multiple magnetic stirrer heater by applying the batch method. Pb^{2+} ions at different concentrations and pHs were treated with adsorbent at different temperatures for varying periods. The amount of Pb^{2+} ion remaining in the solution was determined by UV-vis spectrophotometer at λ = 519 nm after complexing with PAR. Removal%, Q (mg g^{-1}), and Recovery% values were calculated using the equations below.

$$Removal\% = \left[\frac{C_i - C_f}{C_i}\right] x100 \quad (1)$$

$$Q = \left[\frac{C_i - C_f}{m}\right] xV \quad (2)$$

$$Recovery\% = \frac{Q_{des}}{Q_{ads}} x100 \quad (3)$$

Results and Discussion

FT-IR Analysis

When the FT-IR spectrum of Tangerine peel is examined (Fig. 1a), the peak around 3400 cm^{-1} is attributed to the O-H stretching vibrations of free and intermolecularly bonded hydroxyl groups [19]. The peak at 1519 cm^{-1} is attributed to C=C stretching vibrations in the aromatic rings of lignin. The peak at 2930 cm-1 is the vibrations of C-H bonds in cellulose, hemicellulose, and lignin [20]. The peak at 1234 cm^{-1} is attributed to C–O stretching vibrations in hemicellulose and lignin. The peak at 1016cm^{-1} can be attributed to the stretching vibrations of the $–OCH_3$ group of lignin to the C–O and C–H groups in cellulose. The peak at 552 cm^{-1} can be attributed to the bending vibrations of aromatic compounds [21]. In the FT-IR spectrum of the PAA@TP composite (Fig. 1a), characteristic peaks of PAA are observed. The peak at 3320 cm^{-1} is attributed to the $-CONH_2$ group and the peak at 3190 cm^{-1} is attributed to asymmetric N–H stretching vibrations. The peak at 1650 cm^{-1} is attributed to the C=O stretch in the $-CONH_2$ group. The peak at 1323 cm^{-1} is attributed to C–C stretching vibration, the peaks at 500–1300 cm^{-1} are attributed to C–H bending vibrations, and the peaks at 1000–1200 cm^{-1} are attributed to C–N stretching vibrations [22]. Characteristic peaks of TP are also seen in the FT-IR spectrum of the PAA@TP. These peaks are 3321 cm^{-1}, 2918 cm^{-1}, 1653 cm^{-1}, 1409 cm^{-1}, 1021 cm^{-1}, and 533 cm^{-1}. When the FT-IR spectrum of Pb^{2+} adsorbed PAA@TP was examined (Fig. 1b), the changes in the intensities of the peak intensities were considered as evidence of Pb^{2+} ion adsorption.

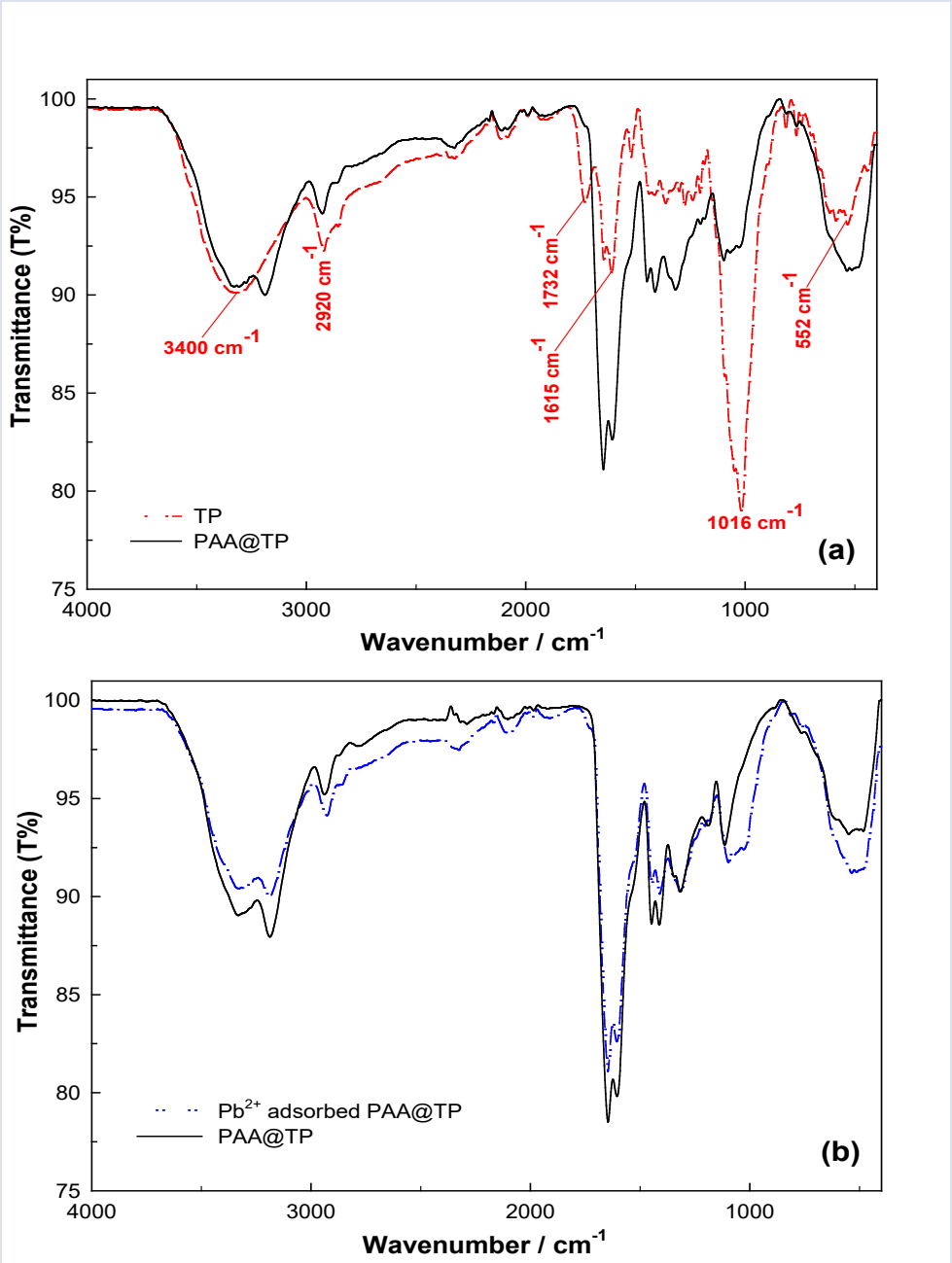

Fig. 1. FT-IR spectra of TP, PAA@TP (a) Pb^{2+} adsorbed PAA@TP (b)

SEM-EDX Analysis

The SEM morphology and EDX spectrum of pure TP (Fig. 2a-d) showed that it had an irregular and porous surface [16]. The surface morphology of the PAA@TP composite clearly shows irregular porous and rod-like structures in TP (Fig. 2b). In the SEM morphology of the Pb^{2+} adsorbed PAA@TP composite, it was seen that the pores were closed and the surface became smooth (Fig. 2c). The morphological changes observed after adsorption are thought to result from the surface complexation between the active sites and Pb^{2+} ions on the surface of the PAA@TP composite. The presence of Pb in the EDX spectrum after adsorption was evaluated as evidence of removal (Fig. 2f).

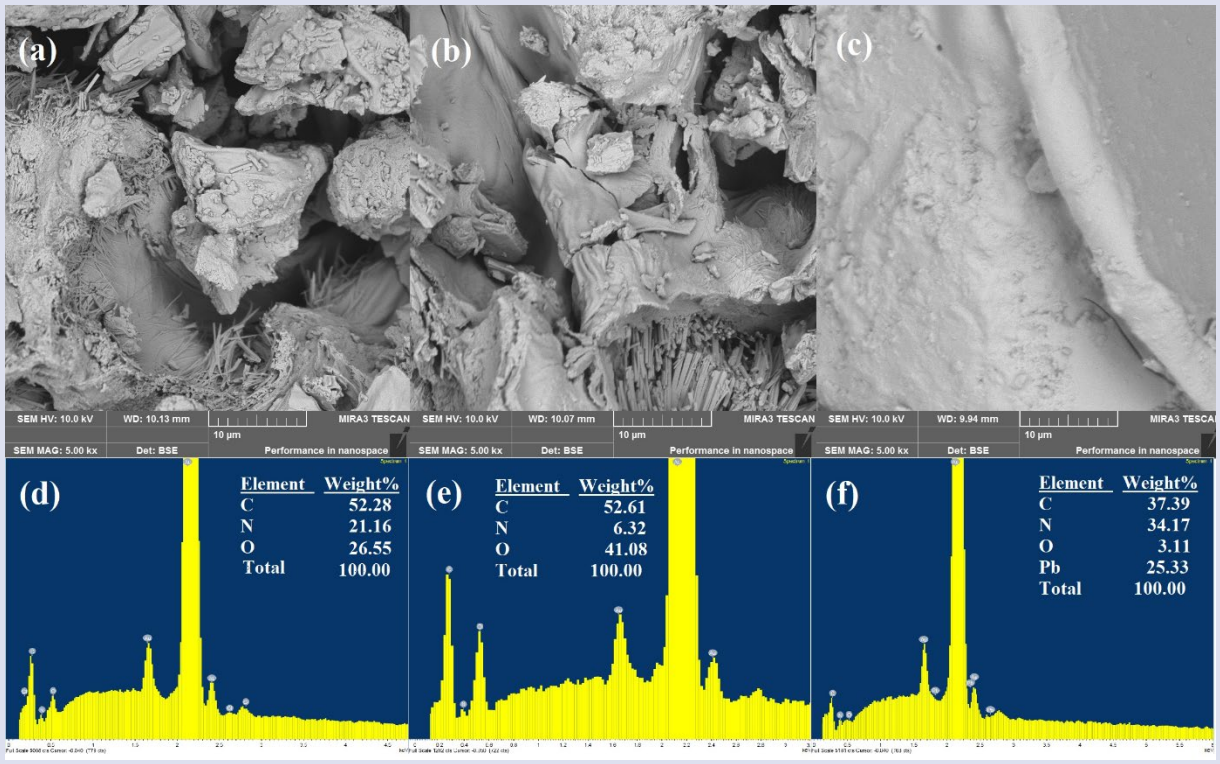

Fig. 2. SEM morphology of TP (a), PAA@TP (b), and Pb^{2+} adsorbed PAA@TP (c), and their EDX spectra, respectively (d-f)

Effect of pH

The effect of initial pH on the adsorption of Pb^{2+} ions on the PAA@TP composite was thoroughly investigated within the pH range of 1.0-5.5. The results were plotted in a pH-Q graph, depicted in Fig. 3. The graph illustrates that as the pH of the aqueous solution increases, the removal of Pb^{2+} ions also increases. At lower pH values (acidic conditions), the adsorbent surface becomes surrounded by H_3O^+ ions, resulting in positively charged surface functional groups. In such acidic conditions, H_3O^+ ions create electrostatic repulsion, hindering the approach of Pb^{2+} ions to the PAA@TP composite surface. Consequently, the efficiency of Pb^{2+} ion adsorption is low under acidic pH conditions (pH 1.0 and 2.0). As the pH of the solution increases, the competition between H_3O^+ ions and Pb^{2+} ions for binding sites on the PAA@TP surface decreases. Simultaneously, the electrostatic interaction between Pb^{2+} ions and the composite surface increases due to the decrease in positive charge density on the PAA@TP surface. This leads to enhanced adsorption efficiency. The deprotonation of active sites on the composite surface increases as the pH rises from 2.0 to 3.5, facilitating stronger electrostatic interaction between Pb^{2+} ions and the PAA@TP surface. Consequently, the adsorption capacity increases. The maximum adsorption of Pb^{2+} ions is achieved at pH 4.5. However, as the pH surpasses 5.0, the removal capacity begins to decrease. In pH regions where pH > 5.0, Pb^{2+} ions may undergo hydrolysis reactions, leading to the formation of various hydroxide species. [23]. Consequently, simultaneous adsorption and precipitation processes occur, resulting in reduced removal capacity. In summary, the pH of the solution significantly influences the adsorption of Pb^{2+} ions on the PAA@TP composite, with optimal adsorption occurring at pH 4.5. Beyond this pH, the formation of non-adsorbable hydroxide species diminishes the removal capacity.

The point of zero charge represents the pH value at which the adsorbent surface becomes electrically neutral. To determine the surface charge of the PAA@TP composite, the solid addition technique was used. In this technique, the same amount of PAA@TP composite was added to a series of solutions with the same ionic strength but different pH values. By measuring the pH values of the equilibrium solutions after waiting 24 hours, the pH at which the surface charge is neutral, that is, pHpzc, was determined. The solid addition technique allows researchers to systematically vary the pH of the solution while keeping other parameters constant. This information is crucial to understand the adsorption behavior of the composite under different pH conditions and to optimize its performance in practical applications [24]. The pHpzc value for the PAA@TP composite was determined to be 5.11, as shown in **Fig. 3.** This pH value indicates the point at which the surface of the composite becomes electrically neutral. At solution pH values lower than the pHpzc value (pHpzc>pH), the surface of the composite carries a net positive charge, while at solution pH values greater than the pHpzc value (pHpzc<pH), it carries a net negative charge on the composite This information is crucial for understanding the adsorption behavior of the PAA@TP composite, especially about pH-dependent processes such as electrostatic interactions with adsorbate species.

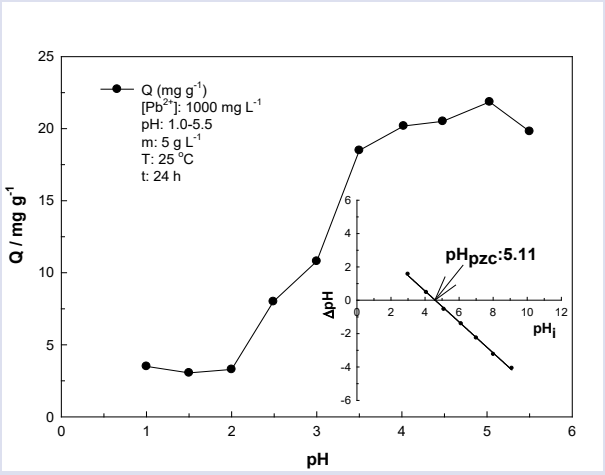

Fig. 3. Effect of pH and pHpzc

Effect of Adsorbent Dose

In experiments designed to evaluate the effect of adsorbent dose, the PAA@TP composite was used in amounts ranging from 1 to 20 g L^{-1}. The relationship between the adsorbent dose and adsorbed amount is shown in Fig. 4. It is seen that as the amount of adsorbent increases, the number of active adsorption sites also increases. Despite the increase in active centers, the concentration of Pb^{2+} ions in the solution remains constant. It was observed that increasing the adsorbent dose from 1 g L^{-1} to 20 g L^{-1} led to an increase in the removal percentage from 12% to 70%. This observation underlines the importance of optimizing the adsorbent dose in adsorption processes. By appropriately adjusting the adsorbent dose, researchers can maximize the use of active adsorption sites and increase the efficiency of removing contaminants from the solution.

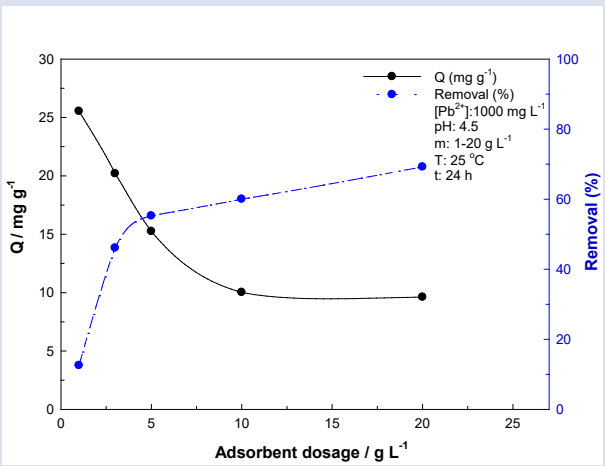

Fig. 4. Effect of adsorbent dose

Adsorption Isotherms

To examine the nature of the adsorption process of Pb^{2+} ions onto the PAA@TP composite, Langmuir, Freundlich, and Dubinin-Radushkevich (D-R) isotherm models were applied to the obtained data. The Langmuir isotherm model [25] is based on the assumption that there is a fixed number of active centers with equal energy on the homogeneous adsorbent surface. The Freundlich isotherm model [26] assumes the existence of different types of adsorptive areas on a heterogeneous surface. The D-R isotherm model [27] examines the nature of adsorption on a heterogeneous surface, especially in porous adsorbents, and evaluates the adsorption process from an energetic perspective.

The fit of the Langmuir, Freundlich, and D-R isotherm models for the adsorption of Pb^{2+} ions onto the PAA@TP composite is shown in Fig. 5, and the parameters of the isotherm models are summarized in Table 1. When the correlation coefficients of the Langmuir and Freundlich isotherm models were examined, it was seen that the correlation coefficient of the Langmuir model was greater than the correlation coefficient of the Freundlich model. This shows that the active centers on the surface of the PAA@TP composite are distributed homogeneously and Pb^{2+} ions form a single layer on this homogeneous surface. The adsorption capacity was determined as 27.3 mg g^{-1}. In addition, the β value of 0.330 obtained from the Freundlich isotherm equation shows the feasibility of adsorption. From the D-R isotherm model, the E_{DR} value calculated as 14.7 kJ mol^{-1} and E_{DR} > 8 kJ mol^{-1}, it can be inferred that the adsorption of Pb^{2+} ions on PAA@TP occurs in the form of chemical adsorption.

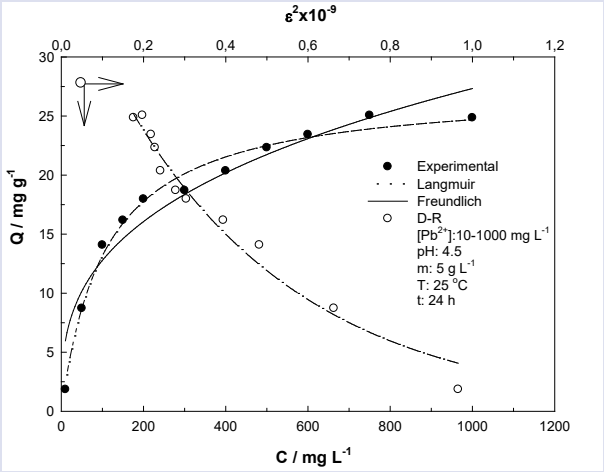

Fig. 5. Adsorption isotherms

Table 1. The parameters of isotherm models

Isotherm Model	Parameter	Value
Langmuir $Q = \frac{Q_L C_e}{1 + K_L C_e}$	Q_L (mg g^{-1})	27.3
	K_L (L mg^{-1})	0.00927
	R^2	0.988
Freundlich $Q = X_F C_e^{\beta}$	X_F	2.79
	β	0.330
	R^2	0.935
D-R $Q = X_{DR} e^{-(K_{DR}\varepsilon^2)}$	X_{DR} (mg g^{-1})	37.8
$\varepsilon = RT\ln\left(1 + \frac{1}{C_e}\right)$	$-K_{DR}x10^9$/mol^2 KJ^{-2}	2.13
$E_{DR} = (2K_{DR})^{-0.5}$	E_{DR}/kJ mol^{-1}	14.7
	R^2	0.973

A comparison of the Pb^{2+} ion adsorption capacity of the PAA@TP composite with other adsorbents reported in the literature is presented in Table 2. Examining Table 2, it was seen that the efficiency of Pb^{2+} ion removal by the PAA@TP composite was higher than that of many other adsorbents. This comparison highlights the superior performance of the PAA@TP composite in removing Pb^{2+} ions from aqueous solutions, highlighting its potential as an effective adsorbent for wastewater treatment and environmental remediation applications.

Table 2. The comparison of Pb^{2+} ion adsorption capacities of various adsorbents found in the literature

Adsorbent	pH	Q/ mg g^{-1} from Langmuir model	Reference
MoS_2-clinoptilolite	6.0	3.45	[28]
Waste beer yeast	1.0-5.0	2.34	[29]
Peels of banana	5.0	2.18	[30]
Waste beer yeast	1.0-5.0	2.34	[29]
Coconut	4.0	4.38	[31]
Okra waste	5.0	5.0	[32]
Pinus Nigra Tree Bark	8.0	12.6	[33]
Chitosan-GLA beads	4.5	14.24	[34]
Coir	4.9	0.127	[35]
Hydroxyapatite–chitosan composite	7.0	12.04	[36]
PAA@TP	4.5	27.3	This study

Adsorption Kinetics

Adsorption kinetics is very important as it provides valuable information about the adsorption mechanism and helps optimize adsorption processes for the effective removal of heavy metal pollutants from wastewater. The effect of interaction time on the adsorption of Pb^{2+} ions by PAA@TP was investigated at time intervals ranging from 10 to 1440 min, as shown in Fig. 6. Looking at Fig. 6, the adsorption occurs quickly due to the presence of empty adsorptive sites on the PAA@TP composite surface. As the equilibrium time is approached, the adsorption rate gradually slows down. This phenomenon indicates that Pb^{2+} ions gradually penetrated the pores of the PAA@TP composite. Further examination of Fig. 6 showed that the time required for Pb^{2+} adsorption to reach equilibrium was approximately 180 min. A significant increase in adsorption was observed beyond this stage, indicating that the adsorption centers had become saturated.

The kinetic models used for describing the adsorption process are represented by the equations given in Table 3. The corresponding graphs of the pseudo-1st-order (PFO) [37], pseudo-2nd-order (PSO) [38], and intra-particle diffusion (IPD) [39] models are depicted in Fig. 6, and the calculated results from these models are summarized in Table 3. Standard regression coefficient (R^2) values were compared to evaluate the applicability of the PFO and PSO models. It was seen that the R^2 value for the PSO model (R^2: 0.907) was greater than the value of the PFO model (R^2: 0.881). It also showed that the PSO model provided a better fit to the experimental data, with the calculated Q_t agreeing more closely with the experimental Q_e values. Additionally, the fit of the experimental data to the IPD model graph was examined to determine the mechanism involved in the adsorption process. The multicollinearity observed in the IPD plot presented in Fig. 6 indicates that two or more steps are involved in the adsorption process. The bilge linearity observed in the IPD plot indicates the presence of both film and pore diffusion mechanisms. Overall, the kinetic results showed that the adsorption process of Pb^{2+} ions onto the PAA@TP composite followed multiple steps characterized by IPD and PSO patterns.

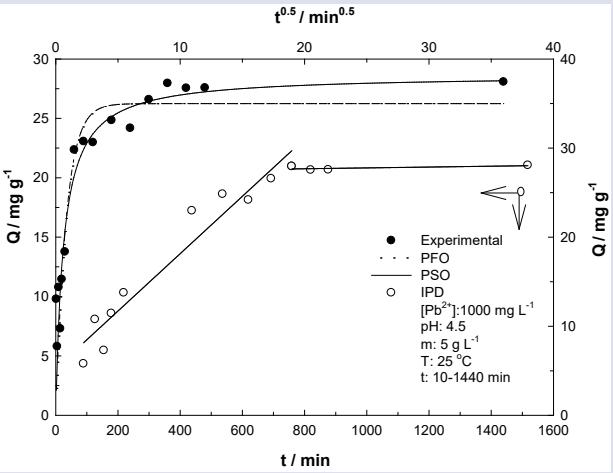

Fig. 6. Adsorption kinetics

Table 3. The parameters of kinetic models

Kinetic model	Parameter	Value
PFO	Q_t / mg g^{-1}	28.1
$Q_t = Q_e[1 - e^{-k_1 t}]$	Q_e / mg g^{-1}	26.2
$H_1 = k_1 Q_e$	k_1 x10^3/min^{-1}	29.3
	H_1x10^3/mg$g^{-1}min^{-1}$	770
	R^2	0.881
PSO	Q_t/ mg g^{-1}	28.1
$Q_t = \frac{t}{\left[\frac{1}{k_2 Q_e^2}\right] + \left[\frac{t}{Q_e}\right]}$	Q_e / mg g^{-1}	28.7
	k_2x10^3/$mg^{-1}gmin^{-1}$	1.39
	H_2x10^3/mg g^{-1} min^{-1}	1145
$H_2 = k_2 Q_e^2$	R^2	0.907
IPD	k_i x10^3/mg g^{-1} $min^{-0.5}$	5261
$Q_t = k_i t^{0.5}$	R^2	0.936

Adsorption Thermodynamics

The effect of temperature on the adsorption process is a critical aspect to consider in adsorption studies. Thermodynamic parameters such as ΔG°, ΔH°, and ΔS° were calculated using the following equations [40].

$$K_d = \frac{Q}{C_e} \quad (4)$$

$$lnK_D = \frac{\Delta S^\circ}{R} - \frac{\Delta H^\circ}{RT} \quad (5)$$

$$\Delta G^o = \Delta H^o - T\Delta S^o \quad (6)$$

The Van't Hoff graph was plotted to observe the effect of temperature on adsorption (Fig. 7), and the resulting thermodynamic parameters are summarized in Table 4. The standard enthalpy value was found to be -22.7 kJ mol^{-1}. The fact that the adsorption process was exothermic showed that increasing the temperature led to a decrease in the adsorption capacity. The entropy value was found to be -47.8 J mol^{-1} K^{-1}. In addition, negative values of ΔG° indicated that the nature of the adsorption was thermodynamically feasible and spontaneous. Overall, these findings showed that the adsorption process was affected by temperature and followed an exothermic path.

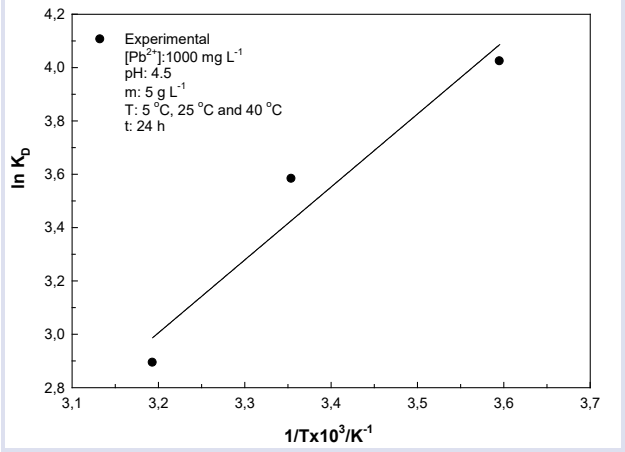

Fig. 7. Adsorption thermodynamics

Tablo 4. Thermodynamic parameters

Temperature/°C	ΔH°/kJ mol^{-1}	ΔG°/kJ mol^{-1}	ΔS°/J mol^{-1} K^{-1}	R²
5		-9.40		
25	-22.7	-8.45	-47.8	0.936
40		-7.73		

Reusability

In adsorption studies, the reusability and recovery of the adsorbent are crucial factors to consider. Therefore, it is essential to investigate the desorption behavior of the PAA@TP composite used for removing Pb^{2+} ions. To examine the desorption of Pb^{2+} ions from the PAA@TP composite, three solvents were utilized: 1 mol L^{-1} solutions of HCl, NaOH, and ethyl alcohol. After subjecting the composite to three desorption cycles, it was observed that HCl achieved the highest yield of desorption, with a rate of 57% (as shown in **Fig. 8**). This finding demonstrated that HCl was the most effective solvent for removing Pb^{2+} ions from the PAA@TP composite, leading to a relatively high recovered ion yield.

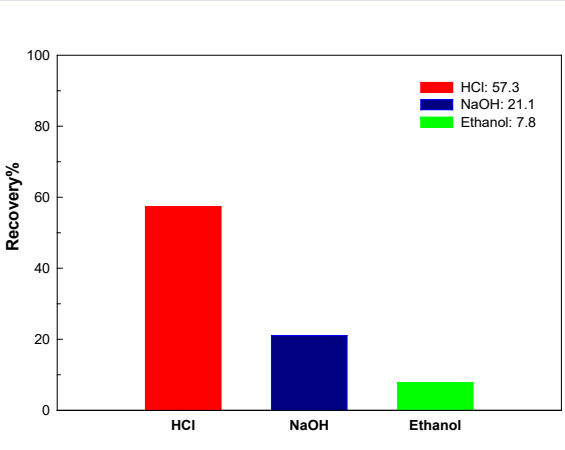

Fig. 8. The effect of desorption on PAA@TP

Conclusion

In this article, the adsorption of Pb^{2+} ions on the PAA@TP composite used as an adsorbent was thoroughly investigated. Various experimental parameters such as pH, contact time, adsorbent dose, initial concentration of the solution, and temperature were systematically varied to optimize the adsorption conditions. Optimum removal conditions were determined as pH 4.5, adsorbent dose 5 g L^{-1}, 24-hour contact time, and 25°C temperature. Experimental data were applied to Langmuir, Freundlich, and D-R isotherms models. Among these models, the Langmuir model showing monolayer adsorption behavior showed the best fit to the experimental data. Under optimum conditions, the monolayer adsorption capacity was determined as 27.3 mg g^{-1}. Adsorption kinetics showed that the adsorption process followed the PSO and IPD models. Adsorption thermodynamics showed that the adsorption process was exothermic and spontaneous. All these findings showed that the PAA@TP composite is a useful, cost-effective, and promising adsorbent for the removal of Pb^{2+} ions from wastewater.

Acknowledgments

The present study was partially supported by the Sivas Cumhuriyet University Projects Commission.

Conflict of interest

The authors declare that they have no competing interests

References

[1] Razzak S.A., Faruque M.O., Alsheikh Z., Alsheikhmohamad L., Alkuroud D., Alfayez A., Hossain S.M.Z., Hossain M.M., A comprehensive review on conventional and biological-driven heavy metals removal from industrial wastewater, *Environ. Adv*., 7 (2022) 100168.

[2] Qu X., Brame J., Li Q., Alvarez P.J.J., Nanotechnology for a safe and sustainable water supply: Enabling integrated water treatment and reuse, *Acc. Chem. Res*., 46(3) (2013) 834-843.

[3] Arbabi M., Hemati S., Amiri M., Removal of lead ions from industrial wastewater: A review of Removal methods, *Int. J. Epidemiol. Res*., 4 (2015) 10.

[4] Jayasri M.A., Suthindhiran K., Effect of zinc and lead on the physiological and biochemical properties of aquatic plant Lemna minor: its potential role in phytoremediation, *Appl. Water Sci*., 7 (2017).

[5] Chaemiso, T. D., Nefo, T. Removal methods of heavy metals from laboratory wastewater, *J. Nat. Sci. Res*., 9(2) (2019) 36-42.

[6] Iftekhar S., Ramasamy D. L., Srivastava V., Asif M. B., Sillanpää M., Understanding the factors affecting the adsorption of Lanthanum using different adsorbents: a critical review. *Chemosphere*., 204 (2018) 413-430.

[7] Feng, N., Guo, X., Liang, S. Adsorption study of copper (II) by chemically modified orange peel, *J. Hazard. Mater*., 164 (2009) 1286-1292.

[8] ElSayed, E. E. . Natural diatomite as an effective adsorbent for heavy metals in water and wastewater treatment (a batch study), *Water Sci.,* 32(1) (2018) 32-43.

[9] Arslan, D. Ş., Ertap, H., Şenol, Z. M., El Messaoudi, N., Mehmeti, V. Preparation of polyacrylamide titanium dioxide hybrid nanocomposite by direct polymerization and its applicability in removing crystal violet from aqueous solution, *J. Polym. Environ*., (2023) 1-15.

[10] Şen, N. E., Şenol, Z. M. Effective removal of Allura red food dye from water using cross-linked chitosan-diatomite composite beads, *Int. J. Biol. Macromol*., 253 (2023) 126632.

[11] Denkova-Kostova, R., Teneva, D., Tomova, T., Goranov, B., Denkova, Z., Shopska, V., Hristova-Ivanova, Y. Chemical composition, antioxidant and antimicrobial activity of essential oils from tangerine (Citrus reticulata L.), grapefruit (Citrus paradisi L.), lemon (Citrus lemon L.) and cinnamon (Cinnamomum zeylanicum Blume), *Sect. C. J. Biosci.,* 76(5-6), (2021) 175-185.

[12] Bureš, M. S., Maslov Bandić, L., Vlahoviček-Kahlina, K. Determination of bioactive components in mandarin fruits: A review, *Crit. Rev. Anal. Chem*., 53(7) (2023) 1489-1514.

[13] da Costa Marques, V. Valorization of Tangerine Peels in the Preparation of Adsorbents for Removal of Ni (II) From Aqueous Solutions (Master's thesis, Instituto Politecnico de Braganca (Portugal), (2020).

[14] Unugul T., Nigiz F. U. Preparation and characterization of an active carbon adsorbent from waste mandarin peel and determination of adsorption behavior on removal of synthetic dye solution, *Air. Soil Pollut.,* 231(11) (2020) 538.

[15] Husein D. Z. Adsorption and removal of mercury ions from aqueous solution using raw and chemically modified Egyptian mandarin peel, *Desalin. Water Treat*., 51(34-36) (2013). 6761-6769.

[16] Yılmaz M., Eldeeb, T. M., Hassaan, M. A., El-Nemr, M. A., Ragab, S., El Nemr, A. The use of mandarin-biochar-O3-TETA (MBT) produced from mandarin peels as a natural adsorbent for the removal of acid red 35 (AR35) dye from water, *Environ. Process*., 9(3) (2022) 44.

[17] Inagaki C. S., Caretta T. D. O., Alfaya R. V. D. S., Alfaya A. A. D. S. Mexerica mandarin (Citrus nobilis) peel as a new biosorbent to remove Cu (II), Cd (II), and Pb (II) from industrial effluent, Desalin, *Water Treat*., 51(28-30) (2013) 5537-5546.

[18] Özdemir N. C., Bilici, Z., Saleh M., Dizge N. Adsorption of phosphate ions and RBBR dye from aqueous solution using thermally activated mandarin peel waste, *Water Pract. Technol*., 19(1) (2024) 170-180.

[19] Torab M. M., Biosorption of lanthanum and cerium from aqueous solutions using tangerine (Citrus reticulata) peel: equilibrium, kinetic and thermodynamic studies, *Chem. Ind. Chem. Eng. Q*., 19(1) (2013) 79-88.

[20] Pavan F. A., Mazzocato A. C., Jacques R. A., Dias, S. L. Ponkan peel: a potential biosorbent for removal of Pb (II) ions from aqueous solution, *Biochem. Eng. J*., 40(2) (2008) 357-362.

[21] Abdić Š., Memić M., Šabanović E., Sulejmanović J., Begić S. Adsorptive removal of eight heavy metals from aqueous solution by unmodified and modified agricultural waste: tangerine peel, *Int. J. Environ. Sci. Technol*. 15 (2018) 2511-2518.

[22] Chiem L. T., Huynh L., Ralston J., Beattie, D. A., An in situ ATR–FTIR study of polyacrylamide adsorption at the talc surface, *J. Colloid Interface Sci*. 297(1), (2006) 54-61.

[23] Yurishcheva A.A., Sorption of Pb^{2+} by magnetite coated with humic acids, *J. Biol. Phys. Chem*. 13 (2013) 61-68.

[24] Şenol Z.M., Gül Ü.D., Gürkan R., Bio-sorption of bisphenol a by the dried- and inactivated-lichen (Pseudoevernia furfuracea) biomass from aqueous solutions, *J. Environ. Heal. Sci. Eng.,* 18 (2020) 853-864.

[25] Langmuir I., The adsorption of gases on plane surfaces of glass, mica and platinum, *J. Am. Chem. Soc.,* 40(9) (1918) 1361-1403.

[26] Freundlich H., Über die Adsorption in Lösungen, *Zeitschrift Für Phys. Chemie.* 57(1) (1907) 385-470.

[27] Hu, Q., & Zhang, Z. (2019). Application of Dubinin–Radushkevich isotherm model at the solid/solution interface: A theoretical analysis, *J. Mol. Liq.,* 277 (2019) 646-648.

[28] Pandey S., Fosso-Kankeu E., Spiro M. J., Waanders, F., Kumar, N., Ray, S. S., Kang, M. Equilibrium, kinetic, and thermodynamic studies of lead ion adsorption from mine wastewater onto MoS2-clinoptilolite composite, *Mater. Today Chem.,* 18 (2020) 100376.

[29] Parvathi K., Nagendran R., Nareshkumar R., Lead biosorption onto waste beer yeast by-product: a means to decontaminate effluent generated from the battery manufacturing industry, *Electron. J. Biotechnol.* 10(1) (2007) 92-105.

[30] Anwar, J., Shafique, U., Salman, M., Dar, A., & Anwar, S. (2010). Removal of Pb (II) and Cd (II) from water by adsorption on peels of banana, *Bioresour. Technol*., 101(6) (2010) 1752-1755.

[31] Gueu, S., Yao, B., Adouby, K., Ado, G. Kinetics and thermodynamics study of lead adsorption on to activated carbons from coconut and seed hull of the palm tree, Int. *J. Environ. Sci. Technol.* 4 (2007) 11-17.

[32] Hashem M. A. (2007). Adsorption of lead ions from aqueous solution by okra wastes, *Int. J. Phys. Sci.,* 2(7) (2007) 178-184.

[33] Argun M. E., Dursun S. Activation of pine bark surface with NaOH for lead removal, *J. Int. Environ. Appl. Sci*., 2 (2007) 5-10.

[34] Ngah, W. W., Fatinathan, S. Pb (II) biosorption using chitosan and chitosan derivatives beads: Equilibrium, ion exchange and mechanism studies, *J. Environ. Sci.,* 22(3) (2010) 338-346.

[35] Shukla S. R., Pai R. S. Removal of Pb (II) from solution using cellulose-containing materials, *J. Chem. Technol. Biotechnol*., 80(2) (2005) 176-183.

[36] Gupta N., Kushwaha A. K., Chattopadhyaya, M. C. Adsorptive removal of Pb2+, Co2+ and Ni2+ by hydroxyapatite/chitosan composite from aqueous solution, *J. Taiwan Inst. Chem. Eng*. 43(1), (2012) 125-131.

[37] Ho, Y. S., McKay, G. Kinetic models for the sorption of dye

from aqueous solution by wood, *Process Saf. Environ. Prot*., 76(2) (1998) 183-191.

[38] Ho, Y. S., McKay, G. Pseudo-second order model for sorption processes, *Process Biochem*., 34(5) (1999) 451-465.

[39] Weber Jr, W. J., Morris, J. C. Kinetics of adsorption on carbon from solution, *J. Sanit. Eng. Div.,* 89(2) (1963) 31-59.

[40] Hong, S., Wen, C., He, J., Gan, F., Ho, Y. S. Adsorption thermodynamics of methylene blue onto bentonite, *J. Hazard. Mater*., 167(1-3) (2009) 630-633.

Cumhuriyet Sci. J., 45(2) (2024) 331-337
DOI: https://doi.org/10.17776/csj.1397903

Cumhuriyet Science Journal

| csj.cumhuriyet.edu.tr | Founded: 2002 ISSN: 2587-2680 e-ISSN: 2587-246X Publisher: Sivas Cumhuriyet University

Age and Peripheral Blood Values Relationship Evaluation of Trichomonas Vaginalis, Candida, and Gardnerella Vaginalis Frequency in Cervicovaginal Pap Smear Screening in Aksaray Province

Şerife Özlem Genç [1,a,*], Melike Ordu [2,b]

[1] *Obstetrics and Gynecology, Faculty of Medicine, Cumhuriyet University, Sivas, Türkiye.*
[2] *Pathology, Faculty of Medicine, Aksaray University, Aksaray, Türkiye.*
**Corresponding author*

Research Article

History
Received: 29/11/2023
Accepted: 19/04/2024

ABSTRACT

This study aimed to explore the correlation between causative agents of vaginitis detected in Pap smear screenings and various hematological indices, alongside the severity of infections observed in Pap smears. We analyzed 348 Pap smear results, which were categorized into normal and abnormal findings and further subdivided into groups based on the presence of Vulvovaginal Candidiasis (VVC), Bacterial Vaginosis (BV), and Trichomoniasis (TV). The degree of inflammation (mild, moderate, severe) was assessed in relation to hematological indices (Platelet Index Value (PIV), Systemic Immune-Inflammation Index (SII), Systemic Inflammatory Response Index (SIRI), Neutrophil to Lymphocyte Ratio (NLR), Platelet to Lymphocyte Ratio (PLR), and Lymphocyte to Monocyte Ratio (LMR)), guided by the 2014 Bethesda System for evaluation. Out of 1654 patients screened, 348 met the inclusion criteria (253 aged below 45 years; 95 aged 45 years and above). In the under-45 age group, 83.3% had normal findings, with prevalence rates for VVC, BV, and TV at 73.4%, 60.2%, and 80.0%, respectively. In the over-45 group, these figures were 16.7% (normal), 26.6% (VVC), 39.8% (BV), and 20% (TV). The prevalence of moderate vaginitis in Pap smears was 45.3% for VVC, 96.1% for mild BV, and 53.3% for moderate TV. In cases of Atypical Squamous Cells of Undetermined Significance (ASCUS), BV was predominant, while VVC and TV were absent in Low-Grade Squamous Intraepithelial Lesion (LSIL) and High-Grade Squamous Intraepithelial Lesion (HSIL) cases. BV was present in 7.8% of normal smears. Significant associations were observed between hematological parameters and the severity of inflammation in the normal smear category ($p<0.001$). In squamous cell anomaly cases, especially ASCUS, differences in SII, NLR, PLR, SIRI, and PIV were noted between severe and mild infections, as well as between moderate and severe infection groups. This research underscores the linkage between the severity of infection and cellular abnormalities identified in cervical cytology, causative agents of vaginitis, and hematological indices with inflammatory parameters, potentially informing clinical management strategies.

Keywords: Smear, Vaginitis agents, Hematological indices.

[a] *drserifeozlemgenc@hotmail.com* *https://orcid.org/0000-0002-9811-2726*
[b] *dr_melike@windowslive.com* *https://orcid.org/0000-0001-8863-817x*

Introduction

Vaginal infections are common health issues faced by women. Those with vaginitis experience local symptoms such as discharge, itching, and burning, leading to predominantly localized treatment. However, vaginitis often recurs, necessitating a better understanding of its systemic effects.

The Pap smear test is a screening method primarily employed to detect cervical cancer, precursor lesions, and certain viral, bacterial, and fungal infections causing vaginitis [1]. Infections causing inflammation in the cervix include primarily Trichomonas vaginalis, Candida albicans, and Gardnerella vaginalis. Additionally, bacterial infections such as Gardnerella mobiluncus, Haemophilus ducreyi, Neisseria gonorrhoeae, Chlamydia trachomatis, Escherichia coli, streptococci, staphylococci, peptostreptococci, and viral infections like HSV can contribute to cervical inflammation [2]. Vulvovaginal candidiasis (VVC) infections are caused by fungi, such as Candida albicans, leading to local symptoms like itching, burning, and vaginal discharge. Neutrophils surrounding squamous epithelial cells and the classic "spindle-shaped" or "dart" appearance may be observed in Pap smears. Trichomonas vaginalis (TV) causes an infection characterized by symptoms such as vaginal itching, malodorous discharge, and painful urination. In Pap smears, it appears as a flagellated microorganism with a pale, vesicular, and eccentrically located nucleus intertwined with inflammatory cells. Bacterial vaginosis (BV) results from an imbalance in vaginal flora, typically causing malodorous vaginal discharge. In Pap smears, the presence of small coccobacilli described as "clue cells" and the covering of squamous cells with a bacterial layer define this condition.

A plethora of studies have explored the role of various systemic inflammatory indices in exacerbating the severity of diseases [3-5]. In the context of this study, our aim was to investigate the systemic effects of vaginitis utilizing systemic inflammatory indices. This research underscores the potential pivotal role of systemic inflammatory indices in evaluating and monitoring the

severity of the disease in clinical applications. In this retrospectively planned study, inflammation indicators observed in Pap smear tests for VVC, BV, and TV cases are categorized. Hematological indices obtained from peripheral blood values are then used to test the hypothesis that vaginal infections may lead to systemic inflammation in addition to local symptoms. A secondary aim is to evaluate the association between the causative agents of vaginitis and cytological abnormalities observed in Pap smear tests. This understanding has the potential to enhance treatment strategies and improve women's health.

Materials and Methods

The study included 348 patients out of 1654 who applied to the Department of Obstetrics and Gynecology at Aksaray University Training and Research Hospital between January 2021 and December 2021 and had smear samples taken. The study encompasses women aged 18 and older, explicitly excluding those who have ingested antibiotics for any purpose in the preceding month, are currently pregnant, or are afflicted with chronic systemic ailments such as diabetes or hypertension. Eligibility extends to participants evidencing infections in vaginal smears, including Vulvovaginal Candidiasis (VVC), Bacterial Vaginosis (BV), and Trichomoniasis (TV), as well as to those exhibiting no infection. In instances of concurrent infections by the pathogens, the predominant infection will be prioritized. Conversely, exclusion criteria are applied to candidates not fulfilling the prerequisites, those combating other active infections, or presenting with indeterminate or analytically unsuitable smear results.

Smear samples were spread using the ThinPrep method in the pathology laboratory, stained with Papanicolaou (Pap), and evaluated by a pathology specialist according to the 2014 Bethesda system [6]. Smear results for those categorized as negative for intraepithelial lesions and malignancy were evaluated under cellular changes reactive to infection, encompassing organisms causing infection (Trichomonas vaginalis, Candida species, and shift towards bacterial vaginosis in the flora). Patients were grouped into three categories based on pathological evaluation of infections: VVC, BV, and TV.

In the smear sample where clue cells are observed, BV is identified (Figure 1).

In the smear sample of Candida infection, pseudo-hyphae, hyphae, and spores are observed (Figure 2).

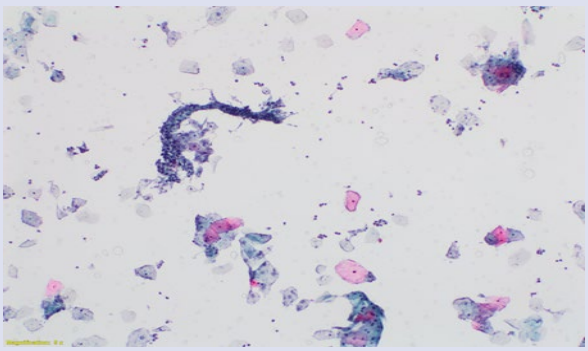

(a)

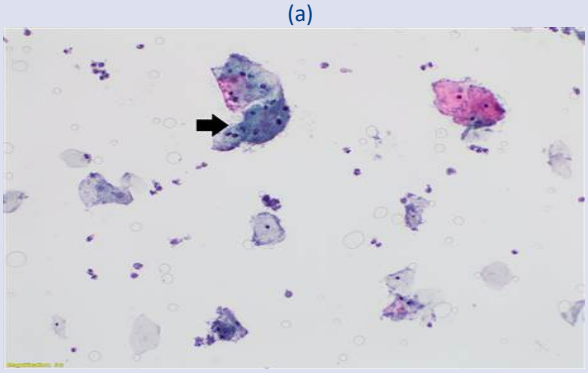

(b)

Figure 1 a- b. The bacterial layer covering the squamous epithelial cell (clue cell) is observed with a black arrow on the ThinPrep Pap-stained smear preparation (x10, x20) using the Olympus Bx43 microscope.

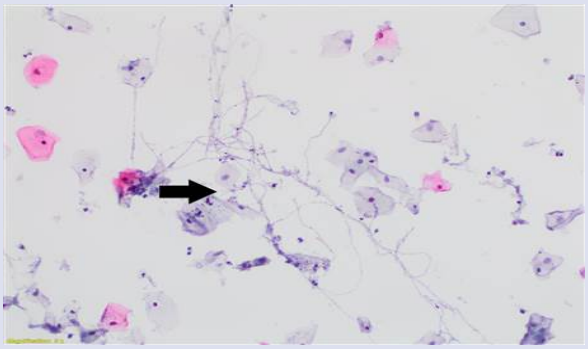

(a)

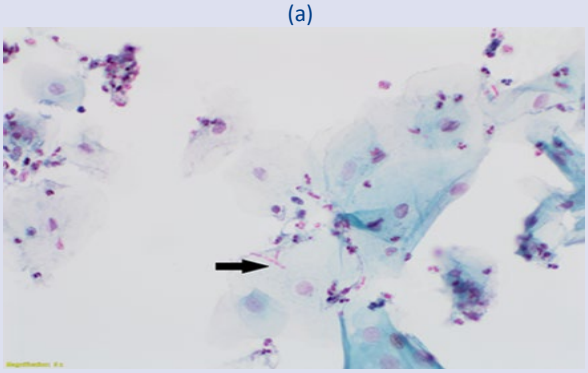

(b)

Figure 2 a- b. The smear sample stained with ThinPrep Pap exhibits a classic 'spindle-shaped' appearance with squamous epithelial cells intertwined with described Candida hyphae and spores. These are indicated by a black arrow on the Olympus Bx43 microscope at magnifications x20 and x40.

The sample shows Trichomonas vaginalis with ovoid or round-shaped nuclei and a sporadically elongated appearance of flagella (Figure 3).

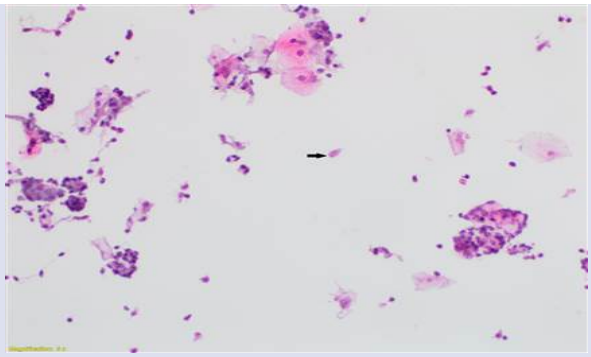

Figure 3: In the ThinPrep Pap-stained smear preparation, an infectious agent with an elongated nucleus consistent with Trichomonas vaginalis is observed (black arrow) among squamous epithelial cells.

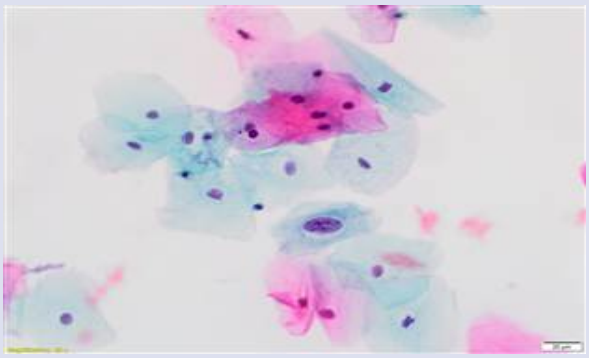

(a)

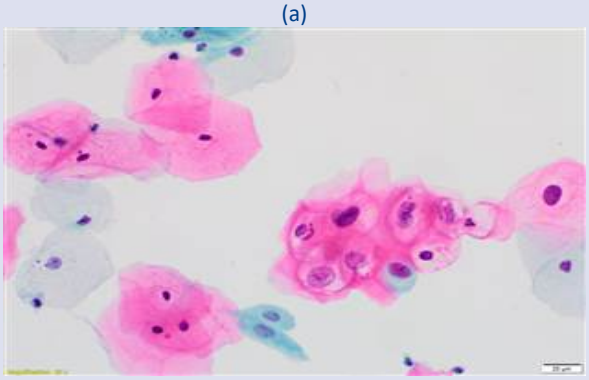

(b)

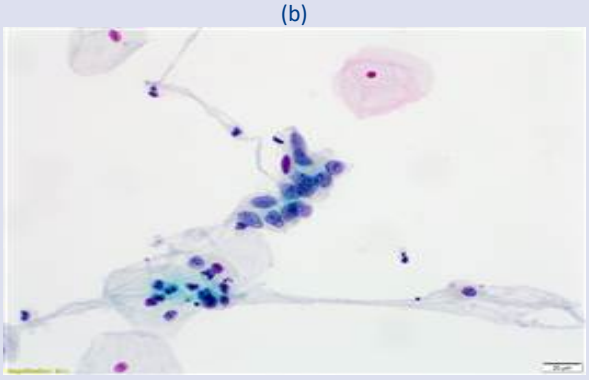

(c)

Figure 4. a. ASCUS example showing abnormalities in squamous epithelial cells, including approximately 3 times the size of the intermediate cell nucleus. b. LGSIL example with nuclear membrane irregularities and perinuclear halo in the ThinPrep Pap-stained smear preparation. c. HGSIL example in the ThinPrep Pap-stained smear preparation, displaying nuclear hyperchromasia.

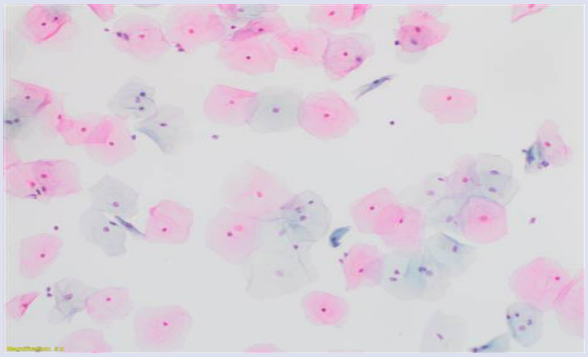

(a)

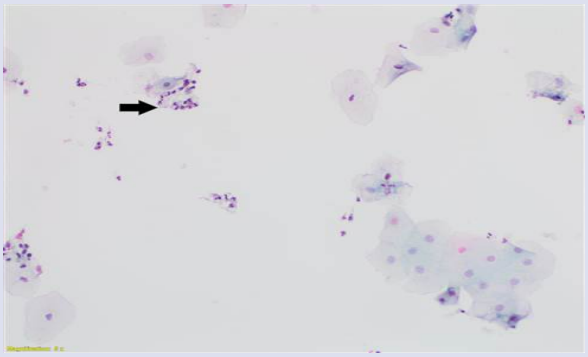

(b)

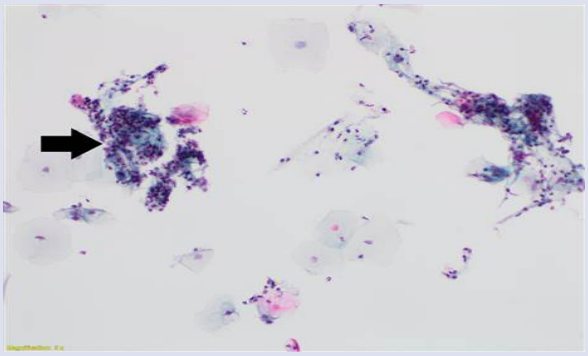

(c)

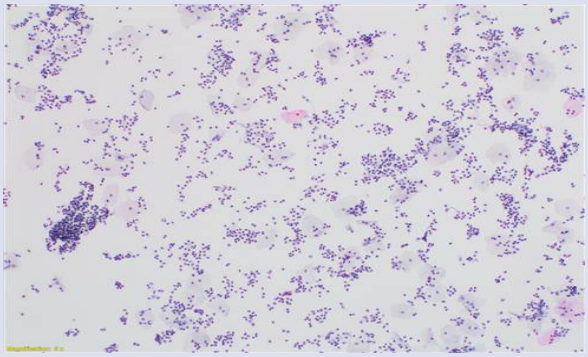

(d)

Figure 5. ThinPrep Pap-stained smear preparation depicting squamous epithelial cells and inflammatory cells overlying or interspersed with epithelial cells: a. Normal sample, b. Mild inflammation, c. Moderate inflammation, d. Severe inflammation.

In the study, the severity of inflammatory cells observed in smear samples was categorized as follows: mild; characterized by a sparse distribution of squamous cells covering a small area in the sample field, moderate; involving a greater coverage of squamous cells compared

to mild, and severe; where squamous epithelium nearly completely covered the field and was extensively present. Within the category of negative for intraepithelial lesions and malignancy, individuals with no observed infectious agents, no cellular abnormalities, and no inflammatory cells in the smear spread were classified as 'Normal' and included as the control group in the study (Figure 5).

The study was conducted to assess the potential variability in systemic impact based on the severity of infection within groups using hematological parameters derived from peripheral blood values. The following parameters were considered: neutrophil-to-lymphocyte ratio (NLR), systemic inflammatory response index (SIRI) calculated as neutrophil count × monocyte count / lymphocyte count, immune inflammation value (PIV) calculated as neutrophil count × platelet count × monocyte count / lymphocyte count, platelet-to-lymphocyte ratio (PLR), lymphocyte-to-monocyte ratio (LMR), and systemic inflammatory index (SII) calculated as neutrophil count × platelet count / lymphocyte count.

Data Analysis

IBM SPSS Statistics for Windows, Version 25.0 (IBM Corp, Armonk, NY) was used for data analysis. In addition to normality tests such as Kolmogorov-Smirnov and Shapiro-Wilk, the appropriateness of variable distributions to normality was examined through relevant distribution graphs. Chi-square and Fisher's exact test was employed for testing the distribution of categorical variables among groups, while Mann-Whitney U test was applied for investigating differences in continuous variables between groups. Kruskal-Wallis Variance Analysis technique was utilized for comparing more than two independent groups. Results were expressed as median (25th-75th percentiles) for continuous variables, and descriptive statistics in terms of frequency distributions and percentages for categorical variables. A statistical significance threshold of $p<0.05$ was considered.

Results

In our study, a total of 348 patients were included, comprising individuals diagnosed with VVC, BV, and TV based on the results of vaginal smear screenings, as well as a control group consisting of individuals with no detected infectious agents and no inflammatory cells. Patients were divided into two groups: those aged 45 and below, and those aged 45 and above. The study comprised 253 patients aged 45 and below and 95 patients aged 45 and above. Among patients aged 45 and below, 85 (83.3%) were reported in the normal category, 94 (73.4%) with VVC, 62 (60.2%) with BV, and 12 (80.0%) with TV (Table 1). In the group without squamous cell anomalies, 113 patients (88.3%) had VVC, 11 patients (73.3%) had TV, and 102 patients (100%) had no infectious agents (Table 1).

In the evaluation of the intensity of inflammatory cells observed in Thin-prep smear specimens; among cases with mild inflammation, 46 (35.9%) had VVC, 99 (96.1%) had BV, and 1 (6.7%) had TV. Among cases with moderate inflammation, 58 (45.3%) had VVC, 4 (3.9%) had BV, and 8 (53.3%) had TV. Cases with severe inflammation included 24 with VVC and 6 with TV (Table 1). These results demonstrate the impact of vaginal smear results and the detected types of infection on systemic inflammation and hematological indices.

Table 1. Age-Based Evaluation of Pap Smear Results and Infection Severity

n (%)	VVC	BV	TV	Normal
Age ≤ 45				
≤45	94 (73.4%)	62 (60.2%)	12 (80%)	85 (83.3%)
>45	34 (26.6%)	41 (39.8%)	3 (20%)	17 (16.7%)
Smear Results				
Normal	113 (88.3%)	0 (0.0%)	11 (73.3%)	102 (100%)
ASCUS	15 (11.7%)	67 (65.0%)	4 (26.7%)	0 (0%)
LSIL	0 (0%)	28 (27.2%)	0 (0%)	0 (0%)
HSIL	0 (0%)	8 (7.8%)	0 (0%)	0 (0%)
Inflammation Severity				
None	0 (0%)	0 (0%)	0 (0%)	102 (100%)
Mild	46 (35.9%)	99 (96.1%)	1 (6.7%)	0 (0%)
Moderate	58 (45.3%)	4 (3.9%)	8 (53.3%)	0 (0%)
Severe	24 (18.8%)	0 (0%)	6 (40%)	0 (0%)

Values are presented as count (percentage). VVC: Vulvovaginal Candidiasis, BV: Bacterial Vaginosis, TV: Trichomoniasis.

When patients were re-evaluated based on age groups for smear results, the presence of infection, the type, and severity of infection, it can be inferred that VVC is most common in the reproductive age, while in older ages, this tendency shifts towards BV (Table 1). Patients diagnosed with ASCUS showed a higher prevalence of BV in their smears. In cases diagnosed with LSIL and HSIL, VVC and TV were not observed, and BV was only seen in 7.8% of cases. According to the findings, the percentage of infection decreases as the degree of cytological abnormality in the smear increases (Table 1). According to the table, in the presence of TV infection, it can be stated that the infection tends to be severe.

An association was found to be significant between hematological parameters and smear inflammation severity in the category considered normal in smear preparations ($p<0.001$) (Table 2). In the category of squamous cell anomalies, in ASCUS cases, significant differences were observed in SII, NLR, PLR, SIRI, and PIV between severe and mild infection groups, and between moderate and severe

groups (p<0.005), with no difference in other hematological parameters. When cases with ASCUS results were grouped according to infection, SII, NLR, and PLR were the most significant parameters (p<0.05, p<0.001). However, no significant differences were found in mild and moderate infection groups (p>0.05). There was no significant difference in LMR values between the moderate infection group and both the mild and severe infection groups (p>0.05). In the category of squamous cell anomalies, there was no significant difference in hematological parameters between the LGSIL and HGSIL groups. In the LSIL and HSIL groups, infection was only observed in mild or moderate severity, and when compared to those with infection, no significance was found in any inflammatory index (p>0.05). On the other hand, in the group without cytological abnormalities in smear findings, it was observed that the control group significantly differed from both the moderate and severe infection groups in all inflammatory markers (p<0.05) (Table 2).

In the peripheral blood values of patients diagnosed with VVC, hematological parameters obtained include SII, NLR, SIRI, PIV, PLR and LMR. Significant differences were observed in the medians of these parameters among mild, moderate, and severe groups (p<0.05, p<0.001). According to the results, a positive correlation was observed between the severity of VVC and all systemic inflammation indices in the study.

In the VVC group, significant disparities were observed across all parameters; notably, SII, NLR, SIRI, PIV, and PLR were found to be significantly elevated (p<0.001) (Table 3). Conversely, the LMR exhibited a decrease, indicating an intensified inflammatory and immune response within this group.

For the BV group, no statistically significant differences were discerned among the evaluated parameters (p>0.05), suggesting a negligible impact of BV on these measures.

In the TV group, no significant variations were detected across SII, NLR, SIRI, PIV, PLR, and LMR parameters (p>0.05), indicating that TV infection does not markedly alter these inflammatory and immunological parameters (Table 3).

These findings elucidate the heterogeneous impact of these three infections on inflammatory and immune responses. VVC appears to significantly affect the examined parameters, whereas BV and TV do not induce substantial changes. These distinctions contribute to a deeper understanding of disease mechanisms and the development of potential therapeutic approaches (Table 3).

Table 2. Assessment of Cellular Changes and Inflammation Severity in Smear Samples

		No inflammation Mean (Min- Max)	Mild Mean (Min- Max)	Moderate Mean (Min- Max)	Severe Mean (Min- Max)	p
Normal	SII	493.82(182.53-1019.64)	402.67(193.72-880.72)	564.57 (373.75 - 1029.76	913.06(479.41-4055.33)	<0.001
	NLR	1.81(0.94 - 3.54)	1.49(0.61-2.69)	2.12(1.22-3.15)	3.15(1.57-14.48)	<0.001
	SIRI	10.55(4.14 - 18.82)	8.48(3.14-25.02)	11.74(3.77-26.44)	18.76(8.02-95.59)	<0.001
	PIV	3036.21 (803.13 - 5706.56)	2341.16 (976.99-5155.06)	3246.54 (1246.97-6524.93)	5058.18 (2444.98-26765.20)	<0.001
	PLR	9.04(3.28 - 14.55)	7.58(4.39-13.72)	9.08(6.19-17.40)	13.01(7.96-46.67)	<0.001
	LMR	5.06(3.66 - 13.45)	6.22(2.31-13.47)	5.09(2.58-15.90)	3.94(0.91-6.96)	<0.001
ASCUS	SII		491.52(283.18-1236.75)	525.07 (268.68 - 758.26)	1026.68(546.17-1455.16)	<0.001
	NLR		1.76(0.98-4.03)	1.76(0.98 - 4.03)	3.58(1.63-5.27)	<0.001
	SIRI		10.25(4.62-34.34)	10.25(4.62 - 34.34)	19.30(7.34-46.51)	0.004
	PIV		3000.34(1370.35-7314.48)	3000.34(1370.35-7314.48)	6004.1(2457.79-14697.12)	0.002
	PLR		8.72(5.22-17.22)	8.72(5.22 - 17.22)	14.28(9.54-19.51)	<0.001
	LMR		5.72(1.89-10.11)	5.72(1.89 - 10.11)	3.98(1.60-7.76)	0.033
LSIL	SII		694.02(277.22-1188.77)	374.10(374.10 - 374.10)		0.286
	NLR		2.35(1.52 - 4.15)	1.83(1.83-1.83)		0.286
	SIRI		13.86(6.94 - 22.55)	9.90(9.90-9.90)		0.500
	PIV		3645.47 (1272.56 - 8255.08)	2020.16 (2020.16-2020.16)		0.286
	PLR		10.62(4.96 - 17.37)	6.28(6.28-6.28)		0.357
	LMR		4.75(2.94 - 9.61)	6.02(6.02-6.02)		0.500
HSIL	SII		895.28(510.98- 196.88)	747.3 (337.01 - 1212.27)		0.571
	NLR		3.25(2.41 - 11.49)	2.92(1.32-3.37)		0.571
	SIRI		20.8(13.01 - 92.07)	15.19(7-19.52)		0.25
	PIV		5461.18 (3213.02- 17678.34)	4334.32 (1786.15-6303.81)		0.571
	PLR		12.11(7.27 - 23.13)	10.42(6.41-13.09)		0.571
	LMR		3.38 (0.88 - 4.98)	6.10(3.67-7.51)		0.143

SII: Systemic inflammatory index (neutrophil x platelet/ lymphocyte count) , NLR: Neutrophil-to-Lymphocyte Ratio, SIRI: Systemic inflammatory response index (neutrophil × monocyte/ lymphocyte count), PIV: Pan-immune inflammation value (neutrophil × platelet x monocyte/lymphocyte count), PLR: Platelet-to-Lymphocyte ratio, LMR: Lymphocyteto- Monocyte Ratio, ASCUS: Atypical Squamous Cells of Undetermined Significance, LSIL: Low-Grade Squamous Intraepithelial Lesion , and HSIL: High-Grade Squamous Intraepithelial Lesion.

Table 3. Investigation of the Relationship Between Infectious Agents and the Severity of Smear Inflammation

		Mean	Min.	Max.	Mean	Min.	Maks.	Mean	Min.	Maks.	p
VVC	SII	402.82	193.72	880.72	563.61	268.68	1019.52	1016.47	513.27	4055.33	**<0.001**
	NLR	1.50	0.61	2.72	2.13	1.20	3.10	3.44	1.63	14.48	**<0.001**
	SIRI	8.50	3.14	25.02	11.73	3.77	26.44	20.10	7.34	95.59	**<0.001**
	PIV	2378.58	976.99	5155.06	3232.70	1246.97	6524.93	6314.49	2457.79	26765.20	**<0.001**
	PLR	7.58	4.39	13.72	9.08	5.80	17.40	14.15	7.96	46.67	**<0.001**
	LMR	6.19	2.31	13.47	5.11	2.58	15.90	3.66	0.91	7.76	**<0.001**
BV	SII	560.52	277.22	1976.88	560.70	337.01	1212.27				0.899
	NLR	2.01	0.98	11.49	2.38	1.32	3.37				0.711
	SIRI	11.03	4.62	92.07	12.55	7.00	19.52				0.863
	PIV	3129.52	1272.56	17678.34	3177.24	1786.15	6303.81				0.736
	PLR	9.25	4.96	23.13	8.41	6.28	13.09				0.558
	LMR	5.40	0.88	10.11	6.06	3.67	7.51				0.558
TV	SII	579.55	579.55	579.55	556.67	429.68	1029.76	620.18	479.41	788.52	0.619
	NLR	2.28	2.28	2.28	1.81	1.58	3.15	2.24	1.57	3.57	0.507
	SIRI	12.09	12.09	12.09	12.11	7.97	16.14	14.55	8.02	16.45	0.57
	PIV	3071.61	3071.61	3071.61	3397.24	2588.34	4777.06	3690.22	2444.98	5182.96	0.869
	PLR	8.94	8.94	8.94	9.40	7.88	14.34	9.68	8.59	11.54	0.869
	LMR	5.36	5.36	5.36	4.86	3.73	7.36	4.80	3.96	6.96	0.869

VVC: Vulvovaginal Candidiasis. BV: Bacterial Vaginosis. TV: Trichomoniasis.

Discussion

Smear is an effective and cost-efficient method used in the screening of cervical cancer. In our country, according to the cervical cancer screening policy of the Ministry of Health, women between the ages of 30-65 undergo smear and HPV screening every five years. Since smear is a routine screening, additional information that can be obtained through it is valuable as it does not require additional procedures for the patient.

Vaginitis is a leading cause of women seeking gynecological clinics, and most women experience vaginitis at some point in their lives [7]. The most common causes of vaginitis are Vulvovaginal Candidiasis (VVC), Bacterial Vaginosis (BV), and Trichomonas vaginalis (TV) [8]. Vaginitis is known to result in societal productivity loss and economic burdens [9,10]. Additionally, studies have shown adverse pregnancy outcomes in women with BV and TV [11,12].

This study investigated the potential effects of VVC, BV, and TV detected in vaginal smear results on systemic inflammation and hematological indices. The significant increases observed in PIV, SII, SIRI, NLR, and PLR support the hypothesis that VVC may lead to systemic inflammation. However, in the treatment of VVC, choosing systemic over local therapy will be important to eliminate the disease and prevent recurrence. Furthermore, the occurrence of TV in the reproductive period, often leading to moderate or severe infection when present, is noteworthy. Despite this severe inflammation, TV did not significantly alter systemic inflammation indices, suggesting that local treatment may be sufficient in TV treatment.

A meta-analysis evaluating the risk of cervical neoplasia associated with TV has indicated a significant increase in cervical neoplasia [13]. In our study, however, TV was not detected except in those with cytological abnormalities, excluding those with ASCUS. In the evaluation of smear samples, TV organisms may be overlooked as squamous cell abnormalities become more prominent in LGSIL and HGSIL cases. Considering this, TV should always be kept in mind in evaluations. TV was not observed in our study in the LGSIL and HGSIL groups.

One of the most important aspects of this study is its presentation of the comparison of smear infection severity, types of vaginitis, and hematological parameters with cytological abnormalities, a topic rarely found in the literature. Another important finding of our study is that, contrary to Candida, which is most commonly associated with ASCUS in the literature, BV was the most commonly associated infection in cases of ASCUS [14]. Additionally, the presence of only BV in those with LSIL and HSIL smear results suggests the need to investigate the role of this factor in cytological abnormalities. In a study evaluating the relationship between cervical intraepithelial lesions and BV, BV was found to be associated with HPV positivity and HSIL [15]. In our study, similarly, BV was the most commonly detected infection in all cytological abnormalities.

A meta-analysis of ten studies compiled in 2023 suggested an increase in aerobic vaginitis, BV, and TV with HPV positivity, but no association was found with VVC concerning cytological abnormalities [16]. In our study, VVC was not observed in patients with LSIL and HSIL, and its prevalence in those with ASCUS was lower (11.7%) compared to TV (26.7%) and BV (65%).

The results of this study emphasize the clinical significance that VVC may contribute not only to local symptoms but also to systemic inflammation. These findings can assist in evaluating treatment strategies for vaginal Candida infections and monitoring systemic inflammation in patients with such infections. Specifically, further research is needed to explore the systemic effects of vaginal Candida infections and their impact on clinical outcomes. Additionally, as a second inference, the relationship between BV and cytological abnormalities, which is still unclear, requires prospective, large-scale studies to be elucidated.

Limitations of the Study

This study has some limitations. Firstly, as it is retrospective, its ability to establish cause-and-effect relationships is limited. Moreover, prospective studies and larger patient groups are needed to better understand the relationship between the severity of infections and systemic inflammation. Finally, the influence of other potential factors (such as age, obesity, immune status) that were not considered or adjusted for should be taken into account. Simultaneous HPV typing could not be performed with smears, and as a result, the distribution of infection types with HPV could not be evaluated. In conclusion, this study, demonstrating the potential effects of VVC, BV, and TV infections detected in vaginal smear results on systemic inflammation and hematological indices, encourages further research in this area. The systemic effects of these infections and their impact on clinical outcomes should be further examined. Additionally, it is important to develop new approaches to minimize the impact of these infections on treatment strategies.

Conflicts of interest

There are no conflicts of interest in this work.

References

[1] Solomon D., Davey D., Kurman R., The 2001 Bethesda System. Terminology for reporting cervical cytology, *JAMA,* 287 (2002) 2114-9.

[2] Schwartz P.E., Hadjimichael O., Lowell D.M., Merino M.J., Janerich D., Rapidly progressive cervical cancer: the Connecticut experience, American Journal of Obstetrics and Gynecology, 175 (1996) 1105–9.

[3] Genç Ş. Ö., Erdal H., Are pan-immune-inflammation value, systemic inflammatory response index and other hematologic inflammatory indexes clinically useful to predict first-trimester pregnancy loss, *Ann. Clin. Anal. Med.*, 14(5) (2023) 473-477.

[4] Erdal H., Yasar E., Tuncer S.Ç., Determination of calprotectin levels in patients with cataract surgery, *Ann. Clin. Anal. Med.*, 14(2) (2023) 148-151.

[5] Erdal H., Gunaydin F., HALP score for chronic spontaneous urticaria: Does it differ from healthy subjects?, *Journal of Experimental and Clinical Medicine*, 40(4) (2023) 677-680.

[6] Nayar R., Wilbur D.C., The Pap test and Bethesda 2014, "The reports of my demise have been greatly exaggerated." (after a quotation from Mark Twain), *Acta Cytol.*, 59(2) (2015) 121–132.

[7] Eleutério Jr. J., Campaner A. B., de Carvalho N. S., Diagnosis and treatment of infectious vaginitis: Proposal for a new algorithm, *Frontiers in Medicine*, 10 (2023) 1040072.

[8] Leclair C., Stenson A., Common causes of vaginitis, *JAMA 327*, (2022) 2238–2239.

[9] Peebles K., Velloza J., Balkus J.E., McClelland R.S., Barnabas R.V., High global burden and costs of bacterial vaginosis, *Sex Transm. Dis.*, 46 (2019) 304–311.

[10] Denning D.W., Kneale M., Sobel J.D., Rautemaa-Richardson R., Global burden of recurrent vulvovaginal candidiasis: a systematic review, *Lancet Infect. Dis.*, 18 (2018) e339–e347.

[11] Force U.P.S.T., Owens D.K., Davidson K.W., Krist A.H., Barry M.J., Cabana M,, Caughey A.B,, Donahue K., Doubeni C.A., Epling J.W., Kubik M., Ogedegbe G., Pbert L., Silverstein M., Simon M.A., Tseng C-W, Wong J.B., US Preventive Services Task Force. Screening for bacterial vaginosis in pregnant persons to prevent preterm delivery, *JAMA 323*, (2020) 1286–1292.

[12] Gerwen O.V., Craig-Kuhn M., Jones A., Schroeder J., Deaver J., Buekens P., Kissinger P., Muzny C., Trichomoniasis and adverse birth outcomes: a systematic review and meta-analysis, *BJOG* 128 (2021) 1907–1915.

[13] Fazlollahpour-Naghibi A., Bagheri K., Almukhtar M., Taha S. R., Zadeh M. S., Moghadam K. B., Rostami A., Trichomonas vaginalis infection and risk of cervical neoplasia: A systematic review and meta-analysis, *Plos One,* 18(7) (2023) e0288443.

[14] Vieira-Baptista P., Lima-Silva J., Pinto C., Saldanha C., Beires J., Martinez-de-Oliveira J., Donders G., Bacterial vaginosis, aerobic vaginitis, vaginal inflammation and major Pap smear abnormalities, *European Journal of Clinical Microbiology & Infectious Diseases*, 35 (2016) 657-664.

[15] Dahoud W., Michael C. W., Gokozan H., Nakanishi A. K., Harbhajanka A., Association of bacterial vaginosis and human papilloma virus infection with cervical squamous intraepithelial lesions, *American Journal of Clinical Pathology,* 152(2) (2019) 185-189.

[16] FuJ., Zhang H., Meta-analysis of the correlation between vaginal microenvironment and HPV infection, *American Journal of Translational Research*, 15 (2) (2023) 630.

Cumhuriyet Sci. J., 45(2) (2024) 338-342
DOI: https://doi.org/10.17776/csj.1422543

Cumhuriyet Science Journal

| csj.cumhuriyet.edu.tr | Founded: 2002 ISSN: 2587-2680 e-ISSN: 2587-246X Publisher: Sivas Cumhuriyet University

Assessment of Serum Beta 2-Microglobulin Levels in Crimean-Congo Hemorrhagic Fever Patients: Implications for Immune Activation and Disease Pathogenesis

Seyit Ali Büyüktuna [1,a,*], Serkan Bolat [2,b], Kübra Doğan [3,c], Yasemin Çakır [1,d], Halef Okan Doğan [2,e]

[1] *Department of Infectious Diseases, School of Medicine, Sivas Cumhuriyet University, Sivas, Türkiye.*
[2] *Department of Medical Biochemistry, School of Medicine, Sivas Cumhuriyet University, Sivas, Türkiye.*
[3] *Department of Biochemistry, Sivas Numune Hospital, Sivas, Türkiye.*
**Corresponding author*

Research Article

History
Received: 19/01/2024
Accepted: 19/04/2024

ABSTRACT

Crimean-Congo Hemorrhagic Fever (CCHF) presents a spectrum of clinical manifestations, ranging from asymptomatic cases to severe, life-threatening conditions. Despite extensive research on CCHF pathogenesis, comprehensive understanding remains elusive. Our investigation focused on assessing serum beta 2-microglobulin (β2M) levels in CCHF patients, aiming to elucidate its potential as an immune activation marker and its involvement in disease pathogenesis. The study enrolled 45 CCHF patients and 45 healthy volunteers as a control group. Serum β2M levels were quantified using the immunoturbidimetric analysis method. The patient group was divided into two groups, mild and moderate-severe, using scoring systems. The mean β2M values for the control, mild, and moderate-severe patient groups were 2.27±0.50, 4.37±1.29, and 5.82±2.62 mg/L, respectively ($p<0.001$). Positive correlations were noted between β2M concentrations and markers such as BUN, creatinine, uric acid, creatine kinase, and aPTT ($p<0.001$, $r=0.684$; $p<0.001$, $r=0.602$; $p=0.003$, $r=0.439$; $p=0.008$, $r=0.392$; $p=0.019$, $r=0.348$, respectively). Conversely, negative correlations were observed with total protein, albumin, and platelet count ($p=0.021$, $r=-0.342$; $p=0.003$, $r=-0.434$; $p=0.048$, $r=-0.296$, respectively). The findings suggest a prominent inflammatory response in CCHF, indicated by elevated β2M levels, implying its potential role in the molecular mechanisms of the disease.

Keywords: Beta 2-microglobulin, Hemorrhagic fever virus, Crimean-Congo, Patient acuity, Viral zoonoses.

[a] *alibuyuktuna@gmail.com* *https://orcid.org/0000-0001-6518-7361*
[b] *drsbolat@gmail.com* *https://orcid.org/0000-0002-8669-8782*
[c] *kubradogan82@hotmail.com* *https://orcid.org/0000-0002-9448-3407*
[d] *yasemincakir2553@gmail.com* *https://orcid.org/0000-0001-5510-3216*
[e] *halefokan@gmail.com* *https://orcid.org/0000-0001-8738-0760*

Introduction

Crimean-Congo Hemorrhagic Fever (CCHF) is a viral zoonotic disease primarily transmitted by ticks, with a clinical spectrum ranging from mild infection to severe illness or even death [1]. The causative agent of CCHF is the CCHF virus, a single-stranded RNA virus belonging to the Orthonairovirus genus of the Nairoviridae family [2]. The disease can be transmitted through tick contact, exposure to the blood or body fluids of an infected animal, or a CCHF patient [3]. The disease is clinically characterized by sudden-onset fever, headache, muscle pain, fatigue, erythema on the face and body, conjunctivitis, petechiae, mucosal bleeding, and, in the advanced stage, multiple organ dysfunction and intraparenchymal hemorrhages. In severe cases, the mortality rate varies between 5-30%, depending on the geographical region and the quality of healthcare services [4].

Although the pathogenesis of the disease is not fully understood, complex molecular mechanisms between the virus and host cells are thought to be responsible for the pathogenesis of CCHF [5]. The main elements mediating this relationship are endothelial and immune cells. The release of cytokines results in increased vascular permeability, vasodilation, multiple organ failure, and shock [6]. Hemorrhage, which is among the important clinical findings of the disease, increases vascular permeability [7]. In addition, viral antigens on endothelial cells indicate that the endothelium is the main target. Activation of endothelial cells plays a critical role in initiating inflammatory reactions, such as the organization of the immune response to infection and increased vascular permeability [8]. Endothelial damage also contributes to the activation of the intrinsic coagulation cascade. Endothelial cells can be activated directly by the virus or indirectly by host-derived mediators induced by the virus [9].

Beta 2-microglobulin (β2M), a component of the lymphocyte HLA complex, is a low molecular weight protein that serves as the light chain of class 1 MHC antigens. It is found in nearly all body fluids and on the surface of nucleated cells. β2M is an indicator of immune activation and proximal tubular function. It increases in conditions associated with high cell turnover and/or immune activation. Conditions accompanied by inflammation such as inflammatory bowel diseases, Crohn's disease, hepatitis, autoimmune diseases, multiple myeloma, chronic kidney failure, lymphoproliferative diseases, myeloproliferative diseases, myelodysplastic diseases, amyloidosis, breast cancer, hepatoma,

hyperthyroidism, vasculitis, tumor necrosis factor, and certain drugs lead to an increase in β2M levels [10].

In infections like CMV, HIV, Epstein-Barr, and influenza A virus, β2M levels rise. This elevation during viral infections may stem from heightened production and release due to lymphocyte activation and increased turnover [11]. Notably, studies, especially in HIV cases, highlight elevated serum β2M levels as HIV targets T-lymphocytes and macrophages, intensifying turnover, and destruction [12, 13]. However, no previous study has investigated the status of β2M levels in CCHF patients.

Accordingly, this study aims to investigate serum β2M levels in CCHF patients, compare them with healthy controls, and assess their impact on the pathogenesis. This study holds significance as it pioneers the investigation of β2M in CCHF patients. Given the absence of prior research in this area, our study fills a critical knowledge gap. Understanding the role of β2M in CCHF could offer valuable insights into the disease's pathogenesis and aid in developing targeted therapeutic interventions.

Materials and Methods

Study Population

This prospective study involves 45 CCHF patients and 45 healthy volunteers without acute or chronic illnesses or medication use. Exclusion criteria for healthy volunteers included suspected clinical infection, liver disease, kidney disease, rheumatic disease, malignancy, pregnancy, or smoking. No specific criteria were applied to exclude any patients from the patient group. None of the patients had a previous acute or chronic kidney disease history. Besides, no deaths occurred in any of the patients included in the study. Demographic data, underlying chronic diseases, treatments used, and outcomes were recorded for the patients. In our study, patients were classified according to the severity score recommended by Bakır et al [15]. Thus, patients were divided into two groups: mild and moderate-severe cases, and correlations between serum β2M levels and disease severity were explored. The procedures were approved by the Ethical Committee of Sivas Cumhuriyet University, following the ethical standards established by the institution (2021-04/02). All procedures were performed by the Helsinki Declaration as revised in 2013. Informed consent was obtained from all individuals included in this study.

Sample Collection and Laboratory Analyses

Samples from the patient group were collected at the time of hospital admission. For participants in the control group, 5 mL venous blood samples were obtained in the morning after an overnight fast. Serum samples were stored at – 80 °C until analyses. β2M levels were measured by using the immune turbidimetric method (Roche Cobas 8000 c702, Germany, Manheim). Ferritin and interleukin-6 (IL-6) levels were measured using the electrochemiluminescence method (Roche Cobas 8000 e801, Germany, Manheim). Various biochemical parameters, including blood urea nitrogen (BUN), creatinine, uric acid, total protein, albumin, alanine aminotransferase (ALT), aspartate aminotransferase (AST), alkaline phosphatase (ALP), gamma-glutamyl transferase (GGT), lactate dehydrogenase (LDH), direct bilirubin (D.bil), total bilirubin (T.bil), creatine kinase (CK) and amylase levels were measured by photometric method (Roche Cobas 8000 c702, Germany, Manheim). Prothrombin time (PT), international normalized ratio (INR), activated partial thromboplastin time (aPTT), fibrinogen, and D-dimer values were measured by using a coagulation analyzer (Sysmex CS-5100, Japan). Complete blood count analyses were conducted employing a hematology analyzer (Sysmex XN-9100, Japan).

Statistical Analyses

Histogram and q-q plots were examined, and Shapiro-Wilk's test was performed to assess the data normality. To compare the differences between groups, a two-sided independent samples t-test or Mann-Whitney U test was used for continuous variables, and Pearson $\chi 2$ analysis or Fisher's exact test was used for categorical variables. Values were expressed as n(%), mean±standard deviation, or median (1st-3rd quartiles). The relationship between quantitative data was analyzed using Pearson correlation analysis. Receiver operating characteristic (ROC) analyses were used to assess the prognostic performance of the parameters to predict CCHF severity. Sensitivity, specificity, positive and negative likelihood ratio value statistics were calculated with 95% confidence intervals. Data were analyzed statistically using IBM SPSS for Windows version 23.00 software (Armonk, New York, United States of America), and GraphPad Prism version 8.3.0 (San Diego, California USA, www.graphpad.com) was used for visualization. A p-value less than 5% was considered statistically significant.

Results

Out of the CCHF patients included in the study, 10 (22%) were female, while 20 (44%) of the control group were female. There were 31 patients with a severity score of 0-4 (mild) and 14 patients with a score of 5 and above (moderate-severe) for determining the severity of CCHF disease. While there was no significant difference between the groups in terms of gender ($p=0.068$), the mean age of moderate-severe patients was higher, and this difference was statistically significant ($p<0.001$). The basic characteristics of the study population are shown in Table 1. Serum β2M concentrations were higher in moderate-severe cases ($p<0.001$). The β2M concentration values for the control, mild, and moderate-severe patient groups were found to be 2.27±0.5, 4.37±1.29, and 5.82±2.62 mg/L, respectively. Positive correlations were observed between serum β2M and BUN ($p<0.001$, $r=0.684$), creatinine ($p<0.001$, $r=0.602$), uric acid ($p=0.003$, $r=0.439$), creatine kinase ($p=0.008$, $r=0.392$), and aPTT ($p=0.019$, $r=0.348$). On the other hand, negative correlations were found between serum β2M concentrations and total protein ($p=0.021$, $r=-0.342$), albumin ($p=0.003$, $r=-0.434$), and platelet count ($p=0.048$, $r=-0.296$) (Figure 1).

Table 1. Baseline characteristics of the study population

Variable	Healthy Cases (n=45)	CCHF Patients		*p* values
		Mild (n=31)	Moderate-Severe (n=14)	
Gender, female (%)	20 (44%)	6 (%19)	4 (%29)	0.068
Age (years)	38±10[a]	43 ± 16[a]	65 ± 10[b]	<0.001
β2M (mg/L)	2.27±0.5[a]	4.37 ± 1.29[b]	5.82 ± 2.62[c]	<0.001
IL-6 (ng/L)		11.2 (5.3-30.4)	20.4 (13.2-138)	0.021
Ferritin (µg/L)		1180 (475-5274)	16275 (5566-22926)	<0.001
BUN (mg/dL)		13.0 (9.9-18.2)	15.5 (11.7-22.0)	0.108
Creatinine (mg/dL)		0.81±0.18	0.91±0.23	0.147
Uric acid (mg/dL)		3.94±1.26	5.39±1.85	0.004
Total protein (g/L)		63.2±4.7	60.5±5.6	0.103
Albumin (g/L)		38±3.2	34.2±4.2	0.002
Amylase (U/L)		65 (45-81)	107 (72-191)	0.001
ALP (U/L)		68 (107-106)	128 (85-165)	0.004
AST (U/L)		78 (40-163)	216 (150-315)	0.001
ALT (U/L)		63 (34-101)	96 (67-173)	0.019
LDH (U/L)		370 (289-573)	581 (472-759)	0.002
CK (U/L)		206 (131-380)	561 (445-866)	0.048
GGT (U/L)		42 (21-92)	121 (75-272)	<0.001
T.bil (mg/dL)		0.43 (0.29-0.57)	0.69 (0.57-1.24)	0.001
D.bil (mg/dL)		0.15 (0.1-0.2)	0.42 (0.21-0.65)	<0.001
PT (sec)		11.7 (11.1-12.2)	11.5 (11.0-12.5)	0.912
INR		1.03 (0.97-1.07)	1.02 (0.96-1.10)	0.922
aPTT (sec)		26.3±4.6	29.7±6.5	0.048
Fibrinogen (mg/dL)		288±75	300±118	0.676
D-dimer (mg/L FEU)		1.88 (1.08-2.87)	3.44 (1.45-29.1)	0.033
WBC (10^9/L)		2.66 (2.08-4.87)	2.6 (1.95-2.91)	0.477
Hemoglobin (g/dL)		13.9±1.7	12.6±2.1	0.028
Platelet (10^9/L)		101 (39-126)	39 (34-64)	0.011

Results are expressed as n (%), mean±standard deviation, or median (1st-3rd quartiles). Different superscripts in the same row indicate a statistically significant difference between groups. Significant p-values are shown in bold. CCHF, Crimean-Congo hemorrhagic fever; β2M, beta 2-microglobulin; IL-6, Interleukin-6; BUN, Blood Urea Nitrogen; ALP, Alkaline phosphatase; AST, Aspartate transaminase; ALT, Alanine aminotransferase; LDH, Lactate dehydrogenase; CK, Creatine kinase; GGT, Gama-glutamyl transferase; T.bil and D.bil, Total and Direct bilirubin; PT, Prothrombin time; INR, International normalization ratio; aPTT, Activated partial thromboplastin time; WBC, white blood count.

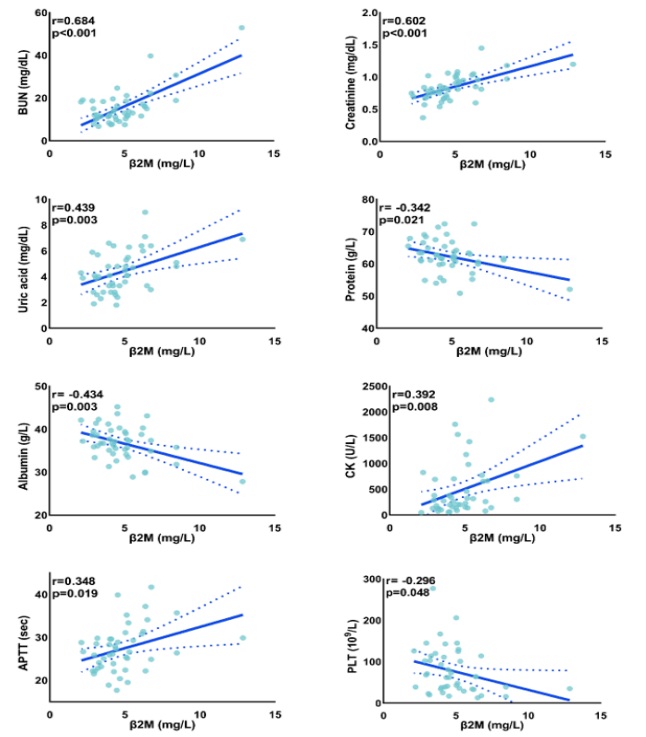

Figure 1. Pearson correlation analysis of β2M levels and laboratory parameters in patients with Crimean-Congo hemorrhagic fever. Linear lines with 95% confidence intervals are given.

Table 2. ROC Analysis Results for Variables in Predicting CCHF Severity

Variable	Cut-off value	AUC	Sensitivity	Specificity	LR(+)	LR(-)
Age (years)	>50	0.88	1.00 (0.77-1.00)	0.68 (0.49-0.83)	3.10 (1.9-5.2)	0
β2M (mg/L)	>5.09	0.7	0.64 (0.35-0.87)	0.77 (0.59-0.90)	2.85 (1.3-6.1)	0.46 (0.2-1.0)
IL-6 (ng/L)	>13.5	0.72	0.79 (0.49-0.95)	0.61 (0.42-0.78)	2.03 (1.2-3.4)	0.35 (0.1-1.0)
Ferritin (µg/L)	>3959	0.84	0.93 (0.66-1.00)	0.71 (0.52-0.86)	3.20 (1.8-5.7)	0.1 (0.02-0.7)
Uric acid (mg/dL)	>4.8	0.75	0.64 (0.35-0.87)	0.84 (0.66-0.95)	3.99 (1.6-9.7)	0.43 (0.2-0.9)
Albumin (g/L)	≤34.1	0.76	0.64 (0.35-0.87)	0.97 (0.83-1.00)	19.9 (2.8-143)	0.37 (0.2-0.7)
Amylase (U/L)	>98	0.81	0.64 (0.35-0.87)	0.94 (0.79-0.99)	9.96 (2.5-40.3)	0.38 (0.2-0.8)
ALP (U/L)	>74	0.77	0.93 (0.66-1.00)	0.61 (0.42-0.78)	2.40 (1.5-3.8)	0.12 (0.02-0.8)
ALT (U/L)	>84	0.72	0.71 (0.42-0.92)	0.71 (0.52-0.86)	2.46 (1.3-4.7)	0.40 (0.2-0.9)
AST (U/L)	>130	0.82	0.79 (0.49-0.95)	0.74 (0.55-0.88)	3.04 (1.6-5.9)	0.29 (0.1-0.8)
LDH (U/L)	>390	0.8	1.00 (0.77-1.00)	0.58 (0.39-0.76)	2.38 (1.6-3.6)	0
CK (U/L)	>343	0.69	0.64 (0.35-0.87)	0.74 (0.55-0.88)	2.49 (1.2-5.1)	0.48 (0.2-1.0)
GGT (U/L)	>101	0.83	0.71 (0.42-0.92)	0.84 (0.66-0.95)	4.43 (1.9-10.6)	0.34 (0.1-0.8)
T.bil (mg/dL)	>0.57	0.82	0.79 (0.49-0.95)	0.77 (0.59-0.90)	3.48 (1.7-7.1)	0.28 (0.10-0.8)
D.bil (mg/dL)	>0.3	0.85	0.71 (0.42-0.92)	0.87 (0.70-0.96)	5.54 (2.1-14.6)	0.33 (0.1-0.8)
aPTT (sec)	>29.3	0.68	0.57 (0.29-0.82)	0.81 (0.63-0.93)	2.95 (1.3-6.9)	0.53 (0.3-1.0)
D-dimer (mg/L FEU)	>2.4	0.7	0.64 (0.35-0.87)	0.74 (0.55-0.88)	2.49 (1.2-5.1)	0.48 (0.2-1.0)
Hemoglobin (g/dL)	≤12.1	0.69	0.50 (0.23-0.77)	0.87 (0.70-0.96)	3.87 (1.4-11.1)	0.57 (0.3-1.0)
Platelet (10^9/L)	≤81	0.74	1.00 (0.77-1.00)	0.55 (0.36-0.73)	2.21 (1.5-3.3)	0

Results are expressed with 95% confidence intervals. CCHF, Crimean-Congo hemorrhagic fever; AUC, Area under the curve; LR, Likelihood ratio; β2M, beta 2-microglobulin; IL-6, Interleukin-6; ALP, Alkaline phosphatase; AST, Aspartate transaminase; ALT, Alanine aminotransferase; LDH, Lactate dehydrogenase; CK, Creatine kinase; Gama-glutamyl transferase; T.bil and D.bil, Total and Direct bilirubin; aPTT, Activated partial thromboplastin time.

ROC analyses were conducted to assess parameters capable of predicting the severity of CCHF. Table 2 presents the Area under the Curve (AUC), sensitivity, specificity, and likelihood ratios for the respective tests. Notably, sensitivities of 100% were observed for cut-off values of age >50 years, LDH >390 U/L, and platelet count <81 *10^9/L. Regarding β2M, a sensitivity of 64% and specificity at 77% was determined for a cut-off value >5.09 mg/L, corresponding to an AUC value of 0.697. ROC curve graphs for age, ferritin, AST, GGT, and direct bilirubin with the highest AUC values are depicted in Figure 2.

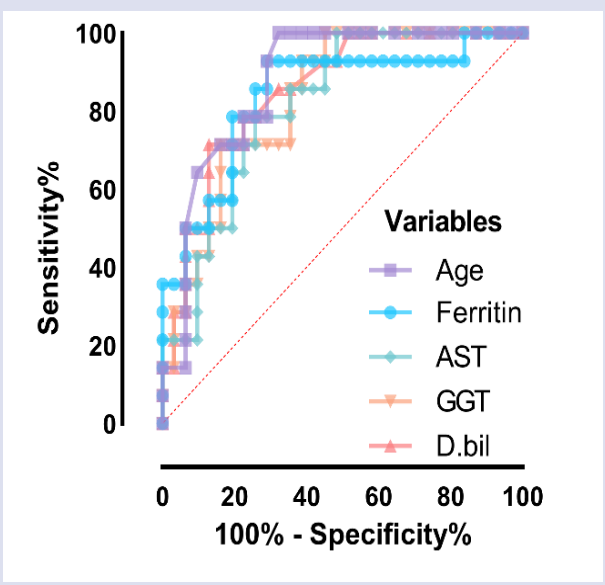

Figure 2. ROC graphs for Variables in Predicting CCHF Severity. According to the data in Table 2, the five variables with the highest AUC values are shown in the graph. AST, Aspartate transaminase; GGT, Gama-glutamyl transferase; D.bil, Direct bilirubin.

Discussion

In this study, significant differences were found in terms of β2M levels between patient and healthy control groups. Additionally, higher β2M levels were associated with a more severe disease course. Our study is the first to determine the associations between serum β2M levels and the course of CCHF disease.

Our study revealed that β2M levels were higher in CCHF patients than in healthy controls. β2M, a protein found in cell membranes of activated immune cells such as T and B lymphocytes and macrophages, is produced by lymphocytes under the influence of interferons and proinflammatory cytokines [14, 15]. Studies in CCHF patients have shown that cytokine storm is one of the factors that play a role in the pathogenesis and prognosis of the disease [16]. Our study found that IL-6 levels were higher in the patient group compared to healthy controls. We also found a statistically significant difference between the two groups in terms of lymphocyte levels. Accordingly, we think changes in lymphocyte levels and increased inflammation may cause elevated β2M levels in CCHF patients.

In the present study, we also determined statistically significant difference between mild and moderate-severe groups. This finding is consistent with a study in which high β2M levels were associated with poor prognosis in individuals with the Omicron variant of COVID-19 [17]. Currently, no specific pharmaceuticals or vaccines are available to combat the disease directly, so the primary therapeutic approach relies heavily on supportive measures. These include interventions such as administering fresh frozen plasma, conducting apheresis procedures, applying platelet treatments, and carefully regulating fluid-electrolyte equilibrium [18]. Given this

context, the early determination of the disease's prognosis emerges as a critical factor in guiding effective treatment strategies. Therefore, integrating the β2M assessment into prognostic evaluations presents an opportunity to refine and optimize the management of therapeutic interventions. By leveraging β2M as an indicator of disease progression and outcome prediction, clinicians may gain valuable insights that facilitate more precise and tailored approaches to patient care. This underscores the importance of proactive prognostic assessments in informing therapeutic decisions and ultimately improving patient outcomes in the absence of specific curative interventions.

β2M is considered an early and sensitive biomarker for acute kidney injury and a structural protein that regulates the immune system in the host. It directly participates in the inflammatory response and can regulate cytokine expression. β2M is implicated in the regulation of immune responses. Changes in β2M concentration can impact the activation and function of immune cells, including T lymphocytes and natural killer (NK) cells. Elevated levels of β2M have also been associated with certain viral infections and inflammatory conditions, indicating its role as a biomarker for immune activation [10, 17]. These findings indicate a progressive elevation of β2M levels with the severity of CCHF. Furthermore, our analysis revealed positive correlations between serum β2M concentrations and several markers, including BUN, creatinine, uric acid, creatine kinase, and aPTT. Conversely, negative correlations were observed with total protein, albumin, and platelet count. The positive correlations with impaired markers of kidney function and prolonged coagulation time suggest a potential association between elevated β2M and organ dysfunction in CCHF. The negative correlations with indicators of overall protein status (total protein and albumin) and platelet count suggest a potential link between increased β2M levels and compromised immune function and coagulation balance.

The study has some limitations. Firstly, no comorbidity that could affect the outcome of CCHF patients has been included in the investigation. Secondly, serum β2M levels were measured only on the first day the patients presented, and a time-dependent evaluation was not performed.

In conclusion, our study suggests that higher β2M levels in CCHF patients may indicate increased immune activation and systemic inflammation. The positive correlations with markers of organ dysfunction and negative correlations with indicators of overall health imply a potential role for β2M as a biomarker for disease severity and prognosis in CCHF.

Conflicts of Interest

There are no conflicts of interest in this work.

References

[1] Ergönül Ö., Crimean-Congo hemorrhagic fever, *Lancet Infect Dis.*, 6(4) (2006) 203-214.

[2] Adams M.J., Lefkowitz E.J., King A.M., Harrach B., Harrison R.L., Knowles, N.J., et al., Changes to taxonomy and the International Code of Virus Classification and Nomenclature ratified by the International Committee on Taxonomy of Viruses (2017), *Arch. Virol,* 162(8) (2017) 2505-2538.

[3] Fillâtre P., Revest M., Tattevin P., Crimean-Congo hemorrhagic fever: An update, *Med. Mal. Infect,* 49(8) (2019) 574-585.

[4] Büyüktuna S.A., Doğan H.O., Diagnosis, Prognosis and Clinical Trial in Crimean-Congo Hemorrhagic Fever. In: Ahmad, S.I. (eds) *Human Viruses: Diseases, Treatments and Vaccines*. Cham: Springer, (2021) 207–219.

[5] Akıncı E., Bodur H., Leblebicioglu H., Pathogenesis of Crimean-Congo hemorrhagic fever, *Vector Borne Zoonotic Dis.*, 13(7) (2013) 429-437.

[6] Akinci E., Bodur H., Sunbul M., Leblebicioglu H., Prognostic factors, pathophysiology and novel biomarkers in Crimean-Congo hemorrhagic fever, *Antiviral Res.,* 132 (2016) 233-243.

[7] Elaldi N., Kaya S., Crimean-Congo hemorrhagic fever, *J Microbiol. Infect Dis.*, 4(5) (2014) 1-9.

[8] Connolly-Andersen A.M., Moll G., Andersson C., Åkerström S., Karlberg H., Douagi I., et al., Crimean-Congo hemorrhagic fever virus activates endothelial cells, *J. Virol*, 85(15) (2011) 7766-7774.

[9] Weber F., Mirazimi A., Interferon and cytokine responses to Crimean Congo hemorrhagic fever virus; an emerging and neglected viral zonoosis, *Cytokine Growth Factor Rev.*, 19(5-6) (2008) 395-404.

[10] Bethea M., Forman D.T., Beta 2-microglobulin: its significance and clinical usefulness, *Ann. Clin. Lab. Sci.,* 20(3) (1990) 163-168.

[11] Cooper E.H., Forbes M.A., Hambling M.H., Serum beta 2-microglobulin and C reactive protein concentrations in viral infections, *J. Clin. Pathol.,* 37(10) (1984) 1140-1143.

[12] Kanekar A., Biomarkers predicting progression of human immunodeficiency virus-related disease, *J. Clin. Med. Res.,* 2(2) (2010) 55-61.

[13] Li L., Dong M., Wang X., The Implication and Significance of Beta 2 Microglobulin: A Conservative Multifunctional Regulator, *Chin. Med. J.,* 129(4) (2016) 448-455.

[14] McPhee C.G., Sproule T.J., Shin D.M., Bubier J.A., Schott W.H., Steinbuck M.P., et al., MHC class I family proteins retard systemic lupus erythematosus autoimmunity and B cell lymphomagenesis, *J. Immunol.,* 187(9) (2011) 4695-4704.

[15] Gamal D.M., Badr F.M., Taha S.I.A.E.F., Moustafa N.M., Teama M.A.E.M., Serum beta-2 microglobulin as a predictor of nephritis, disease activity, and damage score in systemic lupus erythematosus: a cross-sectional study, *Rheumatol Int.*, 43(2) (2023) 323-333.

[16] Parlak E., Ertürk A., Çağ Y., Sebin E., Gümüşdere M., The effect of inflammatory cytokines and the level of vitamin D on prognosis in Crimean-Congo hemorrhagic fever. *Int. J. Clin. Exp. Med.*, 8(10) (2015) 18302.

[17] Gong S., Ma R., Zhu T., Ge X., Xie R., Tao Q., et al., Elevated Serum Beta-2 Microglobulin Level Predicts Short-term Poor Prognosis of Patients with De Novo Acute Omicron Variant COVID-19 Infection, *Front Cell Infect Microbiol.*, 13 (2023) 1204326.

[18] Leblebicioglu H., Bodur H., Dokuzoguz B., Elaldi N., Guner R., Koksal I., et al., Case management and supportive treatment for patients with Crimean-Congo hemorrhagic fever, *Vector Borne Zoonotic Dis.*, 12(9) (2012) 805-811.

Cumhuriyet Sci. J., 45(2) (2024) 343-351
DOI: https://doi.org/10.17776/csj.1380228

Cumhuriyet Science Journal

| csj.cumhuriyet.edu.tr | Founded: 2002 ISSN: 2587-2680 e-ISSN: 2587-246X Publisher: Sivas Cumhuriyet University

Eradication Suggestions For Infectious Diseases Based on the Fractional Guinea-Worm Disease Model

Bahar Acay Öztürk [1,a,*]

[1] *Department of Mathematics, Fırat University, Elazığ, Türkiye.*
**Corresponding author*

Research Article

History
Received: 23/10/2023
Accepted: 26/02/2024

ABSTRACT

Guine-worm disease (GWD) is considered one of the most fascinating infectious diseases that almost no one is aware of. On the other hand, unfortunately, there is no medicine or vaccine to treat this tropical disease transmitted through drinking water. However, GWD is about to be miraculously eradicated. This feature makes it the first parasitic disease to be eradicated without biomedical interventions. Accordingly, this situation brings the question: How can a disease be eradicated without medicine, vaccine or immunity? In light of this question, the current study offers recommendations on how to stop the spread of infectious diseases. One of the best ways to eliminate existing diseases is to benefit from the strategies followed for diseases that have been eradicated. Our results obtained by utilizing the fractional Caputo derivative show that behavior change programs aimed at reducing or stopping the spread of infectious diseases are effective tools in eradicating the disease.

Keywords: Caputo fractional operator, Fractional modeling, Guinea-worm disease, Non-local derivative, Mathematical biology.

[a] *bacay@firat.edu.tr* *https://orcid.org/0000-0002-2350-4872*

Introduction

In the mathematical biology literature, many disease models have been theoretically and numerically investigated using various definitions of non-local fractional operators. As a result of the analyzes and simulations, it is mentioned whether the fractional operators used are advantageous for the model under consideration [1,2]. For example, in [3] the disease model of dengue fever was examined with different types of fractional operators. Also, the behavior of the disease was evaluated by performing comparative analysis, and it was stated that the fractional-order model produced better results than the classical model. In this and many other studies as can be seen in [4-7], diseases have been analyzed in the classical sense or with fractional derivative operators, and discussions have been made on simulations in the light of the parameters affecting the course of the disease. However, in this study, in addition to investigating a disease that has never been investigated before using fractional derivatives, a novel approach to eradicating today's dangerous diseases is given by utilizing a disease that is on the verge of extinction.

Guinea-worm disease (GWD) is one of the most remarkable diseases that nearly no one has heard of [4]. For the treatment of this neglected disease, which is spread through drinking water, there is no drug or vaccination. Regardless, GWD is about to disappear miraculously. Hence, it is the first parasitic disease to be eradicated, as well as the first parasitic disease to be eradicated without the need for biomedical intervention. Also, GWD is a disease that has been going on since ancient times. GWD afflicted 50 million people in most of Africa, Asia, and the Middle East in the 1950s. However, it is now on the verge of extinction, with only three African countries reporting less than 25 human cases in 2016. Therefore, this scourge has almost disappeared, and considering the factors that caused its extinction is a guide for how to eradicate diseases transmitted through contaminated water.

In [8,9] which contains some lessons that can be taken from the eradication process of smallpox for malaria eradication studies, the importance of determining the ways and methods to be followed to achieve this goal is mentioned by making use of smallpox eradication. Similarly, another study [10] has presented a malaria eradication strategy that incorporates lessons learned from the Global Polio Eradication Initiative (GPEI). For this reason, this present study proposes solutions using some popular mathematical tools such as Caputo fractional derivative, fractional numerical method for the eradication of contagious diseases we are still struggling with, using GWD, which is on the verge of extinction and is little-known. The eradication of diseases requires internationally coordinated approaches. Ensuring continuous participation from communities, politicians and funders, efficient organizations and well-managed programs have a very important place in eradication efforts. State and global disease communities should be informed about the experience of other disease eradication programs, including the smallpox eradication program, as they seek to achieve these goals. That is, it is

important to benefit from disease eradication and elimination programs that have been successfully concluded. Problems such as encouraging international support for eradication studies, coordinating the programs organized, and providing the necessary financing should be taken into account. In addition to these, it may be considered a useful approach to review the literature of diseases that have disappeared or are about to disappear to evaluate how the difficulties that are likely to be encountered are overcome. On the other hand, various diseases have been examined using the fractional operators in the literature [11-27].

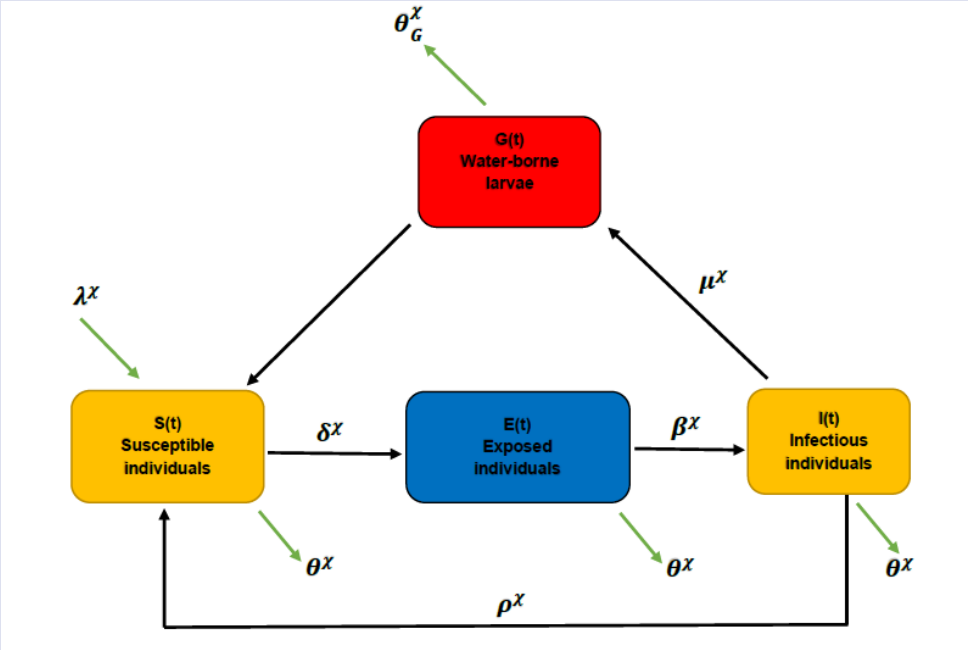

Figure 1. The fractional Guinea-worm disease model diagram.

The remainder of this study is presented as follows. In Section 2, we introduce the formulation of the classical GWD model and its fractional version under non-local Caputo operator including singular kernel. Then, in Section 3, a detailed mathematical analysis of the fractional GWD model is introduced in order to comprehend the dynamical behavior of the system handled. Finally, we present the numerical simulation and discussions section for the GWD model.

Mathematical Formulation of the Guinea-Worm Disease

In this section, we present two subsections wherein we describe the classical (integer-order) and fractional (non-integer order) versions of the GWD model. Thereby, it will be possible to compare the classical and fractional-type models by presenting them separately. Also, fundamental information about the GWD model is given to comprehend the results of the current study. In addition, the advantages of the fractional-order model are emphasized.

Classical GWD Model

We need to follow what comes in and what goes out in order to develop a mathematical model. The human population for GWD is divided into three groups. The first subgroup is susceptible individuals, and there are three possibilities for this group: birth, death, or infection. Individuals who are infectious recover or die, while those who are infected become infectious or die. There is, on the other hand, a worm population. When infected people put their feet in drinking water, the parasite is born as freshwater provides relief, and they die soon after. For model formulation, let S(t) represent susceptible individuals, E(t) represent exposed individuals, I(t) represent infected individuals, and G(t) represent the number of larvae in the water. Also, λ is the human birth rate, δ is the infection rate, β is the worm emergence rate, ρ is the recovery rate, and θ is the death rate. On the other hand, while infected individuals produce new larvae at the μ rate, the larvae are naturally cleared from the water at the θ_G ratio [4].

Interventions to change the course of the disease are carried out in 3 ways: filtration of the water supply, education given to the individuals, and chlorination. Here, the term "education" refers to teaching

individuals not to put infected limbs in the water. As a result, it is clear that the increase in education has a direct decreasing effect on the parasite birth rate, namely μ. Moreover, filtering is a technique for decreasing the parasite's capacity to infect humans-host and thus it has a reducing effect on δ. Also, chlorination has the effect of increasing the parasite death rate θ_G [4].

Now, let us give the mathematical model in the light of the information given above [4]:

$$\frac{ds}{dt} = \lambda - \delta S(t)G(t) - \theta S(t) + \rho I(t),$$
$$\frac{dE}{dt} = \delta S(t)G(t) - \beta E(t) - \theta E(t), \quad (1)$$
$$\frac{dI}{dt} = \beta E(t) - \rho I(t) - \theta I(t),$$
$$\frac{dG}{dt} = \mu I(t) - \theta_G G(t).$$

It should be noted here that state variables S, E, I, and G are not negative. Furthermore, because the quantities given are averages, it is not correct to assume that each person is infected with only one worm at a time. Because there have been instances where people have had seven worms at once. Mass-action transmission is employed because the interaction between aquatic parasites and people is present when humans drink parasite-containing water. Thus, each person's exposure to the parasite is approximately equal, as everyone in the village usually drinks from a single source. Also, we shall emphasize that in some areas, regular disease control can be difficult due to limited resources and infrastructure. In particular, chlorinating water regularly can be difficult or even impossible. The description of all parameters and the values used for this study can be seen in Table 1.

Table 1. Parameter values of GWD model [4].

Parameter	Definition	Sample Value	Units
S	Susceptible individuals	S(0)=λ/θ	people
E	Exposed individuals	E(0)=0	people
I	Infectious individuals	I(0)=0	people
G	Water-borne larvae	G(0)=200	larvae
λ	Birth rate	37	people/years
δ	Transmissibility	0.0255	1/larvae.years
θ	Death rate	0.0142	1/years
ρ	Recovery rate	8.760	1/years
β	Rate of worm emergence	1	1/years
μ	Parasite birth rate	100.000	larvae/people.years
θG	Parasite death rate	26	1/years

θ's average transmissibility can be calculated using (7 drink water per day) ×(365 days)/(100,000 larvae)=0.0255. This calculation shows the ratio of the total annual water ingested to the number of parasites. Also, the average life span of individuals, 1/θ, is assumed to be 70 years while the average infectious time 1/ρ is taken as 1 hour such that ρ=24× 365=8760 $years^{-1}$. The birth rates per 1000 population in the four endemic countries Mali, Ethiopia, Sudan, and Ghana are 46.09, 43.34, 33.25 and 28.09 with an average of 37, respectively [4].

Fractional GWD Model with Caputo Operator

This subsection provides the fractional version of the GWD system (1) under Caputo operator. Systems examined through fractional operators often give more reliable results than systems defined by classical derivatives. Fractional derivatives are used to examine the course of the disease in more detail and to obtain more sensitive results. We define the model as follows, using the Caputo derivative, which is known to be very advantageous in application.

$$ {}_cD^{\chi}_{0,t}S(t) = \frac{1}{1-\chi}\int_0^t \frac{S'(t)}{(t-\tau)^{\chi}} = \lambda^{\chi} - \delta^{\chi}S(t)G(t) - \theta^{\chi}S(t) + \rho^{\chi}I(t),$$
$$ {}_cD^{\chi}_{0,t}E(t) = \frac{1}{1-\chi}\int_0^t \frac{E'(t)}{(t-\tau)^{\chi}} = \delta^{\chi}S(t)G(t) - \beta^{\chi}E(t) - \theta^{\chi}E(t), \quad (2)$$
$$ {}_cD^{\chi}_{0,t}I(t) = \frac{1}{1-\chi}\int_0^t \frac{I'(t)}{(t-\tau)^{\chi}} = \beta^{\chi}E(t) - \rho^{\chi}I(t) - \theta^{\chi}I(t),$$
$$ {}_cD^{\chi}_{0,t}I(t) = \frac{1}{1-\chi}\int_0^t \frac{I'(t)}{(t-\tau)^{\chi}} = \mu^{\chi}I(t) - \theta_G^{\chi}G(t).$$

Now, we present the basic mathematical analysis of the GWD system by using the fractional Caputo derivative and make comments on the process of the disease under consideration.

Fractional Mathematical Analysis of Fractional GWD Model with Caputo Operator

In this section, we introduce some basic information on the proposed fractional system. A positive set of the presented fractional model is given. Also, the disease-free equilibrium (DFE) point is determined for computing the reproduction number (RN). Moreover, we analyze the stability of the system. On the other hand, the fractional model under examination is investigated for understanding the system behavior in detail by means of the Caputo operator. To comment on the eradication or persistence of the GWD, we determine the RN. For this purpose, some basic features of the fractional-order GWD model is presented. For obtaining invariant region of the fractional GWD model, let us consider the following theorem:

Theorem 1. The closed set $\Omega = \{(S,E,I,G) \in R_+^4 : 0 \leq S+E+I+G \leq K\}$ is a positive set of the fractional-order GWD model.

Proof. In order to prove the desired result, we follow that

$$ {}_C D_{0,t}^{\chi} S(t)|_{S(t)=0} = \rho^{\chi} I(t) \geq 0,$$

$$ {}_C D_{0,t}^{\chi} E(t)|_{E(t)=0} = \delta^{\chi} S(t) G(t) \geq 0,$$

$$ {}_C D_{0,t}^{\chi} I(t)|_{I(t)=0} = \beta^{\chi} E(t) \geq 0,$$

$$ {}_C D_{0,t}^{\chi} G(t)|_{G(t)=0} = \mu^{\chi} I(t) \geq 0,$$

and this means that the solutions of the suggested model are non-negative. Furthermore, from the sum of the equations of the GWD model, we obtain

$$ {}_C D_{0,t}^{\chi} N(t) \leq \lambda^{\chi} - \theta^{\chi} N(t),$$

where N(t) is the total population size. Utilizing the property of fractional operator, one can have

$$ N(t) \leq \left(N(0) - \frac{\lambda^{\chi}}{\theta^{\chi}} \right) \boldsymbol{E}_{\chi}(-\theta^{\chi} t^{\chi}) + \frac{\lambda^{\chi}}{\theta^{\chi}}, \tag{3}$$

where $\boldsymbol{E}_{\chi}(.)$ is Mittag-Leffler (M-L) function. Also, if we use the properties of the ML function, the expression (3) can be written as

$$ N(t) \leq \frac{\lambda^{\chi}}{\theta^{\chi}} \cong K,$$

and so we get $N(t) \leq K$. Finally, it can be said that Ω is the positive invariant region of the fractional GWD model including the Caputo differential operator.

On the other hand, we shall note that

$$ {}_C D_{0,t}^{\chi} (S+E+I) = \lambda^{\chi} - \theta^{\chi} (S+E+I),$$

and thus

$$ S(t) + E(t) + I(t) \leq \frac{\lambda^{\chi}}{\theta^{\chi}}. \tag{4}$$

Using (4), we have

$$ {}_C D_{0,t}^{\chi} I \leq \frac{\beta^{\chi} \lambda^{\chi}}{\theta^{\chi}} - (\rho^{\chi} + \theta^{\chi}) I,$$

and from the properties of the fractional derivatives, it can be readily obtained the following result

$$ I(t) \leq \left(I(0) - \frac{\beta^{\chi} \lambda^{\chi}}{\theta^{\chi} (\rho^{\chi} + \theta^{\chi})} \right) \boldsymbol{E}_{\chi}(-(\rho^{\chi} + \theta^{\chi}) t^{\chi}) + \frac{\beta^{\chi} \lambda^{\chi}}{\theta^{\chi} (\rho^{\chi} \theta^{\chi})}.$$

Because of the fact that ρ is large, the M-L function term is small. So, we reach

$$ I(t) \leq \frac{\beta^{\chi} \lambda^{\chi}}{\theta^{\chi} (\rho^{\chi} \theta^{\chi})}.$$

Hence

$$ {}_C D_{0,t}^{\chi} G \leq \frac{\mu^{\chi} \beta^{\chi} \lambda^{\chi}}{\theta^{\chi} (\rho^{\chi} + \theta^{\chi})} - \theta_G^{\chi} G,$$

and so we get

$$ G \leq \frac{\mu^{\chi} \beta^{\chi} \lambda^{\chi}}{\theta^{\chi} \theta_G^{\chi} (\rho^{\chi} + \theta^{\chi})}.$$

The above inequalities may cause the number of parasite in the water to be overestimated. However, they help us to estimate them without solving the fractional system of GWD.

Now, we discuss the dynamical properties of the fractional-order GWD model. DFE point is obtained in order to investigate the RN. Moreover, we analyze the stability of the fractional model under examination. Let $E_0(S^*, E^*, I^*, G^*)$ be the equilibrium points of the proposed model. By setting the right-hand side of all differential equations of the system equal to zero, we get a steady state of the GWD model as follows:

$$ \lambda^{\chi} - \delta^{\chi} S(t) G(t) - \theta^{\chi} S(t) + \rho^{\chi} I(t) = 0,$$

$$ \delta^{\chi} S(t) G(t) - \beta^{\chi} E(t) - \theta^{\chi} E(t) = 0,$$

$$ \beta^{\chi} E(t) - \rho^{\chi} I(t) - \theta^{\chi} I(t) = 0,$$

$$ \mu^{\chi} I(t) - \theta_G^{\chi} G(t) = 0.$$

For obtaining the DFE points, we consider the system in the absence of the GWD. Hence, the suggested model reduces to

$$ \lambda^{\chi} - \theta^{\chi} S = 0,$$

and if we solve, we have $S^* = \frac{\lambda^{\chi}}{\theta^{\chi}}$ Thus, the DFE is

$$E_0(S^*, E^*, I^*, G^*) = \left(\frac{\lambda^\chi}{\theta^\chi}, 0,0,0\right).$$

Now, we calculate the reproductive ratio R_0 of the fractional GWD model by means of the next-generation method (NGM). Here, $R_0 = \rho(FV^{-1})$ such that ρ is the spectral radius of FV^{-1} called next-generation matrix. The matrix **F** includes new infections terms and the matrix **V** including the remaining terms of the fractional GWD model are

$$\boldsymbol{F} = \begin{bmatrix} \delta^\chi SG \\ 0 \\ 0 \end{bmatrix}, \qquad \boldsymbol{V} = \begin{bmatrix} \beta^\chi E + \theta^\chi E \\ \beta^\chi E + \rho^\chi I + \theta^\chi I \\ -\mu^\chi I + \theta_G^\chi G \end{bmatrix},$$

and so we have

$$F = \begin{bmatrix} 0 & 0 & \delta^\chi S \\ 0 & 0 & 0 \\ 0 & 0 & 0 \end{bmatrix}, \qquad V = \begin{bmatrix} \beta^\chi + \theta^\chi & 0 & 0 \\ \beta^\chi & \rho^\chi + \theta^\chi & 0 \\ 0 & -\mu^\chi & \theta_G^\chi \end{bmatrix}$$

Thereby, we can readily obtain that

$$FV^{-1} = \begin{bmatrix} 0 & 0 & \delta^\chi S \\ 0 & 0 & 0 \\ 0 & 0 & 0 \end{bmatrix} \begin{bmatrix} \frac{1}{\beta^\chi + \theta^\chi} & 0 & 0 \\ \frac{\beta^\chi}{(\beta^\chi + \theta^\chi)(\rho^\chi + \theta^\chi)} & \frac{1}{\rho^\chi + \theta^\chi} & 0 \\ \frac{\beta^\chi \mu^\chi}{\theta_G^\chi(\beta^\chi + \theta^\chi)(\rho^\chi + \theta^\chi)} & \frac{\mu^\chi}{\theta_G^\chi(\rho^\chi + \theta^\chi)} & \frac{1}{\theta_G^\chi} \end{bmatrix}$$

$$= \begin{bmatrix} \frac{\delta^\chi \beta^\chi \mu^\chi S^*}{\theta_G^\chi(\beta^\chi + \theta^\chi)(\rho^\chi + \theta^\chi)} & \frac{\delta^\chi \mu^\chi S^*}{\theta_G^\chi(\rho^\chi + \theta^\chi)} & \frac{\delta^\chi S^*}{\theta_G^\chi} \\ 0 & 0 & 0 \\ 0 & 0 & 0 \end{bmatrix}$$

Owing to the property of upper triangular matrix, the eigenvalues of the above matrix are on the diagonal. Thus, if we use the properties of the next-generation method, the largest eigenvalue is obtained as

$$R_0 = \frac{\lambda^\chi \beta^\chi \mu^\chi \delta^\chi}{\theta^\chi(\beta^\chi + \theta^\chi)(\rho^\chi + \theta^\chi)\theta_G^\chi}. \tag{5}$$

Now, let us interpret the resulting R_0 value. If $R_0 < 1$, then it can be said that DFE is stable and is the only equilibrium. If $R_0 > 1$, then DFE is unstable and endemic equilibrium exists. On the other hand, it is useful to note that the value of R_0 increases with $\lambda^\chi, \beta^\chi, \mu^\chi$, and δ^χ, and decreases with $\theta^\chi, \theta_G^\chi$, and Furthermore, the education given to individuals is aimed at preventing people from placing their limbs in drinking water. So, this decreases the value of μ^χ. Additionally, filtering drinking water reduces δ^χ while θ_G^χ increases with continuous chlorination of water. Hence, all these interventions cause a decrease in R_0 [4].

It is worth mentioning that continuous chlorination in the water is neither possible nor desirable, so chlorination is assumed to occur at different t times. During these times, the number of larvae in the water decreases and this gives rise to an impulsive differential equation. Also, in some regions, regular disease control can be quite difficult due to limited resources of infrastructure. In particular, it may be difficult or impossible to chlorinate water at certain times.

To examine the three important control parameters for the GWD model in more detail, fix all the other parameters to the sample values and take $R_0 = 1$. The equation (5) can be solved for the parameter δ^χ (which is trivial) and then μ^χ and θ_G^χ can be taken as independent variables. This situation allows us to obtain a 3D surface plotted in Figure 2. Combinations of parameters below the surface can be said to induce eradication. Furthermore, the disease persists due to a combination of parameters above the surface. Changes in μ^χ have a significant impact on the outcomes. On the other hand, we can not eliminate the disease even if we increase θ_G^χ 100 times, but due to the log scale, we have to drop δ^χ to very low levels. In Figure 2, it can be observed that eradication occurs if the infection rate is greatly reduced by filtration of drinking water and the parasite death rate is increased by more than 100 times by chlorination or the parasite birth rate is reduced to about 1 percent of its current value through education. Moreover, Figure 2 shows the eradication thresholds for the three separate parameters that most affect R_0. Accordingly, eradication will occur if the infection rate is reduced to well below its current value by filtering drinking water, and if the parasite mortality rate is increased more than a

hundredfold by chlorination, or if the parasite birth rate is reduced to 1 percent through education.

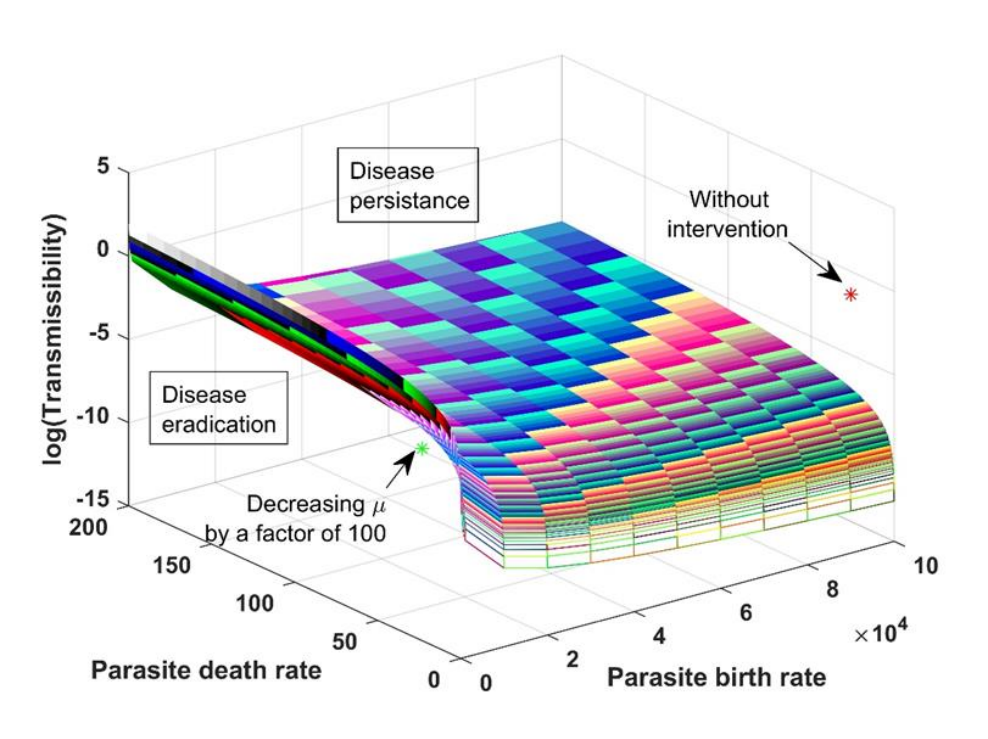

Figure 2. The eradication threshold for the three parameters affects R_0 the most

On the other hand, the endemic equilibrium (EE) is presented for predicting the long-term outcome of the GWD. If the disease continues, we can say that there is an endemic equilibrium, which is shown as $\bar{E} = (\bar{S}, \bar{E}, \bar{I}, \bar{G})$. Also, the DFE is stable when EE does not exist, and hence, we do not have any infection. However, the GWD persists if the EE exists. The EE of the fractional GWD model is as follows:

$$\bar{S} = \frac{\theta_G^{\chi}}{\delta^{\chi}\mu^{\chi}}\left(\rho^{\chi} + \theta^{\chi} + \frac{\rho^{\chi}\theta^{\chi}}{\beta^{\chi}} + \frac{\theta^{2\chi}}{\beta^{\chi}}\right),$$

$$\bar{E} = \frac{\rho^{\chi} + \theta^{\chi}}{\beta^{\chi}}\bar{I},$$

$$\bar{G} = \frac{\mu^{\chi}}{\theta_G^{\chi}}\bar{I},$$

$$\bar{I} = \frac{\lambda^{\chi}\delta^{\chi}\mu^{\chi}\beta^{\chi} - \theta^{\chi}\theta_G^{\chi}(\rho^{\chi}\beta^{\chi} + \theta^{\chi}\beta^{\chi} + \rho^{\chi}\theta^{\chi} + \rho^{\chi}\theta^{2\chi})}{(\beta^{\chi} + \rho^{\chi} + \theta^{\chi})\delta^{\chi}\mu^{\chi}\theta^{\chi}}$$

Numerical Simulation and Discussions

Biological and technical feasibility, costs and benefits, societal and political considerations are listed as distinguishing criteria for eradicating a contagious disease. The model we have presented meets these criteria. It is very important to know which of the ways to be followed may be optimal for the eradication of the disease. Despite the prospects for the extinction of diseases such as malaria, yaws, and yellow fever in the 20th century, and the eradication programs currently underway, such as polio and leprosy, smallpox remains the only disease that has been eradicated. On the other hand, hepatitis A and B, measles, rubella diseases are seen as suitable candidates for eradication. In other words, if necessary efforts are made for these diseases, which are technically and biologically possible to disappear, they will disappear just like smallpox. This study aims to offer solutions by presenting in detail the ways followed for GWD, which has already come to the threshold of eradication. While suggesting these solution proposals, it is aimed to shorten and facilitate the process by making use of the Caputo fractional derivative.

It can be observed that the most effective way to eliminate GWD is to reduce the parasite birth rate. This is possible by training people not to put their infected limbs in water. Although changing people's behavior is generally difficult, GWD eradication programs have been successful in this regard. If 99 percent of people can be persuaded not to put their infected feet in water, GWD will disappear completely. Chlorination, on the other hand, can theoretically control the disease, but numerical simulations clearly show that education is much more effective. Therefore, this study points to the importance of education in the last move towards the eradication of a disease. Although the results show that education is the most important intervention method, a combination of education with chlorination and filtration will be necessary to reach the final steps in a long eradication journey. By bringing together scientific and cultural resources, it will be possible to eradicate one of the oldest diseases in history.

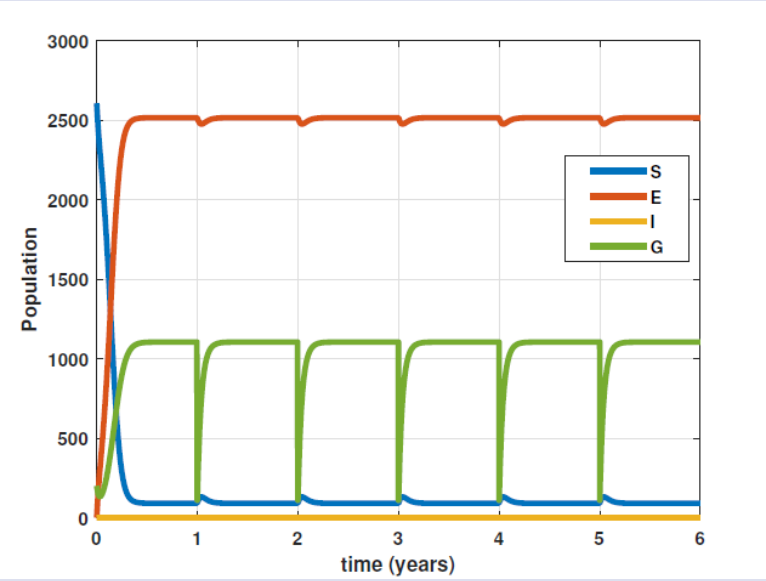

Figure 3. Persistence of the disease as a result of annual chlorination.

The effect of annual chlorination is shown in Figure 3 by using the values in Table 1. Although a significant reduction in larvae numbers is observed after chlorination, the population increases rapidly. While the number of susceptible individuals remains low, nearly all individuals continue to be infected. Additionally, it can be observed that chlorination is applied annually under the assumption that it is 90 percent successful. It is worth mentioning that infection levels are low, as individuals are contagious for a short time when their feet are submerged in water. On the other hand, the parasite birth rate is reduced by 99 percent, as seen in Figure 4. In this situation, the number of people who are exposed and infectious is almost zero, and no one is infected. All values except μ are the same as in Table 1.

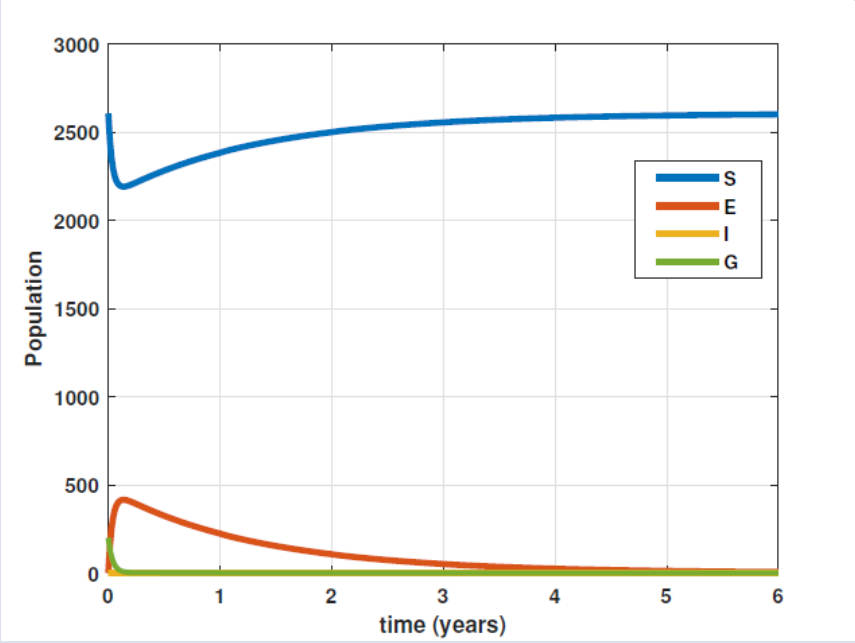

Figure 4. Eradication of the disease in case of reduced parasite birth rate when μ=1000..

Concluding Remarks

Some important results of this study are listed below:

- In the mathematical biology literature, theoretical and numerical results of some diseases have been analyzed using various fractional derivative definitions. As a result of the analyzes and simulations, it is mentioned whether the fractional derivative is advantageous for the model examined. In light of

these studies, GWD, which has not been examined through a fractional derivative before, was analyzed with the Caputo derivative. It is thought that this analysis may be guiding in eradication studies of various diseases.

- The present study's methodology demonstrates that education about disease prevention is the most successful method of intervention. However, depending on the type of disease, a combination of education and certain additional interventions may be needed to reach the final stages of a prolonged eradication process.
- It is necessary to carry out internationally coordinated studies to eliminate the diseases that exist today. It has been emphasized that efficient organizations and well-managed programs are important in disease eradication studies. Therefore, it is crucial to review the literature on diseases that have been or are about to be eradicated to examine how the challenges likely to be faced by disease eradication efforts are addressed.
- Continuous chlorination to eliminate GWD is neither possible nor desirable. Therefore, if it is assumed that chlorination takes place at different t_k times, the following fractional impulsive differential equation system emerges, with the number of larvae in the water decreasing at the rate r:

$$ {}_cD_{0,t}^{\chi} S(t) = \frac{1}{1-\chi}\int_0^t \frac{S'(\tau)}{(t-\tau)^{\chi}} = \lambda^{\chi} - \delta^{\chi} S(t)G(t) - \theta^{\chi} S(t) + \rho^{\chi} I(t), \qquad t \neq t_k $$

$$ {}_cD_{0,t}^{\chi} E(t) = \frac{1}{1-\chi}\int_0^t \frac{E'(t)}{(t-\tau)^{\chi}} = \delta^{\chi} S(t)G(t) - \beta^{\chi} E(t) - \theta^{\chi} E(t), \qquad t \neq t_k $$

$$ {}_cD_{0,t}^{\chi} I(t) = \frac{1}{1-\chi}\int_0^t \frac{I'(\tau)}{(t-\tau)^{\chi}} = \beta^{\chi} E(t) - \rho^{\chi} I(t) - \theta^{\chi} I(t), \qquad t \neq t_k $$

$$ {}_cD_{0,t}^{\chi} I(t) = \frac{1}{1-\chi}\int_0^t \frac{I'(\tau)}{(t-\tau)^{\chi}} = \mu^{\chi} I(t) - \theta_G^{\chi} G(t), \qquad t \neq t_k $$

$$ \Delta G = -rG(t), \qquad t \neq t_k $$

It should be noted that in some regions, regular disease control may be difficult due to limited resources and infrastructure. In particular, it may be difficult or impossible to chlorinate water at constant period. Also, numerical simulations clearly show that education is a much more effective factor in eradicating the disease under investigation.

- As a result, one of the most important conclusions to be drawn from this study is that the precautionary training provided to the public during the eradication studies of a disease can be considered the most important factor. On the other hand, using an effective fractional operator like Caputo derivative can speed up the process of disease eradication.

Conflicts of interest

There are no conflicts of interest in this work.

Ethical Approval Statement

The author of this article declares that the materials and methods used in this study do not require ethical committee permission and/or legal-special permission.

References

[1] Kilbas, A. A., Srivastava, H. M., Trujillo, J. J., Theory and Applications of Fractional Differential Equations, *Elsevier*, (2006) 1-523.

[2] Podlubny, I. Fractional Differential Equations: An Introduction to Fractional Derivatives, Fractional Differential Equations, to Methods of their Solution and Some of their Applications, *Elsevier*, (1998) 1-340.

[3] Gu, Y., Khan, M., Zarin, R., Khan, A., Yusuf, A., Humphries, U. W., Mathematical Analysis of a New Nonlinear Dengue Epidemic Model via Deterministic and Fractional Approach, *Alex. Eng. J.,* 67 (2023) 1-21.

[4] Smith, R., Modelling Disease Ecology with Mathematics, *Springfield: American Institute of Mathematical Sciences,* (2008).

[5] Mandal, S., Sarkar, R. R., Sinha, S., Mathematical Models of Malaria-a Review, *Malaria J*., 10(1) (2011) 1-19.

[6] Hethcote, H. W., The Mathematics of Infectious Diseases, *SIAM review*, 42(4) (2000) 599-653.

[7] Brauer, F., Compartmental models in epidemiology, *Mathematical Epidemiology*, (2008) 19-79.

[8] Cohen, J. M., "Remarkable Solutions to Impossible Problems": Lessons for Malaria from the Eradication of Smallpox, *Malaria J*., 18 (2019) 1-16.

[9] Bernoulli, D., Blower, S., An Attempt at a New Analysis of the Mortality Caused by Smallpox and of the Advantages of Inoculation to Prevent it, *Rev. Med. Virol.,* 14(5) (2004) 275.

[10] Gonzalez-Silva, M., Rabinovich, N. R., Some Lessons for Malaria from the Global Polio Eradication Initiative, *Malaria J.,* 20(1) (2021) 210.

[11] Mustapha, U. T., Qureshi, S., Yusuf, A., Hincal, E., Fractional modeling for the spread of Hookworm infection under Caputo operator, *Chaos, Solitons Fract.,* 137 (2023) 109878.

[12] Berhe, H. W., Qureshi, S., Shaikh, A. A., Deterministic Modeling of Dysentery Diarrhea Epidemic under Fractional Caputo Differential Operator via Real Statistical Analysis, *Chaos, Solitons Fract*., 131 (2020) 109536.

[13] Qureshi, S., Yusuf, A., Mathematical Modeling for the Impacts of Deforestation on Wildlife Species Using Caputo Differential Operator, *Chaos, Solitons Fract.,* 126 (2019) 32-40.

[14] Acay, B., Inc, M., Khan, A., Yusuf, A., Fractional Methicillin-Resistant Staphylococcus Aureus Infection Model under Caputo Operator, *J. Appl. Math. Comput.,* 67(1-2) (2021) 755-783.

[15] Acay, B., Inc, M., Mustapha, U. T., Yusuf, A., Fractional Dynamics and Analysis for a Lana Fever Infectious Ailment with Caputo Operator, *Chaos, Solitons Fract.,* 153 (2021) 111605.

[16] Inc, M., Acay, B., Berhe, H. W., Yusuf, A., Khan, A., Yao, S. W., Analysis of Novel Fractional COVID-19 Model with Real-Life Data Application, *Results Phys.,* 23 (2021) 103968.

[17] Yusuf, A., Acay, B., Mustapha, U. T., Inc, M., Baleanu, D., Mathematical Modeling of Pine Wilt Disease with Caputo Fractional Operator. *Chaos, Solitons Fract.,* 143 (2021) 110569.

[18] Jena, R. M., Chakraverty, S., Yavuz, M., Abdeljawad, T., A New Modeling and Existence–Uniqueness Analysis for Babesiosis Disease of Fractional Order, *Mod. Phys. Lett. B,* 35(30) (2021) 2150443.

[19] Johansyah, M. D., Sambas, A., Qureshi, S., Zheng, S., Abed-Elhameed, T. M., Vaidyanathan, S., Sulaiman, I. M., Investigation of the Hyperchaos and Control in the Fractional Order Financial System with Profit Margin, *Partial Differ. Equ. Appl. Math.,* (2024) 100612.

[20] Şenol, M., Gençyiğit, M., Koksal, M. E., Qureshi, S., New Analytical and Numerical Solutions to the (2+ 1)-Dimensional Conformable cpKP–BKP Equation Arising in Fluid Dynamics, plasma physics, and nonlinear optics, *Opt. Quant. Electron., 56*(3) (2024) 352.

[21] Awadalla, M., Alahmadi, J., Cheneke, K. R., Qureshi, S., Fractional Optimal Control Model and Bifurcation Analysis of Human Syncytial Respiratory Virus Transmission Dynamics, *Fractal Fract., 8*(1) (2024) 44.

[22] Qureshi, S., Argyros, I. K., Soomro, A., Gdawiec, K., Shaikh, A. A., Hincal, E., A New Optimal Root-Finding Iterative Algorithm: Local and Semilocal Analysis With Polynomiography, *Numer. Algorithms*, (2023) 1-31.

[23] Abdulganiy, R. I., Ramos, H., Osilagun, J. A., Okunuga, S. A., Qureshi, S., A Functionally-Fitted Block Hybrid Falkner Method for Kepler Equations and Related Problems, *Comput. and Appl. Math., 42*(8) (2023) 327.

[24] Qureshi, S., Soomro, A., Naseem, A., Gdawiec, K., Argyros, I. K., Alshaery, A. A., Secer, A., From Halley to Secant: Redefining root finding with memory-based methods including convergence and stability, *Math. Method Appl. Sci.,* 7(47) (2024) 5509-5531.

[25] Evirgen, F., Esmehan, U. Ç. A. R., Sümeyra, U. Ç. A. R., Özdemir, N., Modelling Influenza a Disease Dynamics Under Caputo-Fabrizio Fractional Derivative with Distinct Contact Rates, *Mathematical Modelling and Numerical Simulation with Applications*, *3*(1) (2023) 58-72.

[26] ur Rahman, M., Arfan, M., Baleanu, D., Piecewise Fractional Analysis of the Migration Effect in Plant-Pathogen-Herbivore Interactions, *Bull. Math. Biol., 1*(1) (2023) 1-23.

[27] Joshi, H., Yavuz, M., Transition Dynamics Between a Novel Coinfection Model of Fractional-Order for COVID-19 and Tuberculosis via a Treatment Mechanism, *Eur. Phys. J. Plus., 138*(5) (2023) 468.

Cumhuriyet Sci. J., 45(2) (2024) 352-359
DOI: https://doi.org/10.17776/csj.1351460

Cumhuriyet Science Journal

| csj.cumhuriyet.edu.tr | Founded: 2002 ISSN: 2587-2680 e-ISSN: 2587-246X Publisher: Sivas Cumhuriyet University

Polydopamine-mediated facile Silver grown on ZnO Thin Films as High Performance SERS Substrates for R6G Detection

Sami Pekdemir [1,2,a,*]

[1] *Department of Aeronautical Engineering, Faculty of Aeronautics and Astronautics, Erciyes University, Kayseri, 38039,Türkiye.*
[2] *ERNAM - Erciyes University Nanotechnology Application and Research Center, Kayseri, 38039, Türkiye.*
**Corresponding author*

Research Article

History
Received: 28/08/2023
Accepted: 30/05/2024

ABSTRACT

Surface-enhanced Raman spectroscopy (SERS) is a widely known technique that uses plasmonic structures (silver, gold, etc.) to detect low-concentration molecules. However, the limited number of metallic elements with plasmonic properties leads to limitations in their application. The qualitative detection method of SERS holds considerable promise in providing novel platforms for diverse applications, owing to its utilization of hybrid structures. Mussel-inspired polydopamine offers a promising avenue for the fabrication and integration of hybrid structures suitable for the SERS platform. Here, sputtered ZnO thin films were modified with Ag Nanostructures using polydopamine to fabricate a homogeneous Ag@ZnO hybrid high-performance SERS substrate. Ag/ZnO hybrid nanostructures were analyzed by FESEM and XRD to investigate their morphological and structural characterizations. SERS measurements were performed for all silver growth times to understand the effect of the silver growth process and hybrid structure synergy on SERS performance. The Ag@ZnO hybrid structure, cultivated with 24-hour silver growth, exhibited remarkable detectability even at an ultra-low R6G concentration of 10 pM.

Keywords: Polydopamine, Plasmonics, SERS, Ag-ZnO hybrid structures, R6G.

[a] *samipekdemir@erciyes.edu.tr* *https://orcid.org/0000-0002-7929-6849*

Introduction

Surface-Enhanced Raman Spectroscopy (SERS) has emerged as a powerful analytical technique for enhancing the vibrational signals of molecules adsorbed onto metallic surfaces [1]. To further harness the potential of SERS for sensitive and selective molecular detection, the design and fabrication of high-performance SERS substrates are of paramount importance [2]. Among various materials, zinc oxide (ZnO) thin films have attracted attention due to their unique optical and chemical properties, making them promising candidates for SERS applications [3]. Moreover, the incorporation of silver (Ag) nanostructures onto ZnO surfaces can significantly amplify the SERS signal through the localized surface plasmon resonance effect [4]. Achieving controlled Ag nanostructure growth on ZnO substrates, however, remains a challenge [5].

In recent years, the design and fabrication of hybrid plasmonic structures has gained prominence as a strategy to unlock even greater SERS sensitivity and reproducibility [6]. Hybrid structures entail the combination of multiple materials with distinct plasmonic properties, synergistically enhancing the overall SERS performance beyond the capabilities of individual components. The incorporation of Ag nanostructures onto other substrates, such as zinc oxide (ZnO) thin films, presents a promising avenue to achieve such enhanced SERS activity.

In this context, the integration of polydopamine (PDA) as a versatile platform for surface modification and metal ion reduction offers a promising avenue for the controlled synthesis of Ag nanostructures on ZnO thin films [7]. PDA, inspired by the adhesive proteins found in marine mussels, exhibits strong adhesion to various substrates and provides functional groups that facilitate metal ion binding and subsequent reduction [8]. By leveraging the inherent properties of PDA, a facile approach to the controlled growth of Ag nanostructures on ZnO thin films becomes feasible, thereby enhancing the SERS activity of the resulting substrates.

In this study, we delve into the innovative strategy of utilizing PDA-assisted Ag growth on ZnO thin films to fabricate high-performance SERS substrates. ZnO thin films are fabricated through a diverse array of techniques, encompassing RF/DC magnetron sputtering, chemical vapor deposition (CVD), pulsed laser deposition (PLD), organic vapor phase epitaxy (MOVPE), molecular beam epitaxy (MBE), and sol-gel methods [9]. Notably, RF/DC magnetron sputtering facilitates precise manipulation of chemical composition and deposition rates. Additionally, its execution within a high-vacuum environment ensures the creation of thin films characterized by high purity, homogeneity, and exceptional quality. The introduction of surface-bound Ag nanostructures (Ag NSs) onto ZnO thin films was accomplished through the incorporation of polydopamine, inspired by the adhesive properties of mussels [7]. Polydopamine's solution-phase deposition confers flexibility to surface functionalization and

provides the requisite chemical groups for Ag ion reduction. The evaluation of Ag NS size and structure variations due to growth conditions was conducted through field emission scanning electron microscopy (FESEM) imaging. The collaborative effect of PDA-mediated Ag growth and ZnO thin films facilitated the sensitive detection of the R6G analytical molecule, achieving a remarkable detection limit of 10 pM.

Experimental

Materials

Silicon wafers (<100>, N/Phos) were purchased from Wafer World Inc. ZnO sputtering target (99.999% purity, 2 inch diameter) was purchasing from Plasmaterials inc. Dopamine hydrochloride (Sigma H8502), Tris-EDTA buffer solution, $AgNO_3$ salt and Rhodamine 6G (R6G) was purchased from Sigma-Aldrich. Ethanol, was purchased from Merck.

Deposition of ZnO thin Film on Si substrate Fabrication

RF magnetron sputtering was used to deposited ZnO thin films on a Si (100) substrate using the NANOVAK NVTS-400. Fabrication of ZnO films was done using a ZnO target and argon gas (99.999% purity). Si (100) substrates were cleaned with an ultrasonic cleaner using acetone, isopropyl alcohol, ethanol, and dried by blowing nitrogen gas, respectively. After the drying process was completed, the samples were cleaned in vacuum with O_2 plasma system at 15 W power for 10 minutes in order to clean the surface from hydrocarbon residues and for better adhesion of the thin film to the surface. Before to starting the thin film deposition process, the chamber was purged down to a base pressure of $2x10^{-6}$ Torr. Under 3.9 mTorr pressure, 15 sccm argon flow rate, 80 W RF power, and room temperature conditions, thin films were deposited. ZnO thin films with a thickness of 250 nm were deposited at a rate of 0.3 /s. During the growing process, the ZnO films thickness and growth rate were measured using the QCM thickness measuring equipment (Inficon).

Polydopamine-mediated in situ growth of Ag nanostructures on sputtered ZnO thin film

Mussel inspired Polydopamine (PDA) thin film coating on Si (100) substrates ($1x1cm^2$) with a 250 nm thick ZnO film. The substrates were submerged in a dopamine solution for 30 minutes (1 mg/mL in 5 mM Tris-EDTA buffer, pH 8.5) at room temperature. After coating with PDA, the samples were rinsed with distilled water and dried with N_2 gas. The PDA coated substrates were then treated in steady state with silver nitrate solution (50 mM $AgNO_3$ in 5 mL distilled water) at steady state for various Ag growth times (12, 24, and 36 hours).

Characterization of ZnO thin films and Ag@ZnO substrate

The morphology of the substrate was analyzed by scanning electron microscopy (SEM) imaging that was performed at 3 kV (FESEM, Zeiss Gemini 500). X-ray diffraction patterns of silver decorated ZnO thin film hybrid nanostructures (Ag@ZnO) were analyzed by Grazing Incidence X-ray Diffraction (GIXRD) technique in the range of 30^o-85^o 2θ on a Panalytical X-ray diffractometer.

SERS Measurements of Ag decorated ZnO thin films

Plasmonic properties of the Ag@ZnO was investigated by Raman spectroscopy. An analyte molecule dropped Ag@ZnO samples with various silver growth time was performed Raman measurement which called SERS. The SERS activity of the Ag-structured ZnO film was systematically investigated utilizing a confocal Raman microscope (Alpha M+, Witec, Germany), which was equipped with a 532 nm laser. The experimental setup involved the drop-casting of an aqueous solution of Rhodamine 6G (R6G) onto both the unmodified and Ag-decorated ZnO films, wherein the Ag decoration was accomplished via a PDA coating. Unless explicitly specified, a consistent volume of 2 µL and concentration of 100 µM for the R6G solution were maintained. Raman measurements were conducted post the complete evaporation of the water. The acquisition of Raman spectra employed a 100× objective featuring a numerical aperture value of 0.9. The spectral acquisition time was set at 0.05 s, and the laser power was maintained at 0.1 mW.

To map the SERS activity of the surfaces, a spatial resolution of 0.5 µm was employed, encompassing a 40 × 30 μm^2 area. This mapping relied on the distinctive peak of R6G, with the aromatic C–C stretch peak at 1361 cm^{-1} serving as the characteristic marker. The intensity of this peak facilitated both Raman mapping and determination of the detection limit.

To ascertain the limit of detection, the concentration of R6G was systematically varied from 1 µM down to 10 pM. A stock solution of R6G at a concentration of 10 mM was initially prepared, and subsequent lower concentrations were obtained through dilution with deionized water. Each solution, with a volume of 2 µL, was subsequently deposited onto the SERS substrate, and Raman measurements were conducted post evaporation of the water. In this limit of detection investigation, SERS spectra were recorded from a minimum of 10 distinct locations, with each acquisition lasting for 0.1 s.

Results And Discussion

Figure 1 provides a schematic representation of the key stages and outcomes involved in the production of ZnO thin films and the subsequent development of Ag nanostructures on these surfaces.

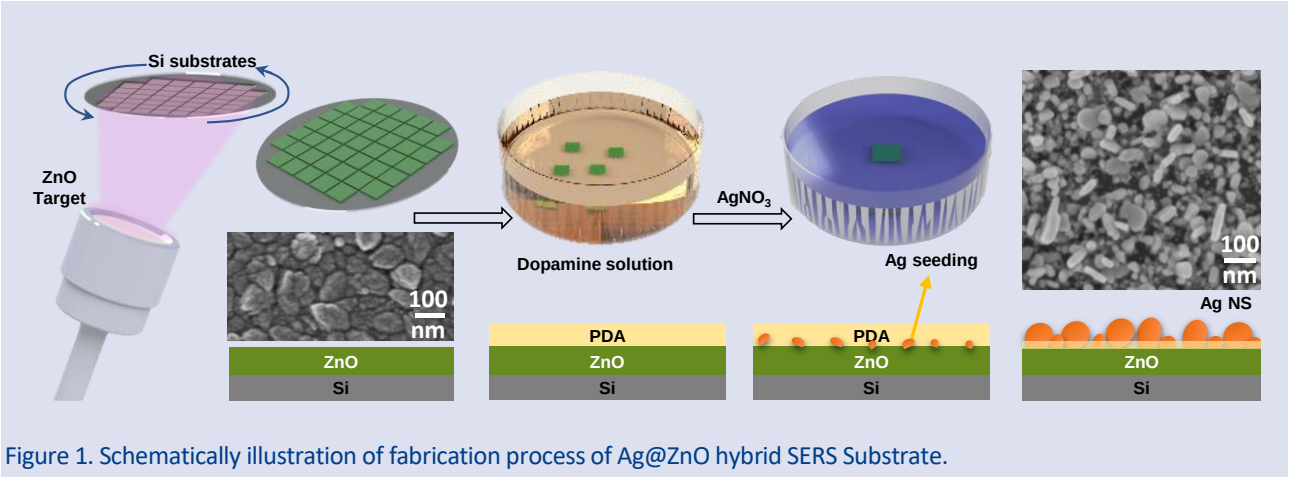

Figure 1. Schematically illustration of fabrication process of Ag@ZnO hybrid SERS Substrate.

Initially, Si substrates, cut into 1x1 cm² dimensions, were meticulously cleaned using acetone, propanol, and ethanol. These square-shaped Si samples were then introduced into the vacuum thin film system. Once the vacuum pumps-initiated operation, the system awaited the attainment of a starting pressure of $3x10^{-7}$ Torr. The coating process commenced by introducing high-purity Ar gas into the system, followed by the activation of the RF power unit to generate plasma. Subsequently, the target material underwent preliminary cleansing via plasma treatment, effectively removing potential contaminants before they could reach the sample surface.

Following this pre-cleaning step, the actual coating process was initiated. This involved opening the shutter positioned in front of the sample and resetting the thin film thickness gauge. As the thickness reading reached 250 nm on the thin film thickness meter system, the cover automatically closed to maintain a consistent film thickness. Once the coating process was complete, the system was halted by deactivating the RF power supply and gas flow, and the sample was extracted from the vacuum environment by introducing gas into the system.

The Si/ZnO samples, now withdrawn from the system, were immersed in a freshly prepared dopamine solution with a pH value of 8.5. These samples were then kept in darkness for a duration of 30 minutes. During this period, the dopamine molecules polymerized in response to the basic environment, resulting in the formation of a PDA thin film on the Si/ZnO sample.

Subsequently, the PDA-coated sample underwent immersion in a 50 mM $AgNO_3$ solution for varying durations (12, 24, and 36 hours) to facilitate the growth of Ag nanostructures. Leveraging the inherent capability of PDA to catalyze the reduction of metallic ions, an observable reduction process occurred. This transformation involved the conversion of dissolved silver ions through interaction with the PDA thin film.

The topological and structural characteristics of Ag-grown ZnO (Ag@ZnO) hybrid structures were investigated through scanning electron microscopy (SEM) imaging. Figure 2 illustrates the influence of the silver growth mechanism on the surface topology of the ZnO thin film.

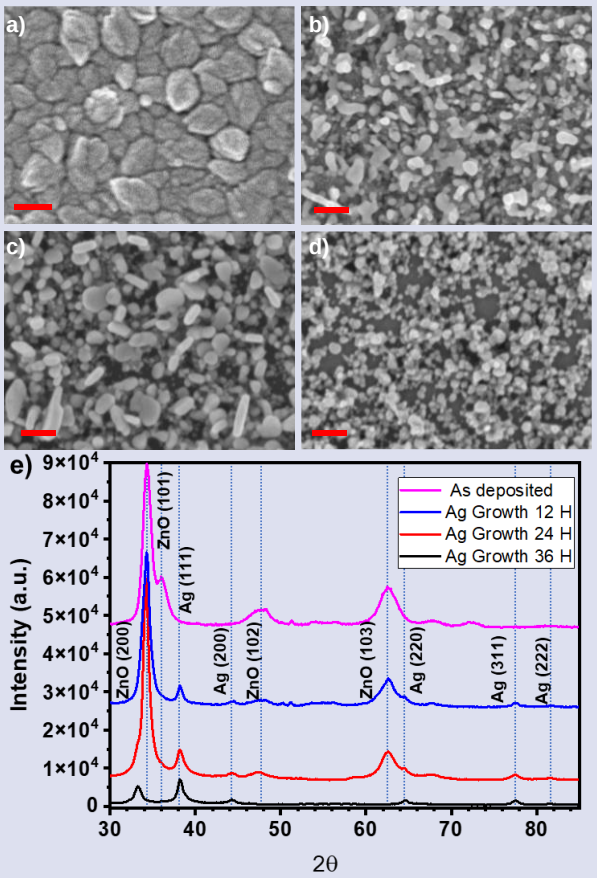

Figure 2. SEM images (scale bar: 100 nm) and XRD measurement. a) SEM image of ZnO thin film as deposited. b) SEM image of Ag@ZnO hybrid structures after 12 h Ag growth. c) SEM image of Ag@ZnO hybrid structures after 24 h Ag growth. d) SEM image of Ag@ZnO hybrid structures after 36 h Ag growth. e) XRD results of the ZnO and Ag@ZnO hybrid structures.

Figure 2a presents an SEM image of the as-deposited ZnO thin film. The ZnO film exhibited high uniformity, devoid of any discernible cracks, and was composed of nanoscale grains. Following the growth of silver, the surface morphology underwent a significant transformation, resulting in the formation of small silver nanoparticles. Notably, in the absence of the PDA coating, noteworthy silver growth was not observed. The growth

of Ag nanostructures on the surface was facilitated through a mussel-inspired PDA thin film.

Morphology was systematically investigated for variations in the substrate in response to different Ag deposition periods. The growth duration exerted a direct influence on the dimensions of the Ag nanostructures (Ag NSs). During a 12-hour growth interval, the production of Ag NSs was incomplete, and their dimensions predominantly remained below 25 nm. However, extending the growth period to 24 hours yielded the development of Ag NSs ranging in size up to 100 nm, excluding those exceeding 50 nm. Subsequently, with a further extension to a 36-hour growth period, the average Ag NS size reduced to 20 nm. This reduction in size is plausibly attributed to potential deterioration of the underlying ZnO film within the aqueous growth solution. It is noteworthy that particles dislodged from the surface were observed in the wastewater subsequent to the growth process termination. Consequently, particles became discernible in the rinse water of the substrate, implying a separation of particles from the surface. The substantiation for this deduction is reinforced by EDX results (Table 1), which exhibit variations in the silver content within the sample (as seen in Figure 3). Notably, the Ag NS-decorated samples showcase consistent Si content. The utilization of normalized EDX counting enables a comparative analysis of element quantities across the samples. Over the course of the silver growth process, the silver content exhibited a gradual increment, culminating in its peak value at the 24-hour growth rate. However, this content exhibited a decline at the 36-hour interval, presumably due to weathering effects.

Table 1. Elemental composition of the Samples.

Samples	% Atomic Si	% Atomic O	% Atomic Zn	% Atomic Ag
ZnO	20.59402	35.63005	43.77593	0
Ag(12h)@ZnO	33.01004	33.4837	21.07815	12.4281
Ag(24h)@ZnO	35.59322	28.66468	13.62803	22.11406
Ag(36h)@ZnO	34.40178	36.51642	13.98998	15.09182

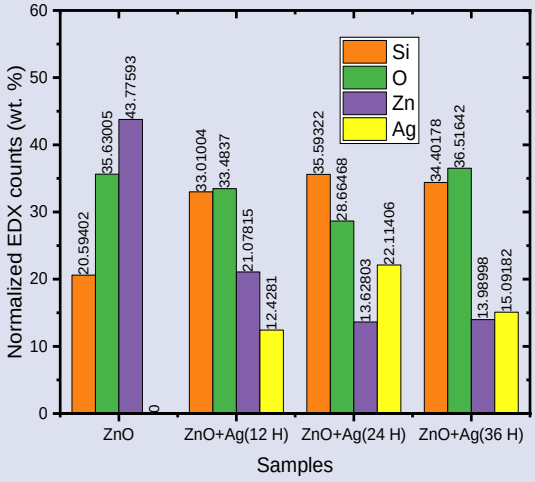

Figure 3. Elemental analyses of Samples by normalization EDX counts

The formation of Ag NSs on the ZnO film can be rationalized through the metal ion reduction capabilities of PDA. Notably, the absence of PDA prevented the development of Ag nanostructures on the ZnO layer (see figure 4). This observation underscores the essential role of functional groups introduced by PDA in facilitating the surface growth of Ag NSs.

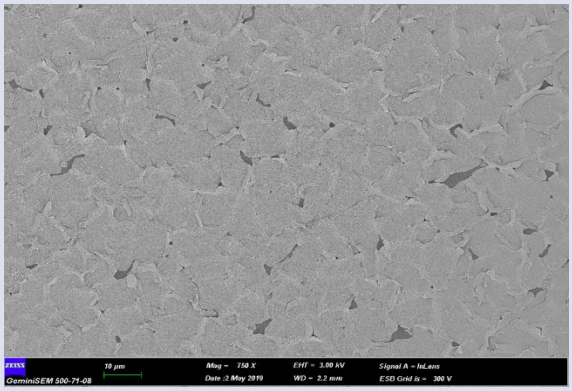

Figure 4. SEM image of decomposed ZnO thin film after the Ag growth process without PDA coating

The diffraction data were acquired through X-ray diffraction (XRD), alongside quantitative analysis. The XRD patterns of both the ZnO thin film and Ag-modified samples, obtained for various Ag growth durations, are depicted in Figure 2.e. The presence of diffraction peaks at 34.5° and 62.6° corresponding to the (200) and (130) crystallographic planes, respectively, substantiates that the ZnO films exhibit excellent agreement with the wurtzite hexagonal crystal structure (JCPDS No. 36-1451) [10]. The peak at 36.1° can be attributed to the (101) crystallographic plane [11], which disappeared during the silver growth process. This is the possible result of the water solubility of ZnO [12], as clearly seen in the SEM images of the 36 h silver growth process and discussed in the section on SEM images. Notably, these peaks were absent in the ZnO thin film subjected to a 36-hour growth period, a result attributed to the decomposition of the ZnO underlayer. Furthermore, the diffraction peak at 38.2° corresponds to the (111) plane of the face-centered cubic Ag structure (JCPDS card # 089-3722) [13]. In comparison, the Ag peak intensity on the uncoated PD-modified ZnO film was notably subdued. Additionally, diffraction peaks corresponding to the (002), (220), (311), and (222) planes, observed at 44.3°, 64.6°, 77.5°, and 81.5°, respectively, can be attributed to silver nanostructures, a direct consequence of the silver growth process.

Optimal peak intensity for both ZnO and Ag was noted in substrates prepared via 24-hour Ag deposition time. The peak intensity of the ZnO (002) plane exhibited an increase with prolonged Ag decoration time. However, after 24 hours, despite the extended Ag decoration period, the intensity of the peak diminished, signifying that adorning Ag for excessive durations disrupts the preferred orientation of ZnO (002).

The average crystallite sizes (D) of the samples were determined utilizing the Debye–Scherrer equation [14]:

$$D = \frac{0.9\times\lambda}{\beta\times\cos\theta} \quad (1)$$

Here, λ, θ, and β represent the wavelength of X-ray radiation, the Bragg's angle of the peaks, and the angular width of peaks at the full width at half maximum (FWHM), respectively. For pure ZnO, the average crystal size was 7.5 nm, exhibiting variations with differing Ag deposition times. Specifically, the average crystallite sizes were 12.55 nm, 13.31 nm, and 11.87 nm for ZnO films decorated with Ag for 12, 24, and 36 hours, respectively. The absence of additional peaks and shifts in peak positions suggests that Ag did not incorporate into the ZnO lattice but remained solely on the surface of ZnO [15].

SEM images and XRD results give us some correlations about the particle sizes (see Figure 5). The particle size analysis shows Ag nanostructures of 13.7 ± 7.6 nm, 15.9 ± 7.8 nm, 10.6 ± 5.1 nm in Ag@ZnO samples with 12, 24, 36 h growth time, respectively. The average particle sizes obtained from SEM images and the crystallite sizes obtained from XRD measurements give comparable results. Based on this correlation, it can be said that the two results support each other and Ag nanostructures are largely composed of single crystal structures.

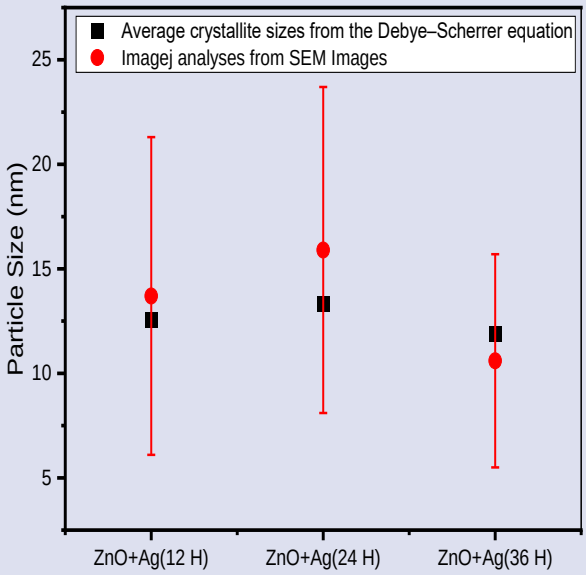

Figure 5. Comparative analysis of average particle sizes obtained from XRD measurement and SEM images

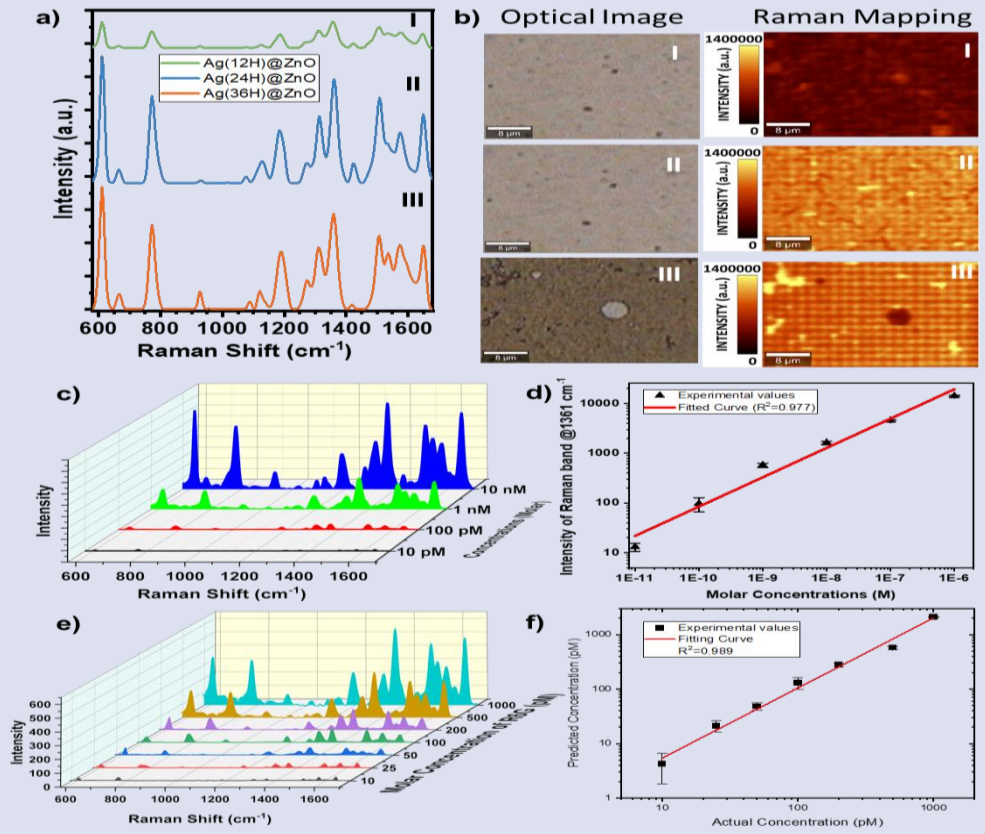

Figure 6. SERS activity of Ag@ZnO nanostructures. a) SERS spectra of R6G on silver decorated ZnO thin films with 12 hours(I), 24 hours(II), 36 hours(III) growth time. b) Optical Images of Raman mapping regions and Raman mapping images of Ag@ZnO with various Ag growth time (12 hours, 24 hours, 36 hours; I, II, III, respectively), obtained by mapping intensities at a Raman shift of 1361 cm^{-1}. c) SERS spectra of R6G at concentrations ranging 10 nM to 10 pM, measured on the Ag(24H)@ZnO. d) Correlation between R6G concentration and SERS intensity at 1361 cm^{-1}. e) SERS measurements were conducted using a distinct set of R6G solutions, spanning concentrations from 1000 pM to 10 pM. f) Calculated concentrations were predicted using the equation mentioned in section (d) for the aforementioned R6G solution batch.

The SERS activity was explored utilizing Rhodamine 6G (R6G) as a probe molecule. An aqueous R6G solution was drop-cast onto Ag@ZnO samples featuring varying Ag deposition times, and SERS measurements were conducted post-water evaporation. The surface SERS activity was analyzed through the mapping of the characteristic vibrational mode of the probe molecule at 1361 cm^{-1}. This mode originates from the robust C–H in-plane bending of R6G [16]. Among the studied Ag@ZnO samples, noteworthy SERS activity was notably observed in the sample subject to a 24-hour Ag growth period (Ag(24H)@ZnO) (refer to Figure 6.a). The SERS signal intensity at 1361 cm^{-1} from Ag(24H)@ZnO surpassed those from Ag(12H)@ZnO and Ag(36H)@ZnO by factors of 5 and 1.1, respectively.

$$S.D. = \sqrt{\frac{\sum_{i=1}^{n}(x_i-\bar{x})^2}{(n-1)}} \quad (2)$$

$$R.S.D = \frac{\sqrt{\frac{\sum_{i=1}^{n}(x_i-\bar{x})^2}{(n-1)}}}{\frac{\sum_{1}^{n} n}{n}}.100 \quad (3)$$

Here; x_i is i labeled data, $\bar{x}$ is average of all data sets, n is number of all data sets.

Moreover, standard deviation (SD) and relative standard deviation (RSD) values (Table 2) were calculated based on the signal intensities of the 1361 cm^{-1} band using equation (2) and (3), elucidating the substrate efficiency. To calculate the standard deviation, approximately 60 spectra were randomly selected from each mapping image (Figure 7). This comprehensive analysis reveals a commendable level of uniformity across the film, with a 9.3% RSD. The SERS intensity from Ag(24H)@ZnO demonstrates a high degree of uniformity (refer to Figure 8), surpassing that of SERS substrates fashioned from colloidal nanoparticle assemblies [17].

Raman mapping images in Figure 6.b depict the spatial distribution of SERS activity. These images were obtained from Ag@ZnO samples featuring varied Ag growth times (12 hours, 24 hours, 36 hours). Specifically, the mapping images labeled as "I" pertain to Ag@ZnO with a 12-hour silver growth period (Ag(12H)@ZnO). The dark orange Raman mapping image highlights an insufficient AgNS growth for effective SERS activity points, known as "hot-spots". In contrast, the Raman mapping of Ag(24H)@ZnO (II) samples illustrates improved, homogeneous distribution of the SERS signal. While some dark orange and yellow regions persist, the darker orange Raman mapping image for Ag(36H)@ZnO (III) is indicative of Ag nanostructure erosion from the surface, likely connected to the decomposition of the ZnO thin film within the water-based solvent. The occurrence of yellow regions represents aggregated R6G on surface cracks due to decomposing. From these outcomes, it is evident that the most efficient SERS substrate emerges from a 24-hour silver growth process.

Table 2. Statistical analysis of SERS activity on Ag@ZnO samples. S. D. refers to the standard deviation and R. S. D. refers to the relative standard deviation.

Region	Raman Intensity @ 1361 cm^{-1}	S.D.	R.S.D. (%)
Ag(12h)@ZnO	367965	60793	16.5
Ag(24h)@ZnO	1048473	98246	9.3
Ag(36h)@ZnO	1003297	145460	14.5

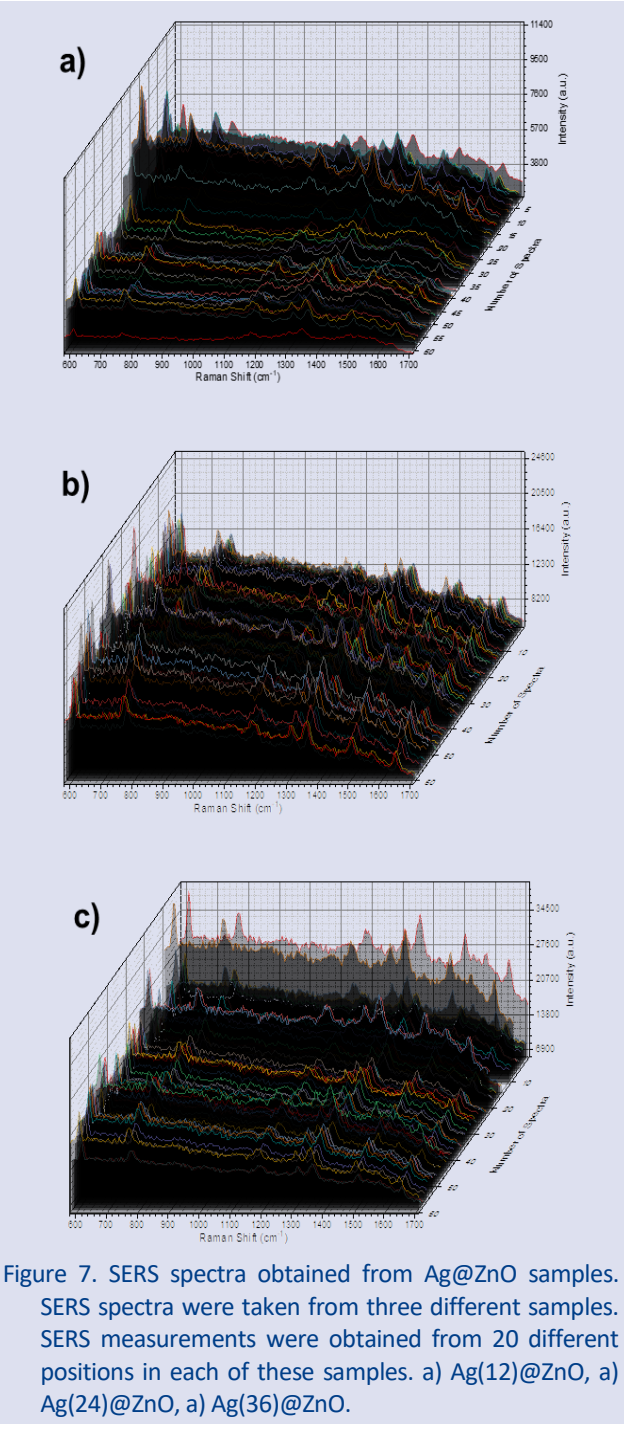

Figure 7. SERS spectra obtained from Ag@ZnO samples. SERS spectra were taken from three different samples. SERS measurements were obtained from 20 different positions in each of these samples. a) Ag(12)@ZnO, a) Ag(24)@ZnO, a) Ag(36)@ZnO.

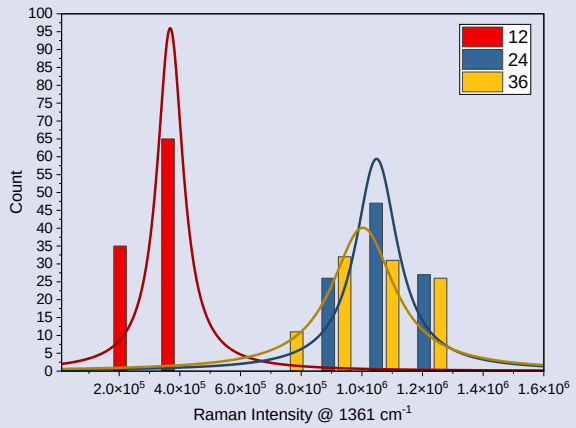

Figure 8. Statistical analysis of SERS activity of Ag@ZnO samples

The limit of detection for SERS-active surfaces represents the lowest detectable concentration through Raman spectroscopy. Raman spectra for varying R6G concentrations (10 nM to 10 pM) are shown in Figure 6.c. The distinct peak of R6G at 1361 cm^{-1} was discernible even at concentrations as low as 10 pM. Overall, the SERS performance of the presented material parallels Ag-ZnO thin film hybrid nanostructures reported in other studies. For instance, in a recent report [15], Ag@ZnO nanoworms were employed as SERS substrates, achieving a detection limit of 100 pM for R6G. In a separate investigation, nanocomposite films were fabricated by cultivating silver nanoparticles on zinc oxide rods[18], which were previously grown on PET substrate using Methenamine. These substrates exhibited surface-enhanced Raman scattering (SERS) detection capabilities, detecting concentrations as low as 100 nM for Malachite green and 1000 pM for p-aminothiophenol. The findings of this study reveal a detection capability that exceeds previous research by a factor of ten or more.

To illustrate the quantitative detection capabilities of Ag(24H)@ZnO, SERS intensity was plotted against the concentration of R6G (Figure 6.d). The resulting curve was well-fitted with the equation , yielding a coefficient of determination (R^2) of 0.981. Furthermore, to underscore the predictive potential of probe molecule concentrations on the presented platform, an additional batch of R6G solutions was prepared, spanning concentrations from 1000 pM to 10 pM. These solutions were then applied to the Ag(24H)@ZnO substrate, and intensity at the 1361 cm^{-1} position was gauged via Raman spectroscopy after water evaporation. Employing the equation derived from the data in Figure 6.d, these intensity values enabled the calculation of solution concentrations. The resultant calculated concentrations represent predicted concentrations and were plotted against actual concentrations (refer to Figure 6.e, 6.f). Notably, a favorable alignment between predicted and calculated concentrations was observed, substantiated by a coefficient of determination (R^2) of 0.989, further affirming the quantitative molecular detection capability of the presented platform.

A quantitative measure of SERS activity is the enhancement factor, which gauges the extent of improvement in Raman scattering intensity relative to a reference substrate. Different enhancement factors have been proposed in the literature [19]. A straightforward definition, known as the analytical enhancement factor (AEF), provides a straightforward and repeatable measurement under predefined conditions [20]. AEF is calculated using the following Eq. (4):

$$\mathrm{AEF} = \frac{\mathrm{I_{SERS}}}{\mathrm{I_{RM}}} \times \frac{\mathrm{C_{RM}}}{\mathrm{C_{SERS}}} \quad (4)$$

In this equation, I_{SERS} (13 counts) and I_{RM} (53 counts) denote the intensity of Raman scattering at 1361 cm^{-1} for the SERS and reference substrates, respectively. For the experiments described herein, the reference substrate consisted of an unmodified glass slide. Similarly, C_{SERS} (10 pM) and C_{RM} (10 mM) refer to the solution concentration of the probe molecule for the SERS and reference substrates, respectively. AEF was calculated as 2.45×10^8 for R6G. This enhancement factor of 10^8 is in line with previous reports [15].

Conclusions

In this study, we have successfully fabricated high-performance SERS substrates by cultivating Ag nanostructures with remarkable uniformity on ZnO thin films. The harmonious interplay between PDA-mediated Ag growth and ZnO thin films offers an auspicious avenue for propelling SERS technology forward, bestowing the capability for precise and selective molecular detection across diverse analytical and sensing applications. Inspired by the adhesive prowess of mussels, we have orchestrated Ag@ZnO hybrid structures, fashioning proficient Ag NS configurations on ZnO thin films through the inherent metal ion reduction propensity of the PDA polymer structure. The symbiotic interplay between metal oxide semiconductors and plasmonic metallic nanostructures has engendered the detection of the R6G analyte molecule with an impressive detection threshold reaching 10 pM. In conclusion, this proves a detection capability that surpasses similar efforts in the literature, thus paving the way for promising avenues of future research.

Conflicts of interest

There are no conflicts of interest in this work.

References

[1] K. Kneipp, Y. Wang, H. Kneipp, L.T. Perelman, I. Itzkan, R.R. Dasari, M.S. Feld, Single Molecule Detection Using Surface-Enhanced Raman Scattering (SERS), *Physical Review Letters*. 78 (1997) 1667–1670..

[2] P.L. Stiles, J.A. Dieringer, N.C. Shah, R.P. Van Duyne, Surface-Enhanced Raman Spectroscopy, *Annual Review of*

Analytical Chemistry. 1 (2008) 601–626.

[3] O. Szabó, S. Flickyngerová, T. Ignat, I. Novotný, V. Tvarozek, Gold nanostructures sputtered on zinc oxide thin film and corning glass substrates, *Facta universitatis - series: Electronics and Energetics*. 29 (2016) 77–88.

[4] A. Guerrero-Martínez, S. Barbosa, I. Pastoriza-Santos, L.M. Liz-Marzán, Nanostars shine bright for you, *Current Opinion in Colloid & Interface Science*. 16 (2011) 118–127.

[5] Y. Fang, N.-H. Seong, D.D. Dlott, Measurement of the Distribution of Site Enhancements in Surface-Enhanced Raman Scattering, *Science*. 321 (2008) 388–392.

[6] X.-S. Zheng, I.J. Jahn, K. Weber, D. Cialla-May, J. Popp, Label-free SERS in biological and biomedical applications: Recent progress, current challenges and opportunities, *Spectrochimica Acta Part A: Molecular and Biomolecular Spectroscopy*. 197 (2018) 56–77.

[7] H. Lee, S.M. Dellatore, W.M. Miller, P.B. Messersmith, Mussel-Inspired Surface Chemistry for Multifunctional Coatings, *Science*. 318 (2007) 426–430.

[8] Y. Cong, T. Xia, M. Zou, Z. Li, B. Peng, D. Guo, Z. Deng, Mussel-inspired polydopamine coating as a versatile platform for synthesizing polystyrene/Ag nanocomposite particles with enhanced antibacterial activities, *J. Mater. Chem. B*. 2 (2014) 3450–3461.

[9] M. Kuru, H. Narsat, The effect of heat treatment temperature and Mg doping on structural and photocatalytic activity of ZnO thin films fabricated by RF magnetron co-sputtering technique, *Journal of Materials Science: Materials in Electronics*. 30 (2019) 18484–18495.

[10] H.L. Cao, X.F. Qian, Q. Gong, W.M. Du, X.D. Ma, Z.K. Zhu, Shape- and size-controlled synthesis of nanometre ZnO from a simple solution route at room temperature, *Nanotechnology*. 17 (2006) 3632–3636.

[11] P. Fageria, S. Gangopadhyay, S. Pande, Synthesis of ZnO/Au and ZnO/Ag nanoparticles and their photocatalytic application using UV and visible light, *RSC Adv.* 4 (2014) 24962–24972.

[12] S. Heinonen, J.-P. Nikkanen, E. Huttunen-Saarivirta, E. Levänen, Investigation of long-term chemical stability of structured ZnO films in aqueous solutions of varying conditions, *Thin Solid Films*. 638 (2017) 410–419.

[13] T. Theivasanthi, M. Alagar, Electrolytic Synthesis and Characterization of Silver Nanopowder, *Nano Biomedicine and Engineering*. 4 (2012). doi:10.5101/nbe.v4i2.p58-65.

[14] B.D. Cullity, C.D. Graham, Introduction to Magnetic Materials, *John Wiley & Sons, Inc.*, Hoboken, NJ, USA, 2008.

[15] N.D. Jayram, S. Sonia, S. Poongodi, P.S. Kumar, Y. Masuda, D. Mangalaraj, N. Ponpandian, C. Viswanathan, Superhydrophobic Ag decorated ZnO nanostructured thin film as effective surface enhanced Raman scattering substrates, *Applied Surface Science*. 355 (2015) 969–977..

[16] S. Nie, S.R. Emory, Probing Single Molecules and Single Nanoparticles by Surface-Enhanced Raman Scattering, *Science*. 275 (1997) 1102–1106..

[17] C. Jiang, S. Markutsya, V. V. Tsukruk, Collective and Individual Plasmon Resonances in Nanoparticle Films Obtained by Spin-Assisted Layer-by-Layer Assembly, *Langmuir*. 20 (2004) 882–890.

[18] D. Cheng, Y. Zhang, C. Yan, Z. Deng, X. Tang, G. Cai, X. Wang, Polydopamine-assisted in situ growth of three-dimensional ZnO/Ag nanocomposites on PET films for SERS and catalytic properties, *Journal of Molecular Liquids*. 338 (2021) 116639.

[19] E.C. Le Ru, E. Blackie, M. Meyer, P.G. Etchegoin, Surface enhanced Raman scattering enhancement factors: a comprehensive study, *The Journal of Physical Chemistry C*. 111 (2007) 13794–13803.

[20] Y.C. Kao, X. Han, Y.H. Lee, H.K. Lee, G.C. Phan-Quang, C.L. Lay, H.Y.F. Sim, V.J.X. Phua, L.S. Ng, C.W. Ku, T.C. Tan, I.Y. Phang, N.S. Tan, X.Y. Ling, Multiplex Surface-Enhanced Raman Scattering Identification and Quantification of Urine Metabolites in Patient Samples within 30 min, *ACS Nano*. 14 (2020) 2542–2552.

Cumhuriyet Sci. J., 45(2) (2024) 360-365
DOI: https://doi.org/10.17776/csj.1462654

Cumhuriyet Science Journal

| csj.cumhuriyet.edu.tr | Founded: 2002 ISSN: 2587-2680 e-ISSN: 2587-246X Publisher: Sivas Cumhuriyet University

Multispectral Imaging and Single-Cell Analysis with Genetically Encoded Biosensors Unveil Complex Interactions between Extracellular ATP and Intracellular Calcium

Emrah Eroglu [1,2,a,*]

[1] *Molecular Biology, Genetics and Bioengineering Program, Faculty of Engineering and Natural Sciences, Sabanci University, Istanbul, Türkiye.*
[2] *Research Institute for Health Sciences and Technologies (SABITA), Istanbul Medipol University, Istanbul, Türkiye.*
**Corresponding author*

Research Article

History
Received: 01/04/2024
Accepted: 07/06/2024

ABSTRACT

The dynamic interplay between extracellular ATP (eATP) and intracellular calcium ($[Ca^{2+}]_i$) serves as a pivotal signaling axis in cellular physiology, influencing a myriad of cellular processes. Traditionally recognized as an energy currency within the cell, ATP has emerged as a multifunctional signaling molecule that orchestrates diverse cellular responses through activation of purinergic receptors. The complex link between ATP signaling and calcium dynamics plays a central role in cellular communication and homeostasis. Advancements in imaging technologies such as development of genetically encoded biosensors have revolutionized the study of cellular signaling dynamics, enabling visualization of the spatiotemporal aspects of eATP and $[Ca^{2+}]_i$ in real-time. The convergence of eATP signaling and $[Ca^{2+}]_i$ dynamics serves as a central hub in cellular communication. In this study, utilizing bicistronic construct biosensors for multispectral imaging of $[Ca^{2+}]_i$ responses to eATP, we show that distinct concentrations of eATP administration reveal complex intracellular $[Ca^{2+}]_i$ responses, potentially attributed to receptor desensitization. Single-cell co-imaging uncovers $[Ca^{2+}]_i$ heterogeneity, emphasizing the significance of individual cell dynamics in eATP-induced calcium signaling. Therefore, this study sheds light on the intricacies of eATP-induced calcium signaling, providing insights valuable for basic research and therapeutic applications.

Keywords: Calcium signaling, ATP signaling, Single cell imaging, Genetically encoded eiosensors, Multispectral imaging.

[a] *Emrah.eroglu@medipol.edu.tr* *https://orcid.org/0000-0002-9373-0808*

Introduction

The dynamic interplay between extracellular ATP (eATP) and intracellular calcium ($[Ca^{2+}]_i$) serves as a pivotal signaling axis in cellular physiology, influencing a myriad of cellular processes ranging from cell proliferation to synaptic transmission [1,2]. ATP, traditionally recognized as an energy currency [3,4] within the cell, has emerged as a multifunctional signaling molecule that orchestrates diverse cellular responses through activation of purinergic receptors [5,6]. Notably, the intricate link between ATP signaling and calcium dynamics plays a central role in cellular communication and homeostasis [7,8].

Adenosine triphosphate (ATP), primarily known for its role in cellular energy transfer, has garnered increasing attention as an extracellular signaling molecule [9]. The recognition of purinergic receptors, encompassing P1 adenosine and P2 purinoceptor families, has established ATP as a key mediator in intercellular communication [10]. Among the P2 purinoceptor family, P2X receptors directly respond to eATP, leading to the influx of calcium ions and subsequent activation of downstream signaling cascades [11]. The coupling of eATP to intracellular calcium signaling is integral for the regulation of cellular responses [12,13], making it a focal point for investigations aimed at unraveling the complexities of cellular communication.

Advancements in imaging technologies have revolutionized the study of cellular signaling dynamics [14], enabling researchers to visualize the spatiotemporal aspects of eATP and $[Ca^{2+}]_i$ in real-time [15-17]. Chemical and genetically encoded biosensors have played pivotal roles in this endeavor [18]. Traditional chemical indicators, such as Fluo-4 and Fura-2, offer high sensitivity but are limited by issues like photobleaching and potential cytotoxicity [19]. Genetically encoded biosensors, on the other hand, provide a versatile and targeted approach by fusing fluorescent proteins with proteins sensitive to specific signaling molecules [18].

This study, employed a bicistronic construct expressing $GRAB_{ATP1.0}$ and RCaMP, genetically encoded biosensors for eATP and $[Ca^{2+}]_i$, respectively [20]. This approach not only allows for the simultaneous monitoring of extracellular ATP and intracellular calcium but also offers the advantage of improved spatial resolution and reduced perturbation compared to traditional chemical indicators. The specific binding and fluorescence changes associated with these genetically encoded biosensors offer a direct and reliable readout of eATP and $[Ca^{2+}]_i$, facilitating a more comprehensive understanding of the signaling events.

While genetically encoded biosensors have significantly advanced live-cell imaging, the importance of multiparametric imaging cannot be overstated [21]. Multispectral imaging involves the simultaneous

acquisition of multiple wavelength bands, allowing for the discrimination of distinct fluorophores [7,22,23]. This study utilizes the $GRAB_{ATP1.0}$ [15] and RCaMP [22] permitting multispectral imaging to capture their unique spectral properties using conventional widefield microscopes, a common challenge in conventional imaging techniques. This approach provides a nuanced perspective, enabling the separation of signals from different probes, thereby refining the accuracy of data interpretation. In the context of eATP and $[Ca^{2+}]_i$ imaging, multispectral analysis would not only improve the reliability of signal detection but also facilitate the identification of potential crosstalk or interference between the two signaling pathways. Thus, the incorporation of multispectral imaging with genetically encoded biosensors is instrumental in advancing the precision and discriminatory power of live-cell imaging studies.

The cellular landscape is inherently heterogeneous, with individual cells within a population often exhibiting diverse characteristics [24]. Single cell heterogeneity is particularly evident in signaling pathways, where cellular responses to external stimuli can vary significantly even within clonal cell lines [25]. Traditional population-level measurements may obscure critical insights into the underlying dynamics of cellular signaling [26]. Single cell imaging techniques provide a powerful tool to unveil this heterogeneity and offer a more granular understanding of cellular responses [27]. In the context of our study, single cell imaging allowed us to discern variable $[Ca^{2+}]_i$ responses despite consistent eATP signals. This discovery underscores the importance of investigating signaling dynamics at the single-cell level. By unraveling the heterogeneity within a cell population, we gain a more comprehensive understanding of the range of responses that cells may exhibit. Single cell imaging enables the identification of subpopulations with distinct signaling profiles, revealing hidden complexities that would otherwise be overlooked in bulk measurements.

Understanding single cell heterogeneity in signaling has profound implications for both basic research and therapeutic applications [28]. It provides insights into the inherent diversity of cellular responses, offering a more accurate representation of the cellular milieu. This knowledge is crucial for designing targeted interventions, as therapies that account for and address the spectrum of cellular responses within a population are likely to be more effective. Consequently, the importance of single cell imaging in elucidating the intricacies of cellular signaling cannot be overstated. It serves as a key tool for refining our understanding of cellular behavior, fostering advancements in both basic science and clinical applications.

The convergence of eATP signaling and $[Ca^{2+}]_i$ dynamics serves as a central hub in cellular communication. Leveraging genetically encoded biosensors, particularly through multispectral imaging, provides a powerful platform for dissecting the complexities of these interconnected signaling pathways. Furthermore, the exploration of single cell heterogeneity sheds light on the diversity of cellular responses, offering a more nuanced understanding of the intricate signaling networks governing cellular behavior. Our study contributes to this ongoing endeavor by employing cutting-edge techniques to unravel the heterogeneity in eATP-induced calcium signaling, paving the way for enhanced precision and reliability in the study of cellular signaling dynamics.

Materials and Methods

Cell Culture and Transfection

Human embryonic kidney cells (HEK293T) were cultured in a high-glucose medium (4.5 g/L) supplemented with 10% FBS, 100 µg/ml streptomycin, and 100 U/ml penicillin. Cells were maintained in a humidified incubator at 37°C with 5% CO_2. 24 hours prior to transfection, cells were seeded at a density of approximately 3×10^5 cells per well on 30 mm glass coverslips No.1 (Glaswarenfabrik Karl Knecht, Sondheim, Germany). When cells reached a confluency of about 70–80%, transfection with $GRAB_{ATP1.0}$-P2A-RCaMP was carried out using the PolyJet transfection reagent, following the manufacturer's guidelines. All imaging experiments took place 24 hours post-transfection.

Imaging Buffers and Solutions

All chemicals were purchased from NeoFroxx except otherwise stated. One hour before the imaging experiment, the culture medium was substituted with a sterile storage buffer (pH=7.43). This buffer comprised 2 mM $CaCl_2$, 5 mM KCl, 138 mM NaCl, 1 mM $MgCl_2$, 1 mM HEPES (Pan-Biotech, Aidenbach, Germany), 0.44 mM KH_2PO_4, 2.6 mM $NaHCO_3$, 0.34 mM NaH_2PO_4, 10 mM D-Glucose, 0.1% MEM Vitamins (Pan-Biotech, Aidenbach, Germany), 0.2% essential amino acids (Pan-Biotech, Aidenbach, Germany), 100 µg/mL penicillin (Pan-Biotech, Aidenbach, Germany), and 100 U/mL streptomycin (Pan-Biotech, Aidenbach, Germany). Cells were kept in the dark outside the incubator for one hour in the storage buffer before performing the imaging experiments. The physiological imaging buffer composition included 2 mM $CaCl_2$, 5 mM KCl, 138 mM NaCl, 1 mM $MgCl_2$, and 10 mM D-Glucose, pH buffered with 10 mM HEPES (7.43). For experiments with ATP administration, the desired concentrations of ATP were prepared in the abovementioned imaging buffer.

Fluorescence Imaging

Real-time imaging experiments utilizing HEK293T cells expressing $GRAB_{ATP1.0}$-P2A-RCaMP were conducted on a Zeiss Axio Observer.Z1/7 (Carl Zeiss AG, Oberkochen, Germany) equipped with a Colibri 7 LED light source (excitation wavelengths: 423/44 nm, 469/38 nm, 555/30 nm), Plan-Apochromat 20×/0.8 dry objective, Plan-Apochromat 40×/1.4 oil immersion objective, and a monochrome CCD camera Axiocam 503. $GRAB_{ATP1.0}$ signals were obtained using a 495 nm excitation filter, and

emission signals were collected through a bandpass filter (BP 525/50). For RCaMP emissions, filter combinations FT570 (BS) and emission filter 605/70 were employed. The data acquisition process utilized Zen Blue 3.1 Pro software (Carl Zeiss AG, Oberkochen, Germany). The administration and washout of the imaging buffers were facilitated by a custom-made perfusion system and a metal perfusion chamber (NGFI, Graz, Austria).

Statistical Analysis

All data analysis was performed using GraphPad Prism software (GraphPad Software, San Diego, CA, USA). One-way ANOVA (Tukey's multiple comparison test) was performed for statistical comparison of the multiple responses.

Results and Discussion

In this study, our primary objective was to establish a correlation between extracellular ATP levels and intracellular calcium responses within cultured HEK293T cells. To achieve this, we employed a novel bicistronic construct that co-expresses the differentially targeted $GRAB_{ATP1.0}$ for extracellular ATP detection and the intracellularly targeted calcium sensor RCaMP (Figure 1A). The distinct spectral properties of both biosensors enabled accurate detection of their emissions in their respective channels. Successful differential targeting was confirmed, and no discernible bleedthrough was observed, as illustrated in (Figure 1B). Notably, despite being separated by a self-cleavage peptide (P2A), both biosensors exhibited robust expression in the cellular environment.

Subsequently, we assessed the functionality of the biosensors and their responses to extracellular ATP, focusing on the impact on intracellular calcium levels. (Figure 1C) demonstrates that the constitutive addition of varying concentrations of extracellular ATP led to a clear and concentration-dependent activation of $GRAB_{ATP1.0}$, validating the correct function of the extracellular ATP sensor in the green channel. Concurrently, the red-fluorescent protein-based RCaMP exhibited functional responsiveness, demonstrating a robust intracellular calcium response even in the presence of low extracellular ATP concentrations.

This experimental setup, performed in transiently transfected HEK293T cells, effectively showcases the full functionality of both probes and allows for the precise correlation of extracellular ATP and intracellular calcium signals. Utilizing a pump-driven super fusion system, we administered and withdrew different concentrations of ATP, as indicated by lines. Intriguingly, we observed rapid activation of intracellular calcium, characterized by characteristic oscillations during ATP treatment. Noteworthy is the observation that upon withdrawal of the agonist from the imaging medium, extracellular ATP signals declined more slowly compared to the corresponding intracellular calcium signals.

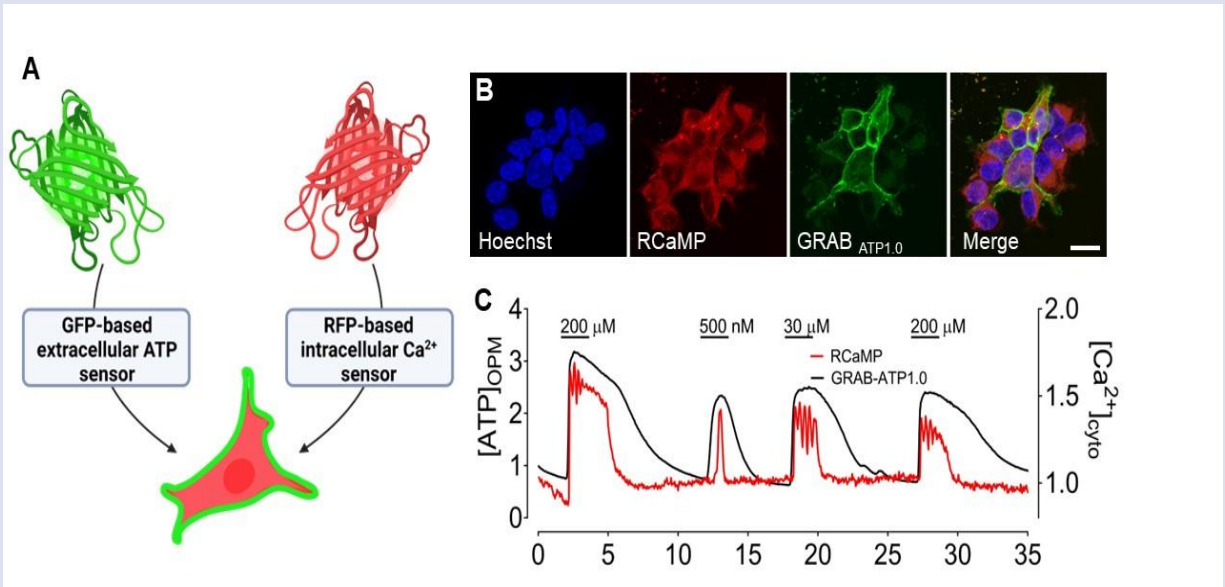

Figure 1. Graphical overview and characterization of $GRAB_{ATP1.0}$-P2A-RCaMP construct. A) Graphic illustrates the localization of GFP-based ATP biosensor ($GRAB_{ATP1.0}$) and RFP-based Ca^{2+} biosensor (RCaMP). B) High resolution confocal images of HEK293T cells expressing $GRAB_{ATP1.0}$-P2A-RCaMP. Left image shows HEK293T cells stained with Hoechst. The second and third image shows the same cells co-expressing RCamP and $GRAB_{ATP1.0}$, respectively. The very right image shows the merged version of the single images. C) Real-time traces of extracellular ATP imaged with $GRAB_{ATP1.0}$ (black curve) and intracellular calcium, imaged with RCaMP (red curve) in response to the indicated concentrations of extracellular ATP using a pump driven super fusion system. Scale bar represents 20 µm.

To further explore the observed phenomena and elucidate the direct relationship between extracellular ATP and intracellular calcium, we refined our perfusion protocols. In this iteration, we administered identical concentrations of extracellular ATP, as illustrated in (Figure 1), but omitted washout steps between the increasing concentrations of ATP. As anticipated, the extracellular ATP biosensor, $GRAB_{ATP1.0}$, exhibited a

pronounced concentration-dependent response in accordance with the increasing levels of ATP administration. Surprisingly, the corresponding intracellular calcium responses displayed non-specific calcium activity.

The observed correlation between extracellular ATP and intracellular calcium responses, as depicted in (Figure 1C), presents an intriguing aspect of cellular signaling dynamics. Notably, this correlation becomes more pronounced when extracellular ATP is subjected to a washout-readdition protocol. A plausible explanation for this phenomenon lies in the concept of receptor desensitization, a complex regulatory mechanism that shapes cellular responses to repeated or sustained ligand exposure [30]. Purinergic receptors, particularly P2 receptors that respond to extracellular ATP, are known to undergo desensitization following prolonged or repetitive stimulation [31]. Desensitization refers to a reduction in receptor responsiveness, often attributed to mechanisms such as receptor internalization, uncoupling from downstream signaling pathways, or alterations in receptor conformation. In the context of our study, repeated exposure to extracellular ATP could induce desensitization of purinergic receptors within the cellular membrane. The washout and subsequent re-addition of ATP in our experimental setup may serve as a resetting mechanism for the desensitized receptors. During the washout phase, any bound ATP molecules are removed, allowing receptors to undergo deactivation and potentially regain sensitivity. Upon re-addition of ATP, receptors that have been reset during the washout phase may exhibit heightened responsiveness to extracellular ATP, leading to the observed correlation with intracellular calcium responses. This phenomenon aligns with the concept of ligand-induced receptor desensitization and resensitization, which has been well-documented in various cellular systems [32]. It reflects the dynamic nature of cellular signaling regulation, where the responsiveness of receptors can be modulated in response to ligand exposure patterns. The washout-readdition protocol in our study provides a controlled experimental context to investigate the temporal aspects of purinergic receptor desensitization and recovery, shedding light on the intricacies of extracellular ATP-mediated signaling events.

(Figure 2) presents three representative multispectral imaging experiments (Figure 2A-C) out of several repeats. In these experiments, while certain cells exhibited minimal and transient intracellular calcium activity, others displayed oscillations irrespective of the extracellular ATP concentrations applied. The statistical analysis of these experiments, as depicted in Figure 2D, revealed a robust and heterogeneous maximum intracellular calcium response. Conversely, the extracellular ATP sensor $GRAB_{ATP1.0}$ exhibited a clear concentration correlation with no observed heterogeneity.

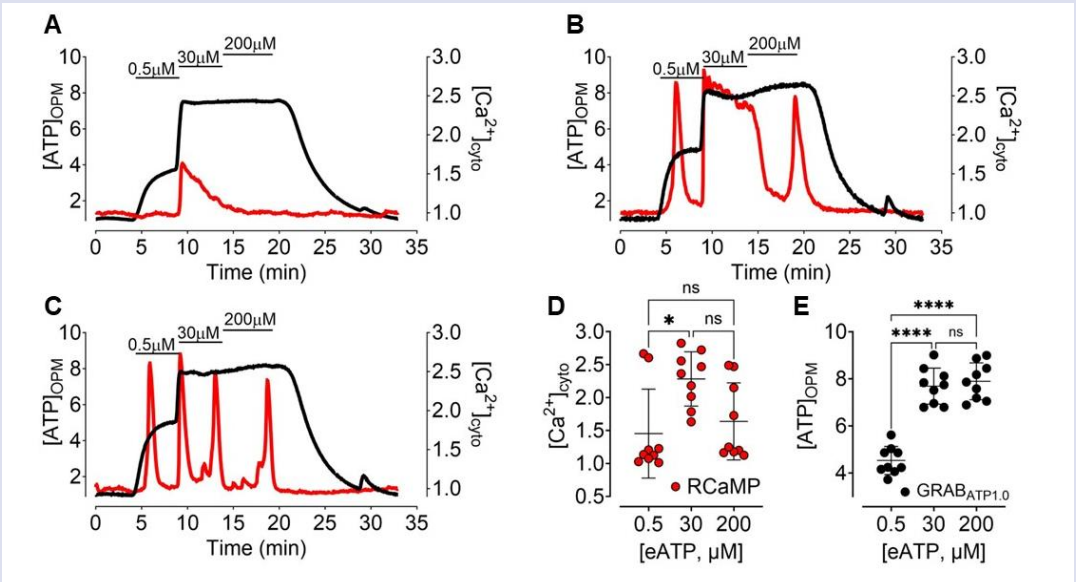

Figure 2. Single cell responses of HEK293T cells to extracellular ATP as indicated in the panels A-C. Extracellular ATP responses detected with $GRAB_{ATP1.0}$ are shown in black curve, left axis; and intracellular calcium responses detected with RCaMP are shown as red curves, right axis. These representative experiments were repeated 9 times. Panel D, shows a scatter dot plot analysis of maximum RCaMP responses (n=9) and panel e shows the statistical analysis of maximum responses of $GRAB_{ATP1.0}$ (n=9) in response to 0,5 µM, 30 µM and 200 µM as indicated in the panels. Error bars show ±SD values..

These findings collectively suggest a significant heterogeneity in intracellular calcium responses within cultured HEK293T cells exposed to identical concentrations of extracellularly applied ATP. The absence of a clear correlation between extracellular ATP and intracellular calcium responses under direct administration suggests a complex and dynamic cellular response. This lack of correlation could be attributed to the rapid and sustained activation of receptors, leading to desensitization and downstream signaling alterations

[30]. The direct administration protocol may induce receptor desensitization, disrupting the usual correlation observed with washout-readdition cycles. Receptor desensitization is a crucial aspect to consider in the interpretation of our results. P2 purinergic receptors, which respond to extracellular ATP, may undergo desensitization upon prolonged or repetitive stimulation. This desensitization could alter intracellular calcium signaling dynamics and contribute to the observed differences in responses between the two experimental setups. This unexpected diversity in the intracellular calcium signaling underscores the complexity of the cellular response to extracellular ATP and prompts further investigation into the underlying mechanisms governing such heterogeneity even in clonal cell lines.

The integration of multispectral imaging techniques has been a key facet of our research endeavors, extending beyond the investigation of extracellular ATP and intracellular calcium dynamics. In previous studies, we applied similar multispectral imaging approaches to correlate intracellular calcium responses with nitric oxide [7] or hydrogen peroxide levels [29]. In a recent investigation, we employed a multiparametric imaging strategy, revealing differential cellular responses at the subcellular level in co-cultured cells [21]. The application of multispectral imaging to simultaneously monitor extracellular ATP and intracellular calcium responses furnishes a significant advantage in our research. This methodological approach not only facilitates the detection of subtle differences in cellular responses but also allows for a nuanced exploration of intricate signaling pathways that may evade detection in conventional single-channel imaging. Our study on the interplay between extracellular ATP and intracellular calcium in HEK293T cells underscores the imperative of employing advanced imaging techniques for a comprehensive understanding of cellular signaling dynamics. Furthermore, our broader research context involving intracellular calcium, nitric oxide, and hydrogen peroxide emphasizes the versatility of multispectral imaging. By expanding our investigative scope, we have successfully unraveled the complex interrelationships governing cellular responses. In a recent multiparametric imaging study, the differential cellular responses observed in co-cultured cells on the subcellular level underscore the power of multispectral imaging in deciphering intricate cellular signaling networks [21].

The application of biosensors in single-cell imaging is paramount in uncovering cellular heterogeneity. Our study emphasizes the significance of biosensors, such as $GRAB_{ATP1.0}$ and RCaMP, in elucidating individual cell responses. Single-cell imaging allows the identification of cell-to-cell variations that would be masked in population-based measurements, providing a more nuanced understanding of cellular signaling dynamics. The detection of heterogeneous intracellular calcium responses underscores the complexity within the cellular population. Understanding this heterogeneity is crucial for several reasons. Firstly, it reflects the diverse nature of cellular responses to extracellular ATP, suggesting the involvement of intricate regulatory mechanisms. Secondly, this information has implications for therapeutic interventions, as targeting specific subpopulations of cells may be necessary for effective treatment strategies.

Conclusion

In conclusion, our study leverages advanced imaging techniques and biosensors to uncover the intricate relationship between extracellular ATP and intracellular calcium in HEK293T cells. The observed heterogeneity and the impact of receptor desensitization underscore the dynamic nature of cellular responses, emphasizing the need for nuanced experimental designs and single-cell imaging approaches in unraveling the complexity of purinergic signaling.

Acknowledgments

This research was supported by funds from the European Molecular Biology Organization EMBO (IG-5322-2023. The author acknowledges Asal Ghaffari Zaki for English language proofreading. Figure 1A was generated with Biorender (License code: ME26EKR3WY).

Conflicts of interest

There are no conflicts of interest in this work.

References

[1] Arcuino G, Lin JHC, Takano T, Liu C, Jiang L, Gao Q, Kang J, Nedergaard M. Intercellular calcium signaling mediated by point-source burst release of ATP, *Proc. Natl. Acad. Sci.*, 99 (15) (2002) 9840–9845.

[2] Cisneros-Mejorado A, Pérez-Samartín A, Gottlieb M, Matute C. ATP signaling in brain: release, excitotoxicity and potential therapeutic targets, *Cell. Mol. Neurobiol.*, 35 (1) (2015) 1–6.

[3] Depaoli MR, Karsten F, Madreiter-Sokolowski CT, Klec C, Gottschalk B, Bischof H, Eroglu E, Waldeck-Weiermair M, Simmen T, Graier WF, Malli R. Real-Time Imaging of Mitochondrial ATP Dynamics Reveals the Metabolic Setting of Single Cells, *Cell Rep.*, 25 (2) (2018) 501-512.

[4] Bonora M, Patergnani S, Rimessi A, De Marchi E, Suski JM, Bononi A, Giorgi C, Marchi S, Missiroli S, Poletti F, Wieckowski MR, Pinton P., ATP synthesis and storage, *Purinergic Signal.*, 8 (3) (2012) 343–357.

[5] Eersapah V, Hugel S, Schlichter R., High-resolution detection of ATP release from single cultured mouse dorsal horn spinal cord glial cells and its modulation by noradrenaline, *Purinergic Signal.*, 15 (3) (2019) 403–420.

[6] Fields RD, Burnstock G., Purinergic signalling in neuron-glia interactions, *Nat. Rev. Neurosci.*, 7 (6) (2006) 423–436.

[7] Eroglu E, Saravi SSS, Sorrentino A, Steinhorn B, Michel T., Discordance between eNOS phosphorylation and activation revealed by multispectral imaging and chemogenetic methods, *Proc. Natl. Acad. Sci. U. S. A.*, 116 (40) (2019) 20210–20217.

[8] Eroglu E, Hallström S, Bischof H, Opelt M, Schmidt K, Mayer B, Waldeck-Weiermair M, Graier WF, Malli R., Real-time visualization of distinct nitric oxide generation of nitric oxide synthase isoforms in single cells, *Nitric Oxide Biol. Chem.*, 70 (2017) 59–67.

[9] Barry VA, Cheek TR., Extracellular ATP triggers two functionally distinct calcium signalling pathways in PC12 cells, *J. Cell Sci.*, 107 (Pt 2) (1994) 451–462.

[10] Burnstock G., Purine and purinergic receptors, *Brain Neurosci. Adv.*, 2 (2018) 2398212818817494.

[11] Molcak H, Jiang K, Campbell CJ, Matsubara JA., Purinergic signaling via P2X receptors and mechanisms of unregulated ATP release in the outer retina and age-related macular degeneration, *Front. Neurosci.*, 17 (2023) 1216489.

[12] Eroglu E, Gottschalk B, Charoensin S, Blass S, Bischof H, Rost R, Madreiter-Sokolowski CT, Pelzmann B, Bernhart E, Sattler W, Hallström S, Malinski T, Waldeck-Weiermair M, Graier WF, Malli R., Development of novel FP-based probes for live-cell imaging of nitric oxide dynamics, *Nat. Commun.*, 7 (1) (2016).

[13] Eroglu E, Rost R, Bischof H, Blass S, Schreilechner A, Gottschalk B, Depaoli MR, Klec C, Charoensin S, Madreiter-Sokolowski CT, Ramadani J, Waldeck-Weiermair M, Graier WF, Malli R., Application of Genetically Encoded Fluorescent Nitric Oxide (NO•) Probes, the geNOps, for Real-time Imaging of NO• Signals in Single Cells, *J. Vis. Exp. JoVE*, (121) (2017) 55486.

[14] Eroglu E, Charoensin S, Bischof H, Ramadani J, Gottschalk B, Depaoli MR, Waldeck-Weiermair M, Graier WF, Malli R., Genetic biosensors for imaging nitric oxide in single cells, *Free Radic. Biol. Med.*, 128 (2018) 50–58.

[15] Wu Z, He K, Chen Y, Li H, Pan S, Li B, Liu T, Xi F, Deng F, Wang H, Du J, Jing M, Li Y., A sensitive GRAB sensor for detecting extracellular ATP in vitro and in vivo, *Neuron*, 110 (5) (2022) 770-782.

[16] Conley JM, Radhakrishnan S, Valentino SA, Tantama M., Imaging extracellular ATP with a genetically-encoded, ratiometric fluorescent sensor, *PLoS ONE*, 12 (11) (2017) e0187481.

[17] Lobas MA, Tao R, Nagai J, Kronschläger MT, Borden PM, Marvin JS, Looger LL, Khakh BS., A genetically encoded single-wavelength sensor for imaging cytosolic and cell surface ATP, *Nat. Commun.*, 10 (1) (2019) 711.

[18] Depaoli MR, Bischof H, Eroglu E, Burgstaller S, Ramadani-Muja J, Rauter T, Schinagl M, Waldeck-Weiermair M, Hay JC, Graier WF, Malli R., Live cell imaging of signaling and metabolic activities, *Pharmacol. Ther.*, 202 (2019) 98–119.

[19] Li ES, Saha MS., Optimizing Calcium Detection Methods in Animal Systems: A Sandbox for Synthetic Biology, *Biomolecules*, 11 (3) (2021) 343.

[20] Ghaffari Zaki A, Yiğit EN, Aydın MŞ, Vatandaslar E, Öztürk G, Eroglu E., Genetically Encoded Biosensors Unveil Neuronal Injury Dynamics via Multichromatic ATP and Calcium Imaging, *ACS Sens.*, 9 (3) (2024) 1261-1271.

[21] Secilmis M, Altun HY, Pilic J, Erdogan YC, Cokluk Z, Ata BN, Sevimli G, Zaki AG, Yigit EN, Öztürk G, Malli R, Eroglu E., A Co-Culture-Based Multiparametric Imaging Technique to Dissect Local H2O2 Signals with Targeted HyPer7, *Biosensors*, 11 (9) (2021) 338.

[22] Akerboom J, Carreras Calderón N, Tian L, Wabnig S, Prigge M, Tolö J, Gordus A, Orger M, Severi K, Macklin J, Patel R, Pulver S, Wardill T, Fischer E, Schüler C, Chen TW, Sarkisyan K, Marvin J, Bargmann C, Kim D, Kügler S, Lagnado L, Hegemann P, Gottschalk A, Schreiter E, Looger L., Genetically encoded calcium indicators for multi-color neural activity imaging and combination with optogenetics, *Front. Mol. Neurosci.*, 6 (2013) Available at: https://www.frontiersin.org/articles/10.3389/fnmol.2013.00002. Retrieved Oct. 23, 2022.

[23] Arai S, Kriszt R, Harada K, Looi LS, Matsuda S, Wongso D, Suo S, Ishiura S, Tseng YH, Raghunath M, Ito T, Tsuboi T, Kitaguchi T., RGB-color intensiometric indicators visualize spatiotemporal dynamics of ATP in single cells, *Angew. Chem. Int. Ed Engl.*, 57 (34) (2018) 10873–10878.

[24] Gupta RK, Kuznicki J., Biological and Medical Importance of Cellular Heterogeneity Deciphered by Single-Cell RNA Sequencing, *Cells*, 9 (8) (2020) 1751.

[25] Hastings JF, Latham SL, Kamili A, Wheatley MS, Han JZR, Wong-Erasmus M, Phimmachanh M, Nobis M, Pantarelli C, Cadell AL, O'Donnell YEI, Leong KH, Lynn S, Geng FS, Cui L, Yan S, Achinger-Kawecka J, Stirzaker C, Norris MD, Haber M, Trahair TN, Speleman F, De Preter K, Cowley MJ, Bogdanovic O, Timpson P, Cox TR, Kolch W, Fletcher JI, Fey D, Croucher DR., Memory of stochastic single-cell apoptotic signaling promotes chemoresistance in neuroblastoma, *Sci. Adv.*, 9 (9) eabp8314.

[26] Handly LN, Yao J, Wollman R., Signal transduction at the single-cell level: Approaches to study the dynamic nature of signaling networks, *J. Mol. Biol.*, 428 (19) (2016) 3669.

[27] Mattiazzi Usaj M, Yeung CHL, Friesen H, Boone C, Andrews BJ., Single-cell image analysis to explore cell-to-cell heterogeneity in isogenic populations, *Cell Syst.*, 12 (6) (2021) 608–621.

[28] Baysoy A, Bai Z, Satija R, Fan R., The technological landscape and applications of single-cell multi-omics, *Nat. Rev. Mol. Cell Biol.*, 24 (10) (2023) 695–713.

[29] Altun HY, Secilmis M, Caglar TA, Vatandaslar E, Öztürk G, Vilain S, Eroglu E., Visualizing H2O2 and NO in endothelial cells: strategies and pitfalls. *bioRxiv*, Available at: https://www.biorxiv.org/content/10.1101/2023.02.15.528776v1. Retrieved Feb. 16, 2023.

[30] Shankaran H, Wiley HS, Resat H., Receptor downregulation and desensitization enhance the information processing ability of signalling receptors, *BMC Syst. Biol.*, 1 (2007) 48.

[31] Rodríguez-Rodríguez R, Yarova P, Winter P, Dora K., Desensitization of endothelial P2Y1 receptors by PKC-dependent mechanisms in pressurized rat small mesenteric arteries, *Br. J. Pharmacol.*, 158 (6) (2009) 1609–1620.

[32] Woolf PJ, Linderman JJ., Untangling Ligand Induced Activation and Desensitization of G-Protein–Coupled Receptors, *Biophys. J.*, 84 (1) (2003) 3–13.

Cumhuriyet Sci. J., 45(2) (2024) 366-378
DOI: https://doi.org/10.17776/csj.1345303

Cumhuriyet Science Journal

| csj.cumhuriyet.edu.tr | Founded: 2002 ISSN: 2587-2680 e-ISSN: 2587-246X Publisher: Sivas Cumhuriyet University

Simulation of Two-Step Block Approach for Solving Oscillatory Differential Equations

Sabo John[1,a] Abdullahi Muhammed Ayinde[2,b], Taiye Oyedepo[3,c*], Adam Ajimoti Ishaq[4,d]

[1] *Department of Mathematics, Adamawa State University, Mubi 650001, Nigeria.*
[2] *University of Abuja, Abuja, Nigeria.*
[3] *Department of Applied Sciences, Federal College of Dental Technology and Therapy, Enugu, Nigeria.*
[4] *Departments of Physical Sciences, Al-Hikmah University, Ilorin, Nigeria.*
**Corresponding author*

Research Article

History
Received: 18/08/2023
Accepted: 03/01/2024

ABSTRACT

This study demonstrates the derivation of a two-step block scheme simulation through a linear block approach. The scheme's fundamental properties were thoroughly analyzed and found to fulfill all necessary conditions. The research focused on examining specific classes of oscillatory differential equations and comparing them to established methods. The findings indicate that the newly proposed methods exhibit superior accuracy and faster convergence compared to the existing methods investigated in this research. Consequently, the results highlight the improved precision and quicker convergence achieved with the new method. All computations were executed using Maple 18 software.

Keywords: Simulation, Linear block approach, Properties of the schemes, Oscillatory differential equation, Accuracy and convergence

[a] sabojohn21@gmail.com https://orcid.org/0000-0002-8402-9219
[b] ayinde.abdullahi@uniabuja.edu.ng https://orcid.org/0000-0002-2563-0952
[c] oyedepotaiye12@gmail.com https://orcid.org/0000-0001-9063-8806
[d] aaishaq@alhikmah.edu.ng https://orcid.org/0000-0002-8931-5708

Introduction

The use of mathematics in demonstrating empirical problems in applied science and other areas of study in which noises are introduced into the deterministic models of differential equations [1]. It was found that the deterministic differential equations were ineffective and inadequate to handle differential equations arising from these fields of study with intrinsically complex systems containing millions or billions of interacting particles [2]. The computations of empirical problems will be used for sampling the first order initial value problem given as:

$$\gamma' = f(u,\gamma), u(0) = 0 \tag{1}$$

Most of the empirical problems and studies mentioned above are coded in numbers and mathematical symbols to form an equation in order to have meaning, construction, and application [3]. One of such equations is known as a differential equation of the form (1) [3]. The differential equation (1) may evolve from empirical problems that involve the rate of change of a given variable in the structure (system) with respect to another. These equations came to prominence in the late 17th century with the independent invention of infinitesimal calculus by an English mathematician, Isaac Newton (1642-1727), and a German mathematician, Gottfried Wilhelm Leibniz (1646-1716).

The computational solution of an empirical problem modeled in (1) has great significance to researchers. A lot has been considered in finding analytic solutions to (1). Among others, [4, 5, 6, 7, 8] developed block methods for solving (1). The study of the Obrechkoff method for solving (1) is considered [9, 10]. The collocation method was employed by [11, 12,13, 14, 15, 16] to investigate the resolution of Volterra-Fredholm integro-differential equations and Volterra-Fredholm fractional order integro-differential equations.

Also, [17, 18, 19,20, 21,22,23,24,25] adopt some methods to solve (1). However, it was noticed that many of the problems leading to this type of equation, especially when they are non-linear, could not be easily solved analytically to get the exact solution. As a result, various numerical methods for solving the equations have been developed in order to obtain an approximate solution to (1) [26].

Mathematical Formulation of the Method

This section shows the formulation of the method. The method is derived using the linear block approach [27].

The linear block approach is of the form

$$y_{n+\xi} = \sum_{i=0}^{2} \frac{(\xi h)^i}{i!} y_n^{(i)} + \sum_{i=0}^{4} \left(\phi_{i\xi} f_{n+i} \right), \quad \xi = 0, m, n, 1, a, b, 2 \tag{2}$$

Differentiating Eq. (2) gives

$$y_{n+\xi}^{(a)} = \sum_{i=0}^{1-a} \frac{(\xi h)^i}{i!} y_n^{(i+a)} + \sum_{i=0}^{4} \kappa_{\xi i a} f_{n+i}, a = 1_{(0,m,n,1,a,b,2)} \tag{3}$$

$\phi_{\xi i} = A^{-1}P$ and $\kappa_{\xi i a} = A^{-1}Q$ where

$$A=\begin{pmatrix}1 & \frac{1}{(m)^1} & \frac{1}{(n)^1} & \frac{1}{(1)^1} & \frac{1}{(a)^1} & \frac{1}{(b)^1} & \frac{1}{(2)^1}\\ 0 & \frac{(m)^2}{1!} & \frac{(n)^2}{1!} & \frac{(1)^2}{1!} & \frac{(a)^2}{1!} & \frac{(b)^2}{1!} & \frac{(2)^2}{1!}\\ 0 & \frac{(m)^3}{2!} & \frac{(n)^3}{2!} & \frac{(1)^3}{2!} & \frac{(a)^3}{2!} & \frac{(b)^3}{2!} & \frac{(2)^3}{2!}\\ 0 & \frac{(m)^4}{3!} & \frac{(n)^4}{3!} & \frac{(1)^4}{3!} & \frac{(a)^4}{3!} & \frac{(b)^4}{3!} & \frac{(2)^4}{3!}\\ 0 & \frac{(m)^5}{4!} & \frac{(n)^5}{4!} & \frac{(1)^5}{4!} & \frac{(a)^5}{4!} & \frac{(b)^5}{4!} & \frac{(2)^5}{4!}\\ 0 & \frac{(m)^6}{5!} & \frac{(n)^6}{5!} & \frac{(1)^6}{5!} & \frac{(a)^6}{5!} & \frac{(b)^6}{5!} & \frac{(2)^6}{5!}\\ 0 & \frac{(m)^7}{6!} & \frac{(n)^7}{6!} & \frac{(1)^7}{6!} & \frac{(a)^7}{6!} & \frac{(b)^7}{6!} & \frac{(2)^7}{6!}\end{pmatrix},\ P=\begin{pmatrix}\frac{(\xi h)^1}{1!}\\ \frac{(\xi h)^2}{2!}\\ \frac{(\xi h)^3}{3!}\\ \frac{(\xi h)^4}{4!}\\ \frac{(\xi h)^5}{5!}\\ \frac{(\xi h)^6}{6!}\\ \frac{(\xi h)^7}{7!}\end{pmatrix},\ Q=\begin{pmatrix}\frac{(\xi h)^{1-a}}{(1-a)!}\\ \frac{(\xi h)^{1-a}}{(1-a)!}\\ \frac{(\xi h)^{1-a}}{(1-a)!}\\ \frac{(\xi h)^{6-1}}{(1-a)!}\\ \frac{(\xi h)^{1-a}}{(1-a)!}\\ \frac{(\xi h)^{1-a}}{(1-a)!}\\ \frac{(\xi h)^{1-a}}{(1-a)!}\end{pmatrix} \tag{4}$$

Eq. (2) and Eq. (3) are solved step by step using linear block approach through

$$\vartheta_\xi,\ \xi=0,\ m,\ n,\ 1,\ a,\ b,\ 2$$

The polynomial $x=x_s+th$, is used in Eq. (3) to yield the block hybrid method of the form:

$$q(x_s th)=\alpha_m y_{s+m}$$
$$h\left(\beta_0 f_s+\beta_m f_{s+m}+\beta_n f_{s+n}+\beta_1 f_{s+1}+\beta_a f_{s+a}+\beta_b f_{s+b}+\beta_2 f_{s+2}\right) \tag{5}$$

Where

$$\alpha_0=1$$

$$\beta_0=\frac{\begin{pmatrix}168\xi^4-210\xi^5+60\xi^6-210a\xi^3+252a\xi^4-70a\xi^5-210b\xi^3+1252b\xi^4-70b\xi^5-210m\xi^3\\ +252m\xi^4-70m\xi^5-210n\xi^3+252n\xi^4-70n\xi^5+280ab\xi^2-315ab\xi^3+84ab\xi^4+\\ 280am\xi^2-315\xi^3+84am\xi^4+280an\xi^2+280bm\xi^2-315an\xi^2-315bm\xi^3+84an\xi^4+\\ 84bm\xi^4+280bn\xi^2-315bn\xi^3+84bn\xi^4+280mn\xi^2-315mn\xi^3+84bn\xi^4+280mn\xi^2\\ -315mn\xi^3+84mn\xi^4-420abm\xi-420abn\xi-420amn\xi-420bmn\xi+420abm\xi^2-\\ 105abm\xi^3+420abn\xi^2-105abn\xi^3+420amn\xi^2-105amn\xi^3+420bmn\xi^2-105mn\xi^3\\ +840abmn-630abmn\xi+140abmn\xi^2\end{pmatrix}}{840abmn}$$

$$\beta_m=-\frac{\xi^2\begin{pmatrix}-168\xi^3-210\xi^4+60\xi^5-210a\xi^2+252a\xi^3-70a\xi^4+210b\xi^2-252b\xi^3+70b\xi^4+210n\xi^2\\ -252n\xi^3+70n\xi^4-280ab\xi-280an\xi-280bn\xi+315ab\xi^2-84ab\xi^3+315an\xi^2-\\ 84an\xi^3+315bn\xi^2+84bn\xi^3+84bn\xi^3+420abn-420abn\xi+105abn\xi^2\end{pmatrix}}{420m(m-1)(m-2)(m-n)(b-m)(a-m)}$$

$$\beta_n=\frac{\xi^2\begin{pmatrix}-168\xi^3+210\xi^4-60\xi^5+210a\xi^2-252a\xi^3+70a\xi^4-210b\xi^2-252b\xi^3+70b\xi^4+210m\xi^2\\ -252m\xi^3+70m\xi^4-280ab\xi-280an\xi-280bm\xi+315ab\xi^2-84ab\xi^3+315an\xi^2-\\ 84am\xi^3+315bm\xi^2+84bm\xi^3+84bm\xi^3+420abm-420abm\xi+105abm\xi^2\end{pmatrix}}{420n(n-1)(n-2)(m-n)(b-n)(a-n)}$$

$$\beta_1=-\frac{\xi^2\begin{pmatrix}-140\xi^4+60\xi^5+168\xi^3-70a\xi^4+168b\xi^3-70b\xi^4+168m\xi^3-70m\xi^4+168n\xi^3-70n\xi^4\\ -210ab\xi^2+84ab\xi^3-210am\xi^2+84am\xi^3-210an\xi^2-210bm\xi^2+84an\xi^3+84bm\xi^3-\\ 210bn\xi^2+84bn\xi^3-210mn\xi^2+84mn\xi^3+280abm\xi+280abn\xi+280amn\xi+280bmn\xi\\ -105abm\xi^2-105abn\xi^2-105amn\xi^2-105bmn\xi^2-420abmn+140abmn\xi\end{pmatrix}}{420(n-1)(m-1)(b-1)(a-1)}$$

$$\beta_a = -\frac{\xi^2\begin{pmatrix}-168\xi^3+210\xi^4-60\xi^5+210b\xi^2-252b\xi^3+70b\xi^4-210m\xi^2-252m\xi^3+70m\xi^4+210n\xi^2\\-252n\xi^3+70n\xi^4-280bm\xi-280bn\xi-280mn\xi+315bm\xi^2-84bm\xi^3+315bn\xi^2-\\84bn\xi^3+315bmn\xi^2+84mn\xi^3+420bmn-420bm\xi+105bmn\xi^2\end{pmatrix}}{420a(a-1)(a-2)(a-n)(a-n)(a-b)}$$

$$\beta_a = -\frac{\xi^2\begin{pmatrix}-168\xi^3+210\xi^4-60\xi^5+210a\xi^2-252a\xi^3+70a\xi^4-210m\xi^2-252m\xi^3+70m\xi^4+210n\xi^2\\-252n\xi^3+70n\xi^4-280bm\xi-280bn\xi-280mn\xi+315am\xi^2-84am\xi^3+315an\xi^2-\\84an\xi^3+315amn\xi^2-84mn\xi^3+420amn-420am\xi+105amn\xi^2\end{pmatrix}}{420b(b-1)(b-2)(b-n)(b-n)(a-b)}$$

$$\beta_1 = \frac{\xi^2\begin{pmatrix}-70\xi^4+60\xi^5+84a\xi^3-70a\xi^4+84b\xi^3-70b\xi^4+84m\xi^3-70m\xi^4+84n\xi^3-70n\xi^4\\-105ab\xi^2+84ab\xi^3-105am\xi^2+84am\xi^3+140abn\xi+140abn\xi+140amn\xi-105abn\xi^2-\\105amn\xi^2-105bmn\xi^2-210abmn+140bmn\xi\end{pmatrix}}{840(n-2)(m-2)(b-2)(a-2)}$$

To get the unknown values of Eq.(3), we simplify $\kappa_{\xi ia} = A^{-1}Q$ to obtain

$$\left.\begin{aligned}
y_{s+m} &= y_s + h\left(\kappa_{11} f_s + \kappa_{12} f_{s+m} + \kappa_{13} f_{s+n} + \kappa_{14} f_{s+1} + \kappa_{15} f_{s+a} + \kappa_{16} f_{s+b} + \kappa_{17} f_{s+2}\right)\\
y_{s+n} &= y_s + h\left(\kappa_{21} f_s + \kappa_{22} f_{s+m} + \kappa_{23} f_{s+n} + \kappa_{24} f_{s+1} + \kappa_{25} f_{s+a} + \kappa_{26} f_{s+b} + \kappa_{27} f_{s+2}\right)\\
y_{s+1} &= y_s + h\left(\kappa_{31} f_s + \kappa_{32} f_{s+m} + \kappa_{33} f_{s+n} + \kappa_{34} f_{s+1} + \kappa_{35} f_{s+a} + \kappa_{36} f_{s+b} + \kappa_{37} f_{s+2}\right)\\
y_{s+a} &= y_s + h\left(\kappa_{41} f_s + \kappa_{42} f_{s+m} + \kappa_{43} f_{s+n} + \kappa_{44} f_{s+1} + \kappa_{45} f_{s+a} + \kappa_{46} f_{s+b} + \kappa_{47} f_{s+2}\right)\\
y_{s+b} &= y_s + h\left(\kappa_{51} f_s + \kappa_{52} f_{s+m} + \kappa_{53} f_{s+n} + \kappa_{54} f_{s+1} + \kappa_{55} f_{s+a} + \kappa_{56} f_{s+b} + \kappa_{57} f_{s+2}\right)\\
y_{s+2} &= y_s + h\left(\kappa_{61} f_s + \kappa_{62} f_{s+m} + \kappa_{63} f_{s+n} + \kappa_{64} f_{s+1} + \kappa_{65} f_{s+a} + \kappa_{66} f_{s+b} + \kappa_{67} f_{s+2}\right)
\end{aligned}\right\} \quad (6)$$

(6)

$$y_{s+m}\begin{pmatrix}\kappa_{11}\\\kappa_{12}\\\kappa_{13}\\\kappa_{14}\\\kappa_{15}\\\kappa_{16}\\\kappa_{17}\end{pmatrix} = \begin{pmatrix}\frac{19087}{181440}\\\frac{2713}{7560}\\-\frac{15487}{60480}\\\frac{586}{2835}\\-\frac{6737}{60480}\\\frac{263}{7560}\\-\frac{863}{181440}\end{pmatrix}, y_{s+n}\begin{pmatrix}\kappa_{21}\\\kappa_{22}\\\kappa_{23}\\\kappa_{24}\\\kappa_{25}\\\kappa_{26}\\\kappa_{27}\end{pmatrix} = \begin{pmatrix}\frac{1139}{11340}\\\frac{94}{189}\\\frac{11}{3780}\\\frac{332}{2835}\\-\frac{269}{3780}\\\frac{22}{945}\\-\frac{37}{11340}\end{pmatrix}, y_{s+1}\begin{pmatrix}\kappa_{31}\\\kappa_{32}\\\kappa_{33}\\\kappa_{34}\\\kappa_{35}\\\kappa_{36}\\\kappa_{37}\end{pmatrix} = \begin{pmatrix}\frac{137}{1344}\\\frac{27}{56}\\\frac{387}{2240}\\\frac{34}{105}\\-\frac{243}{2240}\\\frac{9}{280}\\-\frac{29}{6720}\end{pmatrix},$$

$$y_{s+a}\begin{pmatrix}\kappa_{41}\\\kappa_{42}\\\kappa_{43}\\\kappa_{44}\\\kappa_{45}\\\kappa_{46}\\\kappa_{47}\end{pmatrix} = \begin{pmatrix}\frac{286}{2835}\\\frac{464}{945}\\\frac{128}{945}\\\frac{1504}{2835}\\\frac{58}{945}\\\frac{16}{945}\\-\frac{8}{2835}\end{pmatrix}, y_{s+b}\begin{pmatrix}\kappa_{51}\\\kappa_{52}\\\kappa_{53}\\\kappa_{54}\\\kappa_{55}\\\kappa_{56}\\\kappa_{57}\end{pmatrix} = \begin{pmatrix}\frac{3715}{36288}\\\frac{275}{1512}\\\frac{2125}{12096}\\\frac{250}{567}\\\frac{3875}{12096}\\\frac{235}{1512}\\\frac{275}{36288}\end{pmatrix}, y_{s+2}\begin{pmatrix}\kappa_{61}\\\kappa_{62}\\\kappa_{63}\\\kappa_{64}\\\kappa_{65}\\\kappa_{56}\\\kappa_{67}\end{pmatrix} = \begin{pmatrix}\frac{41}{420}\\\frac{18}{35}\\\frac{9}{140}\\\frac{68}{105}\\\frac{9}{140}\\\frac{18}{35}\\\frac{41}{420}\end{pmatrix}$$

Basic Properties of the Block Method

Order and Error Constant

This subsection establishes the linear operator $\ell[y(x_i);h]$ associated with the newly derived method.

Proposition 1

The local truncation error of the newly derived scheme is $C_{07}h^{07}y^{07}(x_n)+0(h^{08})$.

Proof

The linear difference operators associated with the newly derived method is given as:

$$\left.\begin{aligned}
\ell\left[y\left(x_\eta\right);h\right] &= y\left(x_\eta+mh\right)-\left(\alpha_m\left(x_\eta+mh\right)+h\sum_{j=0}^{k}\left(\beta_j\left(x\right)f_{n+j}+\beta_k\left(x\right)f_{n+k}\right)\right), k=0,\, m,\, n,1,\, a,\, b,\, 2\\
\ell\left[y\left(x_\eta\right);h\right] &= y\left(x_\eta+nh\right)-\left(\alpha_m\left(x_\eta+mh\right)+h\sum_{j=0}^{k}\left(\beta_j\left(x\right)f_{n+j}+\beta_k\left(x\right)f_{n+k}\right)\right), k=0,\, m,\, n,1,\, a,\, b,\, 2\\
\ell\left[y\left(x_\eta\right);h\right] &= y\left(x_\eta+h\right)-\left(\alpha_m\left(x_\eta+mh\right)+h\sum_{j=0}^{k}\left(\beta_j\left(x\right)f_{n+j}+\beta_k\left(x\right)f_{n+k}\right)\right), k=0,\, m,\, n,1,\, a,\, b,\, 2\\
\ell\left[y\left(x_\eta\right);h\right] &= y\left(x_\eta+ah\right)-\left(\alpha_m\left(x_\eta+mh\right)+h\sum_{j=0}^{k}\left(\beta_j\left(x\right)f_{n+j}+\beta_k\left(x\right)f_{n+k}\right)\right), k=0,\, m,\, n,1,\, a,\, b,\, 2\\
\ell\left[y\left(x_\eta\right);h\right] &= y\left(x_\eta+bh\right)-\left(\alpha_m\left(x_\eta+mh\right)+h\sum_{j=0}^{k}\left(\beta_j\left(x\right)f_{n+j}+\beta_k\left(x\right)f_{n+k}\right)\right), k=0,\, m,\, n,1,\, a,\, b,\, 2\\
\ell\left[y\left(x_\eta\right);h\right] &= y\left(x_\eta+2h\right)-\left(\alpha_m\left(x_\eta+mh\right)+h\sum_{j=0}^{k}\left(\beta_j\left(x\right)f_{n+j}+\beta_k\left(x\right)f_{n+k}\right)\right), k=0,\, m,\, n,1,\, a,\, b,\, 2
\end{aligned}\right\} \quad (7)$$

If $y(x)$ is sufficiently differentiable, we can use the Taylor series to expand Eq. (7) in the power of *h*. It is critical to emphasize that the first non-zero term in each formula in Equation (7) is $C_{07}h^{07}y^{07}\left(x_n\right)+0\left(h^{08}\right)$

Definition 1. [28]

A linear multistep method is of order p if it satisfies the condition

$$c_0=c_1=c_2=c_3=\cdots=c_p=c_{p+1}=0,\, c_{p+2}\neq 0,$$

$$\left.\begin{aligned}
c_0 &= \sum_{j=0}^{k}\alpha_j\\
c_1 &= \sum_{j=0}^{k}\left(j\alpha_j-\beta_j\right)\\
&\cdot\\
&\cdot\\
&\cdot\\
c_p &= \sum_{j=0}^{k}\left[\frac{1}{p!}j^p\alpha_j-\frac{1}{(p-1)!}\left(j^{p-1}\beta_j\right)\right],\ p=2,\,3,\,\cdots,\,q+1
\end{aligned}\right\} \quad (8)$$

$$c_0=c_1=c_2=c_3=\cdots=c_p=c_{p+1}=0,\, c_{p+2}\neq 0, \quad \text{where} \quad (8)$$

The parameter $c_{p+2}\neq 0$ is referred to as the error constant with the local truncation error defined as $x_{n+k}=c_{p+2}h^{p+2}y^{(p+2)}\left(x_n\right)+c_{p+3}h^{p+3}y^{(p+3)}\left(x_n\right)+c_{p+4}h^{p+4}y^{(p+4)}\left(x_n\right)+0\left(h^{p+5}\right)$

$$\begin{bmatrix}
\sum_{j=0}^{\infty}\frac{\left(\frac{1}{3}\right)^j}{j!}-y_n-\sum_{j=0}^{\infty}\frac{h^{j+1}}{j!}y_n^{j+1}\left[\frac{2713}{7560}\left(\frac{1}{3}\right)-\frac{15487}{60480}\left(\frac{2}{3}\right)-\frac{586}{2835}(1)-\frac{6737}{60480}\left(\frac{4}{3}\right)+\frac{263}{7560}\left(\frac{5}{3}\right)-\frac{863}{181440}(2)\right]\\
\sum_{j=0}^{\infty}\frac{\left(\frac{2}{3}\right)^j}{j!}-y_n-\sum_{j=0}^{\infty}\frac{h^{j+1}}{j!}y_n^{j+1}\left[\frac{94}{189}\left(\frac{1}{3}\right)-\frac{11}{3780}\left(\frac{2}{3}\right)-\frac{332}{2835}(1)-\frac{269}{3780}\left(\frac{4}{3}\right)+\frac{22}{945}\left(\frac{5}{3}\right)-\frac{37}{11340}(2)\right]\\
\sum_{j=0}^{\infty}\frac{(1)^j}{j!}-y_n-\sum_{j=0}^{\infty}\frac{h^{j+1}}{j!}y_n^{j+1}\left[\frac{27}{56}\left(\frac{1}{3}\right)+\frac{387}{2240}\left(\frac{2}{3}\right)+\frac{34}{105}(1)-\frac{243}{2240}\left(\frac{4}{3}\right)+\frac{9}{280}\left(\frac{5}{3}\right)-\frac{29}{6720}(2)\right]\\
\sum_{j=0}^{\infty}\frac{\left(\frac{4}{3}\right)^j}{j!}-y_n-\sum_{j=0}^{\infty}\frac{h^{j+1}}{j!}y_n^{j+1}\left[\frac{464}{945}\left(\frac{1}{3}\right)+\frac{128}{945}\left(\frac{2}{3}\right)+\frac{1504}{2835}(1)-\frac{58}{945}\left(\frac{4}{3}\right)+\frac{16}{945}\left(\frac{5}{3}\right)-\frac{8}{2835}(2)\right]\\
\sum_{j=0}^{\infty}\frac{\left(\frac{5}{3}\right)^j}{j!}-y_n-\sum_{j=0}^{\infty}\frac{h^{j+1}}{j!}y_n^{j+1}\left[\frac{275}{1512}\left(\frac{1}{3}\right)+\frac{2125}{12096}\left(\frac{2}{3}\right)+\frac{250}{567}(1)-\frac{3875}{12096}\left(\frac{4}{3}\right)+\frac{235}{1512}\left(\frac{5}{3}\right)-\frac{275}{36288}(2)\right]\\
\sum_{j=0}^{\infty}\frac{(2)^j}{j!}-y_n-\sum_{j=0}^{\infty}\frac{h^{j+1}}{j!}y_n^{j+1}\left[\frac{18}{35}\left(\frac{1}{3}\right)+\frac{9}{140}\left(\frac{2}{3}\right)+\frac{68}{105}(1)-\frac{9}{140}\left(\frac{4}{3}\right)+\frac{18}{35}\left(\frac{5}{3}\right)-\frac{41}{420}(2)\right]
\end{bmatrix}$$

Corollary 1 [28].

The newly derived scheme's local truncation error is given by.

$$\left.\begin{array}{l}
\left(1.7326\times10^{-06}\right)C_{07}h^{07}y^{07}\left(x_\eta\right)+0\left(h^{08}\right)\\
\left(1.2903\times10^{-06}\right)C_{07}h^{07}y^{07}\left(x_\eta\right)+0\left(h^{08}\right)\\
\left(1.5310\times10^{-06}\right)C_{07}h^{07}y^{07}\left(x_\eta\right)+0\left(h^{08}\right)\\
\left(1.2903\times10^{-06}\right)C_{07}h^{07}y^{07}\left(x_\eta\right)+0\left(h^{08}\right)\\
\left(1.7326\times10^{-06}\right)C_{07}h^{07}y^{07}\left(x_\eta\right)+0\left(h^{08}\right)\\
\left(1.2661\times10^{-06}\right)C_{07}h^{07}y^{07}\left(x_\eta\right)+0\left(h^{08}\right)
\end{array}\right\} \quad (9)$$

Therefore, the newly derived scheme is of uniform order seven as well as error constant is given by

$$C_9=\begin{pmatrix}
1.7326\times10^{-06}\\
1.2903\times10^{-06}\\
1.5310\times10^{-06}\\
1.2903\times10^{-06}\\
1.7326\times10^{-06}\\
1.2661\times10^{-06}
\end{pmatrix}$$

Consistent

Traditionally, the method is consistent if the order of the method is greater than or equal to one.

Definition 2. [5]

By definition, the method is said to be zero stable as $h\to0$ if the roots of the polynomial $\pi(r)=0$ satisfy $\left|\left[\sum A^0R^{k-1}\right]\right|\le1$, and those roots with R = 1 must be simple.

Hence according to [8] it's found as

$$\pi(r)=\left|r\begin{bmatrix}1&0&0&0&0&0\\0&1&0&0&0&0\\0&0&1&0&0&0\\0&0&0&1&0&0\\0&0&0&1&0&0\\0&0&0&0&1&0\\0&0&0&0&0&1\end{bmatrix}-\begin{bmatrix}0&0&0&0&0&1\\0&0&0&0&0&1\\0&0&0&0&0&1\\0&0&0&0&0&1\\0&0&0&0&0&1\\0&0&0&0&0&1\end{bmatrix}\right|=\left|\begin{bmatrix}r&0&0&0&0&-1\\0&r&0&0&0&-1\\0&0&r&0&0&-1\\0&0&0&r&0&-1\\0&0&0&0&r&-1\\0&0&0&0&0&r-1\end{bmatrix}\right|=r^6(r-1)$$

Then, solving for r in $r^6(r-1)$,

Gives $r=0,\,0,0,\,0,\,1$. Therefore, the method is zero stable.

Dahlquist's theorem states that the scheme is convergent, and consistency and zero-stability are analyzed and fulfilled [29].

Convergence

Theorem 1. [29]

Consistency and zero-stability are both required and sufficient conditions for a linear multistep method to be convergent.

Therefore, the newly derived scheme is convergent since it is consistent and zero-stable.

Linear Stability

Definition 3. [5]

The region of absolute stability of a numerical method is the set of complex values λh for which all solutions of the test problem $y'=-\lambda y$ will remain bounded as $n\to\infty$.

The concept of A-stability according to [8] is discussed by applying the test equation $y^{(k)}=\lambda^{(k)}y$ to yield

$$Y_m=\mu(z)Y_{m-1},\ z=\lambda h \tag{10}$$

Where $\mu(z)$ is the amplification matrix of the form

$$\mu(z)=\left(\xi^0-z\eta^{(0)}-z^1\eta^{(0)}\right)^{-1}\left(\xi^1-z\eta^{(1)}-z^1\eta^{(1)}\right) \tag{11}$$

The matrix $\mu(z)$ has Eigen values $(0,\,0,\,\cdots,\,\xi_k)$ where ξ_k is called the stability function.

Thus, the stability function of the method is given by

$$\zeta=-\frac{\begin{pmatrix}367275240\hat{z}^6-10000752628\hat{z}^5+79785191834\hat{z}^4+5060796756302^3\\+1827771257925\hat{z}^2-4328380929600z+4444263936000\end{pmatrix}}{\begin{pmatrix}870912000\hat{z}^6+-12802406400\hat{z}^5+1060770816004^4-5761082880003^3\\+20575296000002^2-4444263936000z+4444263936000\end{pmatrix}}$$

The boundary locus method is used to generate the hybrid method's stability polynomial. The polynomial is defined as

$$\left.\begin{aligned}\bar{h}(w)=&\left(-\frac{1}{5103}w^5+\frac{1}{5103}w^6\right)h^6+\left(-\frac{7}{2430}w^5-\frac{7}{2430}w^6\right)h^5+\left(-\frac{29}{1215}w^5+\frac{29}{1215}w^6\right)h^4\\&+\left(-\frac{7}{54}w^5-\frac{7}{54}w^6\right)h^3+\left(-\frac{25}{54}w^5+\frac{25}{54}w^6\right)h^2+\left(w^5+w^6\right)h+w^5+w^6\end{aligned}\right\} \tag{12}$$

The polynomial is used to plot the region as:

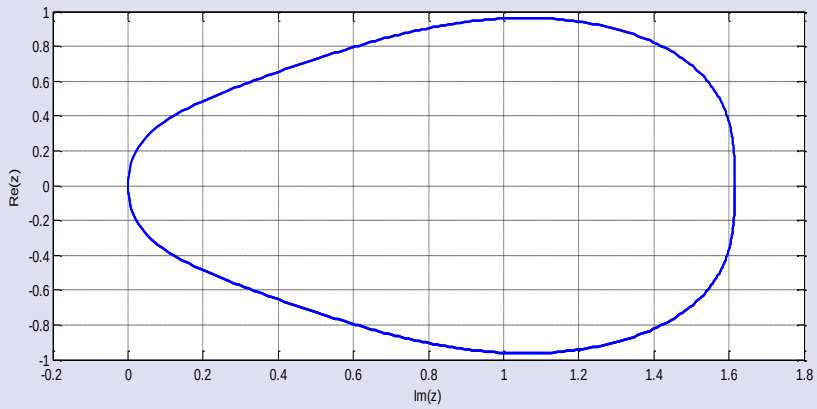

Figure 1. Showing the region of stability of the method.

The region of absolute stability of the method is a region in the complex z plane. The numerical solution of (6) satisfies $y_j \to 0 \; as \; j \to \infty$ for any initial condition [29]. The stability region obtained in Figure 1 is $A-stable$ according [29].

Numerical Problems

To validate the accuracy and convergence of the new method, the following IVPs are considered.
The results obtained from the new method are compared with the existing methods.
The following notations will be used in the tables and figures.
ES means exact solution
CS means computed solution
ENM means error in method
ES11 means error in Sunday 2011 [30]
EJASY means error in James *et al.* 2013 [6]
ESOAJ means error in Sunday *et al.* 2013 [5]
ESJOA means error in Sunday *et al.* 2015 [4]
EOSE means error in Okunuga *et al.* 2013 [31]
E2SEM means error in the Two-Step Implicit Obrechkoff Method of Omar and Adeyeye 2016 [9].
E2SBM means error in New Two-Step Obrechkoff-Type Block Method of Omar and Adeyeye 2016 [9]
EBYP means error in Badmus *et al*., 2015 [20]

Problem 1

A specific radioactive substance is known to decay at a rate proportional to its concentration. A block of this substance with a mass of $100g$ is observed. Its mass is reduced to $90g$ after 40 hours. Find an expression for the mass of the substance at any time and solve this problem for $\forall \; u \in 0,1$ using the new method. The differential equation for the above problem is

$$\frac{du}{dv} = -\mu u, u(0) = 100, \forall \; u \in 0,1. \tag{13}$$

Where u represent the substance's mass at any point in time v and μ are constants that specify the rate at which this particular substance decays. As a result, $100e^{-0.0026v}$ is the theoretical solution to equation (13).
See: [8, 17].

Problem 2: The oscillatory differential equation solved by [4, 5]

$$\frac{du}{dv} = -\sin(v) - 200(u - \cos(v)), h = 0.01, u(0) = 0, \tag{14}$$

with the exact solution

$$u(v) = \cos(v) - e^{-200v} \tag{15}$$

Problem 3: Consider the oscillatory differential equation [4, 32]

$$\frac{du}{dv} = -10(u-1)^2,\ h = 0.01,\ u(0) = 2, \tag{16}$$

with the exact solution

$$u(v) = 1 + \frac{1}{1+10v} \tag{17}$$

Problem 4: Consider the Highly stiff oscillatory differential equation [9, 20]

$$\frac{du}{dv} = -\psi u,\ h = 0.1,\ u(0) = \psi = 1, \tag{18}$$

with the exact solution

$$u(v) = \exp(-v) \tag{19}$$

Results and Discussions

Table 1. Showing the result for (13) with that of [6, 30].

V	ES	CS	ENM	ES11	EJASY
0.1	99.97400337970708570600	99.9740033797070857060 0	0.0000e-00	2.0000e-08	0.0000e-00
0.2	99.94801351765683795200	99.9480135176568379520 0	0.0000e-00	1.0000e-08	1.4211e-14
0.3	99.92203041209234205300	99.9220304120923420530 0	0.0000e-00	0.0000e-00	0.0000e-00
0.4	99.89605406125714006400	99.8960540612571400640 0	0.0000e-00	0.0000e-00	0.0000e-00
0.5	99.87008446339523065700	99.8700844633952306570 0	0.0000e-00	3.0000e-08	1.4211e-14
0.6	99.87008446339523065700	99.8700844633952306570 0	0.0000e-00	0.0000e-00	1.4211e-14
0.7	99.84412161675106900700	99.8441216167510690070 0	0.0000e-00	3.0000e-08	1.4211e-14
0.8	99.81816551956956667200	99.8181655195695666720 0	0.0000e-00	3.0000e-08	0.0000e-00
0.9	99.79221617009609147100	99.7922161700960914710 0	0.0000e-00	0.0000e-00	0.0000e-00
0.1	99.76627356657646737200	99.7662735665764673720 0	0.0000e-00	0.0000e-00	0.0000e-00

Table 2. Showing the result for oscillatory differential equation (13) with that of [4, 5].

V	ES	CS	ENM	ESJOA	ESOAJ
0.001	0.18126874692477177712	0.1812687469220598080 0	2.7120e-12	3.7249e-10	8.5812e-06
0.002	0.32967795396412439246	0.3296779539650273658 4	9.0297e-13	5.2169e-10	2.9379e-06
0.003	0.45118386391042716158	0.4511838639093485663 6	1.0786e-12	6.7870e-10	9.3961e-06
0.004	0.55066303589223450724	0.5506630358934450695 5	1.2106e-12	7.6010e-10	1.1305e-05
0.005	0.63210805885482676508	0.6321080588545993233 7	2.2744e-12	7.4126e-10	7.9107e-06
0.006	0.69878778814058064233	0.6987877881417978385 6	1.2172e-12	7.4495e-10	1.0313e-05
0.007	0.75337853615825529977	0.7533785361584350263 3	1.7973e-13	7.2211e-10	1.0426e-05
0.008	0.79807148217492301264	0.7980714821760108940 9	1.0879e-12	6.5649e-10	7.7981e-05
0.009	0.83466061205144457875	0.8346606120517877235 9	3.4315e-13	6.1326e-10	8.4900e-05
1.000	0.86461471717914105002	0.8646147171800525858 9	9.1154e-13	5.6367e-10	8.0388e-05

Table 3. Showing the result for oscillatory differential equation (15) with that of [4, 31].

V	ES	CS	ENM	ESJOA	EOSE
0.001	1.90909090884750640830	1.9090909088909090909 0	4.3403e-11	2.4025e-08	1.0700e-04
0.002	1.83333333337241953740	1.8333333333333333330	3.9086e-11	3.1560e-08	2.3800e-04
0.003	1.76923076920944483900	1.7692307692307692308 0	2.1324e-11	3.2631e-08	4.5100e-04
0.004	1.71428571432193859870	1.7142857142857142857 0	3.6224e-11	3.1192e-08	6.2000e-04
0.005	1.66666666683042904300	1.6666666666666666670	1.6376e-11	2.8877e-08	8.8400e-04
0.006	1.62500000029558015600	1.6250000000000000000	2.9558e-11	2.6370e-08	1.0300e-03
0.007	1.58823529413888054590	1.5882352941176470588 0	2.1234e-11	2.3953e-08	1.2700e-03
0.008	1.55555555557943834040	1.5555555555555555560	2.3883e-11	2.1734e-08	1.5300e-03

0.009	1.52631578949329163390	1.52631578947368421050	1.9607e-11	1.9740e-08	1.7500e-03
1.000	1.50000000001952055900	1.50000000000000000000	1.9521e-11	1.7969e-08	1.8100e-03

Table 4. Showing the result for oscillatory differential equation (15) with that of [9, 20].

V	ES	*CS*	ENM	E2SEM	E2SBM
0.1	0.90483741803595957316	0.90483741803596084590	1.2727e-15	7.5513e-05	9.0730e-12
0.2	0.81873075307798185867	0.81873075307798400161	2.1429e-15	6.8684e-05	1.1768e-11
0.3	0.74081822068171786607	0.74081822068170938478	8.4813e-15	1.2397e-04	2.3144e-11
0.4	0.67032004603563930074	0.67032004603564280973	3.5090e-15	1.1246e-04	2.8440e-11
0.5	0.60653065971263342360	0.60653065971262806724	5.3564e-15	1.5237e-04	3.1815e-11
0.6	0.54881163609402643263	0.54881163609403074200	4.3094e-15	1.3811e-05	3.4927e-11
0.7	0.49658530379140951470	0.49658530379140642905	3.0857e-15	1.6640e-04	3.6582e-11
0.8	0.44932896411722159143	0.44932896411722629572	4.7043e-15	1.5076e-04	3.8127e-11
0.9	0.40656965974059911188	0.40656965974059764972	1.4622e-15	1.7033e-04	3.8576e-11
1.0	0.36787944117144232160	0.36787944117144713602	4.8144e-15	1.5428e-04	3.9020e-11

Table 5. Showing the result for oscillatory differential equation (15) with that of [9, 20].

V	ES	*CS*	EBYP
0.1	0.90483741803595957316	0.90483741803596084590	1.5476e-10
0.2	0.81873075307798185867	0.81873075307798400161	1.3823e-10
0.3	0.74081822068171786607	0.74081822068170938478	1.3282e-10
0.4	0.67032004603563930074	0.67032004603564280973	1.1733e-10
0.5	0.60653065971263342360	0.60653065971262806724	1.1342e-10
0.6	0.54881163609402643263	0.54881163609403074200	9.9385e-11
0.7	0.49658530379140951470	0.49658530379140642905	9.6770e-11
0.8	0.44932896411722159143	0.44932896411722629572	8.4003e-11
0.9	0.40656965974059911188	0.40656965974059764972	8.2517e-11
1.0	0.36787944117144232160	0.36787944117144713602	7.0848e-11

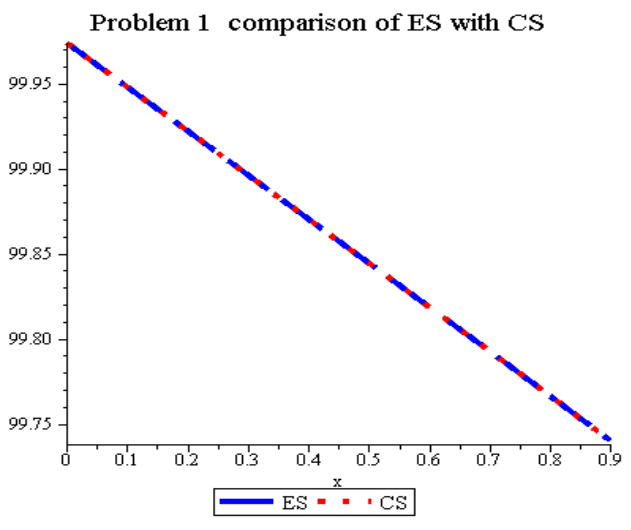

Figure 2. Graphical curves for Problem 1.

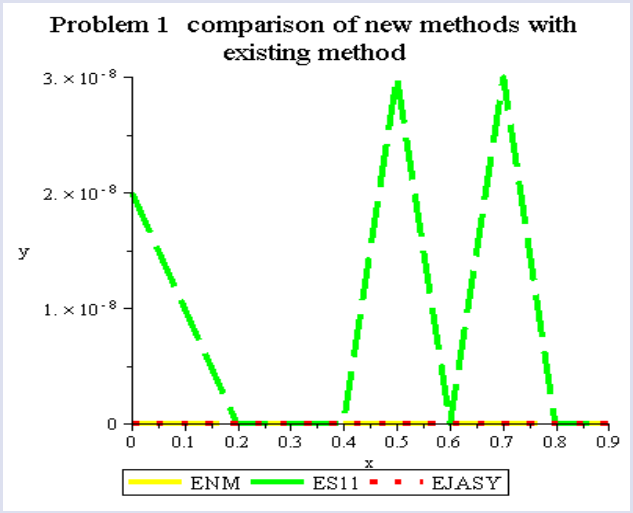

Figure 3. Graphical curves for Problem 1.

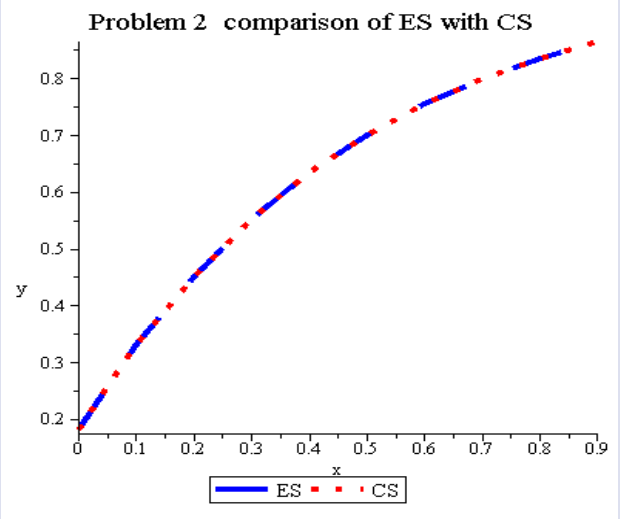

Figure 4. Graphical curves for Problem 2.

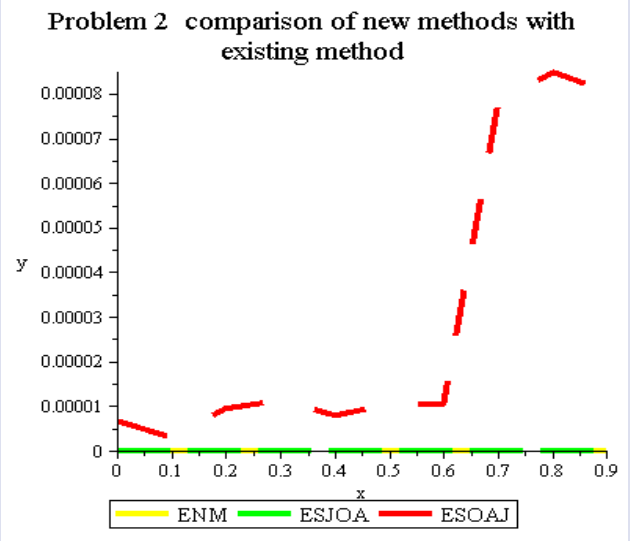

Figure 5. Graphical curves for Problem 2.

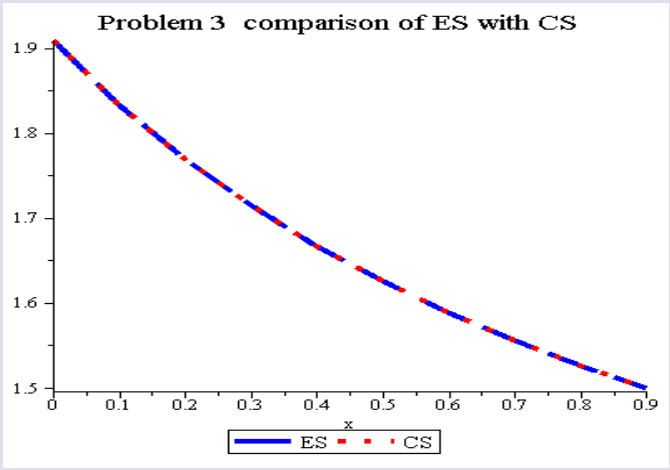

Figure 6. Graphical curves for Problem 3.

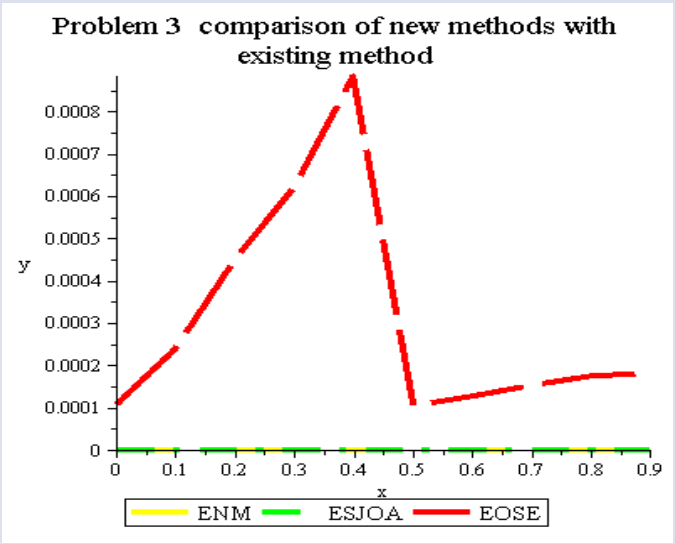

Figure 7. Graphical curves for Problem 3.

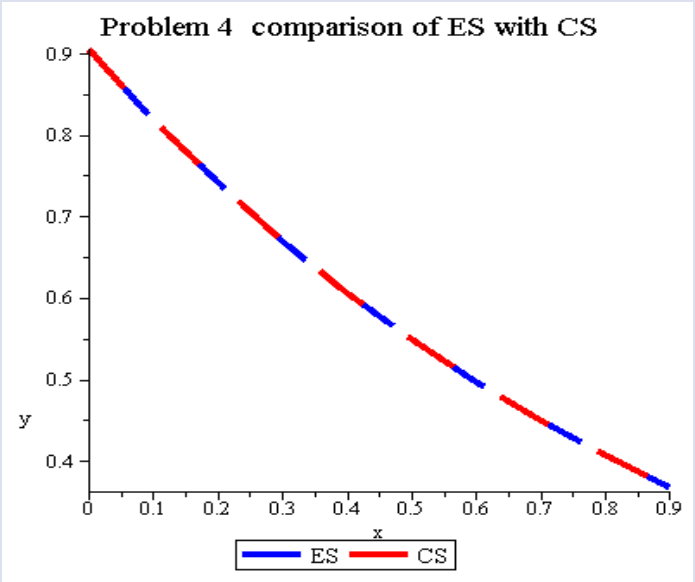

Figure 8. Graphical curves for Problem 4.

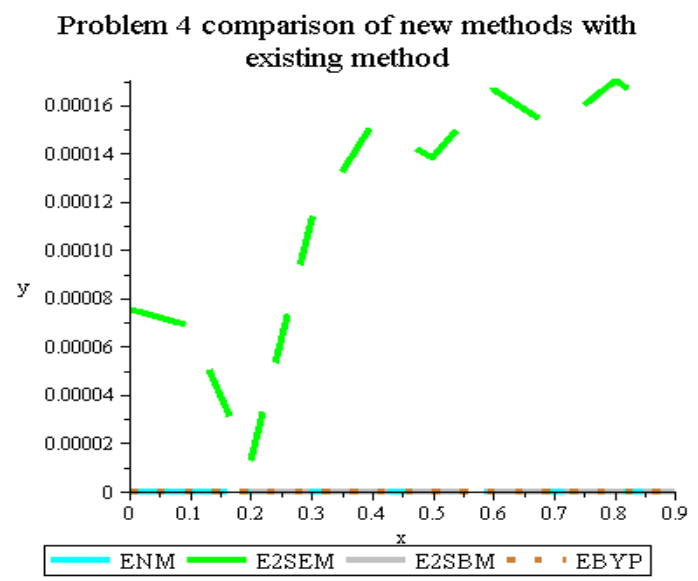

Figure 9. Graphical curves for Problem 4.

Discussion of results

The newly derived method was applied to four sample problems. Problem 1 is the differential equation solved by [6, 30]. From the result obtained in Table 1 above, the new method performs accurately than [6, 30]. Figures 2 and 3 show the graphical curve for problem 1. The oscillatory differential equation in problem 2 was considered by [4, 5]. In Table 2, the proposed method performed accurately than that of [4, 5]. From figures 4 and 5, the textual curve of problem 2 is accurate. The result converges and performs better than that of [4, 5]. The oscillatory differential equation in problem 3 was solved and compared with [4, 31]. The textual results showed the convergence of the new method over the existing one. Finally, the highly stiff oscillatory differential (18) was solved by [20, 30], and the new method was accurate, as seen in tables 4 and 5 and figures 7 and 8 above. Hence, from the results, the new method has shown better accuracy and faster convergence graphically. Figures 3, 5, 7, and 9 have shown the convergence of the new method closer to zero than those in the literature.

Conclusion

In this research, the application of a two-step block scheme is derived using the block approach for solving (1). The basic properties of the scheme were analyzed and satisfied all conditions. Some special classes of differential equations were implemented and compared with existing methods [4, 5, 6, 9, 20, 30, 31]. From tables 1 to 5, the new method proved to have better accuracy and faster convergence than the existing methods considered in this research. The graphical curve for problems 1 to 4 proved the convergence accuracy of the method. Therefore, the new methods have yielded a good result over the existing methods, both graphically and in tabular form.

Conflicts of interest

There are no conflicts of interest in this work.

References

[1] Ajileye, G., Aminu, F. A., A Numerical method using collocation approach for the solution of Volterra-Fredholm integro-differential equations, *African Scientific Reports*, 1(3) (2022) 206.

[2] Raymond, D., Kyagya, T. Y., Sabo, J., Lydia, A., Numerical application of higher order linear block scheme on testing some modeled problems of fourth order problem, *African Scientific Reports*, 2(1) (2023).

[3] Henrici, P., Discrete variable methods in ordinary differential equations, *John Wiley & Sons, Inc., Hoboken, NJ, USA*, (1969).

[4] Sunday, J., James, A. A., Odekunle, M. R., Adesanya, A. O., Chebyshevian basis function-type block method for the solution of first-order initial value problems with oscillating solutions, *J. Math. Comput. Sci.*, 5 (2015) 462-472.

[5] Sunday, J., Odekunle, M. R., Adesanya A. O., James, A. A., Extended block integrator for first-order stiff and oscillatory differential equations, *Amer. J. Comput. Appl. Math.* 3 (2013) 283-290.

[6] James, A. A., Adesanya, A. O., Sunday, J., Yakubu, D. G., Half-step continuous block method for the solution of modeled problems of ordinary differential equations, *American Journal of Computational Mathematics*, 3 (2013) 261- 268.

[7] Skwame, Y., Sabo, J., Kyagya, T. Y., The constructions of implicit one-step block hybrid methods with multiple off-grid points for the solution of stiff differential equations, *Journal of Scientific Research and Report*, 16(1)(2017) 1-7.

[8] Ayinde, A. M., A. A. Ishaq, A. A., T. Latunde, T., Sabo, J., Efficient numerical approximation methods for solving high-order integro-differential equations, *Caliphate Journal of Science & Technology*, 2(3)(2021) 188-195.

[9] Omar, Z., Adeyeye, A., Numerical solution of first order initial value problems using a self-starting implicit two-step Obrechkoff-type block method, *Journal of Mathematic and Statistics*, 12(2)(2016) 127-134.

[10] Shokri, A., Shokri, A. A., The new class of implicit L-stable hybrid Obrechkoff method for the numerical solution of first order initial value problems, *Comput. Phys. Commun*. 184(2013) 529-530.

[11] Ayinde, A.M, James, A.A, Ishaq, A.A., Oyedepo, T. , A new numerical approach using Chebyshev third kind polynomial for solving integro-differential equations of higher order, *Gazi University Journal of Science, Part A: Engineering and Inovation*, 9(3)(2022) 259 -266.

[12] Oyedepo, T., Taiwo, O.A., Adewale, A.J., Ishaq, A.A., Ayinde, A.M., Numerical solution of system of linear fractional integro-differential equations by least squares collocation Chebyshev technique, *Mathematics and Computational Sciences*, 3(2) (2022) 10-21**.**

[13] Oyedepo**,** T., Ayoade, A.A., Ajileye, G., Ikechukwu, N.J., Legendre computational algorithm for linear integro-differential equations, *Cumhuriyet Science Journal*, 44(3) (2023) 561-566.

[14] Oyedepo, T., Ayinde, A.M., E.N. Didigwu, E.N., Vieta-Lucas polynomial computational technique for Volterra integro-differential equations, *Electronic Journal of Mathematical Analysis and Applications*, 12(1) (2024) 1-8. Dio.10.21608/EJMAA.2023.232998.1064

[15] Oyedepo, T., Ishola, C.Y., Ishaq, A.A., Ahmed, O.L., Ayinde, A.M., Computational algorithm for fractional Fredholm integro-differential equations, *Kathmandu University Journal of Science, Engineering and Technology*, 17(1) (2023), 1-7.

[16] Oyedepo, T., Ayoade, A. A., Otaide, I.K., Ayinde, A. M., Second kind Chebyshev collocation technique for Volterra-Fredholm fractional order integro-differential equations, Journal of Natural Sciences and Mathematical Research, 8 (2)(2022) 103-110

[17] Kida, M., Adamu, S., Aduroja, O. O., Pantuvo, T. P., Numerical solution of stiff and oscillatory problems using third derivative trigonometrically fitted block method, *Journal of Nigerian Society of Physical Sciences*, 4(1)(2022) 34-48.

[18] Ajileye, G., James, A. A., Ayinde, A. M., Oyedepo, T., Collocation approach for the computational solution of Fredholm-Volterra fractional order of integro-differential equations, *Journal of Nigerian Society of Physical Sciences*, 4(2022) 1-7.

[19] Hasni, M. M., Majid, Z. A., Senu, N., Numerical solution of linear dirichlet two-point boundary value problems using block method, *Int. J. Pure Applied Math.,* 85(3)(2013) 495-506.

[20] Badmus, A. M., Yahaya, Y. A., Pam, Y. C., Adams type hybrid block methods associated with Chebyshev polynomial for the solution of ordinary differential equations, *British J. Math. Comput. Sci*. 6(6)(2015), 465-472.

[21] Ali, K.K., Mehanna, M.S. and Akbar, M.A., 2022. Approach to a (2+ 1)-dimensional time-dependent date-JimboKashiwara-Miwa equation in real physical phenomena, *Appl. Comput. Math*., 21(2)(2022) 193-206.

[22] Akram, G., Elahi, Z. and Siddiqi, S.S., Use of Laguerre polynomials for solving system of linear differential equations, *Appl. Comput. Math*., 21(2)(2022) 137-146.

[23] Iskandarov, S. and Komartsova, E., On the influence of integral perturbations on the boundedness of solutions of a fourth-order linear differential equation, *TWMS J. Pure Appl. Math*., 13(1)(2022) 3-9.

[24] Ozdemir ME. New refinements of hadamard integral inequality via k-Fractional integrals for p- Convex Function. Turkish Journal of Science, 6(1)(2021) 1-5.

[25] Qi, F. Necessary and sufficient conditions for a difference defined by four derivatives of a function containing trigamma function to be completely monotonic, Appl. Comput. Math., 21(1)(2022) 61-70.

[26] Shaalini, V. J., Fadugba, S. E., A new multistep method for solving delay differential equations using Lagrange interpolation, *Journal of Nigerian Society of Physical Sciences*, 3 (2021) 159-164.

[27] Obarhua, F. O., Adegboro, O.J. Order four continuous numerical method for solving general second order ordinary differential equations, Journal of Nigerian Society of Physical Sciences **3** (2021) 42.

[28] Sabo, J., Skwame, Y., Kyagya, T. Y., Kwanamu, J. A. ,The direct simulation of third order linear problems on single step block method. *Asian Journal of Research in Computer Science.* 12(2)(2021) 1-12.

[29] Dahlquist, G. G., Numerical integration of ordinary differential equations, Mathematica Candinavica, 4(1956) 33-53.

[30] Sunday, J., On Adomian decomposition method for numerical solution of ODEs arising from the natural laws of growth and decay, *The Pacific Journal of Science and Technology*, 12(1)(2011) 237-243.

[31] Okunuga, S. A., Sofoluwe, A. B., Ehigie, J. O., Some block numerical schemes for solving initial value problems in ODEs, *Journal of Mathematical Sciences*, 2(1)(2013) 387-402.

[32] Yan, Y.L., Numerical methods for differential equations, City University of Hong Kong Kowloon (2011).

Cumhuriyet Sci. J., 45(2) (2024) 379-385
DOI: https://doi.org/10.17776/csj.1338905

Cumhuriyet Science Journal

| csj.cumhuriyet.edu.tr | Founded: 2002 ISSN: 2587-2680 e-ISSN: 2587-246X Publisher: Sivas Cumhuriyet University

Determination of Transmission Factors and γ-Ray Linear Attenuation Coefficients of Some Construction Materials Mixed with Ulexite and Borax

Salih Zeki Erzeneoğlu[1,a] Burcu Akça[2,b,*], Hidayet Uyanık[1,c]

[1] *Department of Physics, Faculty of Sciences, Atatürk University, Erzurum, Türkiye.*

[2] *Department of Medical Services and Techniques, Ardahan Health Services Vocational School, Ardahan, Türkiye.*

**Corresponding author*

Research Article

History
Received: 07/08/2023
Accepted: 18/04/2024

ABSTRACT

In the study, transmission factors *(T)* and linear attenuation coefficients (μ) of some construction materials (briquette, sand, marble, paint, adobe, soil, and lime) mixed with ulexite and borax are measured with energy dispersive X-ray fluorescence spectrometer for 59.5 keV energy by using a Si(Li) detector. Ulexite and borax were added to the samples at a rate of 25, 50, and 75 percent. Results are presented and discussed in this paper. Measurements made on these construction materials with technological importance will create new use areas..

Keywords: **C**onstruction material, Radiation isolation, EDXRFS.

[a] *salih@atauni.edu.tr* *https://orcid.org/0000-0002-0890-6099*
[b] *burcuakca@ardahan.edu.tr* *https://orcid.org/0000-0003-2399-5971*
[c] *hidayetuyank@gmail.com* *https://orcid.org/0009-0003-2014-567X*

Introduction

The research on shielding materials is essential to protect human beings from the harmful effects of various ionizing radiations. The most proper materials for shielding according to the radiation energy are specified based on their radiation shielding capacities. In this sense, the most used material is lead because of its properties [1]. It is also necessary to find new materials such as lead. Zayed et al. investigate the effect of boric acid on the physical, mechanical, microstructural, and radiation-shielding properties of serpentine concrete. The results of they showed that the addition of boric acid hindered the hydration of cement[2]. Zahran et al. have studied the attenuation characteristics of some semiconductor compounds at different photon energies [3]. They have estimated interaction parameters in the range of 0.015-15 MeV. Abbasi et al.[4] have discussed the great potential of mesoporous silica nanoparticles for application in cancer immunotherapy. The electronic, atomic, and absorption ability of the composite are analyzed from the irradiation intensity after the X-rays pass through the samples by Anugrah et al. [5]. They have compared the linear attenuation coefficients of different composite gelatin with those of breast phantom. As a result of the study, they obtained a new composite with excellent characteristics for breast phantom. Kumar et al. [6] did experimental studies on the measurement of the mass attenuation coefficient of zirconium and some compounds of zirconium in the range of 17.919–18.664 keV. In a distinct study, Akça et al. [7] investigated the change according to the different voltages of linear attenuation coefficients for some semiconductors by using EDXRFS and Am-241 point source. Saleh et al. have determined the natural radioactivity of different cement raw materials in Yemen[8]. Tyagi et al. [9] did a review on the usage of alternate materials, emphasizing hazardous industrial byproducts, as constituents of radiation shielding concrete. They have expected that the exposition of these research gaps will be helpful in the area of alternate materials in radiation shielding concrete. Akça and Erzeneoğlu [10] have measured the mass attenuation coefficients for compounds of biomedically important elements by using the transmission method. They have obtained shielding parameters from these results. The relative difference between the experimental and theoretical values is given in the article. Böke [11] has computed coherent, incoherent scattering, photoelectric cross sections, and linear attenuation coefficients for liver, kidney, muscle, and fat. Akça et al. [12] have measured shielding parameters for various materials. It was shown that maximum interaction with gamma rays for lime and minimum interaction for polyvinyl chloride. Madej et al. [13] have presented a study on the performance of shielding refractory concretes. Linear attenuation coefficients are determined twice, firstly after casting and drying of concretes, and secondly after sintering. Eke C. [14] has calculated radiation protection coefficients of beach sand samples from Antalya in the energy range of 80–1332 keV by using gamma-ray spectrometry. Erzeneoğlu et al. [15] have measured the mass attenuation coefficients of ternary semiconductors that are InSe and InSe having different holmium concentrations. Samson et al. [16] have made Rhizophora spp. particleboard phantoms using SPI-based adhesives, modified with sodium hydroxide and itaconic acid poly

amidoamine-epichlorohydrin (0, 5, 10, and 15 wt%) by using an X-ray computed tomography imaging system. Koirala et al. [17] have researched the total cross-section of electrons, atoms, and molecules in iron oxides to select the best shielding material for iron oxides in the energy range of 0–10 MeV. Cinan and Yılmaz [18] have obtained the calibration curve by using Rayleigh to Compton scattering ratio. They showed that this curve can be used for qualitative analysis of compounds within a certain range of effective atomic numbers. Kurudirek et al. [19] have determined the chemical compositions of materials. Also, they have investigated some building materials and their admixtures with TSW in terms of radiation shielding parameters by using X-rays at 22.1, 25 keV, and γ-rays at 88 keV photon energies. Gökmen [20] investigated neutron and gamma-ray shielding properties of Inconel 718 reinforced B_4C (0-25 wt%) using PSD software.

Theoretical Basis

The transmission of a beam of monochromatic gamma photons on absorbing material is given by the Lambert-Beer law:

$$I = I_0 e^{-\mu t} \quad (1)$$

where I_0 is the incident photon intensity and I is the reduced photon intensity after passing through the material of thickness t, the linear attenuation coefficient $\mu(cm^{-1})$ and (I/I_0) the transmission factor T.

Experimental Basis

The experimental setup used is given in Figure. 1. In this study, we used a point source of Am-241 of intensity 100 mCi which emits 59.5 keV gamma rays. The source is placed in lead blocks to collimate the rays. We used a Si(Li) detector having a diameter of 3,91 mm and an active area of 12 mm^2 and a resolution of 160 eV at 5,9 keV. Measurements were taken under the same experimental conditions for 600 s. The spectra are recorded in a 4096-channel analyzer. In the experiment, the source, sample, and detector were positioned on the same plane. Ulexite and borax have been added to building materials (briquette, sand, marble, paint, adobe, soil, and lime) in different proportions (0%, 25%, 50%, and 75%) and have been mixed at 20 min by the mixer. Samples have a diameter of 13 mm and are compressed into pellets. The typical spectra for Adobe are shown in Figure 2. Experimental errors are attributed to the deviation from the average value in intensities (<0.9%), sample thickness (<0.5%), the mass of the sample (<0.8%), and systematic errors (<1%).

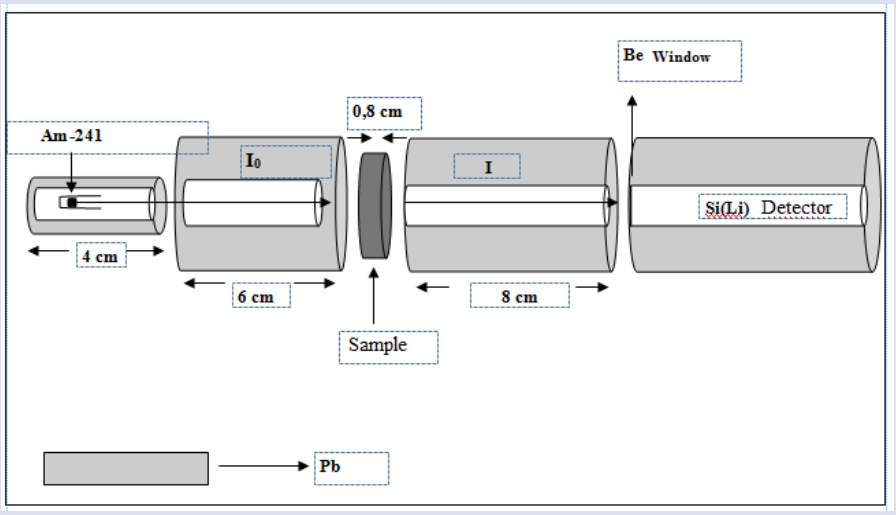

Figure 1. The experimental setup).

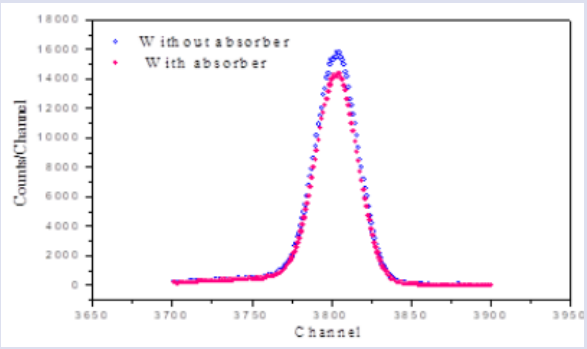

Figure 2. Representative spectrum for Adobe.

Results and Discussion

Borax (Na2B4O7) is widely used in the industry. Some usage areas are glass, agriculture, ceramics, fire retardants, metallurgy, construction, anti-freeze, and adhesive. In Turkey, ulexite (Na2O.2CaO.5B2O3.16H2O) is commonly found in Bigadiç/Balıkesir. Some usage areas of ulexite are glass, ceramics, heat and sound insulation, and fertilizer. It is important to find new uses for boron since Turkey has the highest boron reserves in the world. On the other hand, it is also important to minimize the damage effects of radiation. Radiation has caused diseases such as cancer have affected the quality of life. In this study, we aimed to use different materials for radiation shielding. At the same time, we are researching new uses for future mine boron. T and μ values of construction materials mixed with ulexite and borax are given in Table 1-2. Experimental results are also graphically given in Figures 3-17. As seen in Figure 3, the transmission factors of pure construction materials increase for soil, marble, lime, adobe, paint, briquette, and sand, respectively. When the transmission factors increase, the linear attenuation coefficients decrease, i.e. the absorption decreases. Maximum absorption was obtained for soil and minimum for sand. The experimental linear attenuation coefficient results have been fitted as in Figures 3-17. There are some minor deviations here which may be due to beam collimation and preparation of samples such as mixture. As shown in Figures 4-17, the concentration of ulexite and borax changes the μ values of construction materials. This is a clear result. In Figures 4, 5, 6, 8, 9, 11, 13, 14, 15, and 16, the linear attenuation coefficients decrease with increased ulexite and borax concentration. In other words, when the concentration of ulexite and borax increases, linear attenuation coefficients decrease. In Figures 7, 10, 12, and 17, there is still a decrease with increased ulexite and borax, but the form of change is different from others. On the other hand, When the results with ulexite and borax in Table 1-2 are compared, it is seen that there is no significant difference. Average linear attenuation coefficients for borax are slightly larger than for ulexite. As far as we know, there are no experimental results reported in the literature for these samples, ratios, and energy. Therefore, we could not compare the experimental results with other experimental results.

Table 1. T and μ values of construction materials mixed with Ulexite

Sample	*T*	μ (cm-1)
Briquette	0.231	5.940
Briquette + %25 Ulexite	0.277	4.072
Briquette + %50 Ulexite	0.315	3.554
Briquette + %75 Ulexite	0.250	2.798
Sand	0.266	5.151
Sand + %25 Ulexite	0.295	4.987
Sand + %50 Ulexite	0.261	3.532
Sand + %75 Ulexite	0.130	5.032
Marble	0.097	10.442
Marble + %25 Ulexite	0.601	2.232
Marble + %50 Ulexite	0.631	0.574
Marble + %75 Ulexite	0.150	3.911
Paint	0.194	5.865
Paint + %25 Ulexite	0.301	10.976
Paint + %50 Ulexite	0.274	9.938
Paint + %75 Ulexite	0.063	7.164
Adobe	0.129	6.457
Adobe + %25 Ulexite	0.305	2.933
Adobe + %50 Ulexite	0.334	2.411
Adobe + %75 Ulexite	0.205	3.104
Soil	0.070	9.517
Soil + %25 Ulexite	0.188	7.337
Soil + %50 Ulexite	0.153	5.901
Soil + %75 Ulexite	0.084	6.425
Lime	0.113	2.202
Lime + %25 Ulexite	0.265	3.287
Lime + %50 Ulexite	0.291	3.396
Lime + %75 Ulexite	0.361	2.487

Table 2. T and μ values of construction materials mixed with borax

Sample	*T*	μ (cm-1)
Briquette	0.231	5.940
Briquette + %25 Borax	0.071	7.061
Briquette + %50 Borax	0.083	5.482
Briquette + %75 Borax	0.087	4.980
Sand	0.266	5.151
Sand + %25 Borax	0.144	6.164
Sand + %50 Borax	0.109	5.620
Sand + %75 Borax	0.587	1.301
Marble	0.097	10.442
Marble+ %25 Borax	0.073	9.905
Marble + %50 Borax	0.068	8.507
Marble + %75 Borax	0.086	5.118
Paint	0.194	5.865
Paint+ %25 Borax	0.322	3.432
Paint + %50 Borax	0.364	2.512
Paint + %75 Borax	0.374	1.754
Adobe	0.129	6.457
Adobe + %25 Borax	0.194	6.135
Adobe + %50 Borax	0.185	5.177
Adobe + %75 Borax	0.077	5.288
Soil	0.070	9.517
Soil + %25 Borax	0.252	4.675
Soil + %50 Borax	0.344	3.495
Soil + %75 Borax	0.318	2.464
Lime	0.113	2.202
Lime + %25 Borax	0.198	5.706
Lime + %50 Borax	0.068	6.012
Lime + %75 Borax	0.215	3.170

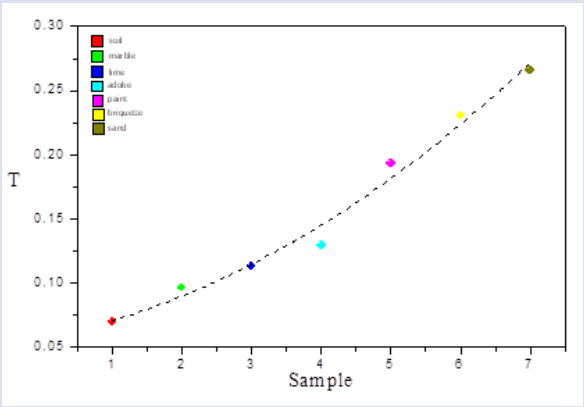

Figure 3. Transmission factors versus sample

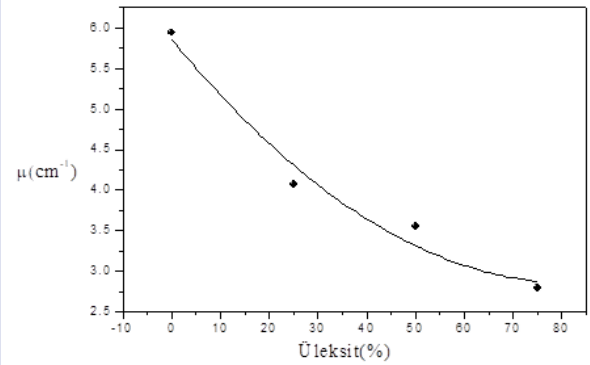

Figure 4. Linear attenuation coefficients versus percent of ulexite for briquette.

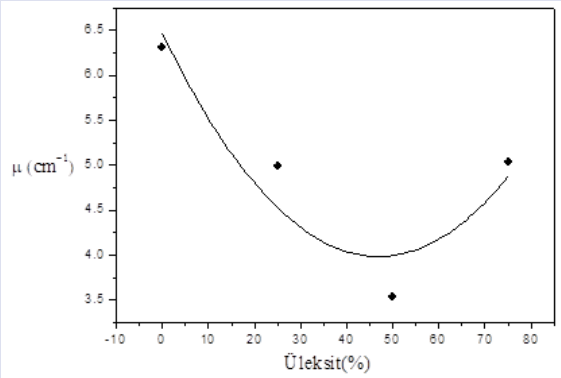

Figure 5. Linear attenuation coefficients versus percent of ulexite for sand.

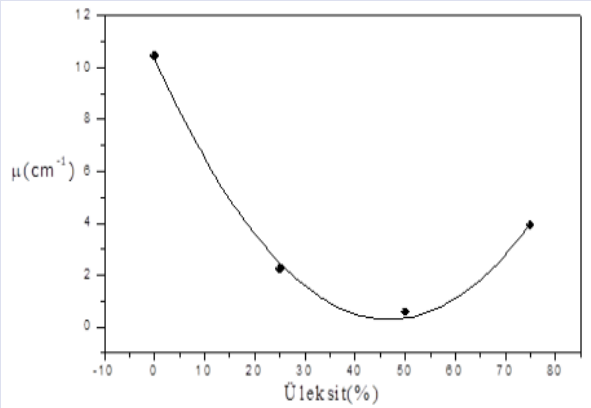

Figure 6. Linear attenuation coefficients versus percent of ulexite for marble.

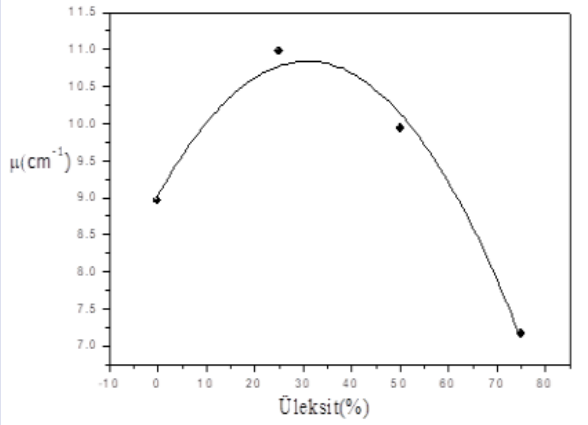

Figure 7. Linear attenuation coefficients versus percent of ulexite for paint.

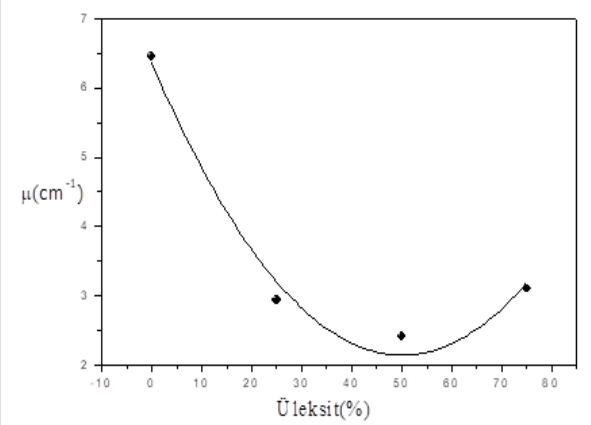

Figure 8. Linear attenuation coefficients versus percent of ulexite for Adobe.

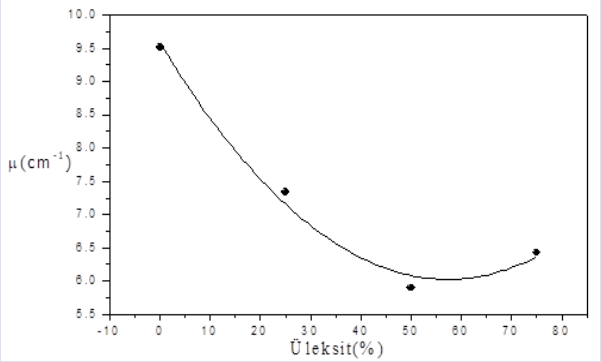

Figure 9. Linear attenuation coefficients versus percent of ulexite for soil

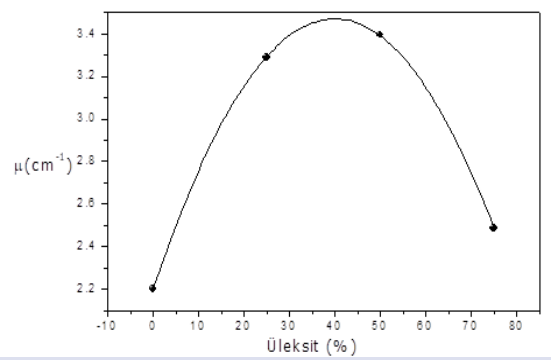

Figure 10. Linear attenuation coefficients versus percent of ulexite for lime.

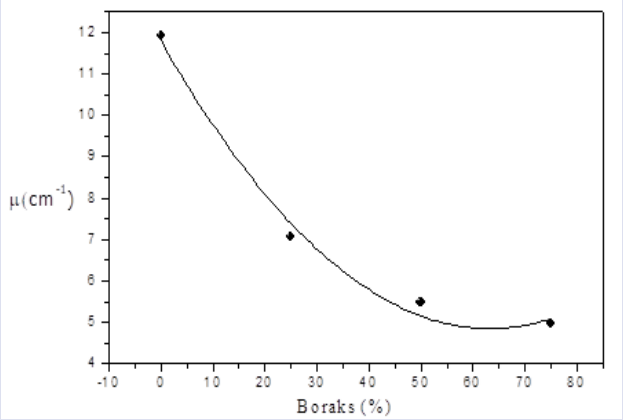

Figure 11. Linear attenuation coefficients versus percent of borax for Briquette.

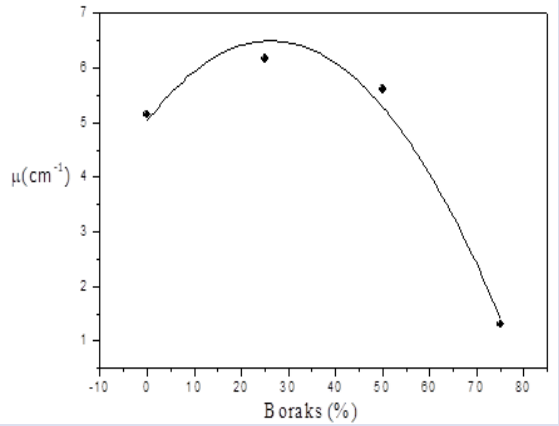

Figure 12. Linear attenuation coefficients versus percent of borax for sand.

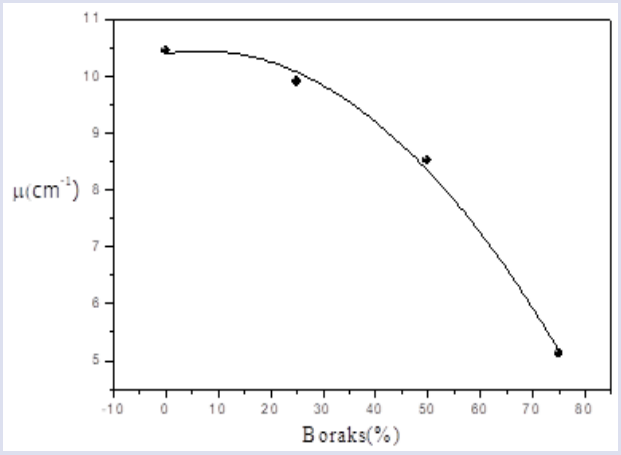

Figure 13. Linear attenuation coefficients versus percent of borax for Marble.

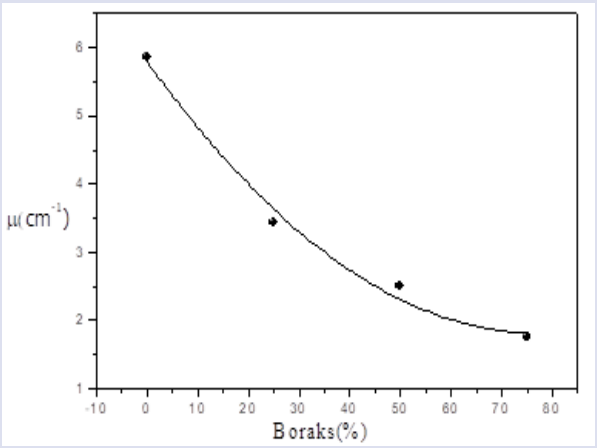

Figure 14. Linear attenuation coefficients versus percent of borax for paint

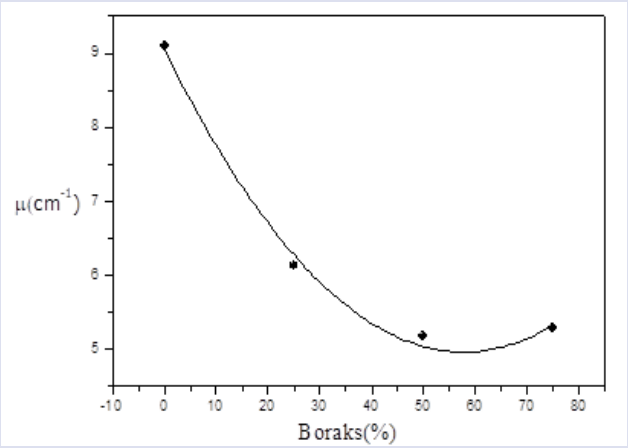

Figure 15. Linear attenuation coefficients versus percent of borax for Adobe.

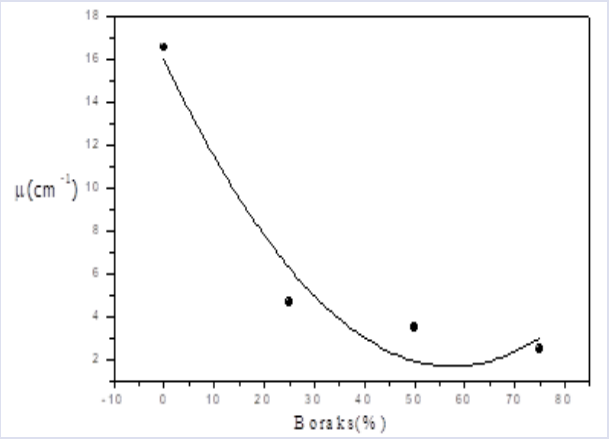

Figure 16. Linear attenuation coefficients versus percent of borax for soil.

.

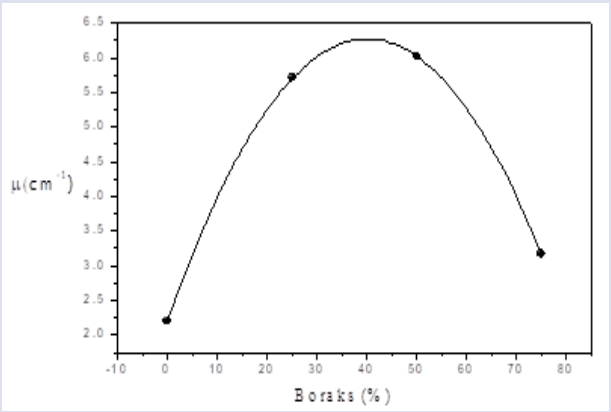

Figure 17.Linear attenuation coefficients versus percent of borax for lime

CONCLUSİON

In this study, we have tested to be used as a shield against gamma radiation of some construction materials mixed with two boron compounds. These construction materials and boron compounds have numerous uses in our lives. The transmission factors and linear attenuation coefficients of these samples were measured and compared to each other. In general, linear attenuation coefficients is decreasing with increasing ratio of ulexite and borax. It was also observed that the transmission factors of sand are higher than the other. We can say that qualitative and quantitative analyzes of the construction materials should be made and the shielding parameters should be measured for a more accurate interpretation of the results. Also, various energies and construction materials can be tried for different usage areas of boron.

Acknowledgments

The authors are thankful to ETİMADEN for the sample

Conflicts of interest

There are no conflicts of interest in this work.

Authors's Contributions

S. Erzeneoğlu: Writing, review, editing, investigation, supervision, project, administration, conceptualization, methodology, **B. Akça:** Writing, review, editing, investigation, data curation, original draft, conceptualization, methodology, **H. Uyanık:** Writing, review, editing, investigation, data curation, conceptualization.

References

[1] Mhareb M. H. A., Mostafa Z., Mohamed E., Alajerami Y. S., Sayyed M. I., Gameel S., Hamad R. M., Hamad M. Kh., Radiation Shielding Features for Various Telluriumbased Alloys: a Comparative Study, *J Mater Sci*: Mater *Electron*, 32 (2021) 26798– 26811.

[2] Zayed A.M., Masoud M.A., Shahien M.G., Gökçe H.S., Sakr K., Kansouh W.A., El-Khayatt A.M., Physical, Mechanical and Radiation Attenuation Properties of Serpentine Concrete Containing Boric Acid, *Construction and Building Materials*, 272 (2021) 121641.

[3] Zahran H.Y., El Sayed Y., Yahia I.S., Novel approach of gamma attenuation performance of Cu2SnZn(S, Se, Te)4 semiconductor materials: Radiation interactions with proton, alpha, carbon, electron, and photon, *Materials Science in Semiconductor Processing*, 123 (2021), 105554.

[4] Milad A., Salar H. G., Mohammad H. N., Kazem J., Zohre M., Ali J., Peyman I., Ali M. A., Mesoporous Silica Nanoparticle: Heralding a Brighter Future in Cancer Nanomedicine, *Microporous and Mesoporous Materials*, 319 (2021) 110967.

[5] Anugrah M. A., Ilyas S., Tahir D., Gelatin/Poly (vinyl alcohol) / Inorganic Filler Composites for Phantom Breasts, *Materials Chemistry and Physics*, 262 (2021) 124333.

[6] Kumar A. M., Manjula G., Nageshwar Rao A.S., Measurement of mass attenuation coefficient of ZIRCONIUM (Zr), Zirconium Chloride (ZrCl4) and Zirconium Silicate (ZrSiO4) near the K-edge using synchrotron Radiation, *Materials Today: Proceedings*, 38 (2021) 2927–2934.

[7] Akça B., Gürbulak B., Erzeneoğlu S. Z., Effect of Voltages on γ-*Ray* Linear Attenuation Coefficients for Some Semiconductors, *Radiation Physics and Chemistry*, 179 (2021) 109208.

[8] [8] Saleh E. E., Mohammed A. K., Elmonem El-Fiki S.A., Radiological and Gamma-ray Shielding Parameters of Cement Raw Materials Samples Used in Yemen, *Eur. Phys. J. Plus*, 136 (2021) 890.

[9] [9] Tyagi G., Singhal A., Routroy S., Bhunia D., Lahoti M., Radiation Shielding Concrete with alternate constituents: An approach to address multiple hazards,, *Journal of Hazardous Materials* 404 (2021) 124201.

[10] Akça B., Erzeneoğlu S. Z., The Mass Attenuation Coefficients, Electronic, Atomic, and Molecular Cross Sections, Effective Atomic Numbers, and Electron Densities for Compounds of Some Biomedically Important Elements at 59.5 keV, *Science and Technology of Nuclear Installations*, (2014) 8 pag.

[11] Böke A., Linear attenuation coefficients of tissues from 1 keV to 150 keV**,** *Radiation Physics and Chemistry,* 102 (2014) 49-59.

[12] Akça B., Ulusoy Ö., Erzeneoğlu S. Z., Total Mass Attenuation Coefficients, Total Photon Interaction Cross Sections, Effective Atomic Numbers and Effective Electron Densities for Some Construction Materials Available in Turkey, *Arabian Journal for Science and Engineering* 6(2022) (2021).

[13] Madej D., Silarski M., Parzych S., Design, Structure, Microstructure and Gamma Radiation Shielding Properties of Refractory Concrete Materials Containing Ba- and Sr-doped Cements, *Materials Chemistry and Physics* 260 (2021) 124095.

[14] Eke C., Investigation of Gamma-ray Attenuation Properties of Beach Sand Samples from Antalya, Turkey, Arabian *Journal of Geosciences* 14(159), (2021).

[15] Erzeneoğlu S., İçelli O., Gürbulak B., Ateş A., Measurement of Mass Attenuation Coefficients for Holmium Doped and Undoped Layered Semiconductors InSe at Different Energies and The Validity of Mixture Rule for Crystals Around The Absorption Edge, *Journal of Quantitative Spectroscopy & Radiative Transfer*, 102 (2006) 343–347.

[16] Samson D. O., Shukri A., Jafri M. Z. M., Hashim R., Sulaiman O., Abdul Aziz M. Z., Yusof M. F. M., Characterization of Rhizophora SPP. Particleboards with SOY Protein Isolate Modified with NaOH/IA-PAE Adhesive for Use as Phantom Material at Photon Energies of 16.59e25.26 keV, *Nuclear Engineering and Technology* 53 (2021) 216-233.

[17] Koirala B., Dhobin S. H., Khadka D., Yadav K., Nakarmi J. J., Poudyal K., Study The Radiation Shielding Material of Iron Oxides on the Basis of Total Cross Section*, IOSR Journal of Applied Physics* (IOSR-JAP), 13(6) (2021) 19-25.

[18] Cinan E., Yılmaz D., Effective Atomic Numbers of Boron Compounds Obtained using Rayleigh to Compton Scattering Intensity Ratio, *Applied Radiation and Isotopes* 174 (2021) 109753.

[19] Kurudirek M., Aygün M., Erzeneoğlu S., Chemical Composition, Effective Atomic Number and Electron Density Study of Trommel Sieve Waste (TSW), Portland Cement, Lime, Pointing and Their Admixtures with TSW in Different Proportions, *Applied Radiation and Isotopes*, 68(6) (2010) 1006-1011.

[20] Gökmen U., Gamma and Neutron Shielding Properties of B_4C Particle Reinforced Inconel 718 Composites, Nuclear Engineering and Technology, 54(3) (2022) 1049-1061.

Cumhuriyet Sci. J., 45(2) (2024) 386-393
DOI: https://doi.org/10.17776/csj.1420790

Cumhuriyet Science Journal

| csj.cumhuriyet.edu.tr | Founded: 2002 ISSN: 2587-2680 e-ISSN: 2587-246X Publisher: Sivas Cumhuriyet University

The Nonlinear Optical Properties of Self-Assembled InAs/GaAs Quantum Dot: Effect of Hydrostatic Pressure and Temperature

M. Jaouane [1,a], K. El-Bakkari [1,b], E. B. Al [2,c,*], A. Sali [1,d], F. Ungan[2,e]

[1] *Department of Physics, Laboratory of Solid-State Physics (LPS), Dhar El Mahraz Sidi Mohamed Ben Abdellah University, Fez 1796, Morocco.*

[2] *Department of Physics, Faculty of Science, Sivas Cumhuriyet University, 58140, Sivas, Türkiye.*

**Corresponding author*

Research Article

History
Received: 21/02/2024
Accepted: 02/05/2024

ABSTRACT

In this study, we have investigated the effects of temperature (T) and hydrostatic pressure (P) on both the nonlinear and linear optical properties of an InAs/GaAs core/shell quantum dot (QD) system with a Screened-Modified Kratzer potential (SMKP). To achieve this objective, we calculated the energy levels and their corresponding wave functions of the structure using the diagonalization method within the framework of the effective mass approximation. Analytical expressions for the absorption coefficients (ACs) and relative refractive index changes (RRICs) were derived using the compact-density-matrix approach. In our numerical calculations, we first determined the variation of the SMKP dependence, the dipole transition matrix element, and the electron energies of the ground (1s) and first excited state (1p) over a range of hydrostatic pressure (P) and temperature (T). As a result, the obtained numerical calculations revealed that changes in P and T influence both the magnitude and position of the resonant peaks that define the ACs and RRICs.

Keywords: Screened Modified Kratzer potential, Temperature, Hydrostatic pressure, Nonlinear optical properties.

[a] *mohammed.jaouane@gmail.com* *https://orcid.org/0000-0002-5779-8055*
[b] *elbakkari.kamal@gmail.com* *https://orcid.org/0000-0003-3649-7373*
[c] *emrebahadiral@hotmail.com* *https://orcid.org/0000-0003-4435-2879*
[d] *sali_ahm@hotmail.com* *https://orcid.org/0000-0003-4153-3404*
[e] *fungan@cumhuriyet.edu.tr* *https://orcid.org/0000-0003-3533-4150*

Introduction

Quantum confinement, observed in low-dimensional systems such as quantum wells [1,2], quantum wires [3], and quantum dots (QDs) [4], gives rise to novel properties. Particularly noteworthy are QDs, which possess naturally occurring atomic-like discrete energy levels. These physical attributes can be manipulated and fine-tuned by adjusting their size, composition, and even their shapes, which encompass a diverse range including approximations of spheres [5,6], rings [7], cubes [8,9], cylinders [10,11], pyramids [12], and ellipsoids [13]. QDs have captured the attention of numerous researchers in both experimental and theoretical [14] realms, rendering them valuable for an array of advanced optoelectronic and quantum devices. Such applications span from solar cells, lasers, batteries, and energy storage systems to light-emitting diodes, transistors, and beyond.

The QDs can be synthesized using a range of semiconductor materials. Within the realm of III-V semiconductors, indium arsenide (InAs) has garnered substantial significance and stands out as the most extensively utilized material for QD fabrication. In the form of a thin layer, InAs can be grown on GaAs substrates despite a notable lattice mismatch of approximately 6.8% [15]. The InAs/GaAs QD structure can be produced using various growth modes, including the Stranski-Krastanov (S-K) mode and the sub-monolayer (SML) mode, both referred to as self-assembled QDs [16]. The application of hydrostatic pressure and temperature to InAs/GaAs QDs renders them versatile materials, finding widespread utility in optical communications [17], laser technology [18], infrared detectors, and quantum-dot diodes [19].

Following the 1960 invention of the laser, nonlinear optics, a sub-discipline within modern optics, has found widespread applications. The behavior of materials in nonlinear optics can be characterized by macroscopic parameters, notably the refractive index and absorption coefficient, both of which are functions of the amplitude of the incident light's electric field [20]. In light of this, numerous scholars have directed their attention in recent years towards the study of these properties. For instance, Al et al. conducted an investigation into the nonlinear optical properties of a double GaAs/$Al_{1-x}Ga_xAs$ QW [21]. Ungan et al. [22] undertook simulations to examine the impact of electric and magnetic fields on nonlinear optical rectification, while Jaouane et al. [23] analyzed numerical outcomes concerning the nonlinear optical properties of multilayer cylindrical QDs. Jaouane et al. [24] conducted simulations to study the optical properties of allowed transitions, specifically the 1s-1p transition, within CdSe/ZnTe core/shell QDs using the screened modified Kratzer potential. Additionally, Edet et al. [25,26] explored the influence of magnetic fields and quantum confinement parameters on the optical properties of GaAs spherical QDs with the screened modified Kratzer potential in their papers. These properties have formed the fundamental basis for a variety of optoelectronic

devices, including far-infrared photodetectors, optical switches, far-infrared laser amplifiers, and optical modulators.

The purpose of this paper is to explore nonlinear optical properties by solving the Schrödinger equation, which describes electron states within quantum dots (QDs). This investigation is grounded in a modeling approach that employs the Screened Modified Kratzer potential (SMKP) to depict quantum confinement. In this context, we initially assessed how changes in temperature and hydrostatic pressure affect the energy eigenvalues and eigenfunctions of an InAs/GaAs core-shell quantum dot enclosed by the SMKP potential. This assessment was conducted using the diagonalization method within the framework of the effective mass approach. Subsequently, we utilized these energy eigenvalues and eigenfunctions to determine the absorption coefficients and refractive index changes of the system. The paper will be organized as follows: Section 2 will be dedicated to our theoretical model. In Section 3, we will present our numerical results along with their analysis, and a comprehensive summary will be provided in Section 4.

Theory

Schrödinger's wave equation

In this study, we considered a QD with SMKP. While $InAs$ forms the core of QD, the shell material is chosen as $GaAs$. We examined the system under pressure (P) and temperature (T) effects. Under these effects, within the framework of the effective mass approach, the Hamiltonian in spherical coordinates for the confined electron takes the form [26]

$$H = -\frac{\hbar^2}{2m^*(P,T)r^2}\left[\frac{\partial}{\partial r}\left(r^2\frac{\partial}{\partial r}\right) + \frac{1}{\sin\theta}\frac{\partial}{\partial\theta}\left(\sin\theta\frac{\partial}{\partial\theta}\right) + \frac{1}{\sin^2\theta}\frac{\partial^2}{\partial\phi^2}\right] + V(r,P,T), \quad (1)$$

where, $\hbar$ is the reduced Planck constant and $m^*(P,T)$ is the conduction band electron effective mass for the Γ valley, which is given by Vurgaftman formula depending on the hydrostatic pressure and temperature as [27,28]

$$(P,T) = \frac{m_0}{1+2\gamma+\left[\frac{E_P^\Gamma\left(E_g^\Gamma+\frac{2}{3}\Delta_{SO}\right)}{E_g^\Gamma\left(E_g^\Gamma+\Delta_{SO}\right)}\right]}, \quad (2)$$

where m_0 is the free electron mass, γ is the Kane parameter, E_P^Γ is the energy associated with the momentum matrix element at Γ, Δ_{SO} is the spin-orbit splitting, and E_g^Γ is the energy gap at Γ defined by the empirical Varshni expression depending on pressure and temperature as [28,29]

$$E_g^\Gamma(P,T) = E_g^\Gamma(0,0) - \frac{\alpha T^2}{\beta+T} + DP, \quad (3)$$

where, $E_g^\Gamma(0,0)$ is the energy gap at $P = 0\ kbar$ and $T = 0\ K$, where D is the pressure coefficient and α and β are the temperature coefficients. All parameters used in our calculations for InAs and GaAs are listed in Table 1.

Table 1. Parameters accepted in our simulations for GaAs and InAs.

Parameters	*InAs*	*GaAs*
$E_g^\Gamma(0,0)\ (meV)$	533	1519
$\alpha\ (meV/K)$	0.276	0.5405
$\beta\ (K)$	83	204
$D\ (meV/kbar)$	7.7	10.8
$\Delta_{SO}\ (meV)$	390	341
$E_P^\Gamma\ (meV)$	21500	28800
γ	-2.9	-1.94

$V(r,P,T)$ given in Eq. (1) is the spherically symmetrical SMKP and it is given as a function of hydrostatic pressure and temperature by [24,25,30],

$$V(r,P,T) = V_c(P,T)\left(q - \frac{r_e e^{-ar}}{r}\right)^2, \quad (4)$$

where, $V_c(P,T) = Q_c\left[E_g^\Gamma(GaAs) - E_g^\Gamma(InAs)\right]$, ($Q_c = 0.7$) is the dissociation energy between InAs and GaAs materials, r_e is the internuclear distance, a is the screening parameter, and q is the control parameter.

In the presence of pressure and temperature, the energy levels and their associated wave functions are obtained with the three-dimensional Schrödinger equation corresponding to the Hamiltonian in Eq. (1) within the framework of the envelope function approach:

$$H\psi_{nlm}(r,\theta,\phi) = E_{nlm}\psi_{nlm}(r,\theta,\phi), \quad (5)$$

where, n, l, and m are the principal, angular and magnetic momentum quantum numbers, respectively. This three-dimensional Schrödinger equation of the system under consideration cannot be solved analytically under the effects of pressure and temperature. Therefore, we have to use the diagonalization method to calculate direct numerical solutions such as energy eigenvalues and envelope wave functions. Thus, the solutions of Eq. (5) can be obtained by the approach based on the extension of electronic states on a complete orthogonal basis in the form

$$\psi_{nlm}(r,\theta,\phi) = \sum_{j=1} c_{n_j}\psi^{(0)}_{n_jlm}(r,\theta,\phi) \quad (6)$$

where, c_n is the expansion coefficient and the electronic states are categorized according to certain l and m values. $\psi^{(0)}_{nlm}(r,\theta,\phi)$ is the total wave function describing the motion of the electron and the exact solution for an electron in a spherical QD with infinite potential is given by

$$\psi^{(0)}_{nlm}(r,\theta,\phi) = \varphi^{(0)}_{nl}(r)Y_{lm}(\theta,\phi), \quad (7)$$

here, $\varphi_{nl}^{(0)}(r)$ is the radial part of the electron eigenfunction and it is given by

$$\varphi_{nl}^{(0)}(r) = \begin{cases} Nj_l(k_n r), & r < r_I \\ 0, & r \geq r_I, \end{cases} \quad (8)$$

where N is the normalization constant, k_n is the nth root of the lth order spherical Bessel function-j_l, and $r_I = 20\ nm$ is the radius of the infinite spherical QD. $Y_{lm}(\theta, \phi)$ in Eq. (7) are spherical harmonics.

Optical properties

After obtaining the energies and their associated envelope wave functions, the effects of pressure and temperature on the ACs and RRICs can be calculated using the density matrix approach. In this study, we use electromagnetic radiation polarized in the z direction. This electromagnetic radiation is considered as

$$E(t) = E_0 \cos \omega t = \bar{E} e^{i\omega t} + \bar{E}^* e^{-i\omega t}, \quad (9)$$

where $\bar{E}$ and ω are the amplitude and angular frequency of the electric field, respectively.

In the two-level system approach, the linear and third-order nonlinear ACs are given respectively by [24]

$$\alpha^{(1)}(\omega) = \sqrt{\frac{\mu}{\varepsilon_r}} \frac{\sigma_s |M_{12}|^2 \hbar\omega \Gamma_{12}}{(E_{12} - \hbar\omega)^2 + (\hbar\Gamma_{12})^2} \quad (10)$$

and

$$\alpha^{(3)}(\omega, I) = -\sqrt{\frac{\mu}{\varepsilon_r}} \frac{2I}{n_r \varepsilon_0 c} \frac{\sigma_s |M_{12}|^4 \hbar\omega \Gamma_{12}}{[(E_{12} - \hbar\omega)^2 + (\hbar\Gamma_{12})^2]^2} \left[1 - \frac{\delta_{12}^2}{4|M_{12}|^2} \frac{3E_{12}^2 - 4E_{12}\hbar\omega + \hbar^2(\omega^2 - \Gamma_{12}^2)}{E_{12}^2 + (\hbar\Gamma_{12})^2}\right], \quad (11)$$

where, $\mu = 4\pi \times 10^{-7}\ H/m$ is the magnetic permeability of the vacuum, $\varepsilon_r = \sqrt{\varepsilon_r(InAs)\varepsilon_r(GaAs)}$ is the average dielectric constant of the QD material, σ_s is the volume density of the carriers in the system, $I = 2\varepsilon_0 n_r c |\bar{E}|^2$ represents the incident optical intensity, $n_r = \sqrt{\varepsilon_r}$ is the refractive index, $\varepsilon_0 = 8.854 \times 10^{-12}\ F/m$ is the dielectric constant of vacuum, c is the speed of light in vacuum, $\delta_{12} = |M_{11} - M_{22}|$ is the mean electron displacement, $M_{12} = \langle \psi_1 | er | \psi_2 \rangle$ are the off-diagonal matrix elements of the electric dipole moment, $E_{12} = E_2 - E_1$ is the intraband transition energy between the first excited state and the ground state, $\hbar\omega$ is the incident photon energy, $\Gamma_{12} = 1/T_{12}$ is the relaxation ratio between the ground and excited state and T_{12} is the damping term associated with the lifetime of the electron involved in the transitions.

The total AC is given as

$$\alpha(\omega, I) = \alpha^{(1)}(\omega) + \alpha^{(3)}(\omega, I) \quad (12)$$

By the same approach, linear, third-order nonlinear and total RRICs are given respectively with [31]

$$\frac{\Delta n^{(1)}(\omega)}{n_r} = \frac{1}{2n_r^2 \varepsilon_0} \frac{\sigma_s (E_{12} - \hbar\omega) |M_{12}|^2}{(E_{12} - \hbar\omega)^2 + (\hbar\Gamma_{12})^2}, \quad (13)$$

$$\frac{\Delta n^{(3)}(\omega, I)}{n_r} = -\frac{\mu c I \sigma_s |M_{12}|^4}{n_r^3 \varepsilon_0} \frac{E_{12} - \hbar\omega}{[(E_{12} - \hbar\omega)^2 + (\hbar\Gamma_{12})^2]^2} \left[1 - \frac{\delta_{12}^2 \left[E_{12}^2 - E_{12}\left(\hbar\omega + \frac{(\hbar\Gamma_{12})^2}{E_{12} - \hbar\omega}\right) - 2(\hbar\Gamma_{12})^2\right]}{4|M_{12}|^2 [E_{12}^2 + (\hbar\Gamma_{12})^2]}\right] \quad (13)$$

and

$$\frac{\Delta n(\omega, I)}{n_r} = \frac{\Delta n^{(1)}(\omega)}{n_r} + \frac{\Delta n^{(3)}(\omega, I)}{n_r}, \quad (14)$$

The intraband optical transition probability amplitude between two electronic states, such as lowest and first excited, is proportional to the matrix element of the electric dipole moment. Except for the selection rules $\Delta l = \pm 1$ and $\Delta m = 0, \pm 1$, the matrix elements of the electric dipole moment become 0. Therefore, in this study, we consider the transition between the $1s$ ($l = 0, m = 0$) and $1p$ ($l = 1, m = 0$) electron states.

Results and discussions

The aim of this study is to adjust and optimize the ACs and RRICs in a QD system with SMKP under the effects of applied pressure and temperature. The parameters adopted in our calculations are as follows: $r_e = 0.5$, $a = 0.05$, $q = 1.1$, $\varepsilon_r(InAs) = 15.15$, $\varepsilon_r(GaAs) = 12.88$, $T_{12} = 0.5\ ps$, $\sigma = 3 \times 10^{22}\ m^{-3}$ and $I = 50\ MW/m^2$.

In this section, we explore the influences of temperature and pressure on the linear and nonlinear optical properties of core/shell QDs with SMKP. Firstly, we have plotted the shape of the SMKP given by Eq. (4) and the electron probability density of the first two states ($1s$ and $1p$) against the distance r for different values of P, where the temperature is set to be $T = 0\ K$ in Figure 1a and for different values of T at $P = 0\ kbar$ in Figure 1b. This figure clearly shows that the $V(r)$ has a local minimum at a critical distance r_c. This minimum value shifts to the left side (lower values of r) with an increment of the hydrostatic pressure (Figure 1a). It caused by the shrinkage of the QD size under the pressure. Whereas the r_c moves to the right side (higher values of r) with the increase of the temperature (Figure 1b), resulting from the extension of interatomic distance due to rising of temperature. In addition, it can be confirmed that the effects of P and T on the $V(r, P, T)$ are not significant for smaller values of the r, due to the strong confinement effect in these regions. Additionally, it can be seen that an enhance in the hydrostatic pressure causes an increase in the well depth, while an increase in the temperature causes a decrease, and therefore, the area localization of the electron is increased (decreased) with the increase of the hydrostatic pressure (temperature), which is totally agree with the results of the electron probability density reported in the same figure. These results show clearly that the influences of the temperature and pressure have a significant impact in the nonlinear and linear optical properties in the core/shell QDs with SMKP.

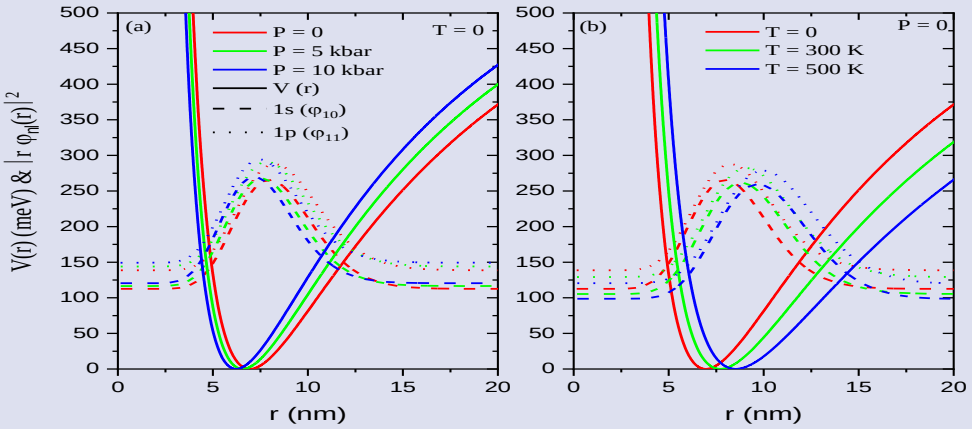

Figure 1. Profiles of SMKP (solid line) and the electron probability density of the first two states $1s$ (dashed line) and $1p$ (pointed line) as a function of r for different values of P $(0, 5\ and\ 10\ kbar)$ at $T = 0K$ (a), and for different values of T $(0, 300$ and $500\ K)$ at $P = 0\ kbar$ (b).

To understand how the energy eigenvalues of electrons change with temperature and pressure, we have plotted Figure 2 the electron energies of the ground 1s and first excited state 1p versus temperature for different values of P. It is clearly seen that the values of the first excited state are higher than those of the ground one, due to the feeble confinement of the electron wave function in the latter, which is confirmed in the results in Figure 1 related to the electron density probability. Furthermore, we can notice that for a fixed value of the T, the rise in hydrostatic pressure increases the energy eigenvalues. This result is due to the augmentation of the electron effective mass and the height of the SMKP with the pressure. On the other hand, for a given value of applied P, the electron energies of the first two states decreases with an increase in the T. This behavior can be explained as follows: An increase in temperature leads to an extension of the interatomic distance, which in turn diminishes the gap energy, thereby reducing quantum confinement [23]. Moreover, as the temperature takes high values, the Bohr radius is increased due to the reducing effective mass. In addition, the contribution of the temperature increases the thermal agitation in the system which can increase the energy of the electron. Therefore, the value of the Rydberg constant decreases, which in turn diminishes the height of the barrier potential. As a consequence, the electron becomes less confined, and the energy eigenvalues decreases with the T.

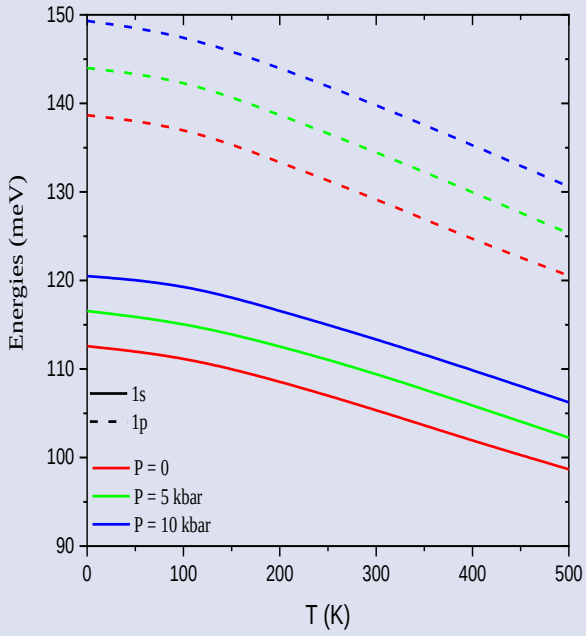

Figure 2. Electron energies of the ground state $1s$ (solid line) and first excited state $1p$ (dashed line) versus the temperature for different values of P $(0, 5\ and\ 10\ kbar)$.

Before presenting our numerical results of the ACs and RRICs in a QD system with SMKP, it is useful to make a study of the changes in the difference energy E_{12} as well as in the electric dipole moment matrix element M_{12}. For this reason, the variation in the E_{12} and M_{12} versus the temperature for three different values of P have been plotted in Figure 3a and Figure 3b respectively. It can be observed that for a given value of T, the transition energy increases when the pressure is enhanced. A comparable behavior was noticed in δ–doped quantum well in $GaAs$ [32]. This is because that the hydrostatic pressure creates

an additional confinement, which makes the electron more confined in the dot and the E_{12} increases with P.

While the opposite occurs in the case of temperature, as it increases, the extension between the energy levels reduces due to diminishing of quantum confinement, making energy transitions less important. This outcome has also been reported Ref. [33].

Furthermore, the observation in Figure 3b shows that for a fixed value of P, the increase of temperature enhances the dipole moment matrix element, which is proportional to the overlap of the electron wavefunctions, the ground and excited states (see Figure 1) consequently, the M_{12} is increased with increasing the temperature. In addition, for a fixed value of T, if the hydrostatic pressure rises, the reverse happens and the M_{12} decreases. This kind of outcome has also been described in different geometries by some authors [34–36]. The reduction in the dipole matrix element with respect to pressure (P) can be explained by the decrease in the area where the electron is localized in our system. This is mainly due to the increase in the depth of the SMKP, as demonstrated in Figure 1b.

To explore the dependence of the optical properties on the external perturbations (P and T) in a QD system with SMKP, we have drawn in Figure 4 the calculation results of the nonlinear (dotted), linear (dashed) and total (solid) ACs for the $1s \rightarrow 1p$ allowed transition, versus the incident photon energy $\hbar\omega$ for various values of pressure at $T = 0\,K$ (Figure 4a) and for different values of temperature at $P = 0$ kbar (Figure 4b). We can note from Eqs. (10) and (11) that the E_{12} and M_{12} are two significant parameters in the determining of ACs. Indeed, the ACs has a maximum value when the incoming photon energy $\hbar\omega$ coincides with the transition energy E_{12}, which is referred as the resonance photon energy and the amplitudes of ACs peaks are proportional to M_{12}. Furthermore, it can be clearly seen from this figure that the hydrostatic pressure P induces a blueshift of the peak of the ACs. These outcomes can be explained in the following way: The application of hydrostatic pressure reinforces the quantum confinement of the electron in the QD and leads to stretching the quantized energy levels hence the growth the energy transition. This is in good agreement with the findings obtained in Figure 3 and also those of Ref. [35].

Additionally, the value of the ACs reduces as the pressure rises from 0 to 10 $kbar$. The physical reason of this result is that as the P goes up, the electron wave functions are extremely confined inside the QD. This outcome is in agreement with Ref. [34]. However, in contrast to the P effect, the amplitude of the resonant peaks of the ACs increases with increasing T from 0 to $500\ K$ as shown in Figure 4b. The reason for this behavior is that the value of the M_{12} increases with T (see Figure 3b). Another finding is that the position of the resonant peaks displays a shift toward the lower incident photon energy as the T increases. This redshift comes from diminishing the confinement potential and effective mass of the electron with growing of the temperature. All these descriptions can be understood by observing the variation of the numerical values of M_{12} and E_{12} with the P and T in the Figure 3.

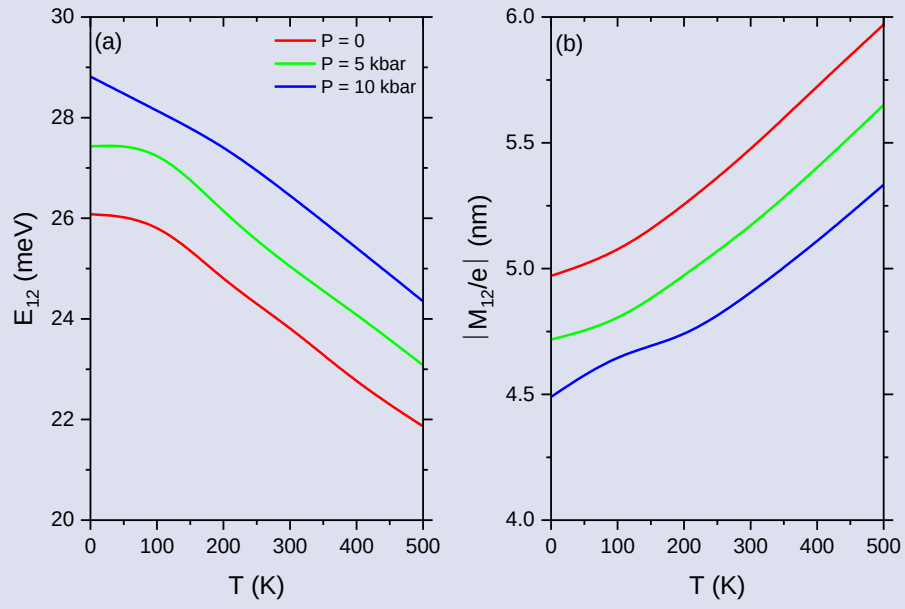

Figure 3. Shows (a) the intraband transition energy between the $1p$ state and the $1s$ state versus temperature, and (b) the matrix elements of the electric dipole moment as a function of T, for different values of P.

In order to investigate the influence of variations of the P and T on the relative refractive index changes, we have computed in Figure 5 the variation of the nonlinear (dotted), linear (dashed) and total (solid) RRICs for the $1s \rightarrow 1p$ against the incident photon energy $\hbar\omega$. The exploited parameters are similar as in the previous Figure

4. This figure clearly displays that the RRICs are related to the hydrostatic pressure and temperature. By increasing the pressure (temperature), maxima and minima of the RRICs decrease (increase) and the peak position shifts toward higher (lower) energies. This is because the transition energy difference E_{12} increases (decreases) when the P (T) rises. Because the physical parameters such as electron effective mass and barrier height increases (decrease) with the P (T). These numerical results are well-matched with the variation of ACs under the effects of P and T in Figure 4. These characteristics make QDs very promising candidates for nonlinear optical materials.

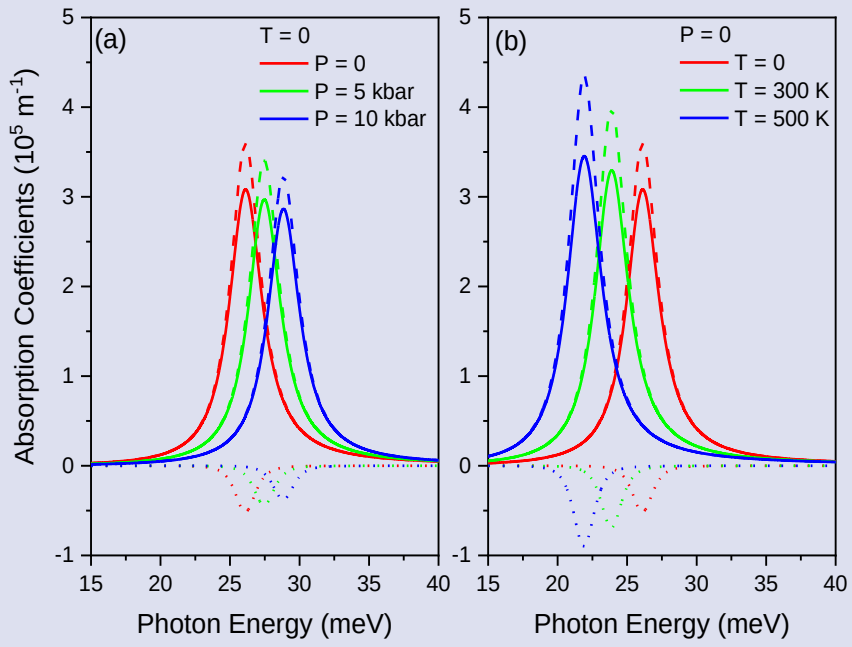

Figure 4. Plot of nonlinear, linear, and total ACs for allowed optical transition 1s→1p against the photon energy for three diverse values of pressures (a) and temperatures (b).

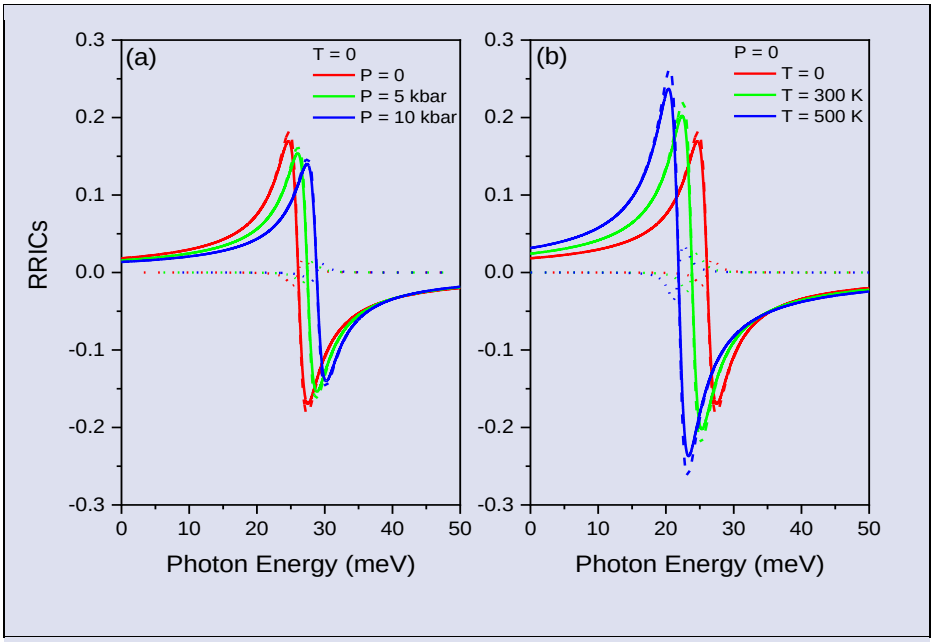

Figure 5. Plot of nonlinear, linear, and total RRICs for the $1s \rightarrow 1p$ transition against the photon energy for three diverse values of pressures (a) and temperatures (b).

Conclusion

In this work, a numerical calculation has been performed to examine the effects of temperature and pressure on the electron probability density of $1s$ and the $1p$ states, transition energy of the electron, dipole moment matrix element, nonlinear and linear ACs and RRICs of a $InAs/GaAs$ core/shell QD system. The electronic quantum confinement is modeled by the SMKP. To derive the wave functions and their associated energy levels, the Schrödinger equation was resolved by diagonalization method. Numerical outcomes reveal that the depth of SMKP, E_{12}, M_{12}, ACs and RRICs of our system are strongly influenced by the variation of the temperature and pressure. It was obtained that the ACs and RRICs are related to the pressure and temperature. As the pressure (temperature) increases, the resonance peaks of ACs and RRICs decrease (increase) and also shift towards higher (lower) energies. It has also been exposed that the effects of P and T on the depth of SMKP are significant in large distance r of QD.

Acknowledgments

M. Jaouane, K. El-Bakkari and A. Sali wrote the “Abstract”, “Introduction”, “Results and discussion”, and “Conclusion” sections of the article.

E. B. Al wrote the program, got the results, drew the graphs, wrote the “Theory” section and edited the article.

F. Ungan determined the problem and the title and edited the article.

Conflicts of interest

There are no conflicts of interest in this work.

Data Availability Statement

Data will be made available on reasonable request.

References

[1] Yesilgul U., Ungan F., Sakiroglu S., Sari H., Kasapoglu E., Sökmen I., Nonlinear optical properties of a semi-exponential quantum wells: Effect of high-frequency intense laser field, *Optik (Stuttg).,* 185 (2019) 311–316.

[2] Belaid W., El Ghazi H., Zaki S.E., Basyooni M.A., Tihtih M., Ennadir R., Kılıç H.Ş., Zorkani I., Jorio A., A theoretical study of the effects of electric field, hydrostatic pressure, and temperature on photoionization cross-section of a donor impurity in (Al, Ga)N/AlN double triangular quantum wells, *Phys. Scr.,* 98 (2023) 045913.

[3] Sali A., Fliyou M., Satori H., Loumrhari H., Photoionization of Impurities in Quantum-Well Wires, *Phys. Status Solidi.,* 211 (1999) 661–670.

[4] Sali A., Satori H., The combined effect of pressure and temperature on the impurity binding energy in a cubic quantum dot using the FEM simulation, *Superlattices Microstruct.,* 69 (2014) 38–52.

[5] Fakkahi A., Sali A., Jaouane M., Arraoui R., Hydrostatic pressure, temperature, and electric field effects on the hydrogenic impurity binding energy in a multilayered spherical quantum dot, *Appl. Phys. A.,* 127 (2021) 908.

[6] Fakkahi A., Sali A., Jaouane M., Arraoui R., A. Ed-Dahmouny, Study of photoionization cross section and binding energy of shallow donor impurity in multilayered spherical quantum dot, *Physica E*., 143 (2022) 115351.

[7] El-Bakkari K., Sali A., Iqraoun E., Ezzarfi A., Polaron and conduction band non-parabolicity effects on the binding energy, diamagnetic susceptibility and polarizability of an impurity in quantum rings, *Superlattices Microstruct.,* 148 (2020) 106729.

[8] Arraoui R., Sali A., Ed-Dahmouny A., Jaouane M., Fakkahi A., Polaronic mass and non-parabolicity effects on the photoionization cross section of an impurity in a double quantum dot, *Superlattices Microstruct*., 159 (2021) 107049.

[9] Ed-Dahmouny A., Sali A., Es-Sbai N., Arraoui R., Jaouane M., Fakkahi A., El-Bakkari K., Duque C.A., Combined effects of hydrostatic pressure and electric field on the donor binding energy, polarizability, and photoionization cross-section in double GaAs/Ga 1-x Al x As quantum dots, *Eur. Phys. J. B*., 95 (2022).

[10] Jaouane M., Sali A., Kasapoglu E., Ungan F., Tuning of nonlinear optical characteristics of a cylindrical quantum dot by external fields and structure parameters, *Philos. Mag*., (2023) 1–19.

[11] Jaouane M., Sali A., A. Ezzarfi A., A. Fakkahi A., Arraoui R., Study of hydrostatic pressure, electric and magnetic fields effects on the donor binding energy in multilayer cylindrical quantum dots, *Physica E*., 127 (2021) 114543.

[12] Jaouane M., Fakkahi A., Ed-Dahmouny A., El-Bakkari K., Tuzemen A.T., Arraoui R., Sali A., Ungan F., Modeling and simulation of the influence of quantum dots density on solar cell properties, *Eur. Phys. J. Plus*., 138 (2023) 148.

[13] Ed-Dahmouny A., Zeiri N., Fakkahi A., Arraoui R., Jaouane M., Sali A., Es-Sbai N., El-Bakkari K., Duque C.A., Impurity photo-ionization cross section and stark shift of ground and two low-lying excited electron-states in a core/shell ellipsoidal quantum dot, *Chem. Phys. Lett*., 812 (2023) 140251.

[14] Tiutiunnyk A., Tulupenko V., Mora-Ramos M.E., Kasapoglu E., Ungan F., Sari H., Sökmen I., Duque C.A., Electron-related optical responses in triangular quantum dots, *Physica E*., 60 (2014) 127–132.

[15] Li G.H., Goñi A.R., Abraham C., Syassen K., Santos P.V., Cantarero A., Brandt O., Ploog K., Photoluminescence from strained InAs monolayers in GaAs under pressure, *Phys. Rev. B*., 50 (1994) 1575–1581.

[16] Du Park G., Du Ha J., Kang T.I., Kim J.S., Kim Y., Lee S.J., Han I.S., Investigation of junction electric fields for InAs quantum dot solar cells with photoreflectance spectroscopy, *Curr. Appl. Phys*., 50 (2023) 46–52.

[17] Zhou P.Y., Dou X.M., Wu X.F., Ding K., Li M.F., Ni H.Q., Niu Z.C., Jiang D.S., Sun B.Q., Single-photon property characterization of 1.3 μm emissions from InAs/GaAs quantum dots using silicon avalanche photodiodes, *Sci. Rep*., 4 (2014) 3633.

[18] Bimberg D., Ledentsov N.N., Grundmann M., Kirstaedter N., Schmidt O.G., Mao M.H., Ustinov V.M., Egorov A.Y., Zhukov A.E., Kopév P.S., Alferov Z.I., Ruvimov S.S., Gösele U., Heydenreich J., InAs-GaAs quantum pyramid lasers: In situ growth, radiative lifetimes and polarization properties, *Japanese J. Appl. Physics*., 35 (1996) 1311–1319.

[19] Wang T., Lee A., Tutu F., Seeds A., Liu H., Jiang Q., Groom K., Hogg R., The effect of growth temperature of GaAs nucleation layer on InAs/GaAs quantum dots monolithically grown on Ge substrates, *Appl. Phys*. Lett., 100 (2012) 052113.

[20] Li C., Nonlinear Optics, Springer Singapore, Singapore, 2017.

[21] Al E.B., Ungan F., Yesilgul U., Kasapoglu E., Sari H., Sökmen I., Effects of applied electric and magnetic fields on the nonlinear optical properties of asymmetric GaAs/Ga1-xAlxAs double inverse parabolic quantum well, *Opt. Mater.,* 47 (2015) 1–6.

[22] Ungan F., Martínez-Orozco J.C., Restrepo R.L., Mora-Ramos M.E., Kasapoglu E., Duque C.A., Nonlinear optical rectification and second-harmonic generation in a semi-parabolic quantum well under intense laser field: Effects of electric and magnetic fields, *Superlattices Microstruct.,* 81 (2015) 26–33.

[23] Jaouane M., Sali A., Fakkahi A., Arraoui R., Ungan F., The effects of temperature and pressure on the optical properties of a donor impurity in (In,Ga)N/GaN multilayer cylindrical quantum dots, *Micro and Nanostructures*, 163 (2022) 107146.

[24] Jaouane M., El-Bakkari K., Al E.B., Sali A., Ungan F., Linear and nonlinear optical properties of CdSe/ZnTe core/shell nanostructures with screened modified Kratzer potential, *Eur. Phys. J. Plus*., 138 (2023) 319.

[25] Edet C.O., Al E.B., Ungan F., Ali N., Ramli M.M., Asjad M., Effects of the confinement potential parameters and optical intensity on the linear and nonlinear optical properties of spherical quantum dots, *Results Phys*., 44 (2023) 106182.

[26] Edet C.O., Al E.B., Ungan F., Ali N., Rusli N., Aljunid S.A., Endut R., Asjad M., Effects of Applied Magnetic Field on the Optical Properties and Binding Energies Spherical GaAs Quantum Dot with Donor Impurity, *Nanomaterials*., 12 (2022) 2741.

[27] Makhlouf D., Choubani M., Saidi F., Maaref H., Applied electric and magnetic fields effects on the nonlinear optical rectification and the carrier's transition lifetime in InAs/GaAs core/shell quantum dot, *Mater. Chem. Phys*., 267 (2021) 124660.

[28] Makhlouf D., Choubani M., Saidi F., Maaref H., Modeling of the second harmonic generation in a lens-shaped InAs/GaAs quantum core/shell dot under temperature, pressure and applied electric field effects, *Results Phys*., 16 (2020) 102961.

[29] Makhlouf D., Choubani M., Saidi F., Maaref H., Applied electric and magnetic fields effects on the nonlinear optical rectification and the carrier's transition lifetime in InAs/GaAs core/shell quantum dot, *Mater. Chem. Phys*., 267 (2021) 124660.

[30] Edet C.O., Al E.B., Ungan F., Ali N., Rusli N., Aljunid S.A., Endut R., Asjad M., Effects of Applied Magnetic Field on the Optical Properties and Binding Energies Spherical GaAs Quantum Dot with Donor Impurity, *Nanomaterials*., 12 (2022) 2741.

[31] Al E.B., Peter A.J., Mora-Ramos M.E., Ungan F., Theoretical investigation of nonlinear optical properties of Mathieu quantum well, *Eur. Phys. J. Plus*, 138 (2023) 49.

[32] Oubram O., Rodríguez-Vargas I., Martínez-Orozco J.C., Refractive index changes in n-type delta-doped GaAs under hydrostatic pressure, *Rev. Mex. Fis*., 60 (2014) 161–167.

[33] Liang S., Xie W., Effects of the hydrostatic pressure and temperature on optical properties of a hydrogenic impurity in the disc-shaped quantum dot, *Physica B*., 406 (2011) 2224–2230.

[34] Farkoush B.A, Safarpour G., Zamani A., Linear and nonlinear optical absorption coefficients and refractive index changes of a spherical quantum dot placed at the center of a cylindrical nano-wire: Effects of hydrostatic pressure and temperature, *Superlattices Microstruct*., 59 (2013) 66–76.

[35] Rezaei G., Kish S.S., Linear and nonlinear optical properties of a hydrogenic impurity confined in a two-dimensional quantum dot: Effects of hydrostatic pressure, external electric and magnetic fields, *Superlattices Microstruct.,* 53 (2013) 99–112.

[36] Zhang Z.H., Yuan J.H., Guo K.X., The combined influence of hydrostatic pressure and temperature on nonlinear optical properties of GaAs/Ga0.7Al0.3As morse quantum well in the presence of an applied magnetic field, *Materials*., 11 (2018) 668.

Cumhuriyet Sci. J., 45(2) (2024) 394-399
DOI: https://doi.org/10.17776/csj.1408773

Cumhuriyet Science Journal

| csj.cumhuriyet.edu.tr | Founded: 2002 ISSN: 2587-2680 e-ISSN: 2587-246X Publisher: Sivas Cumhuriyet University

Orange Emitting SrS: Eu^{2+}, Dy^{3+} Afterglow Phosphor: Structural and Luminescence Properties

Eren Cihan Karsu Asal[1,a,*] Serdar Yıldırım[2,b]

[1] *Department of Electric and Energy, Manisa Celal Bayar University, 45400 Turgutlu - Manisa, Türkiye.*

[2] *Department of Metallurgical and Materials Engineering, Dokuz Eylul University, Buca, 35390, Izmir, Türkiye.*

**Corresponding author*

Research Article

History
Received: 23/12/2023
Accepted: 01/03/2024

ABSTRACT

SrS:Eu is known as an attractive material for imaging, scintillator, or persistent phosphor applications, thanks to its effective photoluminescence (PL) and thermoluminescence (TL) capabilities, but there are still great mysteries of persistent phosphors and attract great interest. Hence, this work investigated the luminescence properties of well-known persistent phosphor based on SrS using various spectroscopic techniques for detailed characterization. Measurements using X-ray photoelectron spectroscopy (XPS) and X-ray diffraction (XRD) were used to analyze the phase and elements of the phosphor. Belongs to the XRD data the microcrystalline phosphor is cubic, and the diameters ranged from 1 to 100 µm. The morphology of the phosphor was examined by scanning electron microscope (SEM). A time-resolved PL system recorded PL properties, namely the emission and excitation spectra of the phosphor. SrS emits around 626 nm with a broad excitation band peaking around 466 nm. A TLD reader system measured the TL glow curve of the phosphors after UVB radiation. The TL glow curve exhibited a broad peak around 160°C. The dose-response of this peak was obtained up to 600 seconds of exposure to UVB radiation, and it was observed that the dose-response curve exhibits a saturating exponential behavior.

Keywords: Persistent phosphor, Thermoluminescence, Time-resolved photoluminescence, Long afterglow phosphors, XPS

[a] *eren.karsu@cbu.edu.tr* *https://orcid.org/0000-0002-0890-6099* [b] *serdar.yildirim@deu.edu.tr* *https://orcid.org/0000-0002-3730-3473*

Introduction

Persistent phosphors are phosphors that emit light even after stopping the excitation. In those phosphors, electrons are liberated by daylight and stored in impurities. Then they are spontaneously released during the nighttime to produce luminescence. The phenomenon is also called afterglow. These phosphor materials are feasible for various uses. For instance, they are used as 'glow in the dark' phosphors in luminous paints or plastics, such as signs that show escape routes in buildings, safety clothing, traffic signs, and road markings, in hospitals and dentistry, such materials, in which X-rays move the electrons to deep capture centers, have now almost entirely replaced traditional X-ray films. Nonetheless, there are not enough effective red-emitting materials. Since the strong nephelauxetic impact of an alkaline earth sulfide phosphor SrS: Eu2+ shifts Eu2+4f65d1→4f7 to red and the weak connection between strontium and sulfide, resulting from the soft base-hard acid character, generates a significant number of intrinsic defects, it remains a promising choice [1].

Alkaline earth sulfide phosphors [1] are used in a wide variety of display applications and lighting [2-5]. They are employed especially in inorganic electroluminescent devices, field emission displays, and wavelength converters in light-emitting diodes (LEDs) for solid-state lighting [2-5]. The alkaline earth sulfides, especially SrS: Eu, have been studied as an inorganic luminescence material for some time [1]. Recently, the presence of up-conversion and optical storage in SrS: Eu has taken a new interest in these phosphors [6,7].

Now one of the most successful practical photoluminescent phosphors is SrS: Eu2+, Dy3+ however, there are still strong background radiations from afterglows [8]. Since both the formation and crystallinity have a substantial impact on the luminescence curves, the first step of our investigation consists of a comprehensive analysis encompassing structural phase analysis, elemental analyses, structure morphology, and particle size. It has long been known that the crystalline phase, which is mainly caused by temperature and pressure, is responsible for all the characteristics of the luminescence phenomenon, including lifetime, efficiency, and emission spectra. Furthermore, the current study intends to achieve the following primary contributions, which are summarized as follows:

- This, in our opinion, is the first time a commercial SrS: Eu2+, Dy3+ phosphor has been thoroughly examined.
- The PL emission and excitation spectrums were studied.
- The PL emission's decay nature was measured.
- Dose response to UV radiation and fading of the glow peak studied by TL measurements.

Material and Method

The samples used in these experiments (SrS: Eu^{2+}, Dy^{3+}) were commercial persistent phosphor. To guarantee the accuracy of the data, three aliquots were utilized in each experiment rather than just one. Each aliquot is 4×10^{-2} g powder.

The samples' phases and crystal structures were identified. through a Thermo Scientific ARL- Kα X-ray diffractometer (XRD). Radiation has been produced using Cu-Kα. For qualitative testing, XRD diagrams were obtained at intervals of $20^o\leq2\theta\leq60^o$ [9,10].

XPS (Thermo-Scientific) was used to investigate the surface chemistry of all samples. It used a monochromatic Al-Kα (1486.7 eV) X-ray source with a 400 nm diameter beam. The gadget was calibrated using $4f^{7/2}$, the gold standard. The pressure was maintained during the collection of spectral data below $5x10^{-10}$ mbar. With a precision of 1 eV and a pass energy of 150 eV, the XPS data were collected between 0 and 700 eV. A single point's ten scans were recorded. The morphology was studied using a COXEM E30 [10].

The microstructures of the particles were examined with a high voltage (30 kV) accelerator and an electron microscope (COXEM EM-30+). The samples were directly attached to sample holders and coated with carbon. There was no surface polishing.

The optical characteristics were investigated using the PL method. The PL studies were performed in a Time-Correlated Single Photon Counting (TCSPC) system with a red-sensitive photomultiplier tube and a spectrofluorometer kit. For steady-state and lifespan measurements, the device was fitted with a normal 15W Xenon light and a microsecond flash bulb, respectively. Throughout the experiment, a non-fluorescing silica aerogel combination (LU-DOX 30%, Sigma Aldrich) in water was utilized to determine the Instrument Response Function (IRF).

All TL measurements were carried out using a Harshaw 3500 TLD Reader. The irradiations were applied via a UVB lamp (310 nm). All measurements were performed in a nitrogen atmosphere with a low constant heating rate of $2^oC/s$, to avoid significant temperature lag, and the samples were heated up to the maximum temperature of 350^oC. To determine the UVB dose response of the material, the following dose-response protocol was applied:

Step 0: Zero dose TL signal (ZDTL) recording

Step 1: Test Dose (TD), immediately recording the TL sensitivity up to 350^oC.

Step 2. Exposure to UVB Radiation with various periods (2-600 s.)

Step 3. TL up to 350^oC

Step 4. Repeat steps 0-4 for a new phosphor.

Result and Discussion

Both the obtained results and their description are provided below.

Using XRD, the phase purity and crystallinity of SrS: Eu^{2+}, Dy^{3+} phosphor were investigated. Figure 1 displays the XRD pattern of the SrS: Eu^{2+}, Dy^{3+} phosphor. The peaks were indexed by the International Centre for Diffraction Data (ICSD) and matched precisely with standard data.

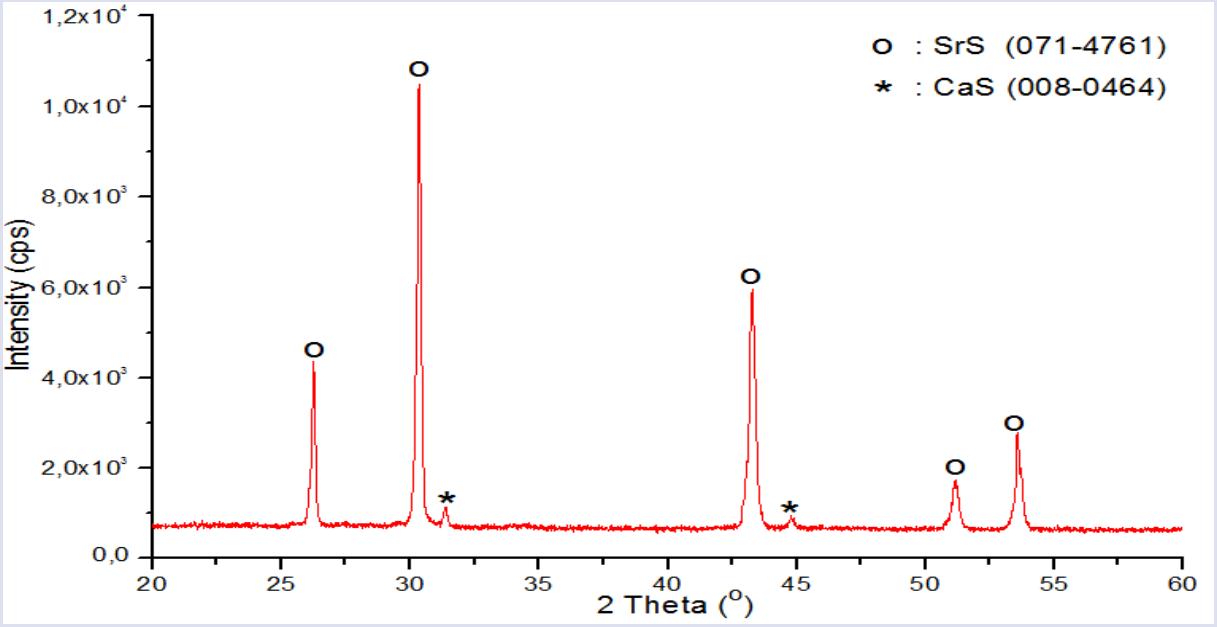

Figure 1. XRD pattern of SrS: Eu^{2+}, Dy^{3+} phosphor.

XRD Patterns are found to be characterized by peaks at 2θ values of 25°, 30°, 42°, 50.5°, and 53° corresponding to the planes (111), (200), (220), (311) and (222) (PDF card No.01-071-4761). These results are verified with already published reports [9-12]. Besides SrS, very little CaS (PDF card No.00-008-0464) phase has been identified in the structure (Figure 1). The structure is cubic.

The valence states, chemical nature, and oxidation of numerous elements in the SrS: Eu^{2+}, Dy^{3+} phosphor aliquots were characterized using XPS, as marked in Figure 2. It is a representation of the findings from the analysis and high-resolution elemental detects of the aliquot.

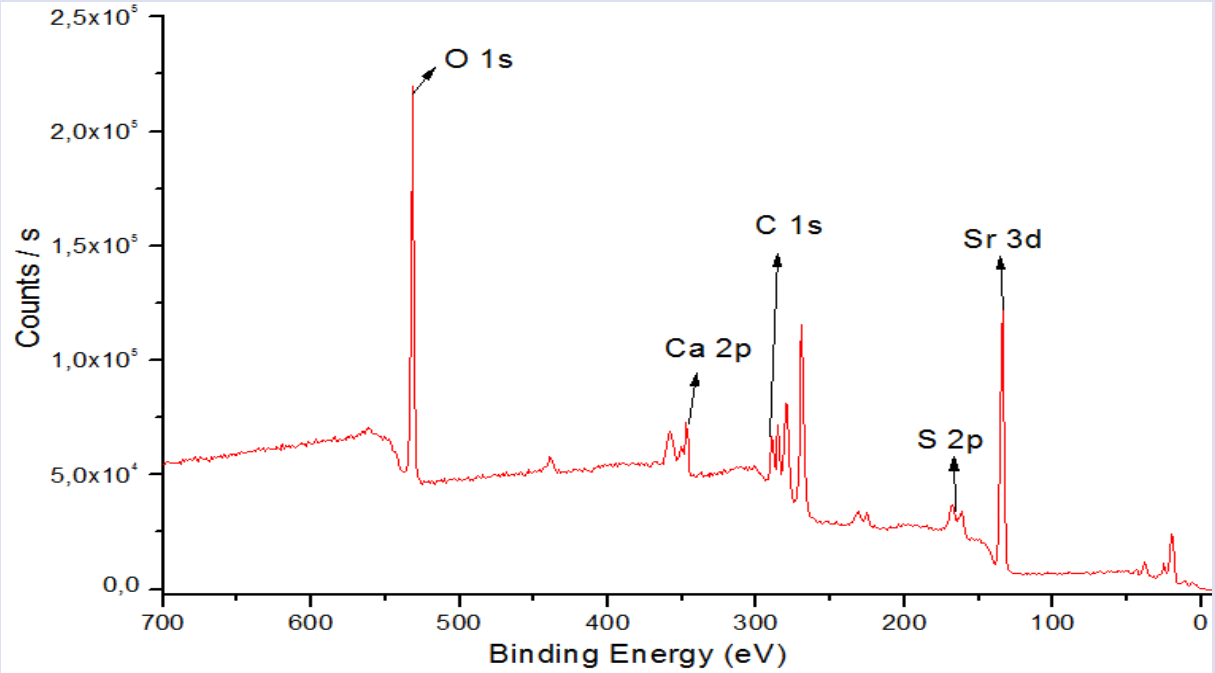

Figure 2. XPS survey spectra of SrS: Eu^{2+}, Dy^{3+} phosphor.

Figure 2 remarks on the regular XPS scanning of the aliquot. Here are the base elements of Sr, Ca, S, O, and C in material structure. The photoelectron peak of Sr 3d becomes evident at the binding energy of 134 eV. Likewise, photoelectron peaks of Ca2p, S2p, O1s, and C1s appear at 347, 167, 531, and 285 eV respectively. The XPS peaks for C1s and O1s (performing as internal standards) were observed because of the contamination from the particles and the accidental hydrocarbon from the XPS equipment. The peak positions line up with the values given in the literature [9].

The peaks obtained at the high-resolution elemental scans, the binding energies, and the weight % values of elements are given in Table 2.

Table 2: XPS outcomes of natural amazonite aliquots

Elements	*Survey Binding Energy (eV)*	*FWHM (eV)*	*Area (Peak) CPS.(eV)*	*Survey Weight (%)*
O1s	531.43	1.683	386805.76	25.21
Sr3d	134.12	3.497	298520.77	50.18
Ca2p	347.09	2.711	59128.21	5.02
S2p	167.78	4.327	63157.26	11.93
C1s	285.16	1.445	61268.59	7.65

Since the crystal structure, particle size, and morphology are important for luminescence properties

Figure 3 shows the SEM images of SrS: Eu^{2+}, Dy^{3+} phosphor powder aliquots.

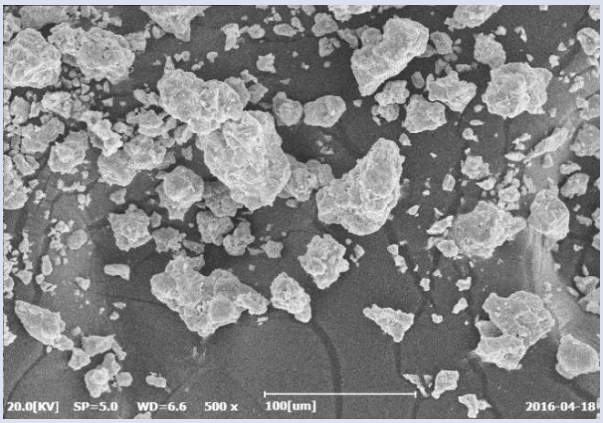

Figure 3. SEM micrograph of SrS: Eu^{2+}, Dy^{3+} phosphor with 500 magnification.

SEM patterns were used to evaluate the surface morphology (Figure 3). SEM images show that the crystal structure is not visible, most of the small particles aggregated together, and the blocky particles of phosphors had irregular morphologies with diameters ranging from 1 µm to 100 µm. These results constrict with the results of J. E. Van Haecke et al [12]

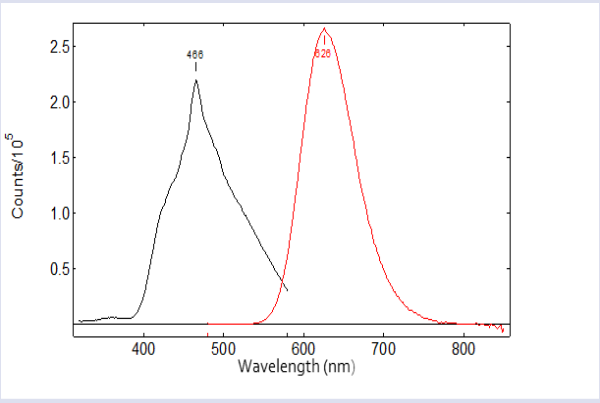

(a) Emission and excitation

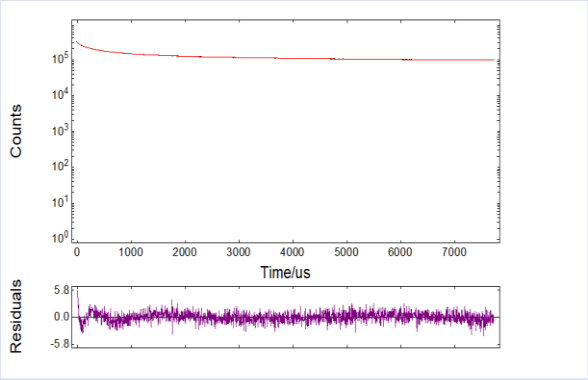

b) 8000µs 1000 channel decaying

Figure 4: (a) PL emission spectrum of SrS: Eu^{2+}, Dy^{3} phosphors. **(b)** Decay curve of SrS: Eu^{2+}, Dy^{3} phosphors

The SrS: Eu2+, Dy3+ phosphors' excitation-emission bands and the PL decay curves at room temperature are shown in Figure 4. The excitation spectrum of emission has a wide band (400- 600 nm) making a peak around 466 nm, corresponding to the host lattice transition. The electromagnetic spectrum's visible area contains the excitation range (Figure 4(a)). When excited, the emission peak appears at 550 nm giving broadband that lasts until about 750 nm. The peak of the emission was found at approximately 626 nm, in the orange portion of the visible spectrum. Both the ground state 8S7/2 of the 4f7 configuration and the excited state T2g of the 4f6 5d1 configuration are where the permitted transitions between them are responsible for the emission of Eu2+ (Laporte's Rule) [1,12]. This allowing transition of Eu2+ is different from the transitions of other activators (f-f and d-d transitions). Furthermore, this transition is due to the strong nephelauxetic effect, and the low stoke shift leading to an excitation band in the blue-green region observed. So, this phosphor is important for several applications like white LEDs [1]. No Dy3+ emission was observed because, Dy3+ does not behave as an emission centre, but supports long afterglow [13]. A long afterglow is observed. The allowed transition period of Eu2+ was determined as around 2.4 ms (Figure 4(b)). The luminescent characteristics of the powder SrS: Eu2+, Dy3+ are comparable with those of crystal aliquots [10-12]. Moreover, since the excitation peak of SrS: Eu2+, Dy3+ phosphors overlaps with the excitation peak of Hg, this phosphor has a great potential to be used for lumination.

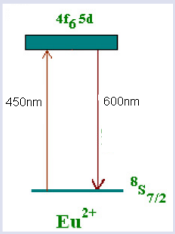

Figure 5. Energy level diagrams for a possible transition of Eu^{2+} ions for Excitation and Emissions.

In Table 3 there are three decaying durations: τ1, τ2, and τ3. The phosphor aliquots of SrS:Eu^{2+},Dy^{3+} exhibited three exponential decaying periods. Three components were identified: the long lifetime (3754.54 µs), the medium lifetime (562.99 µs), and the short lifetime (133.86 µs).

Table 3. Excitation and emission wavelength and decay time measurement outcomes of SrS: Eu2+, Dy3+ phosphor aliquots with standard deviation and percentage allocation.

Sample	Excitation wavelength (nm)	Emission wavelength (nm)	X^2		Decay Period (µs)	Standard Deviation	Rel.%
SrS: Eu^{2+}, Dy^{3+}	426	678	1.187	ζ_1	133.86	1.49459	3.56
				ζ_2	562.99	5.61877	17.41
				ζ_3	3754.54	39.49525	79.03

As a result of radiation, electrons, and holes are trapped in the band gap at local energy levels known as vacancies, interstitials, or contaminants. TL is created when they are liberated from the thermal stimulus and recombined with carriers of the opposite sign. The TL peaks' maximum and shape represent the trap's characteristics. For instance, deeper traps can be empty at higher temperatures (~200 °C), whereas shallow traps can be empty at lower temperatures (~100 °C).

The dose response to UV radiation of SrS: Eu^{2+}, Dy^{3+} is given in Figure 6. Irradiation was performed launching from very short durations and ended at 5 minutes. By increasing the irradiation duration, the height of the glow peak is increased while the speed of increasing decreases

(Figure 7). As seen in Figure 7 there is a saturation at high doses. Up to 75 seconds a linear increase was observed, but especially after 175 seconds, saturation was observed. This observed situation is reasonable. While irradiating the sample radiation affects the traps. Moreover, a shift to high temperatures was observed because of the filling of low-temperature traps with irradiation.

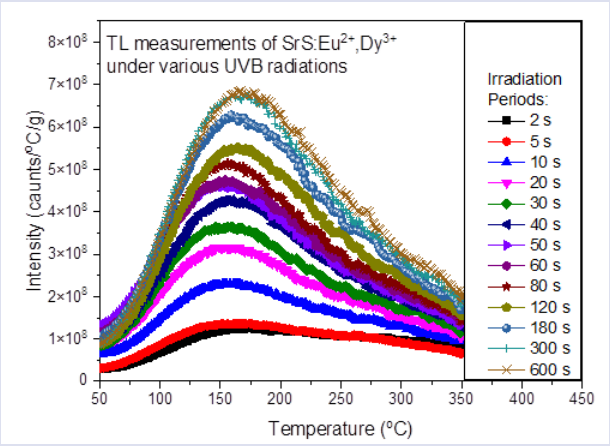

Figure 6. TL glow curves of SrS: Eu^{2+}, Dy^{3+} phosphor immediately after exposure to various UVB radiation.

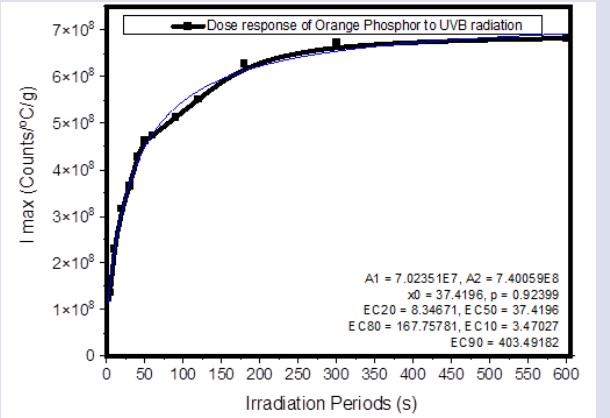

Figure 7. Dose-response curve of SrS: Eu^{2+}, Dy^{3+} phosphor to UVB radiation

To examine the fading of the phosphor, the aliquot was irradiated with 2 min UV radiation and stored in the dark for 5 days, and the TL glow peaks were recorded. As seen in Figure 8 after storing 5 days there is a great luminescence. This low fading property belongs to the cooping of Dy^{3+}

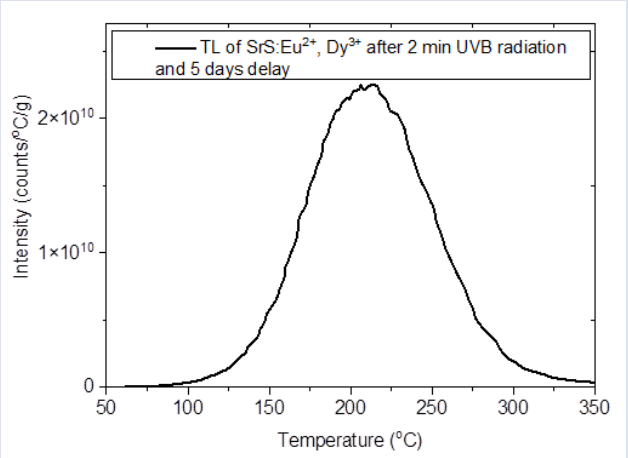

Figure 8. TL Glow curve of SrS: Eu2+, Dy3+ phosphor after 5 days storing at dark atmosphere.

Conclusions

The current conclusions can be summed up as the following:

- A comprehensive overlook of the persistent luminescence behavior of SrS: Eu^{2+}, Dy^{3+} is analyzed.
- XRD patterns indicate that peaks signify the cubic structure of SrS.
- The XPS survey spectra are in good agreement with XRD patterns, the basic elements in the material structure are Sr, Ca, S, O, and C.
- The crystal structure has block particles that bring irregular morphology with diameters ranging from 1 µm to 100 µm.
- SrS phosphors show efficient orange broad-band emission around 626 nm, which originates from the 4f–5d transitions of Eu^{2+} transitions. The co-dopant, Dy^{3+} ions, lengthened the duration of luminescence by behaving as a trapping state. They do not make any emissions. The result is well-matched with literature.
- This phosphor has storage properties, and this is because of Dy^{3+} dopants.
- The allowed transition period of Eu^{2+} was determined as around 2.4 ms.
- The dose-response of this peak was obtained up to 600 seconds of exposure to UVB radiation, and it was observed that the dose-response curve exhibits a saturating exponential behavior.
- These SrS phosphors can be used as a blue phosphor for white or full color. Thin film electroluminescent (TFEL) displays. (Surface Science 454–456 (2000) 529–533)

Conflicts of interest

There are no conflicts of interest in this work.

References

[1] Dos Santos D., Giordano L., Barbara M., Portes M., Pedroso C., Teixeira V., Lastusaari M., L. Rodrigues, Abnormal Co-doping Effect on The Red Persistent Luminescence SrS: Eu^{2+}, RE^{3+} Materials, *Dalton Transactions*, 45 (2020) 16386-16393.

[2] Roa R. P., The Preparation and Thermoluminescence of Alkaline Earth Sulfide Phosphors, *Journal of Materials Science*, 21 (1986) 3357-3386.

[3] Duan X., Huang S., You F., Kang K., Hydrothermal Preparation and Persistence Characteristics of Nanosized Phosphor SrS: Eu^{2+}, Dy^{3+}, *Journal of Rare Earths*, 27 (1) (2009) 43.

[4] Vij A., Lochabb S., Singha S., Kumar R., Singh N., Thermoluminescence Study of UV Irradiated Ce doped SrS Nanostructures, *Journal of Alloys and Compounds*, 486 (2009) 554-558.

[5] Kojima Y., Takahashi A., Umegaki T., Synthesis of Orange-red-emitting Eu^{2+}, Pr^{3+} Codoped SrS Long Afterglow Phosphor, *Journal of Luminescence*, 146 (2014) 42-45.

[6] Summers C. J., Wagner B. K., Tong W., Chaichimansour M., Xin Y. B., Recent Progress in The Development of Full Color SrS-Based Electroluminescent Phosphors, *Journal of Crystal Growth*, 214-215 (2000) 918-925.

[7] Khare A., Mishra S., Kshatri D., Tiwari S., Optical Properties of Rare Earth Doped SrS Phosphor: A Review, *Journal of Electronic Materials*, 46, (2), (2017) 687-708.

[8] Shao S., Du K., Huang K., Cheng L., Mi X., Peng Z., Lin H., Cui S., Lin T., Ba Z.and Zhang X., Rapid Synthesis and Characterization of SrS: Eu, Sm Infrared Up-Conversion Materials, *Advance Powder Technology*, 25 (2014) 1516-1519.

[9] Hu R., Zhang Y., Zhao Y., Wang X., Li G., Wang C., UV–Vis-NIR Broadband-Photo Stimulated Luminescence of $LiTaO_3$:Bi^{3+} Long-Persistent Phosphor and The Optical Storage Properties, *Chemical Engineering Journal*, 392 (2020) 124807.

[10] Kong M., Fang M., Liu M., Shang G. L., Fei G. T., Zhang L., The Investigation on The Mechanism of The Increased Decay Time in Red SrS: Eu^{2+}, Dy^{3+} Phosphor, *Materials Chemistry and Physics*, 207 (2018) 161-166.

[11] Parmentier A., Joos J., Smet P., Poelman D., Luminescence of Ytterbium in CaS and SrS, *Journal of Luminescence*, 154 (2014) 445-451.

[12] Singh V., Tiwari M., Dhoble S., Luminescence studies of SrS and CaS based Phosphors, *Indian Journal of Pure & Applied Physics*, 43 (2005). 1000-1003.

[13] Dobrowolska A., Karsu E. C., Bos A. J.J., Dorenbos P., Spectroscopy, thermoluminescence and afterglow studies of CaLa4(SiO4)3O: Ln (Ln=Ce,Nd,Eu,Tb,Dy), *Journal of Luminescence,* 160 (2015) 321-327.

Cumhuriyet Sci. J., 45(2) (2024) 400-406
DOI: https://doi.org/10.17776/csj.1441702

Cumhuriyet Science Journal

| csj.cumhuriyet.edu.tr | Founded: 2002 ISSN: 2587-2680 e-ISSN: 2587-246X Publisher: Sivas Cumhuriyet University

A Study on the Growth Conditions Role in Defining InGaAs Epitaxial Layer Quality

Meryem Demir [1,a,*], Sezai Elagöz [2,b]

[1] *Aselsan Sivas Precision Optics, 58060, Sivas, Türkiye.*
[2] *Nanophotonics Research and Application Center, Sivas Cumhuriyet University, 58140, Sivas, Türkiye.*
**Corresponding author*

Research Article

History
Received: 22/02/2024
Accepted: 11/03/2024

ABSTRACT

This study delves into the epitaxial growth and characterization of $In_xGa_{1-x}As$ layers on InP substrate, a critical area in the development of high-performance III-V semiconductor devices. $In_xGa_{1-x}As$ is renowned for its superior electron mobility and broad spectral response, making it indispensable in applications ranging from photodetectors to quantum cascade lasers. Employing a horizontal flow reactor MOVPE (metal-organic vapor phase epitaxy) technique, we meticulously grew n-$In_xGa_{1-x}As$ epilayers under varying conditions to investigate the impact of indium content, growth temperature, and V/III ratio on the material's structural, optical, and electrical properties. HRXRD (High-resolution X-ray diffraction) and Hall-effect measurements provided insights into the correlation between growth parameters and epitaxial layer quality, including dislocation density and carrier mobility. Our findings highlight the delicate balance required in the growth process to optimize the $In_xGa_{1-x}As$ /InP structure's performance for advanced semiconductor applications. The research underscores the potential of tailored $In_xGa_{1-x}As$ layers to push the boundaries of current photonics and optoelectronics technologies, emphasizing the importance of growth condition optimization for enhancing device efficiency and thermal stability.

Keywords: $In_xGa_{1-x}As$, Epitaxy, Growth, Indium

[a] *mdemir@aho.com.tr* *https://orcid.org/0009-0009-1234-0081* [b] *sezaielagoz@gmail.com* *https://orcid.org/0000-0002-3600-8640*

Introduction

In the realm of semiconductor materials, Indium Gallium Arsenide ($In_xGa_{1-x}As$) stands out as a pivotal III-V compound, renowned for its exceptional electron mobility and saturation shift rate [1]. This material has carved a niche in various high-tech applications, ranging from remote sensing and environmental monitoring to fiber optic communication and short-wave infrared photodetectors [2-7]. The ability of $In_xGa_{1-x}As$ -based devices to cater to wavelengths within the 0.85–3.60 µm spectral range is a testament to its versatility and technological importance [8]. A critical aspect of $In_xGa_{1-x}As$'s utility lies in its lattice-matched structure with Indium Phosphide (InP), which has been the subject of extensive investigation. Despite certain drawbacks of the InP substrate, such as its relative fragility and higher cost compared to Gallium Arsenide (GaAs) substrates, its electrical properties and reduced lattice mismatch make it theoretically more suitable for base material in certain applications. InP substrates have demonstrated promising performance, especially in the 0.9-1.6µm wavelength region, encompassing a range of applications from photodetectors to photodiodes [9-14]. The evolution of epitaxial growth technologies, including Molecular Beam Epitaxy (MBE), Solid Phase Epitaxy (SPE), Physical Vapor Deposition (PVD), and Metal Organic Vapor Phase Epitaxy (MOVPE), has been a cornerstone in achieving high-performance semiconductor thin films. MOVPE, in particular, has gained prominence since 1968 for its ability to produce high-quality crystal layers at a remarkable growth rate, making it fit for large-scale production [15]. The growth parameters such as substrate temperature, pressure of growth chamber, reactants quantity, semiconductor-alloy-composition, and group V/group III play a pivotal part in defining the characteristics of $In_xGa_{1-x}As$ epitaxial layers [16-21]. The variation of indium concentration in the $In_xGa_{1-x}As$ alloy is a critical factor affecting the crystal quality and optical properties. Studies have shown that increasing indium concentration can lead to greater lattice mismatch and pit dislocation density [22-23]. This variation also impacts the refractive index, as observed in spectroscopic ellipsometry measurements [24]. Additionally, research into the structural and electrical attributes of $In_xGa_{1-x}As$/InP compositions has highlighted the importance of the indium alloy mix and the metal layering process at ambient temperature [8]. Another pivotal aspect of $In_xGa_{1-x}As$ is its energy bandgap, which falls in from the near-infrared to mid-infrared wavelength range. This feature renders $In_xGa_{1-x}As$ a suitable material for infrared device applications. Understanding and optimizing the energy bandgap is crucial for developing detectors with desired properties, including optimal thickness, refractive index, and optical reflection/transmission. The wider range of $In_xGa_{1-x}As$ uses encompasses uncooled infrared sensors, light-emitting devices, field-effect-transistors, and quantum cascade lasers [3, 25-27]. The performance of these

devices is intricately linked to the quality of the $In_xGa_{1-x}As$ layers, influenced by growth conditions and parameters such as growth temperature, rate, and V/III ratio. Carrier localization in In-doped structures is a notable phenomenon, especially in the context of $In_xGa_{1-x}As$ alloys [18]. This aspect is significant due to the compositional inhomogeneity induced by high Indium content and the presence of In-related impurities. The localization effect is observed in various III-V alloys and is manifested in features like temperature-dependent photoluminescence [19]. Theoretical models have been developed to interpret and simulate these phenomena, contributing to a deeper understanding of the optical behavior of these materials.

In this research, the impact of various growth environments on Metalorganic Vapor Phase Epitaxy (MOVPE)-grown $In_xGa_{1-x}As$ epilayers is examined. Techniques such as X-ray diffraction (XRD), in-situ optical reflectivity, and room-temperature Hall-effect measurements are employed to assess the distinct growth conditions of $In_xGa_{1-x}As$ epilayers.

Experimental

In this study, n-InxGa1-xAs epilayers were grown utilizing a state-of-the-art crystal growth system, Aixtron 200/4 RF-S horizontal flow reactor MOCVD system. Epitaxial layers were deposited on 2-inch, (100)-oriented, semi-insulating, double-side polished (dsp) indium phosphide (SI-InP) substrates. The epitaxial growths were achieved at 680 °C. A variety of InxGa1-xAs layers were developed, with thicknesses ranging from 500 to 1000 nm, and varying indium contents (from x = 0.529 to 0.532). Uniform layers in terms of thickness and composition were ensured through gas flow rotation. The group-III precursors used were opto-grade trimethylgallium (TMGa) and trimethylindium (TMIn), while the group-V precursors were high-purity arsine (AsH3) and phosphine (PH3). Silane (SiH4) was employed for n-type doping. The carrier gases used included ultra-highly purified hydrogen (H2) and nitrogen (N2). Growth parameters were meticulously controlled, with reactor temperatures set 680 °C, and reactor pressure maintained at 50 mbar. The AsH3 flow rates varied across different two samples, altering the V/III ratios. Additionally, an InP buffer layer of approximately 500 nm was grown prior to each InxGa1-xAs layer to enhance material quality. For real-time monitoring of growth rate, reflection intensity, and surface quality, a Luxtron 880 nm reflectometer and optical fiber thermometry-light-pipe assembly were incorporated. The MOVPE system was also equipped with a rotating susceptor for substrate rotation, optimizing the epitaxial layer quality.

Structural analysis was carried out using High-Resolution X-Ray Diffraction (HRXRD) on a Rigaku SmartLab diffractometer, which is equipped with a rotating Cu anode and a four-bounce Ge (220) monochromator. The electrical characteristics, such as sheet carrier concentration, mobility, and resistivity, were assessed using a Hall-effect measurement system (HEMS), utilizing the four-probe Van der Pauw method. This thorough methodology facilitated an in-depth exploration of the structural, optical, and electrical attributes of the InxGa1-xAs epilayers. It offered valuable insights into how various growth conditions influence their properties. The growth conditions and parameters for all samples are detailed in Table 1 below.

Table 1. Growth parameters of samples.

Sample	TMIn (sccm)	TMGa (sccm)	AsH_3 (sccm)	SiH_4 (sccm) s/d/i	Growth rate (nm/s)	Thickness (nm)
A	242	9	200	6/400/10	1.32	1000
B	242	9	200	6/350/10	1.33	1000
C	242	9	162	2/500/10	1.43	500

Results and Discussion

On the InP substrate, a buffer layer of InP is first grown, followed by $In_xGa_{1-x}As$ layers for every sample. The in-situ reflectance-temperature graphs of these growths are given by Figure 1, Figure 2, and Figure 3. The blue line in this figure represents the in-situ reflectance intensity and the green one represents the growth temperature of the reactor during the growth. From the in-situ reflectance measurements, it is observed that there are no unwanted conditions on the surface during growth, and also that the surface quality is not degraded during the growth. At the first stage of growth, no interference oscillation is observed in the in-situ reflectance graph since there is no refractive index difference between the InP buffer layer to be grown on the InP substrate and the substrate itself [17]. As shown in Figure 1-Figure 3, after

the successful growth of the InP buffer layer on the InP substrate, doped $In_xGa_{1-x}As$ alloys have been grown.

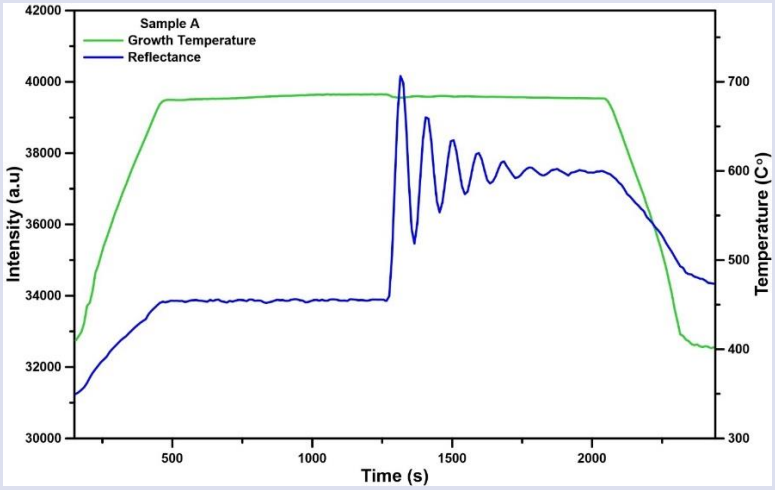

Figure 1. Temperature and in-situ reflectance measurements of sample A.

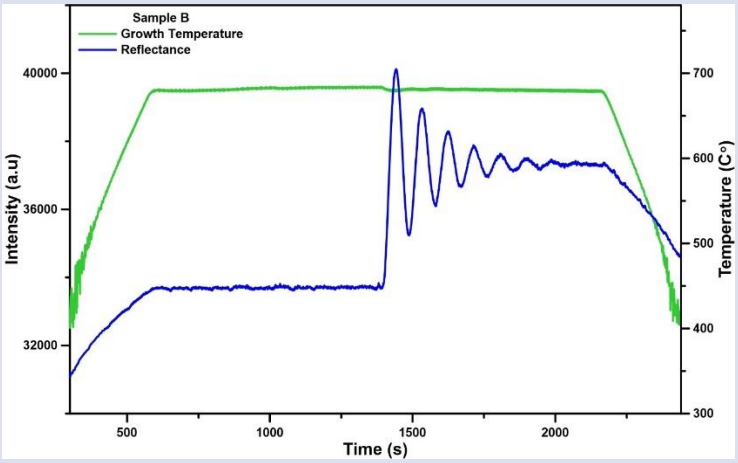

Figure 2. Temperature and in-situ reflectance measurements of sample B.

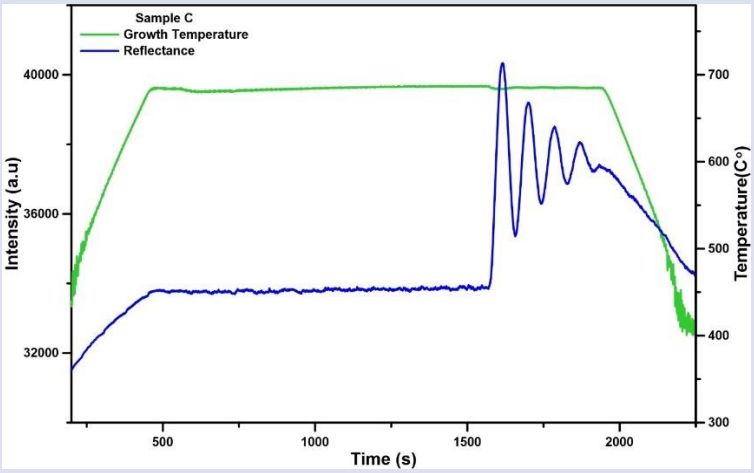

Figure 3. Temperature and in-situ reflectance measurements of sample C.

It was obtained from the in-situ reflectance measurements that the growth rate of sample A, sample B, and sample C are 1.32, 1.33, and 1.43 nm/s, respectively. It can be understood from the comparison of samples A and B that the growth rate is not affected seriously by decreasing the SiH_4 dilute flow which is about the dilution of the SiH_4 precursor. However, it is clear that the growth rate is affected when the AsH_3 flow is changed from 200 sccm to 162 sccm. It is believed that the AsH_3 flow is more effective than the SiH_4 flow considering the growth rate. Literature indicates that an increased presence of AsH_3 in the reactor, or more precisely on the growth surface, results in a reduced growth rate for $In_xGa_{1-x}As$ epitaxial layers [28].

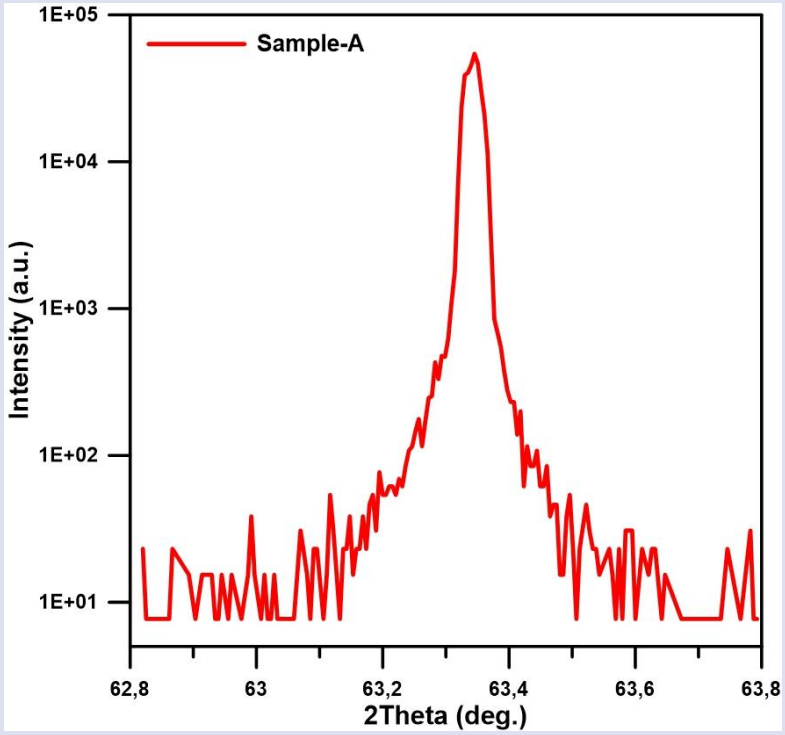

Figure 4. HRXRD measurement of sample A.

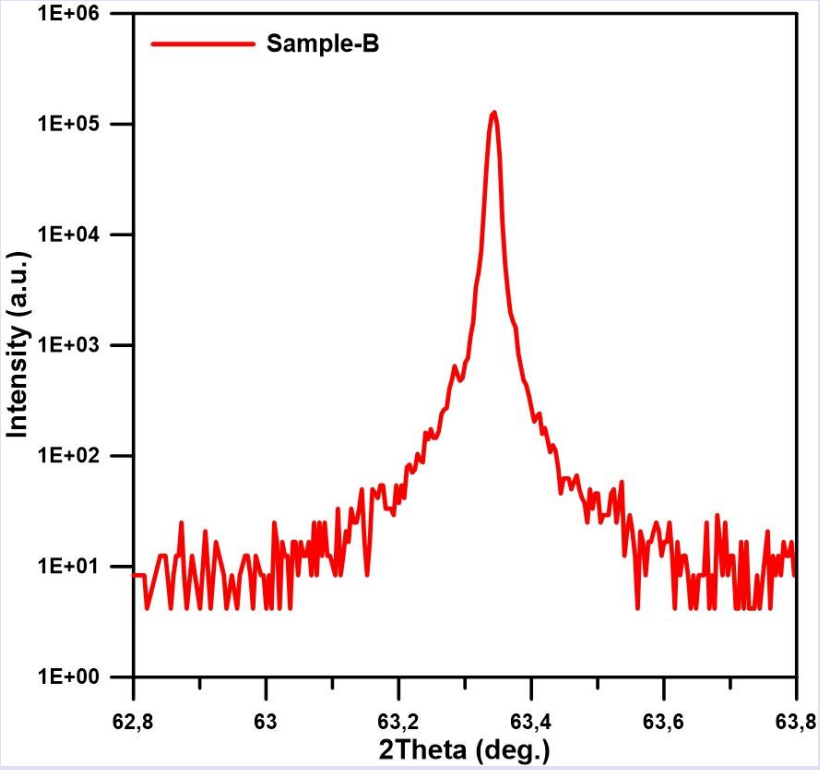

Figure 5. HRXRD measurement of sample B.

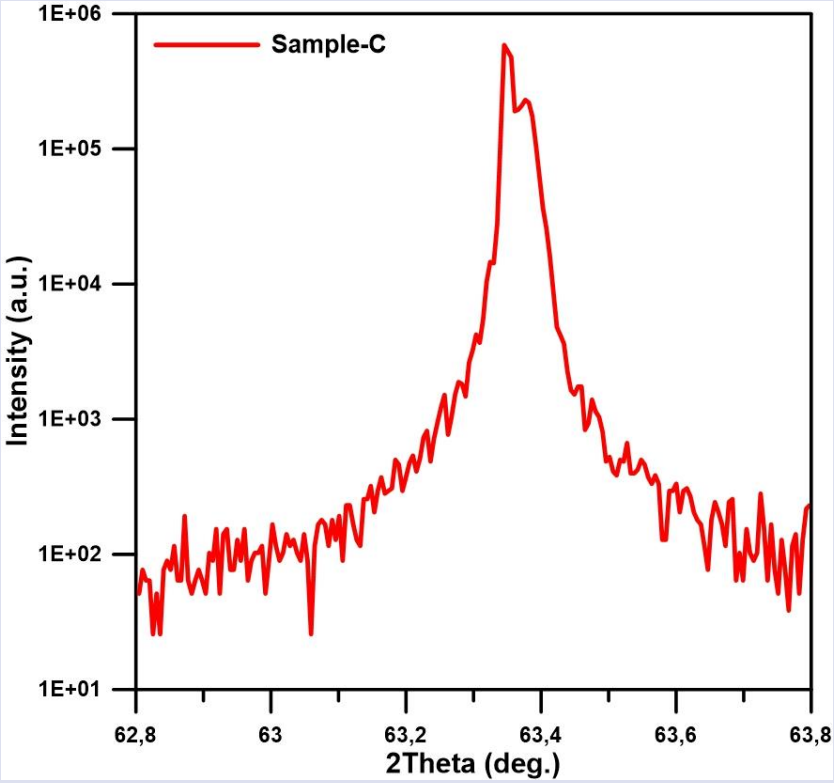

Figure 6. HRXRD measurement of sample C.

XRD is a strong and non-destructive characterization technique to have valuable and detailed information in terms of the alloy concentration, structural properties of epitaxial thin films, and, thickness [24]. The HRXRD 2θ scans of three samples are carried out to investigate the effect of growth conditions. Figure 4, Figure 5, and Figure 6 reveal the HRXRD 2θ patterns of all $In_xGa_{1-x}As$ samples. The selection was made for the interval between 63° and 63.8°, where the (0 0 4) Bragg peaks are situated for both the InP substrate and the $In_xGa_{1-x}As$ epilayer. In this depiction, it is evident that the peaks with the highest intensity and the narrowest Full Width at Half Maximum (FWHM) originated from InP substrates, while the other peaks were attributed to the $In_xGa_{1-x}As$ layers.

When examining the High-Resolution X-Ray Diffraction (HRXRD) scans for samples A, B, and C, it is observed that the $In_xGa_{1-x}As$ peaks are positioned to the left and to the right of the InP substrate peak. This positioning indicates that the $In_xGa_{1-x}As$ epitaxial films are experiencing compressive strain, are lattice-matched, and have tensile strain, which leads to an increase in the out-of-plane lattice parameters. The InAs alloy ratios of the samples, as determined from the measurements and simulations, are 0.533, 0.532, and 0.529 for samples A, B, and C, respectively.

Furthermore, the strain existing between the $In_xGa_{1-x}As$ epitaxial layers and the substrate can be calculated from the HRXRD measurements in the following manner:

$$\frac{\Delta a}{a} = -\frac{\Delta\theta}{\tan(\theta_B)} \quad (1)$$

where Δθ represents the angular difference between the diffraction peaks of the epitaxial $In_xGa_{1-x}As$ layer and the InP substrate, and θ_B is the Bragg angle for the InP substrate. The observation shows that with an increase in indium content and the presence of compressive strain, there is a distinct shift of the Bragg peak toward lower 2θ angles. Furthermore, a greater mismatch between the $In_xGa_{1-x}As$ epilayer and the InP substrate leads to a wider Full Width at Half Maximum (FWHM) of the Bragg peak, despite the film thickness remaining constant. This indicates the emergence of defects, most likely dislocations, which serve to alleviate the misfit strain exerted by the substrate. According to established literature, the density of dislocations (N_{dd}) in epitaxial layers can be estimated using a specific formula, which quantifies the relationship between dislocation density and observed structural characteristics in epitaxial films.

$$N_{dd} = 2 * \frac{(FWHM)^2}{9{a_0}^2} \quad (2)$$

where a_0 is the lattice constant of the $In_xGa_{1-x}As$ epitaxial layer. We then determined here $In_xGa_{1-x}As$ lattice constant is a_0. Based on this, the dislocation density for all samples was determined and is presented in Table 2. Analysis of Table 2 reveals that reducing the indium content, through values of x = 0.533, 0.532, and 0.529 leads to a decrease in lattice constant of $In_xGa_{1-x}As$. The calculated dislocation density values for samples A, B, and C are 2.11, 0.51, and 1.55 (10^9 cm^{-2}), respectively. Notably, the narrowest Full Width at Half Maximum (FWHM) of 58 arcsec was observed for sample B, indicating it has the highest crystalline quality among the samples. Nonetheless, it is evident that all samples exhibit good crystalline quality

Table 2. The HRXRD results of the $In_xGa_{1-x}As$ epitaxial layers

Sample	InAs alloy ratio	Lattice Constant (A)	FWHM (arcsec)	Dislocation Density (10^9 cm^{-2})
A	0.533	5.8674	118	2.11
B	0.532	5.8661	58	0.51
C	0.529	5.8629	101	1.55

Hall effect measurements were performed to explore the impact of varying growth conditions on the electrical properties of the $In_xGa_{1-x}As$ epilayers. This technique allows for the determination of carrier concentration, mobility, and resistivity of the samples, providing valuable insights into how different growth parameters influence the electrical behavior of the fabricated layers. By applying a magnetic field and measuring the voltage generated perpendicular to the current flow, the Hall effect offers a direct method to probe the type and density of charge carriers within a material, as well as their mobility, which are crucial factors in assessing the material's performance for electronic and optoelectronic applications. The net SiH_4 reactant supplied to the reactor is calculated by using the following formula

$$r = i * \frac{s}{s+d} \quad (3)$$

here i is inject, s is source, and d is dilute amount of the mass flow controllers, respectively. So, the net amounts of SiH4 precursors are 0.14, 0.16, and 0.38 µmol/min, respectively. Table 3 shows the room temperature mobility and sheet carrier concentration values of InxGa1-xAs epitaxial layers. Samples A, B, and C have 1.4, 2.0, and 1.9 E+13 cm-2 for sheet carrier concentration and 1.7, 1.5, and 2.4E+4 Vs/cm-2 for mobility, respectively. It is clear from the measurement results that the carrier concentration increases (mobility decreases) of sample B as expected by decreasing the dilution (or increasing the net amount of precursor) of the SiH4 source. It is obtained that even though the SiH4 precursor flow increased more than double, the V/III ratio changes affect the carrier concentration change more than SiH4 amount. As documented in the literature, when the flow rate of arsine (AsH3) is increased during the growth process, there is a significant rise in carrier density alongside a reduction in mobility. This phenomenon is attributed to the enhanced incorporation of arsenic into the material, which can lead to an increase in the number of charge carriers (electrons or holes) within the semiconductor. However, the increased incorporation of arsenic can also introduce additional scattering centers or defects, which adversely affect the mobility of these carriers by impeding their flow through the crystal lattice. Mobility is an essential parameter in semiconductors as it influences how quickly charge carriers can move under the influence of an electric field, impacting the material's electrical conductivity and overall performance in electronic devices [21]. Also, it is known that the effect of the V/III ratio of n-InxGa1-xAs is strong on Si incorporation into the structure [28]. It is thought also that the increase in mobility of sample C can be related to the positive contribution of the AsH3 amount in the reactor.

Table 3. The Hall Effect results of the $In_xGa_{1-x}As$ epitaxial layers.

Sample	Sheet carrier concentration (cm^{-2})	Mobility (Vs/cm^2)
A	1.4E+13	1.7E+4
B	2.0E+13	1.5E+4
C	1.9E+13	2.4E+4

Conclusion

This study has comprehensively explored the properties of $In_xGa_{1-x}As$ epitaxial layers grown on InP substrates, focusing on the impacts of varying growth conditions on the structural, optical, and electrical properties of the layers. Through meticulous experimentation, the research has highlighted the critical role of growth parameters in defining the characteristics of $In_xGa_{1-x}As$ layers, demonstrating how variations in indium content, reactor temperature, and V/III ratio influence layer quality, dislocation density, and carrier mobility. The findings underscore the potential of optimizing $In_xGa_{1-x}As$/InP structures for advanced semiconductor applications, particularly in photodetectors, field-effect transistors, and quantum cascade lasers. Future work should aim at refining growth techniques to further enhance the performance of $In_xGa_{1-x}As$ -based devices, potentially opening new avenues for the application of III-V semiconductors in optoelectronics and photonics, where efficiency, speed, and thermal stability are paramount.

Conflicts of interest

There are no conflicts of interest in this work.

Acknowledge

The authors acknowledge the usage of the Nanophotonics Research and Application Center at Sivas Cumhuriyet University (CUNAM) facilities.

References

[1] Nee T.W., Green, A.K., Optical properties of InGaAs lattice-matched to InP, *J. Appl. Phys.*, 68 (10) (1990) 5314-5317.

[2] Zhao L., Guo Z., Wei Q., Miao Q., Zhao L., The relationship between the dislocations and microstructure in In0.82Ga0.18As/InP heterostructures, *Sci. Rep.*, 6 (1) (2016) 1-7.

[3] Smiri B., Arbia M.B., Demir I., Saidi F., Othmen Z., Dkhil B., Altuntas I., Elagoz S., Hassen F., Maaref H., Optical and structural properties of In-rich InxGa1− xAs epitaxial layers on (1 0 0) InP for SWIR detectors, *Mater. Sci. Eng. B.*, 262 (2020) 114769.

[4] Buckley D. N., The effect of gas phase growth parameters on the composition of InGaAs in the hydride VPE process, *J. Electron. Mater.*, 17 (1) (1988) 15-20.

[5] Vallejo K.D., Cabrera-Perdomo C.I., Garrett T.A., Drake M.D., Liang B., Grossklaus K.A., and Simmonds P.J., Tunable Mid-Infrared Interband Emission from Tensile-Strained InGaAs Quantum Dots, *ACS Nano*, 17 (3) (2023) 2318–2327.

[6] Yan Z., Shi T., Fan Y., Zhou L. and Yuan Z., Compact InGaAs/InP single-photon detector module with ultra-narrowband interference circuits, Advanced Devices & Instrumentation 4, (2023) 0029.

[7] Kalyon G., Mutlu S., Kuruoglu F., Pertikel I., Demir I., Erol A., InGaAs-based Gunn light emitting diode, *Mater. Sci. Semicond. Process* 159, (2023) 107-389.

[8] Asar T., Özçelik S., Özbay E., Structural and electrical characterizations of InxGa1-xAs/InP structures for infrared photodetector applications, *J. Appl. Phys.,* 115 (10) (2014) 104502.

[9] Eckl J. J., Schreiber K. U., Schüler T., Satellite laser ranging in the near-infrared regime, *Photon Counting Applications-SPIE*, (2017) 10229 75-81.

[10] Ma J., Bai B., Wang L.J., Tong C.Z., Jin G., Zhang J., Pan J.W., Design considerations of high-performance InGaAs/InP single-photon avalanche diodes for quantum key distribution, *Appl. Opt.*, 55 (27) (2016) 7497-7502.

[11] Cova S., Ghioni M., Itzler M. A., Bienfang J. C., Restelli A., Semiconductor-based detectors, *Experimental Methods in the Physical Sciences*, 45 (2013) 83-146.

[12] Tosi A., Acerbi F., Dalla Mora A., Itzler M.A., Jiang X., Active area uniformity of InGaAs/InP single-photon avalanche diodes, *IEEE Photonics J.*, 3 (1) (2010) 31-41.

[13] Itzler M.A., Jiang X., Entwistle M., Slomkowski K., Tosi A., Acerbi F., Zappa F. and Cova S., Advances in InGaAsP-based avalanche diode single photon detectors, *J. Mod. Opt.*, 58 (3-4) (2011) 174-200.

[14] Jiang X., Itzler M. A., Ben-Michael R., Slomkowski K., InGaAsP–InP avalanche photodiodes for single photon detection, *IEEE J. Sel. Top. Quantum Electron.,* 13 (4) (2007) 895-905.

[15] Dupuis R.D., III–V semiconductor devices grown by metalorganic chemical vapor deposition—The development of the Swiss Army Knife for semiconductor epitaxial growth, *J. Vac. Sci. Technol. B,* 41 (6) (2023).

[16] Unal D.H., Demir I., InGaAs-Based MSM Photodetector: Researching Absorption Layer, Barrier Layer, and Digital Graded Superlattice Layer with 3D Simulation, *Results Opt.,* 13 (2023) 100581.

[17] Perkitel I., Demir I., Effect of Si-doped and undoped inter-layer transition time on the strain-compensated InGaAs/InAlAs QCL active region grown with MOVPE, *J. Mol. Struct.,* 1272 (2023) 134203.

[18] Arbia M.B., Demir I., Kaur N., Saidi F., Zappa D., Comini E., Altuntaş I. and Maaref H., Experimental insights toward carrier localization in in-rich InGaAs/InP as candidate for SWIR detection: Microstructural analysis combined with optical investigation, *Mater. Sci. Semicond. Process.,* 153 (2023) 107149

[19] Badreddine S., Joshya R.S., Ilkay D., Faouzi S., Ismail A., Lagarde D., Rober C., Xavier M., Hassen M., Systematic optical study of high-x InxGa1-xAs/InP structures for infrared photodetector applications, *Opt. Laser Technol.,* 148 (2022) 107714.

[20] Arbia M.B., Smiri B., Demir I., Saidi F., Altuntas I., Hassen F. and Maaref H., Theoretical analyses of the carrier localization effect on the photoluminescence of In-rich InGaAs layer grown on InP, *Mater. Sci. Semicond. Process.,* 140 (2022) 106411.

[21] Demir I., Altuntas I., and Elagoz S., Arsine flow rate effect on the low growth rate epitaxial InGaAs layers, *Semiconductors* 55 (10) (2021) 816-822.

[22] Alaydın B. O., Tüzemen E. S., Demir I., and Elagöz S., Optical and Structural Properties of MOCVD Grown InxGa1-xAs Epilayers, *Cumhuriyet Sci. J.,* 38 (4) (2017) 681-689.

[23] Gu Y., Huang W., Liu Y., Ma Y., Zhang J., Gong Q., Zhang Y., Shao X., Li X. and Gong H., Effects of buffer doping on the strain relaxation of metamorphic InGaAs photodetector structures, Mater. Sci. Semicond. Process., 120 (2020) 105281.

[24] Kaynar E., Sayrac M., Altuntas I., and Demir I., Determination of Optical Properties of MOVPE-Grown InxGa1-xAs/InP Epitaxial Structures by Spectroscopic Ellipsometry, *Braz. J. Phys.,* 52 (5) (2022) 184.

[25] Demir I., Altuntas I., Bulut B., Ezzedini M., Ergun Y. and Elagoz S., Comprehensive growth and characterization study on highly n-doped InGaAs as a contact layer for quantum cascade laser applications, *Semicond. Sci. Technol.,* 33, (5) (2018) 055005.

[26] Olausson P. and Lind E., Geometrical magnetoresistance as a tool for carrier mobility extraction in InGaAs MOSFETs, *IEEE Trans. Electron Devices,* (2023).

[27] Yang B., Yu Y., Zhang G., Shao X. and Li X., Design and Fabrication of Broadband InGaAs Detectors Integrated with Nanostructures, *Sensors,* 23 (14) (2023) 6556.

[28] Jiang L., Lin T., Wei X., Wang G.H., Zhang,G.Z., Zhang H.B. and Ma X.Y., Effects of V/III ratio on InGaAs and InP grown at low temperature by LP-MOCVD, *J. Cryst. Growth,* 260 (1-2) (2004) 23-27.

Cumhuriyet Sci. J., 45(2) (2024) 407-413
DOI: https://doi.org/10.17776/csj.1429356

Cumhuriyet Science Journal

| csj.cumhuriyet.edu.tr | Founded: 2002 ISSN: 2587-2680 e-ISSN: 2587-246X Publisher: Sivas Cumhuriyet University

Investigation of BSCCO Superconductors with Ga Substitution by Solid State Method

Yasemin Çetin [1,a], Hakan Gündoğmuş [1,b,*]

[1] *Material Science and Engineering, Engineering Faculty, Hakkari University, Hakkari, Türkiye.*

**Corresponding author*

Research Article

History
Received: 31/01/2024
Accepted: 03/04/2024

ABSTRACT

Samples of $(Bi_{2-x}Ga_x)Sr_2CaCu_2O_2$ superconductors with varying Ga substitution levels (x=0, 0.06, 0.12, 0.20) were synthesized using the solid-state reaction method. The effects of partial substitution of bismuth and gallium elements on the BSCCO structure were investigated in terms of their electrical, magnetic, structural, and mechanical properties. X-ray diffraction (XRD) was used to determine the crystalline phases, and samples A and B exhibited sharp peaks, indicating well-crystallized material with no Ga_2O_3 phase. SEM images were used to obtain microscopic views of all samples, and the elemental compositions of each element were determined from EDX spectra. The critical temperature was calculated from R-t measurements, and Sample A exhibited the highest Tc at 96K. Magnetic properties were investigated for all samples, including magnetic hysteresis behavior and magnetic moment. The critical current density (J_c) values were calculated using the Bean model by utilizing magnetic hysteresis.

Keywords: BSCCO, Critical current density, Solid-state method, Superconductivity.

[a] *yasemincetin345@gmail.com* *https://orcid.org/0000-0002-1833-4821* [b] *hakangundogmus@hakkari.edu.tr* *https://orcid.org/0000-0003-4118-0207*

Introduction

Superconductivity is a physical property where electric current passes without resistance. Dutch physicist Heike Kamerlingh Onnes discovered superconductivity with his studies in 1911 [1]. Onnes observed that some metals became less resistive at low temperatures. He then cooled the materials to low temperatures using liquid helium in glass tubes and discovered the superconductivity feature on mercury at 4.2 Kelvin (-268.95 °C) [2] [3]. With this discovery, the foundations of superconductivity were laid and later, it was discovered that many materials were superconducting and studies in the field of superconductivity accelerated. Superconductivity is of great importance for many applications such as magnetic resonance imaging (MRI) systems operating in cryogenic environments, particle accelerators, magnetic levitation [4].

With the study, it was discovered that polyatomic connections can be connected to each other and that semiconductors can also exhibit superconductivity. In 1987, BiSrCaCuO (BSCCO), which has a high critical temperature value presented as Tc value, can reach up to 110 K and is also Cu-O based, showing high-temperature superconductivity properties similar to HgBaCaCuO and TlBaCaCuO [5]. With this invention, studies in this field have intensified considerably by reducing the transition temperature of these materials by cooling them with liquid nitrogen. Among these methods, many theses and articles have been published in many studies and reviews on BSCCO superconducting materials, especially Bismuth (Bi) based. The reason for this is that Bismuth (Bi) based superconducting materials have a very comprehensive field of study due to their suitability for partial replacement applications and doping with the parts of different phases such as Bi-2201, Bi-2212, Bi-2223 [6].

Superconducting materials, also known as BSCCOs, are the subject of intense research due to their remarkable physical and electrical properties, including high-temperature superconductivity. These materials conduct electricity without resistance but are sensitive to magnetic fields [6] [7]. Bi-2212 superconductors, in particular, exhibit high-temperature superconductivity after thermal processing and optimization of their crystal structures [8]. This article presents a thorough review of the structure, synthesis, properties, and potential applications of Bi-2212 BSCCO superconductors. The study is a significant step towards a better comprehension of superconducting materials and their future industrial applications [6].

The primary structural formula, $Bi_2Sr_2Ca_{n-1}Cu_nO_{4+2n}$, represents three phases of bismuth-based superconductors, with the number of CuO_2 layers denoted by 'n' [6]. For the first phase (n=1), Bi-2201 exhibits a T_c of 20K, while for the second phase (n=2), Bi-2212 has a Tc of 80K, and for the third phase (n=3), Bi-2223 has a T_c of 110K. The subunit cells of the Bi-2201, Bi-2212, and Bi-2223 phases vary in the number of CuO_2 layers depending on the value of n [9] [10]. It is suggested that an increase in the number of layers is associated with higher Tc values. Therefore, modifications in superconductors typically target the Cu region, as superconductivity is linked to the CuO_2 layer[11].Furthermore, it is believed that the CuO_2 layers, which contain magnetic Cu^{2+} ions in all HTC superconductors, enhance superconductivity. Recent studies on doping rare earth elements in bismuth-based superconductors have shown that cationic impurities

affect the critical temperature (T_c) of the system. Despite significant changes in carrier density due to cation doping, the primary crystal structure of the system remains unchanged [12].

Samples of superconducting $(Bi_{2-x}Ga_x)Sr_2CaCu_2O_2$ were synthesised in this study by substituting the Bi-Ga part with ratios of x=0, 0.06, 0.12, and 0.20. The aim of this work was to increase the critical current density through a double calcination and sintering process. The materials were prepared using the solid-state reaction method with high-purity elements in stoichiometric ratios. The quality of the synthesised materials and their crystalline structural properties were analysed using X-ray powder diffraction. Surface and grain analysis were conducted using scanning electron microscopy (SEM). The critical temperatures were determined using the four-point resistance method, and the magnetic properties were characterised using a vibrating sample magnetometer (VSM).

MATERIALS AND METHODS

$(Bi_{2-x}Ga_x)Sr_2CaCu_2O_2$ samples with x values of 0, 0.06, 0.12, and 0.20 were prepared using chemical powders with 99% purity of Bi2O3, SrCO3, CaO, CuO, Ga2O3, and $CaCO_3$ in appropriate stoichiometric ratios. Each sample weighed 3 g and was prepared by weighing and mixing the powders in a mortar for 1.5-2 hours to ensure homogeneity. The samples underwent a 12-hour heat treatment for the first calcination. After the initial calcination, the samples were mixed for approximately two hours to ensure homogeneity before undergoing a second calcination. Subsequently, the samples were placed in an oven at 750°C for 12 hours, followed by one hour of grinding. The thoroughly ground samples were then pressed into pellets at a pressure of 4000kg/cm^2 and placed in a crucible inside a cylindrical high-temperature furnace for the sintering phase. The samples were heated from room temperature to 845°C over a period of 100 minutes and held at this temperature in the furnace for 60 hours. Subsequently, they were cooled to 750°C over a period of 100 minutes and held at this temperature for an additional 12 hours. Finally, the samples were cooled from 750°C to room temperature over a period of 100 minutes and were ready for measurement. To avoid confusion, the samples were labelled as A, B, C and D.

RESULTS AND DISCUSSION

X-ray diffraction (XRD) measurements were made to explain the crystal phases of the samples we produced. The patterns for all samples are displayed in Figure 1. samples A and B exhibit sharp peaks, indicating well-crystallized material and the absence of Ga_2O_3 phase. However, Sample D shows additional peaks, indicating the presence of Ga_2O_3 and suggesting that the solubility limit of gallium in the structure has been exceeded. Sample C is similar, suggesting that gallium may be substituting into the structure. The peak intensity across samples indicates good crystallinity of the Bi-2212 phase. However, the variation in peak intensity and broadening, particularly in C and D, may suggest structural changes or strain. The analysis suggests that gallium doping affects the structure of the BSCCO phase and that there is a threshold beyond which gallium forms a separate phase.

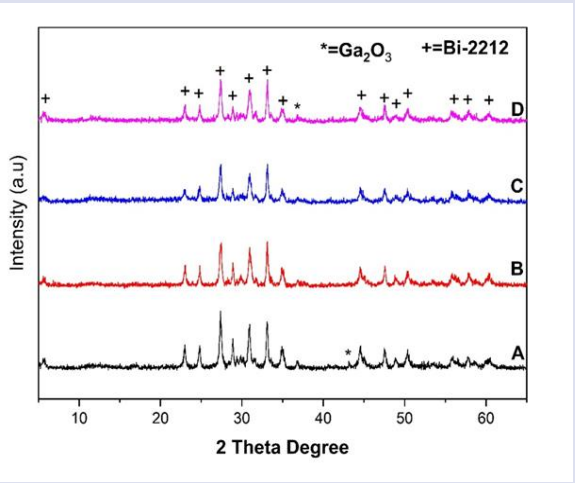

Figure 1. X-ray diffraction patterns of the $(Bi_{2-x}Ga_x)Sr_2CaCu_2O_2$ superconducting samples. (+) Bi-2212 phase, and (∗) Ga_2O_3 secondary phases.

SEM images offer microscopic views of the surface morphology of a sample. Figure 2 a, Figure 2c, Figure 2 e and Figure 2 g, displays the polished grain morphologies of samples A, B, C and D.,respectively. The grain morphology exhibits clear and distinct changes with increasing Ga content. The characteristic flaky grains of (Bi,Pb)-2212 are visible in all samples. At higher Ga contents, the microstructures display secondary phases with round or square edges dispersed within the main matrix. As substitution increases, the homogeneity deteriorates, resulting in the appearance of needle-like structures and particle shrinkage.

This indicates disordered bonding and weakened transmission. Elemental percentages remain consistent across all samples, as observed by EDX analysis and shown also in Figure 2 b, Figure 2 d, Figure 2 f and Figure 2 h, respectively, with corresponding EDX spectra below each SEM image. EDX is employed for elemental analysis and chemical characterisation. The sample is analysed by interacting X-rays with it and identifying the elements based on their unique electromagnetic emission spectra. The spectra show peaks that represent the elements, with the peak position indicating the element and the intensity related to its concentration. The EDX spectra indicate the presence of several elements in each sample, including oxygen (O), carbon (C), silicon (Si), copper (Cu), and aluminium (Al). The results confirm that the materials are composed primarily of the intended substances. However, it is said that the hole concentration in the CuO2 layer, which is one of the variables that changes the Tc value, also affects it. In this case, we can calculate the number of

holes, expressed as p, with equation 1 called the Presland method [13].

$$\frac{T_C}{T_C^{max}} = 1 - 82{,}6(p - 0{,}16)^2 \quad (1)$$

The hole concentration, , T_C^{onset} , T_C^{offset}values and other parameters we calculated for $(Bi_{2-x}Ga_x)Sr_2CaCu_2O_2$ superconductor samples are given in table 1. We can say that as the number of holes decreases in the Bi-2212 system, which is formed with the increase in the displacement of the Bi-Ga part, the superconductivity properties of the system decrease [14].

As can be seen from these limited studies in the literature, no definite interpretation can be made about the dimensions of the contact pin. Therefore, in this study, the detector was modeled in three different ways using the PHITS Monte Carlo simulation program. It is first modeled without including the contact pin, then with the 3.5 mm contact pin, and finally with the 4.5 mm contact, which is the inner hole diameter of the detector. Also, there is one study in the literature on how this contact pin will have an effect on the detector response and the full energy peak efficiency [18]. In this paper, the effect of the copper contact pin on the detector efficiency was examined in the point source geometry in the energy range of 59.5 keV-1408 keV and it was determined that it changed of up to 1.9% in the efficiency of the detector. The current study investigates the effect of a copper contact pin on the full energy peak efficiency by calculating efficiency values for higher gamma ray energies up to 2614.5 keV in both cylindrical and point source geometry in the high-energy region where the effect is dominant.

Table 1. Nominal compositions and structural parameters of $(Bi_{2-x}Ga_x)Sr_2CaCu_2O_2$ (x = 0.0, 0.06, 0.12 and 0.20) compounds.

Samples	Ga dopant, x	Lattice parameters		T_C^{onset} (K)	T_C^{offset} (K)	ΔT_c (K)	hole concentration (p)
		a = b (Å)	c (Å)				
A	x=0			70	55	15	0.259
B	x=0.06			70	55	15	0.259
C	x=0.12			68.75	40	28.5	0.249
D	x=0.20			61.75	43.12	18.63	0.257

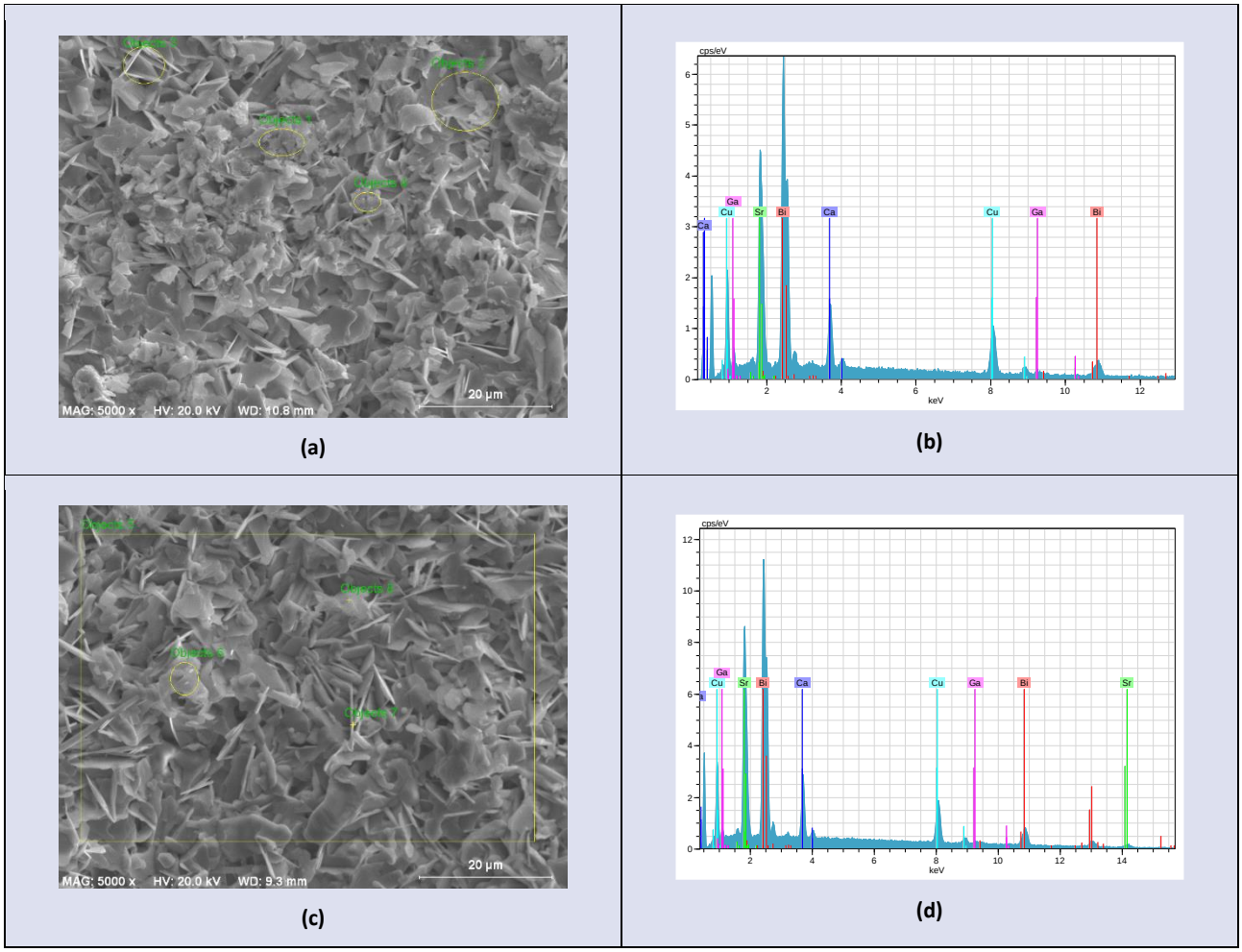

(a) (b) (c) (d)

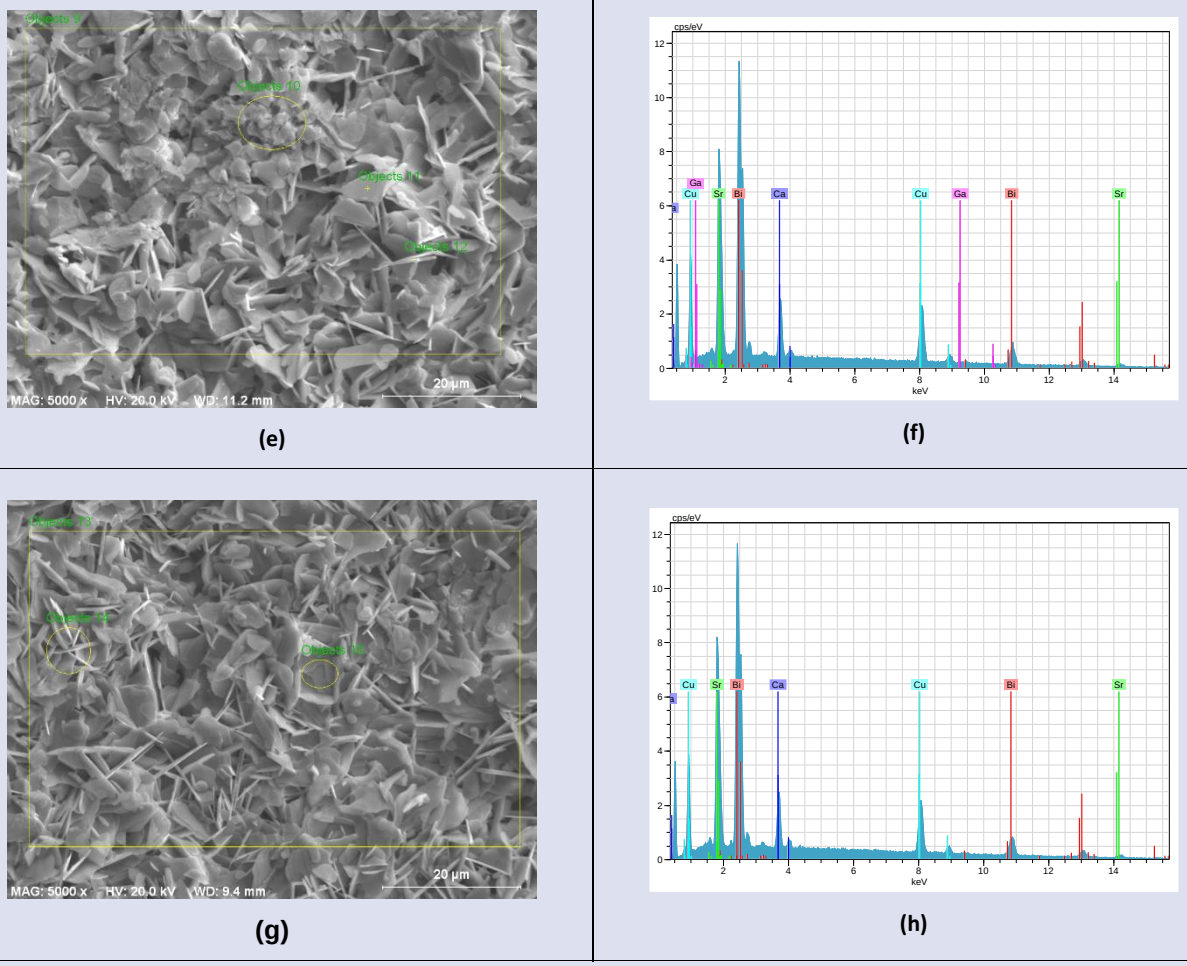

Figure 2. SEM and EDX analysis of all samples (a,c,e and g Sem Images and b,f,d and h EDX analysis).

Figure 3 shows Resistivity measurement vs. temperature for all the samples. The Tc values are similar for all samples, and samples A and B have the same transition temperature, indicating that the x=0.06 substitution does not affect the structure. A single phase transition is observed for all samples, and the resistance decreases with increasing temperature up to a certain point, where a sharp transition occurs. Furthermore, all samples demonstrate metallic behaviour at room temperature, that is, above the transition temperature, and exhibit superconductivity upon cooling. The transition temperature is the point at which a material undergoes a phase change, typically from a non-superconducting to a superconducting state. T_{conset} and $T_{coffset}$ remain the same for samples A and B, but increase for samples C and D as the partial substitution of Bi-Ga increases. The superconducting transition temperature, represented by ΔT, changes correspondingly, with an increase in ΔT indicating a deterioration in the superconducting properties. Electrical resistivity measurements indicate that partial substitution of Bi-Ga degrades the superconducting properties in some aspects. This is a prominent property. The decline in superconductivity can be attributed to the emergence of less doped phases between superconducting particles, the formation of gaps between particles, or the appearance of secondary phases that do not exhibit superconducting properties.

Figure 4 shows M–H hysteresis loops of samples. Magnetic hysteresis curves were measured at a temperature of 10K and over ±10 kOe fields. To expel any trapped magnetic flux, all samples were heated above the superconducting transition temperature before the measurement. The results of the magnetic hysteresis measurements indicate that the M-H curves are nearly symmetrical. As the amount of Bi-Ga partial substitution increases, both the area within the hysteresis curve and the maximum magnetization value increase. The magnetization of the samples resulting from the generated current causes thermal fluctuations that affect the Cooper pair density, leading to a decrease in the area within the M-H curve. When a magnetic field (H) above the critical Hc1 range is applied, flux lines penetrate the sample, narrowing the hysteresis curve. The penetration of the magnetic field into the structure results in the release of a Lenz force, which generates resistance and reduces the critical current density.

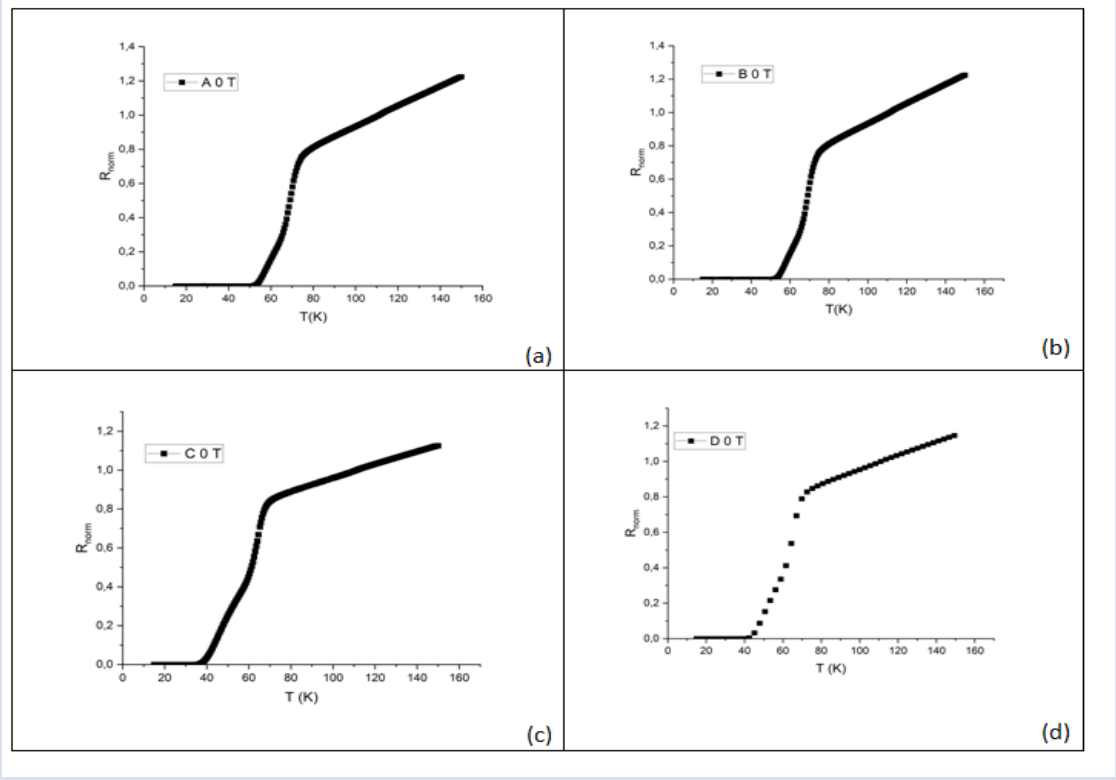

Figure 3. Resistivity measurement vs. temperature for all the samples.

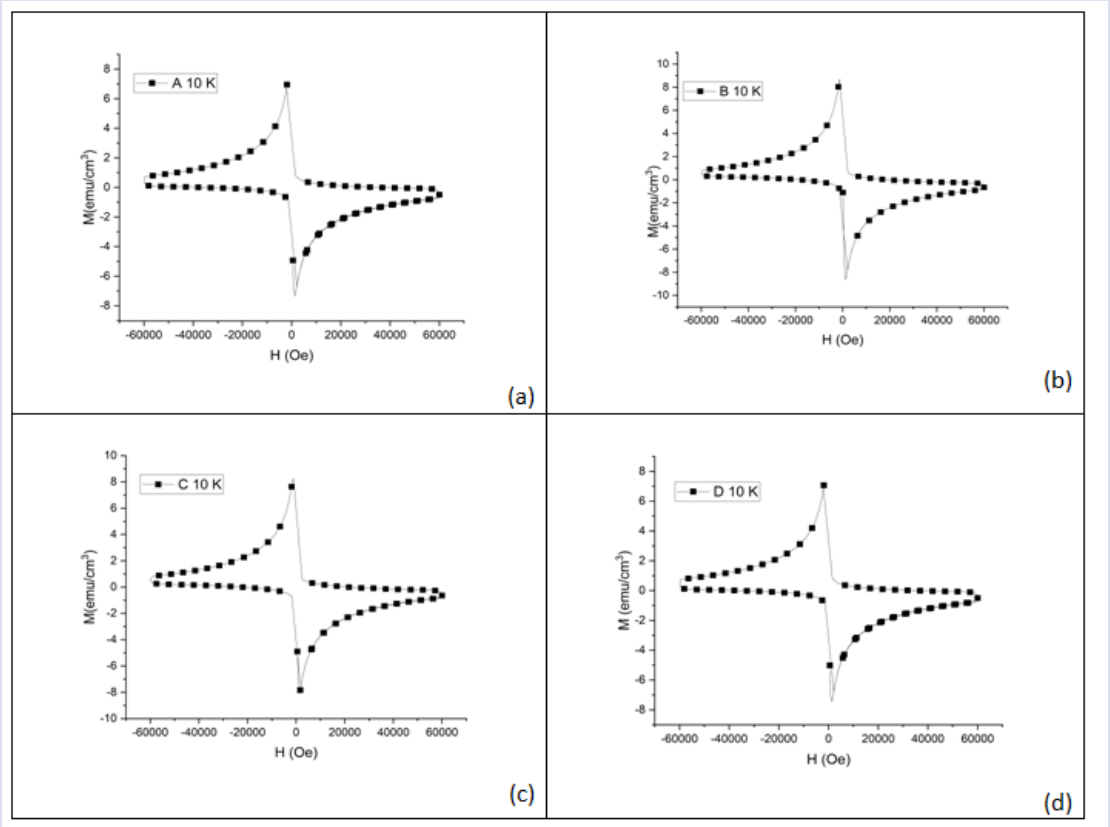

Figure 4. M–H hysteresis loops of samples at T = 10 K and applied external fields of ±10 k

The critical current density (Jc) can be calculated from the M-H curve using the Bean model (Bean 1962) as shown in equation 2. [15]

$$J_c = 20\frac{|\Delta M|}{a(1-\frac{a}{3b})} \quad (2)$$

Figure 5 displays the calculated critical current densities for samples A, B, C, and D as a function of the applied magnetic field at a constant temperature of 10K. The figure illustrates the variation of Jc with respect to the field, where Jc is obtained from the non-zero H portion of the hysteresis curve. The critical current density increases with increasing magnetic field up to a certain value (H) and then decreases at higher magnetic field strengths. At constant temperature, the critical current density theoretically decreases with increasing magnetic field. Increasing the magnetic field to a certain value of H enhances the interparticle interactions and thus the critical current density due to weak interactions between particles in polycrystalline crystals. This is observed as a small region of increase in the curve, and the magnetic field value decreases at higher temperatures, resulting in an increase. Figure 5 shows a decrease in Jc value for sample D at zero magnetic field, while an increase in Jc value is observed for the other samples as the substitution amount increases which is typical for type-II superconductors.

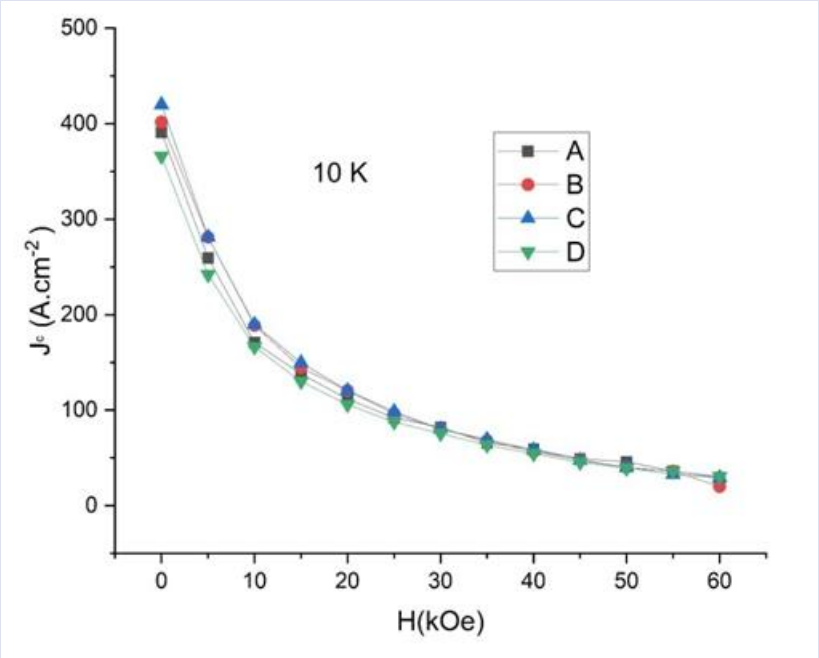

Figure 5. Calculated J_c results of samples at $T = 10$ K from their hysteresis loop.

Figure 6 shows the results as a function of the applied magnetic field. The magnetisation's temperature dependence was measured for all samples under an external magnetic field of 50Oe in the range of 0-100K. The results obtained from partially substituting Ga-Bi indicate that the samples' superconducting properties are lost when the applied magnetic field exceeds the initial T_{conset} value. The magnetic moment usually increases as the temperature decreases, indicating stronger magnetic ordering at lower temperatures. The curves show a significant change in slope at specific temperatures, which may correspond to magnetic or structural phase transitions. The different samples exhibit varying behaviors, which could be due to differences in composition, structure, or magnetic properties.

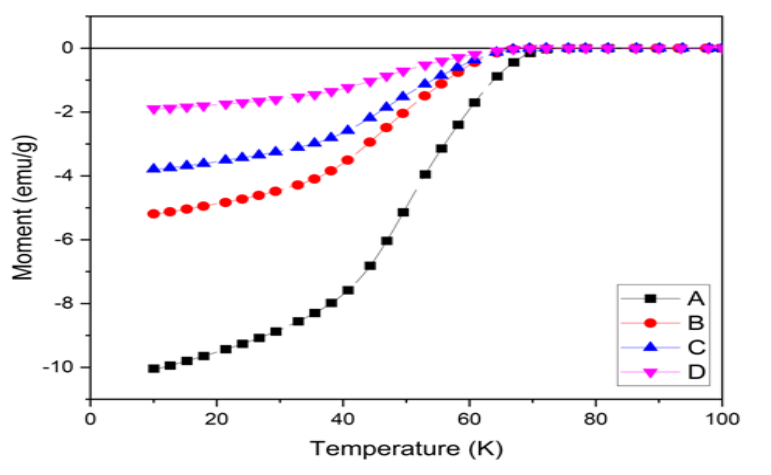

Figure 6. The magnetic moment (moment in emu/g) as a function of temperature (K) for the same samples A, B, C, and D..

CONCLUSION

The $(Bi_{2-x}Ga_x)Sr_2CaCu_2O_2$ system samples (x=0, 0.06, 0.12, 0.20) were synthesized using the solid-state reaction method. The effects of Bi-Ga partial substitution on BSCCO superconductivity were investigated through resistance measurements, EDX, SEM, magnetisation hysteresis measurements, and XRD measurements. The results show that the superconducting transition temperatures, where the resistance becomes zero, decrease as the Bi-Ga partial substitution increases. In contrast, the range of the superconducting transition, ΔT, increases. The electrical resistance measurements indicate that the superconducting properties are degraded by partial substitution. The results of the electrical resistivity measurements are consistent with those of the XRD and SEM analyses.

Acknowledgments

This work was supported by Hakkari University Scientific Research Projects Coordination Office, by the project numbered FM22LTP3.

Conflicts of interest

There are no conflicts of interest in this work.

References

[1] Lönberg B., Lundström T., Norling P., Anti-Meissner Effect in the BiSrCaCuO-System, *Physica C*, 191 (1992) 1365-1366.

[2] Çavdar Ş., Turan N., The Investigation of Bi-Ga Partial Replacement Effect on Magnetic, Mechanical and Microstructural Properties of $Bi_{(1,8-x)}Pb_{0,2}Ga_xSr_2CaCu_2O_y$ Superconductor, *GU J Sci., Part C* (2022) 423-438.

[3] Gul I.H., Rehman M.A., Ali M., Maqsood A., Effect of Vanadium and Barium on the Bi-Based(2223) Superconductors, *Physica C*, 432 (2005) 71-80.

[4] Yazıcı D., Ozcelik B., Altın S., Yakıncı M.E., Effect of Vanadium-Titanium Co-Doping on BPSCCO Superconductor, *Journal of Superconductivity and Novel Magnetism*, 24 (2011) 217-222.

[5] Nkum R.K., Superconductivity in (Bi, Pb) 2Sr2Ca2Cu3-YxOy'j, *J. Mater. Sci.*, 33 (1998) 207-210.

[6] Türk N., Gündoğmuş H., Akyol M., Yakıncı Z.D., Ekicibil A., Özçelik B., Effect of Tungsten (W) Substitution on the Physical Properties of Bi- (2223) Superconductors, *Journal of Superconductivity and Novel Magnetism*, 27 (2013) 711–716.

[7] Ghafoor M., Nabi J., Abbasi J., Effects of Change in Lead Concentration on the Properties of Bi-2223 Superconductor Prepared Via Solid-State Reaction, *Cumhuriyet University Faculty of Science*, 36(7) (2015) 180-191.

[8] Toygun Ş., General Principles of Sol-Gel, *Journal of Engineering and Natural Sciences*, Sigma 31 (2013) 456-476.

[9] Özkartal A., Enis O. N., $Bi_{1.6}Pb_{0.4}Sr_2Ca_3Cu_4O_{12}$ Çubuk Şeklinde Üretilen Süperiletken Üzerinde Doğru Akım Tavlamanın Etkisi, *Yüzüncü Yıl Üniversitesi Fen Bilimleri Enstitüsü Dergisi*, 23 (2) (2018) 123-128.

[10] Türk N., Tungsten Katkılı BSCCO Süperiletken Malzeme Üretimi ve Üretilen Malzemenin Fiziksel Özelliklerinin Araştırılması, yüksek lisans tezi, *Çukurova Üniversitesi, Fen Bilimleri Enstitüsü Fizik Anabilim Dalı*, (2012).

[11] Fujita K., Noda T., Kojima K.M., Eisaki H., Uchida S., Effect of Disorder Outside the CuO_2 Planes on T_c of Copper Oxide Superconductors, *Phys. Rev. Lett*., 95 (097006) (2005).

[12] Abrikasov A. A., Type-II Superconductors and the Vortex Lattice, *Reviews Of Modern Physics*., Volume 76 (2004) 975.

[13] Presland M.R., Tallon J.L., Buckley R.G., Liu R.S., Floeer N.E., General Trends Regarding the Effects of Oxygen Stoichiometry on T_c in Bi and Tl Superconductors, *Physica C*, 176 (1991) 95-105.

[14] Gündoğmuş H., İkinci Tip BSCCO Süperiletkenlerine Y(İtriyum) Katkılamasının Etkileri, *Iğdır Üniversitesi Fen Bilimleri Enstitüsü Dergisi*, 8(2) (2018) 99-105.

[15] Gündoğmuş H., Özçelik B., Özkurt B., Sotelo A., Madre M. A., Physical, Mechanical and Magnetic Properties of the Yb-Substituted $Bi_2Sr_2Ca_1Cu_2O_y$ Textured Superconductor, *Journal of Superconductivity and Novel Magnetism*, 26 (2012) 111–115.

Cumhuriyet Sci. J., 45(2) (2024) 414-425
DOI: https://doi.org/10.17776/csj.1379874

Cumhuriyet Science Journal

| csj.cumhuriyet.edu.tr | Founded: 2002 ISSN: 2587-2680 e-ISSN: 2587-246X Publisher: Sivas Cumhuriyet University

Evaluating the Performance of Two NaI(Tl) Detectors Using a Combined Approach of Experiment and Monte Carlo Simulation

Aydın Yıldırım [1,a,*], Gökçe İnal [1,b]

[1] *Physics Department, Science Faculty, Akdeniz University, Antalya, Türkiye*

**Corresponding author*

Research Article

History
Received: 23/10/2023
Accepted: 29/03/2024

ABSTRACT

The aim of this study is to compare two identical NaI(Tl) detectors under the same conditions to reduce potential sources of error in future experiments. To this end, an experimental setup using both detectors was designed to measure the gamma spectrum of point sources. In order to verify the experimental results, the same setup was conducted by Monte Carlo simulations. The characteristics of the detectors, such as resolution and efficiency, were analyzed simultaneously to obtain possible differences. The resolution and efficiency of the detectors were found to be slightly different when their settings were the same, but within the expected range. The fitted data gave a standard deviation of 20.749±0.00693 keV for detector 1 and 19.698±0.00647 keV for detector 2 at 662 keV. The experimental data showed that one detector had a resolution of 6.9% and the other 7.2%. The simulation results and experimental data are in good agreement. In conclusion, it was observed that the high errors in the experimental data are due to the 20% uncertainty of the point sources.

Keywords: Detector, Efficiency, Geant4, Monte Carlo, NaI.

[a] *aydinyldrm@gmail.com* *https://orcid.org/0000-0003-2141-5355* [b] *gokcealina@gmail.com* *https://orcid.org/0000-0003-4660-8532*

Introduction

Radioactive sources have been used for various purposes since the late 1800s. There are many areas where these radioactive sources can be used, including medicine, academics, archaeology, agriculture, and industry [1-5]. Also, people may encounter natural radioactive sources during their daily lives, in addition to the areas mentioned above [6]. Although these sources, which are used to simplify life, have many benefits, they can be extremely dangerous. Because radioactive sources are both useful and dangerous, they need to be monitored carefully to prevent harm to people and the environment [7]. Detectors are the main tools used to monitor these types of radiation. To obtain accurate and meaningful readings from detectors and minimize undesirable effects, the characteristics of the detectors must be well known [7–9]. As radioactive sources have a wide range of uses, so do the types of detectors that detect them [10–12]. For some detectors, it is sufficient to detect only the presence of radiation in the environment, while for others, the main purpose of the detector is to detect multiple quantities such as the presence of radiation, the type of radiation, the energy of radiation, the activity of the radiation source. Also, if the activity or dose of a source is to be determined with a gamma spectrometer, the efficiency of the detector must be known as a function of distance and energy. In particular, the detectors used by certified institutes or establishments must often be validated, since these institutes measure the activity and dose of drugs that contain radioisotopes.

Bedir et al. (2020) investigated the characterization of a handheld detector for radioguided surgery. They showed that more than one radiotracer can be used to fully assess the size of the tumor (whole tumor and sentinel lymph nodes). In such cases, a detector must have a resolution of less than 10 keV at energies below 159 keV. To develop such a detector, they chose $LaBr_3$ as the scintillator and studied the characteristics of the developed detector for resolution. As an example of a multiple detector system, Ghosh et al. (2016) studied the PARIS (photon array for the studies with radioactive ions and stable beams) $LaBr_3$(Ce)-NaI(Tl) phoswich detectors. The system consists of two phoswich detectors. Both detectors have 9 LaBr3 and 9 NaI scintillator crystals. Gamma energies up to 22.6 MeV have been measured with this configuration. A resolution of 2.1% at E = 22.6 MeV was achieved in the experiments. In addition, FWHM = 315 ps is measured for time resolution with a 60Co source. Akkurt et al. (2015a) emphasized the importance of the resolution of the detector and investigated a $3' \times 3'$ NaI(Tl) detector, similar to this study. They used photon energies of 511, 662, 835, 1173, 1275, and 1332 keV to characterize the resolution of the detector as a function of distance. Guss et al. (2013) investigated different sizes of scintillators for their properties. $CeBr_3$, $LaBr_3$ and NaI were selected for comparison. Detector resolution and efficiency were compared for different crystal sizes, and it was found that $LaBr_3$ has the best resolution for all sizes compared. They indicated that as the size of the crystal

increases, the resolution of all three detectors is reduced but the efficiencies get higher.

In this study, a scintillator type used in gamma spectroscopy is investigated. Gamma spectroscopy is one of the most commonly used techniques for measuring the energy of gamma rays. In gamma spectroscopy, the characterization of the equipment, particularly the characterization of detectors, is crucial for the accuracy of the data taken. NaI(Tl) scintillator detectors have been widely used to measure the activities of low-level radioactive sources in many fields of gamma spectroscopy, especially because of their important characteristics of having high detection efficiency. Nuclear and particle physics experiments today require highly complex setups. Some of the reactions observed during high energy experiments may not be detected with simple detector setups due to their low cross sections. As a solution, research facilities conducting such experiments use a large number of detectors, either of the same type or of different types. In such designs, it is essential to evaluate the readings of each detector separately, as well as the collective readings of all detectors. Also, these high energy reactions produce too much background, and it is very difficult for one detector to handle this background. Increasing the number of detectors reduces the pile-up effect and allows the detector array to make reasonable measurements. Therefore, the thorough examination of the characterization and performance assessment of the systems to be installed is essential due to the extensive usage of comparable systems in research facilities. This is critical to the understanding of the results of the experiments being performed. Accordingly, this investigation will provide valuable insights to research laboratories currently constructing or preparing to construct detector systems that are comparable.

This paper is organized as follows. In Section 2, the methodology of the research is described. First, activity of sources was determined with a hybrid model of experiment and simulation. Then, the experimental method will be presented and followed by simulation method. Section 3 presents all the results for experimental and simulation data. Finally, the study is concluded in Section 4.

Material and Method

Point sources were used as gamma generators for this study. The activity of the sources must be known to calculate the efficiency of detectors. The activity of the source and efficiency of the detector are coupled quantities. It is not possible to calculate the activity of the source or the efficiency of the detector without knowing the value of the other one. The sources are labelled with 1 μCi activity however they have 20% uncertainty and are at least two to three years old. Therefore, Monte Carlo simulations were used to calculate the current activity of the sources [13–16]. The Geant4 simulation toolkit, which is used by many researchers, was employed for the simulations. In Geant4 simulations, the selection of event numbers, Monte Carlo parameters, and variance reduction techniques critically impacts simulation accuracy and efficiency. The count of events reflects the total physical occurrences, such as particle interactions or decays, in the simulation. Optimal selection of event numbers is indispensable in balancing computational resources and ensuring statistically valid results. Increasing the number of events may decrease statistical uncertainties, but it also requires additional computational resources and time. Geant4's Monte Carlo parameters include various configurations, such as step sizes, tracking cuts, and production thresholds, which dictate the precision of particle tracking and interactions in the simulation. Proper parameter tuning is essential to strike the right balance between accuracy and computational efficiency for specific applications [17–19]. It must be mentioned that the variance reduction techniques in Geant4 offer users tools to enhance simulation efficiency and minimize statistical fluctuations. These techniques enable users to give priority to specific interactions, divide particle tracks, and modify tracking weights to improve the accuracy and reliability of results. The process of determining the optimal configuration for simulation outcomes requires users to consider their simulation requirements, computational resources, desired level of statistical precision, and the interplay between the number of events, Monte Carlo parameters, and variance reduction techniques. Achieving effective tailoring of these settings for specific applications is a nuanced endeavor, often involving iterative testing and sensitivity analyses to ensure robust and meaningful results. After the calculation of the current activity of the sources, the characterization of the detectors can be carried out. The last part of this study is to validate the experimental results with Geant4 simulations.

The consistency of detection efficiency and resolution for two NaI(Tl) detectors was investigated by experimentally and computationally via Monte Carlo simulations. The reason for considering such a setup is that when both detectors are used for the same measurement at the same time or in a coincidence experiment, there might be unwanted errors due to incorrectly adjusted settings, or it might create accuracy problems. Detectors were kept under consistent conditions to obtain the most accurate evaluation results. The experiment was conducted for different source-detector distances and gamma energies.

Experimental Setup

The detectors in question were $3' \times 3'$ Ortec's 905-4 NaI(Tl) scintillation detectors. These detectors were connected to a CAEN V1725D 8 Ch. 14 bit 250 MS/s Digitizer. The detectors were covered with lead shielding on all sides. The lead thickness was 5 cm. To determine the efficiency and resolution of detector, four gamma sources were used. These gamma sources were ^{22}Na, ^{54}Mn, ^{60}Co, ^{137}Cs. Because of the gamma peaks of the chosen sources, we had the opportunity to look at a wide range in gamma spectroscopy. These peaks are 511, 662,

835, 1173, 1275 and 1332 keV. The design of the experimental setup can be seen in Figures 1-a, 1-b and 1-c. Figure 1-d shows the image of the detectors and one of the sources.

For each source, measurements were performed at five source-detector distances: 1, 2, 3, 5, and 10 cm. The source was placed in the middle of the setup, and the detectors were moved equally to each distance. All measurements lasted 3600 seconds. The optimum bias voltage for these detectors is between 700 and 850 V, and we fixed the bias voltage for both detectors at 750 V. CAEN Compass software was used for data acquisition. In the Compass software, we used the same acquisition parameters for both detectors to determine the differences for identical setups.

Monte Carlo Simulations

For the Monte Carlo simulations, we used the Geant4 Simulation Toolkit. While performing the Geant4 simulations, the "G4EmLivermorePhysics" library was chosen to model the interaction of the electromagnetic radiation and the detectors. The prepared simulation geometry is illustrated in Figure 2. To obtain a realistic result, we added all the necessary components of the experimental setup. The components in the simulation include the two NaI (Tl) detectors, lead blocks, lead sheets, aluminum cap of detectors, and radioactive sources. Unfortunately, the simulations cannot reflect the electronic or other possible effects coming from radiation-matter interactions, which causes broadening at photo-peaks. The simulations give only single lines for the photo-peaks. It is necessary to add the resolution of the detector, which comes from experimental data to the simulations at this point [5]. To reflect the 1 mCi activity of the point sources, 37×10^6 primaries were selected for the simulations. As previously mentioned, the simulations were adjusted for computational efficiency and accuracy. Additionally, the number of primaries is sufficient to minimize statistical fluctuations while maintaining computational efficiency on an ordinary desktop computer. Using only the NaI crystals as sensitive volumes and killing secondary particles that do not affect the study reduces computational time and output file size

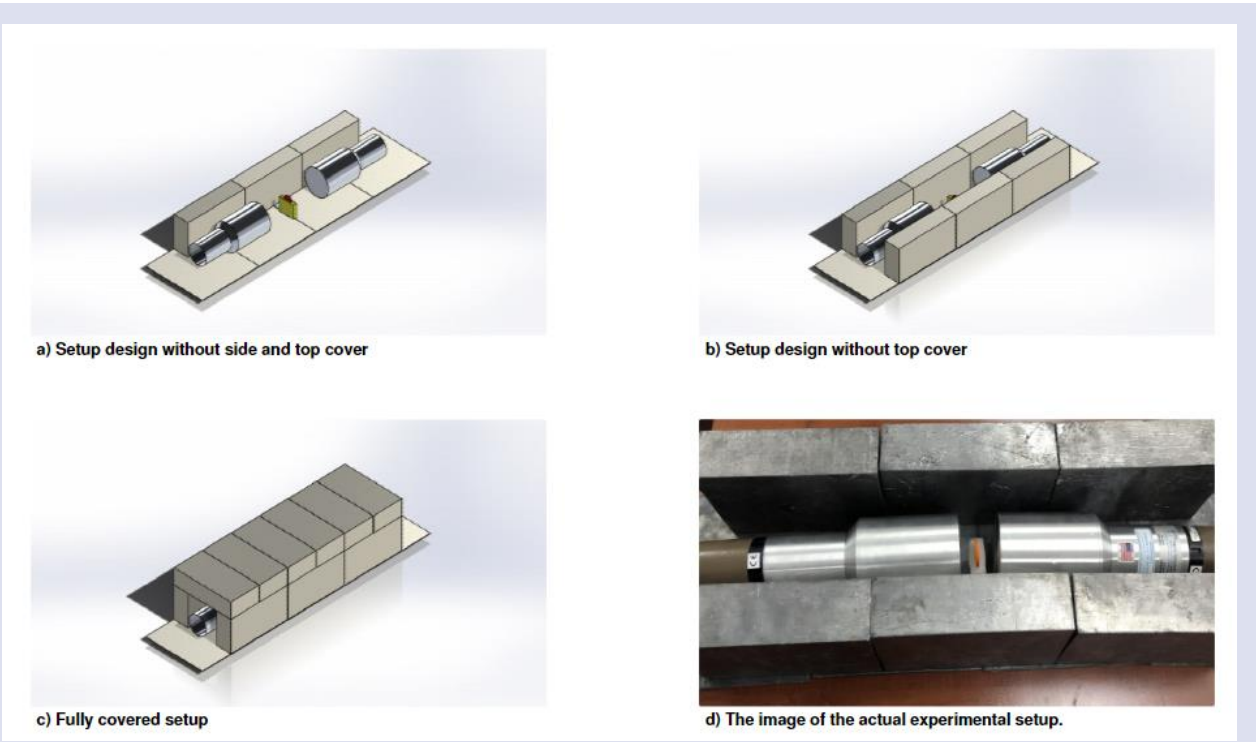

Figure 1. The lead blocks are 5 cm thick, and they covered both detectors and the source. The top blocks were put after the image was taken. The orange disk between the detectors is the gamma source.

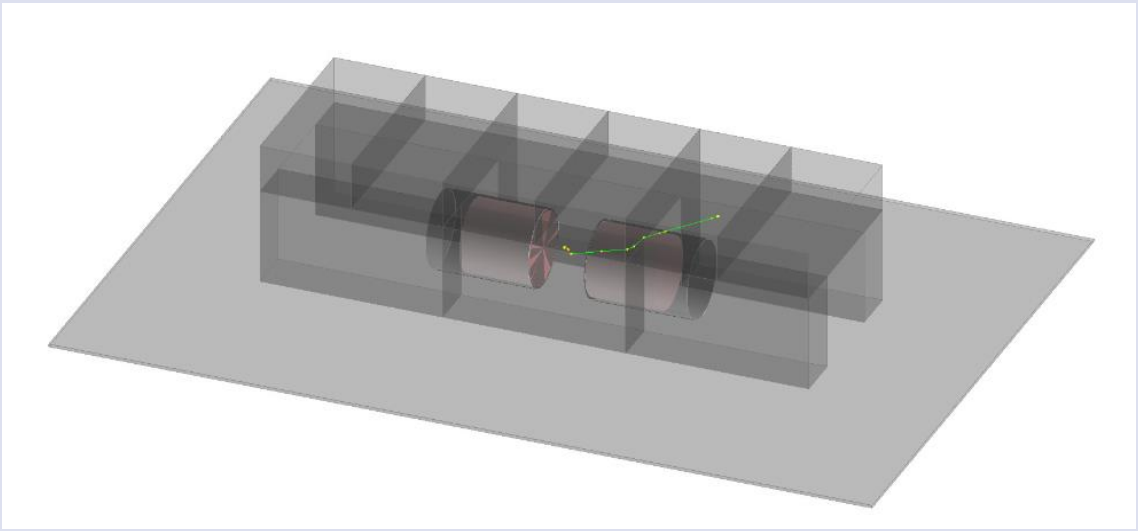

Figure 2. The Geant4 simulation includes lead blocks, lead sheets under the detectors, aluminum covers of the scintillation crystals and the NaI crystals (red cylinders). One gamma was released between two detectors.

Results

We began with the calculation of activity of the sources by using a hybrid model, which includes experiment and simulation. First, we calculated the efficiency of a single NaI (Tl) detector with Monte Carlo method. The next step was to create the same setup in the laboratory environment. The activity of a point source can be calculated with the equation given below [10];

$$A = \frac{N_p}{\epsilon \times \gamma \times t} \quad (1)$$

where A is the activity of the point source, N_p is the total area (or the total counts) under the interested peak, ϵ is the efficiency of the detector for the specific gamma peak of the source, γ is the probability of the source for emitting a gamma photon and t is the time of measurement in second. The current activities of the point sources were given in Table 1.

.**Table 1.** The radioactive sources that were used in this study and their calculated activities. The gamma energies and their emission probabilities are also given in the table.

Nuclide	Energy (keV)	Emission Probability (%)	Current Activity (kBq)
^{22}Na	511.0	179.91	8.85∓1.77
	1274.537	99.940	
^{60}Co	1173.228	99.85	14.7∓2.94
	1332.492	99.9826	
^{137}Cs	661.657	85.10	37.4∓7.48
^{54}Mn	834.848	99.9760	0.80∓0.16

After obtaining the current activities, we proceeded to our intended study. To perform the experiments, we carefully measured each of the distances and fixed the points where the detectors and sources were located. Here, it is essential to prevent extra uncertainties which may arise from miscalculated distances or solid angles.

The Root analysis program was used for all calculations and analyses in the study (see also “ROOT” [software], Release v6.24/06) [20,21]. First, the resolution of the detectors was calculated for the 662 keV gamma peak. The distance of the source-detector was 3 cm for each detector. The spectra which belong to ^{137}Cs for both detectors were given in Figure 3 and these spectra are given for 16384 channels. The Compass software was set to measure between 0 and 2500 keV in 16384 channels.

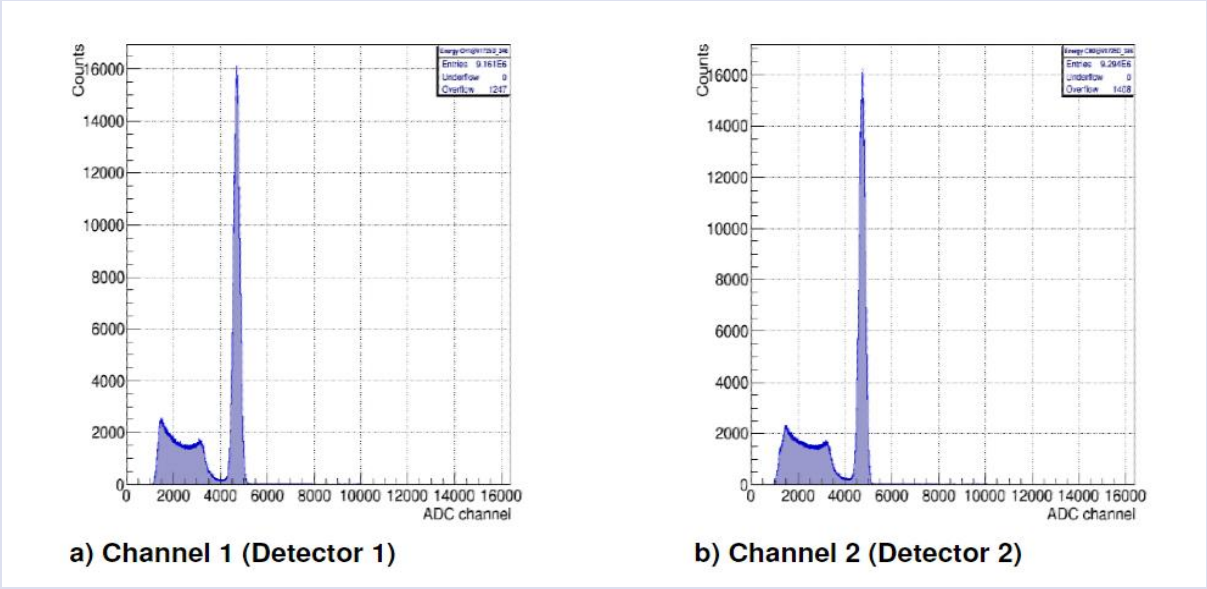

Figure 3. Spectrum of ^{137}Cs at 3 cm source-detector distance. Figure 3-a shows the spectrum of detector 1 and Figure 3-b shows the spectrum of detector 2. The spectra were taken by CAEN's Compass software..

The peaks were fitted using a Gaussian function, and the standard deviation (σ) of the fit function was calculated. Then, using the standard deviations from the fit, the full width at half maximum (FWHM) of the Gaussian was calculated, and the resolutions of the detectors were evaluated. Detector 1 (the detector on the left in Fig. 1) has 7.2% resolution at 662 keV, whereas Detector 2 (the detector on the right in Fig. 1) has 6.9% resolution at 662 keV. The relationship between the σ, FWHM, and the resolution (R) is given by Equation (2) [22].

$$2.335\sigma = FWHM$$
$$R = \frac{FWHM}{E_0} \times 100 \quad (2)$$

As shown in Figure 4, the shape of the fitted data was clearly Gaussian. Therefore, the standard relation given in Equation (2) can be used for the resolution calculations. Although the resolutions were 7.2% and 6.9% for detectors 1 and 2, respectively, it cannot be concluded that there is a difference in the resolution under same conditions since both detectors, photomultipliers (PMTs) and scintillation crystals, are sealed and cannot be opened. An additional analysis of PMT response to single photoelectron (SER) is required to conclude the real difference in resolution [23].

The measured resolutions for both detectors are comparable with those reported in previous works. The resolution values obtained for both detectors were close to 7%, but slightly worse than the datasheet values at 662 keV and at a detector-source distance of 3 cm. Akkurt et al. (2014) used a $3' \times 3'$ NaI(Tl) detector to determine the detector resolution for 5 different gamma energies at a detector-source distance of 0.5 cm. Their study found that the resolution for 662 keV was approximately 7%. Demir et al. (2021) conducted a study on a $3' \times 3'$ NaI(Tl) detector using Fluka Monte Carlo code. They calculated the energy resolution for the ^{137}Cs gamma peak (662 keV), which is traditionally used for resolution determination in NaI(Tl) detectors, as 6.48% [24]. Similarly, Tam et al. (2017) characterized NaI(Tl) both experimentally and using Geant4 Monte Carlo code and found the energy resolution for 662 keV at 20 cm detector-source distance to be 6.44% and 6.54%, respectively. Moszynski et al. (2003) conducted a study on pure crystals of NaI at both room temperature and liquid nitrogen (LN_2) temperature [25]. For their study, three pure NaI crystals were utilized, and the energy resolutions were measured. The resolutions at room temperature were approximately 16%, whereas at LN_2 temperatures, they ranged from 3.8% to 6.2%. The research demonstrates that NaI detectors, when pure, can achieve a resolution similar to that of $LaBr_3$ detectors at LN_2 temperatures.

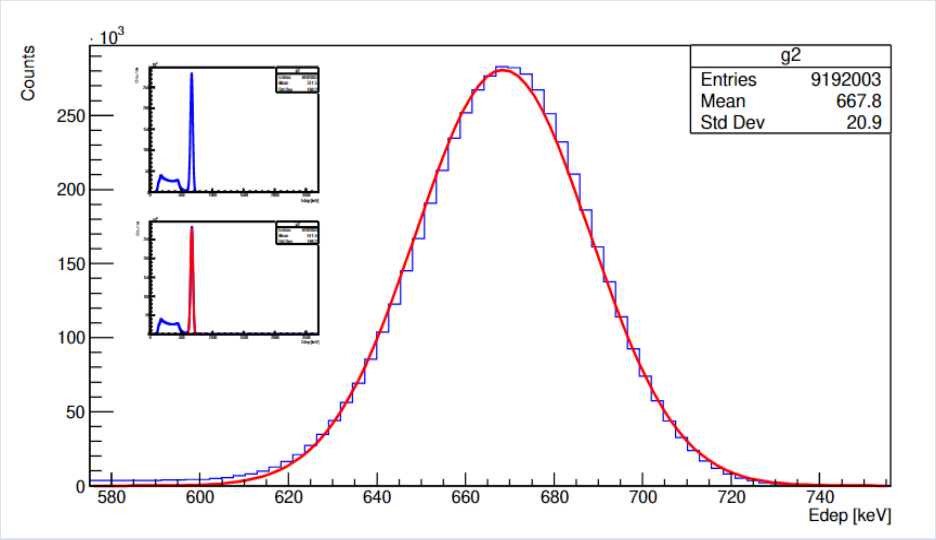

Figure 4. The experimental spectrum of the ^{137}Cs that belongs to one of the detectors. It shows the photo-peak at 662 keV and the gaussian function.

After getting the resolution of detectors, we proceeded to efficiency calculations. We analyzed each photo-peak with ROOT and calculated net area under the peak. By putting the count numbers in the Equation (1), we calculated the efficiencies for both detectors. The solid angles that the detectors saw were also calculated for each source-detector distance. This information is useful for determining the scaling factor for efficiency. The calculated solid angle fractions and scaling factor, or in other words, interaction probabilities are given in Table 2.

Table 2. Calculated interaction probabilities for Detector 1 and 2 from the experimental data.

	Interaction Probability											
Distance (cm)	511 keV		662 keV		835 keV		1173 keV		1275 keV		1332 keV	
	Det.1	Det.2	Det.1	Det.2	Det.1	Det.2	Det.1	Det.2	Det.1	Det.2	Det.1	Det.2
1	0.66	0.58	0.23	0.21	0.26	0.23	0.18	0.16	0.13	0.13	0.15	0.14
2	0.68	0.57	0.22	0.18	0.23	0.21	0.18	0.15	0.14	0.14	0.15	0.13
3	0.65	0.65	0.20	0.19	0.23	0.20	0.18	0.16	0.14	0.15	0.15	0.13
5	0.65	0.76	0.19	0.23	0.22	0.25	0.17	0.20	0.15	0.16	0.15	0.17
10	0.95	0.76	0.24	0.22	0.27	0.27	0.22	0.22	0.19	0.19	0.19	0.19

In following figures (Figures 5 and 6), a comparison of the experimental data and simulation data is given for Detector 1 and Detector 2, respectively. These figures show the change in efficiency with increasing source-detector distance. We also compared the efficiencies with increasing gamma energies. These comparisons are shown in Figures 7 and 8 for detectors 1 and 2, respectively. Figures 5 - 8 show similarities with previous studies and are in good agreement with literature and simulations [8, 13]. Although there are few results that do not agree with the simulations, these results may be due to the large uncertainty of the sources. The main purpose of this study is to determine the differences between two identical detectors with the same settings. We have already mentioned the difference in resolution. Figures 5 - 8 show the differences in terms of efficiency. In particular, the difference in the efficiency of 511 keV for 1 cm is clearly visible for these detectors. As the energy increases, this difference decreases, and this is true for increasing source-detector distance.

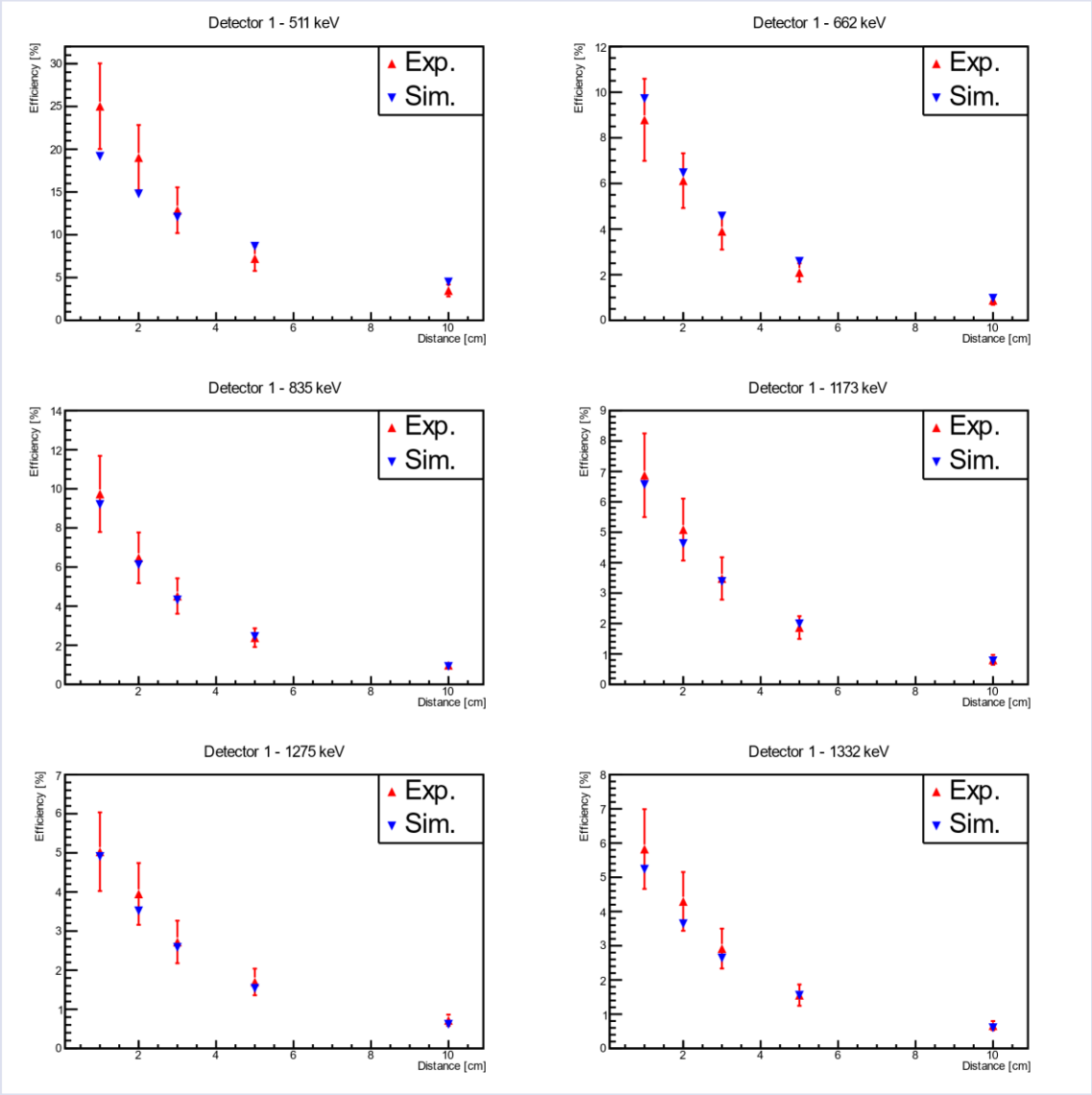

Figure 5. The efficiency graph of the Detector 1 with increasing distance in the x-axis. The simulation results are also in the graphs.

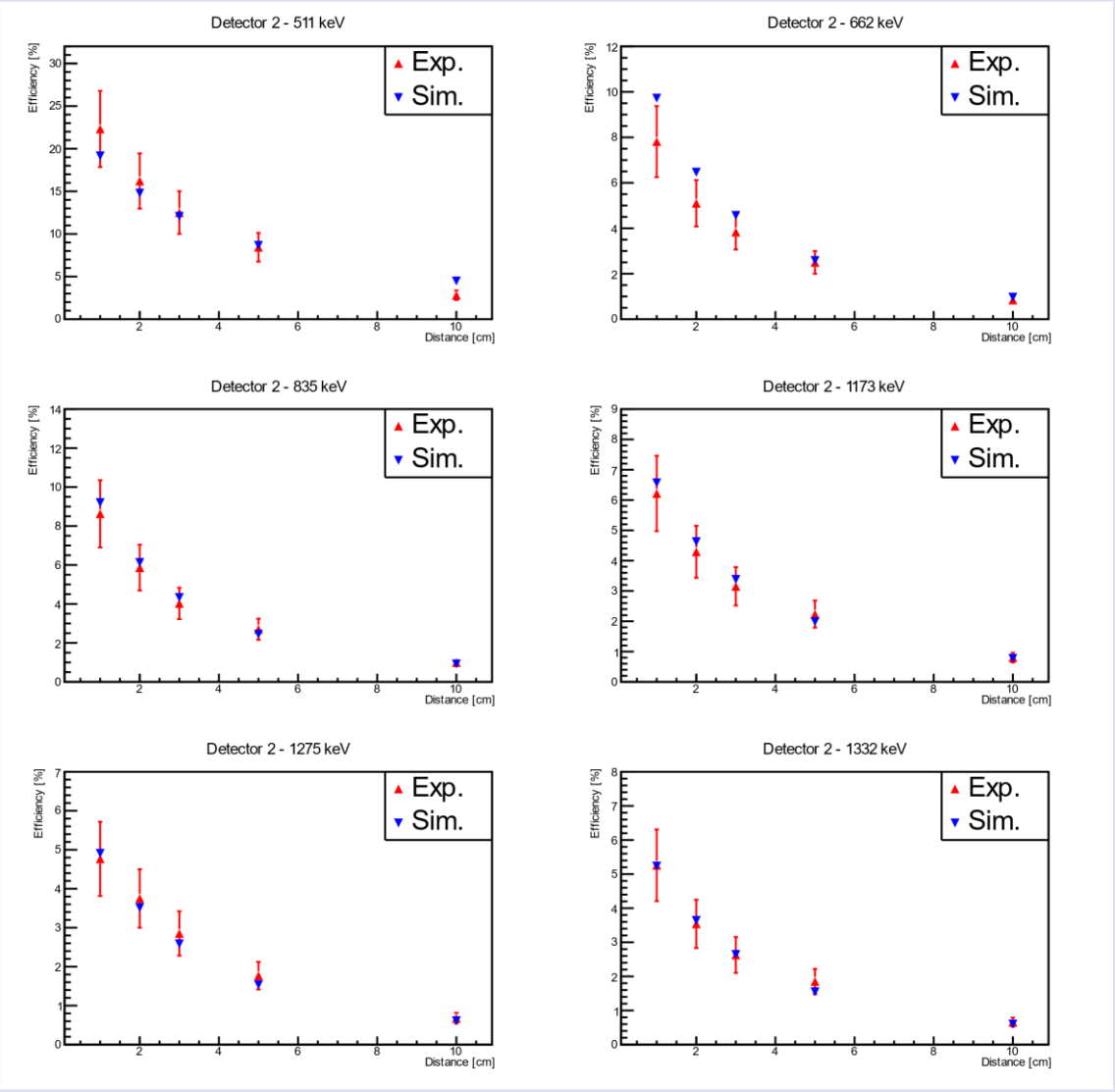

Figure 6. The efficiency graph of the Detector 2 with increasing distance in the x-axis. The simulation results are also in the graphs.

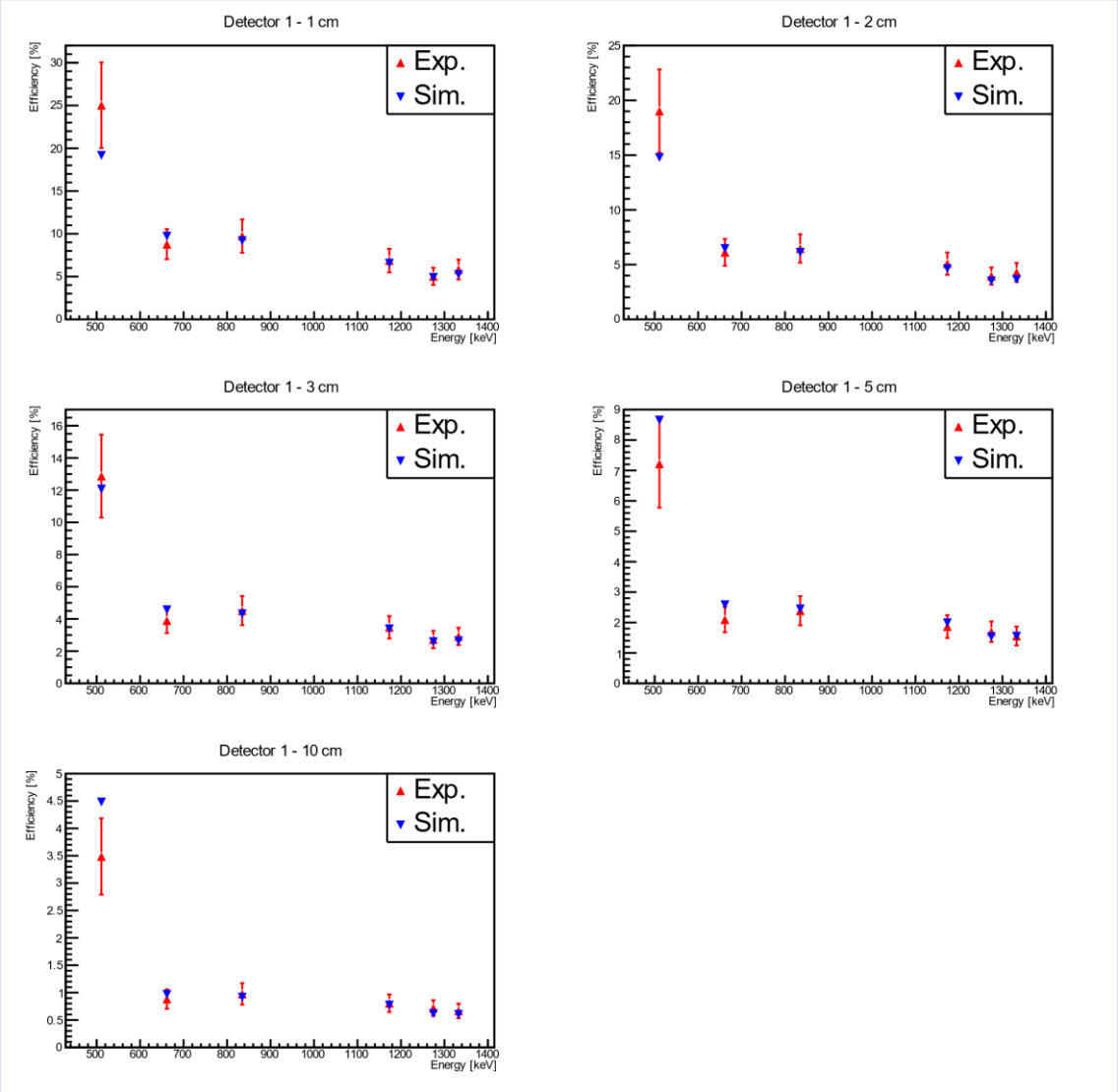

Figure 7. The efficiency graph of the Detector 1 with increasing energy in the x-axis. The simulation results are also in the graphs.

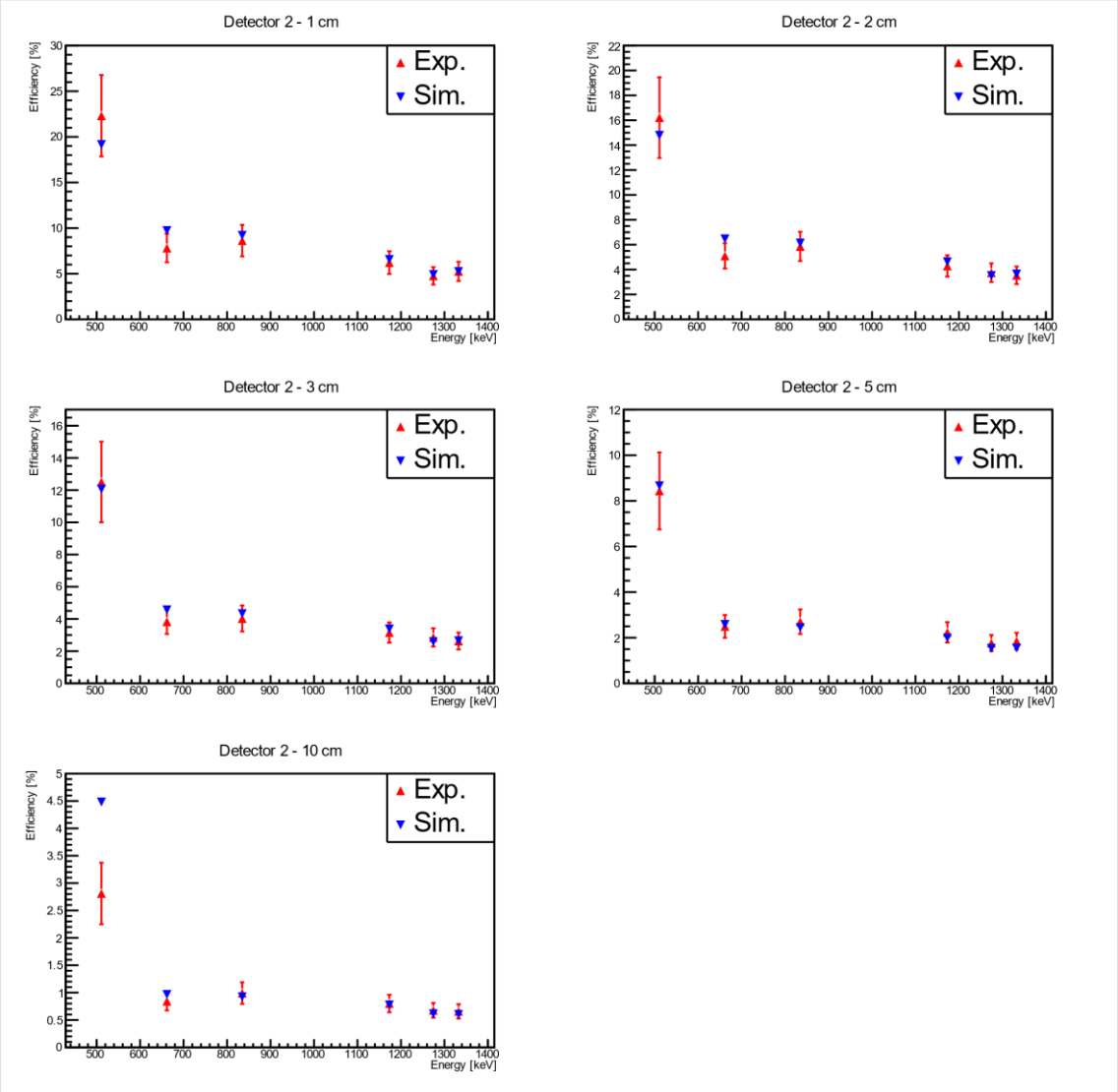

Figure 8. The efficiency graph of the Detector 2 with increasing energy in the x-axis. The simulation results are also in the graphs..

Looking at Figures 5-8, it is clear that Detector 1 has the highest efficiency of 25% and the lowest efficiency of 0.7%, while Detector 2 has the highest efficiency of 22% and the lowest efficiency of 0.7%. However, it is difficult to conclude that the difference in efficiencies at low energies is due to the same detector settings. The error bars indicate that both detectors may have the same efficiency for this setup. It is worth noting that Akkurt et al. (2014) demonstrated that a similar detector has a maximum efficiency of approximately 16% for 511 keV. Both of the detectors investigated in this study have a higher efficiency at lower energy levels. The study indicates that optimizing detector settings can lead to maximum efficiency and improved resolution. It was found that even with two identical detectors, the same performance values could not be achieved at the same settings. Compared to the literature, some similar detectors provided better resolution, but not greater efficiency. However, in high-budget experiments that use multi-gamma detector systems, increasing detection efficiency becomes more important when the detector resolution is deemed sufficient. The efficiency of the detector can also be improved by increasing the number of detectors surrounding the source, which will cover a larger solid angle. Measurements on a smaller scale with a larger number of detectors are more convenient for obtaining data from experiments, as covering a larger solid angle with a single detector leads to pile-up in the spectrum, especially in experiments with high fluxes [26, 27].

Discussion and Conclusion

We studied two identical NaI(Tl) scintillator detectors with the same settings as the bias voltages and software parameters to observe the differences in resolution and efficiency. We also performed Geant4 simulations using the exact experimental setup. While the results of the experiment are in good agreement with the literature values, we have observed some differences with the simulation data. In addition, there are certain differences in the resolution and efficiency with the same settings for both detectors. The first detector had a 7.2% resolution at 662 keV, while the second detector had a 6.9% resolution at 662 keV for a 3 cm source-detector distance. However, as stated in the previous section, this difference in resolution cannot be verified without SER measurements. The source of this difference is therefore not verified. Another difference worth noting is the efficiency of the two detectors. Detector 1 is clearly more efficient than detector 2 for small source-detector distances and low energies. The study's findings will make a valuable contribution to the literature, particularly regarding the use of multi-gamma detectors and effective coincidence/anticoincidence experimental setups. One of the desired features of modern nuclear experiments is an increased detection area for radioactive sources and the ability of the total spectrum to detect gamma rays with low emission probability without experiencing a pile-up effect. This system utilizes two NaI(Tl) detectors and can function as a coincidence setup through offline methods. Alternatively, it can be transformed into an online coincidence/anticoincidence experimental setup by adding a third non-NaI(Tl) detector, such as HPGe.

Conflicts of interest

There are no conflicts of interest in this work.

Acknowledge

We would like to thank Dr. Luciano Pandola for his valuable and useful comments and discussion.

References

[1] Bedir, M.E., Thomadsen, B., Bednarz, B., Development and Characterization of a Handheld Radiation Detector for Radio-Guided Surgery, *Radiat. Meas.*, 135 (2020) 106362.

[2] Borella, A., Camps, J., Paridaens, J., Vidmar, T., Characterization and Monte Carlo Simulations of a 4-Liter NaI Detection System for Use During Nuclear and Radiological Emergencies and for the Detection of Nuclear Materials, *AIP Conf. Proc.*, 1412 (2011) 335–342.

[3] Ghosh, C., Nanal, V., Pillay, R., Anoop, K., Dokania, N., Pal, S., et al., Characterization of Paris $LaBr_3(Ce)$-NaI(Tl) Phoswich Detectors up to E_γ~22 MeV, *J. Instrum.*, 11 (2016) P05023.

[4] Prieto, E., Casanovas, R., Salvado, M., Calibration and Performance of a Real-Time Gamma-Ray Spectrometry Water Monitor Using a $LaBr_3(Ce)$ Detector, *Radiat. Phys. Chem.*, 144 (2018) 444–450.

[5] Heranudin, S.M., van Wyngaardt, W., Guatelli, S., Li, E., Rosenfeld, A., Characterization of a Well-Type NaI(Tl) Detector by Means of a Monte Carlo Simulation for Radionuclide Metrology Application, *Appl. Radiat. Isot.*, 176 (2021) 109889.

[6] Yildirim, A., Solakci, S.O., Eke, C., Boztosun, I., Gamma Spectrometry Measurements of Natural and Artificial Radioactivity of Saklıkent-Antalya and Its Correlation to Quarries, *Arab. J. Geosci.*, 14 (2021) 1–11.

[7] Akkurt, İ., Arda, S., Gunoglu, K., Variation of Energy Resolution with Distance for a NaI(Tl) Detector, *Acta Phys. Pol. A*, 128 (2B) (2015a) B–422.

[8] Akkurt, İ., Gunoglu, K., Arda, S., Detection Efficiency of NaI(Tl) detector in 511–1332 keV Energy Range, *Sci. Technol. Nucl. Ins.*, 2014 (2014) 186798.

[9] Akkurt, İ., Tekin, H., Mesbahi, A., Calculation of Detection Efficiency for the Gamma Detector Using MCNPX, *Acta Phys. Pol. A*, 128 (2B) (2015b) 332–334.

[10] Mouhti, I., Elanique, A., Messous, M., Belhorma, B., Benahmed, A., Validation of a NaI(Tl) and $LaBr_3(Ce)$ Detector's Models via Measurements and Monte Carlo Simulations, *J. Radiat. Res. Appl. Sci.*, 11 (4) (2018) 335–339.

[11] Guss, P., Reed, M., Yuan, D., Beller, D., Cutler, M., Contreras, C., et al., Size Effect on Nuclear Gamma-Ray Energy Spectra Acquired by Different Sized $CeBr_3$, $LaBr_3:Ce$, and NaI:Tl Gamma-Ray Detectors, *Nucl. Technol.*, 185 (3) (2014) 309–321.

[12] Sariyal, R., Mazumdar, I., Sharma, Y., Patel, S., Chavan, P., Ranga, V., et al., Characterization of a Small Volume ($1' \times 1'$) $CeBr_3$ Crystal for γ-Ray Measurements up to 4.4 MeV, *J. Instrum.*, 16 (01) (2021) T01004.

[13] [Akkurt, İ., Waheed, F., Akyildirim, H., Gunoglu, K., Monte Carlo Simulation of a NaI(Tl) Detector Efficiency, *Radiat. Phys. Chem.*, 176 (2020) 109081.

[14] Yalcin, S., Gurler, O., Kaynak, G., Gundogdu, O., Calculation of Total Counting Efficiency of a NaI(Tl) Detector by Hybrid Monte-Carlo Method for Point and Disk sources, *Appl. Radiat. Isot.*, 65 (10) (2007) 1179–1186.

[15] Mitra, P., Tyagi, M., Thomas, R., Kumar, A.V., Gadkari, S., Optimization of Parameters for a CsI(Tl) Scintillator Detector Using Geant4-Based Monte Carlo Simulation Including Optical Photon Transport, *IEEE T. Nucl. Sci.*, 66 (7) (2019) 1870–1878.

[16] Tam, H.D., Yen, N.T.H., Chuong, H.D., Thanh, T.T., et al., Optimization of the Monte Carlo Simulation Model of NaI(Tl) Detector by Geant4 Code, *Appl. Radiat. Isot.*, 130 (2017) 75–79.

[17] Agostinelli, S., Allison, J., Amako, K.A., Apostolakis, J., Araujo, H., Arce, P., et al., Geant4—A simulation Toolkit, *Nucl. Instrum. Methods Phys. Res. A*, 506 (3) (2003) 250–303.

[18] Allison, J., Amako, K., Apostolakis, J., Araujo, H., Dubois, P.A., Asai, M., et al., Geant4 Developments and Applications, *IEEE T. Nucl. Sci.*, 53 (1) (2006) 270–278.

[19] Allison, J., Amako, K., Apostolakis, J., Arce, P., Asai, M., Aso, T., et al., Recent Developments in Geant4, *Nucl. Instrum. Methods Phys. Res. A*, 835 (2016) 186–225.

[20] Brun, R., Rademakers, F., Root — an Object Oriented Data Analysis Framework, *Nucl. Instrum. Methods Phys. Res. A*, 389 (1) (1997) 81-86.

[21] ROOT, Data Analysis Framework. Available at: https://root.cern/releases/release-62406/. Retrieved September 3, 2021.

[22] Knoll, G.F., Radiation detection and measurement. 4th Ed. John Wiley & Sons, (2010) 105-121.

[23] Freitas, E., Fernandes, L., Yahlali, N., Perez, J., Alvarez, V., Borges, F. et al., PMT Calibration of a Scintillation Detector Using Primary Scintillation, *J. Instrum.*, 10 (02) (2015) C02039.

[24] Demir, N., Kuluozturk, Z.N., Determination of energy resolution for a NaI(Tl) detector modeled with FLUKA code, *Nucl. Eng. Technol.*, 53 (2021) 3759-3763.

[25] Moszynski, M., Balcerzyk, M., Czarnacki, W., Kapusta, M., Klamra, et al., Study of Pure NaI at Room and Liquid Nitrogen Temperatures, *IEEE T. Nucl. Sci.*, 50 (4) (2003) 767-773.

[26] Oliveira, J.R.B., Moralles, M., Flechas, D., Carbone, D., Cavallaro, M., et al.,, First comparison of GEANT4 hadrontherapy physics model with experimental data for a NUMEN project reaction case, *Eur. Phys. J. A*, 56 (5) (2020) 153.

[27] Cappuzello, F., Agodi, C., Calabretta L., Calvo, D., Carbone, D., et al., The NUMEN Technical Design Report, *Int. J. Mod. Phys. A*, 36 (30) (2021) 2130018.

Cumhuriyet Sci. J., 45(2) (2024) 426-436
DOI: https://doi.org/10.17776/csj.1401016

Cumhuriyet Science Journal

| csj.cumhuriyet.edu.tr | Founded: 2002 ISSN: 2587-2680 e-ISSN: 2587-246X Publisher: Sivas Cumhuriyet University

Assessment of Indoor and Water Radon Concentrations in Esenyurt and Beylikdüzü Districts of Istanbul, Marmara Region, Turkey

Firdevs Banu Özdemir[1,a,*], Halim Büyükuslu[2,b], Tuba Özdemir Öge[3,c]

[1] *Department of Medical Services and Techniques, Simav Vocational School of Health Sciences, Kütahya Health Sciences University Kütahya, Türkiye.*
[2] *Espiye Vocational School Giresun, Giresun University, Türkiye.*
[3] *Department of Forestry Industry Engineering, Faculty of Forestry Bartin, Bartın University, Türkiye.*
**Corresponding author*

Research Article

History
Received: 06/12/2023
Accepted: 20/05/2024

ABSTRACT

The radon activity concentration measurements for indoor and tap water were studied in Esenyurt and Beylikdüzü districts of Istanbul Province, Turkey. The mean radon concentration value received from thirty-six passive radon detectors was obtained as 63.56 Bq/m^3. The mean annual effective dose for indoor radon measurements is 1.60 mSv/y in this measurement period. The radon activity results of calculated tap water samples were under 0.8 Bq/L. The annual effective doses resulting from ingestion and inhalation were calculated to evaluate the health risk across various age groups. All radon measurement results, and the associated calculated data for ingestion and inhalation remained below the threshold values established by international organizations.

Keywords: Radon, Indoor, Tap Water, LSC, Dose.

[a] *firdevsbanu.ozdemir@ksbu.edu.tr* *https://orcid.org/0000-0002-7935-2062*
[b] *halim.buyukuslu@giresun.edu.* *https://orcid.org/0000-0001-5623-8761*
[c] *tozdemir@bartin.edu.tr* *https://orcid.org/0000-0001-6690-7199*

Introduction

In the nature, radon occurs naturally as a product of α-decay of uranium, and it is the heaviest radioactive gas. Radon (^{222}Rn) is a natural radioactive gas, and its half-life is 3.84 days. Radon, which is in the ^{238}U natural radioactive series, is formed as a result of α emission of ^{226}Ra. The known isotopes of radon, which is a colorless, odorless, and tasteless gas, ^{220}Rn and ^{219}Rn, have very short half-lives, 55 s and 3.9 s, respectively. Therefore, the radon element is dominated by ^{222}Rn. Formation of radon is based on the radioactive decay of natural uranium in soil, rocks and water. The main atoms of this degradation chain can be found in all natural materials. Therefore, radon is released into the environment from all surface rock and soil fragments and building materials. As a result of the potential hazard of radon gas on human health, a vast number of studies on radon monitoring and annual effective dose calculations have been introduced. Radon mixes with the air underground through cracks in soil and rocks and from water coming to the surface. Consequently, studies to assess radon concentration are primarily conducted in water and soil [1]. Büyükuslu et al. (2018) conducted indoor and tap water radon measurements at selected sampling areas of Giresun University. Thirty-eight CR-39 solid-state nuclear track detectors were placed. To measure radon concentrations, water samples were collected from six distinct departments. The average indoor radon concentration was determined to be 193.7 Bq/m^3. Furthermore, the concentrations of radon in tap water samples were observed to vary between 0.98 Bq/L and 27.28 Bq/L [2]. In another study, radon and radium concentrations of well waters in Afyonkarahisar were determined. In this study, the measured maximum values were 28.82 Bq/L and 7.16 Bq/L, for the radon and radium concentrations, respectively. Similarly, the measured minimum concentrations were 0.42 Bq/L and 0.07 Bq/L for radon and radium, respectively [3]. Köksal et al. (1993) conducted measurements of the average indoor ^{222}Rn concentrations across over four hundred homes within the Istanbul province. The radon concentration averages ranged from 10 Bq/m^3 to 260 Bq/m^3, with a median concentration of 50 Bq/m^3 [4]. Tufaner carried out indoor radon measurements in Edirne provincial center in the Marmara Region and reported that the radon concentration measurement results ranged between 2-125 Bq/m^3. The mean radon concentration was determined to be 27.58 Bq/m^3, and the annual effective dose was computed to be 0.728 mSv [5]. Günay et al., performed short term indoor radon measurements in Istanbul and their results varied between 19–53 Bq/m^3. The annual radiation dose values varied between 0.150 mSv -0.402 mSv [6].

Esenyurt and Beylikdüzü, two districts located in the west of Istanbul, have experienced rapid growth and a significant increase in population in recent years. The geological structure of these districts differs from other regions of Istanbul. They are composed of alluviums formed during the Tertiary and Quaternary periods, which typically consist of sand, gravel, and clay. The relationship between radon and geological structure depends on

several factors. Some factors such as uranium content of rocks, soil and rock porosity, groundwater, cracks and fault lines in the earth's crust, geological and topographic features, regional geological structure are critical in determining radon levels and exposure risks in a region. Hence, geological structures must be considered in the process of conducting radon risk assessments.

Depending on the water geology and geological structure of the place where the resources are located, very high concentration values can be detected. Radioactivity concentrations vary over a wide range depending on the geological and chemical composition of the environment [7].

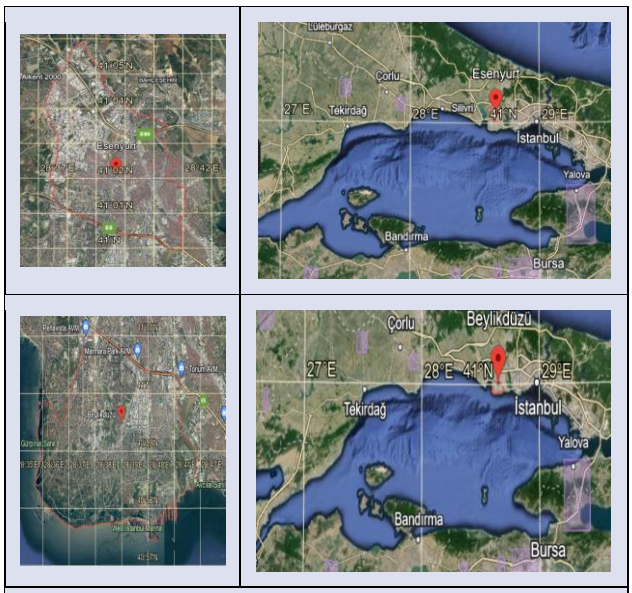

Figure 1. The satellite imagery of the Esenyurt and Beylikdüzü districts was acquired by Google Earth, version 10.49.0.0, on March 20, 2024.

Radon measurement studies aim public health protection, and, in this context, it involves identification of radon concentrations, acquiring knowledge about their impact on human health, and integration of radon mitigation measures in the design and construction of buildings. Radon measurement studies provide the basis for the development of effective strategies to reduce radon exposure and minimize its potential harms on human health. In our research, the primary motivations for performing radon measurements include "Health Effects" and "Environmental Monitoring and Risk Assessment." The results of the measurements were analyzed to provide a basis for public health policies and housing standards. The most serious health-related risk about radon exposure is lung cancer. In this regard, comprehending and minimizing radon exposure is crucial, especially for high-risk groups. Potential risk groups involve individuals such as smokers, miners, underground workers, and residential inhabitants. Radon protection measures include radon testing, ventilation, and engineering controls. In this regard, the present study aims to measure the tap water and indoor radon concentrations in Beylikdüzü and Esenyurt districts of Istanbul Province of Marmara Region. A total of 36 indoor (air) radon concentration measurements were performed for indoor radon measurements. Four (4) sampling locations were determined for tap water measurements to support the indoor radon measurements. The radon activity measurements for indoor and tap water samples were performed using CR-39 detector and LSC system. Passive radon detectors and liquid scintillation counting system are two different methods used to measure environmental radon gas concentration.

Twenty passive radon detectors were placed in the selected residences between two sampling dates (29.05.2019 - 24.09.2019). Sixteen passive radon detectors were placed in the selected residences between two sampling dates (18.02.2020–13.08.2020). Also, radon concentration values of tap water samples taken from four houses on 02.07.2019 were determined. The obtained radon concentration measurements were compared with the literature studies performed in Marmara Region and other regions of Turkey. The factors and parameters likely to be effective on the obtained results were also discussed.

Material and Method

Description of The Study Area

Beylikdüzü is one of the western districts of Istanbul. It is surrounded by the Marmara Sea in the south, Avcılar in the east, Büyükçekmece in the west and Esenyurt in the north. Esenyurt district is in the Trakya sub-region of the Marmara Region, within the boundaries of the Istanbul Metropolitan area. The radon concentration measurements for indoor and tap water radon concentration were performed in Esenyurt and Beylikdüzü districts (Figure 1). The distribution of the sampling locations was specified so as to represent the whole study area. All selected sampling locations for indoor and drinking water measurements are apartments located in the study area. All detectors were placed in rooms that were free of electronic systems or devices, at around 50 cm height from the floor. Passive radon detectors for indoor sampling points were placed in the locations identified in Figure 2 and Figure 3. The satellite view of the sampling points for drinking water samples is shown in Figure 4. The flow diagram for radon measurement is provided in Figure 5, in our study.

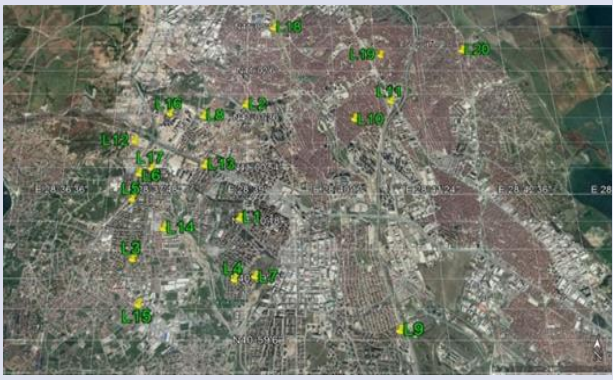

Figure 2. The satellite image of twenty indoor sampling points received by Google Earth Pro (March 14, 2020). Eye altitude 12.26 km. Maxar Technologies 2020 (Google Earth Pro V5 2020).

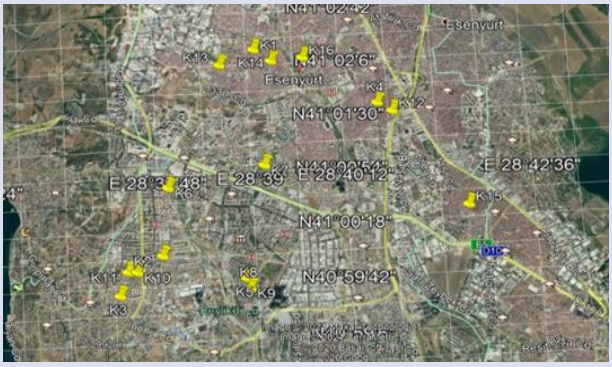

Figure 3. The satellite image of sixteen indoor sampling points received by Google Earth Pro (January 14, 2021). Eye altitude 12.26 km. Maxar Technologies 2020 (Google Earth Pro V5 2020).

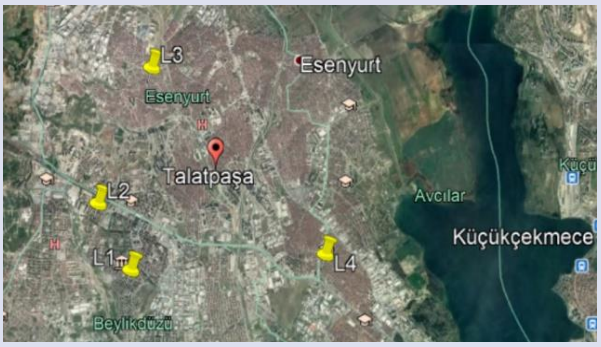

Figure 4. The satellite image of water sampling points received by Google Earth Pro V. (March 26, 2020). Eye altitude 22.39 km. Maxar Technologies 2020 (Google Earth Pro V5 2020).

Passive Radon Detectors (CR-39)

Semiconductor detectors based on CR-39 are often used in nuclear physics and radiation dosimetry. The high energy separation capabilities of semiconductor detectors, which began to be used in the 1960s, as well as their fast-timing characteristics and effective thickness, make them superior to other detectors. Rapid developments in micro-electronics in recent years have led to an increase in the quality of detector fabrication technology and ease in the production of complex structured detectors.

Generally, the responsiveness of CR-39 nuclear track detectors to radon radiation is influenced by a variety of factors, including the configuration of the detector, conditions of exposure, duration of exposure, the methodology employed in the etching process, and the calibration procedure [8]. Detectors play a pivotal role in measuring diverse physical phenomena within the domain of particle physics. The most critical functions include: the identification and detection of particles, the determination of their positions (trajectories), the measurement of time intervals, the assessment of momentum, the evaluation of energy [9].

The passive radon detectors were provided by Turkey Energy, Nuclear and Mining Research Institute (TENMAK). Detection of indoor radon gas is based on the counting of the traces in the film detector (CR-39) in the diffusion container created by alpha particles released as a result of radioactive decay. CR-39 detectors used in both research and public health applications are a popular tool for detecting radioactive gases and they are commonly employed for measuring radon in air, water, and soil. Additionally, because they are easy to use and portable, they are suitable for measuring radon levels in homes and workplaces. CR-39 detectors are typically used in indoor spaces, especially in areas such as basements and ground floors where there is a high probability of radon accumulation. The advantages of CR-39 detectors include high sensitivity, wide measurement range, long-term exposure measurement, low cost, and ease of use. On the other hand, long analysis periods, the need for technical expertise, being single-use, environmental effects, and the inability to perform instant readings lead to limited use of CR-39 detectors. Despite such limitations, CR-39 remains as one of the most widely employed methods for radon measurement across residential, commercial, and industrial domains due to its reliability and effectiveness.

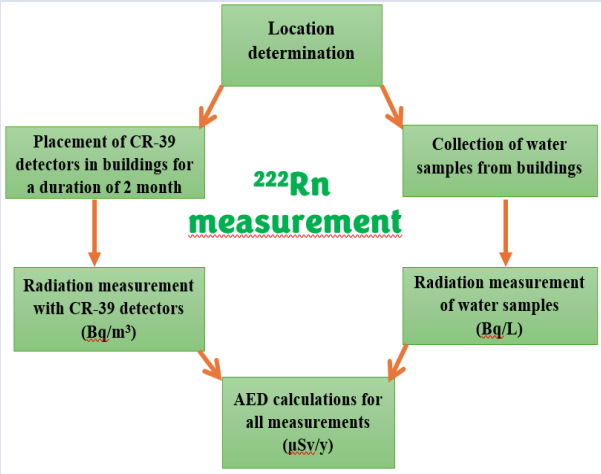

Figure 5. Flow diagram of radon measurement.

Sample Collection for CR-39

CR-39 detectors in cylindrical geometry were placed in aluminum containers and sent to Sarayköy Nuclear Research and Training Center (SANAEM) for analysis. Radon gas concentration values per unit volume of the indoor environment were obtained in Bq/m^3 as given in Figure 6. Thirty-six passive radon detectors were left in the sampling locations for periods ranging between 98-175 days. In the measurements of radon concentration in the air, the CR-39 detector was placed 1 meter above the ground. During this period, they were not relocated, and they were checked at various time intervals.

Liquid Scintillation Counting (LSC)

Scintillation detectors' working principle is based on the emission of visible light in proportion to the amount of radiation they absorb. The intensity of this light is quantified using photomultiplier tubes, enabling the determination of the radiation level. The Liquid Scintillation Counting (LSC) method exhibits high sensitivity in the detection of low-level radioactivity. The Liquid Scintillation Counting (LSC) method is characterized by its broad applicability, facilitating the analysis of liquid, solid, and gaseous samples. As an active measurement technique, LSC systems offer the advantage of immediate measurement, thereby providing instant access to measurement values. Additionally, waste management emerges as a pertinent issue encountered within Liquid Scintillation Counting (LSC) systems. Another concern pertains to the risk of chemical contamination. Chemical interactions between the scintillation fluid and the sample can induce background noise, potentially affecting the measurements. The preparation and processing of samples in the LSC method constitute another area requiring precision. Particularly, the proper mixing of the scintillation fluid with the samples is of significance.

Sample Collection and Preparation

The drinking water samples collected from four sampling locations were put into 250 ml glass bottles. The glass bottles were closed with a cork stopper and a cap to avoid air inlet. This consideration was taken into account for all water samples. Liquid scintillation counting was applied as per ASTM D5072 standard.

Liquid scintillation counting technique is one of the most preferred techniques for radioactivity measurements in water samples. This detection method was used for the analysis of all water samples. Radon gas concentrations in water were obtained in Bq/L. In the ASTM D5072 standard, an aliquot of unaerated water is injected beneath the liquid scintillation mixture of 10 mL. The vials are then capped, shaken, and left to remain 3 hours before the counting process. In the current work, water samples were counted using 1220 Quantulus Ultra Low Level Liquid Scintillation Counter and the scintillation cocktail used is Mineral Oil. 10 ml of water samples were mixed with 10 ml of the scintillation cocktail (Mineral Oil). The counting efficiency was estimated by mixing the Ra-226 standard solution with 10 ml of the scintillation cocktail and leaving it for 30 days. Distilled water was used to prepare the background sample. Both the samples and the solution were prepared using glass vials with 20 ml.

Discussion

In this research, the indoor radon activity concentrations in Esenyurt and Beylikdüzü region were analyzed by CR-39 detector. As indicated in Figure 6, between 29.05.2019 and 24.09.2019, indoor radon concentration values were calculated as 34 Bq/m^3–99 Bq/m^3. The average radon concentration value was also obtained as 60.85 Bq/m^3. Average annual effective doses of indoor radon measurements in these dates ranged from 0.86 to 2.49 mSv/y as shown in Figure 9. Between 18.02.2020 and 13.08.2020, indoor radon concentration values were calculated as 57 Bq/m^3–83 Bq/m^3. The average radon concentration value was also obtained as 66.94 Bq/m^3. According to the Radiation Safety Regulation, the permitted value for radon in dwellings is 400 Bq/m^3 and it cannot exceed 1000 Bq/m^3 in workplaces. This value is not exceeded in the measured areas in this study.

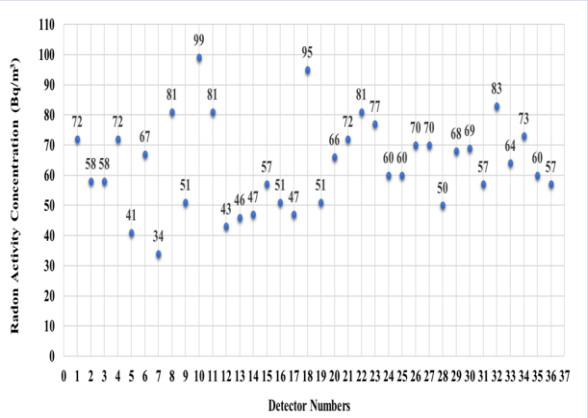

Figure 6. Indoor radon activity concentrations (expressed in becquerels per cubic meter) were quantified using passive detectors over the interval from May 29, 2019, to August 13, 2020.

Radon gas concentrations in Becquerels per m^3 (C_{Rn}) were calculated using Equation 1.

$$C_{Rn} = (CF)(D_{Rn})\left(\frac{1000}{24T}\right) \quad (1)$$

where T is the exposure period in days, CF is the calibration factor, and D_{Rn} is the track density for radon gas [10].

The annual effective dose attributed to indoor radon exposure can be determined through the application of Equation 2 [11]:

$$D = C_{Rn}F\ (O)(DCF) \quad (2)$$

where F represents the equilibrium factor (0.4), C_{Rn} denotes the concentration of radon (Bq/m^3), DCF signifies

the dose conversion factor 9 $nSvh^{-1}$ $(Bqm^{-3})^{-1}$, and O is the occupancy (7000h), utilized in converting the radon concentration to effective dose.

The radon concentration measurement results in Beylikdüzü area were lower than those in Esenyurt area. The highest radon concentration value is in Esenyurt district as 99 Bq/m^3 and the lowest is in Beylikdüzü district as 34 Bq/m^3. The average radon concentration value was obtained as 63.56 Bq/m^3, standard deviation is 14.64 Bq/m^3 and median is 62 Bq/m^3.

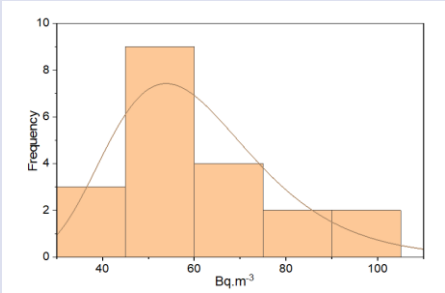

Figure 7. The histogram representing indoor radon measurements.

The histogram of the radon concentration was given in Figure 7. The distribution is consistent with the lognormal distribution. Radon concentration follows approximately lognormal distribution as expected from literature [12-14].

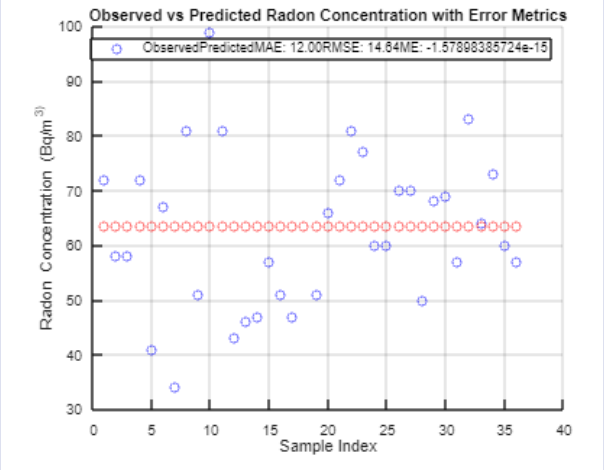

Figure 8. Cross-validation diagrams for indoor radon activity concentrations (measured in becquerels per cubic meter).

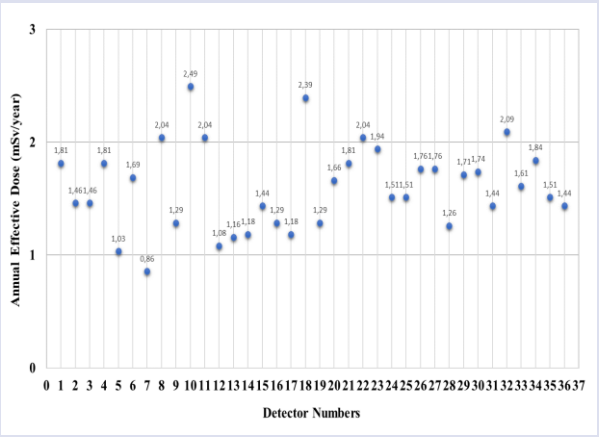

Figure 9. The annual effective dose (measured in millisieverts per year) was computed for indoor measurements spanning the period from May 29, 2019, to August 13, 2020.

Beylikdüzü is a district of Istanbul with a border to Marmara Sea. Esenyurt has no connection with the sea. There are thermal water resources in Esenyurt. This situation explains that the radon concentration level in Esenyurt region is higher than Beylikdüzü region as the thermal water coming from the underground has a high dissolved radon content. The results of annual effective dose calculations ranged from 0.86 to 2.49 mSv/year as given in Figure 9. The mean value of annual effective dose is 1.60 mSv/year.

The performance of the interpolation estimates was evaluated using mean absolute error (MAE), root mean square error (RMSE), and mean error (ME) as performance metrics, as reported by Damla et al. (2022). Cross-validation figures pertaining to indoor radon activity concentrations are depicted in Figure 8.

Spatial interpolation distribution maps are derived from a methodology employed to infer values amidst points within a designated geographic location to utilize point data, such as radon concentrations gathered from diverse sites within an urban environment. Spatial interpolation method applies mathematical models to interpolate or extrapolate the values in interstitial spaces between discrete measurement locations. This methodology facilitates the estimation of anticipated values at arbitrary locations. This approach can be utilized to illustrate the spatial heterogeneity of environmental variables, including but not limited to air quality, aquatic contamination, pedological characteristics, or the dispersion of radon. A spatial interpolation distribution map of the Annual Effective Dose (AED) resulting from ingestion and inhalation across various age demographics, including adults, children, and infants, has been computed as described [15]. The distribution fit of interpolated Annual Effective Dose (AED) values is also shown in Figures 10-15.

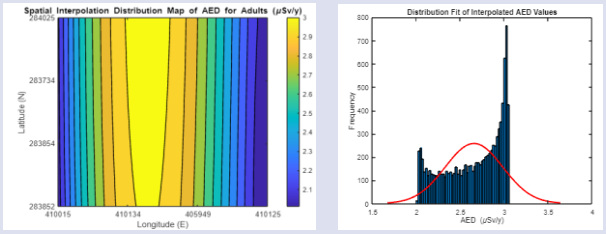

Figure 10. Spatial interpolation distribution map depicting the AED from ingestion for adults.

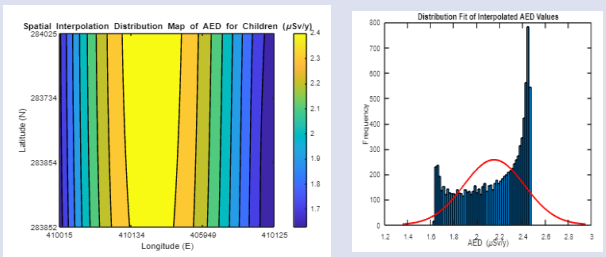

Figure 11. Spatial interpolation distribution map depicting the AED from ingestion for children.

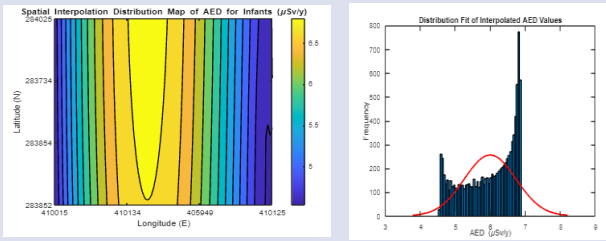

Figure 12. Spatial interpolation distribution map depicting the AED from ingestion for infants.

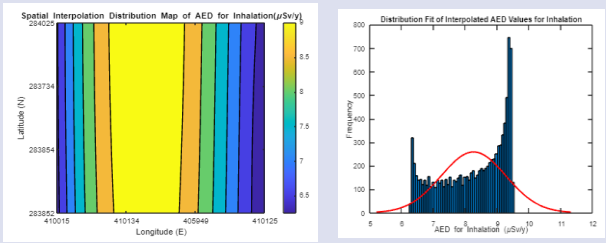

Figure 13. The histogram representing indoor radon measurements.

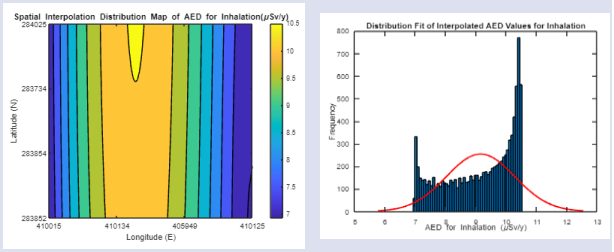

Figure 14. Spatial interpolation distribution map depicting the AED from inhalation for adults.

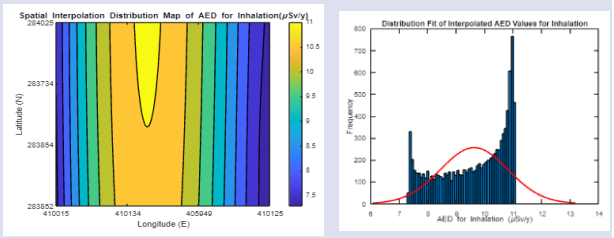

Figure 15. Spatial interpolation distribution map depicting the AED from inhalation for infants.

The colors on the maps indicate the estimated annual effective dose (AED) levels at various latitude and longitude points. It can be observed in Figures 10-15 that colors vary horizontally (longitude) and remain relatively constant vertically (latitude). Contour lines on the map represent equivalent AED levels. The opposite ends of color scale represent the lowest and highest AED values in the interpolation results. The histogram plot shows the frequency distribution of the interpolation results and a distribution fit curve (possibly a normal distribution) superimposed on it. This diagram demonstrates the variation of AED (Annual Effective Dose) values and outlines the general configuration of their distribution, emphasizing the central tendency. It is observed that the interpolation results span in a broad frequency spectrum, suggesting variability within a specific range throughout the interpolation process. The red fit curve exemplifies the anticipated frequencies under the assumption that the data adheres to a normal distribution. Nevertheless, the visualization reveals the presence of an extended tail, particularly on the right flank of the data distribution.

Table 1. The radon activity results for tap water samples

Tap Water	Date: 02.07.2019 Experimental measurement results (Bq/l)	Minimum measured value (Bq/l)
Sample 1	< 0.8 Bq/l	0.8 Bq/l
Sample 2	< 0.8 Bq/l	0.8 Bq/l
Sample 3	< 0.8 Bq/l	0.8 Bq/l
Sample 4	< 0.8 Bq/l	0.8 Bq/l

Table 2. AED due to ingesting and inhalation ^{222}Rn from tap water for adults, children and infants

Tap Water	Ingestion (μSv/y)			Inhalation (μSv/y)		
	Adults	Children	Infants	Adults	Children	Infants
Sample 1	< 2.04	< 1.652	< 4.6	< 6.34	< 7.03	< 7.39
Sample 2	< 2.04	< 1.652	< 4.6	< 6.34	< 7.03	< 7.39
Sample 3	< 2.04	< 1.652	< 4.6	< 6.34	< 7.03	< 7.39
Sample 4	< 2.04	< 1.652	< 4.6	< 6.34	< 7.03	< 7.39

The radon concentration levels in the water samples for Esenyurt and Beylikdüzü regions were analyzed by liquid scintillation counting system as shown in Table 1. During the water radon activity measurements, domestic water samples used by the residents in their daily lives were used. All values were found to remain under the minimum detectable amount (MDA). In a large metropolis such as Istanbul, distribution of water from the source to households can be made through complicated networks and the water is stored by Istanbul Water and Sewage Administration for periods which exceed the half-life of Rn-222 (3.7 days), resulting in significantly low radon concentration levels. Our finding is also under the level of 0.8 Bq/L (Table 1) which is lower than the recommended limit value specified by USEPA as 11 Bq/L [16].

Mamun and Alazmi (2022) conducted a study on the investigation of radon in groundwater utilizing the RAD7 electronic portable radon detector. The radon concentrations in groundwater within the examined area ranged from 0.03 to 3.20 Bq/L, averaging at 1.16 Bq/L. These estimated measurements significantly fall below the safety limits established by international organizations. The calculated total annual effective dose from radon exposure for infants, children, and adults varied between 0.05 and 16.24 μSv/y, with an average dose of 5.89 μSv/y, as reported by [17]. Duong et al. (2023) studied the seasonal 222Rn activity in spring water. The AED for residents who consume the spring water resources were reported to rage within acceptable limits, with average values calculated at 37.9 μSv/year for adults, 29.3 μSv/year for children, and 79.6 μSv/year for infants, respectively [18]. In relation to these values, within the context of our study, the AED_{ing} (ingestion) values for infants, children and adults are < 4.6 μSv/y, < 1.652 μSv/y, and < 2.04 μSv/y, respectively (Table 2). The findings calculated for AED_{ing} and AED_{inh} are summarized in the Table 2. The AED_{inh} (inhalation) values for infants, children and adults are < 7.39 μSv/y, < 7.03 μSv/y, and < 6.34 μSv/y, respectively (Table 2). The estimated AED values for ingestion and inhalation are significantly lower than the recommended threshold of 100 μSv/year, as reported by the World Health Organization (WHO) [19]. These values are also far below the limit values of World Health Organization [19]. These measured and calculated results remain under the specified limit values and pose no risk for human health, however periodical radon monitoring is necessary since various dynamic parameters (such as seismic, geographic, etc.) may be effective on radon levels in water.

Ingestion is calculated as given in Equation 3. The annual effective dose (AED) attributable to the ingestion of 222Rn from water by an individual was determined through the application of the following [11]:

$$AED_{ing}=C_w \text{ X } W_L \text{ X DCF} \quad (3)$$

where AED_{ing} denotes the annual effective dose received by an individual due to the ingestion of radon, C_w is the ^{222}Rn concentration in water (Bq.L^{-1}), W_L represents the annual consumption of water by adults, children, and infants, measured in liters. The values are assumed to be 730 L for adults, 350 L for children, and 250 L for infants, respectively [20-21] and DCF represents the dose conversion factor applicable to radon ingestion. The values are specified as 3.5, 5.9, and 23 nSv/Bq^{-1} for adults, children, and infants, respectively [22-23].

Inhalation is calculated as given in Equation 4. The annual effective dose (AED) attributable to water samples can be determined using the equation provided below [11]:

$$AED_{inh} = C_w \times R_{w/a} \times EF \times ET \times DCF \quad (4)$$

where AED_{inh} denotes the annual effective dose attributable to inhalation, C_w represents the concentration of ^{222}Rn in water, and $R_{w/a}$ indicates the coefficient for radon transfer from water to air (10^{-4}), EF signifies the equilibrium factor between radon and its progeny, possessing a value of 0.4, ET represents the mean exposure time, expressed in hours. ET is assumed to be 7000 hours annually, based on the premise that individuals spend 80% of the year in indoor environments and DCF denotes the dose conversion factor for inhalation of radon. It is 28.3, 31.4 and 33.0 nSv(Bq.h.m^{-3})$^{-1}$ for adults, children and infants, respectively [22, 23, 24].

ELCR is the excess life-time cancer risk and is calculated as given in Equation 5.

$$ELCR = E_W.DL.RF\ (Excess\ life-time\ cancer\ risk) \quad (5)$$

where E_w is the mean effective dose due to radon exposure, DL is the average lifetime (estimated as 70 years), and RF is the fatal cancer risk, and its value is 5.5 x 10^{-2} Sv^{-1} determined by [25]. Radon-induced lung cancer risk was calculated to define the conversion ion factor which is 18 x 10^{-6} mSv^{-1}·y [26, 27].

Table 3. ELCR calculation results

Tap Water	Excess life-time cancer risk ELCR (%)	Radon-induced lung cancer risk (per million persons)
Max C_{Rn}	0.96	44.82
Min C_{Rn}	0.33	15.48
Mean C_{Rn}	0.62	28.82

The calculated excess life-time cancer risk (ELCR) and radon-induced lung cancer risk values for minimum, maximum, and mean radon concentrations are shown in Table 3. The values of excess lifetime cancer risk range from 0.33 % to 0.96 %. The excess lifetime cancer risk values in the present study are lower than the EPA standard for the estimated risk as 1.3% corresponding with radon exposure of 148 Bq/m^3 for the entire population [28, 29].

The results of the published works related to water and indoor radon activity measurements in the Marmara Region and the corresponding calculated annual effective doses in various water sources are presented in Table 4 [30-36]. Tarım et al. (2012) measured Rn-222 concentrations in well and tap water samples from several geological formations in Bursa Province and reported that all measured concentrations were below the limit radon activity concentration value of 100 Bq/L specified by European Union. As reported by the authors, the radon activity concentration of tap water samples was lower than well water samples. They also reported a possible correlation between the activity concentrations and the geological structure of the subject area [30]. Akar (2010) carried out a work on radon activity levels in the thermal waters of Çekirge region in Bursa [31]. The author emphasized the necessity for determination of radioactivity around Bursa province due to the variation in the findings some of which exceeded the recommended value of 11 Bq/L determined by [16] and related this variation to the tectonic activities of North Anatolian Fault Zone and Eskişehir Fault Zone. Alakuş (2013) reported that the values exceeded the limit value of 11 Bq/L in several studied regions [32], which is consistent with the findings of [31] in the same region. Kılıç (2011) reported the radon activity concentration levels in Kükürtlü thermal waters from Bursa province and calculated the corresponding annual effective dose values. They attributed the significantly low concentration levels to the means of storage and escape of radon gas during sampling. The average indoor radon values were reported to range between 7.57 ± 4.35 Bq/m^3 and 179.09 ± 46.50 Bq/m^3 [33]. In a recent work of [34], radon activity concentration measurements were carried out with RAD7 radon detector Geyve, Doğançay and Örencik localities of Sakarya Province which are rich in granite soil in common. Drinking water radon concentrations were measured as 1.66 Bq/L in Geyve, 0.93 Bq/L in Örencik and 1.15 Bq/L in Doğançay [34]. Karahan et al. (1999) reported the activity concentrations of Rn-222 and Ra-226 in lake and tap waters (Bq/L). The concentrations were reported to be between 0.019 Bq/L and 0.048 Bq/L for Rn-222 [35]. In another recent work, Uludağ (2018) evaluated the radon gas levels in the spring water samples from Şile-Kandıra-İzmit in the Marmara Region. The radon measurement levels in the measured spring waters ranged from 0.334 Bq/L to 7.810 Bq/L and average value was 2.110 Bq/L. In the subject area, the results from spring waters did not indicate any health risk as they did not exceed the recommended values. The effective dose in Şile-Kandıra-İzmit regions is in the range of 0.12-1.64 mSvy^{-1} and it has an average value of 0.47 mSvy^{-1} [36].

Domestic use of groundwaters, which are in direct contact with geological formations rich in uranium and its decay products, leads to exposure to natural radiation via ingestion and inhalation of radon gas. Therefore, monitoring of radon activity concentration in waters has become an important task for protection of human health. In Marmara region, many of the drinking water supplies are directly connected to groundwater sources as shown in Table 4, thus monitoring of radon levels in these areas are of great importance. In the present research, on the other hand, the distribution of drinking water for the subject area (Esenyurt and Beylikdüzü districts of Istanbul) is provided indirectly via large water supply networks and after long storage periods which results in reduction in the radon levels due to the short half-life of radon gas until the drinking water reaches the end-users. Thus, the results of the present research in addition to those of the reported study in Table 4 carried out in Istanbul. Ref [35] indicate that, radon activity concentrations in Istanbul are lower than most of the other provinces of Marmara Region, such that, in the present research the measurement results remain under the minimum detectable level. The measurements of indoor radon concentration levels are based on the several factors. Acquisition of diverse measurement results from different study areas increase the importance of radon monitoring studies as well as establishment of a radon database. Aeration of indoor environments, elevation of detectors from the ground level, the subject building's structural material properties, its insulation, ground structure of the study area as well as the geological and seismic activities during the measurement period all contribute to the variance in indoor measurement results. Indoor radon concentration measurements were made in many areas of Turkey. In Table 5, the maximum average concentration values were measured as 793.6 Bq/m^3 in winter in Örencik [34].

Table 4. Radon activity concentrations and calculated annual effective dose values of water samples (min.-max. values, otherwise average values)

Location	Sampling source	Applied radon measurement method/detector	Radon activity concentration range (min.- max. Bq/L)	Annual effective dose	Ref.
Bursa	Well water	AlphaGUARD PQ 2000PRO	(1.46- 53.64)	(0.02 -1.11 µSv/y)	[30]
	Tap water		(0.91-12.58)		
Çekirge-Bursa	Thermal water	AlphaGUARD PQ 2000PRO	(2.513 ± 0.286) – (94.347 ± 4.361)	N/A	[31]
Bursa	Spring water	AlphaGUARD PQ 2000PRO	(0.62 - 50.96)	N/A	[32]
Kükürtlü-Bursa	Thermal water	AlphaGUARD PQ 2000PRO	(2.09 ± 0.145)	(0.0065 ± 0.0004 mSv/y)	[33]
	Pool water		(0.599 ± 0.115)	(0.0019 ± 0.0003 mSv/y)	
Geyve, Örencik and Doğançay - Sakarya	Drinking water	RAD7	(0.93 - 1.66)	N/A	[34]
Istanbul	Various sources	Lucas Radon detector	(0.019-0.048)	N/A	[35]
Şile-Kandıra-İzmit	Spring water	RAD7	(0.334 - 7.810)	(0.12-1.64 mSv/y)	[36]
Esenyurt and Beylikdüzü/Istanbul	Tap water	Liquid scintillation counting system	< 0.8	(Ingestion: 2.04 + Inhalation: 2.02 µSv/y)	Present study
Esenyurt and Beylikdüzü/Istanbul	Tap water	Liquid scintillation counting system	< 0.8	(Ingestion: 2.04 + Inhalation: 2.02 µSv/y)	Present study

Table 5. Radon activity concentrations and calculated values for annual effective dose of indoor samples (min.-max. values, otherwise average values)

Location	Sampling source	Applied radon measurement method/detector	Average indoor Rn-222 concentrations (Bq/m3) (min.- max. Bq/L)	The mean annual effective dose	Ref.
Edirne	Indoor (apartment buildings and houses)	CR-39 nuclear track detectors	49.2 Bq/m3	1.24 mSv/y	(37]
Sakarya	Indoor (classrooms, laboratories and offices)	LR-115 type-II solid state nuclear track detectors	40 ± 5 Bq/m3	1.00 mSv/y	[38]
Kilis, Osmaniye, Antakya	Indoor (houses)	Passive nuclear track detectors	50 Bq/m3 (Kilis) 51 Bq/m3(Osmaniye) 40 Bq/m3 (Antakya)	1.26 mSv/y(Kilis) 1.29 mSv/y(Osmaniye) 1.01 mSv/y(Antakya)	[39]
Erzurum	Indoor (dwellings)	Nuclear track detector LR-115	* 11 ± 6 Bq/m3 - 380 ± 91 Bq/m3 in winter season * 8± 3 Bq/m3 - 356 ± 64 Bq/m3 in summer season	* from 0.278 to 9.59 mSv/y in winter * from 0.202 to 8.98 mSv/y in summer	[40]
Geyve, Örencik, Doğançay	Indoor (dwellings)	LR-115 detectors	in Geyve for winter 221.63 Bq/m3 and for summer 138.37 Bq/m3, in Örencik for winter 793.67 Bq/m3 and for summer 194.00 Bq/m3, in Doğançay for winter 273.67 Bq/m3 and for summer 150.56 Bq/m3	-	[34]
Esenyurt and Beylikdüzü/Istanbul	Indoor (houses)	CR-39 detectors	63.56 Bq/m3	1.60 mSv/y	Present study

The minimum average concentration value was measured as 8 Bq/m^3 in Erzurum during the summer months [40]. As compared to these results, the findings of the present work shown in Table 5 are also lower than several average indoor concentrations values reported in the literature for the other locations in the Marmara Region. Measured radon activity concentration and calculated annual effective dose values of indoor sample was 63.56 Bq/m^3, this value is higher than Edirne indoor study with 49.2 Bq/m^3 [37], Sakarya indoor study with 40 ± 5 Bq/m^3 [38] and Kilis, Osmaniye, Antakya indoor study with 50 Bq/m^3 (Kilis), 51 Bq/m^3 (Osmaniye), 40 Bq/m^3 (Antakya) [39]. As reported in literature studies on indoor radon measurements, indoor radon levels significantly vary depending on the seasonal changes as hot weather conditions require aeration of indoor measurements which results in reduced radon concentration levels. This is also supported by the findings of the present research. In addition to the aeration of indoor environments, the variation in indoor radon measurement results may have also arisen from geological activities of the study area.

Conclusion

In this study, radon concentrations within indoor environments and water samples, collected from the Esenyurt and Beylikdüzü districts of Istanbul Province during the period from May 29, 2019, to August 13, 2020, were analyzed utilizing passive radon detectors and a liquid scintillation counting system.

- A total of 36 measurements of indoor (air) radon concentrations were conducted. The average value of radon concentration was determined to be 63.56 Bq/m³. The average annual effective dose derived from indoor radon measurements amounted to 1.60 mSv/year, which also fell below the recommended threshold values for indoor radon concentrations.

- The outcomes of radon activity measurements for all tap water samples were below 0.8 Bq/L. The AEDing values for infants, children, and adults are less than 4.6 µSv/y, less than 1.652 µSv/y, and less than 2.04 µSv/y, respectively. Similarly, the AEDinh values for infants, children, and adults are less than 7.39 µSv/y, less than 7.03 µSv/y, and less than 6.34 µSv/y, respectively. The estimated AED values for ingestion and inhalation are significantly lower than the recommended threshold of 100 µSv/year, by the World Health Organization (WHO).

- Spatial radiological maps, categorized by ages, were visually constructed within the locations under investigation.

- The majority of radon concentration assessments, including the one presented in this research, are predicated on considerations of human health. Consequently, it is customary for these measurements to be conducted in regions characterized by significant human density. Therefore, two districts have been selected, and radon measurements have been conducted.

- This research was aimed to gather the existing body of radon mapping data for the Marmara Region of Turkey documented in the literature, while also furnishing readers with insights into the water and indoor radon activity levels within the Marmara region.

- Preparation of publicly accessible radon maps for the purpose of regularly monitoring radon levels on regional and national scales, implementing radon reduction measures during the design and construction of new buildings, conducting radon mitigation training among the public, and enhancing awareness of radon's potential health risks, are practical suggestions that can be implemented within public health policies. Furthermore, research should be conducted to better understand the relationship between radon exposure and health outcomes, such as lung cancer.

Acknowledgements

This study was supported by Beykent University Scientific Research Project with 2018-19-BAP-16 project number. The authors thank to Turkey Energy, Nuclear and Mining Research Institute (TENMAK) for the technical support.

Conflicts of Interest

The authors declare no conflict of interest.

References

[1] Akar, Ü. Determination of Radon Concentrations (Rn-222) in Thermal Waters of Bursa-Çekirge Region, Master's Thesis, Uludağ University Institute of Natural Sciences, 2010.

[2] Akbulut S., Taskın H. Determination of natural radioactivity by gross α and β measurements in tap waters in Rize province, *J Radioanal Nucl Chem* 303(1) (2014) 413–420.

[3] Alakuş, F. Measurement of radon gas radioactivity in Bursa water resources, Bozok University Institute of Natural Sciences, Master's Thesis, 2013.

[4] Bossew, P. Radon: exploring the log-normal mystery, *J. Environ. Radioact.* 101 (2010) 826-834.

[5] Bozkurt, A., Kam, E. Indoor Radon Measurement in The City of Edirne, Turkey, *AIP Conference Proceedings*, 899 (2007) 395.

[6] Brudecki K, Li WB, Meisenberg O, Tschiersch J, Hoeschen C, Oeh U Age-dependent inhalation doses to members of the publich from indoor short-lived radon progeny. Radiat Environ Biophys 53 (2014) 535–549.

[7] Büyükuslu, H., Özdemir, F.B., Özdemir Öge T., Gökce, H. Indoor and tap water radon (222 Rn) concentration measurements at Giresun University campus areas. Appl. Radiat. Isot. 139 (2018) 285–291.

[8] Cafaro, C., Giovani, C., Garavaglia, M. Geostatistical simulations for radon indoor with a nested model including the housing factor, *J. Environ. Radioact*. 151 Pt 1, (2016) 264-274.

[9] Can, B., Canbazoğlu, C., Albayrak, N., Çelebi, N., Doğru, M. Measurements of indoor radon concentration levels in Kilis, Osmaniye and Antakya, Turkey during spring season, *J Radioanal Nucl Chem*, 292, (2012)1059–1063.

[10] Choubey V.M., Bartarya S.K., Ramola R.C. Radon in groundwater of eastern Doon valley, Outer Himalaya, *Radiation Measurements* , 36 (2003) 401 – 405.

[11] Damla, N., Alp, M. S., Yesilkanat, C. M., Isık, U. Evaluation and analysis of the spatial distribution of radiation risks caused by radon in drinking water of Batman, Türkiye, *Journal of Radioanalytical and Nuclear Chemistry,* 331 (2022) 5859–5868.

[12] Dwaikat, N., Safarini, G., El-hasan, M., Lida, T., *Nuclear Instruments and Methods in Physics Research A,* 574 (2007) 289–291.

[13] Duong, V. H., Vu, H. D., Nguyen, D. T., Pham, L. T., Tóth, G., Hegedűs, M., & Kovacs, T.. Seasonal 222Rn activity in spring water close to rare earth element and uranium mines in North Vietnam, *Journal of Radioanalytical and Nuclear Chemistry,* (2023)1-9.

[14] Durak, R., Kiran, D., Kavaz E., and Ekinci, N. Indoor radon measurements in Erzurum province of Turkey, Journal of Physics: Conference Series 707 012029, International Physics Conference at the Anatolian Peak (IPCAP2016) (2016).

[15] EPA 402-R-03-003, 2003. EPA Assessment of Risks from Radon in Homes. *Office of Radiation and Indoor Air United States Environmental Protection Agency Washington*, DC 20460.

[16] Günay, O., Aközcan, S., Kulalı, F. Determination of indoor radon concentrations, *European Journal of Science and Technology*, 13 (2018) 91-97.

[17] Haner B., Yilmaz A., Kürkçüoğlu, M. E. Karadem, A. Mencilis (Bulak) Mağarasında Radon Seviyesi Ölçümleri. *Suleyman Demirel University Journal of Natural and Applied Sciences,* 14 (3) (2010) 218–224.

[18] ICRP, International Commission on Radiological Protection. The 2007 Recommendations of the International Commission on Radiological Protection, ICRP Publication 103. Ann. ICRP 37, (2007) 2-4.

[19] ICRP, International Commission on Radiological Protection. Lung Cancer Risk from Exposure to Radon Daughters, ICRP Publication 50. Ann. ICRP 17 (1987) 1.

[20] Karahan, G., Öztürk, N., Bayülgen, A. Natural Radioactivity in Various Surface Waters in Istanbul, Turkey, *Water Research,*. 34 ,18 (2000) 4367-4370.

[21] Kormaz Gorur F., Camgoz H. Natural radioactivity in various samples and radiation dose estimations in Bolu province, *Turk Chemosphere*, 112 (2014) 134–140.

[22] Kılıç, N. Kükürtlü Kaplıcaları Atatürk Rehabilitasyon Merkezindeki Radon Konsansantrasyonunun Belirlenmesi. Yükseklisans Tezi, Uludağ Üniversitesi, Fen Bilimleri Enstitüsü, 2011

[23] Köksal, E. M., Çelebi, N., Özçınar, B.,. Indoor Rn-222 concentrations in Istanbul Houses. Health Physics, 65 (1), (1993) 87-88.

[24] Mamun, A., Alazmi A. S. Investigation of Radon in Groundwater and the Corresponding Human-Health Risk Assessment in Northeastern Saudi Arabia, *Sustainability*, 14(21), (2022) 14515.

[25] Nero, A., Schwehr, Nazaroff, M. W., Revzan K. Distribution of airborne radon- 222 concentrations in U.S. homes, *Science*, 234 (4779), (1986) 992-997.

[26] Ozdemir F.B. Determination of Radon Concentrations (Rn-222) in Well Waters in Afyon and Its Surrounding, Master's Thesis, Afyon Kocatepe University, Institute of Natural and Applied Sciences, Physics Department. 2005.

[27] Rani S, Kansal S, Singala AK, Mehra R. Radiological risk assessment to the publich due to presence of radon in water of Barnala district, Punjap, India, *Environ Geochem Health*, 43(12) (2021) 5011–5024.

[28] Quarto M., Pugliese, Verde, M. G. Loffredo, F. Roca, V. Radon Exposure Assessment and Relative Effective Dose Estimation to Inhabitants of Puglia Region, South Italy. Int., *J. Environ. Res. Public Health,* 12, (2015) 14948-14957.

[29] Sağlam Y. Radon measurement in Geyve District, Dogancay Regıon and Orencik Village. Sakarya University Institute of Natural Sciences, Master's Thesis, 2019

[30] Singala A.K., Kansal S., Mehra R. Quantification of radon contamination in drinking water of Rajasthan, India. *J Radioanal Nucl Chem.,* 327(3) (2021) 1149–1157.

[31] Sherafat, S., Mansour, S. N. Mosaferi M., Aminisani, Yousefi, N. Z. Maleki, S. First indoor radon mapping and assessment excess lifetime cancer risk in Iran, *MethodsX*, 6, (2019)2205–2216.

[32] Tarım, U. A., Gurler, O., Akkaya, G., Kılıç, N., Yalcin, S., Kaynak, G., Gundogdu, O. Evaluation of radon concentration in well and tap waters in Bursa, Turkey, *Radiation Protection Dosimetry*, 150 (2) (2012), 207-212.

[33] Tufaner, F. Indoor Radon Concentration Measurements at Edirne City Center. Trakya University, *Journal of Engineering Sciences*, 19(1), (2018) 1-8.

[34] Uludağ, N. Examining of Regional Radon Gas in Sprıng Water Resources the Area of Sile-Kandıra-Izmit And Sakarya University Radon Awareness Survey, Sakarya University Institute of Natural Sciences, Master's Thesis, 2018.

[35] United States Environmental Protection Agency (USEPA), National primary drinking water regulations for radionuclides. US, Governmental Printing Office, Washington EPA/570/9-91/700 (1991).

[36] United Nations Scientific Committee on the Effects of Atomic Radiation (UNSCEAR) Sources and effects of ionizing radiation. Report of the United Nations Scientific Committee on the Effects of Atomic Radiation to the General Assembly. United Nations, New York. (2000)

[37] Villalba, L., Colmenero Sujo, L., Montero Cabrera, M.E., Cano Jime´nez, A., Renter´ a Villalobos M., Delgado Mendoza C.J., Jurado Tenorio L.A., Da´ vila Rangel I., Herrera Peraza E.F. Radon concentrations in ground and drinking water in the state of Chihuahua, Mexico, Journal of Environmental Radioactivity 80 (2005). 139-151.

[38] Walet, N. P615: Nuclear and Particle Physics, UMITS, Manchester, U.K. (2003)

[39] World Health Organization WHO. Guidelines for drinking water quality: Radiological Aspects 3rd ed, Geneva, Switzerland (2004).

[40] Zenginerler, Z., Ertugral, F., Yakut, H., Tabar, E., Demirci, N., Gunermelikoglu, K. Measurement of Seasonal Indoor Radon Concentration in Sakarya University, Turkey, *ACTA PHYSICA POLONICA A,* 130 (2016).

Cumhuriyet Sci. J., 45(2) (2024) 437-443
DOI: https://doi.org/10.17776/csj.1387861

Cumhuriyet Science Journal

| csj.cumhuriyet.edu.tr | Founded: 2002 ISSN: 2587-2680 e-ISSN: 2587-246X Publisher: Sivas Cumhuriyet University

Log-Linear Model Analysis of Aftershock Sequences: A Review on the 6 February Earthquakes in Turkey

Gökçen Altun [1,a,*]

[1] *Department of Econometrics, Faculty of Economics and Administrative Sciences, Ankara Hacı Bayram Veli University, Ankara, Türkiye.*
**Corresponding author*

Research Article

History
Received: 08/11/2023
Accepted: 15/03/2024

ABSTRACT

Researchers have conducted numerous studies on earthquakes and aftershocks, some of which have utilized statistical analysis methods. However, there is no direct research examining the interaction between variables thought to influence aftershocks following major earthquakes. In this study, 2194 aftershocks with a magnitude of 3 or higher that occurred after two major earthquakes in Turkey on February 6, 2023 were analyzed using log-linear models with respect to variables such as depth, magnitude, time, and city. At the end of the study, all four primary variables - city, magnitude, depth, and time - were found to be statistically significant. Based on the parameter estimation values, it was found that the probability of aftershocks occurring in Malatya was 1.17 times greater than in Adıyaman, 2.82 times greater than in Gaziantep, and 1.38 times greater than in Hatay, while the probability of aftershocks occurring in Kahramanmaraş was 3 times greater than in Malatya. Thus, it can be said that the aftershocks are influenced by the center of the major earthquake. Additionally, it was found that the probability of aftershocks with a magnitude between 3 and 3.5 was 1.4 times greater than those with a magnitude of 4 or higher, and the probability of aftershocks with a depth of less than 10 kilometers was 2 times greater. We believe that the results of this study will provide information on aftershocks that occur after major earthquakes and will be helpful for future studies.

Keywords: Aftershock, Earthquake, Categorical data analysis, Log-linear model.

[a] *gokcenefendioglu@gmail.com* *https://orcid.org/0000-0003-4311-6508*

Introduction

Earthquakes are seismic events that occur due to the movements of fault lines in the earth's crust. These movements occur as a result of the accumulation of stress and tension in the earth's crust. The intensity of earthquakes can be measured using the Richter scale or similar measures. Earthquakes usually occur in the form of main and aftershocks. Studies on earthquakes and aftershocks can address topics such as earthquake prediction, earthquake early warning systems, emergency planning, structural design, earthquake-resistant building materials, and damage reduction techniques. These studies are important for reducing the damage caused by earthquakes and for preparing people for earthquakes.

Many studies have been done by researchers to analyze earthquakes with large and small magnitudes to understand the behavior of the earth crust. Different statistical models such as hidden Markov process, machine learning, extreme value theory, statistical distributions have been used to analyze such data sets. For instance, Pisarenko et al. (2014) proposed a new method by combining generalized extreme value and generalized Pareto distributions to describe the tail probabilities [1]. Ma et al. (2021) used the peaks-over-threshold method to assess the possible damage of large earthquakes in China [2].

Beyreuther and Wassermann (2008) used the hidden Markov model to classify small earthquakes [3]. Yip et al. (2018) proposed a latent Markov process for earthquake prediction. Machine learning techniques are also widely used in seismic analysis [4]. Li et al. (2018) developed an early warning system for earthquakes based on a machine learning technique, generative adversarial network [5]. Mangalathu et al. (2020) classified building damages caused by earthquakes using different machine learning algorithms such as k-nearest neighbors, random forests, and decision trees [6]. Tehseen et al. (2020) reviewed over 70 manuscripts on the earthquake prediction implemented using the expert systems, fuzzy logic and machine learning [7]. In their study, Li et al. recorded the aftershocks following the Kahramanmaraş earthquake in Turkey. The study demonstrated the reliability of earthquake detection, phase picking, and magnitude estimation using deep learning techniques [8].

In this study, we focus on two large earthquakes and their aftershocks occurred on February 6, 2023, Turkey. These two major earthquakes are the deadliest events in the history of Turkey [9]. The earthquakes damaged many historical buildings such as masonry, mosques, and minarets [10]. The aim of this study is to contribute to the literature from a different statistical perspective using such earthquake data. In the study, 2194 aftershock data that occurred after the February 6th earthquake were evaluated in terms of depth, magnitude, time, and city variables. The three-way cross-classified aftershock data were analyzed according to log-linear models. The most

suitable model was found based on the estimated parameters, and the results were interpreted.

The remaining parts of the presented study are organized as follows. Section 2 deals with the used statistical model and its theoretical properties. Section 3 is devoted to the empirical results of the study. Section 4 contains the concluding remarks.

Methods

Log-Linear Models

The concept of log-linear analysis, applied to contingency tables, can be compared to the use of analysis of variance (ANOVA) for continuously distributed factor-response variables. In ANOVA, the response observations are assumed to be continuous and have underlying normal distributions. However, in log-linear analysis, the response observations are considered as counts with Poisson distributions [11].

In cases where more than two categorical variables are involved, determining the relationship between the variables in contingency tables using chi-square independence tests may become difficult or even impossible. In such cases, logarithmic linear models, which allow for testing a larger number of hypotheses compared to chi-square and do not impose restrictions on the number of rows and columns in both two-dimensional and three-dimensional tables, are preferred. In multidimensional contingency tables, a model is created to investigate the relationships between the variables, and the parameters in the model are estimated and tested for significance. The overall goodness-of-fit of a model is assessed by comparing the expected frequencies to the observed cell frequencies for each model. The Pearson chi-square statistics or the likelihood ratio statistic (G^2) can be used to test a model fit, with (G^2)being more commonly used due to its use in maximum likelihood estimation [12].

Table 1. Hierarchical model representation and equations

Model	Model equation
$0\rightarrow X,Y,Z$	$logE_{ijk} = \lambda + \lambda_i^X + \lambda_j^Y + \lambda_k^Z$
$1\rightarrow X,YZ$	$logE_{ijk} = \lambda + \lambda_i^X + \lambda_j^Y + \lambda_k^Z + \lambda_{jk}^{YZ}$
$2\rightarrow Y,XZ$	$logE_{ijk} = \lambda + \lambda_i^X + \lambda_j^Y + \lambda_k^Z + \lambda_{ik}^{XZ}$
$3\rightarrow Z,XY$	$logE_{ijk} = \lambda + \lambda_i^X + \lambda_j^Y + \lambda_k^Z + \lambda_{ij}^{XY}$
$4\rightarrow XZ,YZ$	$logE_{ijk} = \lambda + \lambda_i^X + \lambda_j^Y + \lambda_k^Z + \lambda_{ik}^{XZ} + \lambda_{jk}^{YZ}$
$5\rightarrow XY,YZ$	$logE_{ijk} = \lambda + \lambda_i^X + \lambda_j^Y + \lambda_k^Z + \lambda_{ij}^{XY} + \lambda_{jk}^{YZ}$
$6\rightarrow XY,XZ$	$logE_{ijk} = \lambda + \lambda_i^X + \lambda_j^Y + \lambda_k^Z + \lambda_{ij}^{XY} + \lambda_{ik}^{XZ}$
$7\rightarrow XY,XZ,YZ$	$logE_{ijk} = \lambda + \lambda_i^X + \lambda_j^Y + \lambda_k^Z + \lambda_{ij}^{XY} + \lambda_{ik}^{XZ} + \lambda_{jk}^{YZ}$
$8\rightarrow XYZ$	$logE_{ijk} = \lambda + \lambda_i^X + \lambda_j^Y + \lambda_k^Z + \lambda_{ij}^{XY} + \lambda_{ik}^{XZ} + \lambda_{jk}^{YZ} + \lambda_{ijk}^{XYZ}$

For three-dimensional contingency tables, nine different logarithmic linear models can be created, which can be grouped into five categories: logarithmic linear models with complete independence, logarithmic linear models with partial independence, logarithmic linear models with conditional independence, logarithmic linear models containing all two-way interactions, and logarithmic linear models containing all interactions. These models are referred to as progressive (hierarchical) models.

X, Y and Z show the variables in a three-dimensional contingency table, R, C, and K represent the level numbers of these variables. The explanations of the terms in the models are given below.

E_{ij} is the expected frequency for cell, (i, j and k), which is calculated over the model. λ reflects the constant term. For the logarithmic linear models in Table 1, the following constraints must be met.

$$\sum_{i=1}^{R} \lambda_i^X = \sum_{j=1}^{C} \lambda_j^Y = \sum_{k=1}^{K} \lambda_k^Z = \sum_{i=1}^{R} \lambda_{ij}^{XY} = \sum_{j=1}^{C} \lambda_{ij}^{XY} = \cdots = \sum_{k=1}^{K} \lambda_{ijk}^{XYZ} = 0$$

$\lambda_{ij}^{XY}, \lambda_{ik}^{XZ}, \lambda_{jk}^{YZ}$ and λ_{ijk}^{XYZ} show two-way and three-way interactions, respectively.

Statistical Analysis

The study included 2191 aftershock data. The data source is https://deprem.afad.gov.tr/last-earthquakes.html . Three-dimensional cross-table was obtained according to the dept (<10=1, ≥ 10=2), citys (Adıyaman=1, Gaziantep=2, Hatay=3, Kahramanmaraş=4, Malatya=5), time(00:00-08:00=1, 08:01-16:00=2, 16:01-23:59=3) and magnitude (3-3,4=1, 3,5-4=2, >4,1). The best model was decided by backward stepwise methods. By making parameter estimates of the best model, the variables that are significant are interpreted (p>0.05).

Results

Comparison of Aftershocks According to City, Magnitude, and Depth

Table 2. Number of aftershocks according to city, magnitude, and depth.

Depth	City	Magnitude		
		3-3.4	3.5-4	>4
<10	Adıyaman	109 (106.382)	65 (72.072)	36 (31.546)
	Gaziantep	70 (66.362)	42 (44.959)	19 (19.679)
	Hatay	94 (93.211)	63 (63.149)	27 (27.640)
	Kahramanmaraş	450 (453.388)	313 (307.166)	132 (134.446)
	Malatya	201 (204.658)	143 (138.654)	60 (60.689)
≥10	Adıyaman	24 (21.851)	20 (19.324)	11 (13.824)
	Gaziantep	4 (5.562)	5 (4.919)	5 (3.519)
	Hatay	22 (18.673)	16 (16.514)	9 (11.814)
	Kahramanmaraş	64 (65.951)	63 (58.324)	39 (41.724)
	Malatya	33 (34.962)	26 (30.919)	29 (22.119)

* The values in the parenthesis are the percentages.

When Table 2 is examined in terms of depth, it can be concluded that aftershocks with less depth are more common. This indicates that aftershocks are more likely to be closer to the surface. In terms of city, aftershocks are

observed in Kahramanmaraş and Adıyaman. When the aftershocks following major earthquakes are examined in terms of intensity, it is seen that the number of earthquakes decreases as the magnitude increases. That is, it is possible to say that the magnitude of aftershocks is less compared to the major earthquake that occurred before. However, the occurrence of aftershocks, especially those above 4, is an indicator of how strong the previous earthquake was.

Determination of the Best Model with Backward Stepwise Method

The log-linear models are applied to data used and the main effects and interaction terms are hierarchically tested to decide which terms will be included in the model. Therefore, in the three-way table, the significance of the main effect terms, two-way interaction and three-way interactions are examined.

Table 3. Degrees of freedom (df), p-value and test statistic values for K-Way and higher-order effects.

	K	df	G^2	p-value	χ^2	p-value
K-way and Higher Order Effects	1	29	2559.086	<0.001	3746.930	<0.001
	2	22	45.991	0.002	47.777	0.001
	3	8	6.377	0.605	6.351	0.608
K-way Effects	1	7	2513.095	<0.001	3699.153	<0.001
	2	14	39.614	<0.001	41.426	<0.001
	3	8	6.377	0.605	6.351	0.608

Hypotheses for K-way and higher effects:

H_{01}: One-way and higher effects are not significant.

$p = 0.000 < 0.05$ H_0 is reject; one-way and higher interactions are important.

H_{02}: Two-way and three-way interactions are not significant.

$p = 0.000 < 0.05$ H_0 is reject; Two-way and three-way interactions are significant.

H_{03}: Three-way interaction is not significant.

$p = 0.605 > 0.05$ H_0 is accept; Three-way interaction is not significant.

H_{04}: One-way effect is not significant.

$p = 0.000 < 0.05$ H_0 is reject; one-effect is important.

H_{05}: Two-way interactions are not significant.

$p = 0.000 < 0.05$ H_0 is reject; Two-way interactions are significant.

H_{06}: Three-way interaction is not significant.

$p = 0.608 > 0.05$ H_0 is accept; Three-way interaction is not significant.

Table 4 was obtained to analyze whether two-way interactions and main effects were significant.

Table 4. The degree of freedom, p value and test statistic values of two-way interaction and main effects terms.

Effect	df	X^2	p-value
city*magnitude	8	2.524	.961
city*depth	4	12.236	.016
magnitude *depth	2	24.763	.000
city	4	1101.330	.000
magnitude	2	361.185	.000
depth	1	1050.580	.000

It can be concluded from Table 4 that city and magnitude interaction is not statistically significant (p>0.05). City and depth interactions with magnitude and depth are statistically significant (p<0.05). In addition, three of the main effects were found significant (p<0.05). The parameter estimates of the main effects are as given in Table 5.

Table 5. Parameter estimates of the main effects.

Effects	Parameter	Estimate	Standard error	Z-value	p-value	95% Confidence Interval	
						Lower bound	Upper bound
depth	1	0.756	0.039	19.332	<0.001	0.679	0.832
city	1	-.160	.073	-2.196	.028	-.304	-.017
	2	-1.035	.113	-9.156	.000	-1.257	-.813
	3	-.319	.078	-4.098	.000	-.472	-.167
	4	1.107	.052	21.348	.000	1.005	1.208
magnit.	1	.358	.053	6.715	.000	.253	.462
	2	.092	.054	1.714	.087	-.013	.198

When we refer to Table 5, it can be observed that the probability of aftershocks occurring in Malatya is 1.17 times higher than in Adıyaman, 2.82 times higher than in Gaziantep, and 1.38 times higher than in Hatay. However, the probability of aftershocks occurring in Kahramanmaraş after this major earthquake is three

times higher than in Malatya. Hence, it can be clearly deduced that Kahramanmaraş, which is the epicenter of the earthquake, has the highest probability of aftershocks. Upon examining the table with respect to earthquake magnitude, it can be stated that the probability of aftershocks in the range of 3 to 3.5 is 1.4 times higher than those with a magnitude of 4 or greater. Additionally, it was found that the probability of aftershocks with a depth of less than 10 kilometers is two times greater. The best model selection with backward stepwise method shown in Table 6.

Table 6. Determination of the best model with backward stepwise method.

Step		Effects	χ^2	df	p-value
0	Generating class	city* magnitude *depth	.000	0	.
	Deleted effect	city* magnitude *depth	6.377	8	.605
1	Generating class	city* magnitude, city*depth, magnitude *depth	6.377	8	.605
	Deleted effect	city* magnitude	2.524	8	.961
		city*depth	12.236	4	.016
		Magnitude *depth	24.763	2	.000
2	Generating class	city* magnitude, magnitude *depth	8.901	16	.917
	Deleted effect	city*depth	12.282	4	.015
		magnitude *depth	24.808	2	.000
3	Generating class	city*depth, magnitude *depth	8.901	16	.917

When interpreting Table 6, the generating class expression tests the compatibility of the model, while the deleted effect expression tests the significance of interactions. The steps continue until all examined interactions are statistically significant. In this case, the city-depth and intensity-depth interactions are statistically significant and are included in the model. So, the best model for these three variables is the model represented by XY, XZ. In this case, the model equation is $logE_{ijk} = \lambda + \lambda_i^X + \lambda_j^Y + \lambda_k^Z + \lambda_{ij}^{XY} + \lambda_{ik}^{XZ}$. Although it is expressed by the variables itself, it is in the form of $logE_{ijk} = constant + depth_i + city_j + magnitude_k + depth_i \times city_j + depth_i \times magnitude_k$. The test statistics value of the best model is given in Table 7 which shows that the model is statistically significant.

Table 7: Test statistics and p-value of XY,XZ model.

	Test statistics	df	p-value
G^2	8.901	16	0.917
χ^2	9.015	16	0.913

The parameter estimates of the best fitting model are given in Table 8.

Table 8. Parameter estimates for XY, YZ model

Parameter	Estimate	Standard error	z-value	p-value	95% Confidence Interval	
					Lower bound	Upper bound
Constant	3.096	.139	22.223	.000	2.823	3.370
[city = 1] * [depth= 1]	-.184	.192	-.961	.337	-.560	.192
[city = 2] * [depth = 1]	.712	.305	2.336	.019	.115	1.309
[city = 3] * [depth= 1]	-.159	.201	-.791	.429	-.554	.235
[city = 4] * [depth = 1]	.161	.145	1.110	.267	-.123	.445
[magnitude = 1] * [depth= 1]	.758	.149	5.076	.000	.465	1.050
[magnitude = 2] * [depth = 1]	.491	.154	3.192	.001	.190	.793

The contribution of interaction terms with p > 0.05 to the model is not statistically significant. Interpreting the interaction parameters according to the results in Table 8, it can be said that the risk of occurrence of aftershocks with a depth of less than 10 km increases by 2.1 times when the magnitude of the aftershock is between 3-3.4, and by 1.6 times when it is between 3.5-4.

Comparison of Aftershocks According to time, Magnitude and Depth

Table 9. Number of aftershocks according to time, magnitude and depth.

Depth	Time	Magnitude		
		3-3.4	3.5-4	>4
<10	00:00-08:00	172 (172.962)	152 (151.447)	69 (68.588)
	08:01-16:00	330 (329.573)	203 (207.023)	91 (87.410)
	16:01-23:59	422 (421.465)	271 (267.529)	115 (119.002)
≥10	00:00-08:00	25 (24.038)	27 (27.553)	20 (20.412)
	08:01-16:00	64 (64.426)	57 (52.977)	33 (36.591)
	16:01-23:59	59 (59.536)	46(49.470)	40(35.997)

* The values in the parenthesis are the percentages.

When Table 9 is examined, it is possible to state that aftershocks occurring closer to the surface tend to occur more frequently between the afternoon and night hours (16:01-23:59). On the other hand, aftershocks at greater depths are more likely to occur between the morning and afternoon, as well as between the afternoon and night hours. Although memorable major earthquakes in Turkey are often recalled having happened after midnight, when analyzing earthquakes of magnitude 5.5 and above occurring since the year 2000, it is observed that 48.6% took place between 08:01 and 16:00, 25.7% between 00:00 and 08:00, and another 25.7% between 16:01 and 23:59 (AFAD). These findings support the provided information. The reason behind nocturnal earthquakes leaving a significant impact in people's memory can be attributed to individuals being at home and potentially asleep, thus being caught off guard by the earthquake without being prepared.

Determination of the Best Model with Backward Stepwise Method

The log-linear models are applied to data used and the main effects and interaction terms are hierarchically tested to decide which terms will be included in the model. Therefore, in the three-way table, the significance of the main effect terms, two-way interaction and three-way interactions are examined.

Table 10. Degrees of freedom (df), p-value and test statistic values for K-Way and higher-order effects.

	K	df	G^2	p-value	χ^2	p-value
K-way and Higher Order Effects	1	17	1629.508	<0.001	1885.754	<0.001
	2	12	43.793	<0.001	44.706	0.001
	3	4	1.823	0.768	1.828	0.767
K-way Effects	1	5	1585.715	<0.001	1841.048	<0.001
	2	8	41.970	<0.001	42.878	<0.001
	3	4	1.823	0.768	1.828	0.767

Hypotheses for K-way and higher effects:

H_{01}: One-way and higher effects are not significant.

$p = 0.000 < 0.05$ H_0 is reject; one-way and higher interactions are important.

H_{02}: Two-way and three-way interactions are not significant.

$p = 0.000 < 0.05$ H_0 is reject; Two-way and three-way interactions are significant.

H_{03}: Three-way interaction is not significant.

$p = 0.768 > 0.05$ H_0 is accept; Three-way interaction is not significant.

H_{04}: One-way effect is not significant.

$p = 0.000 < 0.05$ H_0 is reject; one-effect is important.

H_{05}: Two-way interactions are not significant.

$p = 0.000 < 0.05$ H_0 is reject; Two-way interactions are significant.

H_{06}: Three-way interaction is not significant.

$p = 0.767 > 0.05$ H_0 is accept; Three-way interaction is not significant.

Table 11 was obtained to analyze whether two-way interactions and main effects were significant.

Table 11. The degree of freedom, p value and test statistic values of two-way interaction and main effects terms.

Effect	df	χ^2	p-value
time*depth	2	7.854	.020
time* magnitude	4	10.677	.030
depth * magnitude	2	24.934	.000
time	3	175.719	.000
depth	1	1049.425	.000
magnitude	2	360.571	.000

The result indicates that all pairwise interactions are statistically significant starting from Table 11 (p<0.05). The parameter estimates of the main effects are as given in Table 12.

Table 12. Parameter estimates of the main effects.

Effects	Parameter	Estimate	Standard error	Z-value	p-value	95% Confidence Interval	
						Lower bound	Upper bound
depth	1	0.751	0.031	2.,267	<0.001	0.690	0.812
	1	-.411	.049	-8.573	.000	-.507	-.316
time	2	.150	.041	3.633	.000	.069	.232
magnitude	1	.338	.042	8.141	.000	.257	.419
	2	.115	.042	2.722	.006	.032	.198

When Table 12 is examined in terms of time, it can be observed that the probability of aftershocks occurring between the afternoon and midnight following a major earthquake is 1.5 times higher than the probability of occurrence during the hours from midnight until morning. Additionally, the probability of aftershocks occurring between the morning and afternoon is 1.2 times higher

than the probability of occurrence between the afternoon and midnight. Upon examining the table with respect to earthquake magnitude, it can be stated that the probability of aftershocks in the range of 3 to 3.5 is 1.4 times higher than those with a magnitude of 4 or greater. Additionally, it was found that the probability of aftershocks with a depth of less than 10 kilometers is two times greater. The best model selection with backward stepwise method shown in Table 13.

Table 13. Determination of the best model with backward stepwise method.

Step		Effects	χ^2	df	p-value
0	Generating class	time*depth * magnitude	.000	0	.
	Deleted effect	time*depth * magnitude	1.823	4	.768
1	Generating class	time* depth, time* magnitude, depth * magnitude	1.823	4	.768
	Deleted effect	time* depth	7.854	2	.020
		time* magnitude	10.677	4	.030
		depth * magnitude	24.934	2	.000
2	Generating class	time*depth, time * magnitude, depth* magnitude	1.823	4	.768

When interpreting Table 13, the generating class expression tests the compatibility of the model, while the deleted effect expression tests the significance of interactions. The steps continue until all examined interactions are statistically significant. In this case, the time-depth, time-magnitude, and depth-magnitude interactions are statistically significant and are included in the model. So, the best model for these three variables is the model represented by XY, XZ, YZ. In this case, the model equation is $logE_{ijk} = \lambda + \lambda_i^X + \lambda_j^Y + \lambda_k^Z + \lambda_{ij}^{XY} + \lambda_{ik}^{XZ} + \lambda_{jk}^{YZ}$. Although it is expressed by the variables itself, it is in the form of $logE_{ijk} = constant + time_i + depth_j + magnitude_k + time_i \times depth_j + time_i \times magnitude_k + depth_j \times magnitude_k$. The test statistics value of the best model is given in Table 14 which shows that the model is statistically significant.

Table 14: Test statistics and p-value of XY, XZ, YZ model.

	Test statistics	df	p-value
G^2	1.823	4	0.768
χ^2	1.828	4	0.767

The parameter estimates of the best fitting model are given in Table 15.

Table 15. Parameter estimates for XY, XZ, YZ model.

Parameter	Estimate	Standard error	z-value	p-value	95% Confidence Interval	
					Lower bound	Upper bound
Constant	3.583	.134	26.781	.000	3.321	3.846
[time = 1] * [depth= 1]	.016	.158	.103	.918	-.293	.326
[time = 2] * [depth = 1]	-.325	.128	-2.535	.011	-.576	-.074
[time = 1] * [magnitude = 1]	-.340	.159	-2.142	.032	-.650	-.029
[time = 1] * [magnitude = 2]	-.018	.163	-.110	.912	-.337	.302
[time = 2] * [magnitude = 1]	.063	.139	.449	.653	-.211	.336
[time = 2] * [magnitude = 2]	.052	.147	.354	.723	-.237	.341
[depth= 1] * [magnitude = 1]	.761	.150	5.087	.000	.468	1.055
[depth= 1] * [magnitude = 2]	.492	.154	3.191	.001	.190	.794

The contribution of interaction terms with p > 0.05 to the model is not statistically significant. Interpreting the interaction parameters according to the results in Table 15, it can be said that the risk of occurrence of aftershocks with a depth of less than 10 km increases by 2.1 times when the magnitude of the aftershock is between 3-3.4, and by 1.6 times when it is between 3.5-4. Furthermore, the risk of aftershocks occurring between 08:01 and 16:00 increases by 1.38 times when the depth is greater than 10 km, and the risk of aftershocks occurring between 16:01 and 23:59 increases by 1.4 times when the magnitude is between 3-3.4.

Conclusion

In this study, aftershocks that occurred following two major earthquakes on February 6th in Turkey, along with their adverse consequences, were grouped based on the cities where the earthquakes occurred, the intensity of the earthquakes, their depth, and the hours of their occurrence. After this grouping, an analysis was conducted using log-linear models to examine the effects of these variables and the relationships between them. The analysis revealed a higher probability of aftershock occurrence in the epicentral and nearby provinces where the major earthquake occurred. It was observed that a significant portion of the aftershocks had a depth of less than 10 kilometers, indicating their proximity to the surface. Contrary to expectations, it was stated that aftershocks were more likely to occur during the early daylight hours until midnight. The perception that major earthquakes occur at night is likely due to the higher

number of casualties in earthquakes that occur after midnight. The application of the analysis resulted in the determination that most of the aftershocks had an intensity greater than 3 but less than 4. This study demonstrates that the tabulation of qualitative or quantitative variables related to earthquakes and their aftershocks provides us with more detailed and interpretable information.

Conflicts of interest

There are no conflicts of interest in this work.

References

[1] Pisarenko V. F., Sornette A., Sornette D., Rodkin, M. V., Characterization of the tail of the distribution of earthquake magnitudes by combining the GEV and GPD descriptions of extreme value theory, *Pure and Applied Geophysics*, 171 (2014) 1599-1624.

[2] Ma N., Bai Y., Meng S., Return period evaluation of the largest possible earthquake magnitudes in mainland China based on extreme value theory, *Sensors*, 21(10) (2021) 3519.

[3] Beyreuther M., Wassermann J., Continuous earthquake detection and classification using discrete Hidden Markov Models, Geophysical Journal International, 175(3) (2008) 1055-1066.

[4] Yip C. F., Ng W. L., Yau, C. Y., A hidden Markov model for earthquake prediction, *Stochastic Environmental Research and Risk Assessment*, 32 (2018) 1415-1434.

[5] Li Z., Meier M. A., Hauksson E., Zhan Z., Andrews J., Machine learning seismic wave discrimination: Application to earthquake early warning, *Geophysical Research Letters*, 45(10) (2018) 4773-4779.

[6] Mangalathu S., Sun H., Nweke C. C., Yi Z., Burton H. V., Classifying earthquake damage to buildings using machine learning, *Earthquake Spectra*, 36(1) (2020) 183-208.

[7] Tehseen R., Farooq M. S., Abid, A., Earthquake prediction using expert systems: a systematic mapping study, *Sustainability*, 12(6) (2020) 2420.

[8] Li W., Chakraborty M., Köhler J., Quinteros-Cartaya C., Rümpker G., Srivastava N., Earthquake monitoring using deep learning with a case study of the Kahramanmaras Turkey earthquake aftershock sequence, *Solid Earth*, 15(2) (2024) 197-213.

[9] Hussain E., Kalaycıoğlu S., Milline, C. W., Çakir Z., Preconditioning the 2023 Kahramanmaraş (Türkiye) earthquake disaster, *Nature Reviews Earth & Environment*, (2023) 1-3.

[10] Kocaman İ., The effect of the Kahramanmaraş earthquakes (Mw 7.7 and Mw 7.6) on historical masonry mosques and minarets, *Engineering Failure Analysis*, 149 (2023) 107225.

[11] Lawal B., Lawal H. B., Categorical data analysis with SAS and SPSS applications, Psychology Press, (2003).

[12] Agresti A., Categorical data analysis (Vol. 482). John Wiley & Sons, (2003).

Cumhuriyet Sci. J., 45(2) (2024) 444-448
DOI: https://doi.org/10.17776/csj.1326496

Cumhuriyet Science Journal

| csj.cumhuriyet.edu.tr | Founded: 2002 ISSN: 2587-2680 e-ISSN: 2587-246X Publisher: Sivas Cumhuriyet University

Retrospective Examination of Risk Factors Affecting Iron Deficiency Anemia Using Machine Learning Methods

Erol Terzi [1,a,*], Bünyamin Sarıbacak [2,b], Mehmet Şirin Ateş [1,c]

[1] *Department of Statistics, Faculty of Science, Ondokuz Mayıs University, Samsun, Türkiye.*
[2] *Department of Computer Science, Education Faculty, Ondokuz Mayıs University, Samsun, Türkiye.*
**Corresponding author*

Research Article

History
Received: 13/07/2023
Accepted: 22/06/2024

ABSTRACT

Iron deficiency anemia is one of the most common types of anemia worldwide. In recent years, new developments in the field of medicine have offered early diagnosis and treatment opportunities for anemia patients. In the field of data science, in parallel with the developments in medicine, significant developments are taking place in subjects such as data collection, storage, processing, and reporting. Interdisciplinary joint studies positively contribute to patients' quality of life and lifespan. In this study, the accuracy of the statistical results was tested with Machine Learning Method (MLM) while investigating the factors that affect the correct prediction of Iron Deficiency Anemia (IDA) diagnosis. In the first stage, the relationships between all variables in the data set and their effects on the differentiation of disease groups were investigated using univariate and multivariate statistical methods. In the second step, the data set was analyzed in detail using four different methods with Artificial Neural Network (ANN) classifier. Weka 3.8 application was preferred for these operations. In the last stage, the results obtained in both stages were compared. Accordingly, it has been observed that hemoglobin (Hb), mean cell volume (MCV), iron (Fe), and ferritin (FERR) have more effects on IDA. ANN (98.06%) is a better discriminator with a correct classification rate.

Keywords: Iron deficiency anemia, Logistic regression analysis, Artificial neural network, Machine learning.

[a] *eroltrz@omu.edu.tr* *https://orcid.org/0000-0002-2309-827X*
[b] *bunyamin@omu.edu.tr* *https://orcid.org/0000-0003-2775-776X*
[c] *mehmet.ates@omu.edu.tr* *https://orcid.org/0000-0001-9904-6380*

Introduction

Iron deficiency is an essential determinant of anemia and is among the most common types worldwide, according to the World Health Organization (WHO) [1]. Any form of malnutrition has been shown as the main cause of anemia. Despite all efforts to combat malnutrition worldwide, progress has been limited. 614 million women and 280 million children worldwide are struggling with this disease. In particular, it affects 40% of pregnant women, 33% of non-pregnant women, and 42% of children worldwide [1]. In addition to significant and irreversible effects on brain development in children under two, iron deficiency negatively affects learning and school performance in later life [2,3]. Iron deficiency in adults has negative effects such as fatigue, physical performance impairment, and decreased work efficiency and social activities [4,5].

The global prevalence of anemia for the general population is 24.8%, and it is estimated that 1 billion 620 million people are affected by anemia [1]. Despite the positive developments in healthcare services worldwide, the number of people affected by anemia has increased, primarily due to population growth. This result may be due to the ineffective evaluation of the blood analysis given by the clinician whose primary interest is outside this field or the ineffective treatment of anemia.

This study aims to estimate the risk factors affecting Iron Deficiency Anemia (IDA) with acceptable sensitivity. Today, technological developments in the field of computers and especially artificial intelligence are used extensively to solve problems in the field of health [6,7]. Machine learning, a sub-branch of artificial intelligence, consists of systematic techniques developed to make accurate predictions using previous observations [8]. This study establishes a harmonious relationship among statistics, databases and machine learning disciplines. In the first step, univariate statistic analyses were carried out to investigate the effects of selected parameters on individual disease groups. In the second step, logistic regression multivariate statistical analysis was performed in which all parameters found to be significant were added to the model to predict the probability of an outcome with only two values. In the last step, the data were analyzed using the Artificial Neural Network (ANN) machine learning classifier, which includes mathematical methods for analyzing nonlinear functions [9]. It has been investigated which model is more successful in diagnosing the consequences of risk factors affecting IDA.

The paper proceeds as follows. Section 2 describes the Logistic Regression (LR) and ANN models. The third section presents result from the models estimation. A more detailed evaluation of the results is made in the last

section. It is anticipated that the results obtained will be a reference for future scientific studies in this field.

Materials and Method

Collecting Data

Between October 2017 and March 2020, 516 patients diagnosed with malaise and fatigue (ICD-10 code: R53) who applied to the Samsun Training and Research Hospital Hematology Outpatient Clinic were analyzed retrospectively. IDA was diagnosed in 359 patients according to laboratory results. Although the remaining 157 cases were evaluated with the same diagnosis, laboratory values did not give same result as IDA.

Age, gender, complete blood count (CBC) values, Hb, hematocrit (Hct), mean cell volume (MCV), mean cell Hb concentration (MCHC), red cell distribution width (RDW), red blood cell (RBC) and IDA parameters (ferritin, serum iron, serum iron binding capacity, transferrin saturation) of these 516 cases were recorded. The abbreviations above are shown in Table 1.

Table 1. List of laboratory test abbreviations used in this study

Laboratory Test	Abbreviations
Hemoglobin	Hb
Hematocrit	Hct
Mean Cell Volume	MCV
Mean Corpuscular Hemoglobin Concentration	MCHC
Red Blood Cell Count	RBC
Red Blood Cell Distribution Width	RDW
Iron	Fe
Unsaturated Iron Binding Capacity	UIBC
Ferritin	FERR
Disease Diagnosis	DD

Statistical analysis and machine learning techniques were applied to the patients' data to verify these analyses. The conceptual model of the study is shown in Figure 1.

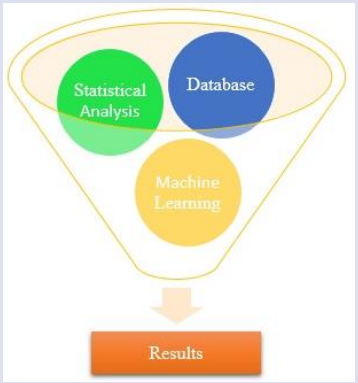

Figure 1. Conceptual model of the study

Statistical Analysis

In the statistical analysis of this study, SPSS 21.0 software was preferred. In all statistical analyzes, the level of significance was accepted as $\alpha = 0.05$. Frequency tables and descriptive statistics were used in the interpretation of the findings. When the data were normally distributed was used "Independent Sample t test" which is one of the parametric tests and when the data were not normally distributed was used "Mann Whitney U test" which is one of the non-parametric tests. In addition, "Binary Logistic Regression (LR)" model was used to classification the factors affecting the disease risk Logistic regression predicts the probability of an outcome that can only have two values [10].

$$Odds = \frac{p}{1-p} \quad (1)$$

The Odds ratio is the ratio of the Odds coefficients of two cases investigated. This ratio is used to explain the effect of the dependent variable on independent variables [11,12]. The basic concept in this model is Logit, and this is shown as

$$\text{Logit}(p) = \ln\left(\frac{p}{1-p}\right) \quad (2)$$

$\text{Logit}(p)$ takes negative values when the probability takes values below 0.5, and $\text{Logit}(p)$ takes positive values when the probability takes values above 0.5. The higher the probability value, the higher the $\text{Logit}(p)$ value [6]. Odds ratio has been widely used in recent years due to its ability to give outstanding estimates with the help of confidence intervals for relationships between binary variables, to investigate the effects of independent variables in studies using logistic regression, and to achieve successful results in case-control studies [13].

Artificial Neural Network (ANN)

ANN is an information-processing technique inspired by the way the human brain works. ANN is widely used today in many applications in various branches of engineering, medicine, and science [14]. ANN consists of connecting artificial neurons called nodes. These connections are assigned a value according to their strength, and the higher the value, the stronger the connection. ANN consists of input, hidden, and exit nodes (Figure 2). ANN networks have forward and feedback features. In the feed-forward, signals in ANN move only in one direction, and the values calculated from the input data are the input values of the next layer. This process continues in all layers until output. They can move in both directions by using loop structures in feedback ANN. They try to create the most appropriate connection by controlling all possible connections between neurons. Using a backpropagation learning algorithm, this study used the hematological dataset to train a Multilayer Perceptron (MLP).

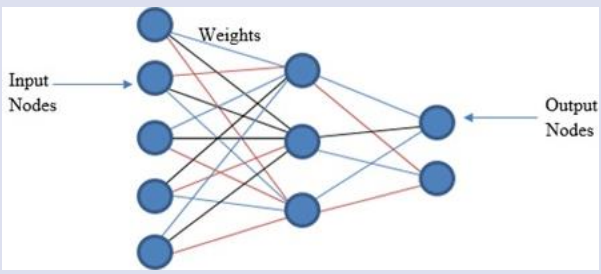

Figure 2. Artificial neural network [17]

Results

In this study, in which risk factors affecting iron deficiency anemia were examined, information on 516 patients subject to the search is given in Table 2. Beforehand, the normality assumption of the data was analyzed using the Kolmogorov Smirnov test. Data are normally distributed. (n>30)

Table 2. Comparison of some parameters according to the groups

Variable (N=516)	Healthy (n=157)		Patient (n=359)		Statistical Analysis* Probability
	$\bar{X} \pm SD$	Median [Min-Max]	$\bar{X} \pm SD$	Median [Min-Max]	
Age (year)	54,37±14,40	54,0 [21,0-89,0]	43,29±14,11	41,0 [17,0-87,0]	Z=-7,969 p=0,000
Hb	13,38±1,28	13,2 [11,0-17,0]	10,32±1,79	10,3 [6,2-15,8]	t=21,906 p=0,000
Hct	38,84±3,62	38,5 [32,0-48,8]	31,20±4,76	31,1 [18,3-48,2]	t=19,955 p=0,000
MCV	84,90±6,38	85,2 [34,9-99,7]	71,76±9,34	71,9 [51,9-111,6]	Z=-14,272 p=0,000
MCH	29,45±2,27	29,4 [21,5-38,3]	23,75±3,86	23,9 [14,6-40,1]	Z=-14,500 p=0,000
MCHC	34,32±1,07	34,3 [25,1-36,2]	32,99±1,34	33,1 [28,2-36,2]	Z=-11,158 p=0,000
RBC	4,50±0,53	4,5 [3,1-5,9]	4,37±0,58	4,4 [2,0-6,6]	Z=-2,650 p=0,008
RDW	15,21±3,48	14,1 [12,0-31,5]	18,39±4,43	17,3 [12,1-46,9]	Z=-11,167 p=0,000
FE	86,49±26,81	80,0 [40,0-217,0]	32,36±38,64	23,0 [10,0-464,0]	Z=-16,174 p=0,000
UIBC	252,68±50,93	251,0 [135,0-404,0]	390,35±96,81	405,0 [68,0-717,0]	Z=-13,987 p=0,000
Saturation (%)	0,36±0,16	0,3 [0,1-0,9]	0,12±0,31	0,1 [0,0-4,6]	Z=-16,150 p=0,0000
FERR	108,68±79,95	83,0 [28,0-640,0]	52,59±170,94	7,0 [10,0-1650,0]	Z=-14,382 p=0,000

* "Independent Sample-t" test (t-table value) in comparison with the measurement values of two independent groups with normal distribution; "Mann-Whitney U" test (Z-table value) statistics were used in comparing the measurement values of two independent groups with no normal distribution

Table 3. Analysis of the relationships between groups and gender

Variable (N=516)	Healthy (n=157)		Patient (n=359)		Statistical Analysis* Probability
Gender	n	%	n	%	
Female	107	68,2	332	92,5	χ^2=49,016
Male	50	31,8	27	7,5	p=0,000

* The χ^2-cross table investigated the relationships between two qualitative variables.

A statistically significant relationship was found between the groups and gender (χ2=49.016; p=0.000). It was determined that 50 people (31.8%) in the healthy group were men, and 332 (92.5%) in the patient group were women.

The created model has a 93.8% correct classification rate (CCR). As a result of Logistic regression (Backward: LR method) performed to determine the disease risk status by including all parameters that were significant in the univariate analysis according to the groups (Table 2), the optimal model consists of the age (year), Hb, MCV, erythrocyte RBC, RDW, Fe, UIBC and saturation (%) parameters. Age, Hb, MCV, Erythrocyte RBC, RDW, Fe, and UIBC values were significant in the model ($p < 0.05$). Some analysis results of the ANN classifier selected to compare the results of univariate and multivariate statistical analyzes are given in Table 5.

Table 4. Examination of the factors affecting the disease status with the LR model.

Variable	β	Standard Error	Wald	df	p	OR	95% Confidence Interval (CI)	
							Lower	Upper
Age (year)	-0,057	0,015	14,670	1	0,000	0,944	0,917	0,972
Hb	-2,710	0,587	21,305	1	0,000	0,067	0,021	0,210
MCV	0,218	0,099	4,832	1	0,028	1,243	1,024	1,509
RBC	4,614	1,522	9,196	1	0,002	1,091	1,011	1,991
RDW	0,123	0,059	4,360	1	0,037	1,131	1,008	1,269
Fe	-0,044	0,016	7,129	1	0,008	0,957	0,927	0,988
UIBC	0,022	0,005	20,919	1	0,000	1,022	1,013	1,032
Saturation (%)	5,726	3,217	3,167	1	0,075	3,068	0,560	16,808
Constant	-8,316	8,537	0,949	1	0,330	0,000		

*Hosmer & Lemeshow test χ^2=2.236; p=0.973; CCR=93.8%

Table 5. Comparative analysis of ANN classifier

Classification output	Model 1	Model 2	Model 3	Model 4
Correctly Classified Instances	93.15%	96.9%	93.03%	98.06%
In Correctly Classified Instances	6.85%	3.1%	6.97%	1.94%
Kappa statistic	0.83	0.928	0.8358	0.955
Mean absolute error (MAE)	0.0802	0.048	0.0808	0.0405
Root mean squared error(RMSE)	0.2466	0.1633	0.2363	0.1451
Relative absolute error (RAE)	19.14%	11.34%	19.07%	9.57%
Root relative squared error	54.98%	35.5%	51.37%	31.54%
AUC	0.94	0.97	0.93	0.98

In Model-1, before the classification process, the data set is divided into 66% training set and 34% test set. In Model-2, the entire data set was used as a training set. In Model 3, the dimension was reduced with Principal Component Analysis (PCA) to highlight the strengths of the data before classification, and then the data set was divided into ten parts by cross-validation method, and nine pieces of the training set were used as one piece of the test set. Average accuracy was obtained as a result of 10 training and testing processes. In Model 4, first, a feature subset (Hb, MCV, Fe, and FERR) was determined by considering the individual prediction ability of each feature and the degree of excess between them. Afterward, a new classification was made in which only the specified features were included in the model, and the entire data set was used as a training set [15]. At the end of this process, the highest correct classification rate was obtained at 98.06%. The evaluation module also provides the correct classification rates as well as Kappa statistics, MAE, RMSE, and relative error (RAE) based on prior probabilities, and it also gives the statistics of the root mean square (RMSE) of the mean square (quadratic) loss [16].

While determining the disease groups in Tables 6 and 7, the ANN classifier uses the Sigmoid function as the transfer function. Nodes consist of the sum of the weights of their inputs. This function was preferred because the value ranges of logistic regression and sigmoid function are [0-1].

Table 6. Power of features to determine disease groups according to ANN

Inputs	Weights					
Attributes	Node 2	Node 3	Node 4	Node 5	Node 6	Node 7
Threshold	-3,0879	-1,3453	-0,2288	-4,3075	0,3793	-8,4297
age	-3,3420	-4,5974	0,1956	-5,2892	2,3902	-0,0890
Hb	-6,1126	-5,2270	0,1856	-2,4230	-10,5547	-3,1134
Hct	-1,1477	-1,5082	0,1452	-0,4477	-8,5774	-0,3969
MCV	2,2419	1,6541	-0,6381	4,5104	-0,4725	6,7628
MCH	-3,5715	-3,1097	-0,2216	-2,3489	-3,7943	-2,9190
MCHC	2,6999	1,0754	0,2470	4,1382	-0,5154	8,2017
RBC	3,8531	2,7593	-0,1178	2,1436	0,2101	3,4655
RDW	1,9810	1,9663	0,5450	1,4202	0,5456	-2,1367
FE	6,7096	5,7775	-0,1225	-4,8643	-0,4588	-23,4869
UIBC	6,0031	3,1920	0,6698	-4,4654	-2,7588	3,1527
FERR	-12,9757	-6,8534	0,1784	-6,1465	5,1607	5,7663

Considering the individual prediction ability of each feature and the degree of excess between them, it is seen that the power of Hb, MCV, Fe, and FERR to determine disease groups is higher.

Table 7. The effects of nodes on disease groups according to ANN

Inputs	Node 0 - Class DD(Yes)	Node 1 - Class DD (No)
	Weights	
Threshold	-7,1850	7,1827
Node 2	6,7132	-6,7180
Node 3	4,6409	-4,6325
Node 4	-0,7723	0,7866
Node 5	4,7579	-4,7584
Node 6	8,3808	-8,3813
Node 7	11,3668	-11,3680

It can be observed that Nodes 2, 6, and 7 have a higher influence on the formation of disease classes.

Conclusion

In this study, the power of age, gender, and results obtained from complete blood count (CBC) analysis in evaluating the diagnosis of IDA of individuals who applied to the hematology service was investigated. RBC indexes consisting of RBC, Hb, Hct, MCV, MCH, MCHC, Fe, UIBC, FERR, and RDW are produced from CBC analysis using automatic devices. According to the first information we obtained from the CBC results, it was found that the age (years), Hb, Hct, MCV, MCH, MCHC, Erythrocyte RBC, Fe, saturation (%), and FERR values of the patients diagnosed with IDA were lower than the healthy group. Likewise, the RDW and UIBC values of the patient group were statistically significantly higher than the healthy group, which is expected (Table 2). It was determined that the women subject to the study were predominantly ill, while the men were predominantly healthy (Table 3). According to the results of Logistic regression performed by including all parameters that were significant according to the groups as a result of univariate analyses (Table 2) to determine the disease risk status, when age (year) increases by 1 unit, the risk of becoming sick 5.6% will decrease by 5.6. When the Hb and MCV value increase by 1 unit, the risk of getting sick will reduce by 93.3% and 24.3%, respectively. When the erythrocyte RBC value increases by 0.01 units, the risk of becoming sick will increase by 9.1%. When the RDW, Iron, and UIBC values increase by 1 unit, the risk of getting sick will increase by 13.1%, 4.4%, and 2.2%, respectively (Table 4).
The results of both univariate (Table 2) and multivariate (Table 4) analyses showed that only one parameter was insufficient to distinguish between two conditions; on the contrary, all parameters effectively separated the two groups. Hb, MCV, RBC, RDW, and Fe were found to be stronger separators in multiple comparison tests (Table 4).

The accuracy of these results was tested by classifying it with machine learning ANN using four methods (Table 5). As a result, it was observed that the correct classification rates of the new subsets, which were compressed and formed by reducing the number of features, changed positively. Although there is a low correlation between the elements of these clusters, it has been observed that there is a high degree of correlation in the classification. As a result of these analyses, the best correct classification rates of LR (93.8%) and ANN (98.06%) were determined, and it was seen that the ANN classifier was a better discriminator in determining the disease groups. The results highly confirm our predictions. It is hoped that advances in data science will significantly contribute to eliminating the difficulty of separating the factors affecting IDA. It is thought that new machine learning techniques to be applied to data sets containing large-scale current IDA disease data free of regional differences will better determine the risk factors affecting anemia.

For this, researchers (medical doctors, data scientists, etc.) who conduct interdisciplinary collaborations will have detailed knowledge about diseases during the data collection, contributing significantly to the data analysis stages. Reducing the number of variables defined initially will greatly facilitate physicians' decision-making processes. In addition, converting the results obtained through many stages into easy-to-use digital applications will significantly reduce the loss of time and effort.

Conflict of Interest

There are no conflicts of interest in this work.

References

[1] World Health Organization. *Anemia*, (2017), https://www.who.int/health-topics/anaemia#tab=tab_1, Accessed 18 Nov 2022.

[2] Allali S., Brousse V., Sacri A. S., Chalumeau M., De Montalembert M., Anemia in Children: Prevalence, Causes, Diagnostic Work-up, and Long-Term Consequences, *Expert Review of Hematology*, 10(11) (2017) 1023-1028.

[3] Cusick S. E., Georgieff M. K., Rao R., *Approaches for Reducing the Risk of Early-Life Iron Deficiency-Induced Brain Dysfunction in Children*, Nutrients 10 (2) (2018) 227.

[4] Andro M., Le Squere P., Estivin S., Gentric A., Anaemia and Cognitive Performances in The Elderly: A Systematic Review, *European Journal of Neurology,* 20(9) (2013) 1234-1240.

[5] Haas J.D., Brownlie T., 4th. Iron Deficiency and Reduced Work Capacity: A Critical Review of the Research to Determine a Causal Relationship, *Journal of Nutrition*, 131 (2S-2) (2001) 676-690.

[6] Hosmer D.W., Lemeshow S., Applied Logistic Regression, John Wiley & Sons, 8-36, New York, 1989.

[7] Khan J. R., Chowdhury S., Islam H., Raheem E., Machine Learning Algorithms to Predict the Childhood Anemia in Bangladesh, *Journal of Data Science,* 17 (1) (2019) 195-218.

[8] Schapire R. E., The Boosting Approach to Machine Learning: An Overview, In Nonlinear Estimation and Classification,149-171, Springer, New York, 2003.

[9] Kumar, N., Narayan Das, N., Gupta, D., Gupta, K., & Bindra, J. (2021). Efficient automated disease diagnosis using machine learning models, *Journal of Healthcare Engineering*, 1 (2021) 9983652.

[10] Alpar R., Applied Multivariate Statistical Methods (Fourth Edition), Detail Publishing, 637-659, Ankara, 2013.

[11] Beam, A. L., Manrai, A. K., & Ghassemi, M. (2020). Challenges to the reproducibility of machine learning models in health care, *Jama*, 323 (4) 305-306.

[12] Mertler C. A., Vannatta R. A., Advanced and Multivariate Statistical Methods: Practical Application and Interpretation, Pyrczak Publishing, Glendale, 2005.

[13] Bland J. M., Altman D.G., The Odds Ratio, *BMJ*, 320 (7247) (2000) 1468.

[14] Haykin S. S., Neural Networks and Learning Machines, Simon Haykin, 2009.

[15] Hall M. A., Correlation-Based Feature Subset Selection for Machine Learning. Hamilton, New Zealand, 1998.

[16] Witten I. H., Frank E., Data Mining: Practical Machine Learning Tools and Techniques with Java Implementations, *Acm Sigmod Record*, 31(1) (2002) 76-77.

[17] http://saedsayad.com/artificial_neural_network.htm, Accessed 13 June 2024